

Dissertation
submitted to the
Combined Faculties for the Natural Sciences and for
Mathematics of the
Ruperto-Carola University of Heidelberg, Germany
for the degree of
Doctor of Natural Sciences

Submitted by
Dipl.-Phys. Michael Deininger
born in Landsberg am Lech
Oral examination: 18. 12. 2013

The European Holocene Climate from the Speleothem's View

**Investigating spatio-temporal coherent changes in
European speleothem proxy time series**

**Reviewer: Prof. Dr. Augusto Mangini
Prof. Dr. Werner Aeschbach-Hertig**

Contents

Abstract	VII
I Introduction	1
1 Speleothems and climate change	3
1.1 Speleothems	3
1.2 Speleothems as climate (change) recorder	6
2 Motivation	9
II Speleothems	11
3 The formation of speleothems	13
3.1 The carbonate system - The chemical properties of the $\text{CO}_2\text{-H}_2\text{O-CaCO}_3$ system	14
3.1.1 The chemical properties of the $\text{CO}_2\text{-H}_2\text{O-CaCO}_3$ system for chemical equilibrium	15
3.1.2 The chemical properties of the $\text{CO}_2\text{-H}_2\text{O-CaCO}_3$ system for chemical non-equilibrium conditions	17
3.1.3 The chemical properties of the $\text{CO}_2\text{-H}_2\text{O-CaCO}_3$ system for thin films	22
3.2 Speleothem growth	23
4 Dating of speleothems	27
4.1 Dating of speleothems by uranium-series disequilibrium - The $^{230}\text{Th-}^{234}\text{U-}^{238}\text{U}$ decay-series: General principles	28
4.2 Dating of speleothems by uranium-series disequilibrium - The $^{230}\text{Th-}^{238}\text{U}$ decay-series: Correction for initial conditions	30
5 Isotope fractionation - Part I	33
5.1 Different states of isotope fractionation	33
5.2 Nomenclature of isotope fractionation	34
5.3 Stable isotopes in speleothem science	35
5.3.1 Isotope fractionation effects of the $\text{CO}_2\text{-H}_2\text{O-CaCO}_3$ system	36
5.3.2 The big debate - Part I	38

6	O and C Isotopes in Speleothems: Concepts	39
6.1	The Rayleigh approach	40
6.2	Limitations of the Rayleigh approach	42
7	O and C Isotopes in Speleothems: Processes	43
7.1	The change of carbon isotope composition of HCO_3^- during the precipitation of calcite	44
7.2	The change of oxygen isotope composition of HCO_3^- during the precipitation of calcite	46
7.3	Multi-box model for the solution layer	49
7.4	Sensitivity of the calcite $\delta^{18}\text{O}$ and $\delta^{13}\text{C}$ values on cave parameters	51
8	Processes above the cave	57
8.1	The source of the water (isotopes) entering a cave	57
8.2	The sources carbon isotopes in the subsurface	60
8.3	Prior calcite precipitation (PCP) - Precipitation of calcite before the formation of a speleothem	62
9	Isotope fractionation - Part II	65
9.1	The big debate - Part II	66
9.2	Prior carbonate precipitation and the effect on isotope fraction factors	67
9.3	The big debate - Part III and concluding remarks	69
III	Methods	71
10	Principal component analysis in speleothem science	73
10.1	Introduction to principal component analysis	74
10.1.1	Problem definition and first steps	74
10.1.2	The calculation of Principal Component(s) Analysis	75
10.1.3	Principal component analysis	76
10.2	PCA in speleothem science	79
10.2.1	Age uncertainty of ages and consequences for the age model	81
10.2.2	Temporal resolution of proxy time series	82
10.2.3	Selection criteria for speleothem proxy time series	85
10.3	How the PCA is performed	85
10.3.1	Procedure of age-depth relation modeling	85
10.3.2	Temporal resolution model	88
10.3.3	Performance of PCA	92
10.3.4	Monte Carlo Approach	93
10.4	Results of PCA with artificial proxy time series	94
10.4.1	The sensitivity of PCA on the age error	96
10.4.2	The sensitivity of PCA on "Gaussian White Noise" time series	98

10.5	Time window length and significance of PCA	104
10.6	Application of PCA on speleothem proxy time series - Spatio-temporal coherence of speleothem proxy time series	110
10.6.1	The behaviour of the distribution of r_s values for proxy time series and the Fork-tool	110
10.6.2	Results of the eigenvalues and test of Preisendorfer's Rule N	116
10.7	Selection rules for PCA	121
 IV Results and Discussion		123
 11 Stable isotopes in Precipitation		124
11.1	Description of the "Stable Isotopes in Precipitation" model	126
11.1.1	Overview of the different components - The physical bases of the SIP model	127
11.1.2	Transect multi-box approach and calibration of model parameters . .	128
11.1.3	Evaporation of water from the oceans	128
11.1.4	Moisture transport in the atmosphere and precipitation	130
11.1.5	Evaporation of water from the continental surfaces	132
11.1.6	Recording of the stable isotope signal by speleothems	132
11.2	Comparison of model results with GNIP values for selected transects in Europe	133
11.2.1	Central European transect - T1	133
11.2.2	Northern European transect - T2	138
11.3	Sensitivity of the model on model parameters for Central Europe (T1) . . .	140
11.4	Comparison of model results with GNIP values for positive and negative NAO phases	145
 12 The Global Speleothem Network		151
12.1	European speleothems within the GSN and pre-selected speleothems for PCA	152
12.1.1	Temporal resolution of speleothem proxy time series	153
12.1.2	Recording period of speleothem proxy time series	156
12.2	Selection of European speleothems for PCA	156
 13 Investigating spatio-temporal coherent changes for the last 8,000 years - PART I: Long-term analysis		159
 14 Investigating spatio-temporal coherent changes for the last 4,000 years		167
14.1	Long-term spatio-temporal coherent changes for the last 4,000 years	167
14.2	Short-term spatio-temporal coherent changes for the last 4,000 years	173
14.2.1	Results for $\delta^{18}\text{O}$ time series	173
14.2.2	Results for $\delta^{13}\text{C}$ time series	176
 15 Investigating spatio-temporal coherent changes for the last 8,000 years -		

PART II: Short-term analysis	187
16 Investigating spatio-temporal coherent changes for the last 10,000 years	197
17 The European Holocene Climate from the speleothems view	205
17.1 Snapshots from the Holocene climate taken by speleothems	205
17.1.1 Investigating the temporal evolution of the $\delta^{18}\text{O}$ gradients by use of the SIP model	206
17.1.2 A revisited interpretation of the results observed by McDermott et al. (2011)	219
17.2 Interpretation of the long-term and short-term 1 st PC time series	220
17.2.1 The physical interpretation of the long-term 1 st PC time series . . .	220
17.2.2 The physical interpretation of the short-term PC time series	228
18 Summary	231
19 Outlook	235
Appendices	237
A Distribution of r_s values for analysed $\delta^{18}\text{O}$ time series for the PCA chap- ter	239
B Model parameters for the SIP model for the transects T1 and T2	252
C Holocene European speleothems	257
D Eigenvalues of the 8,000 year PCA - PART I: Long-term analysis	263
E Results of the application of the Fork-tool onto the 8,000 year runs - PART I: Long-term analysis	266
E.1 Distribution of r_s for short-term coherence pattern for $\delta^{18}\text{O}$ time series . .	266
E.2 Distribution of r_s for short-term coherence pattern for $\delta^{13}\text{C}$ time series . .	272
F Eigenvalues of the 4,000 years runs	278
F.1 4,000 years Long-term runs	278
F.1.1 Eigenvalues of the short-term coherence pattern	278
G Results of the application of the Fork-tool onto the 4000 year long-term runs	283
H Results of the application of the Fork-tool onto the 4000 year short-term runs	292
H.1 Distribution of r_s for short-term coherence pattern for $\delta^{18}\text{O}$ time series . .	292

H.2	Distribution of r_s for short-term coherence pattern for $\delta^{13}C$ time series . . .	321
I	Eigenvalues of the 8,000 years runs - PART II: Short-term analysis	350
J	Results of the application of the Fork-tool onto the 8,000 ka runs - PART II: Short-term analysis	353
J.1	Distribution of r_s for short-term coherence pattern for $\delta^{18}O$ time series . . .	353
J.2	Distribution of r_s for short-term coherence pattern for $\delta^{13}C$ time series . . .	372
K	Eigenvalues of the 10,000 years runs - Long-term analysis	391
L	Results of the application of the Fork-tool onto the 10,000 year runs - Long-term analysis	393
M	Dependence of the slope of the speleothem and precipitation $\delta^{18}O$ gradient on the wNAO index	397
N	Correction of the speleothem $\delta^{18}O$ values at the 10 °W intercept	400
O	Oxygen isotopic composition of evaporative moisture from the ocean	402
P	Comparison of computed 1st PC time series with the original speleothem $\delta^{18}O$ and $\delta^{13}C$ time series for the last 8000 years	404
Listings		453
	List of Figures	453
	List of Tables	463
Acknowledgments		465
References		467

Abstract

Speleothems are recognised as valuable palaeo climate archives. This has led to an increasing number of analysed speleothem proxy time series from caves that are distributed on a global scale. In particular speleothem $\delta^{18}\text{O}$ and $\delta^{13}\text{C}$ time series are investigated. A hotspot of analysed speleothem proxy time series is Europe, which makes it possible to perform spatio-temporal coherency analysis of speleothem proxy time series. For this aim a method is developed that is based on Principal Component Analysis (PCA). The method is based on a Monte Carlo approach and accounts for the speleothem age uncertainty and the different temporal resolution of speleothem proxy time series. This method is applied to compilations of European speleothem $\delta^{18}\text{O}$ and $\delta^{13}\text{C}$ time series. It is demonstrated that the results of the PCA for the compiled $\delta^{18}\text{O}$ time series can be interpreted as a temperature proxy and as a precipitation/hydrology proxy for the compilation of $\delta^{13}\text{C}$ time series. Furthermore, it is shown that the spatio-temporal coherence between the analysed speleothem $\delta^{18}\text{O}$ and $\delta^{13}\text{C}$ time series varied with time. Moreover, a change of the predominant pattern is observed at 4.0 ka.

The second aim of this study is to analyse the change of the observed speleothem $\delta^{18}\text{O}$ gradient for European speleothems. A multi-box Rayleigh approach model is developed (Stable Isotope in Precipitation (SIP) model) that computes the stable isotope composition of precipitation, infiltrated water and calcite. The model is validated with measured precipitation $\delta^{18}\text{O}$ and δD values from the GNIP dataset. It is demonstrated that the SIP model agrees with the observed $\delta^{18}\text{O}$ and δD values for the analysed Central European and Northern European transect. Moreover, it is shown that the precipitation $\delta^{18}\text{O}$ (δD) gradient depends on the North Atlantic Oscillation. This is interpreted as a change of the amount of moisture in the atmosphere for Central Europe. The application of the SIP model of palaeo climate speleothem $\delta^{18}\text{O}$ gradients suggests that the climate was drier in the early- and mid-Holocene compared to present-day. In addition, the past $\delta^{18}\text{O}$ gradients suggest a transition of the atmospheric circulation from a very negative NAO like pattern in the early-Holocene (11 ka) to a very positive NAO like pattern in mid-Holocene (4 ka) and that a reorganisation of the atmospheric circulation occurred at approximately 4 ka when present-day atmospheric circulation established.

Zusammenfassung

Speläotheme werden als aufschlussreiche Klimaarchive angesehen. Dies hat dazu geführt, dass eine Vielzahl von Speläothem Proxy Zeitreihen untersucht wurden. Die analysierten Speläotheme stammen von Höhlen die über die ganze Welt verteilt sind. Insbesondere werden die $\delta^{18}\text{O}$ und $\delta^{13}\text{C}$ Zeitreihen von Speläotheme erforscht. Vor allem in Europe wurden innerhalb des vergangenen Jahrzehnts eine große Menge an Speläothem Daten erhoben, welche ein dichtes räumliches Netz aus Speläothem Proxy Zeitreihen ergeben. Dies ermöglicht es zeitlich kohärente Variationen in den Speläothem Zeitreihen zu erforschen. Zu diesem Zweck wurde eine Methode entwickelt, die auf Principal Component Analysis basiert. Die Methode benutzt einen Monte Carlo Ansatz und berücksichtigt die Altersunsicherheiten von gemessenen Speläothem Altern und die unterschiedliche zeitliche Auflösung von Speläothem Proxy Zeitreihen. Die Methode wurde auf verschiedene Zusammenstellungen von Speläothem $\delta^{18}\text{O}$ und $\delta^{13}\text{C}$ Zeitreihen angewendet. Es konnte gezeigt werden, dass die berechnete gemeinsame zeitliche Komponente der verschiedenen Speläothem $\delta^{18}\text{O}$ Zeitreihen als Temperatur Proxy interpretiert werden kann, während die gemeinsame zeitliche Komponente der verschiedenen Speläothem $\delta^{13}\text{C}$ Zeitreihen als hydrologischer Proxy aufgefasst werden kann. Ferner konnte gezeigt werden, dass sich die dominanten Muster der Korrelation zwischen den untersuchten Speläothem Proxy Zeitreihen und der errechneten gemeinsame zeitliche Komponente um 4000 Jahren vor heute verändert hat. Das zweite Ziel dieser Arbeit war die Interpretation des Speläothem $\delta^{18}\text{O}$ Gradienten der für Europe entdeckt wurde. Hierfür wurde ein multi-box Rayleigh approach Modell entwickelt (Stable Isotope in Precipitation (SIP) Modell), dass die stabile Isotopenzusammensetzung des Niederschlags, der Infiltration und des Kalzits berechnet. Die Ergebnisse des Modells werden validiert mit gemessenen Niederschlags $\delta^{18}\text{O}$ und δD Daten die durch das GNIP Netzwerk erhoben wurden. Es wird gezeigt werden, dass die Modell Ergebnisse mit den gemessenen Niederschlags $\delta^{18}\text{O}$ und δD Werten übereinstimmen. Darüberhinaus wird der entdeckte Zusammenhang zwischen der Nordatlantische Oszillation und dem Niederschlag $\delta^{18}\text{O}$ Gradienten darauf zurückgeführt, dass sich die Luftfeuchte der Atmosphäre ändert für die zwei verschiedenen Phasen der Nordatlantische Oszillation. Des Weiteren wird das SIP Modell dazu verwendet um die Veränderung des Speläothem $\delta^{18}\text{O}$ Gradienten im Holozän zu erklären. Die Veränderungen des Speläothem $\delta^{18}\text{O}$ Gradienten stammen möglicherweise von einem trockenerem Klima im frühen und mittleren Stadium des Holozän ab. Außerdem kann gezeigt werden, dass es eine Veränderung der Atmosphärischen Zirkulation gibt die sich vom frühen zum mittleren Stadium des Holozän vollzieht. Vermutlich findet um 4 ka BP eine Reorganisation der Atmosphärischen Zirkulation zur heutigen hin statt.

Part I

Introduction

„**Speleothem**: from the Greek *spelaion*
(cave) and *thema* (deposit) “

Moore (1952)

1

Speleothems and climate change

1.1 Speleothems

Speleothems are natural cave deposits that occur in caves world wide. Normally they are composed of calcite, a crystal type of calcium carbonate (CaCO_3). The origin of the precipitated mineral lies above the cave within karst zone where limestone (CaCO_3) is dissolved by the percolating water (H_2O) that springs from the precipitation above the karst and soil zone. Thus, the limestone is the provider of the constituent parts of speleothems and the percolating water the conveyor of the dissolved constituents. However, the precondition besides the occurrence of limestone and precipitation is the presence of gaseous carbon dioxide (CO_2) within the soil zone (e.g. [Ford and Williams, 2007](#); [Fairchild and Baker, 2012](#)). The CO_2 accumulates within the soil zone, because of the activity of the vegetation that is growing on the surface and by the decay of organic matter within the soil zone. Usually, the CO_2 concentration within the soil zone is much higher compared to the CO_2 concentration of the atmosphere (e.g. [Salomons and Mook, 1986](#)). The CO_2 within the soil zone is the key ingredient for the formation of speleothems, because it controls the dissolution of limestone. This is due to the fact that CO_2 in combination with H_2O forms carbonic acid (H_2CO_3). In turn, that dissolves CaCO_3 in the karst zone. Hence, the CO_2 in the soil zone is for speleothems what wind is for a sailing-ship. A speleothem is forming if CO_2 is present in the soil zone and the growth of the speleothem stops if the CO_2 is absent within the soil zone. A schematic illustration of the involved processes is given in Fig. 1.1.

The cascade of the processes pictured in Fig. 1.1 is the dissolution of CO_2 by water within the soil zone forming H_2CO_3 , which is described by the chemical reaction



The solution percolating through the soil zone. It gets in contact with CaCO_3 within the

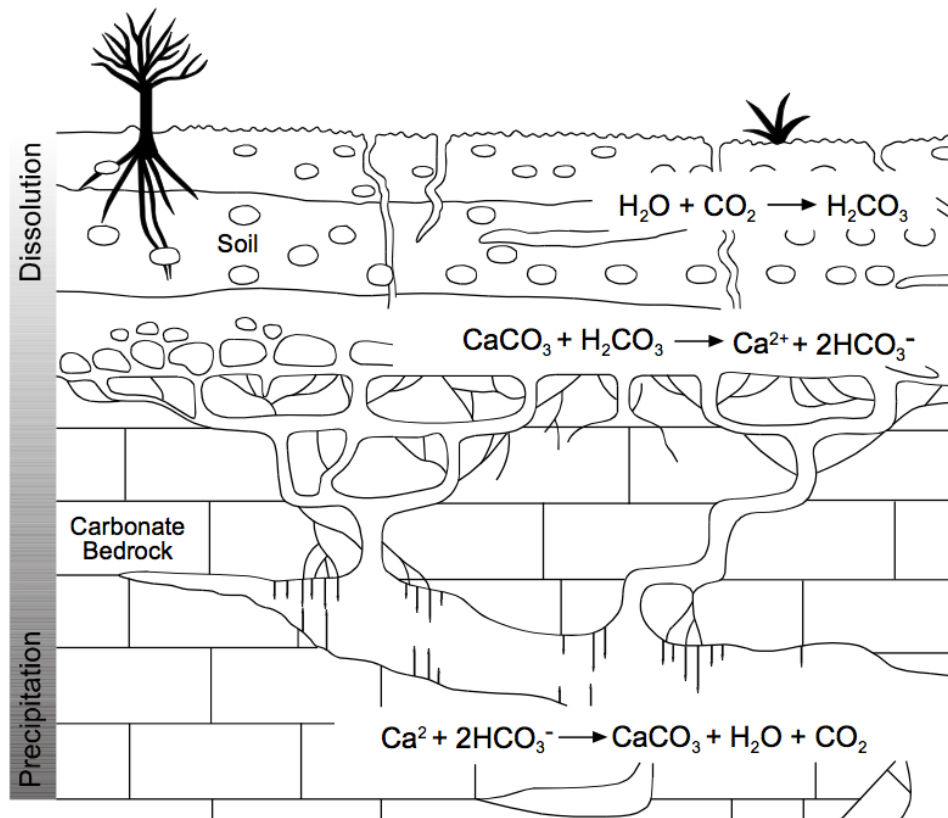
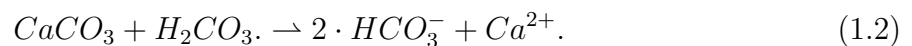
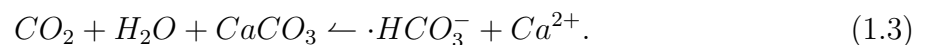


Fig. 1.1: Illustrated are the cascade of processes that occur before ultimately a speleothem is formed. See text for detail (adapted from Fairchild et al., 2006b).

karst zone, where $CaCO_3$ is dissolved:



The solution, that transports at this stage all constituents that are required for the formation of speleothems, ultimately enter a cave by fractures of the karst zone. If the cave atmosphere has lower CO_2 concentration equivalent with respect to the CO_2 concentration of the entering solution, the CO_2 that is dissolved within the solution begins to degas from the solution. This causes that the solution becomes supersaturated with respect to calcite ($CaCO_3$). Calcite is then precipitated from the solution. This is described by the following reaction



The precipitation of calcite causes a great variety of different speleothem shapes inside caves. An example of stalagmites and stalactites shapes is given in Fig. 1.2 that illustrates a picture from the interior of Crag Cave (Ireland). One of the most common stalagmite shapes are "candle like" stalagmites (front stalagmite).



Fig. 1.2: Illustrated is a picture taken inside Crag Cave: stalagmites are growing on the surface and stalactites are forming on the cave ceiling (cc-by Deininger M., 09.08.2012).

1.2 Speleothems as climate (change) recorder

Speleothems are considered as environmental recorders, that is the reason why speleothems and in particular stalagmites, are so valuable for environmental and climate investigations. Speleothems are recording various changes of a multitude of proxy cycles during the their formation by incorporating the individual proxies either directly into the crystal lattice or within the crystal lattice. The different proxies are likewise transported into the cave by the percolating water as the constituents of calcite. Hence, the connection element between the environment (proxy cycles) above the cave and the speleothem-recorder is the percolating water.

A scheme of the role of the speleothem-recorder or the environment is given in Fig. 1.3. It pictures internal and external processes of the environmental (climate) system that determine or modify the different proxy cycles.

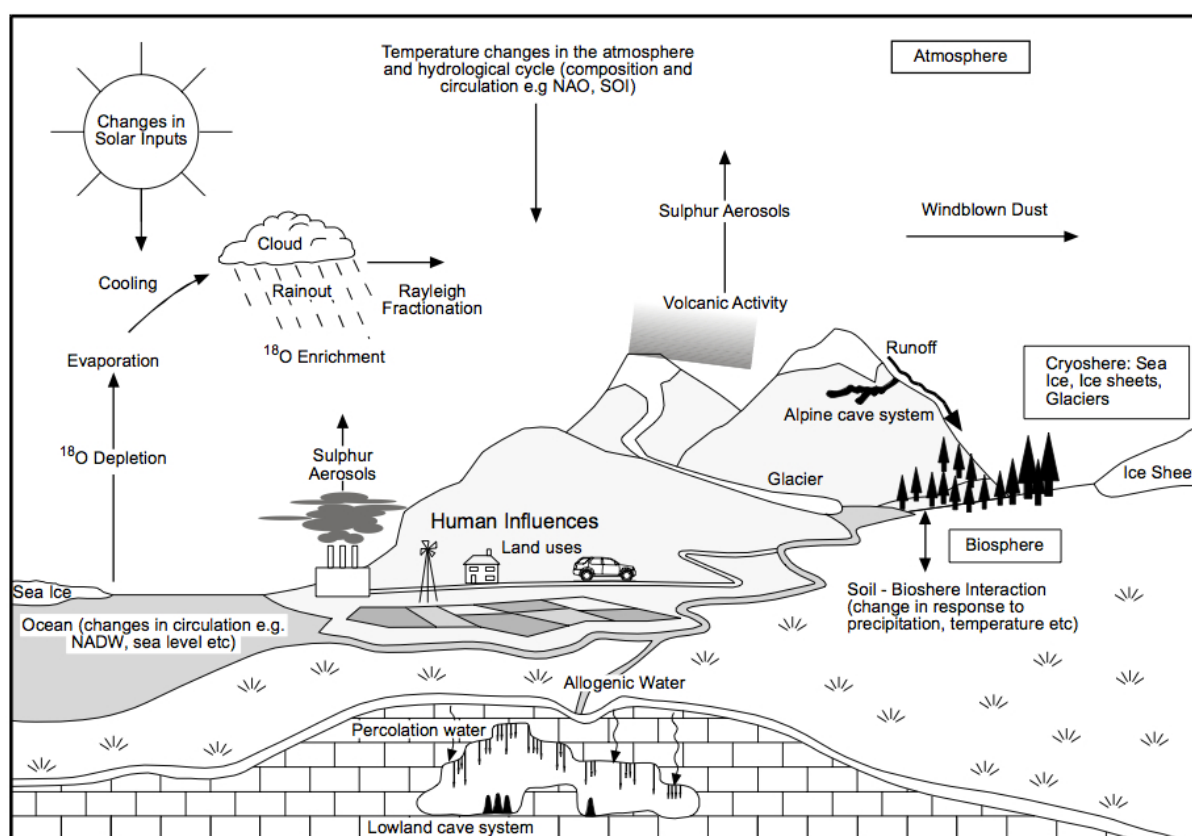


Fig. 1.3: A schematic illustration of the role of the speleothem-recorder within the environment. The figure pictures processes that determine and modify the proxy cycles recorded by speleothems (adapted from Fairchild et al., 2006b).

The most common proxies analysed from speleothems are the stable oxygen isotope composition, the carbon isotope composition and trace element concentration (e.g. Mg, Sr, U,

Si, Al) of the calcite (McDermott, 2004; Fairchild and Treble, 2009). Also, speleothems can be dated with a high precision by the use of U-series disequilibria techniques (Richards and Dorale, 2003). This allows to date speleothems until an age of c. 500,000 years using the isotope ratio of the radioactive isotopes ^{238}U and ^{230}Th and even until the age of the earth if Pb is used instead of Th (Richards and Dorale, 2003). Hence, speleothems are environmental and respectively climate archives that provide several recorded proxy time series from which information on changes of the proxy cycle can be gained. In other words speleothems are high quality palaeoclimate archives. This has induced an abrupt rise of publications that are related to speleothem studies since the 1990s (c.f. Fig. 1 of Fleitmann and Spötl, 2008). Henderson (2006) states: "For paleoclimate, the past two decades have been the age of the ice core. The next two may be the age of the speleothem."

However, the considerable potential of speleothems as palaeoclimate archives was first identified in the late 1960s and 1970s made possible by the foregoing advancement of dating and sampling techniques for the proxies (Hendy and Wilson, 1968; Duplessy et al., 1970a; Schwarcz et al., 1976; Harmon et al., 1979; Gascoyne et al., 1978). Since this early years more than 500 speleothems (with increasing number) were analysed world wide to investigate for past climate changes and from which information have been gained on the climate system (e.g. Bar-Matthews et al., 1996; Neff et al., 2001; Wang et al., 2001; Frisia et al., 2003; Niggemann et al., 2003; Fleitmann et al., 2004; Mangini et al., 2005; Spötl et al., 2006; Winograd et al., 2006; Cruz et al., 2009).

1.2. Speleothems as climate (change) recorder

2

Motivation

The growing number of speleothem studies is steadily increasing the temporal coverage back in time. But another benefit is, that also the spatial coverage is enlarging. This allows for spatio-temporal investigations of speleothem proxy time series of regions and continents which have a high density of analysed speleothems. One particular hotspot of speleothem studies is Europe and the analysed (and published) datasets allow for quantitative investigations of the spatio-temporal coherency of speleothem proxy time series (McDermott et al., 2011; Wackerbarth et al., 2012). McDermott et al. (2011) analysed 53 European speleothems that are distributed all over Europe and determined a linear relationship between present-day speleothem $\delta^{18}\text{O}$ values and the longitude of the respective speleothem location for a selected speleothem $\delta^{18}\text{O}$ time series. In addition McDermott et al. (2011) demonstrated that the $\delta^{18}\text{O}$ gradient changed during the Holocene. McDermott et al. (2011) analysed time slices of 1000 years from 0 ka to 12 ka with a temporal resolution of 100 years. Wackerbarth et al. (2012) performed a more sophisticated method by comparing measured speleothem $\delta^{18}\text{O}$ at a 6 ka with modelled speleothem $\delta^{18}\text{O}$ values. The modelled $\delta^{18}\text{O}$ values were calculated by using the "Oxygen isotope Drip water and Stalagmite Model" applied on the computed $\delta^{18}\text{O}$ values derived by the ECHAM5-wiso General Circulation Model (Werner et al., 2011; Langebroek et al., 2011).

The framework of this work ties in with McDermott et al. (2011) and analyses the spatio-temporal coherency of speleothem $\delta^{18}\text{O}$ AND $\delta^{13}\text{C}$ time series. However, the aim of this work is to determine the common general long-term trends of speleothem $\delta^{18}\text{O}$ and $\delta^{13}\text{C}$ time series, and the short-term variability of $\delta^{18}\text{O}$ and $\delta^{13}\text{C}$ time series. For this purpose Principal Component Analysis are performed on different compilations of speleothem $\delta^{18}\text{O}$ and $\delta^{13}\text{C}$ time series that cover the last 10,000 years. The used speleothems are covering most parts of Europe, except the Mediterranean, and allow therefore spatio-temporal coherency analysis for the Holocene. Furthermore, a "Stable Isotopes in Precipitation" model has been developed to investigate the causes of the temporal change of the $\delta^{18}\text{O}$ gradients discovered by McDermott et al. (2011).

This work is divided in several parts: The first part in the **Chapters 3-9** gives a comprehensive overview on the physics of speleothems. The second part is aimed to the description of the Principal Component Analysis and the application of Principal Component Analysis on speleothem proxy time series (**Chapter 10**). In **Chapter 11** the "Stable Isotopes in Precipitation" model is explained and applied on present-day precipitation stable isotope data. The results of the Principal Component Analysis and Stable Isotopes in Precipitation model are discussed in **Chapters 12-17**.

Part II

Speleothems

3

The formation of speleothems

Speleothems are formed in caves all around the globe and occur in spectacular shapes. Each cave environment is unique and so is the "Lebensraum" for speleothems inside a cave which is also stated as the speleothem incubator [Fairchild and Baker \(2012\)](#). The growth of speleothems is a simple result of the cause-and-effect chain of the CO_2 - H_2O - CaCO_3 system and has been described in many published studies (e.g. [Hendy, 1971](#); [Buhmann and Dreybrodt, 1985a,b](#); [Fairchild et al., 2006a,b](#)) and books (e.g. [Dreybrodt, 1988](#); [Ford and Williams, 2007](#); [Fairchild and Baker, 2012](#)). The cascade of processes ultimately forcing the formation of speleothems is schematically pictured in Fig. 3.1.

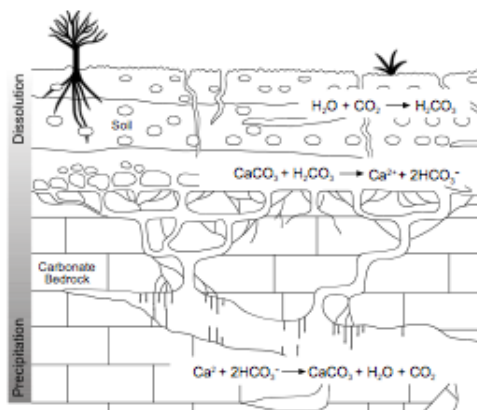


Fig. 3.1: Simplified chart of the karst system and the reactions of the CO_2 - H_2O - CaCO_3 system that take place within the karst system (adapted from [Fairchild et al., 2006b](#)).

Just as for living organisms, water is indispensable for the development of speleothems, transporting the principle constituents of speleothems into caves. These are the carbon bearing species of the CO_2 - H_2O - CaCO_3 system and calcium ions. When a precipitation event occurs in a region where a cave is located the water penetrates the soil zone. Due to plant respiration and the decay of organic matter, which is the source of CO_2 within the soil zone, the soil zone usually has a higher CO_2 concentration compared to the atmosphere above the surface. Therefore, when the water infiltrates the soil zone, the infiltrated water is undersaturated with respect to CO_2 . This results in the dissolution of gaseous CO_2 and the dissolved CO_2 is transformed into carbonic acid, H_2CO_3 in the presence of water. This is indicated by

the reaction $\text{CO}_2 + \text{H}_2\text{O} \rightarrow \text{H}_2\text{CO}_3$ in Fig. 3.1. H_2CO_3 dissociates into hydrogen carbonate, HCO_3^- , and carbonate CO_3^{2-} .

The portion of the carbon bearing species within the solution depends on the gaseous CO₂ concentration in the soil zone, usually quotes as the CO₂ partial pressure, pCO₂, and the temperature of the soil zone. Because CaCO₃ is usually absent in the top layer of the soil zone, the solution is undersaturated with respect to CaCO₃. When the highly corrosive solution penetrates deeper into the soil zone, the solution gets into contact with CaCO₃ at the boundary between the soil and the karst zone. From the moment on that the solution is in contact with CaCO₃, CaCO₃ is dissolved, while the solution is still penetrating deeper and deeper into the karst zone, until the solution is in chemical equilibrium. This can be expressed by the reaction: $\text{CaCO}_3 + \text{H}_2\text{CO}_3 \rightarrow \text{Ca}^{2+} + 2 \cdot \text{HCO}_3^-$ in Fig. 3.1. The chemical equilibrium state of the solution is determined by the chemical laws of the CO₂-H₂O-CaCO₃ system. Within the karst zone caves have developed on geological time scales and are pose a different environment compared to the karst zone above a cave. The key property of caves is that the CO₂ concentration is normally smaller compared to the CO₂ concentration of the soil zone. When the percolating solution enters a cave on its way through the karst zone, it changes its chemical property of being in a chemical equilibrium state into being in a chemical disequilibrium state caused by difference between the pCO₂ of the cave and the soil zone. The chemical disequilibrium forces the degassing of CO₂ from the solution and causes the supersaturation of the solution with respect to calcite. Ultimately, calcite is precipitated from the solution and a speleothem is formed. This is expressed through the reaction $\text{Ca}^{2+} + 2 \cdot \text{HCO}_3^- \rightarrow \text{CO}_2 + \text{H}_2\text{O} + \text{CaCO}_3$ in Fig. 3.1

A short summary has been given in the previous paragraph describing the fundamental processes of speleothem formation. In the following section, the chemical properties of the CO₂-H₂O-CaCO₃ system shall be discussed in detail. In subsequent sections the focus is on the formation of speleothems. In subsequent sections, a focus shall be layed on the formation of speleothems.

3.1 The carbonate system - The chemical properties of the CO₂-H₂O-CaCO₃ system

The growth of speleothems is determined by the chemical properties of the CO₂-H₂O-CaCO₃ system, which is characterized by the relationship of the chemical reactions of the following species: gaseous carbon dioxide, CO₂(g), aqueous carbon dioxide, CO₂(aq), carbonic acid, H₂CO₃, hydrogen carbonate (bicarbonate), HCO₃⁻, carbonate, CO₃²⁻, calcium ions, Ca²⁺ and calcium carbonate, CaCO₃. Many investigations have been performed in the 20th century to understand the complex relationships of the carbonate system, which have been culminated in comprehensive books on karst and speleothem science (e.g. [Dreybrodt, 1988](#); [Ford and Williams, 2007](#); [Fairchild and Baker, 2012](#)). The following discussion on

speleothem formation based on these mentioned books and references therein.

To investigate the chemical properties of the $\text{CO}_2\text{-H}_2\text{O-CaCO}_3$ system, a thought experiment is performed. A vessel is considered that is located in a chamber with a $\text{N}_2\text{-CO}_2$ atmosphere with variable CO_2 partial pressure, $p\text{CO}_2$. The experiment vessel is filled with water, H_2O , and the bottom of the vessel is made of CaCO_3 ; without any limitation of our derived results, the walls of the experiment vessel are made of glass.

In a first though experiment the properties of the $\text{CO}_2\text{-H}_2\text{O-CaCO}_3$ system in chemical equilibrium are investigated, whereas in the second thought experiment the properties of the $\text{CO}_2\text{-H}_2\text{O-CaCO}_3$ system for a chemical non-equilibrium (disequilibrium) scenario are investigated, i.e., the chemical kinetic properties of the carbonate system. The latter includes the dissolution and precipitation of CaCO_3 .

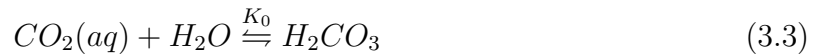
3.1.1 The chemical properties of the $\text{CO}_2\text{-H}_2\text{O-CaCO}_3$ system for chemical equilibrium

The first thought experiment shall illuminate the equilibrium conditions of the $\text{CO}_2\text{-H}_2\text{O-CaCO}_3$ system. For this, the solubility of $\text{CO}_2(\text{g})$ in H_2O is investigated. This is described by Henry's law, which states that the equilibrium concentration of the gas ($\text{CO}_2(\text{aq})$) in the liquid (H_2O) is directly proportional to the partial pressure of the gas ($\text{CO}_2(\text{g})$).



$$K_H = \frac{(\text{CO}_2^{\text{aq}})}{p\text{CO}_2} \quad (3.2)$$

Eq. (3.1) and Eq. (3.2) are the related chemical reaction and Henry's law, respectively, for the exchange of gaseous and aqueous CO_2 in the equilibrium state. The dissolved CO_2 is further transformed into H_2CO_3 when it gets in contact with H_2O . This is described by the chemical reaction in Eq. (3.3) and the related mathematical expression Eq. (3.4).



$$\frac{1}{K_0} = \frac{(\text{H}_2\text{CO}_3)}{(\text{CO}_2(\text{aq}))} \quad (3.4)$$

It is very common to use the abbreviation H_2CO_3^* for the sum of the concentrations of $\text{CO}_2(\text{aq})$ and H_2CO_3 . Eq. (3.2) and Eq. (3.3) can be then combined to

$$1 + \frac{1}{K_0} = \frac{(H_2CO_3^*)}{(CO_2(aq))}. \quad (3.5)$$

H₂CO₃ dissociates then into HCO₃⁻ (Eq. 3.6 and Eq. 3.7) and in a subsequent step HCO₃⁻ into CO₃²⁻ (Eq. 3.8 and Eq. 3.9).

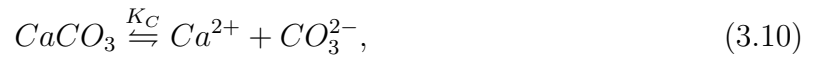


$$K_1 = \frac{(H^+) (HCO_3^-)}{(H_2CO_3^*)} \quad (3.7)$$



$$K_2 = \frac{(H^+) (CO_3^{2-})}{(HCO_3^-)} \quad (3.9)$$

Finally, CO₃²⁻ and Ca²⁺ reacts with the surface of the CaCO₃ crystal, which is described by



$$K_C = (Ca^{2+}) (CO_3^{2-}). \quad (3.11)$$

Eq. (3.1), (3.3), (3.6), (3.8) and (3.10) can be summarized to



Eq. (3.7) and Eq. (3.9) reveal that the first and second dissociation step of H₂CO₃ depends on the concentration of H⁺ ions, i.e., on the pH value of the solution in first and second order, respectively. Consequently, the proportion of the carbonate species (H₂CO₃, HCO₃⁻, CO₃²⁻) varies with changing pH value. This is illustrated in Fig. 3.2 for chemical equilibrium conditions.

Fig. 3.2 depicts the proportion of H₂CO₃, HCO₃⁻ and CO₃²⁻ for pH values between of 0 to 14 for a temperature of 25 °C and TCO₂ of 2 mmol per kg. At a pH range from 0 to c. 6, H₂CO₃ is the dominant species; from c. 7 to 9 HCO₃⁻ dominates and from 11 to 14 CO₃²⁻. At a pH value of c. 6.3 and c. 10.2, H₂CO₃ and HCO₃⁻ and HCO₃⁻ and CO₃²⁻, respectively, have the same proportion.

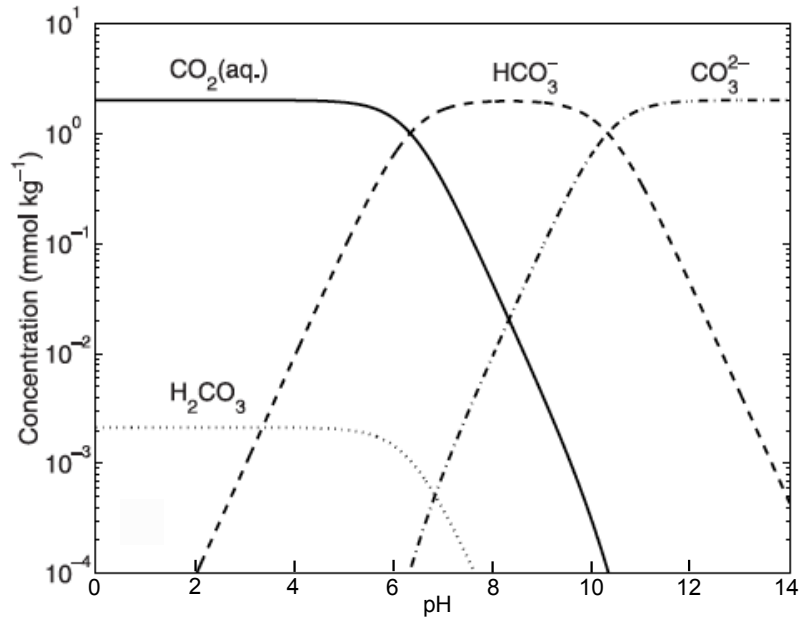


Fig. 3.2: The figure shows the portion of species of the carbonate system in dependence on the pH (adapted from Zeebe, 2007)

3.1.2 The chemical properties of the CO₂-H₂O-CaCO₃ system for chemical non-equilibrium conditions

In contrast to the first thought experiment where the properties of the CO₂-H₂O-CaCO₃ system for chemical equilibrium conditions were studied, the second and third thought experiments are for chemical non-equilibrium conditions - expressed as chemical disequilibrium in the following. This means that the species of the carbonate system are not in a chemical equilibrium, which leads to different reaction rates for the forward and backwards reactions of Eq. (3.1), (3.3), (3.6), (3.8) and (3.10). In the following paragraph, three different chemical disequilibrium scenarios are presented which are conceptually similar to a natural karst system.

In the second thought experiment, the chemical behaviour of the CO₂-H₂O system are studied for the case when water gets in contact with a N₂-CO₂ atmosphere. In the experimental setup, this is realized if the vessel is filled with H₂O and the chamber atmosphere contains only N₂ (the solution of the vessel is stirred with a magnetic stirrer in order to prevent diffusive processes inside the solution). Then CO₂ is injected into the chamber until the pCO₂ value of interest is established. Since the CO₂ molecules diffuse into the H₂O, CO₂ is continuously pumped into the chamber to maintain a constant pCO₂ value. The thought experiment is conceptually identical to the upper soil zone, without the presence of CaCO₃. The CO₂ concentration of the soil voids depends on the CO₂ flux between the atmosphere and soil zone, the CO₂ production by root respiration and the decay of organic matter,

respectively.

The third thought experiment demonstrates the dissolution of CaCO₃. CaCO₃ is dissolved when

$$1 > \frac{(Ca^{2+})(CO_3^{2-})}{K_C} \equiv \Omega. \quad (3.13)$$

Ω is the saturation state of the solution. This is the case for a solution that was in contact with a CO₂ containing atmosphere but without any physical contact to CaCO₃ at the same time. A solution, which fulfils the condition of equation Eq. (3.13), is called an undersaturated (corrosive) solution. For a corrosive solution, there is no equilibrium between the left and right side of equation Eq. (3.11), which leads to a net flux from the left to the right side of equation Eq. (3.10), i.e.,



In nature, the third thought experiment is conceptually identical to the situation of a percolating solution that infiltrates the soil zone. The percolating solution has a higher CO₂ concentration compared to the atmosphere (first thought experiment) and enters the upper karst zone, which contains CaCO₃. [Plummer et al. \(1978\)](#) concluded from their experimental results that the dissolution of *calcite* is a sum of three different reactions Eq. (3.15), (3.16), (3.17) and that the dissolution of *calcite* can be divided into three different regions (Fig. 3.3).

In region 1 (Fig. 3.3), i.e., for low pH values, the dissolution rates have a linear dependence on the pH value of the solution. Furthermore, the results of [Plummer et al. \(1978\)](#) show that the dissolution rates in this regime also depend on the stirring rate, which indicates that the dissolution rate in this regime is controlled by the transport of H⁺ ions to the surface of the calcite crystal ([Plummer et al., 1978](#); [Dreybrodt, 1988](#)). The extension of this dissolution mechanism into region 2 depends on the pCO₂ value: At 1,000,000 ppm (1 atm) the limit shows a pH value of 3.5, whereas at 0 ppm (0 atm) it is pH = 4.5. Fig. 3.3 depicts that in regime 1 the dissolution rates do not depend on the pCO₂ value; this behaviour of the dissolution rates changes and the dissolution rates split into different branches for different pCO₂ values. In region 2, the dependence of the dissolution rate on the stirring rate decreases with increasing pH and is independent at a pH value of c. 5. This indicates that the dissolution rates are limited by surface reactions ([Plummer et al., 1978](#)). However, [Dreybrodt \(1988\)](#) states that this can be used as an approximation as long as the diffusive boundary layer is not less than 10 μm. In region 3, the three branches of dissolution rates for different pCO₂ values show inflection points that depend on the pCO₂ value and a sharp drop of the dissolution rates. The pH value of this drop represents the equilibrium pH value of the solution with the corresponding pCO₂ value ([Plummer et al., 1978](#); [Dreybrodt, 1988](#)).

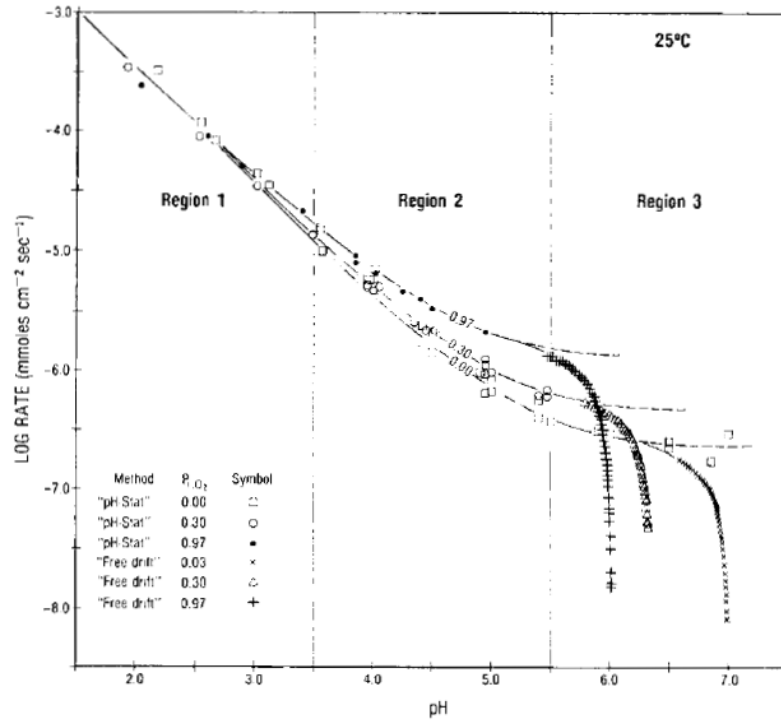
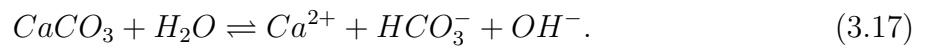
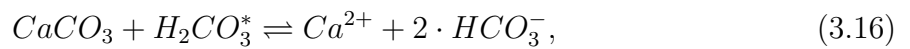
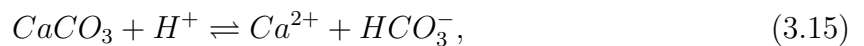


Fig. 3.3: Illustration of the calcite dissolution rate against the pH value. In Region 1 and 2 the dissolution occurs under strong disequilibrium conditions. The dissolution rate is a function of the pCO₂ value of the solution in Region 2 whereas it is independent on the pCO₂ value in Region 1. The dissolution rate decreases rapidly in Region 3 when the equilibrium pH value is reached (adapted from [Plummer et al., 1978](#)).



[Plummer et al. \(1978\)](#) proposed three elemental reactions that take place at the surface of the calcite crystal (Eq. 3.15, 3.16, 3.17) and derived a rate equation for the dissolution:

$$R_D = k_1 \cdot (\text{H}^+) + k_2 \cdot (\text{H}_2\text{CO}_3^*) + k_3 \cdot (\text{H}_2\text{O}). \quad (3.18)$$

Eq. (3.18) is valid in region 1 and 2; in region 3 the dissolution rates are compensated by the precipitation of calcite.

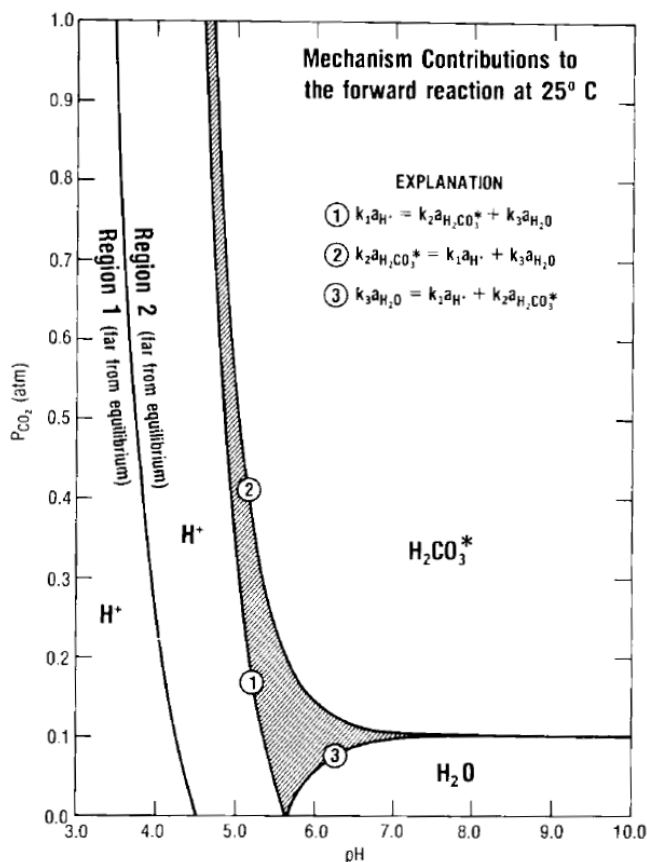
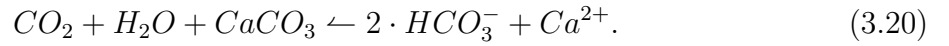


Fig. 3.4: The figure illustrates the three different dissolution mechanisms in dependence of the pH value of the solution and the pCO₂ value of the atmosphere. The thick lines indicate that the dissolution rate of the related dissolution mechanisms is equal for the given set of parameters (adapted from [Plummer et al., 1978](#)).

Fig. 3.4 depicts the contribution of the different dissolution reactions (Eq. 3.15 - 3.17) to the total dissolution of calcite at 25 °C for a pCO₂ range of 0 to 1 atm (0 - 1,000,000 ppm) and pH values between 3 and 10. The non-shaded areas indicate the dominant dissolution reaction, H⁺ stands for reaction (3.15), H₂CO₃^{*} for reaction (3.16) and H₂O for reaction (3.17). The pH value of natural waters is usually between 6.5 and 8.9 for limestone and dolomite areas ([Ford and Williams, 2007](#)); hence reaction (3.17) is the dominant process that contributes to calcite dissolution for these waters since pCO₂ values are in the range between 1,000 and 100,000 ppm (0.1 atm). [Plummer et al. \(1978\)](#) demonstrated that Eq. (3.18) needs to be modified to account for calcite precipitation. This is the topic of the fourth thought experiment. Calcite is precipitated, if the solution is supersaturated and the precipitation rate dominates the calcite dissolution. In this case, Eq. (3.11) is not fulfilled, as the right side of Eq. (3.13) is greater than K_C, i.e. $1 < \Omega$:

$$1 < \frac{(Ca^{2+})(CO_3^{2-})}{K_C}. \quad (3.19)$$

To perform this thought experiment in our experiment vessel, the chamber atmosphere is flushed with a N_2 - CO_2 gas mixture, but with a smaller pCO_2 value compared to the first thought experiment. Consequently the solution is supersaturated with respect to calcite. For a supersaturated solution, the products are on the left side of Eq. (3.12) whereas the reactant are on the right side. For precipitation Eq. (3.12) is formulated as:



To translate this thought experiment, i.e., the precipitation of calcite, into the physical karst world, the solution of the third thought experiment need to enter a hollow space within the karst zone, e.g., a cave. The atmosphere of this hollow space has a smaller pCO_2 value compared to the pCO_2 value at which the solution is in chemical equilibrium. Based on the three dissolution reactions (Eq. 3.15, 3.16, 3.17), [Plummer et al. \(1978\)](#) concluded that the back reaction rate, i.e., precipitation rate, is:

$$\begin{aligned} R_P = R_{P1} + R_{P2} + R_{P3} = & k_{41} \cdot (Ca^{2+}) (HCO_3^-) + \{k_{42} (HCO_3^-)\} \cdot (Ca^{2+}) (HCO_3^-) \\ & + \{k_{43} (OH^-)\} \cdot (Ca^{2+}) (HCO_3^-) = k_4 \cdot (Ca^{2+}) (HCO_3^-) \end{aligned} \quad (3.21)$$

[Plummer et al. \(1978\)](#) discovered that the constants k_1 , k_2 and k_3 depend only on the temperature, whereas k_4 depends also on the pCO_2 value. In region 3 (Fig. 3.3), the precipitation rate becomes more important and Eq. (3.18) is extended by R_P (Eq. 3.21) and results in a comprehensive rate equation. This rate equation is often called PWP equation, after the first letter of the surname of the authors, i.e. **P**lummer, **W**ighley, **P**arkhurst:

$$R = k_1 \cdot (H^+) + k_2 \cdot (H_2CO_3^*) + k_3 \cdot (H_2O) - k_4 \cdot (Ca^{2+}) (HCO_3^-). \quad (3.22)$$

In a following investigation, [Busenberg and Plummer \(1986\)](#) and [Dreybrodt et al. \(1997\)](#) demonstrated that Eq. (3.22) needs to be modified for inhibiting effects for calcite (and aragonite) precipitation for a saturation state between $1.5 < \Omega < 100$ ($2 < \Omega < 100$). [Dreybrodt et al. \(1997\)](#) introduced a factor f that describes the inhibiting behaviours. This can be expressed as in Eq. (3.22):

$$R = k_1 \cdot (H^+) + k_2 \cdot (H_2CO_3^*) + k_3 \cdot (H_2O) - f \cdot k_4 \cdot (Ca^{2+}) (HCO_3^-). \quad (3.23)$$

f is defined by $\left([Ca^{2+}]_{eq} / [Ca^{2+}]_{app}\right)^2$, whereas $[Ca^{2+}]_{eq}$ is the theoretical equilibrium concentration. $[Ca^{2+}]_{app}$ is the apparent quasi-equilibrium concentration (Dreybrodt et al., 1997) found a value of 0.8 for f . Busenberg and Plummer (1986) introduced an equivalent equation for the precipitation rate:

$$R_P = k_4 \cdot \left(C \cdot E - (Ca^{2+}) (HCO_3^-) \right). \quad (3.24)$$

In Eq. (3.24), C is a constant that equates $1/f$ (Dreybrodt et al., 1997) and E is $(Ca^{2+})_{eq}$. From f it follows, that the apparent calcium ion concentration is

$$[Ca^{2+}]_{app} = \frac{[Ca^{2+}]_{eq}}{\sqrt{0.8}}. \quad (3.25)$$

It follows further, that the Eq. (3.25) is the apparent quasi-equilibrium concentration of the calcium ions is elevated by factor of $1/\sqrt{0.8} > 1$ compared to chemical equilibrium. Dreybrodt et al. (1997) interpreted this observations as inhibiting effects, which might be caused by impurities.

3.1.3 The chemical properties of the CO₂-H₂O-CaCO₃ system for thin films

In the previous section we discussed the chemical kinetics of the CO₂-H₂O-CaCO₃ system but neglected physical kinetics of the chemical species within the solution. We argued that due to the continuous stirring of the solution, which can be realized with a magnetic stirrer, physical transportation processes are negligible in comparison to the reaction rates of the chemical reactions, i.e., only the chemical reactions are rate limiting. Buhmann and Dreybrodt (1985a) and Buhmann and Dreybrodt (1985b) investigated the precipitation and dissolution rates for nature-like conditions for open and closed systems, respectively, at which open means an unlimited CO₂(g) source and closed a limited CO₂(g) source. (Buhmann and Dreybrodt, 1985a) demonstrated that the dissolution and precipitation rate are limited by (i) the chemical precipitation and dissolution mechanisms at the crystal surface, described by the PWP-equation, (ii) the slow conversion of hydrogencarbonate (HCO₃⁻) into aqueous CO₂ and (iii) the molecular diffusion of the ions within the solution layer. The results of the authors demonstrate that the dissolution or precipitation rates are a linear function that depends on a rate constant, α_i ($i = D$ for CaCO₃ dissolution; $i = P$ for CaCO₃ precipitation) and on the difference between the solution's actual Ca²⁺ concentration and the apparent Ca²⁺ concentration; the latter is a function of the pCO₂ value of the solution's surrounding cave atmosphere.

$$R_i = \alpha_i \cdot ([Ca^{2+}] - [Ca^{2+}]_{app}) \quad (3.26)$$

In the following paragraph, an emphasize shall be but on open-system conditions and on the precipitation kinetics, as these are the conditions which describe natural cave environments. Based on the work of [Buhmann and Dreybrodt \(1985a\)](#), [Baker et al. \(1998\)](#) determined the value for α_P for nature-like conditions. α_P has been calculated for different solution film thicknesses in the temperature range between 0 and 25 °C. Further results of [Baker et al. \(1998\)](#), suggest that α_P is independent from the cave's pCO₂ value illustrated by Fig. 3 in [Baker et al. \(1998\)](#). Close to chemical equilibrium the functional relationship of α_P on temperature and film thickness might be not valid due to the inhibiting effects for calcite precipitation at the crystal surface ([Dreybrodt et al., 1997](#); [Baker et al., 1998](#)).

3.2 Speleothemgrowth

Speleothemgrowth is the effect of a net flux of calcium ions (Ca²⁺) and carbonate species on an existing crystal surface caused by supersaturation of the solution ($\Omega > 1$). The flux of Ca²⁺ ions to the crystal surface can be calculated with Eq. (3.26) ([Buhmann and Dreybrodt, 1985a](#); [Dreybrodt, 1999](#); [Baker et al., 1998](#)).

$$R_P = \alpha_P \cdot \left([Ca^{2+}] - [Ca^{2+}]_{app} \right) \quad (3.27)$$

To calculate the temporal derivative of the Ca²⁺ concentration we apply the continuity equation (Eq. 3.28),

$$\frac{\partial}{\partial t} \cdot \varrho + \text{div}(\varrho \cdot \vec{v}) = 0, \quad (3.28)$$

on Eq. 3.27, at which ϱ is replaced by the calcium excess, $([Ca^{2+}] - [Ca^{2+}]_{ap})$, and v by the precipitation rate constant, α_P . This yields Eq. 3.29.

$$\frac{\partial}{\partial t} \cdot \left([Ca^{2+}] - [Ca^{2+}]_{app} \right) + \frac{\partial}{\partial x} \left(\left([Ca^{2+}] - [Ca^{2+}]_{app} \right) \cdot \alpha_P \right) = 0 \quad (3.29)$$

For a thin solution layer with height δ , the differential $\partial/\partial x$ can be replaced by $1/\delta$. Transposing Eq. (3.29) for the temporal change of the calcium ion concentration, Eq. (3.30) is obtained, which allows to calculate the precipitation rate for thin solution films.

$$\frac{\partial}{\partial t} \cdot \left([Ca^{2+}] - [Ca^{2+}]_{app} \right) = -\frac{\alpha_P}{\delta} \left([Ca^{2+}] - [Ca^{2+}]_{app} \right) \quad (3.30)$$

Solving equation Eq. (3.30) results in equation Eq. (3.31) and Eq. (3.32), respectively.

$$\left([Ca^{2+}] (t) - [Ca^{2+}]_{app} \right) = \left([Ca^{2+}] (t_0) - [Ca^{2+}]_{app} \right) \cdot \exp \left\{ -\frac{\alpha_P}{\delta} (t - t_0) \right\} \quad (3.31)$$

$$[Ca^{2+}] (t) = \left([Ca^{2+}] (t_0) - [Ca^{2+}]_{app} \right) \cdot \exp \left\{ -\frac{\alpha_P}{\delta} (t - t_0) \right\} + [Ca^{2+}]_{app} \quad (3.32)$$

The temporal evolution of HCO_3^- can be derived from Eq. (3.32). Since HCO_3^- is the dominate carbon bearing species of the CO_2 - H_2O - $CaCO_3$ system for natural karst waters, the electro neutrality conditions require that $2 \cdot [Ca^{2+}] = [HCO_3^-]$. Hence, the temporal evolution of HCO_3^- is given by Eq. (3.33). $[HCO_3^-]_{app}$ is the apparent HCO_3^- concentration and account the inhibiting effects of the calcite precipitation. $[HCO_3^-]_{app}$ can be calculated by $[HCO_3^-]_{app} = [HCO_3^-]_{eq} / \sqrt{0.8}$ whereas $[HCO_3^-]_{eq}$ is the equilibrium concentration of HCO_3^- with respect to the pCO_2 of the atmosphere above the solution.

$$[HCO_3^-] (t) = \left([HCO_3^-] (t_0) - [HCO_3^-]_{app} \right) \cdot \exp \left\{ -\frac{\alpha_P}{\delta} (t - t_0) \right\} + [HCO_3^-]_{app} \quad (3.33)$$

Since every single Ca^{2+} atom (together with a species of the carbonate system) constitutes a $CaCO_3$ molecule, which is incorporated into the calcite lattice, Eq. (3.27) can be used to calculate the speleothem growth rate for a given calcium ion excess and a set of parameter for temperature and solution film thickness, which determines the precipitation rate constant α_P . If we substitute the Ca^{2+} concentration with the functional relationship of the calcium ion concentration on time (Eq. 3.32), Eq. (3.27) changes into a function of time, that can be formulated as follows:

$$R_P (t) = \alpha_P \cdot \left([Ca^{2+}] (t) - [Ca^{2+}]_{app} \right). \quad (3.34)$$

Eq. (3.34) allows to calculate the mean growth rate over a time interval, Δt . With discrete time steps of length dt , the time interval Δt can be divided in n summands. The mean growth rate, $\overline{G_{speleothem}}$, is the sum of precipitated $CaCO_3$ at a given point in time divided by the number of time steps Eq. 3.35.

$$\overline{G_{speleothem}} = \frac{1}{n} \sum_{i=1}^n R_P (t_i) = \frac{1}{n} \cdot \alpha_P \sum_{i=1}^n \left([Ca^{2+}] (t) - [Ca^{2+}] (t + dt) \right) \quad (3.35)$$

For limes $dt \rightarrow 0$, the sum in equation Eq. (3.35) becomes an integral (Eq. 3.36) and can be formulated as:

$$\overline{G_{speleothem}} = \frac{1}{\Delta t} \int_{t_0}^{t_0+\Delta t} dt \cdot \alpha_P \cdot \left([Ca^{2+}](t) - [Ca^{2+}]_{app} \right). \quad (3.36)$$

The solution of equation Eq. 3.36 is ([Dreybrodt, 1999](#))

$$\overline{G_{speleothem}} = \frac{\delta}{\Delta t} \cdot \left([Ca^{2+}](t) - [Ca^{2+}]_{app} \right) \cdot \left(1 - \exp \left\{ \frac{\alpha_P}{\delta} (t_0 + \Delta t - t_0) \right\} \right). \quad (3.37)$$

Equation (3.37) can be applied to different sets of parameters allowing to calculate a theoretical growth rate of a forming speleothem (e.g. [Kaufmann, 2003](#); [Kaufmann and Dreybrodt, 2004](#); [Mühlinghaus et al., 2007](#)).

4

Dating of speleothems

For speleothems several dating techniques can be applied. First speleothem investigations were based on radiocarbon dating (e.g. [Broecker et al., 1960](#)) and uranium-series disequilibrium (e.g. [Rosholt and Antal, 1962](#)). Today, pushed by the advances of mass spectrometry development, the commonly used technique is based on uranium-series disequilibrium ([Edwards et al., 1997](#); [Hoffmann et al., 2007](#)). ^{14}C dating and lamina counting are mostly used to receive additional age information. ^{14}C is frequently applied to verify if speleothems are actively growing tracing the ^{14}C bomb-peak, caused by surficial atomic bombs tests between 1945 and 1963 (e.g. [Scholz et al., 2012a](#)). ^{14}C and $\delta^{13}\text{C}$ is also used as an environmental tracer of the biological activity in the soil zone ([Rudzka et al., 2011](#)) and also to investigate past hydrological conditions in the soil and karst zone ([Griffiths et al., 2012](#)). ^{14}C measurements in speleothems are also used for the calibration of the past atmospheric radiocarbon content ([Hoffmann et al., 2010](#)). All the mentioned examples of the application of ^{14}C , beside radiocarbon dating, have one thing in common: to have dated ages along the growth axis not basing on radio carbon dating. This is mostly done by uranium-series disequilibrium techniques.

Uranium-series disequilibrium techniques are based on the disturbance of the secular equilibrium between parent nuclei (^{238}U , ^{235}U) and the intermediate and long-lived daughter isotopes (^{230}Th , ^{231}Pa) of the radioactive decay-series. From the disequilibrium state between ^{238}U and ^{230}Th it is possible to date samples with ages up to $<\sim 500$ ka; for ^{235}U and ^{231}Pa , samples can be dated with ages $<\sim 200$ ka. Applying the radioactive decay-chain U-Th-Pb samples with ages up to the earth's age can be dated [Richards and Dorale \(2003\)](#). The common procedure is to take carbonate samples along the growth axis, to prepare the samples for the mass spectrometry measurements by separating the uranium and thorium elements by chemical fractionation described by [Frank et al. \(2000\)](#) and [Hoffmann et al. \(2007\)](#).

In the following section the basics of the uranium-series disequilibrium shall be explained following the structure and content of [Richards and Dorale \(2003\)](#). For a comprehensive

review on uranium-series chronology, the reader shall be referred to [Richards and Dorale \(2003\)](#) and references therein.

4.1 Dating of speleothems by uranium-series disequilibrium - The ^{230}Th - ^{234}U - ^{238}U decay-series: General principles

In any material that occurs in nature being undisturbed for millions and millions of years, the parent and daughter isotopes of the ^{238}U radioactive decay series are in secular equilibrium. This is due to the reason that the half-life of parent nuclide is much greater than that of its daughters. For the ^{238}U decay chain, the most important half-lives are that of ^{238}U , ^{234}U and the long lived daughter ^{230}Th being $T_{238} = 4.4683 \pm 0.0048 \cdot 10^9$ years ($\lambda_{238} = \ln(2)/T_{238}$) ([Jaffey et al., 1971](#)), $T_{234} = 234,250 \pm 490$ years ($\lambda_{234} = \ln(2)/T_{234}$) ([Cheng et al., 2000](#)) and $T_{230} = 75,690 \pm 230$ years ($\lambda_{230} = \ln(2)/T_{230}$) ([Cheng et al., 2000](#)). In the earth's continental crust, the average abundance of uranium and thorium are 1.7 and 8.5 $\mu\text{g/g}$ ([Wedepohl, 1995](#)). The secular equilibrium between the parent and its intermediate daughters of a decay chain can be disturbed in secondary precipitates caused by chemical, physical or nuclear fractionation processes. Hence, they are in a disequilibrium state at the time of precipitation. The evolution of the daughter to parent activity ratio can be calculated, if intermediate and daughter products of the decay chain were absent, or in case not, their concentrations are known and the activities can be corrected for. Furthermore, the system has to be closed since the time of formation, i.e., there were no sinks and sources of parent and daughter nuclei. For the ^{238}U radioactive decay-series, this, the extreme fractionation of the parent nuclei ^{238}U and ^{234}U and its long-lived daughter ^{230}Th in the hydrosphere, is, what makes it possible to date speleothems ([Richards and Dorale, 2003](#)). The fractionation between the 238- and 234-uranium isotopes and 230-thorium is caused by the different solubility of the elements, respectively. Uranium is in contrast to thorium readily soluble. This is due to the fact that uranium exists in nature basically as the highly soluble uranyl ion (UO_2^{2+}). In karst waters, the uranyl ion also forms stable carbonate complexes. Thorium usually occurs in nature in its +4 oxidation state. This results in a very high hydrolysis potential and causes that thorium is highly particle-like (inorganic or organic) and very mobile. This explains why secondary carbonates have negligible thorium concentrations while uranium is precipitated with CaCO_3 and so abundant in secondary carbonates ([Richards and Dorale, 2003](#)).

The activity ratio between ^{230}Th and ^{238}U for a closed system under the conditions that the 230-thorium concentration at the time of precipitation is negligible and that the ratio between ^{234}U and ^{238}U is unity can be calculated with Eq. (4.1) ([Richards and Dorale, 2003](#)). $(^{230}\text{Th}/^{238}\text{U})_A$ is the activity ratio between ^{230}Th and ^{238}U , λ_{230} the decay constant of ^{230}Th and t the time.

$$\left(\frac{{}^{230}\text{Th}}{{}^{238}\text{U}}\right)_A = 1 - \exp\{-\lambda_{230} \cdot t\} \quad (4.1)$$

However, the condition that $({}^{234}\text{U}/{}^{238}\text{U}) = 1$ is usually not fulfilled in natural waters and so also for secondary carbonates. This is caused by physical fractionation processes between ${}^{238}\text{U}$ and ${}^{234}\text{U}$ during the dissolution of rocks. However, if the ratio between ${}^{230}\text{Th}$ and ${}^{238}\text{U}$ during the formation of secondary carbonates can be estimated, the temporal evolution of $({}^{234}\text{U}/{}^{238}\text{U})$ can be calculated with Eq. (4.2) (Richards and Dorale, 2003). $\delta^{234}\text{U}(t)$ gives the relative degree of the deviation from the secular equilibrium between ${}^{238}\text{U}$ and ${}^{234}\text{U}$ at time t and is given by the term: $\delta^{234}\text{U} = ({}^{234}\text{U}/{}^{238}\text{U})_m / ({}^{234}\text{U}/{}^{238}\text{U})_{eq} - 1$. The subscripts "m" and "eq" denotes the measured mass ratio and the mass ratio for the secular equilibrium. λ_{234} is the decay constant of ${}^{234}\text{U}$. Usually $\delta^{234}\text{U}$ is given as

$$\delta^{234}\text{U}(t) = \delta^{234}\text{U}(t_0) \cdot \exp\{-\lambda_{234} \cdot t\} \quad (4.2)$$

If $\delta^{234}\text{U}(t_0)$ can be adequately estimated, Eq. (4.2) can be used to calculate carbonate ages. However, generally $\delta^{234}\text{U}(t_0)$ variations are observed and are thus limiting the use of Eq. (4.2) (Richards and Dorale, 2003). As a consequence of the disequilibrium between ${}^{238}\text{U}$ and ${}^{234}\text{U}$ activity ratios in natural waters, the use of Eq. (4.1) is also limited. Usually, $({}^{234}\text{U}/{}^{238}\text{U})_A$ is larger than unity and can have values up to 30 (Osmond et al., 1983; Richards and Dorale, 2003). Hence, Eq. (4.1) must be extended to account for the state of disequilibrium between ${}^{238}\text{U}$ and ${}^{234}\text{U}$ and is resulting in Eq. (4.3) (from Kaufman and Broecker, 1965).

$$\left(\frac{{}^{230}\text{Th}}{{}^{238}\text{U}}\right)_A = 1 - \exp\{-\lambda_{230} \cdot t\} + \delta^{234}\text{U}(t) \cdot \left(\frac{\lambda_{230}}{\lambda_{230} - \lambda_{234}}\right) (1 - \exp\{(\lambda_{234} - \lambda_{230}) t\}) \quad (4.3)$$

The solution of Eq. (4.3) is illustrated in Fig. 4.1 for different $\delta^{234}\text{U}(t_0)$ values. Further assumptions have been, that the system is closed and that the initial concentration of ${}^{230}\text{Th} = 0$. With evolving time, a secular equilibrium between parent and daughter nuclei is reached and the activity ratio between ${}^{230}\text{Th}$ and ${}^{238}\text{U}$ reaches unity. Using Eq. (4.3), the age of a carbonate sample from a speleothem can be calculated iteratively using numerical algorithms.

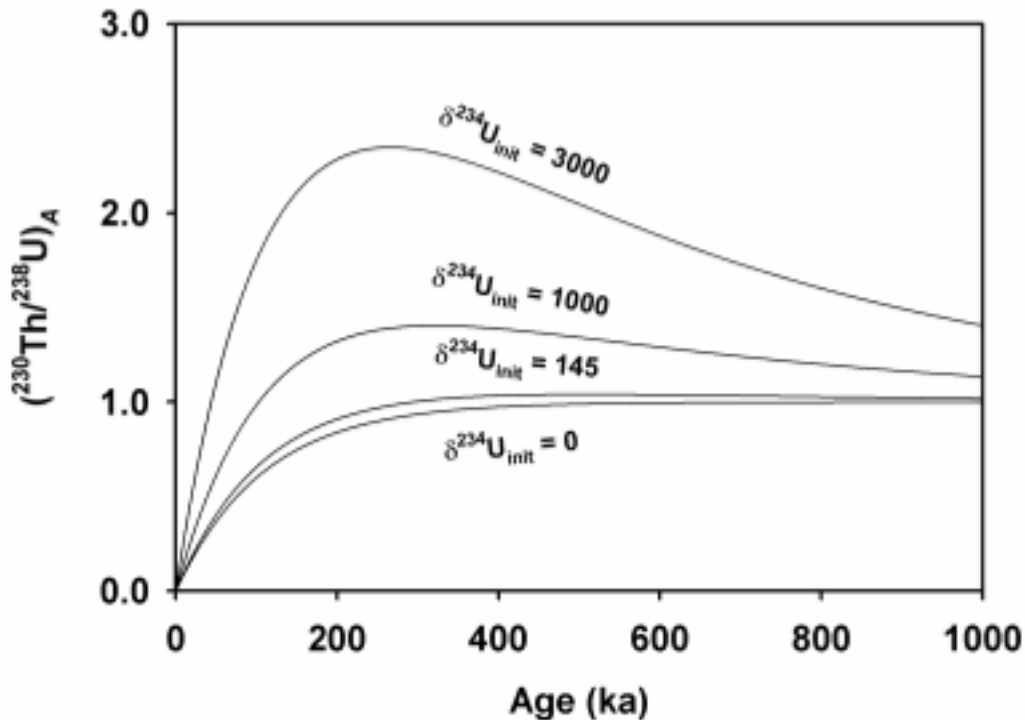


Fig. 4.1: Temporal evolution of the activity ratio between ^{230}Th and ^{238}U , $(^{234}\text{U}/^{238}\text{U})_A$, for different $\delta^{234}\text{U}(t_0)$ values under closed system conditions and the assumption that initial ^{230}Th were absent (adapted from [Richards and Dorale, 2003](#)).

4.2 Dating of speleothems by uranium-series disequilibrium - The ^{230}Th - ^{238}U decay-series: Correction for initial conditions

One assumption of the derivation of Eq. (4.3) is that the initial ^{230}Th concentration is negligible at the time of formation of secondary carbonates. However, when analysing whole-samples of carbonate, not only the autigenic phase is contributing to the radiogenic isotopes but also a detrital component composed of particles having adsorbed Th^{4+} . Hence, the condition that the initial $^{230}\text{Th} = 0$ is not fulfilled ([Richards and Dorale, 2003](#), and references therein). To correct the measured $(^{230}\text{Th}/^{238}\text{U})$ activity ratio for the detrital ^{230}Th component, the long-lived ^{232}Th is used with a half-time of $1.401 \cdot 10^{10}$ years ([Richards and Dorale, 2003](#)). For this, the initial $^{230}\text{Th}/^{232}\text{Th}$ ratio of the detritus is assumed and the measured $(^{230}\text{Th}/^{238}\text{U})$ activity ratio is corrected for it yielding Eq. (4.4). With the corrected $(^{230}\text{Th}/^{238}\text{U})$ activity ratio, the age of the carbonate sample can be calculated applying Eq. (4.3).

$$\left(\frac{{}^{230}\text{Th}^{corr}}{{}^{238}\text{U}}\right)_A = \left(\frac{{}^{230}\text{Th}}{{}^{238}\text{U}}\right)_{Am} - \left(\frac{{}^{232}\text{Th}}{{}^{238}\text{U}}\right) \cdot R_0 \cdot \exp\{-\lambda_{230}t\} \quad (4.4)$$

$({}^{230}\text{Th}/{}^{238}\text{U})_{Am}$ is the measured activity ratio including the autigenic and detrital ${}^{230}\text{Th}$ component. The last term is accounting for the detrital ${}^{230}\text{Th}$ component. $({}^{232}\text{Th}/{}^{238}\text{U})_A$ is the activity ratio between ${}^{232}\text{Th}$ and ${}^{238}\text{U}$, R_0 is the initial activity ratio between ${}^{230}\text{Th}$ and ${}^{232}\text{Th}$ and the exponential function is accounting for the decay of the initial ${}^{230}\text{Th}$ isotopes. For R_0 , several values are published and [Richards and Dorale \(2003\)](#) states that "there is a significance difference the arbitrary value adopted in published studies". However, where there is little contamination, the effect of an incorrect R_0 is minimal ([Richards and Dorale, 2003](#)). To determine R_0 , drip water samples can be investigated. [Richards and Dorale \(2003\)](#) cite studies giving values for R_0 of 1.7 ± 1.4 (2-sigma) basing on (shells, molluscs, tufas) ([Kaufman, 1993](#)) and $R_0 = 0.8 \pm 0.8$ (2-sigma) predicted from the U/Th ratio in the upper continental crust ([Taylor and McLennan, 1995](#); [Wedepohl, 1995](#)) and the secular equilibrium between ${}^{230}\text{Th}$ and ${}^{238}\text{U}$ ([Rogers and Adams, 1969](#)).

4.2. Dating of speleothems by uranium-series disequilibrium - The ^{230}Th - ^{238}U decay-series:
Correction for initial conditions

5

Isotope fractionation - Part I

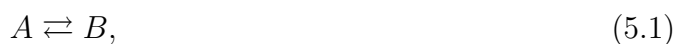
Molecules are composed of a certain number of elements. CaCO_3 is composed of the elements calcium (Ca), carbon (C) and oxygen (O). Elements are composed of an atomic core, composed of the element's specific number of protons and a certain number of neutrons, and electrons being distributed around the atomic core. However, the element's atomic core can be composed of different numbers of neutrons, and these compounds are called isotopes. The name "isotope" is deduced from Greek and its meaning is "equal place" expressing the fact the isotopes of the same element occupy the same place in the periodic table of elements. The isotopes of an element can be divided into groups of stable isotopes and instable isotopes (radioactive). The latter are decaying by α , β and γ decays, depending on the radioactive decay chain of the isotope. The different mass of isotopes from an element causes small changes in their physiochemical properties, called "isotope effects". This leads to a considerable fractionation of isotopes with different masses during physical processes and chemical reactions, stated as "isotope fractionation". The isotope effects of a chemical reaction, e.g., calcite precipitation, or a physical process, e.g., condensation or evaporation of water, causes fractionation of isotopes with different masses and provides insights into ongoing physiochemical processes. Therefore, the scope of applications of stable isotopes is wide (Mook and de Vries, 2000; Mook, 2006; Sharp, 2007; Hoefs, 2009). For the environmental system, isotopes are used as tracers to gain information on the multitude of processes that occur (e.g. Dansgaard, 1964; McDermott et al., 2011). In the following section, a brief introduction shall be given on the principals of isotope fractionation whereas the rest of the chapter shall be dedicated to isotope fractionation in speleothem science.

5.1 Different states of isotope fractionation

Isotope fractionation can be subdivided into two classes, *equilibrium* isotope fractionation and *kinetic* isotope fractionation and an intermediate class between equilibrium and kinetic

5.2. Nomenclature of isotope fractionation

isotope fractionation stated as *disequilibrium* isotope fractionation (e.g. Mook and de Vries, 2000; Mook, 2006). Assuming a chemical reaction or a physical process between two substances A and B,



where isotopes are exchanged continuously, whereas the substance with the rare isotope is quoted with an *, Eq. (5.1) reads as follows:



Now, the difference between equilibrium and kinetic isotope fractionation is that for equilibrium isotope fractionation the two substances A and B are interacting with each other by chemical or physical processes and are in an equilibrium state, which can be expressed by \rightleftharpoons in Eq. (5.1), whereas for kinetic isotope fractionation, it is a "one-way" reaction or physical process, respectively. The \rightleftharpoons in Eq. (5.1) must be replaced in this case by \rightarrow . Hence, the substances are not interacting with each other. The consequence for the isotopic composition of substance A and B is that in case of equilibrium isotope fractionation the isotopic compositions of A and B are constant with time; they are in an isotopic equilibrium with respect to the isotope fractionation processes. For kinetic isotope fractionation however, the isotopic composition of A and B are constantly changing because of the isotope selective behaviour of the chemical reaction or physical process. Disequilibrium isotope fractionation is an intermediate state between equilibrium and kinetic isotope fractionation, expressing that the process is neither a pure equilibrium nor a pure kinetic one.

5.2 Nomenclature of isotope fractionation

The isotopic composition of a substance is usually expressed in its isotope ratio R, whereas as R is calculated by the ratio between the rare and the abundant isotope. Like for CO₂, the carbon isotopic ratio between ¹³C, the rare carbon isotope and ¹²C is given by

$${}^{13}R_{CO_2} = \frac{n^{13}C}{n^{12}C}, \quad (5.3)$$

at which $n^{13}C$ and $n^{12}C$ is the number of CO₂ molecules bearing a ¹³C or a ¹²C isotope, respectively. For better comparisons, the isotopic ratio of a substance is usually given through its δ -notation which expresses the relative deviation from a standard isotopic ratio R_{std} . For the carbon isotopic ratio of CO₂, the δ -notation of Eq. (5.3) yields

$$\delta^{13}C_{CO_2} = \frac{{}^{13}R_{CO_2}}{{}^{13}R_{std}} - 1. \quad (5.4)$$

Due to the small value derived by the δ -notation it usually given in per mill (‰).

The effect of the isotope fractionation between two substances is expressed with the isotope fractionation factor α for a given chemical reaction or physical process, respectively. For Eq. (5.1) the isotope fractionation factor is

$$\alpha_{B/A} = \frac{R_B}{R_A}, \quad (5.5)$$

whereas R_B and R_A is the isotopic ratio of substance B and A, respectively. If $\alpha_{B/A}$ is >1 , the rare isotopes are preferentially incorporated by substance B and if $\alpha_{B/A} <1$, it is vice versa. Due to the fact that the value of $\alpha_{B/A}$ is usually ≈ 1 , it is also expressed by the so called isotope enrichment factor $\epsilon_{B/A}$ (Eq. 5.6) given in per mill (‰).

$$\epsilon_{B/A} = \alpha_{B/A} - 1 \quad (5.6)$$

A comprehensive overview on isotope fractionation and the application in earth sciences is given by [Mook and de Vries \(2000\)](#), [Mook \(2006\)](#), [Sharp \(2007\)](#) and [Hoefs \(2009\)](#).

5.3 Stable isotopes in speleothem science

In speleothem science the most common isotopes being used are stable oxygen and carbon isotopes. For oxygen isotopes, the isotopic ratio between ^{18}O and ^{16}O is analysed and for carbon isotopes the isotopic ratio between ^{13}C and ^{12}C . The reason for this is rather simple: calcite, the most common crystal structure of secondary carbonates in nature, is composed of carbon and oxygen isotopes. By measuring the oxygen and carbon isotopic composition of a speleothem, the analysed calcite provides isotopic information at the time of formation. For this, the oxygen and carbon isotopic ratios are measured long the growth axis of a stalagmite being most representative location of the isotopic composition of the drip water falling from the cave ceiling. Another advantage of measuring the isotopic composition along the growth axis, is that the growth rate is highest at the impact point of the drip water allowing to measure at a higher spacial resolution.

In the following sections, an overview of the carbon and oxygen isotopes of the $\text{CO}_2\text{-H}_2\text{O-CaCO}_3$ system shall be given and discussed. In Chapter 6 and 7, the processes are discussed in detail and the dependency of the oxygen and carbon isotope composition of calcite on various parameter shall be discussed. In the subsequent chapters (Chapter 8), processes shall be discussed that determine the oxygen and carbon isotopic composition of the drip

water inside caves. In Chapter 9, the second part of "Isotope Fractionation" shall present the latest investigations and observations.

5.3.1 Isotope fractionation effects of the $\text{CO}_2\text{-H}_2\text{O-CaCO}_3$ system

The precipitation of calcite inside a cave is the reaction of the $\text{CO}_2\text{-H}_2\text{O-CaCO}_3$ system and is caused by the outgassing of CO_2 from the solution due to a smaller $p\text{CO}_2$ of the cave atmosphere compared to the $p\text{CO}_2$ of the solution (Chapter 3). Each chemical reaction is accompanied by oxygen and carbon isotope fractionation effects. A first comprehensive study on the isotopic system was published by [Hendy \(1971\)](#) who distinguished between three different kinds of isotope fractionation of calcite precipitation. The first two, being separated by the rate of CO_2 loss. If the rate of CO_2 loss is sufficiently slow, isotopic equilibration between the carbon and oxygen bearing species can be maintained. This is in particular important for the oxygen isotope of composition of the precipitated calcite, because an isotope exchange between water and the carbon bearing species is only possible via the dehydration of HCO_3^- and hydration of aqueous CO_2 . But these two chemical reactions are the slowest of the $\text{CO}_2\text{-H}_2\text{O-CaCO}_3$ system ([Hendy \(1971\)](#) and references therein). If the CO_2 loss is rapid, [Hendy \(1971\)](#) states it as kinetic isotope fractionation because there is no time to maintain chemical equilibrium conditions and hence no isotopic equilibrium. The third class of isotope fractionation is the precipitation of calcite caused by evaporation of water. However, since most caves have an relative humidity above 95 %, evaporative effects might be of subordinated order ([Deininger et al., 2012](#); [Dreybrodt and Deininger, accepted manuscript](#)).

fractionation factor α	enrichment factor ϵ	reference
carbon		
$\alpha_{CO_2(g)/HCO_3^-}^{13} = \epsilon_{CO_2(g)/HCO_3^-}^{13} - 1$	$\epsilon_{CO_2(g)/HCO_3^-}^{13} = \exp \left\{ \left(\frac{9483}{T_K} + 23.89 \right) \cdot 10^{-3} \right\} - 1$	O'Neil et al. (1969)
$\alpha_{calcite/HCO_3^-}^{13} = \epsilon_{calcite/HCO_3^-}^{13} - 1$	$\epsilon_{calcite/HCO_3^-}^{13} = \left(\frac{4132}{T_K} + 15.10 \right) \cdot 10^{-3}$	Beck et al. (2005)
oxygen		
$\alpha_{H_2O(l)/HCO_3^-}^{18} = \epsilon_{H_2O(l)/HCO_3^-}^{18} - 1$	$\epsilon_{H_2O(l)/HCO_3^-}^{18} = \exp \left\{ \left(\frac{-259000}{T_K^2} - 1.89 \right) \cdot 10^{-3} \right\} - 1$	Beck et al. (2005)
$\alpha_{CO_2(l)/H_2O(l)}^{18} = \epsilon_{CO_2(l)/H_2O(l)}^{18} - 1$	$\epsilon_{CO_2(l)/H_2O(l)}^{18} = \exp \left\{ \left(\frac{2520000}{T_K^2} + 12.12 \right) \cdot 10^{-3} \right\} - 1$	O'Neil et al. (1969)
$\alpha_{CO_2(g)/CO_2(l)}^{18} = \epsilon_{CO_2(g)/CO_2(l)}^{18} - 1$	$\epsilon_{CO_2(g)/CO_2(l)}^{18} = \exp \left\{ \left(\frac{-160515}{T_K^2} + \frac{1441.76}{T_K} - 1.9585 \right) \cdot 10^{-3} \right\} - 1$	Thorstenson and Parkhurst (2004)
$\alpha_{calcite/H_2O(l)}^{18} = \epsilon_{calcite/H_2O(l)}^{18} - 1$	$\epsilon_{calcite/H_2O(l)}^{18} = \exp \left\{ \left(\frac{18030}{T_K} - 32.42 \right) \cdot 10^{-3} \right\} - 1$	Kim and O'Neil (1997)
$\alpha_{H_2O(v)/H_2O(l)}^{18} = \epsilon_{H_2O(v)/H_2O(l)}^{18} - 1$	$\epsilon_{H_2O(v)/H_2O(l)}^{18} = \left(\frac{-7356}{T_K} + 15.38 \right) \cdot 10^{-3}$	Majoube (1971b)
$\alpha_{H_2O(v)/H_2O(l)}^{18} = \epsilon_{H_2O(v)/H_2O(l)}^{18} - 1$	$\epsilon_{H_2O(v)/H_2O(s)}^{18} = \left(\frac{-11839}{T_K} + 28.224 \right) \cdot 10^{-3}$	Majoube (1971a)
${}^k \alpha_{H_2O(l)/H_2O(v)}^{18} = {}^k \epsilon_{H_2O(l)/H_2O(v)}^{18} - 1$	${}^k \epsilon_{H_2O(l)/H_2O(v)}^{18} = 0.08$	Mook (2006)

Tab. 5.1: The table lists the equilibrium isotope fractionation factors used within this work. Kinetic fractionation factors quoted with the subscript k . The indices g, l and s expresses the phase of the substances, g for gaseous, l for liquid and s for solid.

Recent publications suggest that calcite precipitation occurs under kinetic or disequilibrium isotope fractionation effects as derived by the comparison of the oxygen isotope composition of cave drip water and calcite (Mickler et al., 2006; Tremaine et al., 2011; McDermott et al., 2011) or from measurements from the underwater cave Devil’s Hole with calcite precipitated on the ground of the cave Coplen (2007). Also the loss of CO₂ from the solution is rather fast compared to the exchange time for oxygen isotopes between HCO₃⁻ and H₂O (Dreybrodt, 2012) provoking that the precipitation of calcite occurs under kinetic or disequilibrium isotope conditions. The isotope fractionation factors and -enrichment factors for each chemical reaction or physical process of the carbon and oxygen isotopes, respectively, are listed in Tab. 5.1; T_K is the temperature given in degree Kelvin.

5.3.2 The big debate - Part I

The comparison between the oxygen isotopic composition of calcites and those of the solutions, indicates that calcite precipitation occurs under kinetic or disequilibrium isotope fractionation effects (Mickler et al., 2006; Coplen, 2007; Tremaine et al., 2011; McDermott et al., 2011). However, to be able to compare the calcite and water oxygen isotope compositions a oxygen isotope fractionation factor must be applied to account for the isotope fractionation effects between calcite and water. For the oxygen isotope fractionation $^{18}\alpha_{\text{calcite}/\text{H}_2\text{O}}$ between calcite and water, this is the widely accepted relationship derived by Kim and O’Neil (1997). However, Coplen (2007) questioned the $^{18}\alpha_{\text{calcite}/\text{H}_2\text{O}}$ derived by Kim and O’Neil (1997) claiming that it underestimated oxygen isotope fractionation effects for the analysed samples, assuming that the analysed calcite was precipitated under isotope equilibrium conditions. The studies of Tremaine et al. (2011) and McDermott et al. (2011) do also observe an underestimation of oxygen isotope fractionation effects and supports Coplen (2007) conclusion that $^{18}\alpha_{\text{calcite}/\text{H}_2\text{O}}$ measured by Kim and O’Neil (1997) does not describe equilibrium isotope fractionation effects, or that at least disequilibrium effects modify the isotopic composition of speleothem calcite. However, the question whether the relation of $^{18}\alpha_{\text{calcite}/\text{H}_2\text{O}}$ derived by Kim and O’Neil (1997) describes equilibrium isotope fractionation or not, is yet not answered. Another complication to answer this question is that disequilibrium isotope fractionation effects do modify the oxygen and carbon isotopic composition of precipitated calcite as demonstrated by laboratory experiments (Wiedner et al. (2008); Polag et al. (2010)). Furthermore, theoretical models have been derived to explain the observed disequilibrium effects. These models indicate that the oxygen and carbon isotopic composition depends besides from temperature on the drip interval, the drip pCO₂ value and the cave pCO₂ value (Mühlinghaus et al., 2007, 2009; Deininger et al., 2012).

6

Oxygen and carbon isotopes in speleothems: Basic concepts

Speleothems provide an unique climate archive that has recorded variations in the proxy cycles of hydrogen, oxygen and carbon isotopes. First studies used these environmental tracers in the late 1960s and 70s pushing speleothem science forward and highlighting the potential of stable hydrogen, oxygen and carbon isotopes in speleothems (Hendy and Wilson, 1968; Duplessy et al., 1970b; Harmon et al., 1978; Gascoyne et al., 1978). At the same time that investigations of stable isotopes in speleothems were conducted, concepts were missing that keep at hand explanations for observed variations. A milestone was achieved by Hendy (1971)s investigation of the processes in karst zones and caves that were responsible for the modifications of the carbon and oxygen isotopes of speleothems. Usdowski et al. (1979) applied an approach originally published by Rayleigh (1902) to calculate the isotopic evolution of a solution during the precipitation of inorganic CaCO_3 . This approach has inspired many studies in the last decade focussing on the complex relationships of the isotope system of the CO_2 - H_2O - CaCO_3 system (Mühlinghaus et al., 2007, 2009; Dreybrodt, 2008; Scholz et al., 2009; Deininger et al., 2012). Complete studies were conducted to understand the whole proxy-cycle of carbon and oxygen isotopes (e.g. Salomons and Mook, 1986; Dansgaard, 1964). Salomons and Mook (1986) summarised processes in the weathering zone affecting the carbon isotope composition of aqueous solutions. Concerning oxygen and hydrogen isotopes in precipitation, Dansgaard (1964) published a comprehensive review that highlights several processes that could change the stable isotopic composition of precipitation.

In the following section, a focus shall be put on the Rayleigh approach that has been applied in many publications in order to understand variations in calcite's $\delta^{18}\text{O}$ and $\delta^{13}\text{C}$ values (Usdowski et al., 1979; Salomons and Mook, 1986; Mühlinghaus et al., 2007, 2009; Scholz et al., 2009; Deininger et al., 2012). The cited studies were addressed to explain the observed disequilibrium effects in natural $\delta^{18}\text{O}$ and $\delta^{13}\text{C}$ values of speleothems (e.g. Mickler

et al., 2006; Coplen, 2007; Tremaine et al., 2011; McDermott et al., 2011). A comprehensive overview of Rayleigh approach and its applications is given by Mook and de Vries (2000).

6.1 The Rayleigh approach

The concept of the Rayleigh approach (Rayleigh, 1902) describes the isotopic evolution of a reservoir from which fractions are removed constantly. This is exactly the case for the precipitation of calcite whose reservoir is HCO_3^- . However, two assumptions are necessary to be made to apply a Rayleigh approach: (i) the reservoir must be in a state of isotopic equilibrium with the fraction being removed and (ii) the removed part can not interact with the reservoir after it's separation. This scenario is schematically illustrated in Fig. 6.1. The grey box on the right pictures the state of the reservoir before the removal of a fraction, with a volume or amount of particle/molecules N and an isotopic ratio R ; the grey box on the left represents the state of the reservoir after the removal of the fraction with a changed volume or amount of particles/molecules $N+dN$ and a changed isotopic ratio $R+dR$. The isotopic ratio of the removed fraction (dark grey box) is determined by the isotope fractionation factor α and the isotopic ratio of the reservoir. In the same manner, addition sources and sinks can be added to the boxes illustrated in Fig. 6.1 (e.g. Mook and de Vries, 2000). Nevertheless, for the explanation of the Rayleigh approach, the description is limited on the boxes of Fig. 6.1.

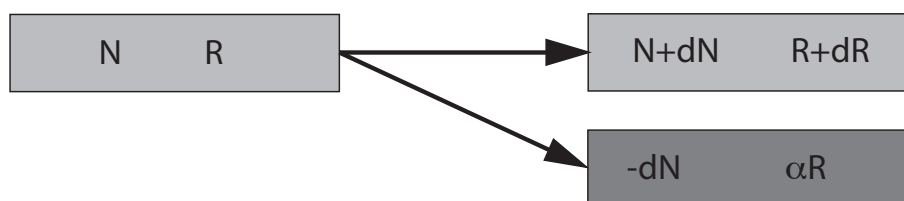


Fig. 6.1: The chart pictures the very basic concept of a Rayleigh process. From a given reservoir with volume or amount of particles, N , with isotope ratio R , a specific amount dN of volume or particles is removed by a physical or chemical process. The removal is accompanied by isotope fractionation processes, forced by the physical laws beyond the ongoing processes, causing that dN has a isotope ratio determined by the isotope fractionation factor α and the isotope ratio R .

The basic scheme of the Rayleigh approach illustrated in Fig. 6.1 highlights a simple fact beyond the concept: the mass conservation between the box(es) on the left side and the boxes on the right side. This can be expressed in an equation. The reservoir N is composed of abundant (light) N_a and rare (heavy) N_r molecules and N is simply the sum of both of them.

$$N = N_a + N_r \quad (6.1)$$

Since R is the ratio between rare and abundant molecules, N_a and N_r can be calculated with the following equations using only N and R:

$$N_a = \frac{N}{1 + R}, \quad (6.2)$$

$$N_r = \frac{R \cdot N}{1 + R}. \quad (6.3)$$

To calculate the evolution of R in dependence of the amount of removed fractions from the reservoir, Eq. (6.3) can be used to express the mass conservation for rare molecules, resulting in following equation:

$$\frac{R}{1 + R} \cdot N = \frac{R + dR}{1 + R + dR} \cdot (N + dN) + \frac{\alpha \cdot R}{1 + \alpha \cdot R} \cdot (-dN). \quad (6.4)$$

The left side of Eq. (6.4) is the amount of rare molecules before the fraction $-dN$ was removed from the reservoir. The fraction $-dN$ was composed of rare N_r molecules, which is expressed by the second term on the right side of Eq. (6.4). The first term on the right of Eq. (6.4) is the amount of rare molecules that remain in the reservoir after the removal of $-dN$; dR quotes the change in the isotopic ratio of the reservoir. The evolution of R can be calculated by solving Eq. (6.4) after separating the variables and assuming that $(1+R) \approx (1+R+dR) \approx (1+\alpha R)$, because the change dR is small compared to R and $\alpha \approx 1$ (e.g. [Mook and de Vries, 2000](#)). The solution is

$$R(N) = R_0 \cdot \left(\frac{N}{N_0} \right)^{1-\alpha}. \quad (6.5)$$

If N is a function of time, Eq. (6.5) can be formulated as:

$$R(t) = R_0 \cdot \left(\frac{N(t)}{N_0} \right)^{1-\alpha}. \quad (6.6)$$

The solution of Eq. (6.4) describes the isotopic evolution of the reservoir, expressed by R and is dependent on the evolution of N, whereas N is a function of time and so is, consequently, R. The temporal evolution of R is determined by the ratio between N and N_0 , which is the amount of molecules at time $t=0$; R_0 is the isotopic ratio of the reservoir at time $t=0$. Furthermore, R depends on the isotope fractionation factor α .

6.2 Limitations of the Rayleigh approach

As stated in the previous section, the Rayleigh approach is based on the two assumptions. Namely, that the reservoir is in a state of isotopic equilibrium and that the fraction being removed is not interacting with the reservoir after it's removal. The first assumption is likely not fulfilled and has been questioned by [Dreybrodt \(2008\)](#) where he presented a kinetic model for the stable isotope evolution of the $\text{CO}_2\text{-H}_2\text{O-CaCO}_3$ system. The main argument of [Dreybrodt \(2008\)](#) is that equilibrium isotope fractionation factors are applied by most studies using a Rayleigh approach ([Mühlinghaus et al., 2007, 2009](#); [Scholz et al., 2009](#); [Deininger et al., 2012](#)). However, even though this argument is true, it is lacking one important fact: kinetic isotope fractionation factors are unknown for the $\text{CO}_2\text{-H}_2\text{O-CaCO}_3$ system that is stated in the mentioned articles. Furthermore, comparison of the Rayleigh approach and the kinetic approach has shown that the difference in the isotopic evolution of carbon and oxygen isotopes in HCO_3^- is small during calcite precipitation ([Deininger et al., 2012](#); [Dreybrodt and Deininger, accepted manuscript](#)). Consequently, the difference in the oxygen and carbon isotope ratio of the precipitated calcite should be small. Another challenge of the kinetic approach of [Dreybrodt \(2008\)](#) is a new parameter γ which is not verified by laboratory experiments yet. A proof, whether the Rayleigh approach or the kinetic approach describes the evolution of the oxygen and carbon isotope ratio is still missing. Though the use of the Rayleigh approach is acceptable for calculating the isotopic dependencies of calcite's $\delta^{18}\text{O}$ and $\delta^{13}\text{C}$ values and shall be discussed in Chapter 7 and subsequent chapters. In Chapter 5 and 9 the aspects of isotope fractionation shall be discussed in detail. In particular Chapter 9 shall illuminate the question on the validity of oxygen isotope fractionation factor derived by [Kim and O'Neil \(1997\)](#).

7

Oxygen and carbon isotopes in speleothems: Processes

To understand, speak and write a foreign language, we need to learn the vocabulary of the language and the pronunciation of each word. After a lot of effort, we are able to speak the language fluently and we can have lively debates with our new learned skill. The situation is comparable with the isotope language of speleothems; to understand the meaning of the oxygen and carbon isotopes in speleothems, an "isotope dictionary" is needed to translate the speleothem's story into climate history. Hence, it is necessary to know where the oxygen and carbon isotopes we would like to read, have their origins. The oxygen and carbon isotopes of speleothems have their origin in the liquid components of the $\text{CO}_2\text{-H}_2\text{O-CaCO}_3$ system (e.g. [Hendy, 1971](#)). Therefore, to understand changes in the isotope composition of speleothems, namely, the isotope composition of CaCO_3 , the processes causing these changes need to be investigated. The formation of speleothems can be described by the summarizing chemical reaction (3.12), which is valid if HCO_3^- is the dominant carbon bearing molecule. This is the case in most natural karst areas (e.g. [Ford and Williams, 2007](#)).



The speleothem that is created by the precipitated CaCO_3 incorporates the fingerprint caused by specific signals of oxygen and carbon isotopes in HCO_3^- (Eq. 3.12). To formulate an "isotope dictionary" applying the $\delta^{18}\text{O}$ and $\delta^{13}\text{C}$ values specific for speleothems, two processes need to be investigated: (i) the processes that modify the isotope composition of HCO_3^- and (ii) the isotope fractionation effect that occur by the precipitation of CaCO_3 between HCO_3^- and CaCO_3 , respectively. Several studies have been performed during the last decades to investigate for this processes (e.g. [Hendy, 1971](#); [Usdowski et al., 1979](#)); the first study, investigating these effects in detail was published by [Hendy \(1971\)](#). In the

7.1. The change of carbon isotope composition of HCO_3^- during the precipitation of calcite

following section, a focus shall be put on the Rayleigh approach. The content of this chapter shall further be based on several selected, published studies (Mühlinghaus et al., 2007, 2009; Scholz et al., 2009; Deininger et al., 2012) and shall summarize key-points therein. The selected studies used the Rayleigh approach to calculate the oxygen and carbon isotope evolution of HCO_3^- during the precipitation of CaCO_3 . Three processes determine the isotopic evolution of HCO_3^- and as well as of the precipitated CaCO_3 (Hendy, 1971): (i) the precipitation of CaCO_3 itself; (ii) the oxygen isotope exchange between water and HCO_3^- and (iii) the evaporation of water. The latter modifies the isotopic composition in two different ways: first, the evaporation of water causes an increase in the amount of precipitated CaCO_3 . This forces stronger disequilibrium effects, i.e., by changing the influence of the precipitated CaCO_3 itself (i). Second, the evaporation of water favours light water molecules and causes an increase of heavy water molecules in the solution, altering the oxygen isotope composition via (ii). To complete this section, a fourth process shall be mentioned as well: the CO_2 exchange with the cave atmosphere. However, Dreybrodt (2008), Scholz et al. (2009) and Dreybrodt and Deininger (accepted manuscript) state that the effect of the CO_2 exchange of the solution with the cave atmosphere on the oxygen and carbon isotope composition of HCO_3^- is negligible because the exchange time is too long, to have a significant influence on the isotopic composition. The estimates of the mentioned three studies were based on theoretical considerations but an experimental examination of their assumption is not conducted yet.

In Sec. 7.1, the Rayleigh approach for the calculation of the carbon isotope composition of HCO_3^- shall be presented. The subsequent Sec. 7.2, discusses the Rayleigh approach for the oxygen isotopes of HCO_3^- is discussed. The last section, Sec. 7.4, shall give an introduction to the sensitivities of the oxygen and carbon isotope composition of calcite. Chapter 7 as a whole can be seen as one chapter of the "isotope dictionary". The other dictionary chapters include source effects (Sec. 8.1) and processes in the soil and karst zone (Sec. 8.2 and 8.3).

7.1 The change of carbon isotope composition of HCO_3^- during the precipitation of calcite

For the two different carbon isotopologues of HCO_3^- , $\text{H}^{12}\text{CO}_3^-$ and $\text{H}^{13}\text{CO}_3^-$, the isotope fractionation effects need to be accounted, that are associated with the conversion of HCO_3^- into $\text{CO}_2(\text{aq})$ and CaCO_3 need to be accounted. Applying the Rayleigh approach on this carbon isotope system, two sinks for the carbon isotopes need to be considered: CO_2 and CaCO_3 (Salomons and Mook, 1986). This is illustrated in Fig. 7.1. The box on the left side equates the state of HCO_3^- (N) before the removal of the fraction dN of HCO_3^- ; the carbon isotopic ratio is quoted as R. The 1st box on the left side (from top to bottom) represents the changed reservoir of HCO_3^- molecules with its new carbon isotopic ratio R+dR and with a changed amount of molecules N+dN. The second box represents the 1st sink, the released CO_2 , which has an amount of $-f_1\text{dN}$ and a carbon isotope ratio of $\alpha_1\text{R}$; α_1 is the

carbon isotope fractionation factor between HCO_3^- and CO_2 . The third box represents the precipitated calcite, which has an amount of $-f_3dN$ a carbon isotopic ratio determined by α_2R ; α_2 is the carbon isotope fractionation factor between HCO_3^- and calcite. The factors f_1 and f_2 are determined by the fraction of carbon isotopes being distributed by the reaction (3.12). Since the carbon isotopes are equally distributed between CO_2 and CaCO_3 , $f_1=f_2=1/2$ (reaction 3.12).

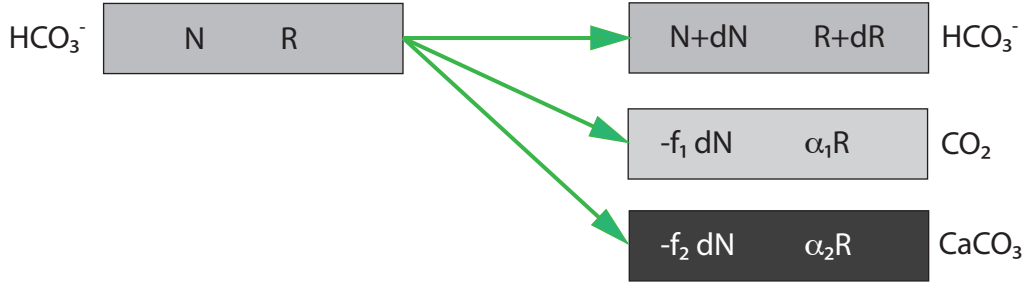


Fig. 7.1: Schematic chart of the carbon isotope system for the precipitation of calcite based on a Rayleigh approach (see text for detail).

The mass conservation for the rare isotopologue $\text{H}^{13}\text{CO}_3^-$ is according to Fig. 14.1 given by Eq. (7.1). The subscripts "13" and " HCO_3^- " of R denote that R is the stable carbon isotopic ratio between ^{13}C and ^{12}C of HCO_3^- . Furthermore, $n\text{HCO}_3^-$ is the molar mass of HCO_3^- . α_1 and α_2 are the carbon isotope fractionation factors between HCO_3^- , CO_2 and calcite, respectively; $\alpha_1 \equiv {}^{13}\alpha_{\text{CO}_2/\text{HCO}_3^-}$ and $\alpha_2 \equiv {}^{13}\alpha_{\text{calcite}/\text{HCO}_3^-}$.

$$\begin{aligned} {}^{13}R_{\text{HCO}_3^-} \cdot n\text{HCO}_3^- &= \left({}^{13}R_{\text{HCO}_3^-} + d^{13}R_{\text{HCO}_3^-} \right) \cdot \left(n\text{HCO}_3^- + dn\text{HCO}_3^- \right) \\ &+ \alpha_1 {}^{13}R_{\text{HCO}_3^-} \cdot \left(-\frac{1}{2} dn\text{HCO}_3^- \right) + \alpha_2 {}^{13}R_{\text{HCO}_3^-} \cdot \left(-\frac{1}{2} dn\text{HCO}_3^- \right) \end{aligned} \quad (7.1)$$

Eq. (7.1) can be solved by the separation of the variables. The solution is given by the following equation (Salomons and Mook, 1986; Mühlinghaus et al., 2007):

$${}^{13}R_{\text{HCO}_3^-}(t) = {}^{13}R_{\text{HCO}_3^-}(t_0) \cdot \left(\frac{n\text{HCO}_3^-(t)}{n\text{HCO}_3^-(t_0)} \right)^{\frac{1}{2}(\alpha_1 + \alpha_2) - 1}. \quad (7.2)$$

Equation (7.2) describes the temporal evolution of the stable carbon isotopic ratio of HCO_3^- , in dependence on the time-dependent evolution of HCO_3^- given by Eq. (3.33). ${}^{13}R_{\text{HCO}_3^-}(t)$ depends on the temperature dependent carbon isotope fractionation between HCO_3^- , CO_2 and calcite, respectively, and on the temperature dependence of the calcite

precipitation. Furthermore, $^{13}\text{R}_{\text{HCO}_3^-}$ depends on excess of HCO_3^- molecules, given by $[\text{HCO}_3^-](t_0) - [\text{HCO}_3^-]_{app}$, determining the degree of isotopic enrichment (Mühlinghaus et al., 2007, 2009; Scholz et al., 2009; Deininger et al., 2012). Furthermore, Deininger et al. (2012) and Dreybrodt and Deininger (accepted manuscript) demonstrated that the enrichment in ^{13}C of HCO_3^- is stronger when the evaporation of water from the solution occurs. However, Deininger et al. (2012) and Dreybrodt and Deininger (accepted manuscript) stated that the influence is only significant, if the relative humidity inside the cave is below 85 % and the wind velocity above the solution is higher than 0.2 m/s. Since the relative humidity is mostly > 95 % in cave environments, the effect of evaporation on $^{13}\text{R}_{\text{HCO}_3^-}$ and consequently on $\delta^{13}\text{C}_{calcite}$ is not discussed in the following section, because it is negligible.

7.2 The change of oxygen isotope composition of HCO_3^- during the precipitation of calcite

For the temporal evolution of the oxygen isotope composition of HCO_3^- the two isotopologues of HCO_3^- , $\text{HC}^{16}\text{O}_3^-$ and $\text{HC}^{18}\text{O}^{16}\text{O}_2^-$ are part of a complex isotope conveyor system. In addition to the oxygen isotope fractionation effect caused by the precipitation of calcite (Dreybrodt, 2008; Scholz et al., 2009), the oxygen isotope exchange between H_2O and HCO_3^- (Dreybrodt, 2008; Scholz et al., 2009) and the evaporation of H_2O (Deininger et al., 2012) from the solution must be considered. The Rayleigh approach for this complex system, composed of oxygen isotope sinks and sources, is illustrated in Fig. 7.2. The grey box frames the Rayleigh approach of Scholz et al. (2009), considering the alteration of the oxygen isotope composition of HCO_3^- by the precipitation of calcite and the oxygen isotope exchange between HCO_3^- and H_2O (reaction 3.12). The mass fluxes of H_2O out- and inside the box consider the loss (arrow 6) and input (arrow 7) of heavy HCO_3^- oxygen isotopologues by evaporation of water from the solution layer and the condensation of water vapour inside the cave, respectively. The precipitation of calcite is accompanied by the conversion of HCO_3^- into H_2O and CO_2 (reaction 3.12). The three chemical conversions inhere isotope fractionation effects quoted by the numbered arrows in Fig. 7.2. Arrow 1 quotes the conversion of HCO_3^- into calcite, arrow 2 states the conversion of HCO_3^- into CO_2 and arrow 3 expresses the conversion of HCO_3^- into H_2O . The oxygen isotope exchange between HCO_3^- and H_2O is indicated by arrow 4, depicts the loss of rare HCO_3^- oxygen isotopologues and arrow 5 illustrates the gain of rare HCO_3^- oxygen isotopologues.

The mass balance of the rare isotopologue $\text{HC}^{18}\text{O}^{16}\text{O}_2^-$ is based on the Rayleigh approach for the oxygen isotope system pictured in Fig. 7.2 and is further mathematically formulated in Eq. (7.3). The term on left side of Eq. (7.3) represents the number of rare $\text{HC}^{18}\text{O}^{16}\text{O}_2^-$ molecules. The first term on the right side is the number of rare $\text{HC}^{18}\text{O}^{16}\text{O}_2^-$ molecules after the time dt , calculated by $(^{18}\text{R}_{\text{HCO}_3^-} + d^{18}\text{R}_{\text{HCO}_3^-}) \cdot (n\text{HCO}_3^- + dn\text{HCO}_3^-)$. $(^{18}\text{R}_{\text{HCO}_3^-} + d^{18}\text{R}_{\text{HCO}_3^-})$ is the changed oxygen isotope ratio and $(n\text{HCO}_3^- + dn\text{HCO}_3^-)$ the

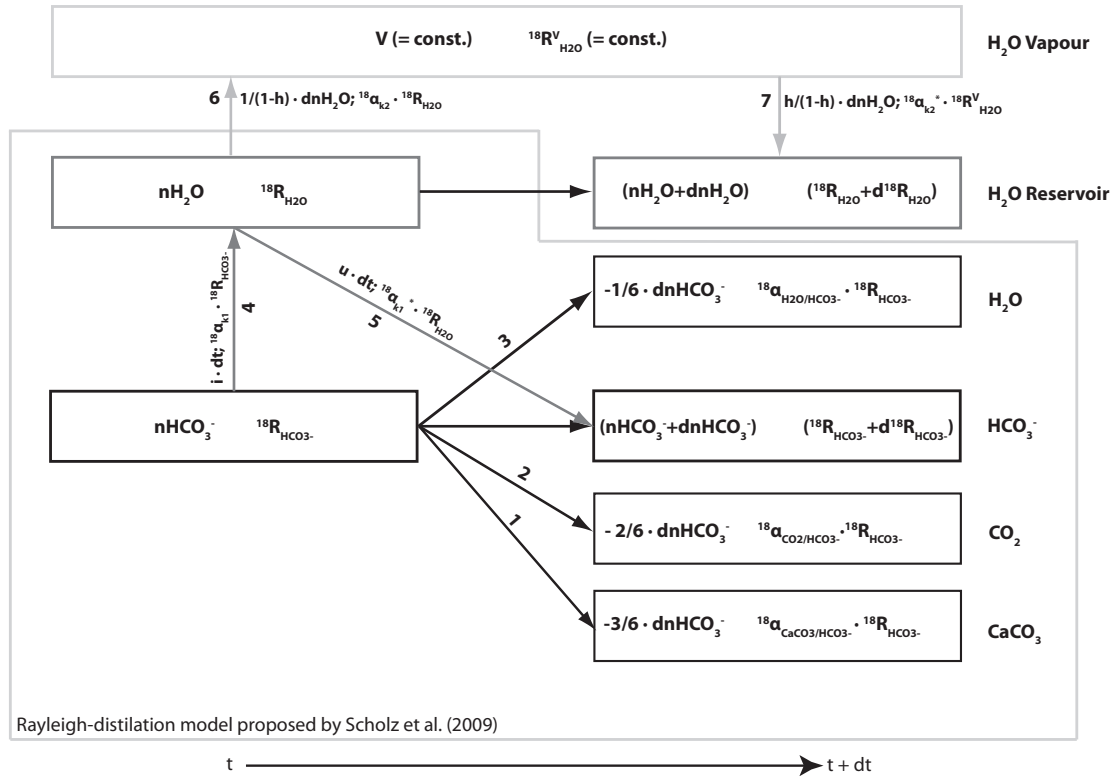


Fig. 7.2: Rayleigh approach for the oxygen isotope system of the $\text{CO}_2\text{-H}_2\text{O-CaCO}_3$ system. See text for detail (adapted from [Deininger et al., 2012](#)).

changed mass of HCO_3^- . The second, third and fourth term account for the loss of rare $\text{HC}^{18}\text{O}^{16}\text{O}_2^-$ isotopes by the conversion of HCO_3^- into CO_2 , calcite and H_2O . The weight factor of each term results from the number of oxygen atoms in each molecule. The last two terms consider the loss and gain of rare $\text{HC}^{18}\text{O}^{16}\text{O}_2^-$ isotopes by the oxygen isotope exchange between HCO_3^- and H_2O .

$$\begin{aligned}
 {}^{18}R_{\text{HCO}_3^-} \cdot n\text{HCO}_3^- &= \left({}^{18}R_{\text{HCO}_3^-} + d^{18}R_{\text{HCO}_3^-} \right) \cdot \left(n\text{HCO}_3^- + dn\text{HCO}_3^- \right) \\
 &+ \alpha_1 {}^{18}R_{\text{HCO}_3^-} \cdot \left(-\frac{2}{6} dn\text{HCO}_3^- \right) + \alpha_2 {}^{18}R_{\text{HCO}_3^-} \cdot \left(-\frac{3}{6} dn\text{HCO}_3^- \right) \\
 &+ \alpha_3 {}^{18}R_{\text{HCO}_3^-} \cdot \left(-\frac{1}{6} dn\text{HCO}_3^- \right) + \alpha_{k1} {}^{18}R_{\text{HCO}_3^-} \cdot i dt - \alpha_{k1}^* {}^{18}R_{\text{H}_2\text{O}} \cdot u dt
 \end{aligned} \quad (7.3)$$

The solution of the mass balance (Eq. 7.3) of rate $\text{HC}^{18}\text{O}^{16}\text{O}_2^-$ isotopes is ([Scholz et al., 2009](#); [Deininger et al., 2012](#)):

7.2. The change of oxygen isotope composition of HCO_3^- during the precipitation of calcite

$$\begin{aligned} \frac{d^{18}R_{\text{HCO}_3^-}}{dt} \Big|_{t^*} &= \frac{\frac{dn\text{HCO}_3^-}{dt} \Big|_{t^*} \cdot {}^{18}R_{\text{HCO}_3^-}(t^*) \left(\sum_j f_j \cdot \alpha_j - 1 \right)}{n\text{HCO}_3^-(t^*)} \\ &+ \frac{1}{\tau_B} \cdot \left(\frac{\alpha_{k1}}{\alpha_{k1}^*} \cdot {}^{18}R_{\text{H}_2\text{O}}(t^*) - {}^{18}R_{\text{HCO}_3^-}(t^*) \right). \end{aligned} \quad (7.4)$$

Eq. 7.4 can be solved numerically using the Newton procedure (Scholz et al., 2009; Mühlinghaus et al., 2009; Deininger et al., 2012) if there is no evaporation and ${}^{18}R_{\text{H}_2\text{O}}$ is constant. This is usually the case excluding evaporation, due to the larger number of H_2O molecules compared to the number HCO_3^- molecules (Dreybrodt, 2008; Scholz et al., 2009). The time constant τ_B stands for the exchange time between HCO_3^- and H_2O and lies in the range between c. 125,000 and c. 10,000 s within a temperature range between 0 and 20 °C (Dreybrodt and Scholz, 2011). α_{k1} and α_{k1}^* are the kinetic isotope fractionation factors between HCO_3^- and H_2O and vice versa. In case of evaporation, the oxygen isotope evolution of H_2O must be calculated. Likewise for the rare $\text{HC}^{18}\text{O}^{16}\text{O}_2^-$, a mass balance can be developed for the rare H_2^{18}O . The mass balance follows the oxygen isotope system shown in Fig. 7.2 and is given by (Deininger et al., 2012):

$$\begin{aligned} {}^{18}R_{\text{H}_2\text{O}} \cdot n\text{H}_2\text{O} &= \left({}^{18}R_{\text{H}_2\text{O}} + d^{18}R_{\text{H}_2\text{O}} \right) (n\text{H}_2\text{O} + dn\text{H}_2\text{O}) \\ -\frac{1}{6}\alpha_3 {}^{18}R_{\text{HCO}_3^-} \left(-d\text{HCO}_3^- \right) &+ \alpha_{k1}^* {}^{18}R_{\text{H}_2\text{O}} (udt) - \alpha_{k1} {}^{18}R_{\text{HCO}_3^-} (idt) \\ -\alpha_{k2}^* {}^{18}R_{\text{H}_2\text{O}}^V \frac{h}{1-h} \left(-d\text{H}_2\text{O} \right) &+ \alpha_{k2} {}^{18}R_{\text{H}_2\text{O}} \frac{1}{1-h} \left(-d\text{H}_2\text{O} \right). \end{aligned} \quad (7.5)$$

The term on the left side of Eq. (7.5) shows number of rare $\text{HC}^{18}\text{O}^{16}\text{O}_2^-$ isotopologues of H_2O before the mass $n\text{H}_2\text{O}$ has changed by $dn\text{H}_2\text{O}$. The term $\left({}^{18}R_{\text{H}_2\text{O}} + d^{18}R_{\text{H}_2\text{O}} \right) (n\text{H}_2\text{O} + dn\text{H}_2\text{O})$ on the right side is number of rare $\text{HC}^{18}\text{O}^{16}\text{O}_2^-$ isotopologues after the mass change of H_2O . The second term on right side accounts for the gain of H_2^{18}O . The second and third terms consider the loss and gain of $\text{HC}^{18}\text{O}^{16}\text{O}_2^-$ by the oxygen isotope exchange between HCO_3^- and H_2O . The last two terms show the gain and loss of $\text{HC}^{18}\text{O}^{16}\text{O}_2^-$ through the condensation of vaporous H_2O from the cave atmosphere and the evaporation of H_2O from the solution layer; h denotes the relative humidity inside the cave. α_{k2} and α_{k2}^* are the kinetic oxygen isotope fractionation factors between H_2O in the liquid and vaporous phase and vice versa. ${}^{18}R_{\text{H}_2\text{O}}^V$ is the oxygen isotope ratio of the water vapour inside the cave and is assumed to be constant (Deininger et al., 2012). The solution of Eq. (7.5) is stated by

$$\begin{aligned} \frac{{}^{18}R_{\text{H}_2\text{O}}}{dt} \Big|_{t^*} &= \left(\frac{\alpha_{k2}^* \alpha_{v/l} \frac{1}{1-h} \frac{dn\text{H}_2\text{O}}{dt}}{d\text{H}_2\text{O}(t^*)} - \frac{\frac{dn\text{H}_2\text{O}}{dt}}{dn\text{H}_2\text{O}(t^*)} - \frac{\alpha_3 n\text{HCO}_3^-}{\tau_B dn\text{H}_2\text{O}(t^*)} \right) \cdot {}^{18}R_{\text{H}_2\text{O}} \\ &+ \left(\frac{n\text{HCO}_3^-}{\tau_b n\text{H}_2\text{O}} - \frac{\alpha_3 \frac{1}{6} \frac{dn\text{HCO}_3^-}{dt}}{n\text{H}_2\text{O}} \right) \cdot {}^{18}R_{\text{HCO}_3^-} + \left(\frac{\alpha_{k2}^* \frac{h}{1-h} \frac{dn\text{H}_2\text{O}}{dt}}{n\text{H}_2\text{O}} \right) \cdot {}^{18}R_{\text{H}_2\text{O}}^V. \end{aligned} \quad (7.6)$$

In case of evaporation, Eq. (7.4) and Eq. (7.6) must be solved numerically with the Newton procedure, as they are a coupled differential equation system (Deininger et al., 2012). However, the enrichment of water with ^{18}O that is caused by evaporation has only a minor influence on the oxygen isotope composition of HCO_3^- in the time range that calcite precipitation occurs. The reason for this is, that the exchange time between HCO_3^- and H_2O is much longer compared to the precipitation time constant that lies within the range of c. 2000 and 300 s between 20 and 0 °C (Deininger et al., 2012; Dreybrodt and Deininger, accepted manuscript). In the same manner as the carbon isotope composition, evaporation has only a strong influence on the evolution of the oxygen isotope composition of HCO_3^- under the condition that the relative humidity inside the cave is below 85 % and the wind velocity above the solution layer is higher than 0.2 m/s (Deininger et al., 2012; Dreybrodt and Deininger, accepted manuscript). Since most caves have a relative humidity higher than 95 %, the effect of evaporation on the oxygen isotope composition is not discussed here.

7.3 Multi-box model for the solution layer

When a water drop falls from a cave ceiling and hits a stalagmite surface, splashing effects can occur. For this reason, Mühlinghaus et al. (2007) introduced a box model to account for the mixing between the falling drop and the solution layer at the top of the stalagmite. To achieve this, the solution layer is partitioned into single boxes with a distinct volume, usually 0.1 ml, being a reasonable value for the volume of drops inside caves (Mühlinghaus et al., 2007). The multi-box model for a solution layer at the top of a stalagmite is schematically illustrated in Fig. 7.3.

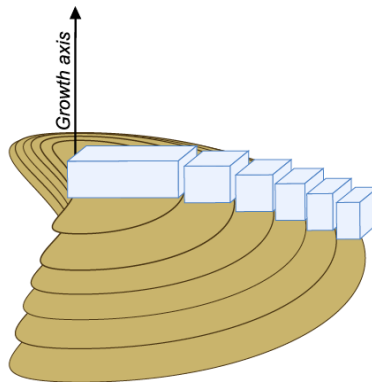


Fig. 7.3: Schematic picture of the multi-box model, that divides the solution layer into single boxes (azure boxes) (adapted from Mühlinghaus et al., 2007).

To calculate the isotope composition at the growth axis of a stalagmite only the first box of the multi-box model is of interest (Fig. 7.4). For this reason, the discussion is restricted

to the first box of the multi-box model. The mixing between the first box and the drip is expressed by a mixing coefficient ϕ , quantifying the fracture of the drop that mixes with the related box at the stalagmite centre. The whole procedure is schematically illustrated in Fig. 7.4.

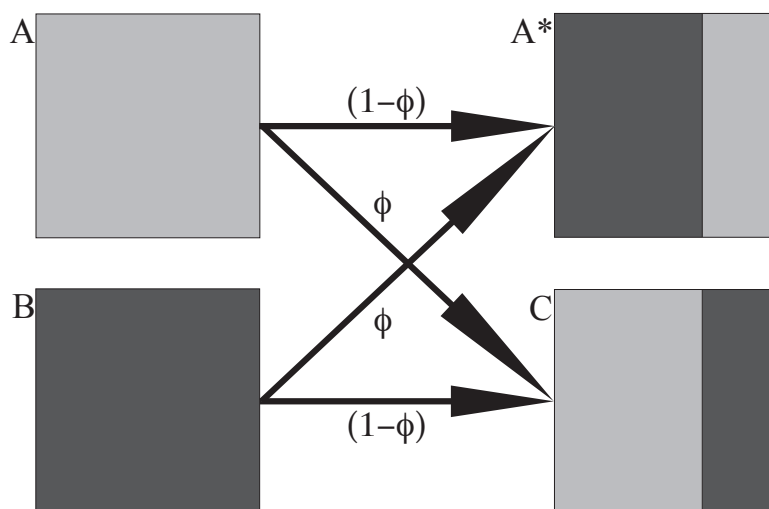


Fig. 7.4: Basic principle of the box model for the solution layer (see text for detail).

Two initial solutions with equal volumes are mixed. Box A is the first box of the solution layer at the stalagmite centre and box B represents the falling drop. The degree of mixing is determined by the mixing coefficient ϕ that expresses the fraction of the drip that replaces the fraction ϕ of box A and that mixes with the remaining fraction $(1-\phi)$ of box A. This results in a new chemical composition of box A, quoted as A*. Box C in contrast is determined in the same way but is the composition of the fraction ϕ of box A and the fraction $(1-\phi)$ of box B. In the same way as volumes, chemical concentrations or masses, the isotopic compositions are mixed. Nevertheless, this time, the isotope mixing coefficient ϕ_R for HCO_3^- is (Mühlinghaus et al., 2009):

$$\phi_R = \frac{1}{1 + \frac{1-\phi}{\phi} \frac{n\text{HCO}_3^- \text{ solution}}{n\text{HCO}_3^- \text{ drip}}} \quad (7.7)$$

For H_2O , Eq. 7.7

stays the same, only two expressions are adapted: $n\text{H}_2\text{O}_{\text{solution}}$ and $n\text{H}_2\text{O}_{\text{drip}}$. The effects of mixing on the isotopic evolution of $^{18}\text{R}_{\text{HCO}_3^-}$ and $^{13}\text{R}_{\text{HCO}_3^-}$ is discussed in detail by Mühlinghaus et al. (2009) and Deininger et al. (2012).

7.4 Sensitivity of the calcite $\delta^{18}\text{O}$ and $\delta^{13}\text{C}$ values on cave parameters

The oxygen and carbon isotopic evolution of HCO_3^- ($^{13}R_{\text{HCO}_3^-}^{eq}$, $^{18}R_{\text{HCO}_3^-}^{eq}$) that has been calculated with the Rayleigh approach (Sec. 7.1, 7.2 and 7.3) can be used to calculate the $\delta^{18}\text{O}$ and $\delta^{13}\text{C}$ values of CaCO_3 . To achieve this, the mean oxygen and carbon isotopic value of HCO_3^- are calculated ($\overline{^{13}R_{\text{HCO}_3^-}^{eq}}$, $\overline{^{18}R_{\text{HCO}_3^-}^{eq}}$) by folding the temporal evolution of the oxygen or carbon isotope composition ($^{18}R_{\text{HCO}_3^-}(t)$, $^{13}R_{\text{HCO}_3^-}(t)$) with a weight function Π , which is based on the temporal evolution of the Ca^{2+} concentration (Eq. 7.8) (Mühlinghaus et al., 2009).

$$\overline{^iR_{\text{HCO}_3^-}^{eq}} = \frac{\sum_{j=1}^n \overline{^iR_{\text{HCO}_3^-}^{eq}(\Delta t_j)} \cdot \Delta \text{Ca}^{2+}(\Delta t_j)}{[\text{Ca}^{2+}](t_0) - [\text{Ca}^{2+}](t_0 + d)} = \sum_{j=1}^n \Pi_j \cdot \overline{^iR_{\text{HCO}_3^-}^{eq}(\Delta t_j)}, i = 13, 18. \quad (7.8)$$

In Eq. (7.8), the length of Δt_j determines in how many time intervals the drip interval, d , is split in order to be able to apply a numerical use an numerical approach, namely the Newton approach; the number of time intervals is given by the number n . Therefore, Δt_j refers to the j 's time interval. Usually, a value of 1 s is chosen for the length of Δt_j . $\overline{^iR_{\text{HCO}_3^-}^{eq}(\Delta t_j)}$ is the mean oxygen ($i = 18$) or carbon ($i = 13$) isotope composition of HCO_3^- in the time interval Δt_j . $\Delta \text{Ca}^{2+}(\Delta t_j)$ is the change in the Ca^{2+} concentration in the solution during the time interval Δt_j ; the difference $[\text{Ca}^{2+}](t_0) - [\text{Ca}^{2+}](d)$ describes the change in the Ca^{2+} concentration during the drip interval, d . Hence, the ratio between the amount of converted Ca^{2+} ions during the time interval Δt_j and the total amount of converted Ca^{2+} ions within the drip interval (between t_0 and $t_0 + d$), $\Delta \text{Ca}^{2+}(\Delta t_j) / ([\text{Ca}^{2+}](t_0) - [\text{Ca}^{2+}](d))$, is the weight factor Δt_j for the time interval. The mean oxygen or carbon isotopic composition of the precipitated CaCO_3 can then be easily calculated from the mean oxygen or carbon isotopic composition of HCO_3^- , $\overline{^iR_{\text{HCO}_3^-}^{eq}}$ by multiplying $\overline{^iR_{\text{HCO}_3^-}^{eq}}$ with the isotope fractionation factor between HCO_3^- and CaCO_3 , $^i\alpha_{\text{CaCO}_3/\text{HCO}_3^-}$ for the related stable isotope, i.e., oxygen ($i = 18$) or carbon ($i = 13$) (Eq. 7.9) (see Mühlinghaus et al., 2009; Deininger et al., 2012, for detail).

$$\overline{^iR_{\text{CaCO}_3}^{eq}} = ^i\alpha_{\text{CaCO}_3/\text{HCO}_3^-} \cdot \overline{^iR_{\text{HCO}_3^-}^{eq}}, i = 13, 18. \quad (7.9)$$

The sensitivity of the calcite $\delta^{18}\text{O}$ or $\delta^{13}\text{C}$ values on specific cave parameter, namely temperature, T , drip interval, d , $\text{pCO}_{2,\text{drip}}$ and $\text{pCO}_{2,\text{cave}}$, can be calculated from Eq. (7.9) by varying the parameters of interest and keeping the remaining parameters constant. This is illustrated for the sensitivity of calcite the $\delta^{18}\text{O}$ or $\delta^{13}\text{C}$ values on temperature and drip interval in Fig. 7.5 and on $\text{pCO}_{2,\text{drip}}$ and $\text{pCO}_{2,\text{cave}}$ in Fig. 7.6, respectively.

Comparing the sensitivity of the calcite $\delta^{18}\text{O}$ and $\delta^{13}\text{C}$ values on temperature reveals that $\delta^{18}\text{O}$ has a negative sensitivity on temperature changes whereas $\delta^{13}\text{C}$ has a positive sensitivity on temperature changes. Furthermore, $\delta^{18}\text{O}$ has a higher sensitivity on temperature changes compared to $\delta^{13}\text{C}$. Only for moderate drip intervals (500 - 1,800 s) and low temperatures ($T < \approx 2\text{ }^\circ\text{C}$), the temperature sensitivity of $\delta^{18}\text{O}$ or $\delta^{13}\text{C}$ is of comparable magnitude and ranges between -0.16 and -0.18 ‰/°C for $\delta^{18}\text{O}$ and between 0.12 and 0.14 ‰/°C for $\delta^{13}\text{C}$ (Fig. 7.5 a and b). For short drip intervals (1 and 50 s), the temperature sensitivity of precipitated calcite $\delta^{18}\text{O}$ values decreases linearly with higher temperatures and has a temperature sensitivity between -0.24 and -0.23 ‰/°C at 0 °C and between -0.19 and -0.21 at 20 °C. The temperature sensitivity of the calcite $\delta^{13}\text{C}$ values in contrast, is constant for short drip intervals, and ranges between 0.05 and 0.07 ‰/°C within a temperature interval between 0 and 20 °C. However, the temperature sensitivity of the calcite $\delta^{13}\text{C}$ values is one order of magnitude smaller compared to temperature sensitivity of the calcite $\delta^{18}\text{O}$ values (Fig. Fig. 7.5 a and b). For moderate drip intervals, the shape of the temperature sensitivity is similar for $\delta^{18}\text{O}$ and $\delta^{13}\text{C}$. However, while the temperature sensitivity for $\delta^{18}\text{O}$ is increasing for higher temperatures, the temperature sensitivity is decreasing for $\delta^{13}\text{C}$ (Fig. 7.5 a and b). [Deininger et al. \(2012\)](#) stated that the complex behaviour of the temperature sensitivity of precipitated calcite $\delta^{18}\text{O}$ and $\delta^{13}\text{C}$ values is caused by the interplay of stable isotope fractionation and precipitation kinetics.

The dependence of the calcite $\delta^{18}\text{O}$ and $\delta^{13}\text{C}$ values on the drip interval is illustrated in Fig. 7.5 c and d for various temperatures. Both stable isotope compositions have a similar dependence on the drip rate with a decreasing sensitivity on drip interval changes for longer drip intervals. Furthermore, the sensitivities of the $\delta^{18}\text{O}$ and $\delta^{13}\text{C}$ values on drip interval change have the same order of magnitude and range between 0.002 and 0.008 ‰/s within the given temperature interval between 0 and 20 °C. Fig. 7.5 c and d reveal that the sensitivity on drip interval changes has its highest values for smaller drip intervals, with the highest sensitivity for a temperature of 20 °C and the lowest sensitivity for a temperature of 0 °C. [Deininger et al. \(2012\)](#) explained this feature of the $\delta^{18}\text{O}$ and $\delta^{13}\text{C}$ sensitivity on drip interval changes through the change of the amount of precipitated calcite. This is due to the fact that the precipitation rate is higher for higher temperatures, and consequently, disequilibrium effects are more dominant for higher temperatures and vice versa. Since the amount of precipitated calcite decreases exponentially with time, the weight function Π_j becomes smaller with a prolonged precipitation time; the effect of drip interval changes on the mean stable isotope composition of precipitated calcite is higher for drip interval changes at short drip intervals, and smaller for drip interval changes at longer drip intervals.

In addition to temperature and drip interval changes, variations in $\text{pCO}_{2,drip}$ and $\text{pCO}_{2,cave}$ can also change the mean stable isotope composition of precipitated calcite ([Deininger et al., 2012](#)). This is depicted in Fig. 7.6: The upper two figures (Fig. 7.6 a and b) illustrate the sensitivity of the calcite $\delta^{18}\text{O}$ and $\delta^{13}\text{C}$ values due to changes in $\text{pCO}_{2,cave}$ (Fig. 7.6c) and due to changes in $\text{pCO}_{2,drip}$ (Fig. 7.6d). [Deininger et al. \(2012\)](#) demonstrated that the dependence of the calcite $\delta^{18}\text{O}$ and $\delta^{13}\text{C}$ values on these two variables is based on the same process, namely the chemical $[\text{Ca}^{2+}]$ excess (see Chapter 3 for details about the $[\text{Ca}^{2+}]$

excess). This explains the different algebraic sign of the $\delta^{18}\text{O}$ and $\delta^{13}\text{C}$ sensitivity on changes of pCO_2 .*drip* and pCO_2 .*cave*. An increase of pCO_2 .*drip* results in a higher precipitation rate and further in stronger isotope disequilibrium effects; whereas an increase of pCO_2 .*cave* forces a slower precipitation rate and consequently weaker isotope disequilibrium effects and vice versa (Deininger et al., 2012). The magnitude of changes in the mean calcite $\delta^{18}\text{O}$ and $\delta^{13}\text{C}$ values is in the range of ± 0.0015 ‰/ ppm.

7.4. Sensitivity of the calcite $\delta^{18}\text{O}$ and $\delta^{13}\text{C}$ values on cave parameters

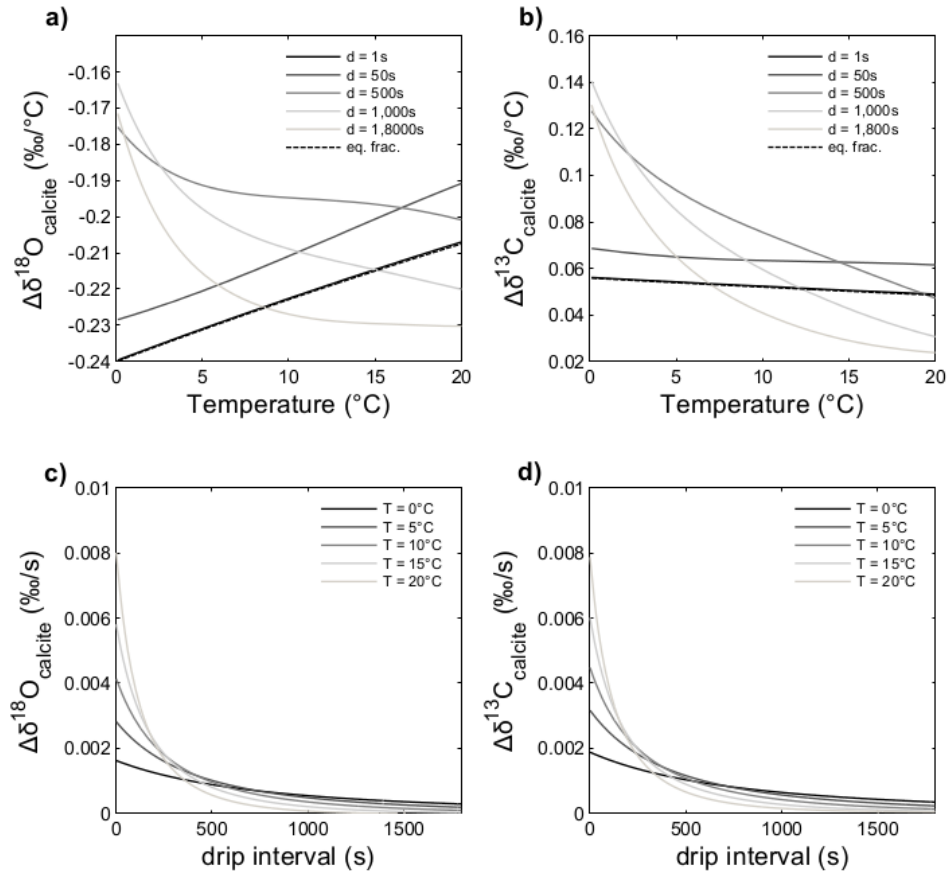


Fig. 7.5: Panels (a) and (b) picture the sensitivity of the calcite $\delta^{18}\text{O}$ and $\delta^{13}\text{C}$ values on the temperature for different drip intervals. Panels (c) and (d) illustrate the sensitivity of the calcite $\delta^{18}\text{O}$ and $\delta^{13}\text{C}$ values on the drip interval for different temperatures (adapted from [Deininger et al., 2012](#)).

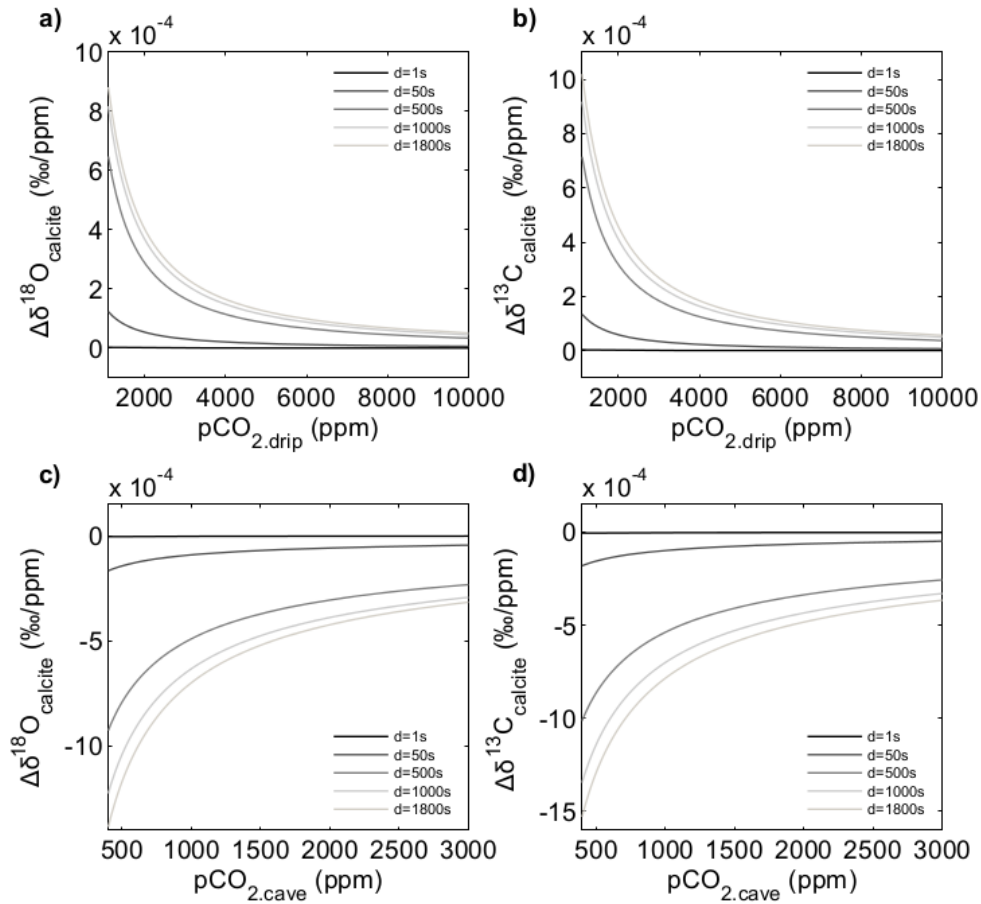


Fig. 7.6: Panels (a) and (b) picture the sensitivity of the calcite $\delta^{18}\text{O}$ and $\delta^{13}\text{C}$ values on the pCO₂ value of the drip water (solution) for different drip intervals. Panels (c) and (d) illustrate the sensitivity of the calcite $\delta^{18}\text{O}$ and $\delta^{13}\text{C}$ values on the pCO₂ value of the cave atmosphere for different drip intervals (adapted from [Deininger et al., 2012](#)).

8

Processes above the cave: From the source to the cave

In the previous chapters (Chapter 5-7) the isotope fractionation processes were discussed that may modify the oxygen and carbon isotopic composition of the precipitated calcite. However, it was ignored that the oxygen and carbon isotopic composition of drip water may naturally change during the growth history of a speleothem due to surficial climate changes. The reason for this is, that the seepage transfers the oxygen isotope composition of the precipitation and the carbon isotopic composition of the CO₂ in the soil zone through the soil and karst zone and becomes drip water when entering a cave. On the pathway through the subsurface a handful of processes, however, can modify the original isotopic fingerprint of the different oxygen and carbon isotope sources. In the following sections the effects that alter the oxygen (Sec. 8.1) and carbon (Sec. 8.2) isotopic fingerprint of the sources shall be discussed.

8.1 The source of the water (isotopes) entering a cave

The water dripping from a cave ceiling originates from the water that is infiltrated in the karst zone. The latter is the difference between the amount of precipitation and the amount of water that is lost from the soil zone by evaporation and plant transpiration (evapo-transpiration). Hence, the oxygen isotope composition of the drip water inheres the oxygen isotope fingerprint of the local precipitation above the cave. Accordingly, to understand the oxygen isotope composition of a speleothem during its growth history the processes that alter the stable isotope composition of the local precipitation need to be considered (e.g. [McDermott, 2004](#); [Fairchild et al., 2006a](#); [Lachniet, 2009](#); [Wackerbarth et al., 2010](#); [Langebroek et al., 2011](#); [Jex et al., 2013](#)). In Fig. 8.1 a schematic chart of the hydrological cycle and the involved fractionation effects are illustrated. It includes all processes that occur until a stalagmite is formed, beginning with the evaporation of oceanic

8.1. The source of the water (isotopes) entering a cave

surface waters and ending with the fall of the drip from the cave ceiling.

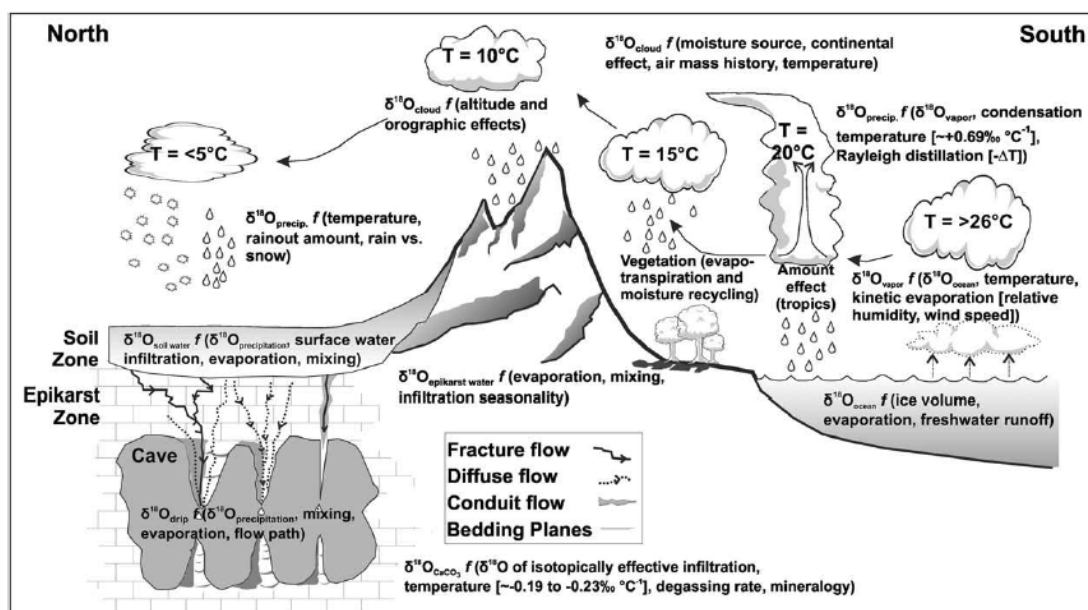


Fig. 8.1: The figure is illustrating the hydrological cycle and the fractionation effects that occur during the various processes until ultimately the drip falls from the cave ceiling (adapted from Lachniet, 2009).

From a simplified point of view, caves drip waters origin from the largest water reservoirs of our planet, the oceans, and are an intermediate component of the hydrological cycle. In this respect the discussion of the various processes affecting the stable isotopic composition of the precipitation starts with the processes that determine the stable isotopic composition of the oceans. The ocean stable isotopic composition is determined by the stable isotopic composition of the sources and sinks of the fresh water (e.g. Mook and de Vries, 2000; Gat, 1996). The two main sources are the runoff of freshwater from the continents and input of freshwater by the deglaciation of the ice sheets. The latter has an effect of approximately $0.011 \text{‰}/\text{m}$ (Fairbanks, 1989). Moreover, the evaporated water ($\delta^{18}\text{O}_{\text{vapour}}$) from the surface ocean waters causes a preferential selection of light water isotopologues and is determined from the stable isotopic composition of the ocean surface water ($\delta^{18}\text{O}_{\text{ocean}}$) and the stable isotope fractionation effect of the evaporation (Merlivat and Jouzel, 1979) (*source effect*). The stable isotope fractionation of the evaporation depends on the sea surface temperature (SST), the relative humidity and the wind velocity above the ocean surface (Merlivat and Jouzel, 1979). The evaporated water is lifted and transported by the atmospheric circulation. The uplift of the atmospheric moisture causes a cooling due to the conversion of thermic energy into potential energy. As long as the air temperature is higher than the dew point the cooling can be described with a dry adiabatic uplift and if the temperature is below the dew point, the condensation of the atmospheric moisture occur, i.e., the formation of clouds and precipitation, and cooling can be calculated with a moist adiabatic

uplift (Dansgaard, 1964). The isotopic composition of the condensate depends on the air temperature at the moment of condensation and the isotopic composition of the atmospheric moisture and can be calculated with a Rayleigh approach (Rayleigh, 1902; Dansgaard, 1964) (*temperature effect*). The continuous condensation of atmospheric moisture over the continent and the subsequently precipitation causes a progressive depletion of heavy water isotopologues in the atmospheric moisture. Hence, the stable isotopic composition of the precipitation is decreasing as an effect of the depletion of heavy isotopes in the atmospheric moisture (*continental effect*). Recently, McDermott et al. (2011) demonstrated that the continental effect observed in the European precipitation is preserved by speleothems $\delta^{18}\text{O}$ values. Moreover, in tropical regions convective rainfall events are causing a depletion of the stable isotopes in precipitation that depends on the amount of precipitation (*amount effect*) (Dansgaard, 1964).

When the precipitation impacts the surface, with a certain stable isotopic composition $\delta^{18}\text{O}_{\text{precipitation}}$, enters the soil zone. Within the soil zone, the soilwater can be lost due to evaporation or by the take up of plants Gat (1996). Both processes have only a subordinate effect on the stable isotopic composition of the soilwater ($\delta^{18}\text{O}_{\text{soilwater}}$). This is due to the reason that the take up of water by plants is mainly not accompanied by fractionation effects (Münnich, 1978; Gat, 1996). The evaporation of water has usually no effect on the isotopy of the residual soilwater, because the water that is evaporated within the top soil is replaced by soilwater from below. However, for semi-arid and arid regions, where precipitation events are interrupted by a dry intervals, evaporation of water during the dry intervals can cause an enrichment of heavy isotopes in the soilwater (Zimmermann et al., 1967; Münnich, 1978; Gat, 1996). For a steady state system, the isotopy of the evaporated and transpired water has the same isotopy as soilwater, i.e., it has the same isotopic composition as the precipitation (Münnich, 1978; Gat, 1996) - evaporation and transpiration are usually referred as evapo-transpiration. The residual soilwater is then pushed ahead when new precipitation events occur and transfers the isotopic fingerprint of the precipitation (only for non semi-arid and arid regions) and infiltrates the deeper layers of the soil zone and subsequently the karst zone. The annual isotopic composition of the infiltrated water depends on seasonal amount of precipitation and evapo-transpiration and can be consequently seasonally biased. In the soil zone the water becomes into contact with gaseous CO_2 - the major source of carbon isotopes in the soil zone-, that origin from root respiration and the decomposition of organic mater, and dissolves CO_2 (Salomons and Mook, 1986).

The oxygen isotope composition of the $\text{CO}_2\text{-H}_2\text{O-CaCO}_3$ system is determined by the oxygen isotope composition of the infiltrated water. The carbon bearing species are equilibrating with the oxygen isotope composition of H_2O by the hydration of aqueous CO_2 and the dehydration of HCO_3^- (Mills and Urey, 1940; Hendy, 1971) with respect to the oxygen isotope fractionation factors between all species. Due to the fact that the amount of water molecules is much higher ($\approx 10^5$) compared to the total dissolved carbonates (CO_2 , H_2CO_3 , HCO_3^- , CO_3^{2-}) the influence on the oxygen isotope composition of water is negligible (e.g. Dreybrodt, 2008; Scholz et al., 2009). The exchange time for the oxygen isotope exchange

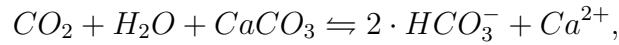
τ_B is according to [Dreybrodt and Scholz \(2011\)](#) between 125,700 s (c. 1. 46 days) at a temperature of 0 °C and 6200 s at a temperature of 25 °C (c. 1.72 h); for a temperature of 10 °C the exchange time τ_B is 35,300 s (c. 9.80 h). After 4 times τ_B the oxygen isotope system of the CO₂-H₂O-CaCO₃ system is almost in isotope equilibrium (> 98 %). For the most European regions with a mean annual air temperature of c. 10 °C and under the assumption that the temperature in the karst zone equates the mean annual air temperature the CO₂-H₂O-CaCO₃ system is in oxygen isotope equilibrium (> 98 %) after c. 1.63 days. If the transition time through the limestone is longer than the equilibration time the CO₂-H₂O-CaCO₃ system is in oxygen isotope equilibrium. Hence, if no further effects occur after the dissolution of CaCO₃ in the karst zone until point of time when a stalagmite is formed on the cave ground (Sec. 8.3), the drip water falling from the cave ceiling has the same oxygen isotope composition as the precipitation above the cave (e.g. [Hendy, 1971](#)).

8.2 The sources carbon isotopes in the subsurface

The atmospheric CO₂ concentration has a value of ≈ 395 ppm and is constantly increasing since the last 100 years. It has been demonstrated by [Keeling \(1958\)](#) that the $\delta^{13}\text{C}$ value of the atmospheric CO₂ concentration has a relation to the atmospheric CO₂ concentration, caused by the combustion of fossil fuels and biospheric activity ([Suess, 1955](#); [Keeling, 1979](#)). However, the input of CO₂ in the soil zone, due to the take up of drops is only of subordinate order ([Gorham, 1955](#)) and the major sources of CO₂ in the soil zone are the vegetation and the decay of organic matter ([Salomons and Mook, 1986](#)). The pCO₂ value within the soil zone can be between 300 ppm and 11,500 ppm ([Atkinson, 1977](#); [McDermott, 2004](#)). Usually, the CO₂ concentration depends on the plant activity and can vary within a year ([Salomons and Mook, 1986](#)). The $\delta^{13}\text{C}$ value of the CO₂ that originates from plants depends on the photosynthetic cycle of the corresponding plant; these cycles are the Calvin cycle (C₃), the Hatch-Slack cycle (C₄) and the Crassulacean acid metabolism cycle (CAM), which is an intermediate cycle between the C₃ and C₄ cycle (see [Deines, 1980](#), for a review). For the C₃ cycle the $\delta^{13}\text{C}$ values vary between -22 ‰ -34 ‰ with a maximum of the distribution at -27 ± 2 ‰. The $\delta^{13}\text{C}$ values for the C₄ cycle are vary between -9 ‰ and -19 ‰ with a maximum of the distribution at 12 ± 2 ‰ ([Salomons and Mook, 1986](#)).

The water that is infiltrated into the upper soil zone is equilibrating with the CO₂ concentration within the soil zone and the carbon bearing species of the CO₂-H₂O system is in isotopic equilibrium with the present CO₂. Hence, the soilwater becomes a corrosive solution with respect to CaCO₃ after equilibration with the CO₂ that is present in soil zone. After the transition the soilwater infiltrates the karst zone, where carbonate rocks are present (Fig. 3.1).

When the corrosive solution comes into contact with the limestone carbonate, CaCO₃ is dissolved in accordance with the overall chemical reaction



for the $\text{CO}_2\text{-H}_2\text{O-CaCO}_3$ system. Two different modes of CaCO_3 dissolution are possible (Hendy, 1971) (i) the dissolution under "open system" conditions where the solution is in contact with a CO_2 reservoir that balances the loss of CO_2 caused by the CaCO_3 dissolution. Hence, the CO_2 concentration of the solution is unchanged during the dissolution process; (ii) the dissolution under "closed system" conditions where the solution is separated from any additional CO_2 reservoir in the karst zone until the solution enters the cave. The state of dissolution of CaCO_3 has two consequences onto the $\text{CO}_2\text{-H}_2\text{O-CaCO}_3$ system: it first determines the amount of CaCO_3 that can be dissolved by the corrosive solution. Assuming a similar pCO_2 value in the soil zone for open and closed system conditions, then more CaCO_3 is dissolved under open system conditions, because more CO_2 is available during the dissolution in comparison to a closed system state Hendy (1971). As a consequence of the dissolution, the $\delta^{13}\text{C}$ value of the original solution is modified because the $\delta^{13}\text{C}$ of the limestone is usually ≈ 0 ‰ (e.g. Salomons and Mook, 1986) and is therefore more positive than the usual $\delta^{13}\text{C}$ value of the solution, which is determined by the vegetation (C3, C4, CAM) above the soil and karst zone. Hence, the $\delta^{13}\text{C}$ value of the solution is determined by the amount of carbon bearing species in the solution before the dissolution of CaCO_3 and the amount of dissolved CaCO_3 and the $\delta^{13}\text{C}$ value of CaCO_3 . The amount of dissolved CaCO_3 depends on the karst system configuration and so does the $\delta^{13}\text{C}$ value of the carbon bearing species of the solution Hendy (1971). The effect is that after the dissolution of CaCO_3 the $\delta^{13}\text{C}$ value of the solution for a given pCO_2 value in the soil zone is more positive for a closed system than for an open system (Salomons and Mook, 1986). Furthermore, the $\delta^{13}\text{C}$ value of the solution depends on the pCO_2 value of the soil zone. Salomons and Mook (1986) demonstrate that for a solution that is in chemical equilibrium (i.e., after the dissolution of CaCO_3) the $\delta^{13}\text{C}$ value of the solution decreases with increasing pCO_2 . Another aspect of the dissolution within the karst zone is the incongruent dissolution, that occurs for example if the solution comes into contact with dolomite. Assuming that the solution was in chemical equilibrium with respect to calcite then calcite would be precipitated and dolomite would be dissolved which would also modify the isotopy of the solution (Reardon and Fritz, 1978; Wigley et al., 1978; Salomons and Mook, 1986). This context is not further discussed here. If no additional processes occur during percolation of the solution through the limestone then the carbon isotopic composition of the drip water inside a cave is similar to the carbon isotopic composition of the solution after chemical equilibration (i.e., after the dissolution of CaCO_3) and is determined (for a constant temperature) by the pCO_2 of the soil zone and the system configuration of the karst zone. The latter can be an open system, a closed system or an intermediate between both - an intermediate state is, if the dissolution of CaCO_3 occurs partly under an open system and a under closed system configuration (Hendy, 1971; Buhmann and Dreybrodt, 1985a,b; Fohlmeister et al., 2011; Dreybrodt and Scholz, 2011).

8.3 Prior calcite precipitation (PCP) - Precipitation of calcite before the formation of a speleothem

As mentioned in the foregoing sections, the oxygen and the carbon isotope composition of the drip water equates the isotope composition of the percolating solution if no further processes have occurred after the dissolution of CaCO_3 . However, it is possible that the solution enters a fracture within the host rock that has a lower pCO_2 value at which the solution is supersaturated with respect to calcite. Hence, calcite is precipitated which would cause an enrichment of ^{18}O and ^{13}C in the solution (Hendy, 1971; Salomons and Mook, 1986; Mühlinghaus et al., 2007; Dreybrodt, 2008; Scholz et al., 2009). Another effect forcing calcite precipitation within the karst zone is the evaporation of water from solution (Hendy, 1971). The precipitation of calcite before the formation of a speleothem is stated as "*prior calcite precipitation*" (PCP). The precipitation is different in an "*open system*" and a "*closed system*" (Hendy, 1971; Salomons and Mook, 1986). For an open system the solution is in active contact with an atmosphere and exchanges CO_2 with the atmosphere, whereas for a closed system the solution is not in contact with a atmosphere and only CO_2 is degassed from the solution - the CO_2 originates from the calcite precipitation. Hendy (1971) states that open systems behave like closed systems if the pCO_2 of the solution is higher than 0.1 % atm (1000 ppm). If, however, the pCO_2 of the solution is 0.03 % (300 ppm) the system must be considered as an open system Hendy (1971). The pCO_2 value within the soil and karst zones is in the range of 0.03 % (300 ppm) to 11.5 % (11,500 ppm) (mean value 0.9 %; 9000 ppm). For this reason the effect of calcite precipitation within veins is considered as a closed system. The difference of calcite precipitation within a cave from the precipitation of calcite inside a vein is, that the CO_2 which forms during the calcite precipitation is accumulated inside the vein whereas it has a negligible effect on the pCO_2 value of the cave because of the large volume of caves.

If calcite is precipitated from a solution the oxygen and the carbon isotopic composition of the $\text{CO}_2\text{-H}_2\text{O-CaCO}_3$ system in solution becomes enriched in ^{18}O and ^{13}C - if the solution was in chemical equilibrium before PCP, the pH value of the solution is c. 8 and therefore the carbonate system consists mainly of HCO_3^- (e.g. Dreybrodt, 1988). For this reason the discussion is restricted to HCO_3^- instead of the terminus " $\text{CO}_2\text{-H}_2\text{O-CaCO}_3$ system". Hendy (1971) used a Rayleigh approach to calculate the effect of calcite precipitation under closed system conditions and demonstrated that the $\delta^{13}\text{C}$ value of the precipitated calcite increases with decreasing a pCO_2 value of the solution. Later studies have also shown that the $\delta^{18}\text{O}$ value of calcite increases with supersaturation of the solution by applying a Rayleigh approach (Mühlinghaus et al., 2009). Scholz et al. (2009) have presented that the $\delta^{18}\text{O}$ and $\delta^{13}\text{C}$ value of HCO_3^- increases during the precipitation of calcite by using a Rayleigh approach. Therefore, the results of (Scholz et al., 2009; Hendy, 1971; Mühlinghaus et al., 2009) show that the on one hand the carbon and oxygen isotope composition of HCO_3^- become enriched in ^{18}O and ^{13}C during the precipitation of calcite and that on the other hand the $\delta^{18}\text{O}$ and the $\delta^{13}\text{C}$ values of the precipitated calcite increase with decreasing

HCO_3^- concentration (i.e. supersaturation). The enrichment of calcite in ^{18}O and ^{13}C during the precipitation has been also experimentally proofed by [Wiedner et al. \(2008\)](#); [Polag et al. \(2010\)](#) who analysed the $\delta^{18}\text{O}$ and $\delta^{13}\text{C}$ value of precipitated calcite in a channel. But not only the precipitation of calcite in veins must be considered as PCP also the precipitation of calcite on cave ceilings is a form of PCP, i.e., the formation of stalactites. [Wiedner et al. \(2008\)](#) showed for instance for a temperature of 17.9 °C and a drip rate of 0.12 ml/min (this equates a drip interval of 50 s) that the $\delta^{18}\text{O}$ value and the $\delta^{13}\text{C}$ value is increasing with a slope of 0.027 ‰/cm and 0.031 ‰/cm, respectively, with increasing distance from the drip point (in cm). It has been also demonstrated the slope is a function of the drip rate with steeper slopes for smaller drip rates ([Wiedner et al., 2008](#)). In summary the precipitation of calcite within the karst zone or on the cave ceiling can be described by a closed system precipitation ([Hendy, 1971](#)) and the $\delta^{18}\text{O}$ and $\delta^{13}\text{C}$ value and the solution and of the precipitated calcite increases with the total amount of precipitated calcite ([Hendy, 1971](#); [Scholz et al., 2009](#); [Mühlinghaus et al., 2009](#); [Wiedner et al., 2008](#); [Polag et al., 2010](#)).

The enrichment of HCO_3^- in ^{18}O and ^{13}C during PCP has a consequence for the oxygen and carbon isotopic composition of speleothems that are formed from the solution, because the oxygen and carbon isotopic composition of the solution is modified by PCP. However, the two isotope systems must be discussed separately, because the oxygen isotope system has a large reservoir that can balance the enrichment in ^{18}O of HCO_3^- , the water, whereas the carbon isotope system has no such reservoir. If the $\text{CO}_2\text{-H}_2\text{O-CaCO}_3$ system was in oxygen isotope equilibrium before PCP occurred, the change of the oxygen isotope composition caused by PCP, is balanced by the oxygen isotope exchange between H_2O and HCO_3^- . If the transition time of the solution until the formation of a stalagmite from the precipitated solution is sufficiently long, the oxygen isotope equilibrium of the $\text{CO}_2\text{-H}_2\text{O-CaCO}_3$ system is established again. The time constants for the exchange time τ_b are given by [Dreybrodt and Scholz \(2011\)](#) (see above). The carbon isotope system of the $\text{CO}_2\text{-H}_2\text{O-CaCO}_3$ system has no reservoir and the shift in the $\delta^{13}\text{C}$ values are preserved by the percolation solution. The consequence for stalagmite $\delta^{18}\text{O}$ and $\delta^{13}\text{C}$ values is, that if PCP occurs within the karst zone and the transition time is long enough to re-establish the oxygen isotope equilibrium of the solution, the $\delta^{18}\text{O}$ values of the stalagmite reflects the oxygen isotope composition of the rain water whereas the $\delta^{13}\text{C}$ value of the stalagmite is modified by PCP. A crucial case of PCP is the formation of a stalactite above a stalagmite, because the transition time is not long enough to re-establish the oxygen isotope equilibrium of the solution and consequently, in addition to the $\delta^{13}\text{C}$, the $\delta^{18}\text{O}$ value of the stalagmite is modified and does not reflect the original oxygen isotope fingerprint of the rain water. Hence, the $\delta^{18}\text{O}$ and the $\delta^{13}\text{C}$ value of the stalagmite are shifted towards more positive values.

8.3. Prior calcite precipitation (PCP) - Precipitation of calcite before the formation of a speleothem

9

Isotope fractionation - Part II

In the previous chapters, the oxygen and the carbon isotopic behaviour of the CO₂-H₂O-CaCO₃ system have been illuminated and all aspects of the carbon and oxygen isotope cycle have been discussed, putting special focus on the isotope-recording speleothem. In Chapter 5, the isotope fraction of calcite precipitation was differentiated between equilibrium and kinetic or disequilibrium isotope fractionation, respectively, in dependence on the loss rate of CO₂ from the solution [Hendy \(1971\)](#). Recently, [Dreybrodt and Scholz \(2011\)](#) have highlighted that loss of CO₂, is 8 s at 0 °C and 2 s at 25 °C, is much faster compared to precipitation rate, 2,000 s at 0 °C and 230 s at 25 °C. Following the argumentation of [Hendy \(1971\)](#), the precipitation of calcite is without any doubt a kinetic or disequilibrium isotope fractionation process. This is based on the fact that the time constant for the oxygen isotope exchange between HCO₃⁻ and H₂O is between the time range of 125,700 and 6200 s for a temperature range between 0 and 25 °C ([Dreybrodt and Scholz, 2011](#)). Further, it is at least 2 orders of magnitude greater than the precipitation time constant. In Sec. 5.3.2, the big debate has been intoned has been introduced. An emphasis was put on the question whether the observed discrepancies between cave-calcite-derived $^{18}\alpha_{\text{calcite}/\text{H}_2\text{O}}$ values and the values for $^{18}\alpha_{\text{calcite}/\text{H}_2\text{O}}$ based on the relationship of [Kim and O'Neil \(1997\)](#) are caused by kinetic or disequilibrium isotope fractionation effects or not. But is the kinetic or disequilibrium isotope fractionation the only cause for the observed discrepancies or could other processes explain the offset between the relationship of [Kim and O'Neil \(1997\)](#) and the observed $^{18}\alpha_{\text{calcite}/\text{H}_2\text{O}}$ from cave calcites? This question shall be discussed in the following sections in more detail as in Sec. 5.3.2 but also at greater distance from the stalagmites, meaning that not only effects at the speleothem's surface are considered but also effects that could happen above it. Effects, that could modify the oxygen isotope composition of the drip water as well as the calcite.

9.1 The big debate - Part II

When Coplen (2007) questioned if $^{18}\alpha_{\text{calcite}/\text{H}_2\text{O}}$ derived by Kim and O'Neil (1997) is representative for the equilibrium isotope fractionation during calcite precipitation, he set off an avalanche. Although, it was well known that many speleothems show kinetic or disequilibrium isotope fractionation effects (Mickler et al., 2006). Tremaine et al. (2011) summarised values of $^{18}\alpha_{\text{calcite}/\text{H}_2\text{O}}$, which were available from several studies, and compared those values with the temperature relationship described by Kim and O'Neil (1997). An updated plot of Tremaine et al. (2011) is shown in Fig. 9.1; $^{18}\alpha_{\text{calcite}/\text{H}_2\text{O}}$ values of Johnston et al. (2013), Feng et al. (2012) and Riechelmann et al. (2012) are included additionally. Fig. 9.1 impressively demonstrates, that almost all values of $^{18}\alpha_{\text{calcite}/\text{H}_2\text{O}}$ derived from cave calcites are greater than the values derived by the relation for $^{18}\alpha_{\text{calcite}/\text{H}_2\text{O}}$ after Kim and O'Neil (1997).

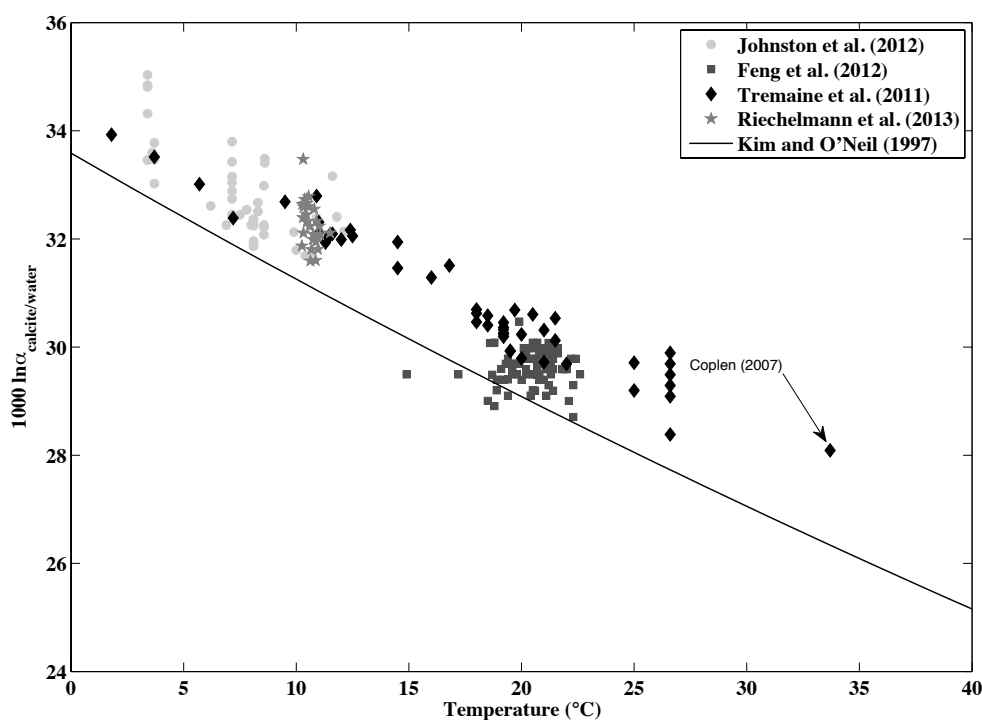


Fig. 9.1: The figure shows $^{18}\alpha_{\text{calcite}/\text{H}_2\text{O}}$ values derived from speleothem and drip water $\delta^{18}\text{O}$ values pictured in dependence on the cave air temperature. The straight line determines the value for $^{18}\alpha_{\text{calcite}/\text{H}_2\text{O}}$ calculated from the temperature relation of Kim and O'Neil (1997) (adapted and modified after Tremaine et al., 2011).

Several studies discuss the effect of isotope fractionation and in particular of oxygen isotope fractionation during the precipitation of calcite with focus on disequilibrium effects (Zeebe,

1999, 2007; Watson, 2004; Wiedner et al., 2008; Dietzel et al., 2009; Polag et al., 2010; DePaolo, 2011; Day and Henderson, 2011). Watson (2004) developed a theory based on solid state diffusion within the calcite lattice. It describes the propagation of trace-metals within the crystal, but may also be applied to stable isotopes. However, Hendy (1971) stated a value of c. 1000 years at a temperature of 20 °C for the exchange time of 50 % of the oxygen and carbon isotopes through one unit cell below the surface, based on experimental results of diffusion coefficients of oxygen and carbon isotopes in calcite (Haul and Stein, 1955; Anderson, 1969). Hence, solid state diffusion of oxygen and carbon isotopes is by far too slow to explain the observed kinetic or disequilibrium effects, which is also stated by (DePaolo, 2011). The studies by (Zeebe, 1999, 2007) demonstrated, that under the assumption that H_2CO_3 , HCO_3^- and CO_3^{2-} contribute to the precipitated calcite in proportion to their fraction of DIC, the oxygen isotope fractionation factor between water and calcite is also a function of the pH value of the precipitation solution and not only of the temperature. A reason for this is the fact that the fraction of the carbon species depend on the pH value (Fig. 3.2). Since the oxygen isotope fractionation is different between every species, the overall oxygen isotope fractionation factor is a weighted mean of all oxygen isotope fractionation factors with respect to their relative abundance. The concept of DePaolo (2011) is based on the relative strength between the precipitation and the dissolution rate of calcite. Apart from the theoretical approaches (Zeebe, 1999, 2007; Watson, 2004; DePaolo, 2011), Dietzel et al. (2009) investigated the dependence of $^{18}\alpha_{\text{calcite}/\text{H}_2\text{O}}$ on several parameters experimentally. The parameters are the temperature, the precipitation rate and the pH value of the solution. The results of Dietzel et al. (2009) indicate, that $^{18}\alpha_{\text{calcite}/\text{H}_2\text{O}}$ is also a function of the precipitation rate and of the pH value.

9.2 Prior carbonate precipitation and the effect on isotope fraction factors

Several experiments (Wiedner et al., 2008; Polag et al., 2010; Day and Henderson, 2011) have been performed under cave-like conditions in most cases using a ramp on which a supersaturated solution is flowing down and calcite is precipitating along its way down. The results of Wiedner et al. (2008) indicate that the precipitated calcite gets enriched in ^{18}O and ^{13}C isotopes along the flow path. For the oxygen isotope ratio of calcite, it could be shown that, the enrichment along the flow path depends on the pump(flow) rate. For a pump rate of 0.24 ml/min and 0.12 ml/min, the enrichment in the $\delta^{18}\text{O}$ values of the precipitated calcite is approximately 1.0 ‰ and 1.5 ‰ for a path length of 50 cm, respectively, at a temperature of 21.7 °C. Assuming a drop volume of 0.1 ml, the pump rate of 0.24 ml/min equates a drip interval of 25 s and the pump rate of 0.12 ml/min a drip interval of 50 s. For $\delta^{13}\text{C}$ values of the precipitated calcite, it could be demonstrated, that it is enriched by about 1.4 ‰ for a path length of 50 cm, at a temperature of 17.9 °C and a pump rate of 12 ml/min. Similar results were derived by Polag et al. (2010). This could be

explained by the observation that the mass of precipitated calcite decreases exponentially with the length of the path due to precipitation kinetics (Polag et al., 2010; Hansen et al., 2013). Hence, the solution becomes enriched in ^{18}O and ^{13}C with increasing flow length. This is a result of the disequilibrium isotope fractionation effects (Scholz et al., 2009). What has been demonstrated by the experiments is (i) that whenever calcite is precipitated, the solution becomes enriched in ^{18}O and ^{13}C with increasing flow distance and furthermore, (ii) that calcite, that is precipitated along a flow path, becomes enriched along its way, too. What has been demonstrated by the studies of Wiedner et al. (2008) and Polag et al. (2010), describes furthermore the evolution of the decoration of cave ceilings, namely, the formation of stalactites and other sinter shapes on the cave ceiling. In caves, it not unlikely that a stalactite is above a stalagmite or that the drip water is first flowing along the cave ceiling before it drips from it and falls onto a stalagmite surface or the cave ground. Both situations are accompanied by calcite precipitation in case of supersaturated solutions. It is also possible that calcite is precipitated inside veins of the karst zone. Those cases are usually summarized under the term "prior calcite precipitation" (PCP), meaning, prior to the stalagmite formation, which is than stated as secondary calcite precipitation. Like the studies of Wiedner et al. (2008) and Polag et al. (2010) have shown, PCP is also accompanied by isotope fractionation effects causing an enrichment of the solution in ^{18}O and ^{13}C with the flow length. If a growing stalagmite is under a drip side and is fed by a solution from which calcite is precipitated by PCP, the stalagmite's $\delta^{18}\text{O}$ and $\delta^{13}\text{C}$ value would be greater, compared to the case, when no calcite is precipitated from the solution before the stalagmite formation. This is a simple fact of the disequilibrium isotope fraction effects proofed by Wiedner et al. (2008) and Polag et al. (2010). The effect can be quite high: Note that only for a length of 50 cm and a drip interval of 50 s, the enrichment is already in the order of c. 1.4 ‰ at a temperature of c. 20 °C.

The question is, what has PCP to do with the determination of $^{18}\alpha_{\text{calcite}/\text{H}_2\text{O}}$? A lot! The idea goes as follows: to calculate $^{18}\alpha_{\text{calcite}/\text{H}_2\text{O}}$, two values for the oxygen isotope ratio are necessary, one of the stalagmite's calcite sample from the top or the calcite from a watch glass and the second from the water sample feeding the stalagmite or watch glass, respectively. Both samples are carried to a laboratory, where the oxygen isotope ratio is determined with a mass spectrometer. In the end, two values for the oxygen isotope ratio of calcite and water are determined and $^{18}\alpha_{\text{calcite}/\text{H}_2\text{O}}$ can be calculated. But is the oxygen isotope ratio of the measured water representative for the oxygen isotope ratio of the solution's HCO_3^- ? Yes!, and No! If there has not been any PCP and both HCO_3^- and water are in oxygen isotope equilibrium, the measured oxygen isotope ratio of water is representative and the calculated $^{18}\alpha_{\text{calcite}/\text{H}_2\text{O}}$ expresses the real isotope fractionation factor. But in the case that PCP did occur, HCO_3^- is enriched in ^{18}O and ^{13}C at the time of calcite precipitation and the resulting $\delta^{18}\text{O}$ and $\delta^{13}\text{C}$ value are greater compared to the case without PCP. The water sample does therefore not represent the oxygen isotope state of the solution at the time of the calcite precipitation. This is due to the fact, that the amount of water is so much higher compared to the carbon bearing species and further the effect of the greater amount of ^{18}O isotopes in the solution is negligible for water. Furthermore, the oxygen isotope exchange between HCO_3^- and water forces an oxygen isotope re-equilibrium

between HCO_3^- and water and would consequently balance the enrichment caused by PCP. For example, if the sampled solution has a constant temperature of approximately 10 °C, the oxygen isotope equilibrium between HCO_3^- and H_2O is re-established after c. 1.64 days (98 %) (Dreybrodt and Scholz, 2011). This is usually the case for water samples being kept in a fridge for several days until the samples are analysed. Hence, the derived $^{18}\alpha_{\text{calcite}/\text{H}_2\text{O}}$ is overestimating the isotope fractionation effects in case of PCP.

9.3 The big debate - Part III and concluding remarks

Most of the studies from which the $^{18}\alpha_{\text{calcite}/\text{H}_2\text{O}}$ values of Fig. 9.1 origin have not investigated for PCP. Some of these studies even mentioned kinetic effects or "highly decorative cave ceiling" as being a hint for PCP. Hence, PCP could explain the offset between the reference-line set by the relation of Kim and O'Neil (1997) and the $^{18}\alpha_{\text{calcite}/\text{H}_2\text{O}}$ values derived from drip water and calcite samples. As long as PCP is not excluded from processes affecting the drip water isotopic composition, no $^{18}\alpha_{\text{calcite}/\text{H}_2\text{O}}$ values derived from calcite and drip water samples should be used to derive $^{18}\alpha_{\text{calcite}/\text{H}_2\text{O}}$ values. However, the devil lies in the detail, because the calcite and water sample analysed by Coplen (2007) originate from an under-water cave in Nevada, Texas, called the Devil's Hole. Therefore, no PCP occurs and can not be the reason for the offset between the derived $^{18}\alpha_{\text{calcite}/\text{H}_2\text{O}}$ values and the Kim and O'Neil (1997) relationship for $^{18}\alpha_{\text{calcite}/\text{H}_2\text{O}}$. The argument by Coplen (2007), that the derived $^{18}\alpha_{\text{calcite}/\text{H}_2\text{O}}$ value represents isotope equilibrium conditions, is that the calcite precipitation rate is so slow, being between 0.1 and 0.8 μ/a (Winograd et al., 2006), compared to growth rates of speleothems, being between 10 and 1000 μ/a (McDermott, 2004), that calcite precipitation is likely to be an equilibrium oxygen isotope fractionation effect. A possible reason for this could be the circumstance, that the mass transport within the solution, which is limiting the precipitation rate, is gaining importance for an increasing height of the solution film (Buhmann and Dreybrodt, 1985a,b). Consequently, the same applies for the under-water calcite sample of Devil's Hole. Furthermore, disequilibrium effects, as discussed in Chapter 7 for thin solution films, might be of subordinate order for under-water-calcite samples. Assuming a boundary layer with a finite thickness between the bulk solution above the calcite surface and the calcite surface, the solution within the boundary layer is constantly renewed by molecular diffusion, or in case of currents, by turbulent diffusion, too. Considering the exchange time, only molecular diffusion is considered being an upper limit for the exchange time; the occurrence of turbulent diffusion, the exchange time becomes smaller. The time constant for the exchange of HCO_3^- molecules, being the most abundant carbon bearing species in the solution ($\text{pH} \approx 7.4$ Coplen, 2007), between the boundary layer and the bulk solution is formulated by dreybrodt1988

$$\tau_D^{\text{HCO}_3^-} = \frac{1}{3} D_M^{\text{HCO}_3^-} \delta^2, \quad (9.1)$$

whereas $D_M^{HCO_3^-}$ is the molecular diffusion coefficient for HCO_3^- and δ the height of the boundary layer. The values for $D_M^{HCO_3^-}$ are calculated with the relation of Zeebe (2011). After $3 \cdot \tau_D$, about 95 % of the HCO_3^- molecules are exchanged. This occurs after c. 18.3 s at a temperature for 0 °C. Hence, for higher temperatures the exchange time is smaller. Consequently, it is very unlikely that HCO_3^- molecules, that are situated within the boundary layer, get further enriched in ^{18}O and ^{13}C . This is due to the fact, that the precipitation time constant is at least one order of magnitude greater than the exchange time. Applying this results on the calcite samples of Devils Hole (with a water temperature of 33.7 °C) shows, that the calcite $\delta^{18}O$ and $\delta^{13}C$ values should be precipitated in oxygen and carbon isotope equilibrium. This has been already demonstrated by Coplen et al. (1994) in case for the carbon isotopes. If the argument of Coplen (2007) are right, the relationship of Kim and O'Neil (1997) does not equates the oxygen isotope equilibrium state for calcite precipitation. However, the hydrological parameter of Devil's Hole water has one major difference to drip waters inside cave, having usually a pH value of c. 8.2; the water of Devil's Hole in contrast has a value of c. 7.4. According to the theory of (Zeebe, 1999, 2007), different pH values of the solution form which calcite is precipitated can have an effect on the precipitated calcite. If the water from Devil's Hole would have a pH value comparable with cave drip water the precipitated calcite would be c. 0.5 ‰ higher compared to it's measured value. Nevertheless, this does not explain the difference of c. 1.8 ‰ between the $^{18}\alpha_{calcite/H_2O}$ values derived by Coplen (2007) and the ones derived by Kim and O'Neil (1997). However, Dietzel et al. (2009) demonstrated that the pH-effect on precipitated calcite can be even stronger than calculated by (Zeebe, 1999, 2007). Fig. 4 of Dietzel et al. (2009) shows that at a temperature of 40 °C, $^{18}\alpha_{calcite/H_2O}$ varies by about 8 ‰ in the pH range between 8 and 10. Hence, for a pH difference of 0.5, the change in $^{18}\alpha_{calcite/H_2O}$ would be c. 2 ‰. Although, the water temperature at Devil's Hole is cooler by about 6 °C compared to experiment temperatures under experimental conditions in the laboratory of 40 °C the change in $^{18}\alpha_{calcite/H_2O}$ is comparable in magnitude and could explain the offset of c. 1.8 ‰ between the temperature relationship for $^{18}\alpha_{calcite/H_2O}$ found by Coplen (2007) and Kim and O'Neil (1997).

The previous discussion has demonstrated, that there is yet no straight forward explanation for the difference between cave-calcite-derived $^{18}\alpha_{calcite/H_2O}$ values and that the $^{18}\alpha_{calcite/H_2O}$ values calculated with the relationship of Kim and O'Neil (1997). PCP, disequilibrium effects and additional fractionation effects may modify the isotope fractionation effects of calcite precipitation (Zeebe, 1999, 2007; Wiedner et al., 2008; Dietzel et al., 2009; Polag et al., 2010; DePaolo, 2011; Day and Henderson, 2011) and a direct comparison of $^{18}\alpha_{calcite/H_2O}$ values is challenging, unless all parameters are known. The question whether $^{18}\alpha_{calcite/H_2O}$ derived by Kim and O'Neil (1997) represents isotope equilibrium conditions or not is yet to be answered.

Part III
Methods

10

Principal component analysis in speleothem science

Principal component analysis (PCA) is a widely-used statistical method in meteorology and climate science to investigate coherent variations in data records ([Preisendorfer and Mobley, 1988](#); [Von Storch and Zwiers, 2001](#); [Jolliffe, 2002](#)) and other branches of science ([Jolliffe, 2002](#)). The data records consist of different proxy time series, e.g. temperature, air pressure or precipitation. All variables have to be measured at the same station over a period of time or have to be a multitude of proxy time series recorded simultaneously at different stations. PCA is also referred to as empirical orthogonal functions (EOF) and it is often not differentiated between these two terminus in literature ([Jolliffe, 2002](#)). The expression empirical orthogonal function adumbrates that the subject is based on orthogonal functions, which in turn are used to describe the variations of the data record. An introduction to the mathematical concept behind PCA (EOF) is given in Sec. 10.1. PCA is a meaningful tool. Both, temporal coherent variations and spatio-temporal coherent changes can be investigated. Thereby, the investigated data can include different spacial scales. [Wallace and Gutzler \(1981\)](#) for example used PCA to investigate coherent changes in the winter geopotential high field in the Northern Hemisphere. Recently, [Anchukaitis and Tierney \(2012\)](#) used Monte Carlo based PCA to determine spatio-temporal changes in palaeoclimatic time series derived from lake sediments in East Africa. This is, to the knowledge of the author, the first time that PCA has been applied on proxy time series that adhere an age error.

In this work, Monte Carlo based PCA are applied on speleothem proxy time series to explore coherent spacial-temporal variations in European speleothems during the Holocene. In addition to the age uncertainty of measured speleothem ages, speleothems have usually a non-constant growth rate causing a different temporal resolution of the proxy time series ([Spötl and Matthey, 2006](#)). This feature has not been discussed by [Anchukaitis and Tierney \(2012\)](#). In general, it is no challenge comparing speleothem proxy time series from different

locations visually. However, it might get difficult when using PCA, due to of different temporal resolutions (Sec. 10.2). The method presented here considers the age uncertainty of speleothem ages and the different temporal resolution of speleothem proxy time series. This allows to investigate for coeval spacial-temporal changes in speleothem proxy time series. However, there are manifold processes altering the recorded proxies (Chapter 7 and 8). This makes it challenging to search for synchronous variations in speleothem proxy time series from speleothems that have grown in different regions. Nevertheless, with the application of PCA on a collection of speleothem proxy time series (data records) from different locations, hidden common variations in the speleothems proxy time series can be uncovered.

In the following section a brief overview shall be given on the mathematical concept of PCA (EOF) (Sec. 10.1) that is based on the first chapters of Jolliffe (2002). Subsequently, the application of PCA on speleothem proxy time series is discussed (Sec. 10.2), followed by the explanation of the source code (Sec. 10.3). Ultimately, PCA is applied on artificial and real proxy time series to derive significance criteria for the selection of leading modes of "shared" variations (Sec. 10.4, 10.5, 10.6, 10.7).

10.1 Introduction to principal component analysis

10.1.1 Problem definition and first steps

When a large number m of variables (time series) are investigated for common variations the classical correlation methods become impractical. For example, to test the temporal coherency of 10 variables a total of 45 ($\frac{1}{2}m(m-1)$) correlations or covariances must be analysed. Hence, other methods must be applied, that allow to investigate large numbers of variables, but reduce the dimensionality of the dataset. This is the concept of principal component analysis (PCA). Assuming a vector \mathbf{X} that is composed of m variables, then \mathbf{X} is given by

$$\mathbf{X} = [\mathbf{x}_1, \mathbf{x}_2, \dots, \mathbf{x}_m], \quad (10.1)$$

with \mathbf{x}_i being

$$\mathbf{x}_i = (x_i(t_1), x_i(t_2), \dots, x_i(t_n)), \quad (10.2)$$

whereas the $x_i(t_k)$ ($k=1, 2, \dots, n$) are observations. If the x_i s are independent variables, e.g., $\delta^{18}\text{O}$ time series of different speleothems, then $x_i(t_k)$ is the $\delta^{18}\text{O}$ value of the i^{th} speleothem at the time t_k . The idea of PCA is to find a linear function $\alpha_1^T \mathbf{X}$ that explains most of the variance of the elements of \mathbf{X} . The subscript T denotes that α is transposed. Hence, the linear function $\alpha_1^T \mathbf{X}$ is given by

$$\alpha_1^T \mathbf{X} = \alpha_{11} \mathbf{x}_1 + \alpha_{12} \mathbf{x}_2 + \dots + \alpha_{1m} \mathbf{x}_m = \sum_{i=1}^m \alpha_{1i} \mathbf{x}_i. \quad (10.3)$$

The next step is to find a linear function $\alpha_2^T \mathbf{X}$ that is orthogonal to $\alpha_1^T \mathbf{X}$, i.e. $\langle \alpha_1^T \mathbf{X}, \alpha_2^T \mathbf{X} \rangle = 0$ ($\langle \cdot, \cdot \rangle$ is the standard scalar product) and explains most of the variance. The k^{th} ($k \leq m$) linear function $\alpha_k^T \mathbf{X}$ is orthogonal to $\alpha_1^T \mathbf{X}, \alpha_2^T \mathbf{X}, \dots, \alpha_{k-1}^T \mathbf{X}$ and explains most of the variance and so on and so force until $k=m$. The $\alpha_k^T \mathbf{X}$ are refereed as the k^{th} principal component (PC) or as the k^{th} empirical orthogonal function (EOF). If the PCA was successful, than most of the variance of \mathbf{X} is explained by only a few PCs ($p \ll m$) (e.g. Jolliffe, 2002).

10.1.2 The calculation of Principal Component(s) Analysis

To derive the PCs values for α_i must be determined that fulfil the conditions of orthogonality and of having maximum variance (Sec. 10.1.1). For the 1st PC this yields that $var [\alpha_1^T \mathbf{X}] = \alpha_1^T \Sigma \alpha_1$ is maximal and that $\alpha_1^T \alpha_1 = 1$ (e.g. Jolliffe, 2002). Σ is the covariance matrix of \mathbf{X} . To solve this problem the technique of Lagrange multipliers can be used. Hence, the task is to maximise Eq. (10.4) at which λ is the Lagrange multiplier.

$$max (\alpha_1^T \Sigma \alpha_1 - \lambda (\alpha_1^T \alpha_1 - 1)). \quad (10.4)$$

After differentiation of Eq. (10.4) with respect to α_1 yields

$$\Sigma \alpha_1 - \lambda_1 \alpha_1 \stackrel{!}{=} 0. \quad (10.5)$$

Hence, the problem is reduced to an eigenvalue-problem where α_1 is an eigenvector of Σ and λ the corresponding eigenvalue. Because $\alpha_1^T \Sigma \alpha_1$ need to be maximal, the solution of Eq. (10.5) is eigenvector with the largest eigenvalue because $\alpha_1^T \Sigma \alpha_1 = \lambda_1$. It can be demonstrated that all other α_k^{th} are also eigenvectors of Σ with corresponding eigenvalues λ_k (Jolliffe, 2002). Hence, the PCA is described by

$$\Sigma = \mathbf{A} \mathbf{\Lambda} \mathbf{A}^T \quad (10.6)$$

where the order of the eigenvectors is in accordance with the size of the eigenvalues. α_1 has the largest eigenvalue, α_2 the second largest, α_3 the third largest etc. pp. It follows that the portion of the explained total variance of \mathbf{X} by α_k is given by

$$\frac{\lambda_k}{\sum_{i=1}^m \lambda_i}. \quad (10.7)$$

If the \mathbf{x}_i^{th} are standardized the covariance matrix equates the correlation matrix ($\Sigma \equiv R$) and Eq. (10.6) gives

$$\mathbf{R} = \mathbf{A}\mathbf{A}\mathbf{A}^T. \quad (10.8)$$

Because the $\alpha_{\mathbf{k}}^{th}$ are orthonormal, they span a new space of dimension n that allow to transform the observations of the vector \mathbf{X} into the new space (Eq. 10.3). Hence, the "observations" of the $\alpha_{\mathbf{k}}^{th}$ are given by

$$\chi_{\mathbf{k}} = \alpha_{\mathbf{k}}^T \mathbf{X}. \quad (10.9)$$

The $\chi_{\mathbf{k}}$ are referred as PC time series in the following. Hence, χ_1 is explaining most of the total variance of \mathbf{X} , χ_2 the second most etc. pp. Eq. (10.3) shows that the contribution of the \mathbf{x}_i 's vector to $\chi_{\mathbf{k}}$ is determined by the components α_{ki} of the corresponding eigenvectors $\alpha_{\mathbf{k}}$ and are often quoted as "loadings" in the literature. Another approach is to calculate the correlation between $\chi_{\mathbf{k}}$ and the \mathbf{x}_i 's to test whether a computed PC time series explains the variability of a certain \mathbf{x}_i . Within this framework, the correlation between a PC time series and the \mathbf{x}_i 's is calculated with the Spearman's rank correlation coefficient (r_s).

10.1.3 Principal component analysis

Within this section a PCA is applied on two variables (time series) \mathbf{x}_1 and \mathbf{x}_2 . The components of the \mathbf{x}_1 and \mathbf{x}_2 are calculated with Eqs. (10.11).

$$x_1(t_i^1) = \sin\left(\frac{t_i^1}{100}\right) + \Gamma \quad (10.10)$$

$$x_2(t_i^2) = -\sin\left(\frac{t_i^2}{100}\right) + \Gamma \quad (10.11)$$

The variables \mathbf{x}_1 and \mathbf{x}_2 are described by anti-correlated sinus-function with a period of $2\pi 100$ years (arbitrarily chosen). Each component of the two variables is calculated with Eqs. (10.11), whereat Γ is a white noise function. The t_i 's are varied from 0 to 5000 years, whereat the difference between subsequent ages is 10 years. Furthermore, each age is allowed to vary by 0.3 years (1-sigma). The parameter are chosen (arbitrarily) to be consistent with speleothem time series having a limited proxy resolution and an age uncertainty and inhere an "uncertainty". To demonstrate the effect of the "uncertainty" in the variables a total of 500 Monte Carlo approach is performed, at which a PCA is applied on \mathbf{x}_1 and \mathbf{x}_2 for each Monte Carlo run. The ensemble of the time series \mathbf{x}_1 (red) and \mathbf{x}_2 (blue) are illustrated in Fig. 10.1.

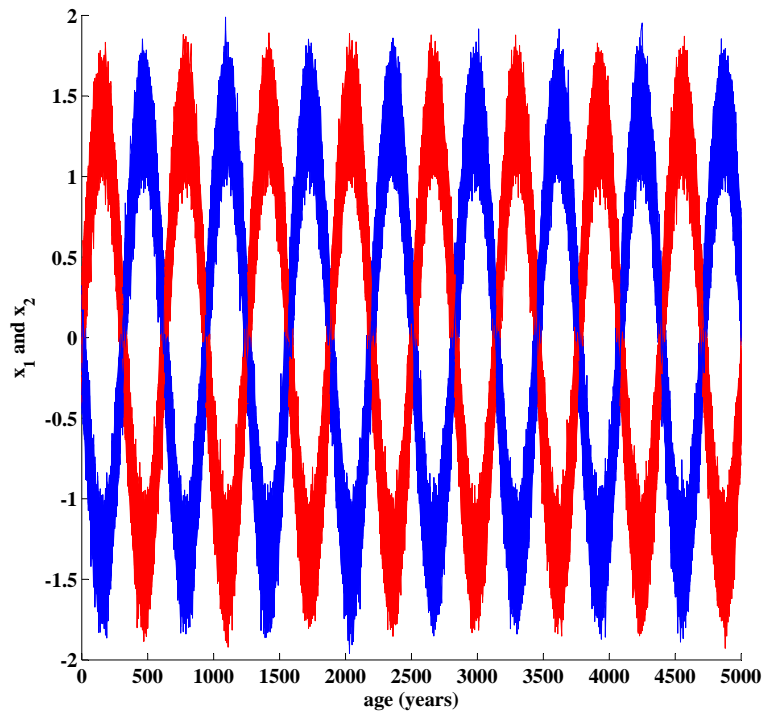


Fig. 10.1: Illustrated are the ensemble of two variables \mathbf{x}_1 (red) and \mathbf{x}_2 (blue) which are uncorrelated. Each ensemble is composed of 500 individual time series, whereas each component is calculated with Eqs. (10.11).

The variables \mathbf{x}_1 and \mathbf{x}_2 are illustrated against each other in Fig. 10.2 (blue closed dots). The figure illustrates that the variability of \mathbf{x}_1 and \mathbf{x}_2 occurs in both directions (dimensions) x_1 and x_2 with an equal variability. The "uncertainty" of the variables (scatter of the circles) is a result of the white noise function and the time uncertainty. After the application of a PCA on the variables \mathbf{x}_1 and \mathbf{x}_2 the two PCs are computed. For both exists a PC variable (time series) χ_1 and χ_2 . For the illustrated example (Fig. 10.2) the 1st PC explains c. 99 % of the total variance of \mathbf{x}_1 and \mathbf{x}_2 whereas the 2nd PC only accounts of less than 1 % of the total variance. This is also depicted in Fig. 10.2 where χ_1 is plotted against χ_2 for the illustrated variables \mathbf{x}_1 and \mathbf{x}_2 . The variance of χ_1 and χ_2 is in comparison to \mathbf{x}_1 and \mathbf{x}_2 mainly in one direction, χ_1 s. Hence, the two variables \mathbf{x}_1 and \mathbf{x}_2 can be represent by χ_1 .

The variable χ_1 of the PCA Monte Carlo approach for $\mathbf{X} = [\mathbf{x}_1, \mathbf{x}_2]$ is illustrated in Fig. 10.3. The figure pictures that two different phase relations are observed for the computed χ_1 's, having a phase relation of $\varphi = 0$ ($\chi_1^{\varphi=0}$) (magenta) and $\varphi = \pi$ ($\chi_1^{\varphi=\pi}$) (cyan) and can be described by

$$\chi_1^\varphi = \Psi \cdot \exp^{i\pi\varphi}. \quad (10.12)$$

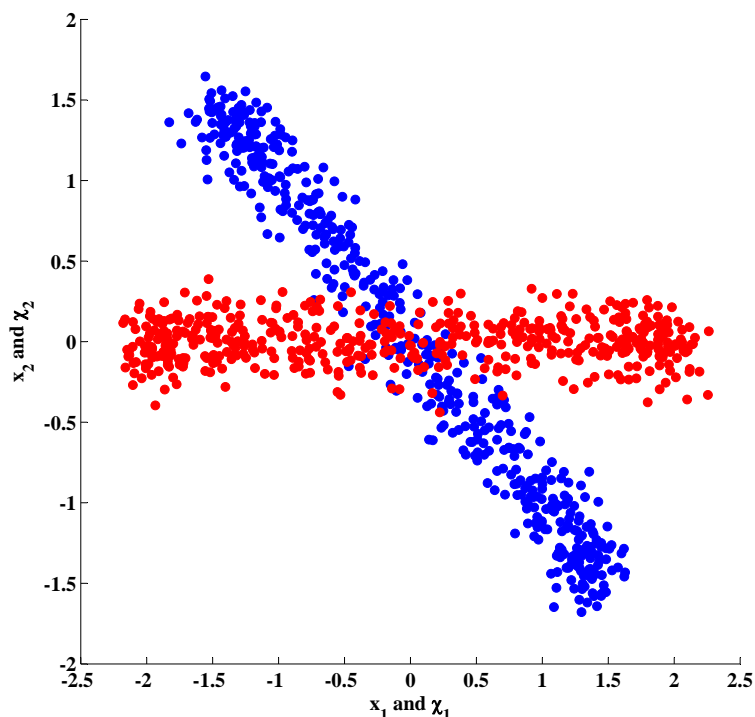


Fig. 10.2: The figure is picturing the relationship between the two variables \mathbf{x}_1 and \mathbf{x}_2 (blue closed circles) and χ_1 and χ_2 derived from the PCA on \mathbf{x}_1 and \mathbf{x}_2 (red closed circles), respectively.

This effect, which is quoted as the "up-side-down effect" in the following, is a result of the PCA of $\mathbf{X} = [\mathbf{x}_1, \mathbf{x}_2]$ that can be only discovered by a Monte Carlo approach, because it allows to vary the variance of \mathbf{x}_1 and \mathbf{x}_2 for each Monte Carlo run, as the white noise component and the time uncertainty of the components of \mathbf{x}_1 and \mathbf{x}_2 is different for each Monte Carlo run. Hence, the different phase relations of χ_1 observed for the Monte Carlo approach originate from the different variances of \mathbf{x}_1 and \mathbf{x}_2 for each subset of the ensemble. It is a result of the mathematical concept of PCA, that the dimensionality of a compilation of variables shall be reduced. For the example: if \mathbf{x}_1 has a higher variance than \mathbf{x}_2 , the phase relation is $\varphi = 0$. In contrast, if \mathbf{x}_2 has a higher variance than \mathbf{x}_1 , the phase relation is $\varphi = \pi$. Note that both curves that are illustrated in Fig. 10.3 are describing the variables \mathbf{x}_1 and \mathbf{x}_2 and are solutions of the primary problem to describe the total variance of $\mathbf{X} = [\mathbf{x}_1, \mathbf{x}_2]$ by only one PC time series. If the Spearman's rank correlation coefficient (r_s) is calculated between \mathbf{x}_1 and $\chi_1^{\varphi=0}$, the value for r_s is positive. The r_s value for the correlation between \mathbf{x}_2 and $\chi_1^{\varphi=0}$ is negative. If the correlation is calculated for $\chi_1^{\varphi=\pi}$ the correlation is vice versa. The up-side-down effect only occurs, if the variances of the variables $\mathbf{x}_1, \mathbf{x}_2, \dots, \mathbf{x}_m$ are variable.

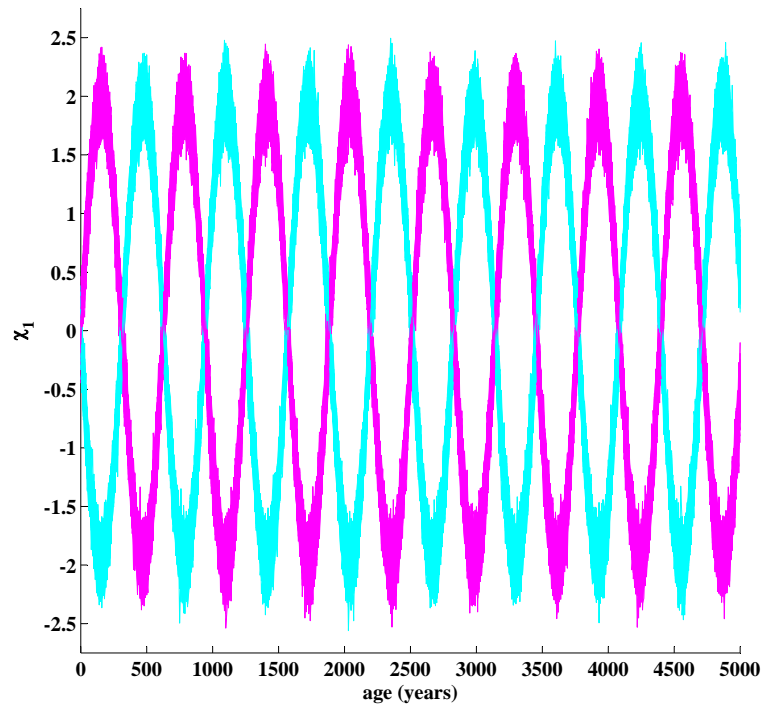


Fig. 10.3: The figure is illustrating the derived ensemble of PC time series χ_1 for the compilation of variables \mathbf{x}_1 and \mathbf{x}_2 . The different phase relation of χ_1 is caused by the different variances of \mathbf{x}_1 and \mathbf{x}_2 for each Monte Carlo run. If \mathbf{x}_1 has the highest variance in comparison to \mathbf{x}_2 the magenta coloured curves are derived for χ_1 . If \mathbf{x}_2 has the highest variance the cyan coloured curves are computed for χ_1 . Assuming that magenta coloured curves have a phase relation of $\varphi = 0$ than the cyan coloured curves have a phase relation of $\varphi = \pi$.

10.2 PCA in speleothem science

As previously mentioned, PCA makes it possible to explore coherent spacial-temporal variations in a compilation of speleothem proxy time series. This is of high interest, as it allows conclusions about the climate system and its dynamics. However, for the forgoing time of the instrumental age, only proxy time series derived from palaeo climate archives enable to investigate for simultaneous variations in different regions. For example [Spötl et al. \(2006\)](#) compared the $\delta^{18}\text{O}$ time series of two speleothems from the Austrian Alps with that of Greenland ice cores. Another study was published by [Wang et al. \(2001\)](#) comparing the $\delta^{18}\text{O}$ time series of five speleothem from Hulu Cave (China) with the GISP2 ice core and the insolation at 33°N . For a more sophisticated comparison of speleothem proxy time series, PCA is applied on a selection of European speleothem $\delta^{18}\text{O}$ and $\delta^{13}\text{C}$ time series. Although PCA has been used in climate science for decades ([Preisendorfer and](#)

Mobley, 1988) it has not been applied to speleothem proxy time series for spatio-temporal exploration. Two characteristics adherent to speleothems are possible explanations for this: the age uncertainty of the dated speleothem ages and the variable growth rate of a speleothem. This makes it challenging to apply PCA on a selection of speleothem proxy time series.

The measured ages of a speleothem have an uncertainty which results from the dating technique (Chapter 4). This allows to vary each age within its given age uncertainty. Consequently, a derived age-depth relation is only one of many solutions. Hence, every age-depth relation has its own proxy-age relation, which is derived from the proxy-depth and age-depth relation. Accompanied by different age-depth relations is the varying growth rate. This puts another issue forth. The proxy values are derived by specific sampling techniques, e.g., micro milling or laser ablation. All the different techniques have different spacial resolutions (Spötl and Matthey, 2006). The sampling resolution is limited by the technique. Thus, the temporal resolution of a proxy time series of a speleothem varies along the speleothem's growth axis due to its varying growth rate. Since PCA analyses variations, it is necessary that the proxy time series have similar temporal resolutions. In the following section two technical challenges shall be discussed in more detail. The data of five speleothems is applied in this chapter. These speleothems grew in different caves and are distributed throughout Europe (Fig. 10.4).

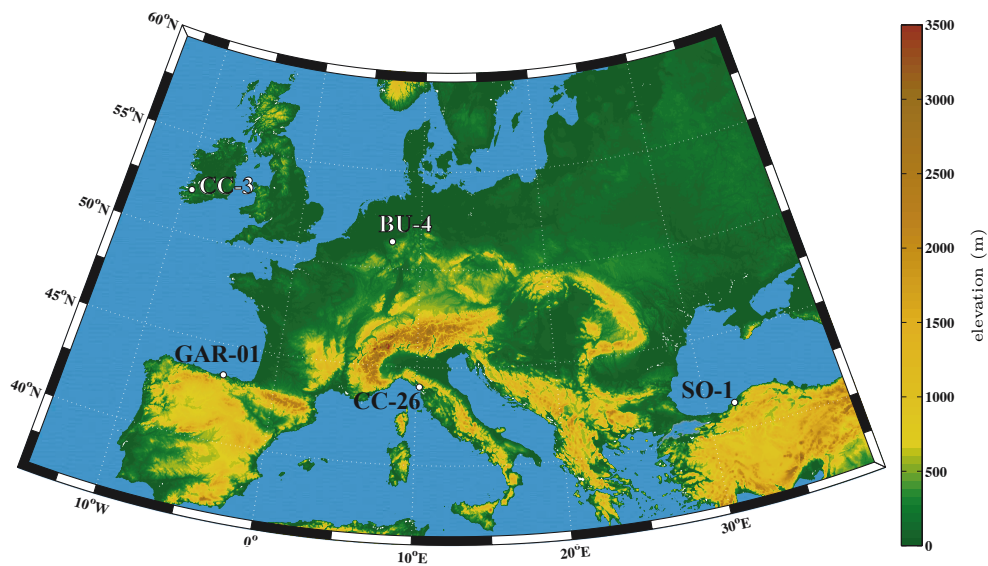


Fig. 10.4: Map showing the location of five European speleothems: BU-4 from Bunker Cave (Germany); CC-3 from Craig Cave (Ireland); CC-26 from Corcia Cave (Italy); GAR-01 from La Garma Cave (Spain) and SO-1 from Sofular Cave (Turkey).

10.2.1 Age uncertainty of ages and consequences for the age model

The age uncertainty of speleothem ages expresses that the determined ages are not unique solutions (Chapter 4). This is illustrated in Fig. 10.5 which shows the age-depth relation of the stalagmites BU-4, CC-26, CC-3, GAR-01 and SO-1. All ages are shown with their 1-sigma age uncertainty.

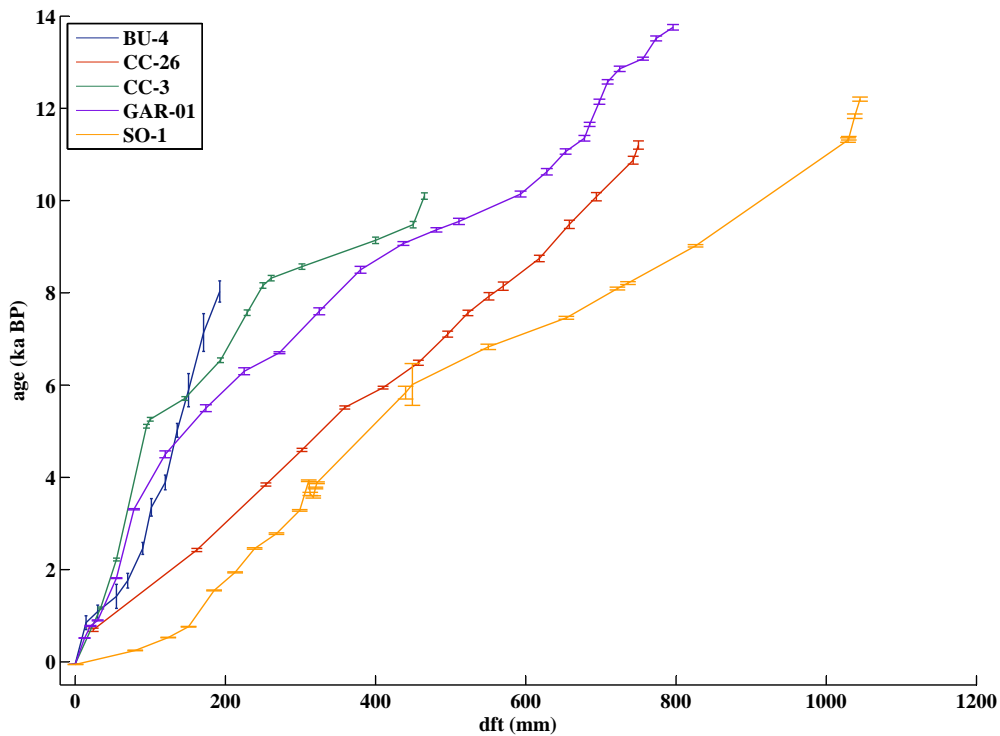


Fig. 10.5: Figure illustrating the age-depth relation of the stalagmites BU-4, CC-26, CC-3, GAR-01 and SO-1. The age-depth relation is given by the determined ages given in ka BP and the related position along the growth axis referred as distance from top (dft) given in mm. It highlights that the growth history of a speleothem is not smooth but lively. The growth of a speleothem depends on several parameters resulting in a great variety of speleothem shapes and speleothem growth rates (see Chapter 3).

To define the age-depth relation of a speleothem, the ordinary procedure is to date several carbonate samples along the growth axis. The first step is to cut out the carbonate samples along the growth axis of the speleothem. These carbonate samples are then prepared by

chemical procedures (e.g. [Frank et al., 2000](#)). Finally, the prepared carbonate samples are analysed with a mass spectrometer. The location of the carbonate samples on the growth axis and the samples' ages are then defining the age-depth relation, i.e., the age model of the speleothem. In the best-case scenario the carbonate sample size is not finite and the age uncertainty of the age determination can be neglected in comparison to the absolute age. This would allow for numerous age determinations along the growth axis, yielding a robust age model due to its high age density along the growth axis. However, in most cases there are technical and financial limitations, allowing only manageable amount of age determinations. In addition, the age uncertainty is not negligible compared to the absolute age. Hence, certain assumptions must be made for the age-depth interpolation between measured ages. Concerning speleothems, only a couple speleothem age-model algorithms are published considering the age uncertainty of the age determinations. The age-models are based on different assumptions regarding the age interpolation (see [Scholz et al., 2012b](#), and references therein). [Scholz et al. \(2012b\)](#) have presented a comprehensive overview of the reliable models published so far. However, the most convenient interpolation technique between ages is a linear interpolation that is also used in sophisticated age models (e.g. [Scholz and Hoffmann, 2011](#)) - A linear interpolation has been also applied on the measured ages in Fig. 10.5, resulting in a linear age-depth relation for each speleothem. The basic assumption of a linear interpolation between the ages is that environmental changes force a linear response of the speleothem's growth rate. However, the age-depth relations depicted in Fig. 10.5 are only one possible solution for each speleothem. The age uncertainty of each age allows to vary all the ages within their given ranges. This results in a multitude of age-depth relations, which then determine the age-depth transfer function for the proxy record. This needs to be considered when speleothem proxy time series are compared by PCA.

10.2.2 Temporal resolution of proxy time series

Besides the age-depth relation of a speleothem, the proxy-depth relation along the growth axis of a speleothem provides insights into climate history (see Chapter 1). In combination with the age-depth relation, the proxy-depth relation can be transformed into a proxy-age relation, i.e., a proxy time series. Therefore, the temporal resolution of the proxy time series depends on the spatial resolution of the proxy and the growth rate along the growth axis of the speleothem, respectively. In most cases, the temporal resolution of speleothem proxy time series are not equal and the "endurance" of different speleothems, too. Thus, the different temporal resolution of speleothem proxy time series allows only qualitative comparisons between different speleothems.

The proxy-depth relation of five different speleothems is shown in Fig. 10.6 - the illustrated proxy is in this case $\delta^{18}\text{O}$. However, a proxy-depth relation by its own does not allow for inter-comparisons between proxy-depth relations derived from different speleothems. Only in combination with the speleothem's age-depth relation (Fig. 10.5) a qualitative and

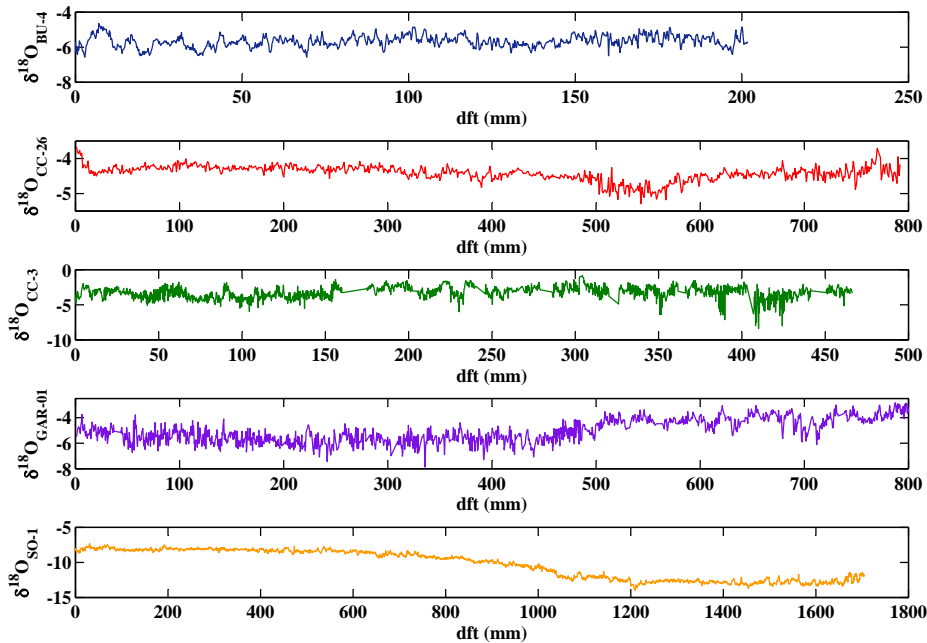


Fig. 10.6: The five $\delta^{18}\text{O}$ -depth relations of speleothem BU-4, CC-26, CC-3, GAR-01, and SO-1 (from top to bottom) picture the variability of the $\delta^{18}\text{O}$ signal along the growth axis quoted as distance from top (dft) given in mm. The comparison of the $\delta^{18}\text{O}$ -depth relations illustrates that both the length of the speleothem as well as the variability of the speleothem $\delta^{18}\text{O}$ values are different from speleothem to speleothem. It highlights that every single speleothem has an unique history that defines its characteristics. Only in combination with the speleothem's age-depth relation, the $\delta^{18}\text{O}$ -depth relation can be transformed into $\delta^{18}\text{O}$ time series and allows for inter-comparison with other $\delta^{18}\text{O}$ time series.

quantitative investigation of different speleothem proxy time series can be conducted.

If an age-depth and a proxy-depth relation of a speleothem are combined into a proxy-age relation, the temporal resolution of a speleothem is simply the age difference between two neighbouring proxy values. The temporal resolution of a speleothem proxy time series is constant if the growth rate as well as the spacial sampling solution are constant. However, as demonstrated in Fig. 10.5 this does not usually apply to speleothems and results in different temporal resolutions of the proxy time series along the growth axis. The temporal resolution of the stalagmites BU-4, CC-26, CC-3, GAR-01 and SO-1 is pictured in Fig. 10.7. To account for the age uncertainty of each measured age a Monte Carlo (MC) approach was used. The speleothem ages were varied within their 1-sigma age uncertainty and a

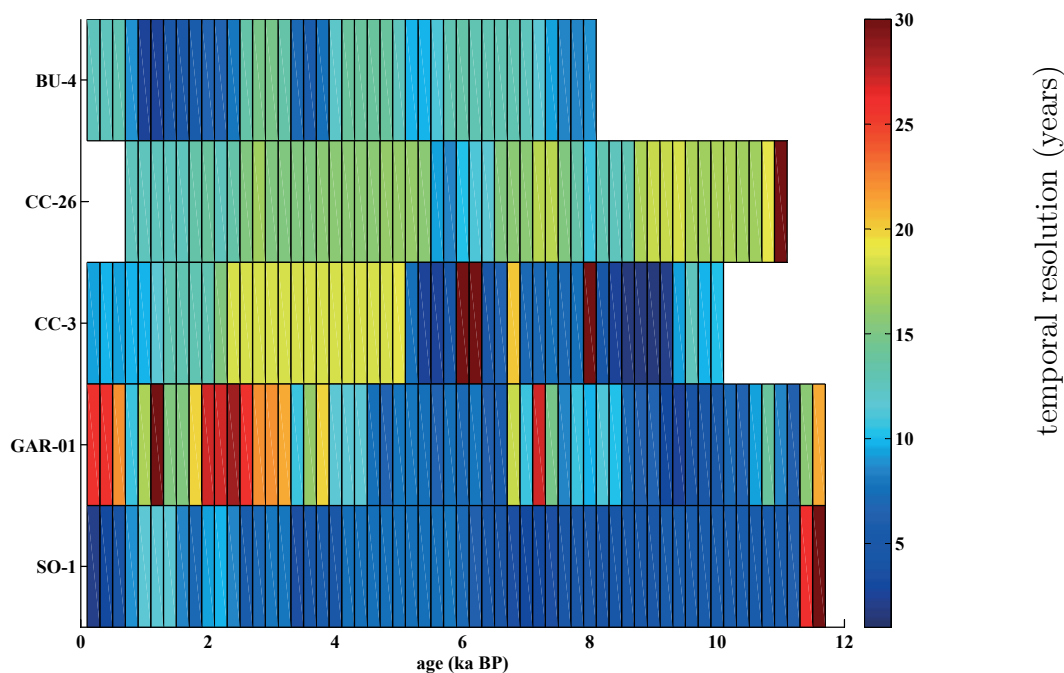


Fig. 10.7: The figure is illustrating the mean temporal resolution of the $\delta^{18}\text{O}$ time series of the stalagmites BU-4, CC-26, CC-3, GAR-01 and SO-1. To account for the age uncertainty of the measured a MC approach is applied to the age-model of each speleothem. Each rectangle is showing the mean temporal resolution at the corresponding age. The temporal resolution is indicated by the coloured shading.

linear interpolation between the ages was used for each of the MC runs, resulting in a linear age model for each speleothem. A total amount of 1000 MC runs has been performed. Based on the ensemble of 1000 runs, the mean temporal resolution is calculated for each speleothem by using a moving average of 100 years. This is illustrated in Fig. 10.7 where the coloured shading gives information on the mean temporal resolution for each 100 year time frame (rectangle). The colours differentiate between a temporal resolution smaller than 30 years. The temporal resolution of the five speleothems shows a high variability and differs from speleothem to speleothem (Fig. 10.7). While SO-1 has an almost constant temporal resolution throughout the Holocene, the temporal resolution of GAR-01 has a more variable growth rate. According to Fig. 10.7 the temporal resolution of GAR-01 is c. 25 years during the last 400 years of GAR-01's growth history. There is even a hiatus between 1.0 and 1.2 ka BP. In the mid-Holocene, 4.0 to 6.0 ka BP, the temporal resolution of GAR-01 is smaller than 10 years. It is posed by Fig. 10.7 that analysing different speleothem proxy time series with more sophisticated statistical tools, such as PCA, is not straight forward. This is due to the requirement that the temporal resolution of all speleothems must be

equal for detailed statistical analysis and consequently must be equalised.

10.2.3 Selection criteria for speleothem proxy time series

The preceding paragraphs have highlighted that investigating speleothem proxy time series for spatial-temporal coherent changes with principal component analysis, requires a preparation of the proxy time series. This includes a robust age-depth relation, which means that the uncertainty of the age determination should be small in comparison to the determined age. For this reason, only speleothems are used that have been dated with TIMS or ICP-MS techniques. In addition, the temporal resolution of the proxy time series should be smaller than 30 years. Furthermore, only speleothems are used that have a non-changing crystal configuration. This is due to the reason that the isotope fractionation effects are changed for different crystal configuration (Rubinson and Clayton, 1969; Romanek et al., 1992). Moreover, the speleothems should be equally distributed in order to avoid that a region is overvalued. However, the most important issue is to apply PCA not randomly on a selection of speleothem proxy time series. The proxy time series that are investigated should be related to each other. An example are $\delta^{18}\text{O}$ or $\delta^{13}\text{C}$ values of a speleothem that provide information on the water cycle and the vegetation, respectively.

10.3 How the PCA is performed

To apply PCA on speleothem proxy time series, the proxy time series need to be prepared beforehand. The age-depth relations illustrated in Fig. 10.6 (straight lines), are only one possible solution for the age-depth relation based on the measured ages of each speleothem. For this reason, a Monte-Carlo (MC) approach is applied to create an ensemble of age-depth relations, which are used to translate the proxy-depth relation into a proxy-age relation. The temporal resolution of the proxy time series of each MC run is equalised in a subsequent step. Finally, the PCA is applied on the ensemble of prepared proxy time series. The different steps of the procedure shall be explained in the following sections.

10.3.1 Procedure of age-depth relation modeling

To describe the procedure of how each age-model is constructed, the discussion is limited on the age-model of stalagmite BU-4 for simplicity. Fig. 10.8 illustrates the measured ages with their 1-sigma uncertainty. The straight line links the mean ages of each age that has been determined, whereas "mean" refers to the most likely age according to the statistics of the measurement, though other age-depth relations are also possible solution providing that the ages are within the age uncertainties.

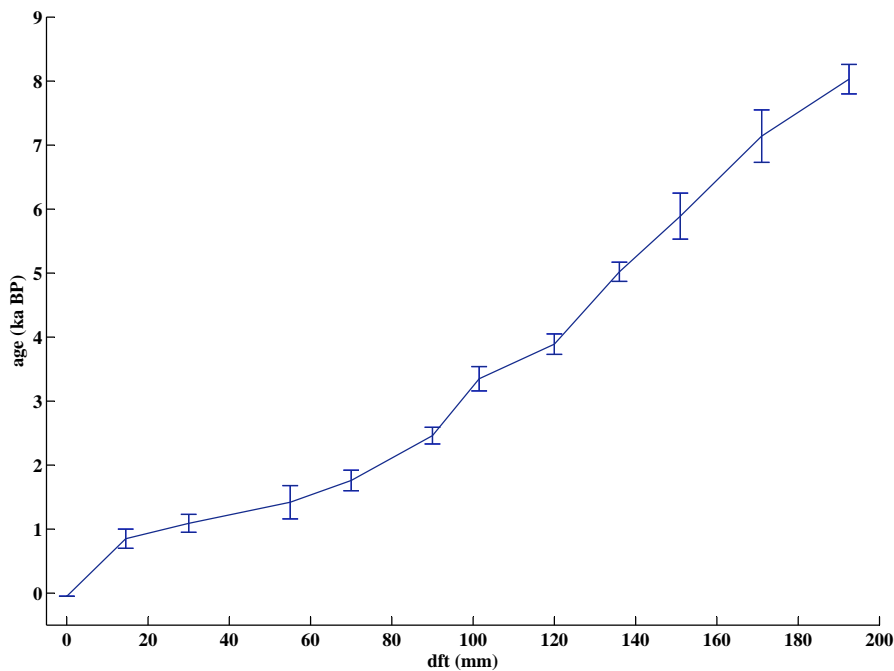


Fig. 10.8: Illustrated is the age-depth relation of stalagmite BU-4. The ages are pictured with the corresponding 1-sigma standard uncertainty and a linear interpolation method is applied.

To construct an age-depth relation, the stratigraphic order of the ages must be fulfilled, i.e., starting with the youngest age at the tip of a speleothem, the subsequent age must be older than the youngest age and the next age must be older than the foregoing. This requirement must be fulfilled by all ages along the growth axis. However, if the domain of values for ages is defined by the 1-sigma range of each individual age along the growth axis and the 1-sigma range of neighbouring ages are overlapping, there are certain age-depth relations possible at which the stratigraphic order of the age-depth relation is not fulfilled; i.e., the age-depth relation has age inversions. Accordingly, a routine must be developed to handle the age inversion of this certain age-depth relation.

10.3.1.1 Routines for age inversions

The first two ages:

To test each age-depth relation for age inversions, the youngest age is used as a tie-point. The subsequent 2^{nd} age of the age-depth relation is then compared to the 1^{st} age.

(*Scenario I*): In the case that the 2nd age of the age-depth relation is younger or equal than the 1st age it is not used for the constructed age-depth relations - "constructed" age-depth relations shall be defined as the original age-depth relation, that has been tested and corrected for age inversions, respectively. The same procedure is applied to the 3rd age. (*Scenario II*): If the 2nd age is older versus the 1st age it is compared with the 2nd's following age, the 3rd age. This is due to the reason, that the 2nd age can be older than the 3rd age in case that the 1-sigma ranges of the 2nd and 3rd age are overlapping. Thus, an age-inversion is possible. For this routine the two subsequent ages of the 2nd age, i.e., the 3rd and the 4th age are used, to distinguish between the cases, whether the 2nd and 3rd age are in stratigraphic order or not, and, in case not, if the 2nd age is too old or the 3rd age too young - for the last two cases the 4th age is used. (*Scenario IIa*): In the case that the 3rd age is older than the 2nd age, i.e., the stratigraphic order is fulfilled, the 2nd age is used for the constructed age-depth relation - note that for this case the 1st and 2nd age are in stratigraphic order. If the stratigraphic of the 2nd and 3rd ages is not fulfilled the 1st and 3rd age are compared. (*Scenario IIb*): If the 3rd age is older than the 1st age, the 2nd age is not used for the constructed age-depth relation. (*Scenario IIc*): Is even the 3rd age younger than the 1st age the 4th age is used as a further age reference - this case means technically that the 1- σ range of three succeeding ages are overlapping and the oldest age of the 1- σ range of the 1st age is older than the youngest age of the 1- σ range of the 3rd age. If the 4th age is older than the 2nd age, the 2nd age is used for constructing the age-depth relation. For a "chaotic" age-depth relation, where the 1- σ ranges of the first four ages are overlapping, it is likely that even the 4th age is younger than the 1st age. The routine is not designed for such complicated age-depth relations, and the original age-depth relation must be checked manually for such complicated age-depth sections.

The third and subsequent ages of the constructed age-depth relation:

When the first two ages of the constructed age-depth relation are determined all following ages are determined, by the similar procedure. For the 3rd age of the age-depth relation this means that instead of the 1st age (t_1) the 2nd age (t_2) of the constructed age-depth relation is the new tie-point. Hence, $t_1 \Rightarrow t_2$, $t_2 \Rightarrow t_3$, $t_3 \Rightarrow t_4$ and $t_4 \Rightarrow t_5$. Fig. 10.9 shows the ensemble of age-depth relations based on 1000 MC simulations for stalagmite BU-4. A linear interpolation method has been applied on the constructed age-depth relation. The universe of the ensemble covers the 1-sigma range of the age-depth relation. At the younger part of the speleothem, where the 1-sigma ranges of the 2nd and 3rd age and the 3rd and 4th age are overlapping, some constructed age-depth relations do not contain the 2nd and 3rd age, respectively. This is due to the reason that an age-inversion has occurred.

10.3.1.2 Interpolation between ages for age-depth modelling

After the constructed age-depth relation is finished, an interpolation method must be applied on it in order to assure that the proxy-depth relation can be translated into a

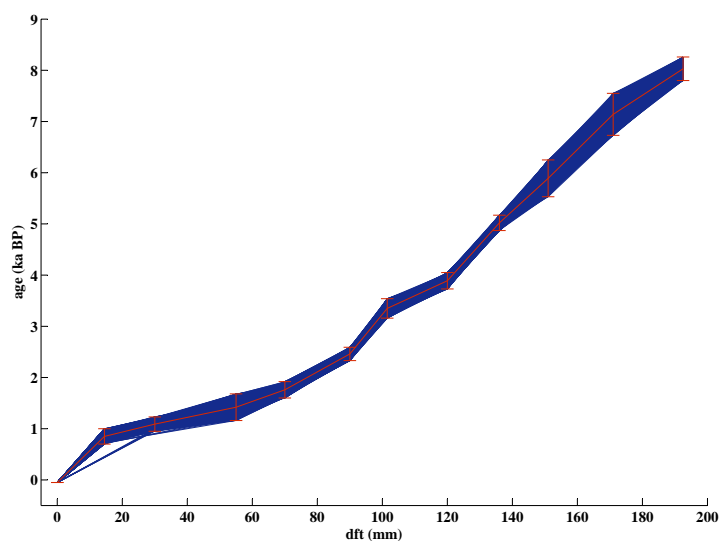


Fig. 10.9: Illustrated is the original age-depth relation of stalagmite BU-4 (red line). The blue shading area indicates the range of possible age-depth relations (see text for detail).

proxy-age relation. In the past, different models using different interpolation methods have been developed for age-depth modelling. [Scholz et al. \(2012b\)](#) presented a comprehensive overview and discussion on these models. Here a linear interpolation method is used following [Scholz and Hoffmann \(2011\)](#). This is due to the reason that a linear interpolation between ages is the simplest method that can be applied on speleothem age-depth relations. This interpolation method implies that the growth rate of the speleothem responds linearly to environmental changes which affect the growth rate.

Fig. 10.10 illustrates the age-depth relation (blue) including the 1-sigma age uncertainty of each measured age. A linear age interpolation is applied on the age-depth relation. Presented is only the case where the most likely ages were applied for the age-depth relation. The $\delta^{18}\text{O}$ -depth relation is indicated by the red curve. Combining both the age-depth relation and the proxy-depth relation enables a transformation of the proxy-depth relation into a proxy-age relation. For each MC run, the proxy-age relations must be equalised in order to gain a similar temporal resolution. This proxy-age relation can then be used for further analysis.

10.3.2 Temporal resolution model

When the proxy-age relation is constructed for all speleothems, the temporal resolution along the growth axis is usually not constant and varies with the age of the speleothem. This

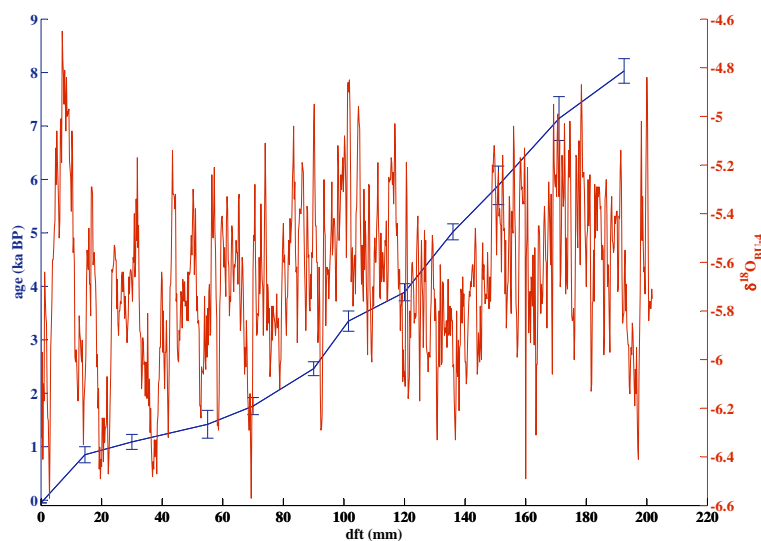


Fig. 10.10: The blue curve illustrates the age-depth relation of stalagmite BU-4; the blue errorbars indicate the $1\text{-}\sigma$ uncertainty of each measured age. A linear age interpolation is applied. The $\delta^{18}\text{O}$ -depth relation of stalagmite BU-4 is indicated in red.

is illustrated in Fig. 10.7 for five different speleothems (BU-4, CC-26, CC-3, GAR-01, SO-1). The coloured shading indicates the temporal resolution for each speleothem. To equalise the temporal resolution for all speleothem proxy-age relations, it must be considered that a section with a higher temporal resolution, i.e., a smaller value for the temporal resolution, contains more information compared to a section with a smaller temporal resolution. In order not to create non-existing temporal information of a speleothem time series, the temporal resolution of all analysed speleothem proxy time series must be equalised with respect to the lowest temporal resolution. However, as Fig. 10.7 illustrates, the temporal resolution of each speleothem varies with its growth history. Taking GAR-01 as an example, at some stages of GAR-01's growing phase, e.g, between 2.0 and 3.0 ka BP, the stalagmite has the highest values for the temporal resolution compared to the other four stalagmites. However, between 4.0 and 5.0 ka BP it has also smaller values compared to highest value for the temporal resolution of all stalagmites - here stalagmite CC-3 has the highest values for the temporal resolution. In order to not to loose information, the speleothem time series are scanned for the lowest temporal resolution at each point of time for their coeval growth history. In following step, the speleothem time series are then equalised according to the lowest temporal resolution during their growth history. If that the lowest resolution alternates between the speleothems for different ages, the evolution of the lowest temporal resolution is then a function of all speleothem time series. The procedure shall be introduced in the following paragraphs.

10.3. How the PCA is performed

Determination of coeval growth history: The first step is to find the period in which all speleothems have grown simultaneously. The youngest age of this period, τ_1 , representing the oldest age of the collection of all youngest ages. Mathematically this means that

$$\tau_1 = \max \{t_1^i\}_{i=1:n}, \quad (10.13)$$

whereas t_1^i is the youngest age of speleothem i ; n denotes the number of speleothems. For the oldest age, τ_{end} , of the period, the youngest age of the collection of all oldest ages is chosen. The mathematical formulation of this condition is

$$\tau_{end} = \min \{t_{end}^i\}_{i=1:n}. \quad (10.14)$$

Here, t_{end}^i is the oldest age of speleothem i ; n is the number of speleothems again. When the youngest and oldest age are determined, the temporal evolution of the temporal resolution within the time interval of coeval growth history needs to be calculated.

Determination of the temporal evolution of the temporal resolution: The subsequent step of the routine is to determine the temporal resolution for all speleothem proxy time series during the coeval growth history. For this, it is considered that the temporal resolution at any point of time can not be smaller than the maximum of the compilation of all values for the temporal resolution of all speleothems at the given point of time. After the beginning of the coeval growth history is defined by τ_1 , the 2nd age is determined in the following way: for all speleothem time series the age difference, Δt_{12} , between τ_1 and the successive age, t_j^i , with $t_j^i > \tau_1$, of the time series is calculated, whereas i is a placeholder for the speleothem and j denotes the number of the proxy value of the speleothem's time series.

$$\Delta t_{12} = \{t_j^i - \tau_1\}_{i=1:n}. \quad (10.15)$$

Δt_{12} is the temporal resolution at τ_1 . Hence, the second age, τ_2 , is given by the maximum value of Δt_{12} and τ_1 :

$$\tau_2 = \tau_1 + \max(\Delta t_{12}). \quad (10.16)$$

All other values are calculated with the same procedure until $\tau_k \geq \tau_{end}$:

$$\tau_k = \tau_{k-1} + \max(\Delta t_{(k-1)k}). \quad (10.17)$$

τ_k is the k^{th} age of the constructed time series, τ_{k-1} is the previous age and $\Delta t_{(k-1)k}$ is the age difference between τ_{k-1} and the subsequent ages of the speleothem proxy time series. The ages of the constructed time series, T , are given by the compilation of all ages τ_k ; if m is the number of ages, T_i is given by

$$T_i = \{\tau_1, \tau_2, \dots, \tau_{k-1}, \tau_k, \dots, \tau_{m-1}, \tau_m\}, i = 1, 2, \dots, n. \quad (10.18)$$

Note, that T_i is the same for all speleothems.

Determination of proxy values: The proxy values at time τ_k for each speleothem proxy time series are calculated as follows: if τ_k is part of the ages of a speleothem proxy time series, the proxy value of the time series at τ_k is used; this is the case when the considered speleothem time series has the lowest temporal resolution during corresponding time interval. For all other cases, τ_k lies in between two subsequent ages t_j^i and t_{j+1}^i ($i = 1, 2, \dots, n$) of the speleothem proxy time series and the related proxy value is calculated with a linear interpolation between the proxy values at t_j^i and t_{j+1}^i . Mathematically expressed that means: If $\tau_k \in [t_1^i \dots t_{end}^i]$ ($i = 1, 2, \dots, n$) and $\tau_k = t_j^i$ then the proxy value for the new time series T^i for speleothem i is

$$T^i(\tau_k) = \Gamma^i(t_j), \quad (10.19)$$

whereas $\Gamma^i(t_j)$ is the proxy value of the speleothem i at time t_j . In case that $t_j^i < \tau_k < t_{j+1}^i$, the proxy value for T_i at τ_k is calculated using a linear interpolation between the ages t_j^i and t_{j+1}^i :

$$T^i(\tau_k) = \frac{\Gamma^i(t_{j+1}) - \Gamma^i(t_j)}{(t_{j+1} - t_j)}(\tau_k - t_j) + \Gamma^i(t_j). \quad (10.20)$$

$\Gamma^i(t_{j+1})$ and $\Gamma^i(t_j)$ are the proxy values of speleothem i at time t_{j+1} and t_j . This procedure results in n constructed time series T^i with an equal resolution that can be investigated performing a PCA.

Fig. 10.11 is picturing BU-4's $\delta^{18}\text{O}$ time series for one MC run before the temporal resolution is equalised (blue dashed line) and after the temporal resolution is equalised (red straight line); the blue squares and red circles indicate the corresponding proxy values, here $\delta^{18}\text{O}$ for both time series, respectively. Furthermore, Fig. 10.7 illustrates that BU-4 has the lowest temporal resolution in comparison to the other four speleothems (CC-26, CC-3, GAR-01, SO-1) between 5.5 and 6.5 ka BP (except the hiatus of CC-3 between 5.9 and 6.3 ka BP). This feature is also depicted in Fig. 10.11. Here the $\delta^{18}\text{O}$ values correspond to the constructed time series T^{BU-4} of the original, which is the non modified $\delta^{18}\text{O}$ time series of stalagmite BU-4. To gain a better illustration of the time frame between 5.0 and 8.0 ka BP, a zoom function of the $\delta^{18}\text{O}$ time series is illustrated in Fig. 10.12.

The $\delta^{18}\text{O}$ time series for stalagmite BU-4, CC-26, CC-3, GAR-01, SO-1 is pictured in Fig. 10.13 (from top to bottom). One MC runs was performed and the blue function is picturing the $\delta^{18}\text{O}$ time series of the speleothems before the equalisation of the temporal resolution whereas the red function is illustrating the $\delta^{18}\text{O}$ time series after the equalisation

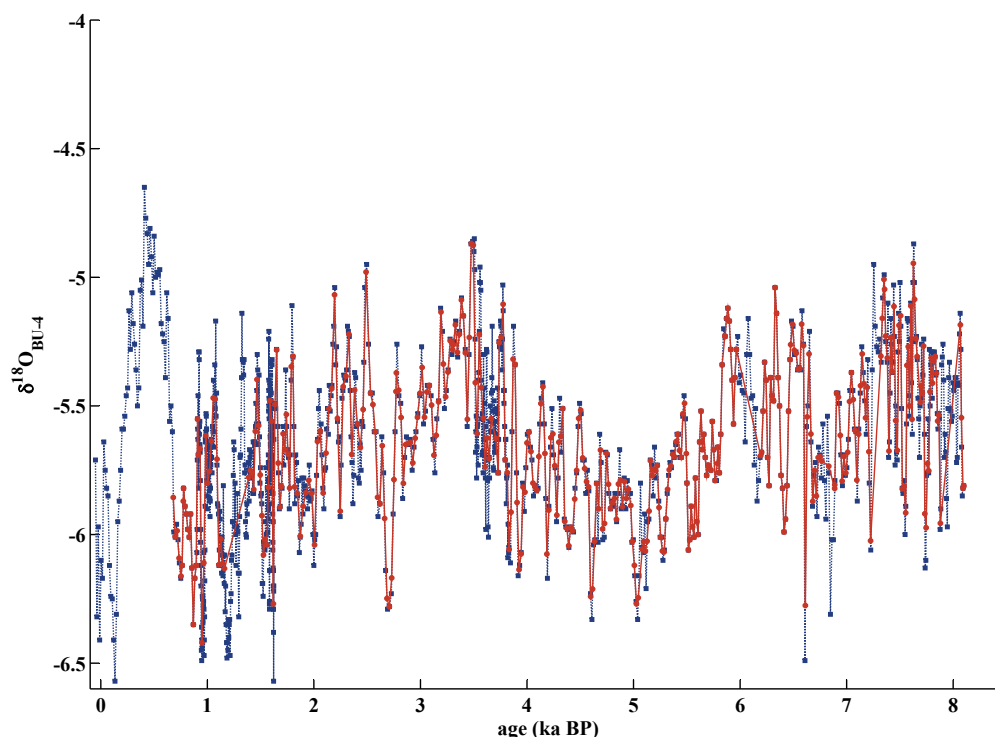


Fig. 10.11: Illustrated are the age-proxy ($\delta^{18}O$) relations of stalagmite BU-4 for one MC run: the blue curve is the age-proxy relation before the equalisation of the temporal resolution with the age-proxy relations of the stalagmites CC-3, CC-26, GAR-01 and SO-1. The red curve is the age-proxy relation of stalagmite BU-4 after the equalisation of the age-proxy relations.

of the temporal resolution. The figure shall point out that the characteristics of each proxy ($\delta^{18}O$) time series are preserved by the procedure.

10.3.3 Performance of PCA

After the time series T^i ($i = 1, 2, \dots, n$) are assembled, each T^i is rescaled for a mean value of 0 and a variance of 1. Then a PCA is applied on the compilation of time series T^i . From the PCA it is obtained: (i) n principal components (PC), (ii) the PC's eigenvalues λ_i , (iii) the loadings of each T_i for every PC and (iv) after the projection of the time series T^i with the PCs the PC's time series, χ_i . In addition to the loadings, the Spearman's rank correlation coefficient, r_s , between T^i with χ^i is calculated. See section 10.1 for details

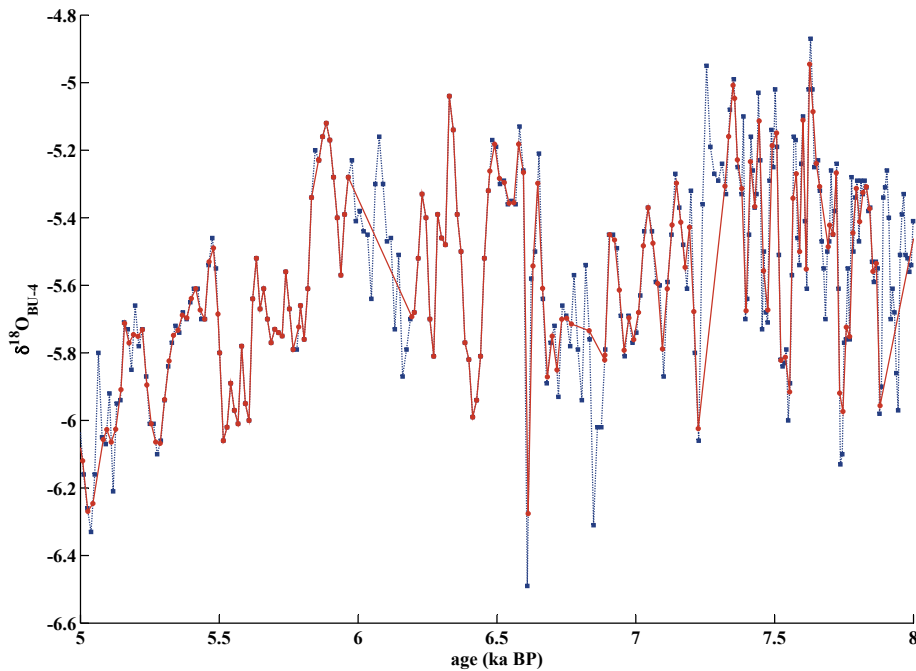


Fig. 10.12: Same as Fig. 10.11 but between 8 ka BP and 5 ka BP.

about the mathematical aspects of PCA.

10.3.4 Monte Carlo Approach

The Monte Carlo approach defines a computer simulation that is repeated several times, which is in this framework the construction of proxy-age relations for the used speleothems. This results in an ensemble of input time series T^i on which PCA is applied to every T^i . Therefore, for every performed PCA PCs, λ , χ^i and r_s are obtained. The results are analysed subsequently. The ensemble of χ^i 's are then "re-sampled" to derive a mean value and a standard deviation from the ensemble. In order not to create non-existing temporal information, the different temporal resolutions of the proxy time series T^i must be considered. Though only proxy time series T^i whose temporal resolution was smaller than 30 years are considered - this is one of our selection rules for speleothem proxy time series - a 30 year running mean is calculated from the ensemble of PC time series.

Fig. 10.14 pictures the 1st PC time series (blue dots), i.e., χ^1 , derived from a compilation of five different speleothem $\delta^{18}\text{O}$ time series (BU-4, CC-26, CC-3, GAR-01, SO-1) after a total of 1000 MC simulations. The red circles are the mean values for the 30-year time windows.

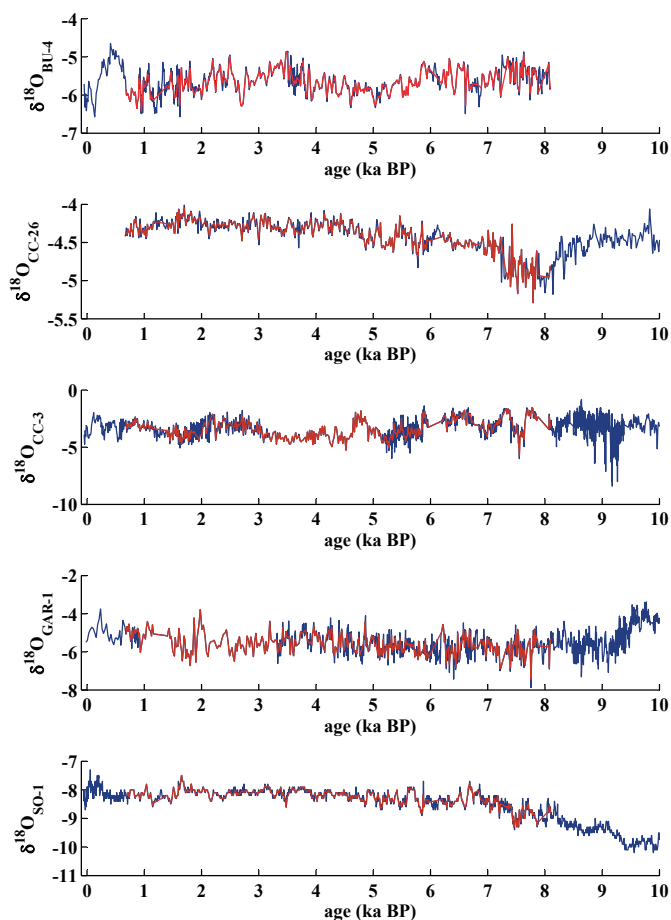


Fig. 10.13: The figure is illustrating the age-proxy ($\delta^{18}\text{O}$) relation of the stalagmites BU-4, CC-26, CC-3, GAR-01 and SO-1 before the equalisation of the temporal resolution (blue line) and after the equalisation (red lines).

The red lines indicate the corresponding 1-sigma standard deviation from the mean value.

10.4 Results of PCA with artificial proxy time series

In the previous section (Sec. 10.3) the procedure for the PCA was explained. Within this section the behaviour of PCA on different boundary conditions of the compilation of speleothem proxy time series shall be discussed. Boundary conditions are the age

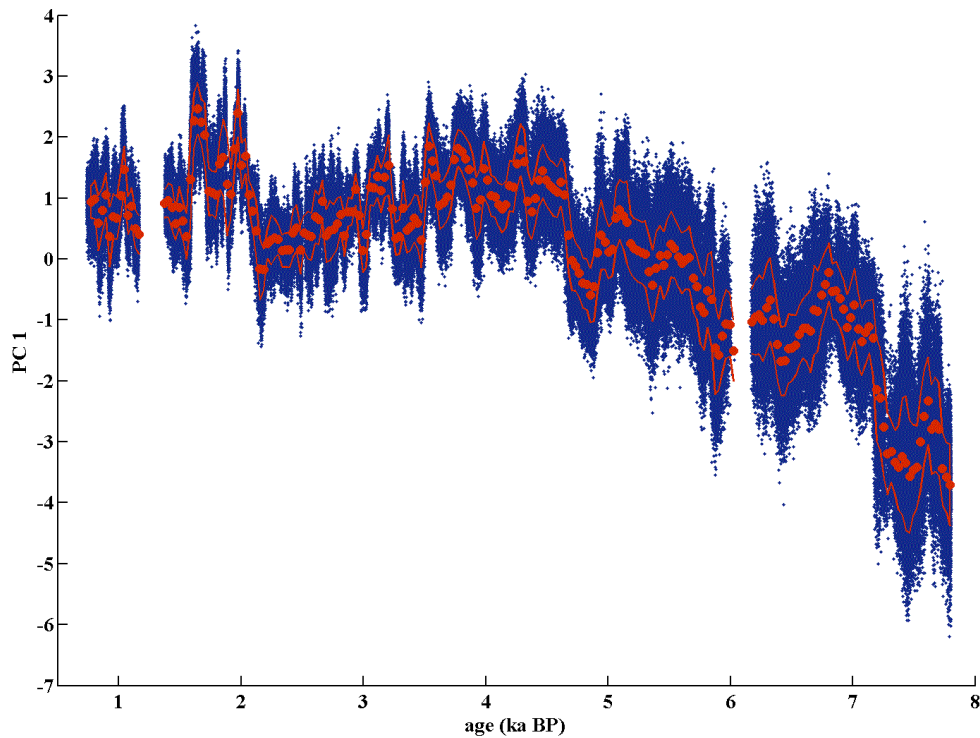


Fig. 10.14: The ensemble of χ^1 (PC 1) (blue dots) for 1000 MC simulations for the PCA of five speleothems (BU-4, CC-26, CC-3, GAR-01, SO-1) is re-sampled. The red circles show the mean value of each 30 year time window and the red lines indicate the 1-sigma standard deviation of the corresponding mean value.

uncertainty of the age models, the number of investigated speleothems and the number of MC runs. For these three different kind of artificial compilations of speleothem proxy time series are investigated. The first boundary condition, the age uncertainty of the age models, is composed of only one real speleothem proxy time series, being the "best-case" scenario, in the meaning that all investigated speleothems have recorded the same proxy signal. This is quoted as the single speleothem experiment. Here, the speleothem age-depth and $\delta^{18}\text{O}$ -depth relation of stalagmite BU-4 is used. The second and third compilations are assembled of proxy time series that are based on an auto-regressive time series. The second one having a memory effect, i.e., it has a persistence, and the third one having no memory effect. For the second artificial time series, the properties of the proxy time series of BU-4 is used and is then computed based on an AR-1 process. The third time series is simply a Gaussian white noise time series.

10.4.1 The sensitivity of PCA on the age error

To test the sensitivity of PCA results on the number of used speleothem records and the age uncertainty, several experiments were performed, in which the sensitivity of the eigenvalues on the age uncertainty is investigated for 0-sigma, 1-sigma and 2-sigma. Furthermore, the sensitivity on the number of speleothem proxy time series is tested for 2, 4, 8 and 16 speleothems. The PCA is conducted for 10, 100, 1000 and 2000 MC simulations to verify the convergence of the PCA's results.

10.4.1.1 The 0-sigma experiment

The evolution of the eigenvalues for the single speleothem experiment is illustrated in Fig. 10.15 for 2, 4, 8, and 16 speleothem time series (top to bottom) when the ages have no age uncertainty; for all cases a total of 10, 100, 1000 and 2000 MC runs were performed, respectively. Since the age uncertainty is 0 ka, the age model of the performed MC runs is unchanged for different runs. Hence, there is no difference in the results if 10, 100, 1000, 2000 MC runs or just 1 MC run is conducted. The absolute value of the 1st eigenvalue increases with the number of speleothem proxy time series, with a value of 2, 4, 8 and 16 for 2, 4, 8, and 16 speleothem proxy time series, respectively. All other eigenvalues are 0. This is because all speleothem proxy time series are identical, i.e., linearly dependent. In terms of PCA, this means that the speleothem proxy time series contains no noisy component, which is not surprising as the same speleothem proxy time series is used and the ages have no age uncertainty.

10.4.1.2 The 1-sigma experiment

The 0-sigma experiment demonstrates that for identical speleothem proxy time series whose age uncertainty is 0, only the first leading mode, i.e., only the 1st eigenvector, accounts for the variance of all time series. Fig. 10.16 shows the evolution of the mean eigenvalues derived for 2, 4, 8 and 16 speleothem proxy time series (here BU-4's $\delta^{18}\text{O}$ time series) (top to bottom) for 10 (blue), 100 (red), 1000 (green) and 2000 (purple) MC runs. The errorbars indicate the 1-sigma standard deviation of each mean eigenvalue based on the ensemble of eigenvalues. Fig. 10.16 reveals that, if the ages of the age-model vary within their 1-sigma age uncertainty, the absolute value of the 1st eigenvalue decreases whereas the values of eigenvalues of higher order increase in comparison to the 0-sigma experiment. However, the 1st eigenvalue has still the highest value compared to eigenvalues of higher order and the eigenvalues are monotonously decreasing with higher order.

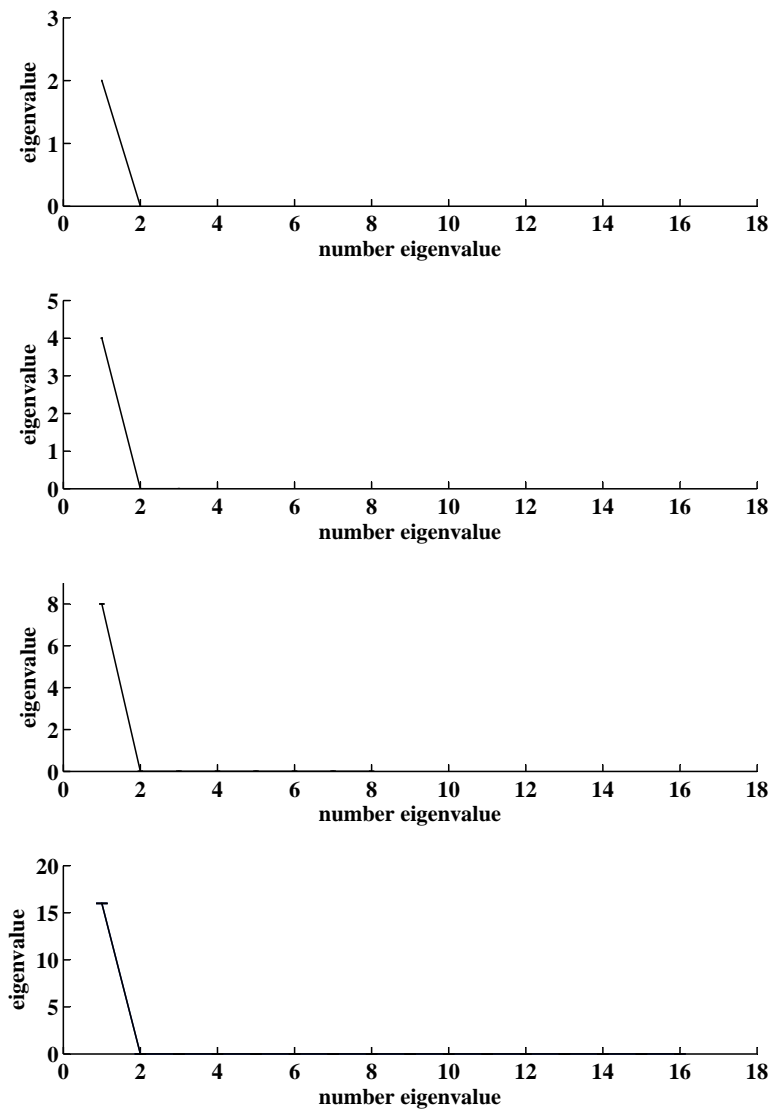


Fig. 10.15: The figure is illustrating the convergence of the eigenvalues for 2, 4, 8 and 16 speleothems (from top to bottom panel) for an assumed age uncertainty of 0-sigma.

10.4.1.3 The 2-sigma experiment

Fig. 10.17 shows the same as Fig. 10.16, the evolution of the mean eigenvalues for different numbers of speleothem proxy time series, but for a 2-sigma age uncertainty. The errorbars indicate the 1-sigma standard deviation of the mean eigenvalue. Compared to Fig. 10.16 and Fig. 10.15 the absolute value of the 1st eigenvalue has decreased whereas the absolute value of eigenvalues of higher order increased. Although the eigenvalues are monotonously decreasing with higher order. The 1-sigma standard deviation for the mean eigenvalues has increased in comparison to 1-sigma experiment, which is a result of the larger age uncertainties.

10.4.1.4 Discussion of the results based on the three experiments

Comparing the evolution of eigenvalues of Fig. 10.15, Fig. 10.16 and Fig. 10.17 for different number of MC runs, the convergence behaviour of the eigenvalues reveals that the eigenvalues converge within 1000 MC runs. Furthermore, the 1-sigma standard deviation of the mean eigenvalues is increasing with increasing age uncertainty of speleothem's ages. For a better illustration, Fig. 10.18 shows the evolution of the mean eigenvalues for a age uncertainty of 0, 1 and 2-sigma (top to bottom) of the speleothem's ages for 2, 4, 8 and 16 speleothems, respectively, based on 1000 MC runs. With increasing age uncertainty, the 1st eigenvalue decreases whereas the eigenvalues of higher orders are increasing. This means that the eigenvectors of 2nd and higher orders also contribute to the speleothem proxy time series when the age uncertainty of speleothem's ages is not 0; the percentage of the contribution is even increasing with a higher age uncertainty. This is due to the fact that the higher the age uncertainty is, the more the time series are shifted against each other, which results in a loss of correlation between the speleothem proxy time series. Consequently, the other PCs (eigenvectors) become more important. Though the age uncertainty varies within the 1-sigma (2-sigma) range, the 1st PC still explains 71.3 (65.2), 58.3 (49.3), 52.2 (41.2) and 49.3 (37.6) % of the total variance for 2, 4, 8 and 16 speleothem proxy time series, respectively; for 0-sigma the 1st PC explains 100 % of the total variance. Hence, the 1st PC is still the dominant signal. However, since PCs of higher order are mostly interpreted as a noisy component of the original speleothem proxy time series and since they become more dominant for higher age uncertainties, all following PCA are conducted with ages varying in the 1-sigma range for the speleothem's ages parameter space.

10.4.2 The sensitivity of PCA on "Gaussian White Noise" time series

In the preceding section, the evolution of the eigenvalues for a compilation of identical speleothem proxy time series were investigated - the eigenvalues are indicating the the contribution of each PC to the total explained variance. However, speleothem proxy time

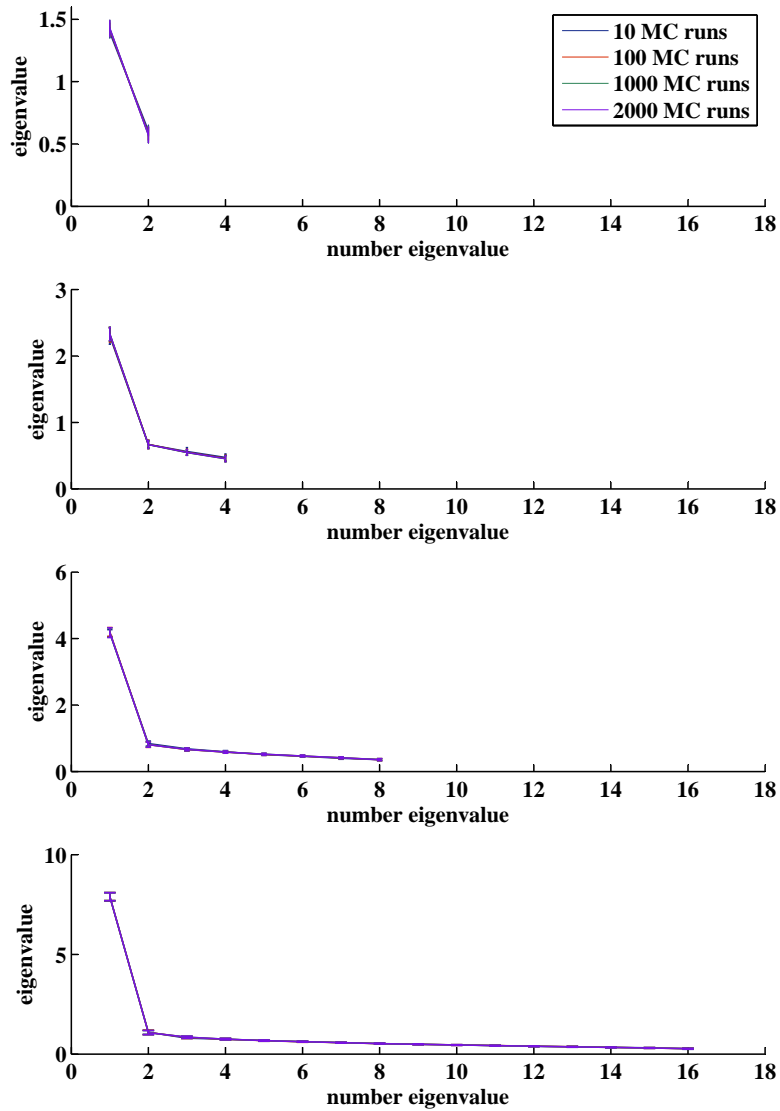


Fig. 10.16: The figure is illustrating the convergence of the eigenvalues for 2, 4, 8 and 16 speleothems (from top to bottom panel) for an assumed age uncertainty of 1-sigma.

series are influenced by several processes causing differences in the temporal evolution of proxy time series from different speleothems. For this, the behaviour of PCA on two more datasets artificial time series is investigated. The datasets are, (i) a compilation of AR-1

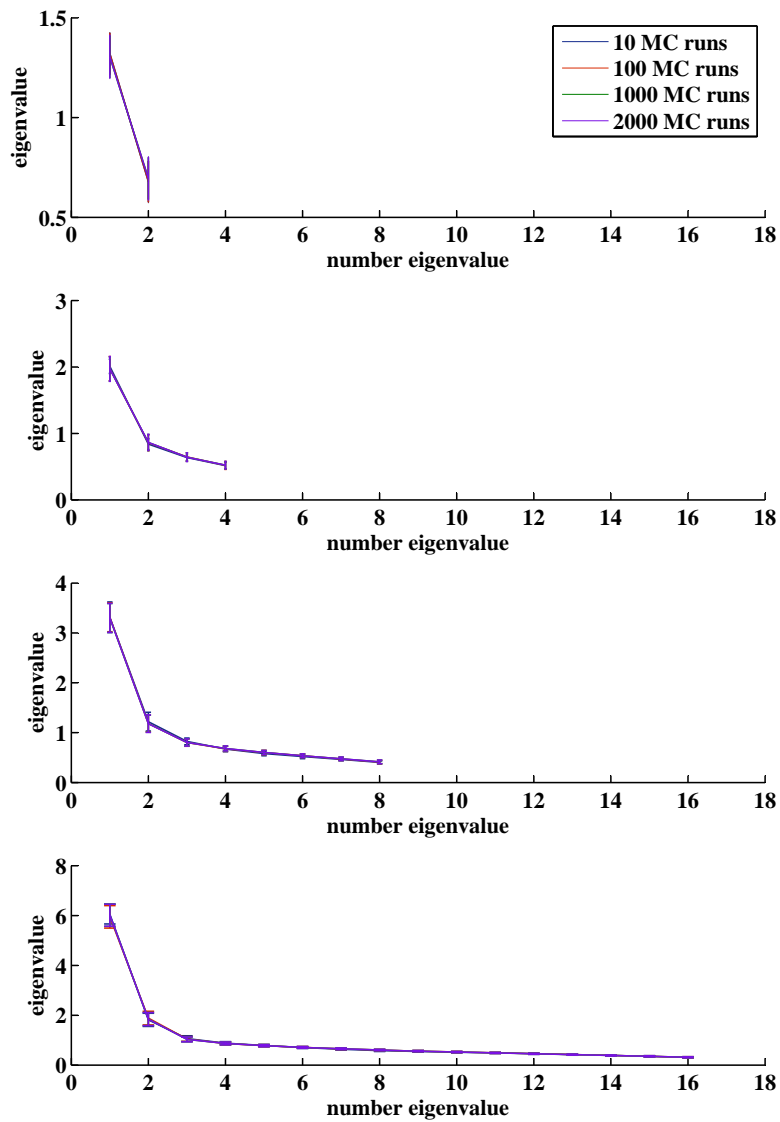


Fig. 10.17: The figure is illustrating the convergence of the eigenvalues for 2, 4, 8 and 16 speleothems (from top to bottom panel) for an assumed age uncertainty of 2-sigma.

time series with a memory effect for the foregoing proxy value - AR-1 time series are based on autoregressive model of first order - and (ii) a compilation of Gaussian white noise (WN) time series. Fig. 10.18 illustrates the evolution of eigenvalues for 2 (blue), 4 (red), 8

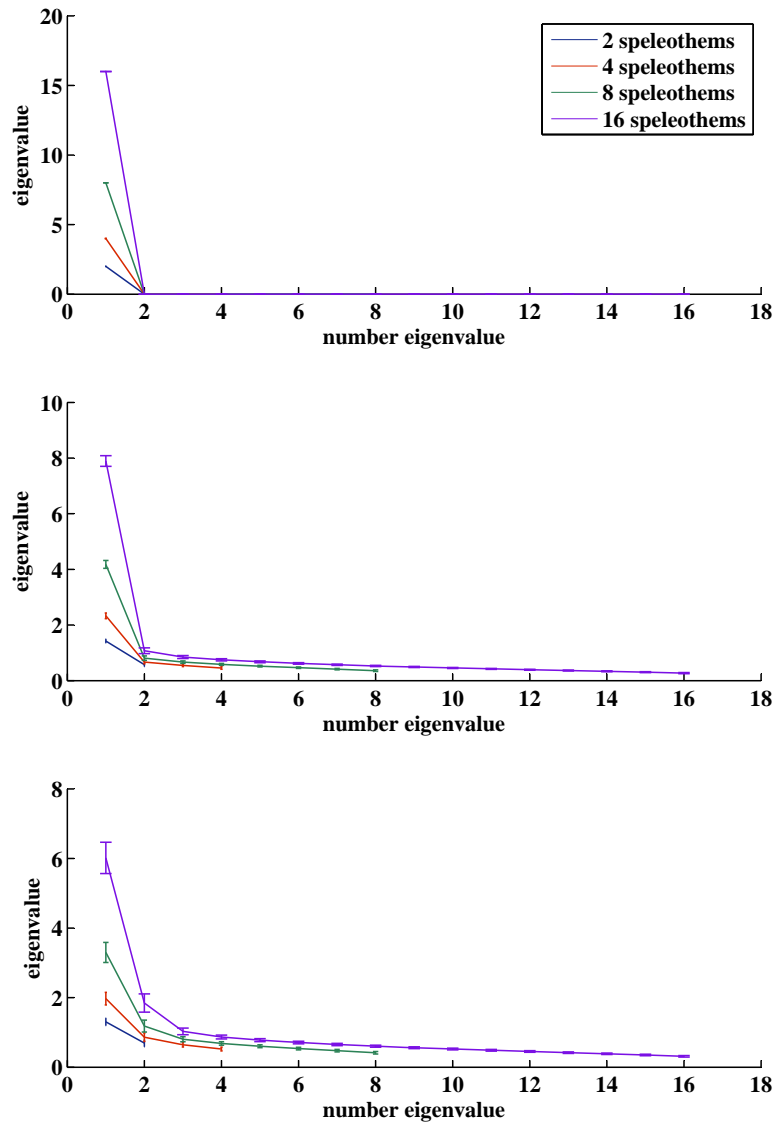


Fig. 10.18: Evolution of eigenvalues and age uncertainty within the 0, 1 and 2-sigma range (top to bottom panel) based on a total 1000 MC runs for 2 (blue), 4 (red), 8 (green) and 16 (purple) speleothems. All eigenvalues are illustrated with the corresponding 1-sigma error.

(green) and 16 (purple) speleothems for 1000 MC runs, using only the proxy time series of stalagmite BU-4; the ages are varying within the 1-sigma range. The figure depicts that

the eigenvalues are decreasing with higher order. However, there is no a priori criterion for the significance of eigenvalues (and eigenvectors). To test the significance of variables, it is common in time series analysis to use artificial time series with certain properties for this purpose (Preisendorfer and Mobley, 1988). Here, the properties of the AR-1 and WN time series are used to determine the significance of PC. The AR 1 time series are determined by the properties of the investigated time series and based on the following equation for unequal spacing (Mudelsee, 2010):

$$x(1) \sim N(0; 1), \quad (10.21)$$

$$x(i) = x(i-1) \cdot a^{[t(i)-t(i-1)]} + \epsilon(i), i = 2, \dots, n, \quad (10.22)$$

whereas a is the autocorrelation parameter and ranges between -1 and 1; ϵ is Gaussian random process with a mean value of 0 and a standard deviation of 1. The artificial time series are assembled as follows: For the Gaussian white noise time series the original speleothem proxy values are replaced by random values with a mean value of 0 and a standard deviation of 1. To assemble the AR 1 time series, the speleothem proxy values are replaced by values calculated with Eq. (10.22). Then, the usual MC procedure is applied on the compilation of artificial time series. Preisendorfer and Mobley (1988) compared the 95 % confidence interval of the eigenvalues of the artificial time series with the eigenvalues of the original proxy time series and stated that all values that are above the 95 % level are significant. This rule is called "Rule N" or "Preisendorfer's Rule N". However, the authors also comment that "there is [...] some evidence that Rule N may not be very robust when the data are highly non-normal in distribution." The limits in Preisendorfer's Rule N shall be discussed later in this chapter.

Fig. 10.19 illustrates the area between the 5 % and 95 % confidence level of the computed eigenvalues for artificial AR 1 time series (red shading), for artificial white noise time series (green shading) and the mean eigenvalues (blue), including the 1-sigma standard deviation (blue error bars) of a single speleothem compilation, here the $\delta^{18}\text{O}$ time series of stalagmite BU-4. The parameter of the AR-1 model is also base on the $\delta^{18}\text{O}$ time series of stalagmite BU-4. It is illustrated for compilations of 2, 4, 8 and 16 speleothems, respectively. In all four cases, for 2, 4, 8 and 16 speleothem time series, the mean of the eigenvalue of the 1st PC is higher compared to the 95 % level, whereas the mean value of the eigenvalues of 2nd and higher orders are all below the 95 % level for both, the AR 1 time series and the white noise time series, respectively. In terms of the significance of PCs, the 1st PC is significant and is interpreted physically. PCs of 2nd and higher order are insignificant and are interpreted as noise, which results from variations of the ages of the speleothem's age models. Another feature which is revealed by Fig. 10.19, is that for PCs of higher order, the 95 % level for AR 1 time series is below the 95 % level interval of white noise time series.

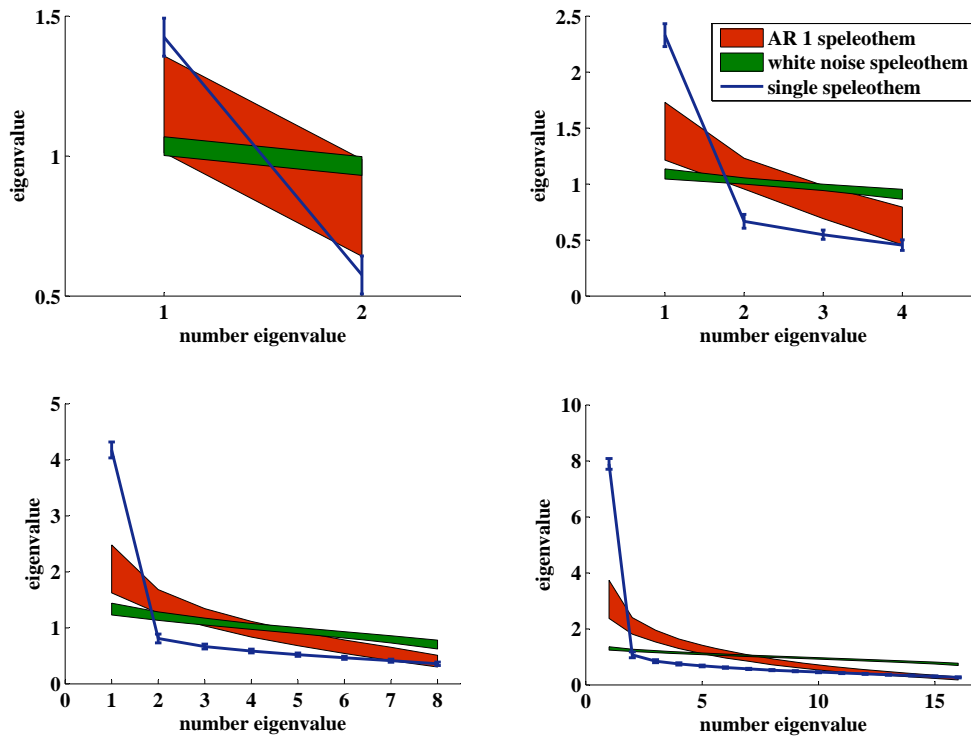


Fig. 10.19: The red shading area indicate the 95 % confidence interval of eigenvalues for an AR 1 time series, the green shading area depicts the 95 % confidence interval of eigenvalues for white noise time series. The mean eigenvalues for the single speleothem experiment are indicated in blue, including their 1-sigma standard deviation (see text for detail).

10.4.2.1 Discussion of the results for "Gaussian White Noise" time series

Preisendorfer's Rule N provides a practical tool for the estimation, whether PCs are significant or not. This is illustrated in Fig. 10.19. Here, the 1st eigenvalue is significant compared to the 95 % level of the AR 1 and white noise time series, regardless if 2, 4, 8 or 16 speleothems time series are analysed. PCs of higher order are all insignificant. This result is somewhat intuitive, as the original compilation of speleothem proxy time series consists only of one single speleothem proxy time series (here stalagmite BU-4's $\delta^{18}\text{O}$ time series), but is used 2, 4, 8 and 16 times. Hence, the 1st PC is physically interpreted as the $\delta^{18}\text{O}$ signal of the original speleothem proxy time series, namely as the temporal evolution of the $\delta^{18}\text{O}$ signal of stalagmite BU-4. The PC of 2nd and higher orders are insignificant and interpreted as noise and do not have any physical meaning. This noisy signal results from the age uncertainty of the speleothem's age models, which shifts the time series against each

other and anticipates a total temporal coherence, i.e., congruency. Congruency occurs in the 0-sigma experiments, where the 1st PC explains 100 % of the total variance of the time series compilation. Certainly, such academic compilations of speleothem proxy time series are investigated and such compilations with PCA are especially essential for research due to their "perfect" coherence. But if speleothem proxy time series are investigated from different regions that have grown simultaneously, there is a priori no reason why the proxy time series are coherent. In other words, there is no reason why speleothem proxy time series should correlate; a posteriori, there can be a spatio-temporal coherence between speleothem proxies from different regions, if the proxies are sensitive for similar environmental changes, e.g., temperature, or are part of the same proxy cycle as $\delta^{18}\text{O}$.

10.5 Time window length and significance of PCA

The advantage of the PCA procedure is that the time window's boundaries, i.e., the length and start point of the time window, are not only limited on the beginning and ending of the speleothems coeval growth history, but can vary within these boundaries. On one hand, this opens up the possibility to track changes of the spatio-temporal coherence pattern and of the PCs time series - and for the latter to test the robustness of the derived PC time series (see below). But on the other hand, this introduces the challenge to determine whether possible changes of the spacial temporal coherence pattern are significant or not. It further defines the limitations of the boundary values, in particular the length of the time window. To investigate the effect of changed boundary conditions of the time window on the behaviour of PCA results, the artificial speleothem proxy time series (see Sec. 10.4) are used. Only a total number of 8 and 16 speleothem proxy time series were included, respectively. For this purpose, the window length is reduced from 8.0 ka to 4.0 ka to 2.0 ka to 1.0 ka, using the same start point for all runs (Fig. 10.20). In a second experiment, the effect of the start point and the window length on the PCA results is compared for two different window lengths of 1.0 ka and 0.5 ka and two different start points, respectively - note that for the last experiment the compilation of speleothem proxy time series consists only of the $\delta^{18}\text{O}$ time series of stalagmite BU-4. To test the significance of the compilation of speleothem proxy time series, the derived eigenvalues are compared with the eigenvalues for two compilations of artificial time series; a composition of time series is based on an AR-1 model and of white noise model, respectively. A total amount of 1000 MC runs were performed, where the ages of the speleothems varied within their 1-sigma range.

Fig. 10.20 illustrates the eigenvalues for four different time windows with varying time window length. The red and orange shading area indicate values between the 5 % confidence level and the 95 % confidence level of the eigenvalues for artificial AR 1 time series for 8 and 16 speleothems, respectively; the dark (8 speleothems) and light green (16 speleothems) shading areas show the same but for artificial white noise (WN) time series. The dark blue line represents the evolution of the mean eigenvalues for 8 speleothems; the errorbars

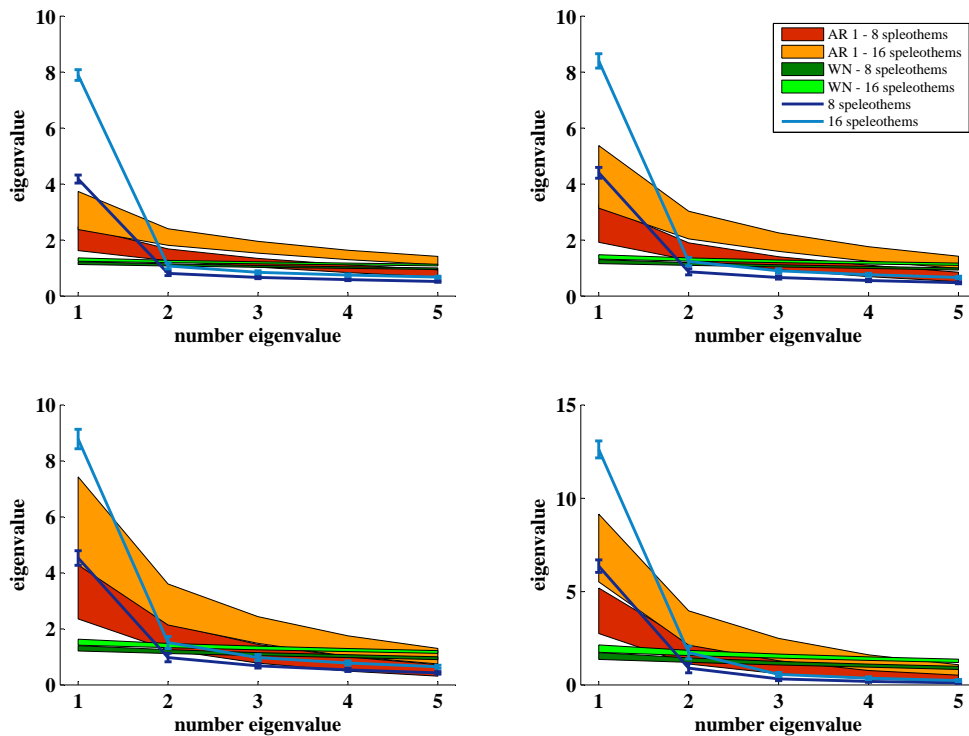


Fig. 10.20: The figure illustrates the comparison between the mean eigenvalues for a compilation of 8 (dark blue) and 16 speleothems (light blue) with the respective 95 % confidence interval of eigenvalues computed from compilations of AR-1 time series (red and orange) and WN time series (dark green and bright green for different time window lengths). The top left panel is for a window length of 8.0 ka; the top right panel for a window length of 4 ka; the bottom left panel for 2 ka and the bottom right panel for 1 ka. All time windows end at 0.0 ka BP (see text for detail).

indicate the 1-sigma standard deviation from the mean value; the light blue line illustrates the mean eigenvalues for 16 speleothems and the errorbars represent the 1-sigma standard deviation. All investigated time windows end at 0.03 ka BP (1920 CE) and have a time length of 8.0 ka, 4.0 ka, 2.0 ka and 1.0 ka, respectively. Comparing the results of the eigenvalues for a window length of 8.0, 4.0, 2.0 and 1.0 ka, Fig. 10.20 reveals that the mean eigenvalue of the 1st PC for compilation of BU-4 time series is approximately between 4 and 5 and 8 and 9. for a window length of 8, 4 and 2 ka for 8 and 16 speleothems, respectively, and c. 7 and c. 13 for a window length of 1.0 ka for 8 and 16 speleothems, respectively. The 95 % level of the AR-1 and WN time series is increasing with decreasing time window length. This is a challenging feature which makes it more difficult to identify significant PCs and which shall be discussed in the following section.

The sensitivity of the eigenvalues on the time window length of artificial time series and especially for artificial AR 1 time series, is simply a consequence of the sampling procedure. With a smaller time window length, the number of proxy values that lie in between the start and end point of the time window decreases as the temporal resolution is unchanged; e.g, for a speleothem proxy time series with a temporal resolution of 30 years, a time window with a length of 4 ka and 2 ka consists of 133 and 66 proxy values, respectively. Hence for an artificial time series, in particular for artificial time series with a memory effect, the possibility that time series correlate by chance is higher for a smaller window length. For that reason, the effect on the distribution of eigenvalues for artificial AR 1 time series is more dominant compared to the distribution of eigenvalues for artificial WN time series (Fig. 10.20). The time window effect is illustrated in Fig. 10.21. Here, the histograms depict the number of counts of Spearman's Rank coefficients, r_s , between two artificial AR 1 time series, based on the persistence of stalagmite BU-4's $\delta^{18}\text{O}$ time series, for a time window length of 8, 4, 2 and 1 ka, respectively. As the investigated artificial AR-1 time series are all based on the same speleothem time series, the correlation of the two selected artificial time series between each other describes also the correlation between 3, 4, 5, ... artificial time series.

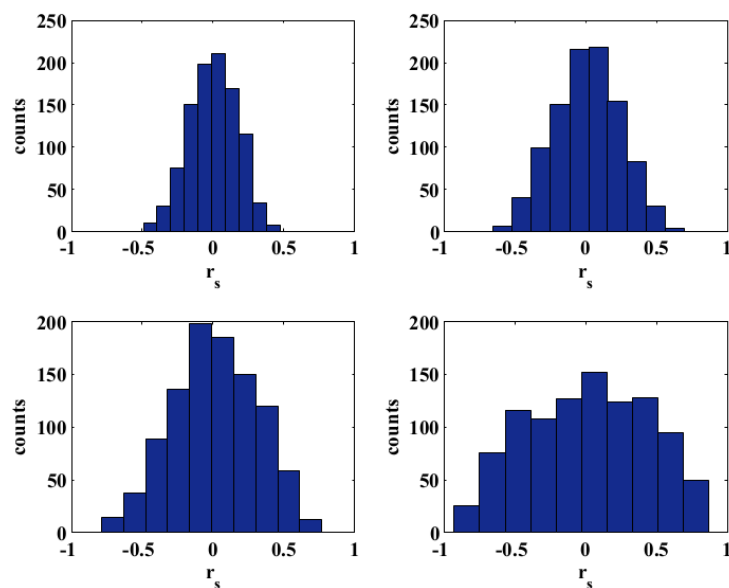


Fig. 10.21: Illustration of the distribution of r_s values between two AR-1 time series for four different window length. The top left panel is for a window length of 8.0 ka; the top right panel for a window length of 4 ka; the bottom left panel for 2 ka and the bottom right panel for 1 ka. All time windows end at 0.0 ka BP (see text for detail).

The distribution of r_s values reveals that the mean value is approximately 0 for the four time window lengths. Nevertheless, the variance is increasing. The standard deviation is ± 0.17 , ± 0.23 , ± 0.30 and ± 0.42 for a time window length of 8, 4, 2 and 1 ka, respectively. Hence, the chance to find two artificial AR-1 time series with high correlation is higher for

a smaller time window length. This proves the relationship between the eigenvalues and the time-window length. For the same reason, the distribution of eigenvalues of the compilation of speleothem proxy time series (here only BU-4's $\delta^{18}\text{O}$ time series) is not changing, except for the time window between -0.03 and 0.97 ka BP. This is due to the fact that the mean correlation between the speleothem proxy time series is not changing for the investigated time windows. However, for a window length of 1 ka, the mean eigenvalue of the 1st PC is c. 7 and c. 13 for 8 and 16 speleothems, respectively (Fig. 10.20). Fig. 10.22 illustrates the distribution of r_s values between two identical speleothem proxy time series, here stalagmite BU-4's $\delta^{18}\text{O}$ time series, for four different time windows; the first time window covers the period from c. 0.0-8.0 ka BP; the second from 0.0-4.0 ka BP; the third from 0.0-2.0 ka BP and the fourth from 0.0-1.0 ka BP. Fig. 10.10 and Fig. 10.22 help to explain this effect. The $\delta^{18}\text{O}$ time series of the last 1000 years of BU-4's growth history shows a distinct peak and the $\delta^{18}\text{O}$ values increase from c. -6.4 to -4.6 ‰ between c. 1 ka BP and c. 0.5 ka BP until the $\delta^{18}\text{O}$ decreasing again and ending with a value of c. -6.4 ‰. The longer time windows do not cover periods of BU-4's $\delta^{18}\text{O}$ history that show such additional strong peaks. For this reason, the mean eigenvalue of the time windows with a length of 8, 4 and 2 ka are only changing marginally compared to the time window with a length of 1ka. This is also depict in the distribution of the r_s values (Fig. 10.22). The mean value of the distribution is 0.41 ± 0.06 , 0.42 ± 0.08 and 0.35 ± 0.13 (1-sigma) for a time window length of 8.0, 4.0 and 2.0 ka, respectively, whereas the mean value of the distribution is 0.70 ± 0.17 for a time window length of 1.0 ka.

To underline this effect, four additional time windows are investigated. They end at -0.03 ka and 3 ka BP and have a length of 1.0 and 0.5 ka (Fig. 10.23), respectively.

Fig. 10.23 illustrates the characteristics of the mean eigenvalue for the compilation of 8 (dark blue) and 16 (light blue) identical speleothem proxy time series, which are based on the $\delta^{18}\text{O}$ time series of stalagmite BU-4 for four different time windows. In comparison to Fig. 10.20, Fig. 10.23 depicts only the characteristics of two different time window lengths, 1.0 and 0.5 ka ending at -0.03 and 3.0 ka BP, respectively. In addition to the mean eigenvalues, the 95 % confidence interval of the eigenvalues of the compilations of AR-1 and WN time series is illustrated in Fig. 10.23 - the indication of the coloured shading is the same as in Fig. 10.20. The evolution of the 95 % confidence level of the artificial AR-1 and WN time series, respectively, is the same as for the other experiments. The 95 % level is shifted towards more positive values. The comparison of the mean eigenvalues of the compilations of single speleothem time series for the two time periods, i.e., for the time between c. 4.0 and 3.0 ka BP and 1.0 and 0.0 ka BP, respectively, indicates that the mean eigenvalues of the 1st PC for the earlier time period (4.0 until 3.0 ka BP) are c. twice as small compared with mean eigenvalues of the 1st PC of the later time period (1.0 until 0.0 ka BP). Furthermore, the mean eigenvalue lies within the 95 % interval of the artificial AR-1 time series for a window length of 1.0 ka and even below for a window length of 0.5 ka. For the later time period, the mean eigenvalues of the 1st PC are above the 95 % interval of the artificial AR-1 time series. In addition, the mean eigenvalue of the 2nd PC for the later time period is below the 95 % interval of the artificial WN time series but

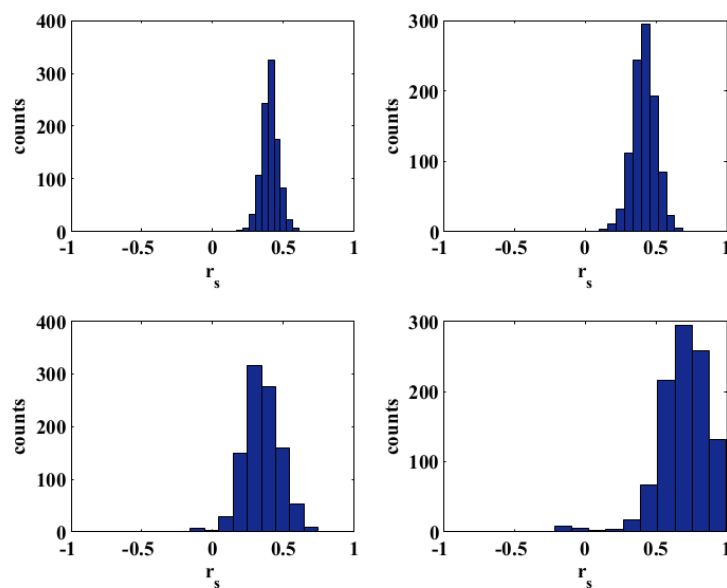


Fig. 10.22: Illustration of the distribution of r_s values between two identical speleothem proxy time series for four different window length. Here the $\delta^{18}\text{O}$ time series of stalagmite BU-4 is used. The top left panel is for a window length of 8.0 ka; the top right panel for a window length of 4 ka; the bottom left panel for 2 ka and the bottom right panel for 1 ka. All time windows end at 0.0 ka BP (see text for detail).

above for the early time period.

Summing up in terms of whether a PC is significant or not, it has been demonstrated that Preisendorfer's Rule N is under certain circumstances an adequate tool. However, it has been highlighted too, that Preisendorfer's Rule N has its limitation if the length of the time window is decreasing. This is caused on one hand by the fact that the mean correlation between artificial AR-1 or WN time series is increasing and on the other hand that the mean correlation between the investigated time series is depending on the variability of the proxy time series. The latter is resulting in different changing distributions for the different eigenvalues. In particular the distribution of the 1st eigenvalue is affected by this effect, causing a higher mean eigenvalue for periods with a higher mean correlation between the investigated proxy time series and a smaller mean eigenvalue for those periods during which the mean correlation is small (Fig. 10.22). The 95 % level of the distribution of eigenvalues derived from the compilation of artificial AR-1 and WN time series on the other side is increasing with a decreasing time window length (Fig. 10.21). As Preisendorfer's Rule N significance criteria is that all significant eigenvalues must be above the 95 % level of the eigenvalues of the compilation artificial time series, the time window effects makes it difficult to decide whether the derived PCs are significant or not (Fig. 10.20 and 10.23). This makes it challenging to conduct short-term analysis applying PCA and using Preisendorfer's Rule N alone as a significance criteria. For this an additional significance criteria is developed

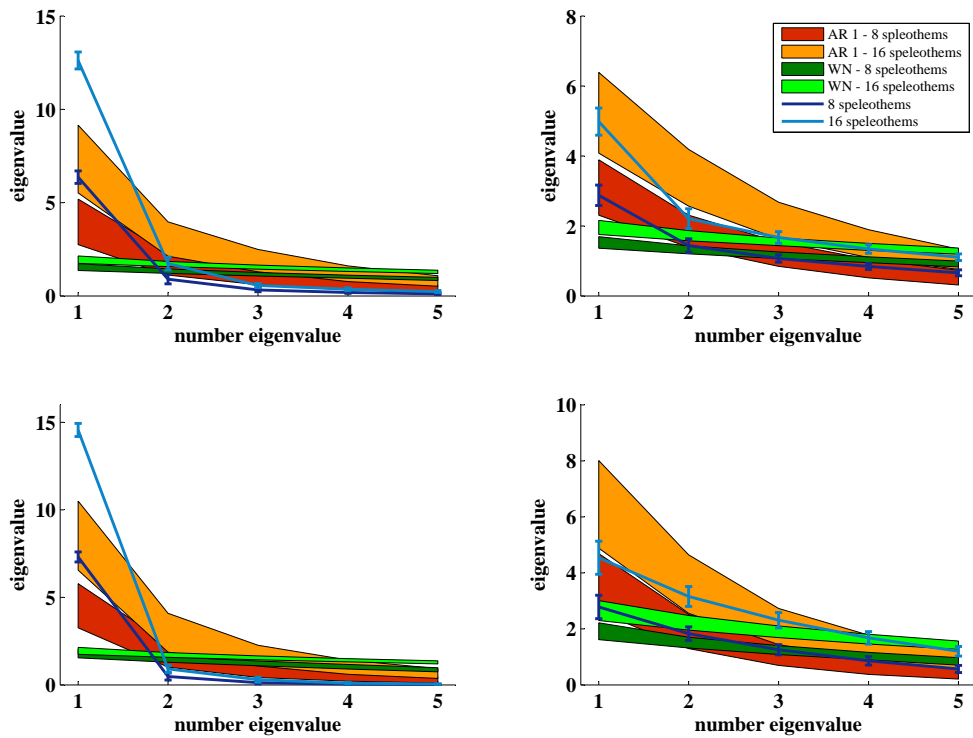


Fig. 10.23: The figure is illustrating the comparison between the mean eigenvalues for a compilation of 8 (dark blue) and 16 speleothems (light blue) with the respective 95 % confidence interval of eigenvalues computed from compilations of AR-1 time series (red and orange) and WN time series (dark green and bright green for different time windows). The top left panel is for the time interval between 4.0 ka BP and 3.0 ka BP; the top right panel is for the time window between 3.5 ka BP and 3.0 ka BP; the bottom left panel is for the time window between 1.0 ka BP and 0.0 ka BP and the bottom right panel for the time window between 0.5 ka BP and 0.0 ka BP (see text for detail).

in the next section that is using the correlation between the proxy time series and the computed PC time series.

10.6 Application of PCA on speleothem proxy time series - Spatio-temporal coherence of speleothem proxy time series

PCA allow to uncover common variations in proxy time series and to classify the derived PC time series if they are significant in the sense that a PC time series describes a simultaneous variation (signal) that is contained by the original time series. In climate science, those signals can be pressure, temperature, precipitation and many more factors depending on the proxy which is analysed and the question beyond the investigation. Above all, not only shared dynamics of proxy time series can be discovered but also patterns of coherent changes, if for example pressure fields are explored; i.e., pressure time series from various meteorological stations, which are distributed over a local, regional or global area, respectively. [Wallace and Gutzler \(1981\)](#) for example investigated the correlation (teleconnections) between winter pressure time series that were measured on the northern hemisphere, and used apart from other techniques PCA, and found several teleconnection patterns. To uncover spacial correlation pattern for a PC time series, i.e., a common variation that is contained in all speleothem proxy time series, the Spearman's rank correlation coefficient, r_s , between each speleothem proxy time series and the computed PC time series for each of the MC runs is calculated. This allows further investigations: First, the distribution of r_s values allows to decide whether a speleothem proxy time series correlates with a PC time series or not. Furthermore, the properties of the distribution of r_s values enable to discriminate if a PC is significant or not, because the properties of the distribution is different for WN, AR-1 and single speleothem time series. From this a second significance criteria is derived.

10.6.1 The behaviour of the distribution of r_s values for proxy time series and the Fork-tool

In the previous sections (Sec. 10.4 and 10.5), the distribution of eigenvalues of PCs were used to decide whether a certain PC is significant or not (Preisendorfer's Rule N). However, another property of a PC is its correlation with the investigated proxy time series. If a computed PC time series (to the corresponding PC) shares common variations of the proxy time series that are researched, the correlation between the PC time series and the proxy time series is significant. The value of the correlation coefficient r_s indicates the degree of the correlation - r_s is the Spearman's rank correlation coefficient. This property shall be explained in detail in the following part. Moreover, a further criteria for the significance of a PC (and of the related PC time series) shall be developed on this properties. For this compilations of four artificial AR-1 and WN time series (Sec. 10.4 and 10.5) are used. Furthermore, a compilation of four speleothem proxy series used; the four time series shall be similar, in order to achieve a perfect correlation. Here, the $\delta^{18}\text{O}$ time series of

stalagmite BU-4 is used. A total amount of 1000 MC simulations are performed resulting in ensembles composed of 1000 eigenvalues and time series for each PCs, respectively. According to Preisendorfer's Rule N the 1st PC is significant and all PCs of higher orders are not significant, because only the mean eigenvalue of the 1st PC is above the 95 % level of the eigenvalues for the compilation of AR-1 and WN time series, respectively (Fig. 10.19). However, in addition to the computed eigenvalues of each PC, the Spearman's rank correlation coefficient (r_s) can be calculated between each PC time series and each proxy time series. Hence, for each MC run r_s is calculated between the derived PC time series and the proxy time series (in the example conducted here these are four proxy time series). Consequently, a total amount of 1000 r_s values are calculated for the correlation between each PC time series and each proxy time series. This results in n^2 distributions of r_s values, where n is the number of investigated proxy time series. The distribution of r_s -values between the proxy time series and the 1st PC for the WN time series, the AR-1 time series and the single speleothem collection is illustrated in the left panels of Fig. 10.24, 10.25 and 10.26, respectively. Only values for r_s are shown if the p-values are smaller than 0.05. For the WN and AR-1 time series the shape of the distribution is bimodal, with a minimum centred at $r_s=0$. The distribution for the single speleothem selection on the other hand depicts a Gaussian distribution with a mean value of c. 0.7. Furthermore, it is visible that the variance of the WN and AR-1 time series' distribution for each peak is higher compared to the variance of the single speleothem collection. The bimodal distribution of r_s values is a result of the up-side-down effect and a result of the mathematical theory behind PCA (Sec. 10.1). The properties of the bimodal distribution of r_s values allow to decide whether a PC is significant or not. Moreover, it makes it possible to reveal, which of the investigated proxy time series is correlated with the related PC time series. The following problem might occur: if an ensemble of PC time series is investigated and the distribution of r_s values between the PC time series and the speleothem proxy time series is bimodal, only those PC time series are analysed which have a phase relation ($\exp\{i \cdot \phi\}$) of $\phi=0$ or π . Consequently, only one part of the bimodal distribution for each speleothem proxy time series is considered if the speleothem proxy time series have shared a common signal. For time series that are a priori not correlated with each other (as WN and AR-1 time series) and consequently do not share a common signal, there should not be such an outcome. To proof this assumption, only one part of the bimodal distribution between a PC time series and a selected speleothem is chosen (the positive or the negative) and the behaviour of the distribution of r_s values between the selected PC time series and the remaining speleothems is investigated. If the remaining speleothems are correlated with the PC series the distribution of r_s values should be sensitive to the selection and not if they are not correlated with the PC time series. This procedure is called the "Fork-tool" and shall be explained in the following.

For the WN and AR-1 time series the positive part of the bimodal distribution of the WN and AR-1 time series 1, respectively, is selected (Fig. 10.24, 10.25; right column); before the application of the Fork-tool on the bimodal distribution of WN and AR-1 time series 1, 948 and 965 r_s values contributed to the distributions, whereas after the application 599 and

10.6. Application of PCA on speleothem proxy time series - Spatio-temporal coherence of speleothem proxy time series

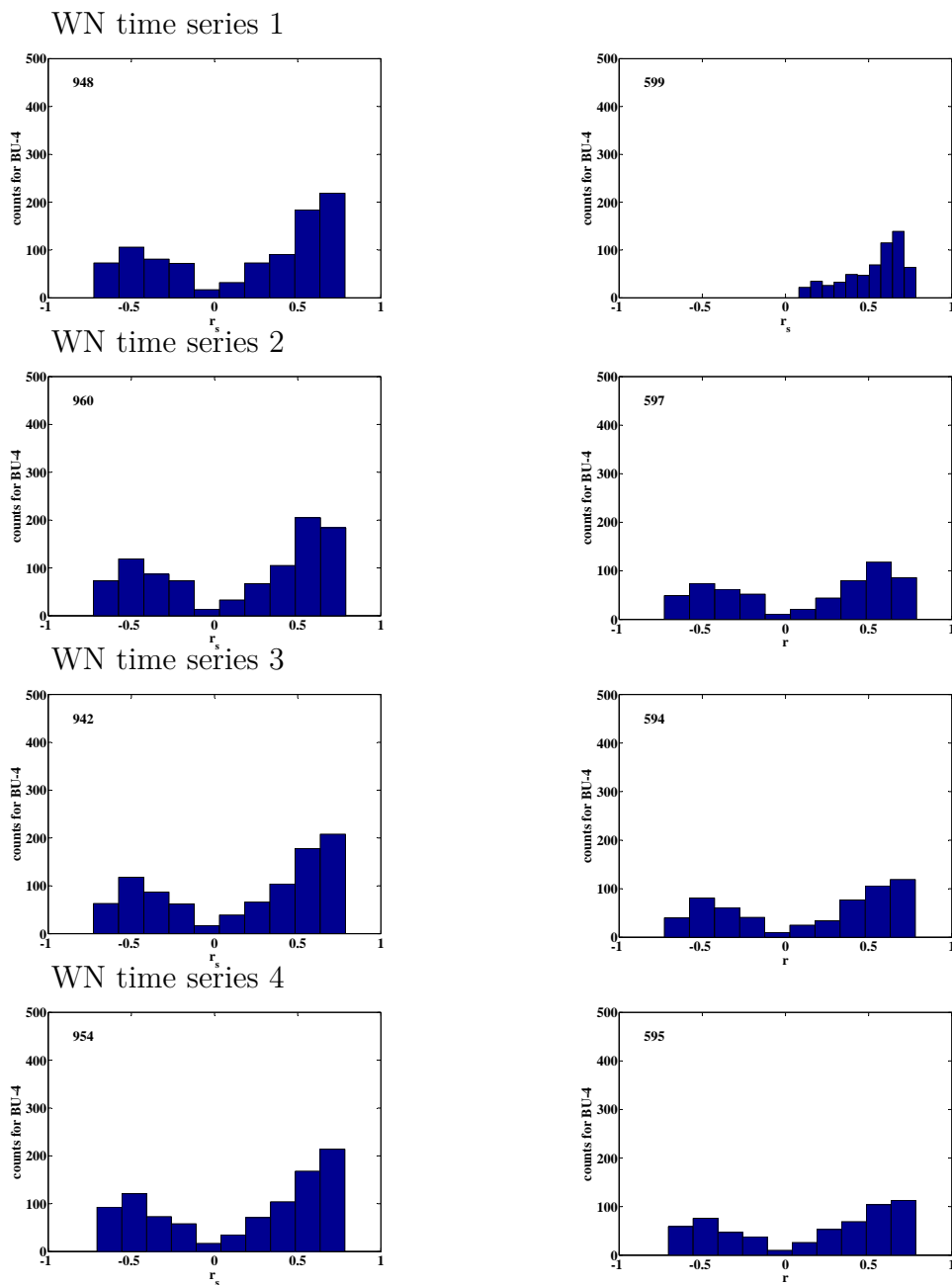


Fig. 10.24: Illustrated is the distribution of r_s values between WN time series and the computed 1st PC time series for four different time series. The labelling of the y-axis indicates the proxy-age relation of stalagmite BU-4 used as the basis for the WN time series. The panels on the left side depict the distribution before the application of the Fork-tool and the panels on the right side after the application of the Fork-tool.

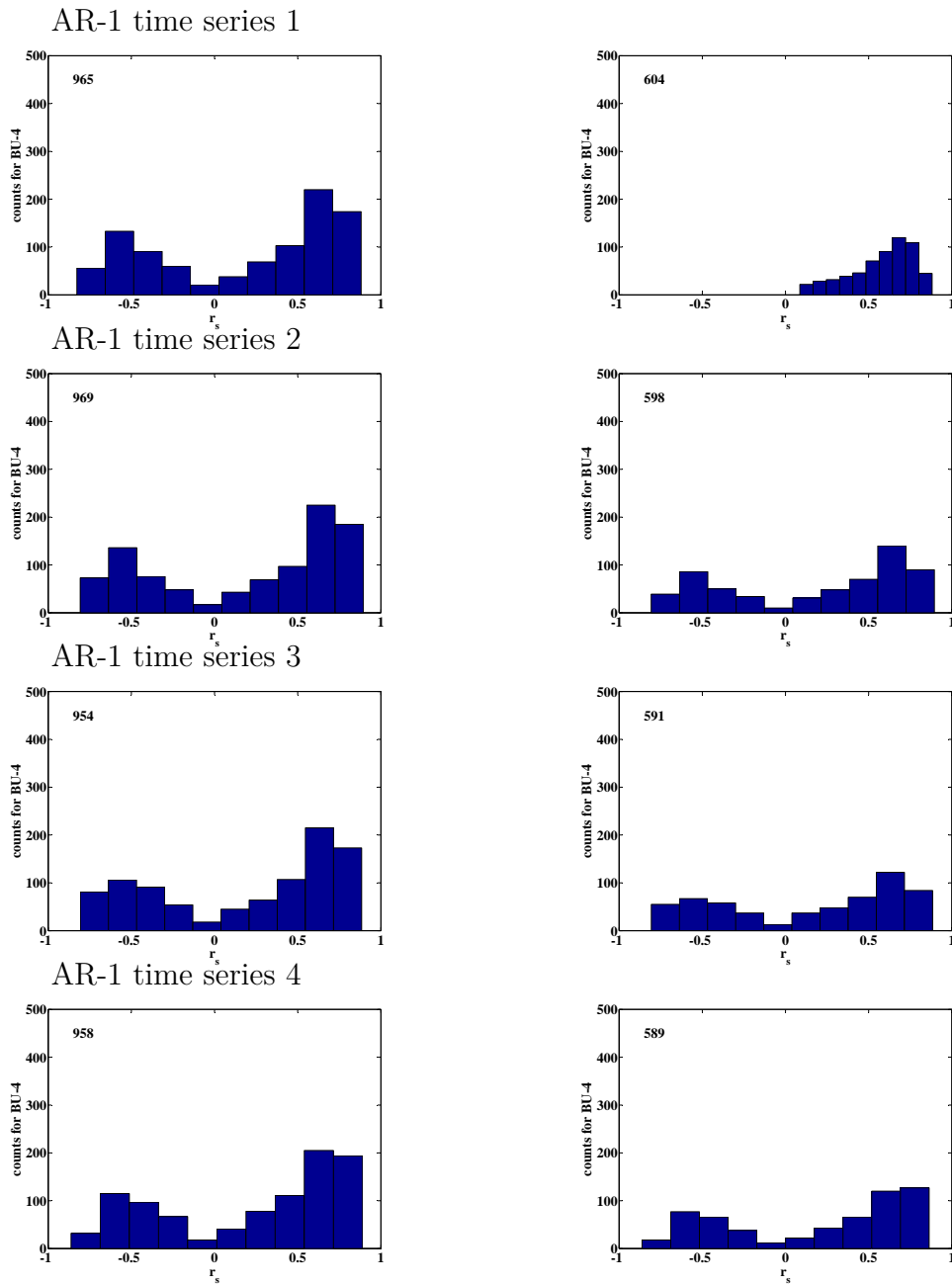


Fig. 10.25: Illustrated is the distribution of r_s values between AR-1 time series and the computed 1st PC time series for four different time series. The labelling of the y-axis indicates the proxy-age relation of stalagmite BU-4 used as the basis for the AR-1 time series. The panels on the left side depict the distribution before the application of the Fork-tool and the panels on the right side after the application of the Fork-tool.

10.6. Application of PCA on speleothem proxy time series - Spatio-temporal coherence of speleothem proxy time series

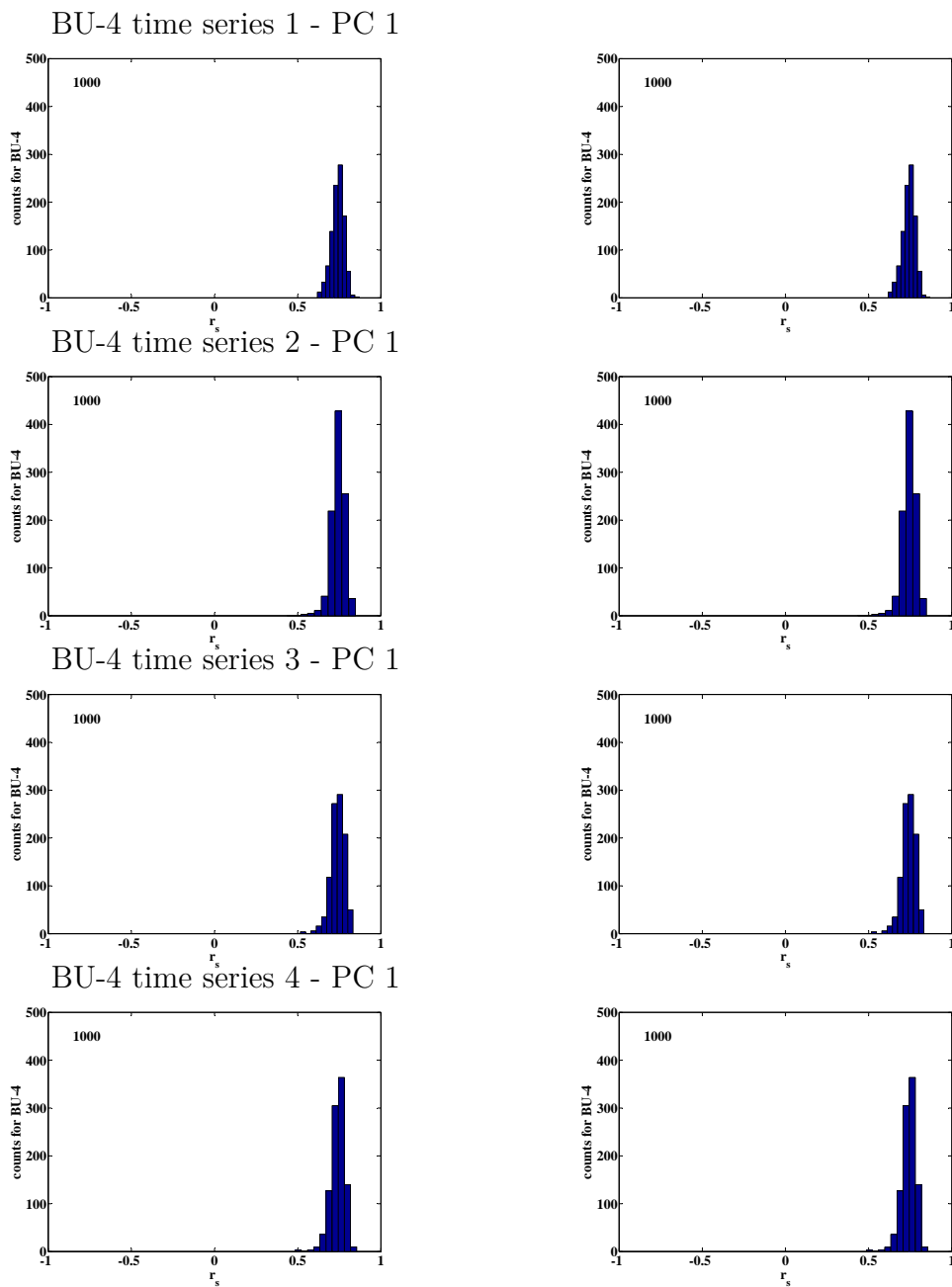


Fig. 10.26: Illustrated is the distribution of r_s values between identical speleothem proxy time series and the computed 1st PC time series for four different time series. Here, the $\delta^{18}\text{O}$ time series of BU-4 is used. The panels on the left side depict the distribution before the application of the Fork-tool and the panels on the right side after the application of the Fork-tool.

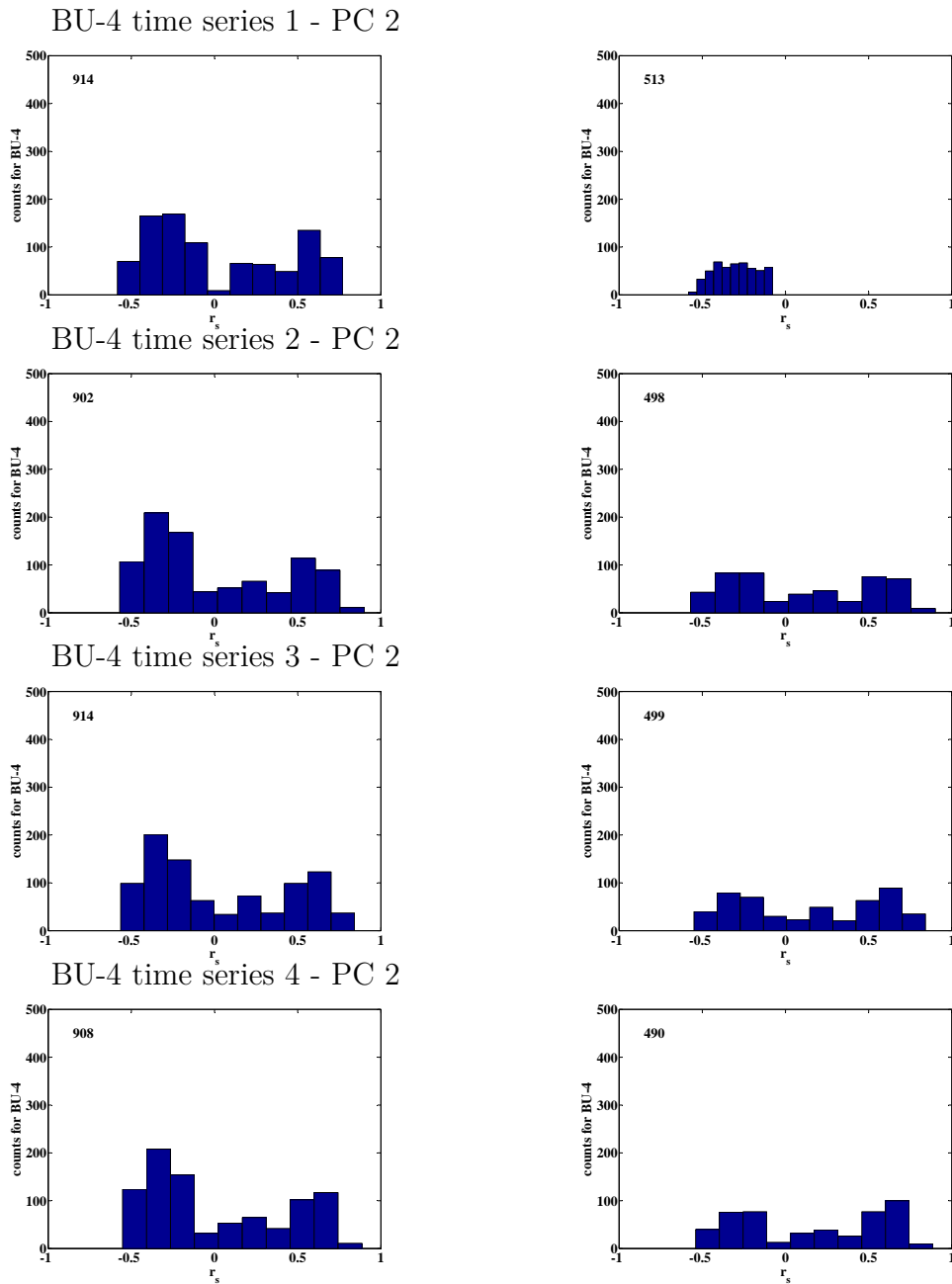


Fig. 10.27: Illustrated is the distribution of r_s values between identical speleothem proxy time series and the computed 2^{st} PC time series for four different time series. Here, the $\delta^{18}\text{O}$ time series of BU-4 is used. The panels on the left side depict the distribution before the application of the Fork-tool and the panels on the right side after the application of the Fork-tool.

604 r_s values contribute to both distributions, respectively. Similar numbers can be found for the other distributions of time series 2, 3 and 4. However, the shape of the distributions of these time series compared to the distribution of time series 1 is different and maintains the bimodal distribution. From this result, it can be concluded that if proxy time series are not correlated with each other, the application of the Fork-tool on the bimodal distribution does not change the shape of the other distributions. There is also an equivalent for the results under permutation of the application of the Fork-tool on the time series and the positive or negative part of the bimodal distribution.

The distribution of r_s values between the ensemble of the single time series with the 1st PC (Fig. 10.26 left column) illustrates that all four time series correlate with the PC. Consequently, after application of the Fork-tool on the distribution of the ensemble of time series 1 all other distributions are unchanged (Fig. 10.26 right panels). Hence, the 1st PC is significant and represents a common signal in all four time series. This result is intuitive, since all four time series are based on the same $\delta^{18}\text{O}$ time series, but it provides a tool to decide whether a derived PC represents a signal that is common in many proxy time series or only in one. Application of Preisendorfer's Rule N on the derived PCs for the single speleothem experiment of four speleothems shows that only the 1st PC is significant and all PCs of an order higher than 1 not (Fig. 10.19). A similar result can be achieved by the application of the Fork-tool on the distribution of r_s values for the single speleothem ensemble and the 2nd PC, which shows a bimodal distribution for all four time series (Fig. 10.27, left column). The application of the Fork-tool on the negative part of the bimodal distribution of time series 1 reveals that the shape of the remaining distributions are unchanged (Fig. 10.27, right column). Hence, the 2nd PC time series behaves like WN and AR-1 time series and does not contain a common signal of the four time series.

The behaviour of the distributions of r_s values on the selection of PC time series, i.e., positive or negative phase relation, uncovers if a PC time series is a common signal of the investigated speleothem proxy time series or not and is an additional selection rule to Preisendorfer's Rule N.

10.6.2 Results of the eigenvalues and test of Preisendorfer's Rule N

The experiments that were described in the previous sections represent academic case studies. In those case studies, PCA were applied on collections of time series (AR-1, WN, single) that base on the same proxy time series. Even though insights were gained on the performance of PCA and about evaluation criteria, Preisendorfer's Rule N (Preisendorfer and Mobley, 1988) must be tested for it's practical performance and applicability onto selections of speleothem proxy time series. For this, PCA were performed on five speleothem $\delta^{18}\text{O}$ time series. The sampling locations of the speleothems are shown in Fig. 10.4 and include sampling locations for the speleothms BU-4, CC-26, CC-3, GAR-01 and SO-1. This compilation of speleothems covers an area that ranges from Ireland (CC-3) to Turkey

(SO-1) with tie points in Northern Spain (GAR-01), Central Germany (BU-4) and Northern Italy (CC-26). The speleothems overlap between the time period of approximately 8 ka BP to 0.75 ka BP; the end points are determined by the initial growth phase of BU-4 at c. 8 ka BP and the growth stop of CC-26 at c. 0.75 ka BP (Fig. 10.7). During the contemporaneous growth history of the speleothems, stalagmite GAR-01 has a hiatus, i.e., a temporary growth stop, between 1.1 and 1.3 ka BP and stalagmite CC-3 between 5.9 and 6.3 ka BP (Fig. 10.7). Apart from stalagmite GAR-01 and except for the hiatus of GAR-01 and CC-3, respectively, all stalagmites have a temporal resolution that is smaller than 20 years; stalagmite GAR-01 has a temporal resolution that is smaller than 20 years for the first 8,000 years of its growth history and for the last 4,000 years the temporal resolution varies between 10 and 30 years (Fig. 10.7).

For the PCA, a total amount of 1,000 MC runs is performed and the speleothem's ages varied within their 1-sigma age uncertainty as it is described in Sec. 10.3. To test whether a derived PC is significant or not, Preisendorfer's Rule N is applied on mean eigenvalues of the derived PCs. This is illustrated in Fig. 10.28. Here, the mean eigenvalue (2-sigma) is compared with the 95 % level of WN time series. The red shading area indicates the parameter space which is limited by the 5 % and 95 % level of the eigenvalues derived for the compilation of WN time series. The 95 % level is the upper limit of the red shading area. The mean eigenvalue for the compilation of speleothems (blue line) is, apart from the time window of run #1 (0.75-7.8 ka BP) and #2 (4.0-7.8ka BP), below the 95% level for the eigenvalues of the WN time series (upper limit of the red shading area) (Fig. 10.28). This is due to the fact that the 95% confidence interval of the eigenvalues of the WN time series is covering a greater range of eigenvalues with smaller time window length, as it is the case for time series based on an AR-1 process (Sec. 10.4.2). This is an evidence that Preisendorfer's Rule N is not applicable for certain window length that depend on the temporal resolution of the investigated time series, as it is emphasised in Fig. 10.28. To decide whether the results of a conducted PCA for a certain time window length and period of time are significant or not in case that the mean eigenvalue of the speleothem selection is below the 95% level of WN time series, the Fork-tool is applied on the ensemble of PCs time series, i.e., on the distribution of r_s values. Furthermore, the PC time series for the shorter window length are compared with the temporal evolution of the 1st PC time series of the time window from 7.8 until 0.75 ka BP, which is significant after Preisendorfer's Rule N.

The comparison of the derived 1st PC time series shows that short-term 1st PC time series do fit the temporal variability of the long-term 1st PC time series (Fig. 10.29 and 10.30). Fig. 10.29 illustrates the mean 1st PC time series for the time windows of 7.8-0.75 ka BP (black), 7.8-4.0 ka BP (red) and 5.0-4.0 ka BP (blue). The shaded area indicates the 1-sigma standard deviation of the mean value; the colour of the shading area indicates the related mean 1st PC time series. It shows that the overall comparison between the different time series is very good and all features of the long-term 1st PC time series are captured by the short-term 1st PC time series, although there are differences of higher order. This is in particular visible for the short-term 1st PC time series derived for the time window between

10.6. Application of PCA on speleothem proxy time series - Spatio-temporal coherence of speleothem proxy time series

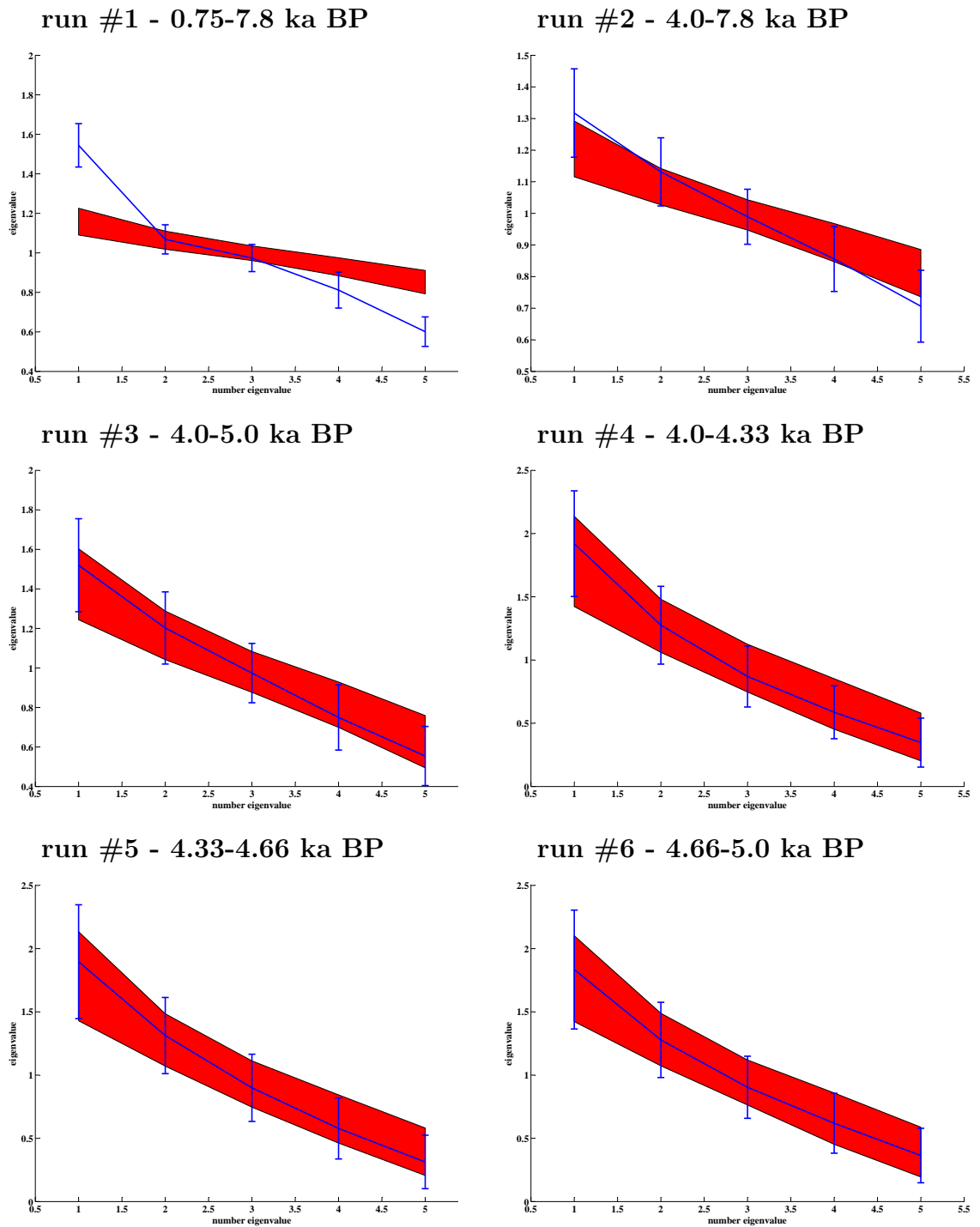


Fig. 10.28: Illustration of the mean eigenvalues (blue lines) for different time windows and the corresponding 95 % confidence interval for WN time series (red shading area). All eigenvalues are pictures with the respective 1-sigma standard deviation (see text for detail).

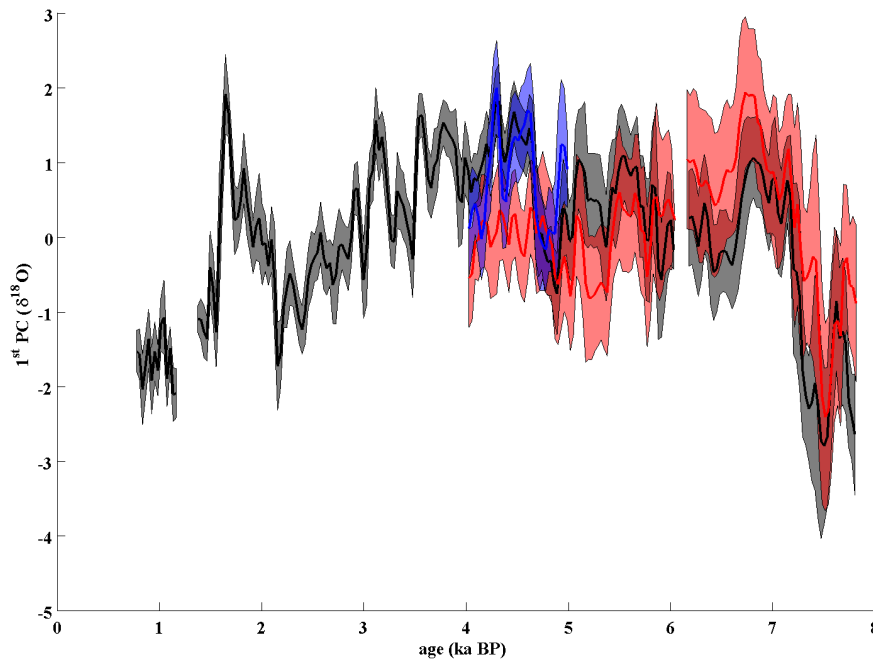


Fig. 10.29: Comparison between the mean long-term 1st PC time series (black) with the mean short-term 1st PC time series covering the time between 4 and 7.8 ka BP (red) and 4 and 5 ka BP, respectively (blue). The shading area indicates the 1-sigma standard deviation of the mean value.

7.8 and 4 ka BP in the time between 5 and 4 ka BP. In this time, the long-term 1st PC time series (black straight line) has a local maximum, whereas the short-term 1st PC time series (red straight line) has a higher variability with alternating maxima and minima. However, between 7.8 and 5 ka BP the two 1st PC time series agree well. A reason for the different shape of both 1st PC time series can be the different length and hence different scaling of the $\delta^{18}\text{O}$ time series before the PCA is applied. The comparison between long-term (black straight line) and short-term (5-4 ka BP; blue straight line) 1st PC time series reveals an even better accordance, also illustrated in Fig. 10.30. Hence, the derived short-term 1st PC time series inherit a common signal of the five speleothem $\delta^{18}\text{O}$ time series, though, according to Preisendorfer's Rule N the derived 1st PC is not significant. The distributions of r_s values between the speleothem $\delta^{18}\text{O}$ time series and the 1st PC time series show that for the long-term (7.8-0.75 ka BP) and the first short-term time window (7.8-4.0 ka BP), the distributions for the speleothems CC-26, CC-3 and SO-1 have distinct peaks, whereas the bimodal distribution of r_s values of speleothem BU-4 and GAR-01 is unchanged by applying the Fork-tool (Fig. A.1 and A.2 for the time window between 7.8-0.75 ka BP; Fig. A.3 and A.4 for the time window between 7.8-4.0 ka BP). For the time window between

10.6. Application of PCA on speleothem proxy time series - Spatio-temporal coherence of speleothem proxy time series

5 and 4 ka BP, the distribution of r_s -values shows a bimodal-like shape for all investigated stalagmites. After the application of the Fork-tool, the bimodal distribution is unchanged for stalagmite BU-4 and CC-26, but shows a single peak for stalagmite CC-3, GAR-01 and SO-1. Hence, the 1st PC time series is significant and explains the mean variability of CC-3, GAR-01 and SO-1 in this time interval, although Preisendorfer's Rule N suggests, that the 1st PC is not significant (Fig. A.5 and A.6 for the time window between 5.0-4.0 ka BP).

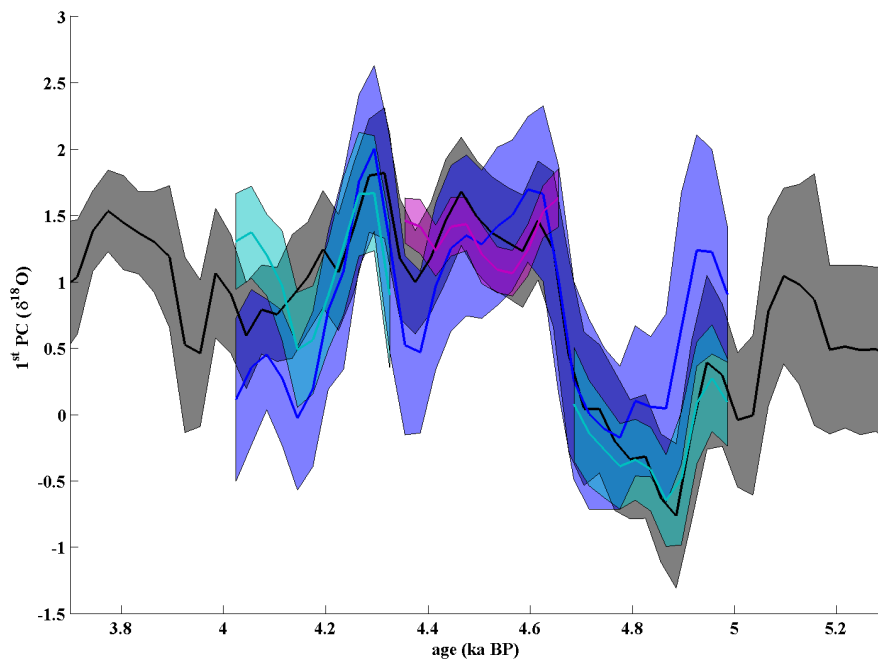


Fig. 10.30: Comparison between the mean long-term 1st PC time series (black) and the mean short-term 1st PC time series covering the time between 4 and 5 ka BP (blue) and three window length of 0.33 ka covering the time interval between 4 and 5 ka BP. The colour of the short-term 1st PC time series (cyan-blue or purple) indicates an up-side-down effect was observed in comparison to the long-term 1st PC time series; the mean value is coloured in purple if there was no up-side-down effect observed and in cyan-blue if there was an up-side-down effect. The shading area indicates the 1-sigma standard deviation of the mean value.

The short-term 1st PC time series pictured in Fig. 10.29 are intermediate time windows regarding their length (blue and red straight lines). It has also been shown that the 1st PC time series computed for the shorter time window (blue straight line), covering the time between 5 and 4 ka BP, is in better agreement with the long-term 1st PC time series (black straight line) than the intermediate-term 1st PC time series (red straight line). This is also depicted in Fig. 10.30. In addition to the two 1st PC time series, three 1st PC time series

are illustrated that cover the time period between 5 and 4.66 ka BP, 4.66 and 4.33 ka BP and 4.33 and 4 ka BP, respectively. The three 1st PC time series are illustrated in purple when the 1st PC time series is not shown up-side-down and in cyan-blue if the 1st PC time series is illustrated up-side-down. The overall comparison between the three short-term 1st PC time series and the long-term 1st PC time series (black straight line) reveals that the 1st PC time series of the first (5-4.66 ka BP) and third time window (4.33-4.0) covers the variability of the long-term 1st PC time series. The 1st PC time series of the second time window (4.66-4.33 ka BP) however is not consistent with variability of the long-term 1st PC time series.

The application of the Fork-tool on the first (5-4.66 ka BP) and third investigated short-term time interval (4.33-4 ka BP) shows that the 1st PC time series can explain the variability of the compilation of $\delta^{18}\text{O}$ time series. This is indicated by the behaviour of bimodal distributions (Fig. A.7 and A.8 for the time window between 4.33-4.0 ka BP; Fig. A.11 and A.12 for the time window between 5.0-4.66 ka BP). Before the application of the Fork-tool, the distributions of r_s values show a bimodal-like shape, whereas afterwards, the single peak is visible for 4 of 5 speleothems. For the first time window the bimodal distribution of stalagmite SO-1 is unchanged and for the third time interval that of stalagmite BU-4. For the second time window however, the Fork-tool results in a negative significance-test. Hence, the derived short-term 1st PC time series is not significant (Fig. A.9 and A.10 for the time window between 4.66-4.33 ka BP).

The previous examples with real compilations of speleothem proxy ($\delta^{18}\text{O}$) time series have shown that Preisendorfer's Rule N can be used for long time series but fails for shorter ones. Here, the comparison of the derived PC time series in combination with the application of the Fork-tool provides a better tool to decide whether the derived PC are significant or not, in dependence on the behaviour of the distribution of r_s values. Furthermore, the decreasing window size has shown that long-term time series are representing a superposition of different short-term states being uncovered also by the behaviour of the r_s distributions.

10.7 Selection rules for PCA

In the previous sections, principal component analysis has been introduced as a novel method in speleothem science to investigate spatio-temporal coherency of speleothem proxy time series. In Chapters 13, 14, 15 and 16 PCA is used to investigate common variations in European speleothem $\delta^{18}\text{O}$ and $\delta^{13}\text{C}$ time series. Though PCA is a powerful tool, it has been also demonstrated that not all derived PC contain a collective variation of the used speleothem proxy time series. To separate the information-bearing PC from the noise-bearing PC, two different criteria are used. The first is "Preisendorfer's Rule N" (Preisendorfer and Mobley, 1988) that is applied on the long-term speleothem proxy time series - long-term means that PCA is applied on the entire time period during which all speleothems were actively growing. After this first step the long-term PC time series are

derived which contain common variations of the compilation of speleothem proxy time series. The correlation between the long-term PC time series and the used speleothem proxy time series can be calculated gaining a long-term spatial information for the entire time period of simultaneous speleothem growth. However, recent studies suggest that the spatio-temporal correlation between speleothem proxy time series are changing with time, due to different boundary conditions ([Wassenburg et al., 2013](#)). Hence, short-term PCA are necessary. Nevertheless, it as been shown that "Preisendorfer's Rule N" loses its reliability on shorter time scales and the second criteria for the evaluation of PCA is used (time window effect). For this purpose, the derived short-term PC time series is compared with its corresponding long-term PC time series in order to validate if the short-term PC time series shows the same variability as the long-term PC time series. If yes, the short-term PC time series is used. This allows to derive short-term spatio-temporal coherence patterns. Furthermore, the fork tool has been developed to investigate the behaviour of the distribution of correlation coefficients between the PC time series and the speleothem proxy time series. The fork tool makes it possible to investigate if single speleothem proxy time series are correlated significantly with a PC time series.

Part IV

Results and Discussion

11

Stable isotopes in Precipitation

The $\delta^{18}\text{O}$ value of speleothems is predominantly determined by the oxygen isotope signature of the water that is infiltrating the soil and karst zone ([McDermott, 2004](#); [Lachniet, 2009](#)); see also Chapter 7 and 8.2. For the interpretation of $\delta^{18}\text{O}$ variations in a speleothem $\delta^{18}\text{O}$ time series, it is essential to know the source of rain water and the processes that modify the source water (Chapter 8.1). This knowledge is important for the interpretation of $\delta^{18}\text{O}$ time series in speleothems, for ice core $\delta^{18}\text{O}$ time series and ground water $\delta^{18}\text{O}$ values. For this reason the International Atomic Energy Agency (IAEA) and the World Meteorological Organization (WMO) set up a global network to measure the oxygen and hydrogen isotope composition of rain. The "Global Network of Isotopes in Precipitation" (GNIP) was founded in 1961. Till this day about 900 stations have been built up world wide (Fig. 11.1).

The first comprehensive review on the GNIP stable isotope data has been conducted by ([Dansgaard, 1964](#)). At this time the GNIP was composed of about 100 stations. In addition to the review [Dansgaard \(1964\)](#) used a Rayleigh process to gain deeper insights into the findings. This approach was later continued by [Rozanski et al. \(1982\)](#) using a multi-box model to calculate stable isotopes in precipitation, that bases on a Rayleigh approach. The advantage of such basic models in comparison to complex Global Circulation Models (GCM) and inter-mediate complex climate models is the less computer power and real-calculation time. For this reason, a remake of the multi-box model is presented here that is based on a Rayleigh process. The aim is to compare the calculated values for the stable isotopes in precipitation with GNIP stable isotope data. In addition, the multi-box Rayleigh model is extended by an ocean component. This is based on first principle physics derived for GCMs (see [Hoffmann et al., 1998](#)). It allows to calculate changes in the stable isotopic composition of the evaporated water, i.e., the atmospheric moisture and the precipitated water. Another advantage of the here presented model is that it has a palaeo-version allowing to vary temperature and precipitation for palaeo climate scenarios. In Chapter 17 the palaeo version is used to model gradients of speleothem $\delta^{18}\text{O}$ values along a central European transect ([McDermott et al. \(2011\)](#)). However, at the beginning, the processes are introduced that

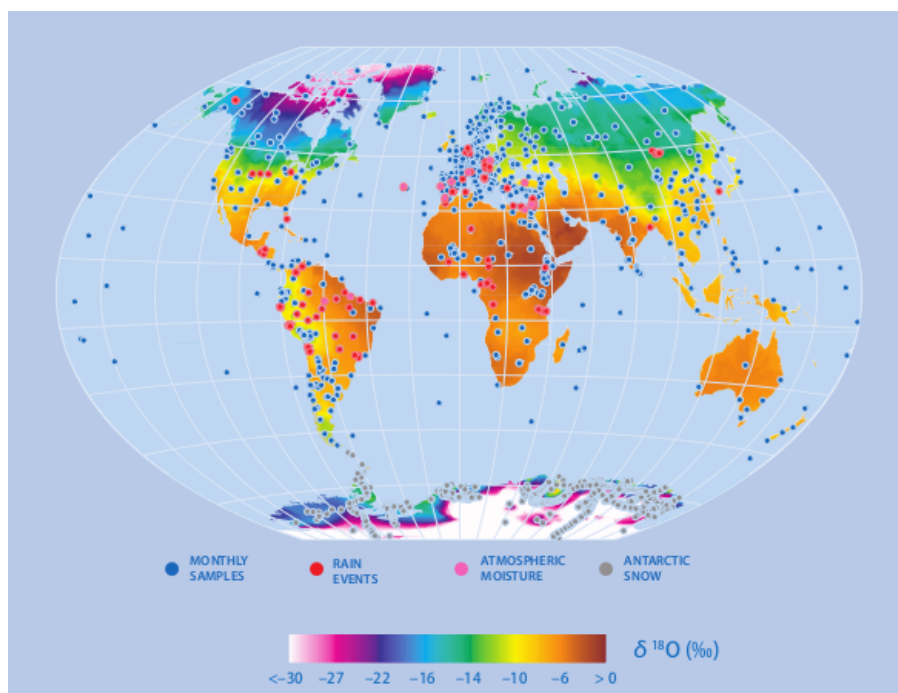


Fig. 11.1: The earth is laced with meteorological stations that are part of the Global Network of Isotopes in Precipitation (GNIP). It is composed of about 900 stations monitoring temperature, amount of precipitation. In addition water samples are analysed for their stable isotope composition managed by the IAEA and WMO. The colour shading of the continents illustrates the $\delta^{18}\text{O}$ value of precipitation derived from long term annual means (GNIP Team, 2013).

alter the precipitation's stable isotopic composition, meaning the components of the water cycle Fig. 8.1. This is an important requirement not only to understand how the stable isotopic composition changes but also for the interpretation of speleothem $\delta^{18}\text{O}$ time series (Lachniet, 2009).

The components of the water cycle are schematically illustrated in Fig. 8.1. Approximately there is a equilibrium between the water sources and sinks of the world oceans (Mook and de Vries, 2000; Mook, 2006). The main sink is the evaporation of water from the ocean surfaces; the sources are precipitation of water over the ocean, river and ground water discharge, respectively. The evaporation process is accompanied by the isotope fractionation of oxygen and hydrogen isotopes (e.g. Dansgaard, 1964). When the water evaporates from the ocean surface it enters the atmosphere and is then transported by atmospheric circulation. The atmospheric circulation is the primary water conveyor transporting water to the continents. If a certain air parcel cools on it's way and becomes oversaturated with respect to water, the water vapour condenses; clouds are developing and if the drops are heavy (big) enough, it starts raining. If the temperature is cold enough, the vapour does

not convert to its liquid phase but to its solid phase. If the ice crystals are heavy enough, it starts snowing. This is particularly important for mountains and for very cold regions like Greenland and Antarctica. Here it finally forms mountain glaciers or becomes part of the ice caps. The conversion of the liquid and solid phase of water is again accompanied by isotope fractionation effects (e.g. [Dansgaard, 1964](#)). If the liquid (solid) water is precipitated over the ocean it becomes part of its source again. Rain precipitated over the continent and infiltrates the soil zone. Parts are taken up by vegetation and are transpired into the atmosphere again. The fraction depends on the vegetation type, vegetation density and in particular the season at which it rains. The latter depends on the region. In the tropics the seasonal effect might be small because of very stable conditions all around the year, but it is very variable for regions that have seasons, like Europe. Another effect is evaporation of water directly at the surface. However, [Rozanski et al. \(1982\)](#) argues on conclusions of [Zimmermann et al. \(1967\)](#) and [Münnich \(1978\)](#) that the evaporation of water and take-up of water by vegetation has no effect on the stable isotopic composition of the remaining water that is infiltrated. The infiltrated water finally forms ground water. In addition precipitated water can contribute to surface aquifers like lakes and rivers. Another source of fresh water for surface aquifers is the melted water of glaciers. The groundwater and the rivers are ending in the oceans again and closing the water cycle.

In the following the "Stable Isotopes in Precipitation" model is explained. For this every component and the physics beyond it is explained. In succession the Stable Isotopes in Precipitation model is applied with focus on Europe. The isotope values of the precipitation of two transects, a Central European and a Northern European, are calculated. The results are compared with GNIP station data. Finally the effect of the NAO on the stable isotopes in European precipitation is investigated, that is observed for precipitation $\delta^{18}\text{O}$ values obtained from the GNIP stations from Europe ([Baldini et al., 2008](#)) and for precipitation $\delta^{18}\text{O}$ values computed with the ECHAM5-wiso GCM ([Langebroek et al., 2011](#)).

11.1 Description of the "Stable Isotopes in Precipitation" model

The scope of the Stable Isotopes in Precipitation (SIP) model is the prediction of precipitation's stable isotopes that is formed along a specific transect. It is based on a multi-box Rayleigh approach model in analogy to [Rozanski et al. \(1982\)](#). To account for isotope fractionation effects modifying the stable isotopic signature of atmosphere's moisture and consequently of the rain, the model uses physical principles, which are explained in the following sections.

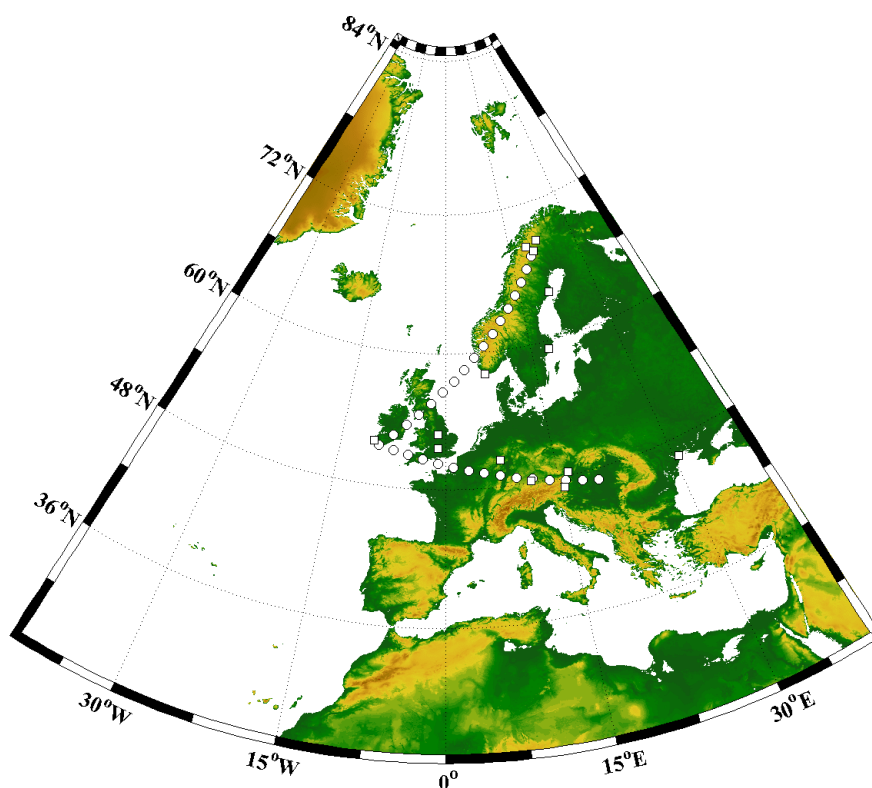


Fig. 11.2: Map showing the Central- and Northern European transect T1 and T2, respectively (open white circles). The white squares are selected GNIP stations distributed along the two transects.

11.1.1 Overview of the different components - The physical bases of the SIP model

The SIP model is physically based on stable isotope fractionation effects. Those have been intensively investigated over the last decades (Merlivat and Jouzel, 1979, and references therein) and are also used for GCMs (e.g. Jouzel et al., 1987; Hoffmann et al., 1998; Werner et al., 2011). To calculate the isotopic composition of the precipitation and the infiltrated water several processes need to be considered (Fig. 8.1).

The SIP accounts for the input of water vapour into the atmosphere due to evaporation of water of large water bodies, e.g., oceans (Sec. 11.1.3). Furthermore, the fractionation effects are considered that occur by the phase change of atmospheric moisture (water vapour) to liquid water or to ice, respectively (Sec. 11.1.4). At the surface, the isotope

fractionation effects of the evaporation of soilwater and the transpiration of water by plants are included in the SIP model (evapo-transpiration) (Sec. 11.1.5). Ultimately, the oxygen isotope composition of speleothems is calculated for oxygen isotope equilibrium conditions based on the oxygen isotopic fingerprint of the infiltrated water.

The movement of water vapour, i.e., the atmospheric circulation, along a transect is defined by the operator. The length and the shape of the transect can be chosen arbitrary, however should base on observation - otherwise the results of the SIP are not comparable to the physical reality, i.e., observations. For this, the transect is divided into square boxes with a defined spatial resolution. Temperature, amount of precipitation and evapo-transpiration are calculated for each box based on CRU-TS3.1 dataset (Mitchell and Jones, 2005) compiled by the Climate Research Unit (CRU) of the University of East Anglia (Sec. 11.1.2). These parameters are then used to calculate the stable isotope composition of precipitation and the water infiltrating the soil and karst zone. In addition, the mixing of different air masses is not included in the SIP model.

11.1.2 Transect multi-box approach and calibration of model parameters

For the calibration of temperature, precipitation and evapo-transpiration for each box, the SIP model uses the CRU-TS3.1 dataset Mitchell and Jones (2005). It has a spatial resolution of $0.5^\circ \times 0.5^\circ$ over the continent and is composed of monthly values based on daily interpolated available station data for the period between January 1901 and December 2009. That makes a total of 1308 monthly values for each parameter and grid point - the network of meteorological stations used for the CRU-TS3.1 dataset for Europe can be found in the supplementary material in Comas-Bru and McDermott (2013). To calculate the values for each box and each month, the grids of the CRU-TS3.1 dataset are framed by each box.

Furthermore, the monthly mean long-term GNIP data is used to calibrate the stable isotope composition of the precipitation of the first box, available from the GNIP webpage. For this, GNIP stations were selected whose location is close to the investigated transects. The GNIP data is also used to validate the SIP model results for the stable isotope fingerprint of the precipitation along the Northern- and Central European transect. To investigate the effect of the winter NAO on the evolution of the stable isotopes in precipitation for the Central European transect, the monthly values of the selected GNIP stations are utilized as well. From this, only those years of the monthly GNIP station time series are used during which the winter NAO index (mean index for the months December-March) has a value < 0.8 (NAO minus) or > 0.8 (NAO plus).

11.1.3 Evaporation of water from the oceans

In the past, especially in the 1950s, 60s and 70s many theories for the evaporation of water have been proposed (see Merlivat and Coantic, 1975, and references therein). Merlivat

and Coantic (1975) undertook the research to test the different evaporation theories by stable isotope techniques that were put forward by Craig et al. (1963) and Craig and Gordon (1965). Based on this work Merlivat and Jouzel (1979) derived a formula describing the stable isotope fractionation during evaporation of water. This formula is still used in GCMs, like the GISS or ECHAM model (e.g. Jouzel et al., 1987; Hoffmann et al., 1998; Werner et al., 2011). According to Merlivat and Jouzel (1979) the isotopic composition of evaporated water δ_E from the ocean is given by

$$\delta_E + 1 = \frac{(1 - k)}{1 - h} \left(\frac{1 + \delta_L}{\alpha_{l/v}} - h(1 + \delta_{V_0}) \right), \quad (11.1)$$

whereas δ_L is the isotopic composition of the ocean surface given in it's delta notation; δ_{V_0} is the isotopic composition of the water vapour in the complete atmosphere being in isotopic equilibrium with the ocean. According to Jouzel and Koster (1996) δ_{V_0} can vary on a regional scale. $\alpha_{l/v}$ is the isotope fractionation factor between the liquid and vaporious phase of water. h ist the relative humidity. The term $(1 - k)$ accounts for the kinetic effects during the evaporation of water and is given by Eq. (11.2) (Merlivat and Jouzel, 1979):

$$1 - k = 1 - \frac{(1 + \epsilon_D)^n - 1}{(1 + \epsilon_D)^n - \frac{\rho_T}{\rho_M}}. \quad (11.2)$$

In Eq. (11.2) ϵ_D is the difference of the molecular diffusion of the isotopes in air and is according to Merlivat (1978b) 25.1 ‰ for δD and 28.5 ‰ for $\delta^{18}O$. ρ_M and ρ_T is molecular and turbulent resistances, respectively. ρ_T/ρ_M can be calculated with the theory of (Brutsaert, 1975b,a) that has been verified to be in good agreement with experimental results Merlivat (1978a). For the term ρ_T/ρ_M it must be differentiated between two cases: a smooth and rough water-air-interface, as a function of the surface roughness Reynolds number R_{es} . If $R_{es} < 1$, the relation for a smooth surface is used. For a rough surface R_{es} has to be higher than 1 (Merlivat and Jouzel, 1979). R_{es} will be calculated as followed:

$$R_{es} = \frac{u_* z_0}{\nu}, \quad (11.3)$$

with z_0 being the surface roughness, u_* the friction velocity and ν is the kinematic viscosity of air. z_0 can be calculated by $z_0 = u_*^2 / (81.8 \cdot g)$, whereat g is the acceleration of gravity. Therefore z_0 and u_* are not independent. z_0 can be also calculated from the distribution of the wind velocity versus the height z ,

$$u = \frac{u_*}{\chi} \ln \left\{ \frac{z}{z_0} \right\}, \quad (11.4)$$

whereat χ is the Von Karman constant and is 0.4 (Merlivat and Jouzel, 1979).

For a smooth water-air-interface ($R_{es} < 1$) the equation for ρ_T/ρ_M is

$$\frac{\rho_T}{\rho_M} = \frac{1}{\chi} \cdot \ln \left\{ \frac{u_* z}{30\nu} \right\} / 13.6 \left(\frac{\nu}{D} \right)^{2/3}, \quad n = 2/3. \quad (11.5)$$

For a rough water-air-interface ($R_{es} > 1$) the relation for ρ_T/ρ_M is

$$\frac{\rho_T}{\rho_M} = \frac{1}{\chi} \ln \left\{ \frac{z}{z_0} \right\} - 5/7.3 R_{es}^{1/4} \left(\frac{\nu}{D} \right)^{1/2}, \quad n = 1/2. \quad (11.6)$$

The isotopic composition of the evaporated water can be therefore computed as a function of the surface temperature of the ocean, the relative humidity of the water-air-interface and the wind velocity at 10 m (u_{10}) above the ocean surface.

11.1.4 Moisture transport in the atmosphere and precipitation

The moisture that has evaporated from the ocean is lifted into the atmosphere by its thermal energy where it contributes to the atmospheric moisture. The lifting causes a cooling of the air parcel, because of the conversion of thermal energy into potential energy. If the temperature falls below the dew point the condensation of the atmospheric moisture starts and clouds form. According to [Rozanski et al. \(1982\)](#), the average cloud base level is at 850 mbar. Therefore the SIP model uses the temperature at 850 mbar to calculate the isotope fractionation effects for the condensation of the vaporous phase into the liquid or solid phase of water, respectively. To calculate the temperature at 850 mbar it is assumed that it varies parallel to the surface temperature [Dansgaard \(1964\)](#) and the uplift of air is described by a dry adiabatic uplift (as long as the ground level is below 850 mbar). For continental areas where the elevation is higher than the average cloud base level, i.e. where the air pressure is smaller than 850 mbar, the condensation temperature is calculated by a moist adiabatic uplift [Dansgaard \(1964\)](#). For this, the CRU TS 2.0, TYN SC 2.0 topography dataset is used. For each grid point the air pressure is calculated with the barometric height formula for ideal gases (Eq. 11.7), assuming an air pressure (p_0) at sea level ($z_0 = 0$ meters) of 1013,23 mbar; M is the molar mass for dry air $M=28.97$ g/mol, g the acceleration of gravity, R the ideal gas constant and T the absolute temperature in K,

$$p = p_0 \exp \left\{ -\frac{Mg}{RT} \cdot (z - z_0) \right\}. \quad (11.7)$$

To calculate the temperature at the cloud level the following equation is used for the temperature gradient,

$$\frac{dT}{dz} = -\frac{Mg}{C_p}, \quad (11.8)$$

based on a dry adiabatic uplift, i.e., a process where no condensation of water occurs. C_p is the heat capacity of dry air $C_p=28.97\text{J/K/mol}$. The result of dT/dz is $-0.981\text{K}/100\text{m}$. It means that a dry air parcel cools by 0.981 K per 100 m height difference. However, when air cools the water saturation pressure decreases and the condensation of water can occur during the lifting. Under these circumstances Eq. (11.8) can not be used, but Eq. (11.9) that describes a moist adiabatic uplift. L is the latent heat of evaporation $L\approx 2500\text{ J/g}$ and q_{sat} the water saturation pressure after Sonntag (1990).

$$\frac{dT}{dz} = -\frac{Mgp}{LRT \cdot \frac{dq_{sat}}{dT} + C_p p}. \quad (11.9)$$

Dansgaard (1964) and Sonntag et al. (1979) applied a Rayleigh approach for the condensation process appearing in the atmosphere, basing on the assumption that it is an equilibrium process, i.e., the condensate is in isotope equilibrium with the atmospheric water vapour and is immediately removed after condensation. This is a good assumption for rain and snow, although it must be modified for temperate regions (Jouzel and Merlivat, 1984, and references therein). For temperatures smaller than $-10\text{ }^\circ\text{C}$ Jouzel et al. (1987) an additional kinetic fractionation factor has to be included accounting for kinetic effects during snow formation (Jouzel and Merlivat, 1984). When a certain amount of precipitation dN is formed from the atmospheric moisture, then the Rayleigh approach for the isotopic composition of the residual atmospheric moisture

$$R_{moisture} = R_0 \left(\frac{N}{N_0} \right)^{\alpha-1}, \quad (11.10)$$

whereat R_0 is the isotopic composition of the atmospheric moisture before evaporation, N_0 is the amount of moisture in the atmosphere before evaporation, N the amount of moisture in the atmosphere after the evaporation process, i.e., $N = N_0 - dN$ and α the isotope fractionation factor depending on the local temperature of cloud base calculated with the surface temperature and Eq. (11.8) and Eq. (11.9), respectively. The isotopic composition of the formed precipitation with respect to Eq. (11.10) is

$$R_{precipitation} = R_0 \frac{1 - \left(\frac{N}{N_0} \right)^\alpha}{1 - \frac{N}{N_0}} \quad (11.11)$$

N_0 can be calculated as followed with

$$N_0 = \gamma \cdot \sum P_i, \quad (11.12)$$

at which γ is a free fit parameter and P_i is the amount of precipitation in box i . The sum includes all boxes. The fit parameter γ accounts for the fact when the amount of moisture in the last box is not 0, i.e., that the relative humidity in the atmosphere is not 0.

11.1.5 Evaporation of water from the continental surfaces

The formed precipitation with isotopic ratio $R_{precipitation}$ reaches the continental surface where it is absorbed by the upper soil zone. The water within the soil zone can be modified by two different processes: the evaporation from the upper soil zone and the water uptake by the vegetation (Zimmermann et al., 1967; Münnich, 1978; Gat, 1996). The water that has been up taken by plants is then removed to the atmosphere by the transpiration of the plants. The uptake of soilwater by the vegetation is not accompanied by isotope fractionation effects and is therefore not modifying the isotopic signature of the remaining soil water. Furthermore, the water that is released by transpiration has the same isotopic composition as the water from the soil zone (Münnich, 1978; Gat, 1996). Zimmermann et al. (1967); Münnich (1978) also demonstrate that the isotopic composition of the soilwater is not altered by the evaporation of water. The argument is, that due to the evaporation of water a deficiency of water occurs within the top soil layer that forces a flux of water from the soil zone below by capillary forces. Hence, the isotopic composition of the evaporated water is the same as the isotopic composition from the water within the soil zone (Zimmermann et al., 1967; Münnich, 1978). Zimmermann et al. (1967) noted, that there are also inner-soil evaporative processes possible, causing isotope fractionation effects in the soil zone for very dry periods. However, this might be only important for semi-arid and arid regions (Gat, 1996) and is therefore not included in the SIP model. The residual soilwater then percolates through the soil zone and enters the karst zone.

11.1.6 Recording of the stable isotope signal by speleothems

While the water percolates through the karst zone, oxygen isotopes are continuously exchanged between water and the species of the $\text{CO}_2\text{-H}_2\text{-CaCO}_3$ system. This results in an equilibration of the oxygen isotope compositions between all species of the $\text{CO}_2\text{-H}_2\text{-CaCO}_3$ system with respect to the oxygen isotopic composition of the water (Chapter 7). The water has the same isotopic composition as the local precipitation. The SIP model does not include any further processes modifying the isotope signature of the carbon bearing species, i.e., no prior calcite precipitation (Chapter 8.2) and no disequilibrium effects during the precipitation of calcite on a speleothem surface (Chapter 7). In sum, the SIP model only accounts for equilibrium isotope fractionation during the precipitation of calcite. For the isotope fractionation effect of the precipitation, the isotope fractionation factor between water and calcite of Kim and O'Neil (1997) is used and it is assumed that the cave air temperature is the mean annual air temperature above the cave.

11.2 Comparison of model results with GNIP values for selected transects in Europe

In the following the SIP model is tested for its reliability on precipitation's stable isotope composition of two European transects. The two transects are chosen in accordance to the two transects in recent and past speleothem $\delta^{18}\text{O}$ values identified by [McDermott et al. \(2011\)](#). The investigated transects depicted in Fig. 11.2 are indicated by the open white circles. The first transect T1, the Central European transect, starts in south-west Ireland and ends in Romania. The second transect T2, the Northern European transect starts also in south-west Ireland but ends in northern Sweden. Both transects are separated into square boxes with a size of $2^\circ \times 2^\circ$. The centre of each box is indicated by the open white circles (see Fig. 11.2). The derived values for the precipitation $\delta^{18}\text{O}$ and δD values are compared with measured $\delta^{18}\text{O}$ and δD values from selected selected GNIP station (open white squares).

11.2.1 Central European transect - T1

The isotopic composition of precipitation along transect T1 is illustrated in Fig. 11.3. The circles are picturing the results for $\delta^{18}\text{O}$ and δD derived from the SIP model. The values of the selected GNIP stations are illustrated by the open squares (Tab. 11.1). The results for the winter month (October-March) are illustrated in blue and for the summer month (April-September) in red. The bottom figure shows the $\delta^{18}\text{O}$ - δD relation for T1. To fit the $\delta^{18}\text{O}$ values of the GNIP stations the fit parameter γ is 1.4 for the winter months and 1.1 for the summer months. The values are in accordance with the values found by [Rozanski et al. \(1982\)](#). The isotopic composition of precipitation computed with the SIP model is a weighted average of the mean value for the related winter (October-March) or summer period (April-September) weighted with the amount of precipitation. The GNIP values are mean values for the winter and summer session derived from the long-term mean values for each month. Temperature, precipitation and evapo-transpiration are calculated from the CRU-TS3.1 dataset for each session using the related months of the years 1901 to 2009 (Fig. B.1). The $\delta^{18}\text{O}$ and δD gradient of the GNIP data is much steeper for the winter values compared to the summer values (Fig. 11.3). This has been also observed by [Rozanski et al. \(1982\)](#) for the δD values. The reason for this observation is the recycling of moisture by evapo-transpiration. Evapo-transpiration is much higher in summer compared to winter (Fig. B.1) [Rozanski et al. \(1982\)](#). The modelled $\delta^{18}\text{O}$ and δD values fit with the winter values, however, the modelled summer values are too positive compared to the GNIP values. A reason for this discrepancy is, that a fraction of the winter precipitation is also recycled during the summer month, when evapo-transpiration is greater compared to the amount of precipitation. Hence, water that is more depleted in heavy stable isotopes evaporate and modify the isotopic composition of the atmosphere and consequently that of the precipitation ([Rozanski et al., 1982](#)). [Rozanski et al. \(1982\)](#) state that a total of 35

11.2. Comparison of model results with GNIP values for selected transects in Europe

% of the winter precipitation was necessary to explain the summer gradient of δD values. The difference between the summer precipitation and evapo-transpiration also suggests a negative water budget in the soil zone, in particular in area between -5 and 12 °E (Fig. B.1). In comparison with the computed $\delta^{18}\text{O}$ - δD relation, the relation obtained by GNIP station values illustrates no kinetic effects, at least on a long-term time scale.

station	longitude °E	latitude °N	$w\delta^{18}\text{O}$ (1-sigma) ‰	$w\delta D$ (1-sigma) ‰	$s\delta^{18}\text{O}$ (1-sigma) ‰	$s\delta D$ (1-sigma) ‰
Valentine	-10,25	51,93	-5.8±0.3	-36.9±2.0	-4.6±0.5	-30.3±3.0
Wallingford	-1,1	51,6	-7.6±0.4	-51.1±3.3	-5.8±0.8	-39.1±4.8
Koblenz	7,58	50,35	-11.9±1.1	-87.7±8.9	-7.9±1.4	-56.0±11.3
Neuherberg	11,33	48,15	-12.1±1.3	-88.6±10.5	-8.4±1.5	-58.8±11.6
Graz (University)	15,45	47,06	-12.4±1.9	-90.0±15.8	-7.5±1.0	-51.4±7.6
Vienna (Hohe Varte)	16,35	48,35	-12.0±1.5	-88.0±12.5	-7.4±1.0	-53.4±7.9
Odessa	36,4	50	-10.9±1.3	-75.8±19.9	-7.2±0.7	-45.8±5.3

Tab. 11.1: Table of selected GNIP station data whose mean values are illustrated in Fig.11.3. The subscripts w and s indicate the $\delta^{18}\text{O}$ and δD values. The mean $\delta^{18}\text{O}$ and δD values are stated with their related 1-sigma standard deviation.

To calculate the stable isotopic composition of the drip water the stable isotopic composition of the infiltrated water is used. This is simply the isotopic composition of the rain (Sec. 11.1.5). Hence, the isotopic composition of the drip water shows the same behaviour as the stable isotopic composition of the rain, with a steeper gradient for the winter month compared to the summer month (Fig. 11.4; only for $\delta^{18}\text{O}$ values). However, the infiltration in summer is negligible in comparison to the winter infiltration. Therefore, the drip water's isotopic composition is mainly determined by the winter precipitation's $\delta^{18}\text{O}$ and δD values. The comparison with drip water $\delta^{18}\text{O}$ values samples in several caves along T1 (black squares), based on values composed by [McDermott et al. \(2011\)](#), illustrates, however, that the computed values are too negative in comparison to the measured $\delta^{18}\text{O}$ values. At first, the observed effect can be due to of evaporative processes at the soil-atmosphere interface. As a result of the evaporation the remaining water would be enriched in heavy isotopes. In addition that would lead to an enrichment of light isotopes in the atmospheric moisture and consequently a much steeper gradient as observed. The second reason could be the amount of water N_0 in the atmosphere. The higher the amount of atmospheric moisture is, the shallower is the $\delta^{18}\text{O}$ gradient. This is simply caused by the Rayleigh approach, because the sensitivity of the isotopic depletion in the atmosphere depends on the quotient of N/N_0 (Eq. 11.10). At last, the differences between the computed and the measured $\delta^{18}\text{O}$ values in the reference could be also due to the too small sampling interval in the caves.

Based on the $\delta^{18}\text{O}$ values of the drip water and the mean annual air temperature above the cave (Fig. B.1) the $\delta^{18}\text{O}$ value of calcite, being precipitated under equilibrium isotope fractionation effects (Sec. 5), can be calculated using the isotope fractionation factor between

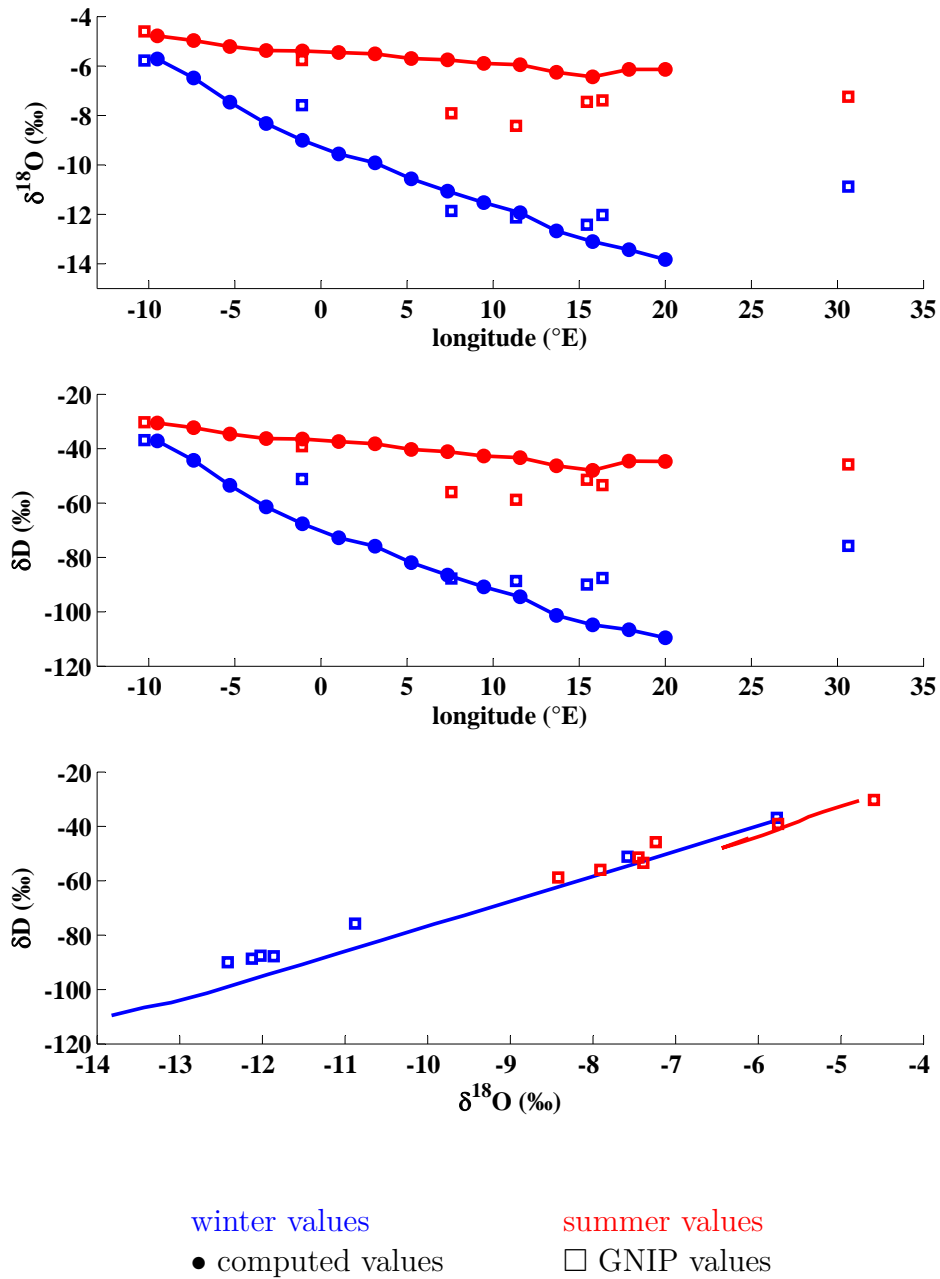


Fig. 11.3: The figure shows the computed $\delta^{18}\text{O}$ and δD values (circles) in precipitation along T1 for winter (October-March) and summer (April-September). In comparison, the GNIP values are illustrated as open squares. Winter values are shown in blue; summer values in red (see text for detail).

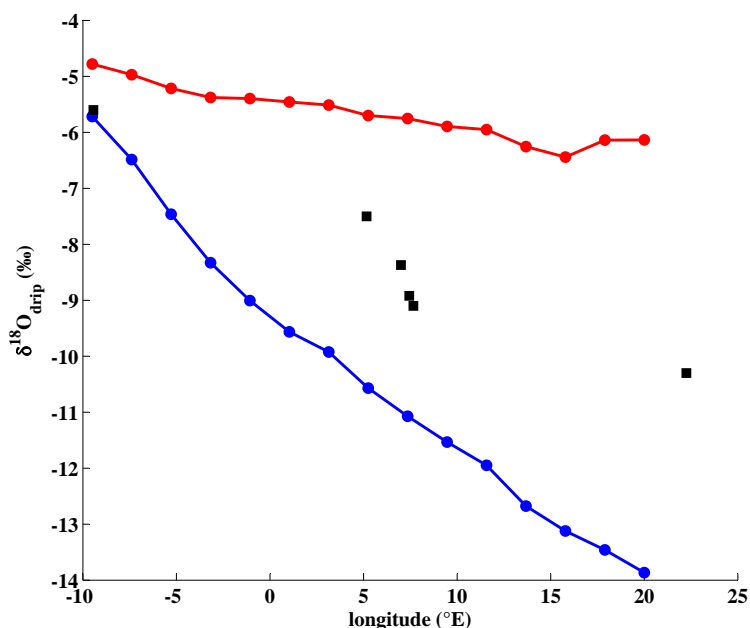


Fig. 11.4: Illustrated are the computed $\delta^{18}\text{O}$ value of the infiltrating water for T1 (closed circles) for the winter months (October-March) (blue) and summer months (April-September) (red). The black squares are measured drip water $\delta^{18}\text{O}$ values from caves that are close to T1. The cave sites are Crag Cave, Pere Noel, Han-sur-Lesse, B7 Cave, Attahöhle and Ursilor. The drip water $\delta^{18}\text{O}$ values are stated by McDermott et al. (2011).

water and calcite of Kim and O'Neil (1997). The gradient of calculated calcite winter (blue) and summer (red) $\delta^{18}\text{O}$ values is illustrated in Fig. 11.5. Furthermore, the $\delta^{18}\text{O}$ values of calcite samples (black squares) pictured in Fig. 11.5, picturing that winter $\delta^{18}\text{O}$ values (as well as the summer $\delta^{18}\text{O}$ values) are too depleted in ^{18}O , both yielding too negative ^{18}O values for the calcite. The difference between the computed and the measured calcite ^{18}O values can have several reasons. Since the SIP model only accounts for equilibrium isotope fractionation effects, disequilibrium effects can cause an additional enrichment in the measured calcite $\delta^{18}\text{O}$ values (Sec. 7). Furthermore, the used oxygen isotope fractionation factor between water and calcite is questioned by several studies, observing more enriched calcite ^{18}O values as suggested by Kim and O'Neil (1997) (Coplen, 2007; Tremaine et al., 2011; McDermott et al., 2011). Furthermore, prior calcite precipitation (PCP) can cause an additional enrichment in calcite ^{18}O values, which can not be detected only by drip water measurements (Sec. 9).

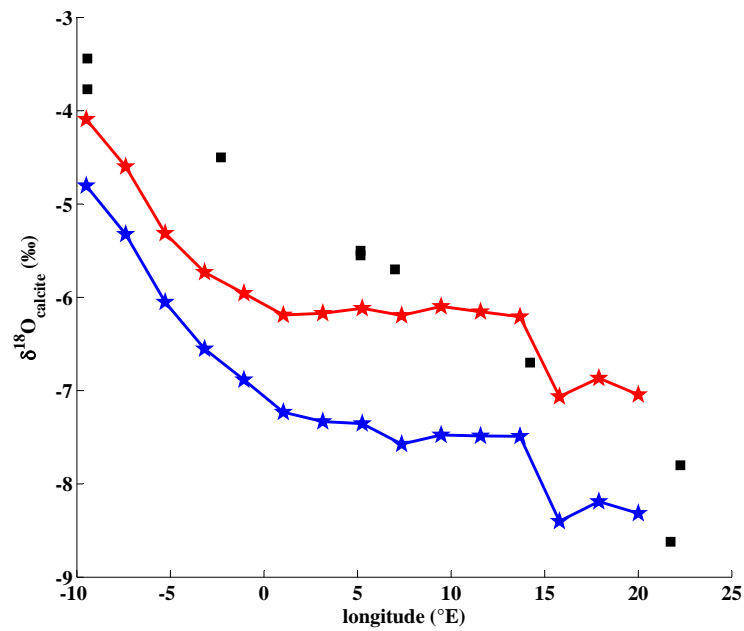


Fig. 11.5: Illustrated are the computed calcite $\delta^{18}\text{O}$ values (stars) for T1 for the winter months (October-March) (blue) and summer months (April-September) (red). The values are calculated from the corresponding drip water $\delta^{18}\text{O}$ values and the oxygen isotope fractionation factor of [Kim and O'Neil \(1997\)](#). For the temperature, the mean annual temperature of the respective box is used. The black squares depict present-day calcite $\delta^{18}\text{O}$ values from cave sides close to T1. The stalagmites are CC-3, Bilbo, BFM9, PN95, Prosperine, B7, Pos-stm4, PP4 and PU2. The speleothem $\delta^{18}\text{O}$ values are reported by [McDermott et al. \(2011\)](#).

11.2.2 Northern European transect - T2

The second transect T2 in speleothem $\delta^{18}\text{O}$ values identified by McDermott et al. (2011) is a northern transect starting in Ireland and ending in northern Sweden. The results of the SIP model for T2, the computed $\delta^{18}\text{O}$ and δD values for T2, are plotted in Fig. 11.6. Like in Fig. 11.3 the computed winter values (October-March) are illustrated in blue circles, whereas the summer values are depicted as red circles. The GNIP station values for the corresponding periods are illustrated as squares (Tab. 11.2). The gap in the transect between 0 and 5 °E corresponds to the Northern Sea. Furthermore, the fit parameter γ for the initial amount of moisture in the atmosphere is 1.4 for the winter session and 1.0 for the summer session. The computed $\delta^{18}\text{O}$ gradient for the winter session fits to the GNIP station values between -10 and 0 °E and to the GNIP station values of Kiruna, Abisko and Naimakka. The values of Stockholm and Ricklea might be also influenced by evaporated water from the Baltic Sea, because of their location. This could explain the more positive values compared to the other GNIP stations at the same longitude and also the deviation from the modelled winter $\delta^{18}\text{O}$ transect. The computed summer gradient for the $\delta^{18}\text{O}$ values is too flat and does not fit to the summer GNIP station values around 20 °E. This can be, as discussed for T1, caused by recycled winter precipitation, because of the deficiency of water in the soil zone during the summer months. However, for the summer period the amount of precipitation and evapo-transpiration is almost equal (Fig. B.2). The computed gradients for the δD values pictures a similar behaviour for the winter and summer period as the $\delta^{18}\text{O}$ gradient does. For the summer months the gradient is too flat to explain the GNIP station data at c. 22 °E. The winter value GNIP station value has also a too negative value compared to modelled winter gradient for δD values. However, for both periods, the δD values are too limited. That is the reason why in the following only the $\delta^{18}\text{O}$ values are discussed.

station	longitude °E	latitude °N	$w\delta^{18}\text{O}$ (1-sigma) ‰	$w\delta\text{D}$ (1-sigma) ‰	$s\delta^{18}\text{O}$ (1-sigma) ‰	$s\delta\text{D}$ (1-sigma) ‰
Valentine	-10.25	51.93	-5.8 ± 0.3	-36.9 ± 2.2	-4.6 ± 0.5	-30.3 ± 3.3
Keyworth	-1.08	52.88	-8.5 ± 0.6	-56.9 ± 4.9	-6.3 ± 0.9	-42.6 ± 6.8
Stockholm	18.03	59.32	-10.6 ± 1.6		-9.7 ± 0.7	
Ricklea	20.91	64.12	-14.1 ± 1.0		-10.8 ± 1.1	
Kiruna	20.23	67.87	-17.1 ± 2.4		-11.1 ± 0.9	
Abisko	18.82	68.35	-14.7 ± 1.3		-12.2 ± 1.5	
Naimakka	21.53	68.68	-19.4 ± 1.5	-144.7 ± 10.5	-13.6 ± 1.9	-99.4 ± 11.6

Tab. 11.2: Table of selected GNIP station data whose mean values are illustrated in Fig.11.6. The subscripts w and s indicate the $\delta^{18}\text{O}$ and δD values, respectively. The mean $\delta^{18}\text{O}$ and δD values are stated with their related 1-sigma standard deviation.

The $\delta^{18}\text{O}$ value of the calcite along the Northern transect is calculated from the oxygen

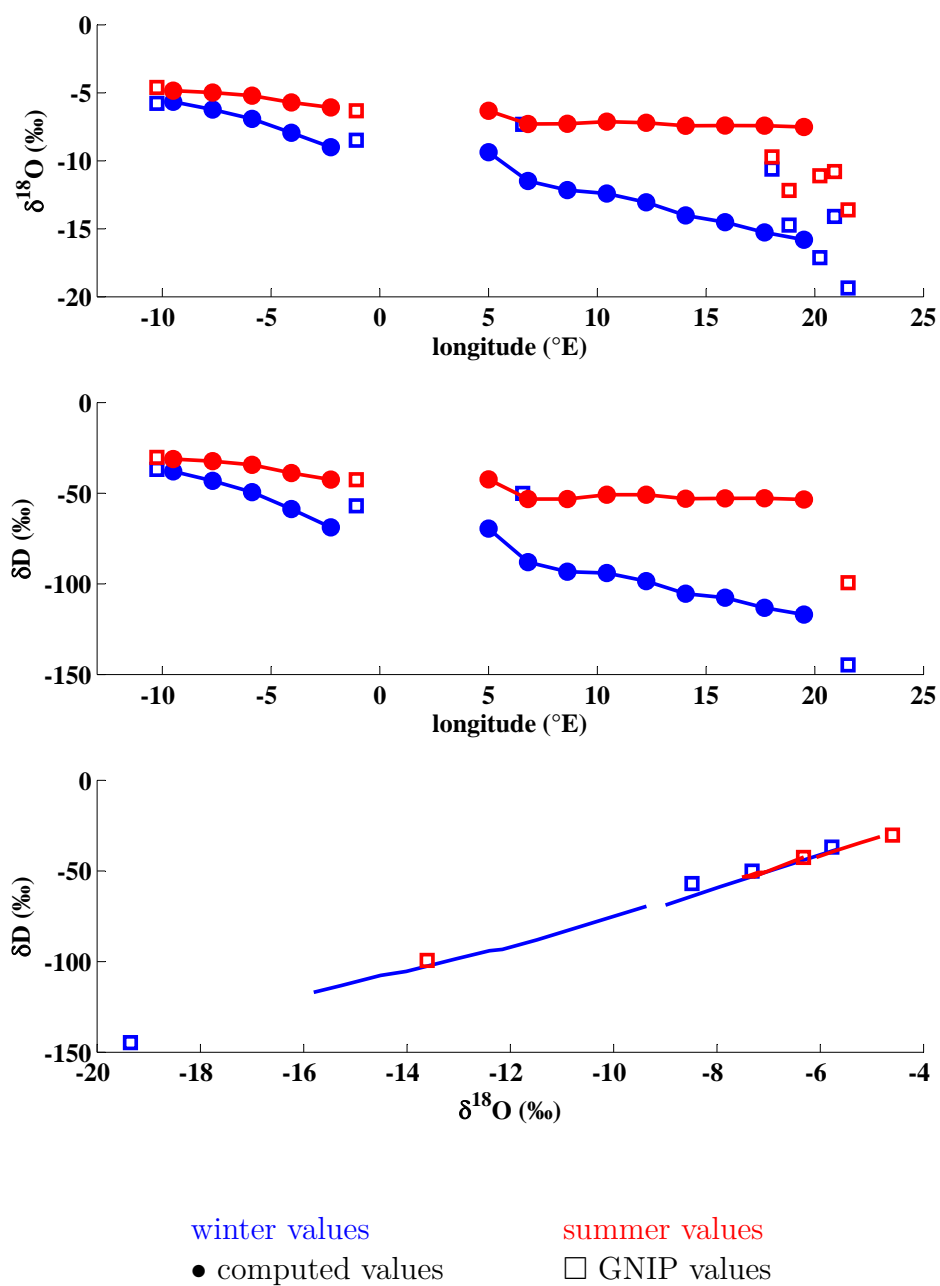


Fig. 11.6: The figure shows the $\delta^{18}\text{O}$ and δD (circles) values in precipitation along T2 for winter (blue) and summer (red). For comparison GNIP values are illustrated (open squares). Winter values are shown in blue; summer values in red. (see text for detail)

isotope composition of rain under the assumption that the calcite has been formed under isotope equilibrium conditions using the relation derived by [Kim and O'Neil \(1997\)](#) for the oxygen isotope fractionation factor between water and calcite. The oxygen isotope composition of drip water equates the oxygen isotopic composition of the rain, since no isotope fractionation processes affect the infiltrated water (Sec. 11.1.3). The calculated calcite $\delta^{18}\text{O}$ values for each box are illustrated in Fig. 11.7. The blue circles correspond to the winter months and the red circles to the summer months. Note, that the fraction of summer infiltration that contributes to the annual infiltration is negligible in comparison to the winter infiltration. Only for the boxes, which are close to the Northern Sea, does the summer infiltration affect the isotopic composition annual infiltration (Fig. B.2). Hence, the focus is on the $\delta^{18}\text{O}$ values in the following. The $\delta^{18}\text{O}$ gradient depends on the gradient of the drip water, i.e., the gradient of the oxygen isotopic composition of the precipitation and the gradient of the mean annual air temperature. Since the temperature gradient is negative along T2 (Fig. 11.7) the equilibrium oxygen isotope fractionation counteracts with the depletion of the drip water in ^{18}O along the transect. This results in the change of the slope for calcite $\delta^{18}\text{O}$ values (Fig. 11.7) compared to the slope for the oxygen isotope composition of the precipitation (Fig. 11.6). The computed gradient for calcite [Kim and O'Neil \(1997\)](#) fits to values from cave-calcite samples of Rana (Norway) and Korrallgrotten cave (Sweden) (Fig. 11.7).

11.3 Sensitivity of the model on model parameters for Central Europe (T1)

In the previous sections two precipitation $\delta^{18}\text{O}$ gradients and the related gradients in calcite $\delta^{18}\text{O}$ values were discussed based on the climate conditions in the period between 1901 and 2009. However, within the Holocene the slope of the Central European gradient of speleothem $\delta^{18}\text{O}$ values has changed ([McDermott et al., 2011](#)). To address this question, the reference winter period between 1901 and 2009 is used to study the sensitivity of the slope in precipitation $\delta^{18}\text{O}$ values and the corresponding calcite $\delta^{18}\text{O}$ values by changing the temperature and the amount of precipitation. In the following the discussion is focused on T1 with the objective to investigate the changed trends in speleothem $\delta^{18}\text{O}$ gradients in Central Europe during the Holocene. In the first sensitivity scenario, the monthly temperature is changed by ± 3 °C, resulting in an annual air temperature that is warmer and colder by 3 °C, respectively (Fig. B.3). The results for the stable isotopic composition of the precipitation are shown in Fig. 11.8. The discussion is limited on the $\delta^{18}\text{O}$ values and is also valid for the δD values. For the temperature scenario the results for the $\delta^{18}\text{O}$ values are illustrated by the closed circles; red indicates the +3 °C scenario, whereas blue indicates the -3 °C scenario. The blue and red squares are the GNIP station values for winter and summer months (Tab. 11.1). The change in the isotopic composition of the precipitation between the two temperature scenarios (+3 °C and -3 °C) is negligible in

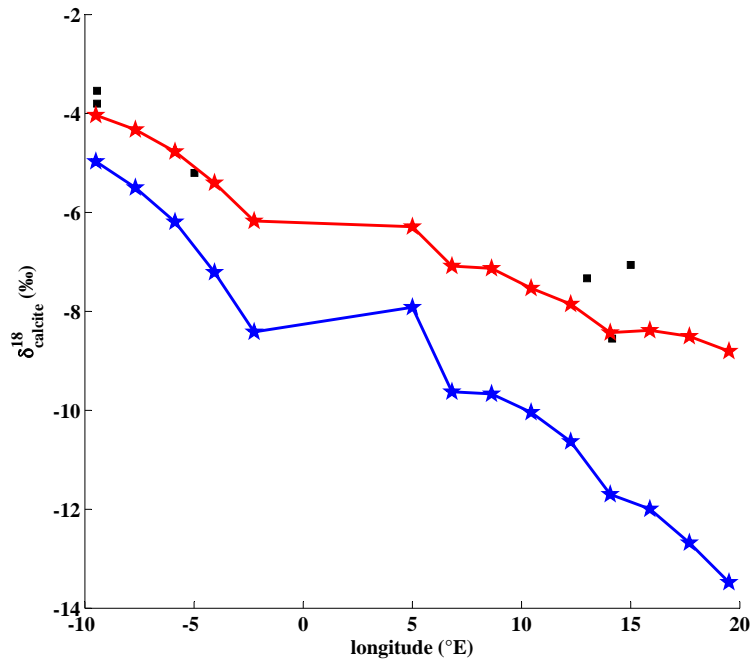


Fig. 11.7: Illustrated are the computed calcite $\delta^{18}\text{O}$ values for T2 for the winter months (October-March) (blue stars) and the summer months (April-September) (red stars). The values are calculated from the corresponding drip water $\delta^{18}\text{O}$ values and the oxygen isotope fractionation factor of [Kim and O'Neil \(1997\)](#). For the temperature, the mean annual temperature of the respective box is used. The closed black squares are present-day calcite $\delta^{18}\text{O}$ values from several stalagmites locates close to T2. The speleothems are CC-3, Bilbo, SG-95, SU, K1 and FM-3. The speleothem $\delta^{18}\text{O}$ values are reported by [McDermott et al. \(2011\)](#).

comparison to the evolution of the precipitation $\delta^{18}\text{O}$ gradient. This is an effect of the Rayleigh approach, at which the isotopic composition of the formed rain is more sensitive on the amount of formed precipitation than on the changes of the temperature dependent isotope fractionation investigated here. However, colder temperatures leads to a steeper gradient, because more H_2^{18}O molecules are condensed, causing a stronger depletion in ^{18}O of the remaining moisture in the atmosphere.

The $\delta^{18}\text{O}$ gradient of precipitation for the precipitation scenario, where the amount of precipitation changes in every box by $\pm 30\%$, is illustrated by the closed circles in Fig. 11.8. The $+30\%$ precipitation (wetter) scenario is visualized in red and the -30% precipitation (drier) scenario in blue (Fig. B.3). Note that the initial amount of precipitation in the atmosphere does not change and is equivalent to the reference winter period. For the $+30\%$ precipitation scenario the slope of the $\delta^{18}\text{O}$ gradient is much steeper compared to both slopes of the temperature scenarios, whereas the slope for the -30% precipitation scenario is much flatter. This is caused by the changed amounts of precipitation and the fact that

the initial amount of precipitation is constant. Hence, for a wetter climate, the atmospheric moisture becomes more depleted in ^{18}O along the transect, which is simply a result of the Rayleigh approach. For a drier climate it acts opposed, because less moisture condenses and consequently more ^{18}O remains in the atmospheric moisture. A similar result would be observed if not the amount of precipitation would have been changed but the initial amount of moisture, because the two variables are equivalent. The reason for this is the nature of the Rayleigh approach. Hereby the degree of isotopic fractionation is determined by the ratio of N/N_0 (Eq. 11.10). Hence, if more moisture is in the atmosphere, the slope is less steep, whereas less moisture leads to a steeper gradient.

The effect of the temperature and the precipitation scenarios is illustrated in Fig. 11.9. Thereby the reference scenario is the winter session of Fig. 11.3. It is indicated by the grey closed circles. For the temperature scenario (closed circles) the absolute values are shifted towards more negative values for +3 °C scenario (red). In contrast they are shifted towards more positive values for the -3 °C scenario (blue). The reason for this effect is that the counteracting of the isotope fractionation effect of the by the oxygen equilibrium isotope fractionation effects during the calcite formation. Since the sensitivity of oxygen isotope fractionation factor between water and calcite is negative (Fig. 7.5, dotted line), a warming forces a calcite oxygen isotopic composition, that is more depleted in ^{18}O . A cooling in contrast, results in an enrichment of ^{18}O . The slope of the $\delta^{18}\text{O}$ gradient does not change for the temperature scenarios in comparison to the reference scenario. This is mainly determined by the fact that the slope of the $\delta^{18}\text{O}$ gradient of the precipitation is almost unchanged for the two temperature scenarios and the the temperature gradient of T1 was changed parallel in all boxes. Only, if there would was an additional temperature gradient added to the reference temperature gradient, the slope would have changed. As an example: if the temperature in West Europe (Ireland) would be colder by 3 °C and warmer by 3 °C in East Europe (Romania), the observed calcite $\delta^{18}\text{O}$ gradient would be a super-position of the +3 °C and -3 °C scenarios. Consequently, the slope of the calcite $\delta^{18}\text{O}$ gradient becomes steeper and shallower if there was a warming in West Europe and a cooling in East Europe.

For the precipitation scenarios (open circles) the slope of the calcite $\delta^{18}\text{O}$ gradient changes, whereas the absolute value in the first box is almost unchanged. For the temperature scenarios in contrast the absolute $\delta^{18}\text{O}$ value of the precipitated calcite shifts by c. ± 1 ‰ caused by the temperature dependent isotope fractionation effects. If the amount of precipitation changes, under the assumption that the initial amount of moisture in the atmosphere is unchanged, the slope of the precipitation $\delta^{18}\text{O}$ gradient would change (Fig. 11.8). This change is transferred into the cave by the percolation water. Since the temperature is unchanged in the precipitation scenarios the oxygen isotope fractionation effects during the calcite precipitation are the same as for the reference scenario. This results in a steeper slope of the calcite $\delta^{18}\text{O}$ gradient for the +30 % precipitation scenario (red) whereas the slope for the -30 % scenario (blue) is flatter (Fig. 11.9).

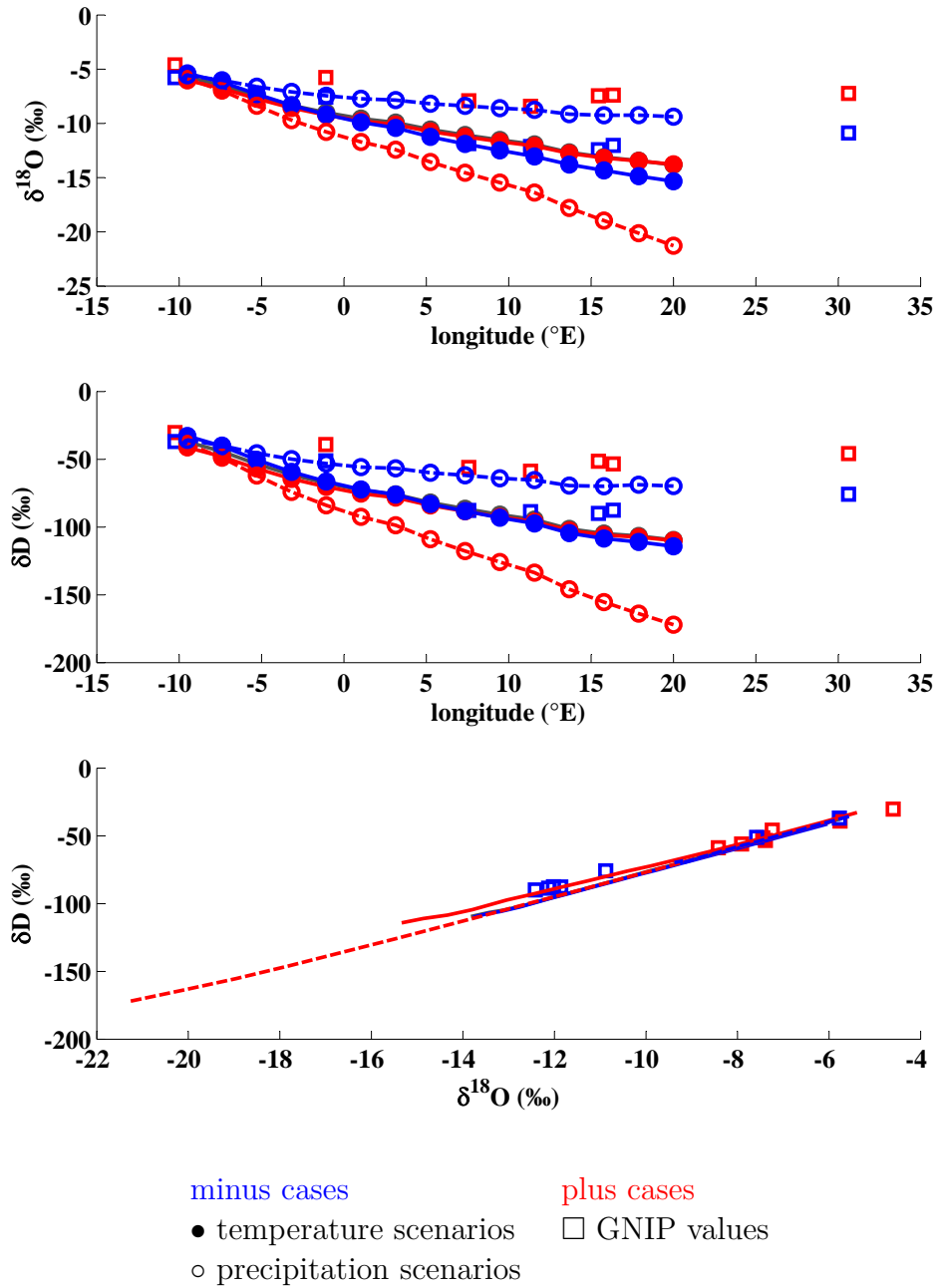


Fig. 11.8: Illustrated are the computed $\delta^{18}\text{O}$ and δD for T1 for different sensitivity studies (closed circles). The closed circles (line) indicate the temperature sensitivity study for an increase of the temperature of +3 °C (red) and -3 °C (blue). The open circles (dotted line) depicts the precipitation sensitivity study whereas the amount of precipitation is changed in each box by +30 % (red) and -30 % (blue). The open squares picturing the GNIP station data for the winter months (blue) and the summer months (red).

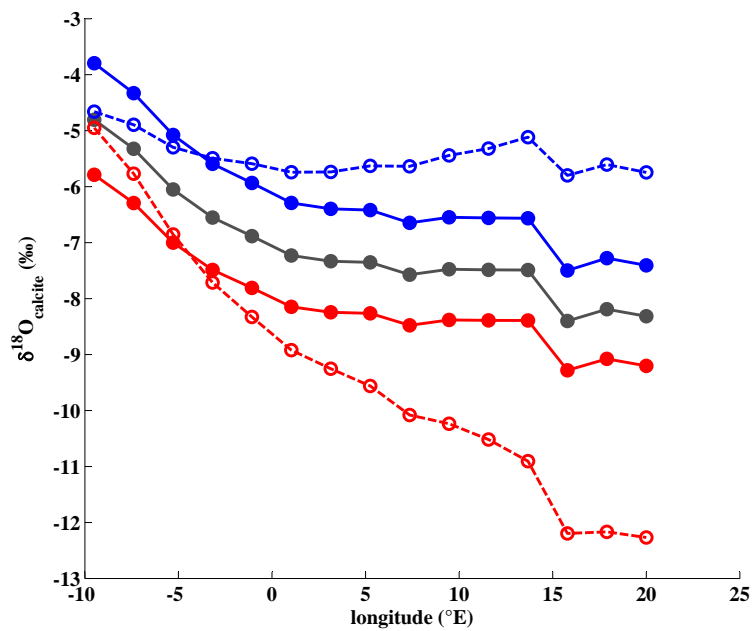


Fig. 11.9: Illustrated are the computed calcite $\delta^{18}\text{O}$ values for the sensitivity studies (coloured circles). The closed circles indicate the results of temperature sensitivity study: the red closed circles are the results of the +3 °C scenario and the blue closed circles for the -3 °C scenario. The open circles picturing the results for the precipitation sensitivity study: the red open circles are the results for the +30 % scenario and the blue open circles for the -30 % scenario. The black closed circles illustrate the computed $\delta^{18}\text{O}$ values for the reference scenario.

11.4 Comparison of model results with GNIP values for positive and negative NAO phases

In the previous sections GNIP station values have been used to test the performance of the SIP model. The comparison shows that the SIP model can compute the observed gradients for the winter months (October-March) and the summer months (April-September) observed in GNIP station $\delta^{18}\text{O}$ values, although the summer gradients are too flat. This might be caused by the deficiency of water stored in the soil zone. A negative water balance of the soil zone during the summer months is caused by the difference between the amount of precipitation and evapo-transpiration (Fig. B.1). Hence, water from the winter months is possibly recycled in the summer months, causing a steeper gradient (Rozanski et al., 1982). However, the gradient for the winter months is well reproduced by the SIP model. In the following the focus is only on the winter month, because the water that has been infiltrated in the soil and karst zone precipitates mostly in the winter months in Central and eastern Europe (Fig. B.1). Hence, the drip water in cave conforms the infiltrated water and so does the isotopic composition.

To investigate the effect of different NAO phases on the GNIP station values, the $\delta^{18}\text{O}$ and δD values from October to March are used during which the winter NAO index (December-March) has values >0.8 (positive NAO phase) and <-0.8 (negative NAO phase). The results for the selected GNIP stations is listed in Tab. 11.3. It lists the mean NAO index of those years which are selected by their winter NAO index and the related mean $\delta^{18}\text{O}$ and δD values for the winter months (October-March). All mean values are stated with the 1-sigma standard deviation. The number in brackets behind the mean NAO indexes is the number of selected years.

station	longitude	latitude	positive	negative	$\delta^{18}\text{O}$ (1-sigma)	δD (1-sigma)	$\delta^{18}\text{O}$ (1-sigma)	δD (1-sigma)
			\overline{wNAO}	\overline{wNAO}	(+) $wNAO$	(+) $wNAO$	(-) $wNAO$	(-) $wNAO$
	°E	°N			‰	‰	‰	‰
Valentine	-10,25	51,93	1.8±0.5 (14)	-1.5±0.7 (6)	-5.7±0.7	-35.4±5.3	-6.0±1.0	-40.2±6.1
Wallingford	-1,1	51,6	1.9±0.5 (11)	-2.3±0.0 (1)	-7.3±0.5	-49.4±4.3	-8.3±0.0	-54.0±0.0
Koblenz	7,58	50,35	1.8±0.6 (10)	-2.3±0.0 (1)	-7.9±1.1	-57.3±9.3	-9.7±0.0	-74.0±0.0
Neuherberg	11,33	48,15	1.9±0.6 (8)	-2.3±0.0 (1)	-12.1±1.1	-87.4±9.0	-13.0±0.0	-95.3±0.0
Graz (U)	15,45	47,06	1.7±0.6 (12)	-1.6±0.6 (3)	-12.5±1.2	-91.0±9.2	-13.3±1.1	-96.7±8.5
Vienna (HV)	16,35	48,35	1.7±0.5 (16)	-1.6±0.7 (7)	-11.3±1.5	-82.8±11.4	-13.5±1.4	-95.3±9.5
Odessa	36,4	50	1.6±1.0 (2)		-9.5±0.7	-57.0±12.0		

Tab. 11.3: Table of mean winter $\delta^{18}\text{O}$ and δD values for positive and negative NAO phases for selected GNIP stations. The values are illustrated in Fig.11.10. All values are given with the related 1-sigma standard deviation.

The results of the stable isotopic composition are illustrated in Fig. 11.10. The values for a positive NAO phase are indicated by red squares, whereas the values for a negative NAO

11.4. Comparison of model results with GNIP values for positive and negative NAO phases

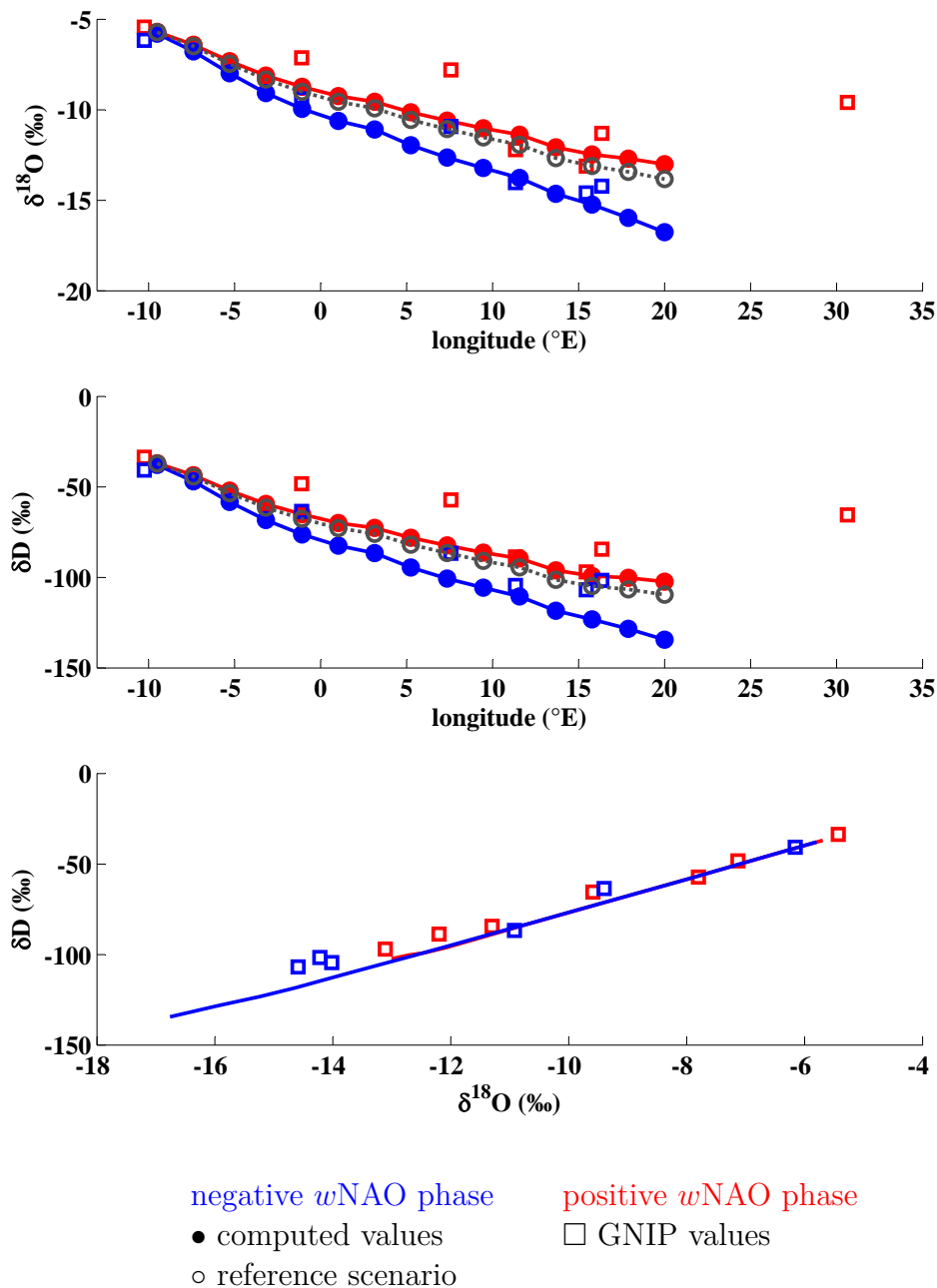


Fig. 11.10: The figures picture the dependence of winter (Oct.-March) $\delta^{18}\text{O}$ and δD values in precipitation. Values for positive (> 0.8) and negative (< 0.8) NAO phases are illustrated in red and blue, respectively (closed circles). The closed squares show GNIP values for positive (> 0.8) (red) and negative (< 0.8) (blue) NAO values. The grey circles illustrating the mean values for all winters (Oct.-March).

phase are illustrated by blue squares. In comparison to the GNIP station data for the long-term $\delta^{18}\text{O}$ and δD values in Fig. 11.3 the $\delta^{18}\text{O}$ and δD values are clearly separated for positive and negative NAO phases. The gradient of $\delta^{18}\text{O}$ (δD) is steeper for negative NAO phases as for positive NAO phases (Fig. 11.10). To fit the $\delta^{18}\text{O}$ GNIP station data values with the computed $\delta^{18}\text{O}$ values, the fit parameter $\gamma=1.5$ in case of the positive NAO phase and $=1.2$ for the negative NAO phase. This is due to the reason that the amount of precipitation is almost identical along the transect for both NAO scenarios and the effect of the temperature difference between positive and negative NAO phases on the $\delta^{18}\text{O}$ (δD) gradient is negligible (Fig. B.4). However, the result, that the initial amount of moisture in the atmosphere varies in dependence on the NAO phases, is reasonable. The NAO is a multi-pattern of different high and low pressure systems (Comas-Bru and McDermott, 2013, and references therein) that modulates the westerlies, which are the moisture conveyor belt for the European continent. In dependence on the NAO phase the westerlies are shifted north- or southwards causing a change of the initial amount of moisture at the western boundary of the European continent. Hence, for a positive NAO phase more moisture enters the European Continent from West and is transported over Central Europe. For a negative NAO phase the effect is the opposite, because the moist air is then transported southwards and causes a higher initial amount of moisture in the atmosphere in the Western Mediterranean region. Consequently, less moisture is transported by the atmosphere to Central Europe. This effect is proofed by the results of the SIP model. If the isotopic composition of the precipitation is not modulated at the surface (Rozanski et al., 1982, and references therein), the different slopes for the $\delta^{18}\text{O}$ gradient of T1 for positive and negative NAO phases should be also observed in cave drip water. This can be an explanation for the observed dependency of the precipitation $\delta^{18}\text{O}$ values on the NAO for the GNIP stations in Europe (Baldini et al., 2008) and ECHAM5-wiso data (Langebroek et al., 2011).

In Sec. 11.2.1 the computed $\delta^{18}\text{O}$ gradient for cave drip water was too steep to explain the $\delta^{18}\text{O}$ values measured in cave drip waters (Fig. 11.4). However, for the calibration of the SIP model the long-term GNIP stations were used, consisting of positive and partly negative NAO phases. Since the GNIP program has started in 1961 the NAO has had mostly a positive wNAO index. The mean wNAO (December-March) between 1961 and 2009 is 0.32. It had a distinct positive phase in the 1990s with a mean value (between 1990 and 1999) of 0.90. This explains why the $\delta^{18}\text{O}$ gradient of the reference winter period in Fig. 11.11 (open grey circles) is closer to the computed $\delta^{18}\text{O}$ gradient for the positive wNAO scenario (red closed circles) than for the calculated $\delta^{18}\text{O}$ gradient for the negative wNAO scenario (blue closed circles) (Fig. 11.11). The illustrated measured $\delta^{18}\text{O}$ values of cave drip water (black squares) are based on the collection of McDermott et al. (2011). However, most of the studies were published between 2003 and 2006 and the monthly $\delta^{18}\text{O}$ values of GNIP station in Koblenz (7,58 °E) exhibits values between -8.6 and -7 ‰ of the local precipitation. This is an explanation why (i) the computed $\delta^{18}\text{O}$ gradient of cave drip water of Fig. 11.4 is not explained by the SIP model. This is simply because the model was calibrated for the long-term GNIP $\delta^{18}\text{O}$ values having a mean oxygen isotopic composition of c. -12 ‰ between 7.6 and 11.3 °E (Tab. 11.1). (ii) The computed $\delta^{18}\text{O}$ gradient for the

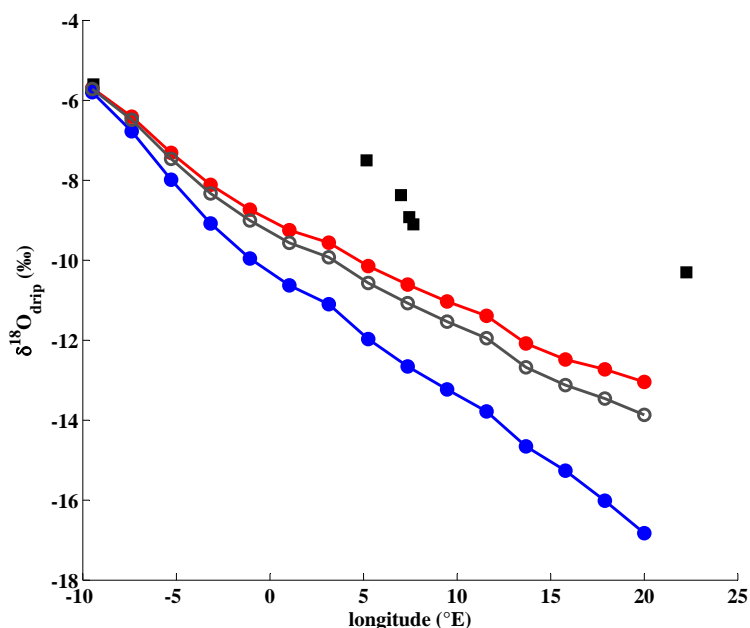


Fig. 11.11: The figure shows the dependence of drip water $\delta^{18}\text{O}$ values against longitude for transect T1 for positive (> 0.8) and negative (< 0.8) NAO phases. The black closed squares visualize drip water samples (McDermott et al., 2011).

cave drip water does not fit to the cave water $\delta^{18}\text{O}$ values. Hence, the observed difference between the modelled and measured $\delta^{18}\text{O}$ values is simply caused by the averaging of the GNIP $\delta^{18}\text{O}$ values and the subsequent calibration of the SIP model.

From the computed $\delta^{18}\text{O}$ drip water values the oxygen isotopic composition of calcite, that is precipitated under isotope equilibrium conditions, can be calculated using the oxygen isotope fractionation factor between water and calcite derived by Kim and O'Neil (1997) and the mean annual air temperature (Fig. B.4). The derived results for the gradient of calcite $\delta^{18}\text{O}$ values are illustrated in Fig. 11.12. The positive NAO scenario is indicated by the red closed circles, whereas the negative NAO scenario is pictured by the blue closed circles. The reference scenario is indicated by the open grey circles. The slope of the calcite $\delta^{18}\text{O}$ gradient is steeper for the negative NAO scenario in comparison to the reference of the positive NAO scenarios, whereas the positive NAO scenario is flatter compared to the reference scenario. This is caused by the fact that the change of the mean annual air temperature (Fig. B.4) is not significant in comparison to the change caused by the different hydrological conditions forcing the different slopes of the gradient in precipitation and drip water $\delta^{18}\text{O}$ values. Hence, calcite $\delta^{18}\text{O}$ values are only modulated by the change of the mean annual air temperature along the transect, but not by the temperature difference between the positive and negative NAO scenario.

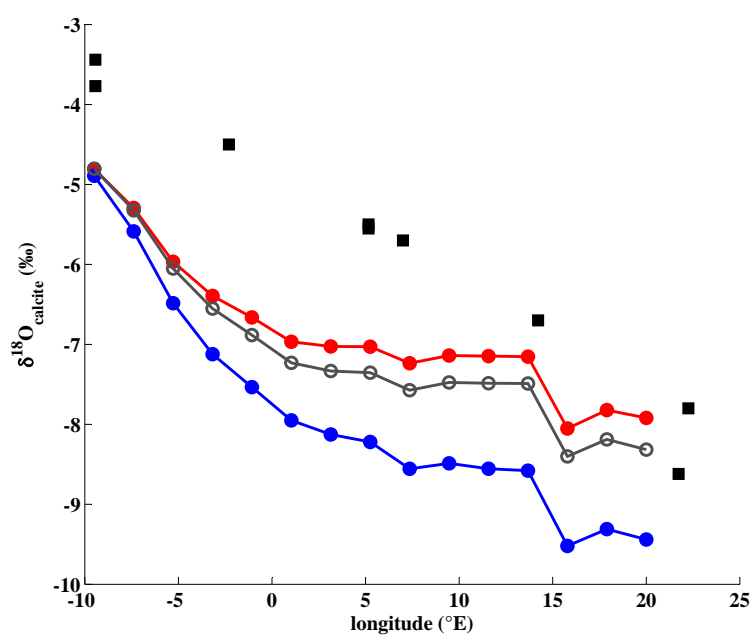


Fig. 11.12: The figure shows calcite $\delta^{18}\text{O}$ values for positive (> 0.8) (red) and negative (< 0.8) (blue) NAO phases; the values are calculated with drip water $\delta^{18}\text{O}$ values (Fig. 11.11) and the oxygen isotope fractionation factor between water and calcite after [Kim and O'Neil \(1997\)](#).

11.4. Comparison of model results with GNIP values for positive and negative NAO phases

12

The Global Speleothem Network

Since the early 90's the number of publications in speleothem science has rapidly increased (Fleitmann and Spötl, 2008) and speleothem science is progressing since ever even faster (e.g. Fairchild and Baker, 2012). At the same time the number of investigated speleothems is increasing. By now, more than 500 speleothems from caves worldwide were investigated.

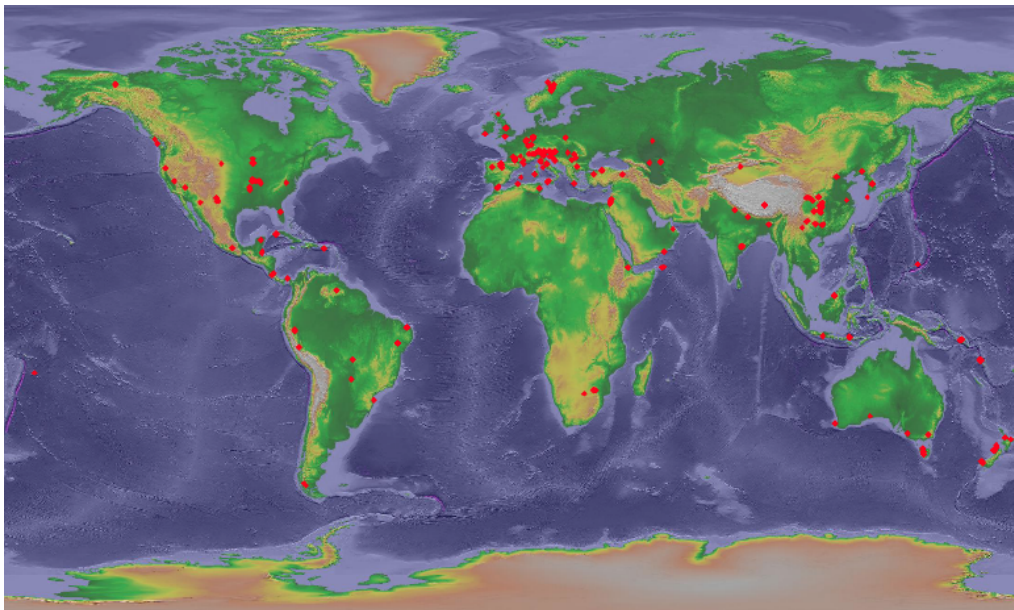


Fig. 12.1: The Global Speleothem Network: The red dots indicate a cave where speleothems have been collected and analysed.

The world map (Fig. 12.1) illustrates this impressively. The red dots are cave locations at which speleothems were analysed or being still investigated. The speleothem data compose a global speleothem network (GSN) that has recorded past climate changes over thousands

of years on all continents - note that the illustrated speleothem studies in Fig. 12.1 is not up to date since the number of investigated speleothems is continuously increasing. This achievement of last decades has introduced a new level in speleothem science, because it allows quantitative comparisons of speleothem proxy time series in space and time. The advance is accompanied with the development of more sophisticated methods, like PCA, that enable to uncover similarities of the speleothem proxy time series. From the speleothems illustrated in Fig. 12.1 39.6 % of the speleothems were collected in Europe, 17.3 % in Asia, 13.1 % in North America and the remaining are distributed over Oceania, the Middle East, South America, Middle America and Africa. Most of the speleothems recorded climate changes during the Holocene and the Last Glacial (MIS 4 to MIS 1). The palaeo climate proxy of choice of the studies was $\delta^{18}\text{O}$ and $\delta^{13}\text{C}$, followed by trace elements and lamina thickness (Dambach, 2012). The highest spacial density of investigated speleothems is achieved in Europe (Fig. 12.1), whereas most of them have grown during the Holocene. Therefore European speleothems are appropriate to apply PCA on their $\delta^{18}\text{O}$ and $\delta^{13}\text{C}$ time series, respectively, to investigate for coherent variations in space and time.

12.1 European speleothems within the GSN and pre-selected speleothems for PCA

The spatial coverage shows that most studied speleothems are situated in Central Europe (Fig. C.1). By using the PCA selection criteria for speleothems (Sec. 10.2.3) however, most of the speleothems fail the criteria and only a limited number of speleothems can be used for PCA. Another external limiting criteria is the availability of the data. Hence, within this framework only data have been used that are either available on the NOAA palaeo climate database or that have been provided by authors. The speleothem proxy time series that fulfil the criteria, that the ages have measured by TIMS or ICP-MS techniques and where the $\delta^{18}\text{O}$ and $\delta^{13}\text{C}$ time series were available are listed in Tab. 12.1 and graphically illustrated in Fig. 12.2. They belong to a pre-selection of speleothems that is ultimately used for PCA. The speleothem proxy time series cover an area that ranges from West Europe, tied by the speleothem CC-3 and GAR-01 formed in Crag Cave and La Garma Cave, respectively. The stalagmites FM-3 and K-1 that grew in Norway and North Sweden are palaeo climate recorders for North Europe. Stalagmite SU 96-7, formed in North Scotland, supplements the most northern speleothems CC-3, FM-3 and K-1. In Central and East Europe the stalagmites BU-4 (Germany), C09-2 (Romania), CC-26 (Italy), SPA-12 (Austria) and SV-1 (Italy) form the most dense network of palaeo climate recorders. In South Europe, stalagmites CL-26 (France) and CR-1 (Italy) and in the East stalagmite SO-1, respectively, are completing the usable speleothems. However, most of the speleothems have not grown during the entire Holocene but only during limited periods (Tab. 12.1). From the selected speleothems, at least 10 were actively growing between 0 and 7.5 ka BP (Fig. C.2). The number of speleothems that have recorded the early Holocene climate

(> 7.5 ka BP) is progressively decreasing. At 12 ka only 3 of the selected speleothems formed. This highlights that in dependence on the focus of the PCA, whether short-term or long-term variations are investigated, only a limited number of the speleothems listed in Tab. 12.1 can be used.

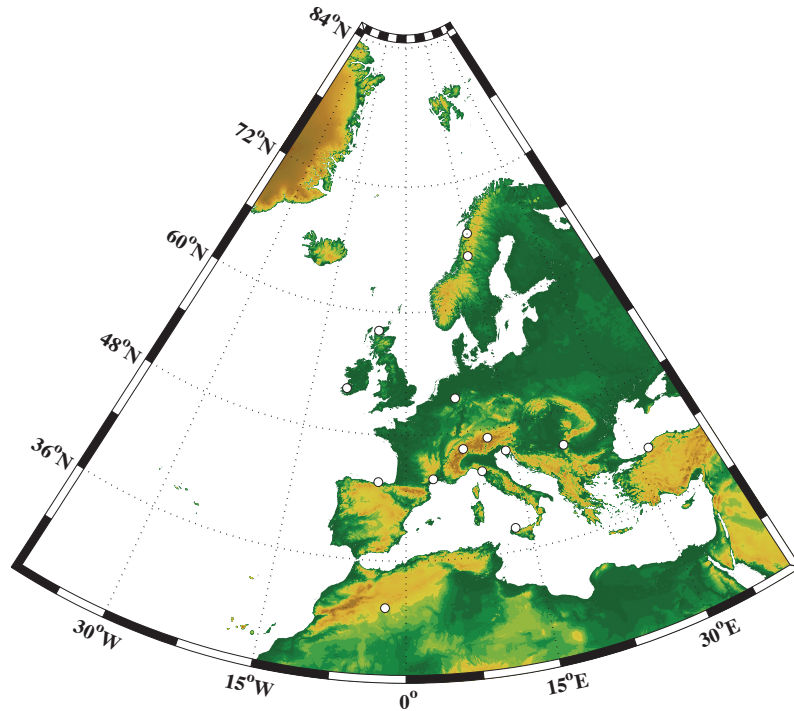


Fig. 12.2: Map of European speleothems (Tab. 12.1) that can be analysed with PCA (see text for detail).

12.1.1 Temporal resolution of speleothem proxy time series

Another criteria for the PCA was, that the temporal resolution of the proxy record should be smaller than 30 years allowing for short-term investigations. To test the pre-selection of speleothems (Tab. 12.1) a total of 1000 MC runs have been performed to calculate the mean temporal resolution for each speleothem during it's active growing section. The result of the MC runs is illustrated in Fig. 12.3 showing the mean temporal resolution for a 200 year running average. The color of each rectangle indicates the mean temporal resolution which is given by the color bar on right side.

name	cave	latitude	longitude	altitude	actual cave	growth	growth	dating	proxies	reference
		°N	°E	(m)	air temperature (°C)	stop (ka BP)	begin (ka BP)			
BU-4	Bunker Cave	51,37	7,666	184	10,8	-0,6	8,2	TIMS	$\delta^{18}\text{O}$, $\delta^{13}\text{C}$	Fohlmeister et al. (2012)
C09-2	Closani Cave	45,07	22,79	80	11	-0,3	4,0	TIMS	$\delta^{18}\text{O}$, $\delta^{13}\text{C}$	daphne et al. (in prep.)
CC-26	Corchia Cave	44,00	10,22	1300	7,5	0,8	11,3	MC-ICP-MS	$\delta^{18}\text{O}$, $\delta^{13}\text{C}$	Zanchetta et al. 2007)
CC-3	Crag Cave	52,23	-9,44	60	10,4	-0,05	10,1	TIMS	$\delta^{18}\text{O}$, $\delta^{13}\text{C}$	McDermott et al. (1999)
CL-26	Clamouse Cave	43,70	3,6	75	14,5	0,3	11,1	TIMS	$\delta^{18}\text{O}$, $\delta^{13}\text{C}$	McDermott et al. 1999
CR-1	Carburangeli Cave	38,15	13,2	22	19,4	1,1	9,9	TIMS	$\delta^{18}\text{O}$, $\delta^{13}\text{C}$	Frisia et al. (2006)
FM-3	Okshala Cave	67	15	200	3,2	-0,05	7,5	TIMS	$\delta^{18}\text{O}$, $\delta^{13}\text{C}$	Linge et al. (2009)
GAR-01	Garma Cave	43,43	-3,66	75	12,1	-0,03	13,9	TIMS/ICP-MS	$\delta^{18}\text{O}$, $\delta^{13}\text{C}$	Baldini et al. (in prep.)
GP-2	Grotte de Piste	31,67	-2,23	1260		2,8	11,0	TIMS/ICP-MS	$\delta^{18}\text{O}$	Wassenburg et al. (in prep.)
K-1	Korallgrottan	64,88	14,15	570	2,7	-0,06	3,8	TIMS	$\delta^{18}\text{O}$, $\delta^{13}\text{C}$	Sundquist et al. (2010)
MB-3	Milchbach Cave	46,37	8,05	1840	2,5	2,2	9,2	MC-ICP-MS	$\delta^{18}\text{O}$, $\delta^{13}\text{C}$	Luetscher et al. (2011)
SO-1	Sofular Cave	41,42	31,93	442	12	-0,06	50,3	MC-ICP-MS	$\delta^{18}\text{O}$, $\delta^{13}\text{C}$	Fleitmann et al. (2009)
SPA-12	Spannagel Cave	47,12	11,67	2531	1,8	0,02	4,8	TIMS	$\delta^{18}\text{O}$, $\delta^{13}\text{C}$	Mangini et al. (2005)
SU 96-7	Uamh an Tartair	58,15	-4,98	220	7,1	-0,04	0,95	TIMS/Laminae counting	$\delta^{18}\text{O}$	Baker et al. (2011)
SV-1	Grotta Savi	45,61	13,88	441	12,3	-0,04	17,6	MC-ICP-MS	$\delta^{18}\text{O}$, $\delta^{13}\text{C}$	Stoykova et al. (2005)

Tab. 12.1: The table is a compilation of pre-selected European speleothems that can be used for PCA. The speleothems which are selected for PCA are indicated by the blue color of their name (1st column).

A mean temporal resolution below 30 years is indicated by blue colors whereas mean temporal resolution that is greater than 30 years is indicated by yellow and red colors. If the mean temporal resolution is exactly 30 years it is indicated by green. For the speleothems CL-26, CR-1 and SV-1 it reveals that the temporal resolution is mostly greater than 30 years. Stalagmite FM-3 has a temporal resolution higher than 30 years in first 4000 years with phases of a temporal resolution that is smaller than 30 years. In the first 3000 years it's growing session, FM-3 has a temporal resolution that is between 20 and 30 years. All other speleothems have a temporal resolution of the proxy record that is smaller than 30 years. Speleothem CC-3 has a hiatus between 6.0 and 6.2 ka BP and GAR-01 between 1.1 and 1.3 ka BP.

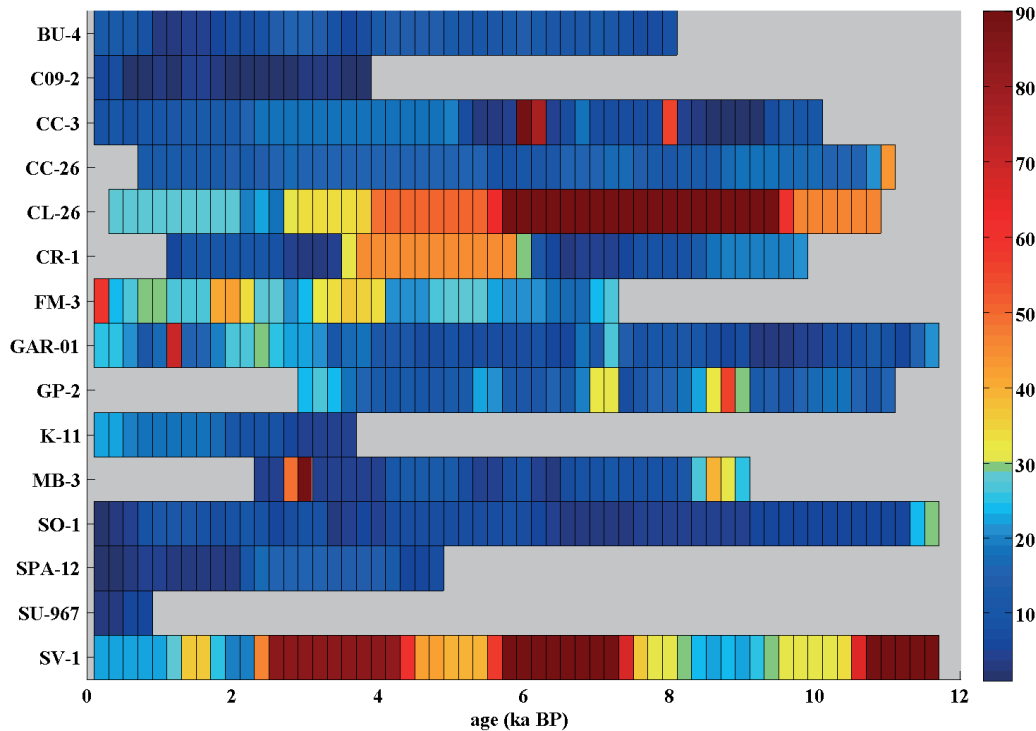


Fig. 12.3: Illustration of the mean temporal resolution of the listed speleothem proxy time series (Tab. 12.1). The mean temporal resolution is based on a total of 1000 MC runs and is calculated by a 200 year running average. The color of each rectangle indicates the mean temporal resolution, given by the color bar on the right side.

12.1.2 Recording period of speleothem proxy time series

In addition to the temporal resolution of the speleothem proxy time series, the period during which the water infiltrated in the karst zone and subsequently entered a cave is another important criteria when speleothem proxy time series are compared. To compare the infiltration period of each pre-selected speleothem (Tab. 12.1) the mean infiltration was calculated by using the CRU-TS3.1 dataset (Sec. 11.1.2). The procedure is to average the mean precipitation and evapo-transpiration for each month for the available years (1901-2009) and to calculate the difference between the two terms. The mean infiltration \bar{I} for month i is

$$\bar{I}_i = \bar{P}_i - \overline{ET}_i \quad (12.1)$$

with \bar{P} being the mean amount of precipitation and \overline{ET} is the mean amount of evapo-transpiration of a $2^\circ \times 2^\circ$ grid around the cave location - the CRU-TS3.1 dataset is composed of a $0.5^\circ \times 0.5^\circ$ grid, hence, the mean values are calculated by 16 values. The results of Eq. (12.1) are illustrated for each month in Fig. 12.4. If the mean infiltration is positive it is indicated by blue colors and if the mean infiltration is negative it is indicated by red. The illustration of the mean infiltration shows, that apart from the Alpine stalagmites MB-3 and SPA-12 having a rather constant infiltration, the infiltration has a maximum during the winter months (October-March). The Mediterranean speleothems CC-26, CL-26, CR-1, GAR-01 and also SO-1 have clear deficiency of water during the summer months (April-September). Stalagmite GP-2, from Morocco, has negative infiltration all year long. The Central European and Northern European speleothems BU-4, C09-2, FM-3 and K-1 have a positive infiltration during the winter months and a negative water budget of the soil zone during the summer period. The speleothems CC-3 and SU-96-7 from Ireland and Scotland, which grew close to the coast line, have a positive infiltration for almost all months but with a clear peak during the winter months.

12.2 Selection of European speleothems for PCA

To analyses speleothem proxy time series, in which the speleothem proxies used within this framework are $\delta^{18}\text{O}$ and $\delta^{13}\text{C}$, certain criteria must be fulfilled (Sec. 10.7). Furthermore, it must be ensured that a region is not overweighted in the way that the speleothem density is different for specific regions. In the graphical illustration of the location of the pre-selected speleothems (Fig. 12.2) it is visible that the Alps and the region of the Northern European speleothems are overweighted regions in comparison to the areal coverage of the other speleothems. Under consideration of the other selection criteria stalagmite CL-26 and SV-1 drop out of the pre-selected speleothem proxy time series, because the temporal resolution of the proxy records is greater than 30 years for most of the time. Although this means a loss of temporal information stalagmite MB-3 is not used, because it would

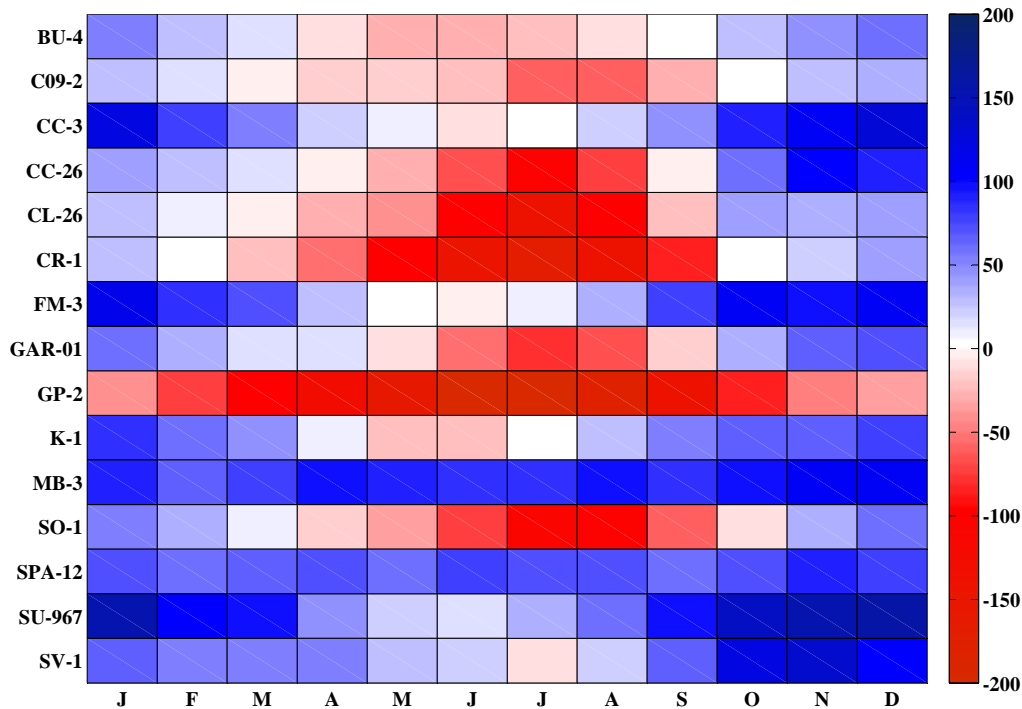


Fig. 12.4: The figure illustrates the monthly mean infiltration of water at the specific cave locations in the period between 1901 and 2009 based on the CRU-TS3.1 dataset. A positive infiltration is indicated by blue values, whereas a negative infiltration is indicated by red values (see text for details).

overweight the Alps. Furthermore, the Mediterranean stalagmites CR-1 and GP-2 are not used. This is due to the reason that the $\delta^{18}\text{O}$ signal on the one hand is modified by Mediterranean Sea and is not only determined by isotopic composition of the Atlantic and precipitation and evapo-transpiration processes, respectively. Although the precipitation above Sofular Cave, and consequently the drip water of stalagmite SO-1, origins mainly from the Black Sea (Fleitmann et al., 2009), the $\delta^{18}\text{O}$ and $\delta^{13}\text{C}$ records of SO-1 are used to test whether the climate in the region around SO-1 has simultaneous variations with the West-, Northern- and Central European climate. This is motivated by the fact that the oxygen isotopic composition is an end member of the $\delta^{18}\text{O}$ gradients of European speleothem $\delta^{18}\text{O}$ values derived by McDermott et al. (2011) for speleothems from West- and Central Europe. From the pre-selected 15 speleothems, nine are used to investigate for a spatio-temporal coherency between their $\delta^{18}\text{O}$ and $\delta^{13}\text{C}$ time series; the stalagmites are BU-4, C09-2, CC-26, CC-3, FM-3, GAR-01, K-1, SO-1 and SPA-12 (Tab. 12.1). The area

which they cover ranges from 41.41 to 71 °N and from -9.5 to 31.92 °E determined by the stalagmites SO-1 and FM-3 and CC-3 and SO-1, respectively. Since the not all speleothems selected for PCA grew continuously during the Holocene, i.e., the last 10,000 years, is subdivided into smaller periods. The first period includes the last 4,000 years and covers the late- and late mid-Holocene and the speleothems BU-4, C09-2, CC-3, GAR-01, K-1, SO-1 and SPA-12 are used for PCA. Stalagmite CC-26 and FM-3 are not used because this would cause that the proxy records from the Alps and from Northern Europe are over-presented in the compilation of speleothem $\delta^{18}\text{O}$ and $\delta^{13}\text{C}$ records. The limits of this time interval are determined by the growing period of stalagmite K-1 and SPA-12 which have started growing at c. 3.6 and 4.8 ka BP. The second periods covers the early mid-Holocene ranging from 7,000 to 4,000 years BP and includes the speleothems BU-4, CC-26, CC-3, FM-3, GAR-01 and SO-1. The stalagmites K-1 and SPA-12 can not be used for this period of time because they were not growing at this time (Fig. 12.3). The limits of the time interval is on the one hand determined by the boundaries of the first time interval and by the temporal coverage of FM-3, which starts growing at c. 7.5 ka BP. Furthermore, stalagmite SO-1 might be influenced by the change of the water isotopy of the Black Sea until 7,000 years BP indicated by $\delta^{18}\text{O}$ values origin from foraminifera (Fleitmann et al., 2009). The third and last period investigates the time between 10,000 and 7,000 years BP and includes stalagmites CC-26, CC-3, GAR-01 and SO-1.

13

Investigating spatio-temporal coherent changes for the last 8,000 years - PART I: Long-term analysis

The Holocene can be divided into different stages: the early-Holocene ($> 6,000$ years), the mid-Holocene (c. 6,000-3,000 years) and the late-Holocene ($< 3,000$ years). Palaeo climate proxies can be compared to get a comprehensive picture on past climate changes during the Holocene (e.g. [Wanner et al., 2008](#)). Since the last decade global and regional temperature reconstructions, derived from temperature sensitive proxies, are in the focus of palaeo climate research ([Mann et al., 2008](#); [Ahmed et al., 2013](#)). However, the reconstructions the reconstructions mainly base on tree rings and therefore are biased for summer temperatures rather than winter- and annual temperatures ([Mann et al., 2008](#); [Ahmed et al., 2013](#)). Alternative studies use a multiproxy approach to derive palaeo climate temperatures ([Christiansen and Charpentier Ljungqvist, 2012](#); [Marcott et al., 2013](#)). However, most of the studies are limited to the last 2,000 years ([Mann et al., 2008](#); [Christiansen and Charpentier Ljungqvist, 2012](#); [Ahmed et al., 2013](#)). Only [Marcott et al. \(2013\)](#) present temperature reconstructions that cover the entire Holocene until 11,300 years. In this study the focus is on European speleothem $\delta^{18}\text{O}$ and $\delta^{13}\text{C}$ time series. The time series covering the complete Holocene period allowing to compare the PCA results with the temperature reconstructions. Although published Holocene speleothem data are available from various places in Europe (Fig. C.1) only a few can be used for PCA (Fig. 12.2). The number of speleothem time series covering the Holocene has its peak at c. 3.0 ka BP and decreases progressively towards the early Holocene ending with 3 records at 12 ka BP (Fig. C.2). This is also illustrated in Fig. 12.3 picturing the temporal resolution of the usable speleothem time series. Within this chapter PCA shall be conducted for the last 8,000 years focused on long-term spatio-temporal coherency. In the subsequent Chapter 14, PCA shall be applied, to investigate for the long-term and short-term spatio-temporal coherency for the last 4,000

years. In the Chapter 15, the short-term spatio-temporal coherency is analysed for the time interval between 4,000 and 7,000 years BP completing the short-term analysis for the last 4,000 years. Finally the time between for last 10,000 years shall be investigated with PCA (Chapter 16).

run #	time window (ka BP)	TEV ($\delta^{18}\text{O}$) (%)	TEV ($\delta^{13}\text{C}$) (%)	Fork-tool $\delta^{18}\text{O}$ and $\delta^{13}\text{C}$
1	0.01-7.8	29.9 ± 1.4	43.1 ± 1.3	Fig. E.1 & E.6
2	0.75-7.8	30.5 ± 0.9	34.2 ± 1.0	Fig. E.2 & E.6
3	0.75-7.3	25.1 ± 1.0	30.9 ± 1.2	Fig. E.4 & E.9

Tab. 13.1: The table lists the results for the mean total explained variance and the related 1-sigma error of the 1st PC for run #1, #2 and #3 that are based on different compilations of speleothem $\delta^{18}\text{O}$ and $\delta^{13}\text{C}$ time series. In addition the related figure is linked for the results of the application of the Fork-tool on the distribution of r_s values. The results base on a total of 1,000 MC simulations.

For the long-term 8,000 years (8k) analysis three compilations of speleothem $\delta^{18}\text{O}$ and $\delta^{13}\text{C}$ time series are used. For run #1 the time series of speleothem BU-4, CC-3, GAR-01 and SO-1 are included; for run #2 the time series of speleothem CC-26 is added and finally the time series of speleothem FM-3 is used in addition to the other five speleothem time series. Although stalagmite FM-3 has some growth phases at which the temporal resolution is slightly higher than 30 years, the derived results are still of high value, allowing for comparison with the results of run #1 and #2 (Fig D.1). The age-models for the six speleothems are illustrated in Fig. 13.1. For each compilation a total of 1,000 MC simulations is performed. The presented results of the 1st PC representing the mean value of the related ensemble.

The distribution of the eigenvalues for run #1 and #2 shows that only the 1st PC is significant. Only the distribution for the 1st PC of run #1 of the $\delta^{18}\text{O}$ time series is partly covering the 95 % confidence interval for the WN time series (Fig D.1). For run #3 the 1st PC is significant for both the $\delta^{18}\text{O}$ and the $\delta^{13}\text{C}$ time series (Fig D.2). For run #2 and #3 the 2nd PC for the $\delta^{13}\text{C}$ time series is also significant in terms of Preisendorfer's Rule N. All other PCs with higher order than 2 are not significant. The application of the Fork tool on the distribution of r_s values is supporting this conclusion (Fig. E.1, E.2, E.3, E.4, E.5 for the $\delta^{18}\text{O}$ time series and Fig. E.6, E.7, E.8, E.9, E.10 for the $\delta^{13}\text{C}$ time series). However, it reveals that stalagmite BU-4's $\delta^{18}\text{O}$ time series does not correlate with the 1st PC time series for run #2 and #3, at least for long-term correlations. In general the 1st PC time series derived from the compilations of $\delta^{13}\text{C}$ time series explains more common variations than the 1st PC time series computed from the compilation of $\delta^{18}\text{O}$ time series (Tab. 13.1). One reason for this observation can be, that the variability of the $\delta^{18}\text{O}$ time series is greater compared to the speleothem $\delta^{13}\text{C}$ time series on a longer time scale. In addition, the long-term coherence of the speleothem $\delta^{13}\text{C}$ time series can be greater than the long-term

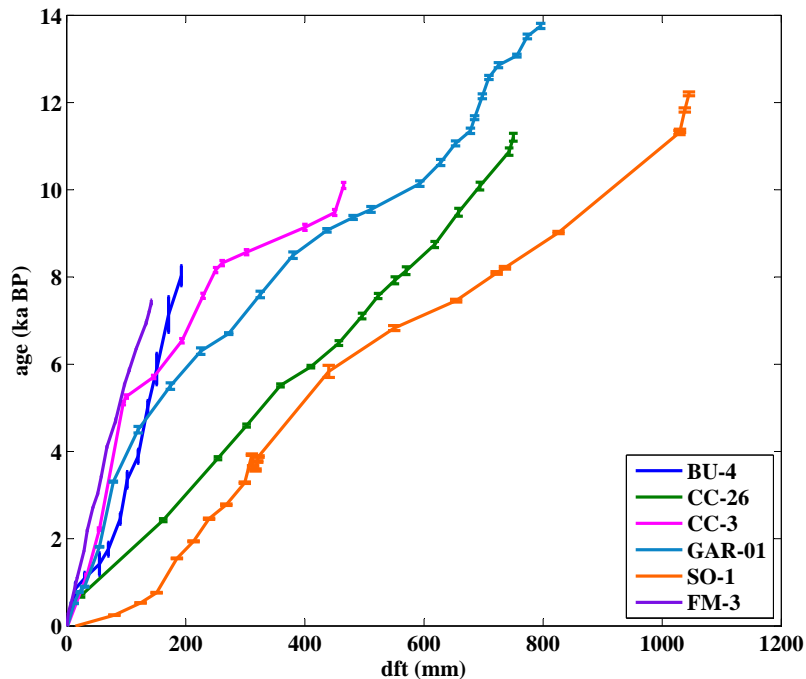


Fig. 13.1: The figure is illustrating the age-models of the speleothems used for the long-term PCA for the last 8000 years.

coherence of the $\delta^{18}\text{O}$ time series. The variability of spatio-temporal coherency on smaller time scales shall be investigated in subsequent chapters. In the following the long-term variability of the derived 1st PC is investigated. In the following, it is only focused on the 1st PC, which is significant according to the significance criteria.

The overall comparison of the derived mean 1st PC time series (straight line) and the related 1-sigma error (shading area) for all three compilations of $\delta^{18}\text{O}$ and $\delta^{13}\text{C}$ time series show that all three 1st PC time series are similar capture common features (Fig. 13.2 and 13.3). This is even more visible for the $\delta^{13}\text{C}$ time series. For run #1 the results are coloured in bright blue and green, respectively. Run #2 and #3 have different colour gradation with the darkest blue and green for run #3.

The detailed comparison of the 1st PC time series for the compilations of $\delta^{18}\text{O}$ time series illustrate that between 0.0 and 4.0 ka BP the derived 1st PC time series have a similar long- and short-term variability. In this period a major minimum is located at c. 500 years BP. A global maximum is located at c. 1.8 ka BP. High values of the 1st PC time series are also common between 3.0 and 4.0 ka BP. Between the 2.0 and 3.0 ka a minimum is centred at c. 2.3 ka BP. In the time between 4.0 and 8.0 ka BP the derived 1st PC time series clearly picture that they share the variability on longer time scales. However there are differences on shorter time scales. For example, this is visible for the maxima between 5.0 and 5.2 ka

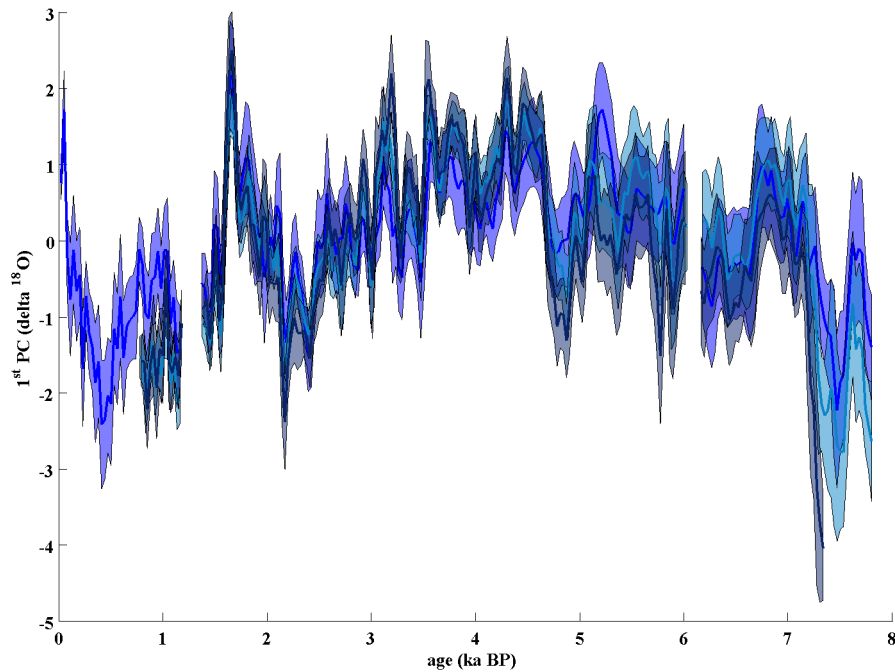


Fig. 13.2: The figure shows the three 1st PC time series (straight line) and the related 1-sigma standard deviation (shading area) based on three different compilations of $\delta^{18}\text{O}$ time series. The results base on 1,000 MC simulations. The first compilations (run #1) includes the $\delta^{18}\text{O}$ time series of BU-4, CC-3, GAR-01 and SO-1. The mean 1st PC time series is illustrated in blue. The shading area indicates the 1-sigma standard deviation of the mean value. Run #2 is indicated by cyan blue, whereas run #3 by grey blue.

BP that are located at different times for all three 1st PC time series. This can be a result of the increasing age uncertainty with time for the measured speleothem age. However, the comparison clearly indicates that for the three compilation of $\delta^{18}\text{O}$ time series the derived 1st PC time series are similar in their variability.

The comparison of the 1st PC time series (straight line) and their related 1-sigma standard deviation for the three different compilations of $\delta^{13}\text{C}$ time series clearly show, that they have a similar long- and short term variability during the last 8,000 years (Fig. 13.3). For run #1 the values are illustrated in bright green; run #2 is illustrated in green and run #3 in dark green. The 1st PC time series show high values between 0.0 and 3.0 ka BP and 6.0 and 8.0 ka BP. Between these two periods, the 1st PC time series depict low values. Apart from these low frequency variations there are superposed variations of higher frequency. There are local minima centred at c. 7.6, 5.5, 4.5, 3.3, 2.2, 1.8 and 0.8 ka BP. Clear maxima

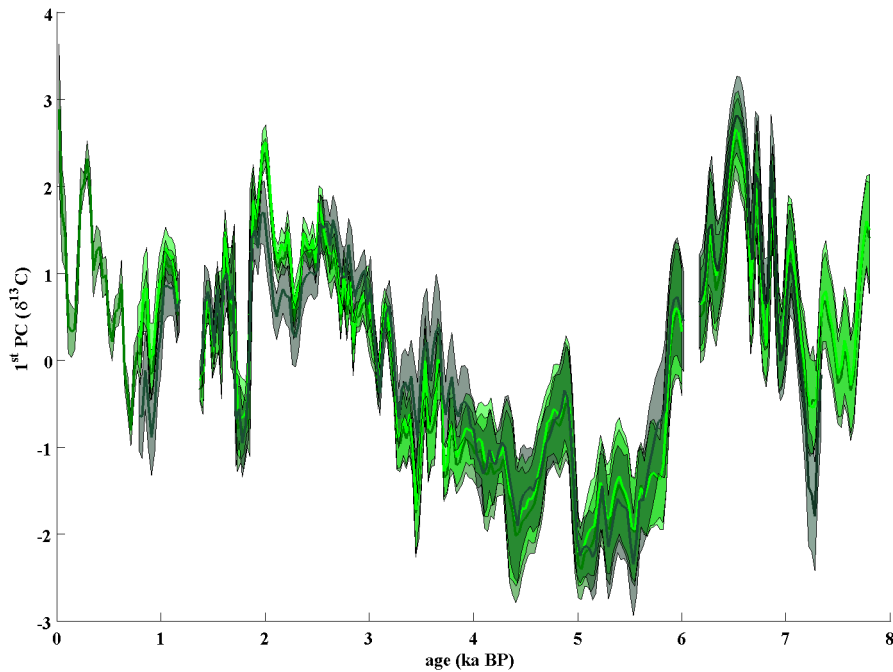


Fig. 13.3: The figure illustrates three different mean 1st PC time series (straight line) and the related 1-sigma standard deviation (shading area) from the ensemble of 1st PC time series derived a total of 1,000 MC simulations for three different compilations of $\delta^{13}\text{C}$ time series, respectively. Run #1, including the $\delta^{13}\text{C}$ time series speleothem BU-4, CC-3, GAR-01 and SO-1, is illustrated in bright green; run #2, is completed with stalagmite CC-26, is indicated by green and run #3, that included stalagmite FM-3 in addition, is pictured in dark green.

are visible at c. 6.5, 4.8 and 2.0 ka BP.

The spacial-temporal coherency pattern, i.e., the mean r_s value of the ensemble of r_s values between the speleothem $\delta^{18}\text{O}$ and $\delta^{13}\text{C}$ time series and the 1st PC time series, for run #1, #2 and #3 are pictured in Fig. 13.4. On the left side the compilations $\delta^{18}\text{O}$ time series are illustrated; the compilations of $\delta^{13}\text{C}$ time series are depicted on the right side. The red "plus" sign for all spacial-temporal coherency pattern indicates that the 1st PC time series in Fig. 13.2 and 13.3 are not illustrated up-side-down due to the up-side-down effect (Chapter 10). For the compilation of $\delta^{18}\text{O}$ ($\delta^{13}\text{C}$) time series, the shading area of the spatio-temporal coherency pattern is illustrated in red (green) and blue (orange) for positive and negative r_s values, respectively. The highest and smallest values for r_s is +1 and -1, respectively.

For the $\delta^{18}\text{O}$ time series Fig. 13.4 shows that the speleothems from Southern Europe (CC-26,

GAR-01 and SO-1) have a positive correlation with the 1st PC time series (Fig. 13.2) for run #2 and #3. For run #1 GAR-01 has a negative correlation with the 1st PC time series whereas the mean correlation for SO-1 is also positive. The Central European stalagmite BU-4 and the Irish speleothem CC-3 have a negative correlation with the 1st PC time series for run #1. For run #2 and #3 the mean correlation of stalagmite CC-3's $\delta^{18}\text{O}$ time series with the 1st PC time series is negative whereas the mean correlation is 0 for stalagmite BU-4. The mean correlation of FM-3's $\delta^{18}\text{O}$ time series with the 1st PC time series is negative for run #3. The change of the mean correlation for BU-4 and GAR-01 for different runs is possibly caused by the different length of the investigated time windows for run #1, #2 and #3. The reason for this is that spatio-temporal coherence pattern of higher order could be covered within the results for the long-term investigations. To uncover these spatio-temporal coherence pattern further investigations on a shorter time scale are conducted in Chapter 14 and 15 for the last 7,000 years. The overall comparison of the spatio-temporal coherence pattern for the long-term investigations for $\delta^{18}\text{O}$ time series, i.e., the entire last 8,000 years, is picturing a dipole with a positive correlation for the southern speleothems and a negative correlation for the northern speleothems with the 1st PC time series pictured in Fig. 13.2.

The spatio-temporal coherence pattern of run #1 for the $\delta^{13}\text{C}$ time series shows positive mean correlations for all four speleothems. Including stalagmite CC-26's and FM-3's $\delta^{13}\text{C}$ time series does not change the 1st PC time series (Fig. 13.3). However, the spatio-temporal coherence pattern for run #2 and #3 reveal that the mean correlation between the $\delta^{13}\text{C}$ time series and 1st PC time series is c. 0.

This could be resulting out of the absence of common variations between these two speleothem $\delta^{13}\text{C}$ time series and the other $\delta^{13}\text{C}$ time series. However, the results reveal that on longer time scales, the speleothem $\delta^{13}\text{C}$ time series of Western Europe, Central Europe and Eastern Europe have similar variations whereas stalagmite CC-26 (Southern Europe) and FM-3 (Northern Europe) have no correlation to the derived 1st PC time series that is illustrated in Fig. 13.3.

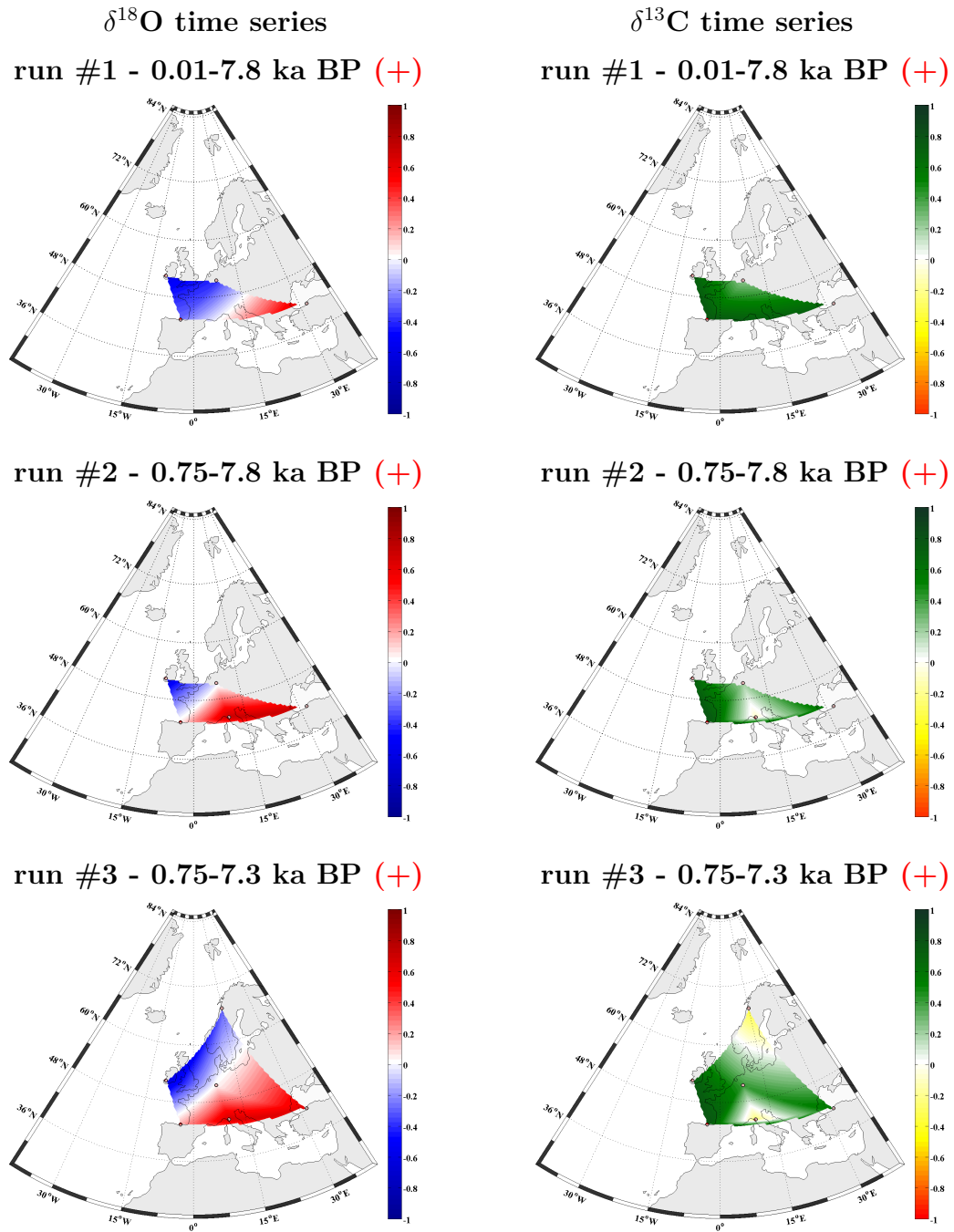


Fig. 13.4: The figure illustrates the spatio-temporal coherency pattern of the 1st PC time series for three different compilations of $\delta^{18}\text{O}$ (right column) and $\delta^{13}\text{C}$ (left column) time series. For this the mean r_s values between the 1st PC time series and the speleothem proxy time series are illustrated.



14

Investigating spatio-temporal coherent changes for the last 4,000 years

To investigate for spatio-temporal coherent changes of speleothem $\delta^{18}\text{O}$ and $\delta^{13}\text{C}$ time series during the last 4000 years, this chapter is divided in two sections: Sec. 14.1 investigates for the long-term spatio-temporal coherency whereas Sec. 14.2 investigates for the short-term coherency. Fig. 12.3 illustrates, that for this period the $\delta^{18}\text{O}$ and $\delta^{13}\text{C}$ time series of stalagmites BU-4, C09-2, CC-3, CC-26, GAR-01, K-1, SO-1 and SPA-12 have a temporal resolution that is smaller than 30 years for the continuous time interval; from this pre-selection all stalagmites, except stalagmite CC-26, grew until 1900 CE. Furthermore, only stalagmite GAR-01 has a hiatus between c. 1.15 and 1.36 ka BP. As illustrated by Fig. 12.2, the used speleothems are distributed equally over Europe. Fig. 12.2 pictures that the pre-selection of stalagmites does not cover the Mediterranean region and Eastern Europe perfectly. However, apart from this regions, the pre-selection covers a wide area of Europe that ranges from Western Europe to Northern Turkey.

14.1 Long-term spatio-temporal coherent changes for the last 4,000 years

The first PCA which is performed, investigates the long-term correlation between the $\delta^{18}\text{O}$ and $\delta^{13}\text{C}$ time series of used stalagmites. Fig. 14.1 illustrates the age models of the pre-selection stalagmites, showing the ages and the related 1-sigma age uncertainty of each stalagmite. The age model of each stalagmite bases on a linear interpolation between the stalagmite's mean ages.

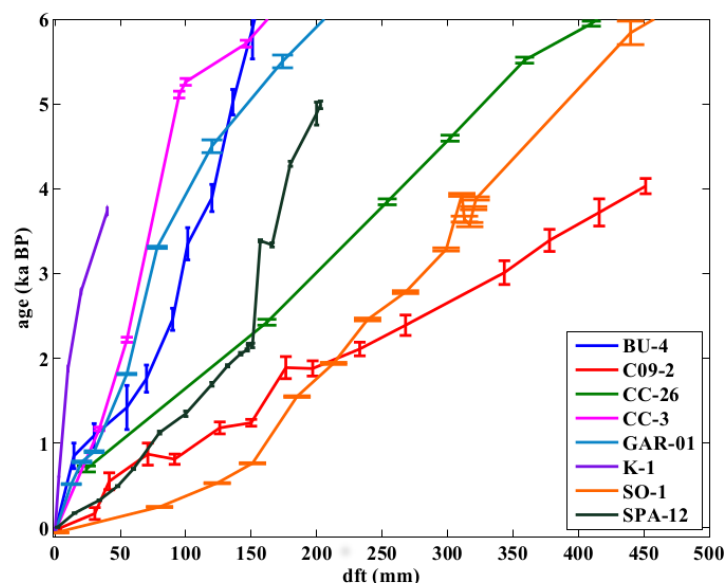


Fig. 14.1: The figure illustrates the age-models of the speleothems used for the long-term PCA for the last 4000 years.

During the last 4000 years the stalagmites have a rather constant growth rate (Fig. 14.1). Only stalagmite SPA-12 show a prominent change in its growth rate at c. 2.1 ka BP, with a higher growth rate for the younger parts of the stalagmite ranging from 0-151 mm (dft). Another feature pictured by Fig. 14.1 is the age uncertainty of stalagmite BU-4 and C09-2, which is greater compared to that of the other stalagmites. This is on one hand due to the reason that the concentration of measured radio-nucleus differs from stalagmite to stalagmite, e.g., SPA-12 and BU-4, and on the other hand different mass spectrometry techniques (TIMS and ICP-MS) are applied to age the stalagmite carbonate samples, which are taken along the growth axis.

For the PCA, 1,000 MC runs are performed (see Chapter 10 for details about the PCA). The time window for the 7 speleothem selection (BU-4, C09-2, CC-3, GAR-01, K-11, SO-1, SPA-12) covers the period from 0.33 until 3.6 ka BP, whereas the 8 speleothem selection (7 speleothem selection + CC-26) starts at 0.75 ka BP and ends at 3.6 ka BP. The beginning of the time interval, i.e., 3.6 ka BP, is determined by the start of growth of stalagmite K-1 (Fig. 14.1). Fig. F.1 shows a comparison of derived eigenvalues for artificial WN time series for 7 (red) and 8 (orange) speleothem and the mean eigenvalues for the $\delta^{18}\text{O}$ (blue) and $\delta^{13}\text{C}$ (green) time series of the compilations of 7 (dark) and 8 (light) speleothems. Fig. F.1 shows that the eigenvalues for the 1st PC of the $\delta^{13}\text{C}$ time series for the 7 speleothems compilation and for the $\delta^{18}\text{O}$ and $\delta^{13}\text{C}$ time series for the 8 speleothem compilation are significant. This is indicated by the comparison of the computed mean eigenvalues for each PCs and the 95 % level of the eigenvalues for the compilation of artificial WN time series. The eigenvalues of the 1st PC of the $\delta^{18}\text{O}$ time series for the 7 speleothem selection are not

significant in term of the difference between the mean eigenvalue and the related 1-sigma error of the 1st PC and the 95% confidence interval for the eigenvalues of the artificial WN time series (see Chapter 10 for details about the evaluation PCA results). For the 2nd PC and PCs of higher order only the 2nd PC of the $\delta^{13}\text{C}$ time series of the 8 speleothem selection is significant (Fig. F.1). For this reason, only the 1st PC is investigated for spatio-temporal changes. The application of the Fork-tool onto the results of the four different ensembles of MC runs reveals, that the 1st PC has a significant correlation to all speleothem $\delta^{18}\text{O}$ and $\delta^{13}\text{C}$ time series, respectively (Chapter G). Only for the 8 speleothem selection, the $\delta^{18}\text{O}$ time series of stalagmite BU-4 has no correlation with the 1st PC.

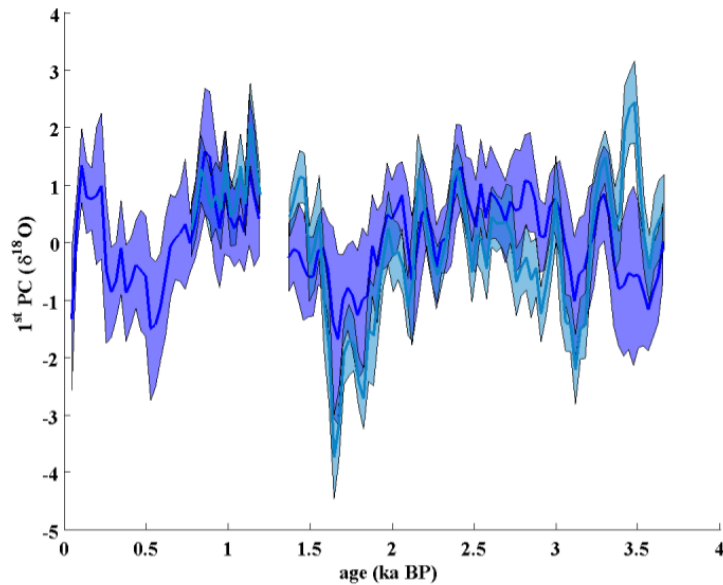


Fig. 14.2: The figure illustrates the 1st PC time series of the long-term PCA for the last 4000 years for two compilations of speleothem $\delta^{18}\text{O}$ time series. The dark line is the 1st PC time series that results from the PCA of the compilation $\delta^{18}\text{O}$ time series of stalagmites BU-4, C09-2, CC-3, GAR-01, K-1, SO-1 and SPA-12. The azure blue line is the 1st PC time series that results from the PCA of the compilation $\delta^{18}\text{O}$ time series of stalagmite BU-4, C09-2, CC-3, CC-26, GAR-01, K-1, SO-1 and SPA-12. The shading area depicts the 1-sigma standard deviation from the mean.

For the two compilations of 7 and 8 speleothem $\delta^{18}\text{O}$ time series the derived 1st PC time series explain $20.8 \pm 0.9\%$ and $23.4 \pm 1.0\%$ of the total variance, respectively and $23.5 \pm 0.9\%$ (7 speleothems) and $24.1 \pm 1.1\%$ (8 speleothems) for the two compilations of speleothem $\delta^{13}\text{C}$ time series. The 1st PC time series derived from the compilation of $\delta^{18}\text{O}$ and $\delta^{13}\text{C}$ time series are visualized in Fig. 14.2 and 14.3, respectively. The straight line is the mean value of the ensemble of computed 1st PC time series, with a resolution of 30 years. The shading area the related 1-sigma error. For the compilations of the $\delta^{18}\text{O}$ time series, the 7 speleothem selection is indicated by the blue color and the 8 speleothem selection by the light-blue

color (Fig. 14.2). Considering the 1st PC time series for the compilations of $\delta^{13}\text{C}$ time series, the 7 speleothem selection is pictures in green, whereas the 8 speleothem selection is illustrated in light-green (Fig. 14.3). The 1st PCs time series that is computed from the compilation of used 8 $\delta^{18}\text{O}$ time series is pictures up-side-down due to the up-side-down effect (see Chapter 10 for details about the up-side-down effect). Fig. 14.2 illustrates that the both 1st PC that are derived from the $\delta^{18}\text{O}$ time series reveal similar variations of the 1st PC with time, although the time that is covered by the individual PCA and the number of used speleothem $\delta^{18}\text{O}$ time series is different. Only at c. 3.5 ka BP, a difference between the two 1st PC time series is visible; the blue curve shows a minimum that is modified by a local maxima whereas the light blue curve has a global maximum hat this time. Both temporal evolutions have minimum at c. 3.1 and 1.7 ka BP and maxima between 3.0 and 2.0 ka BP and 1.1 and 0.7 ka BP. The blue curve has an additional minimum that is centred at c. 0.45 ka BP and starts at c. 0.6 ka BP and lasts for c. 400 years. The minimum is followed by a peak at c. 0.2 ka BP.

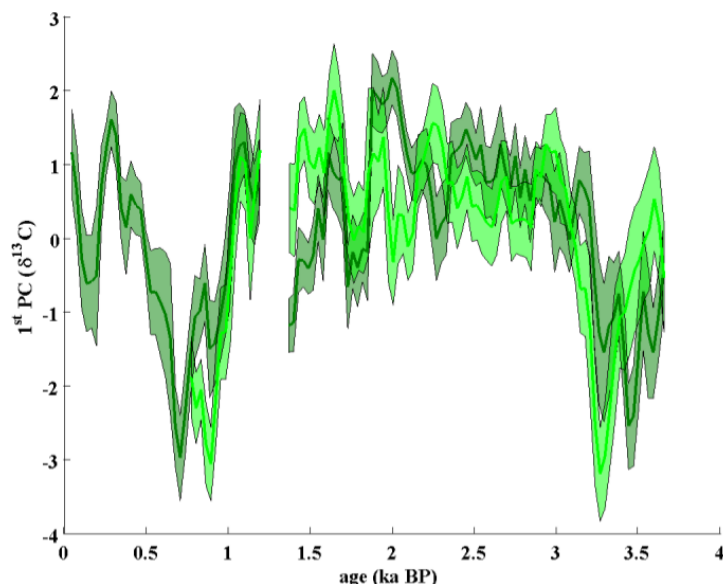


Fig. 14.3: The figure illustrates the 1st PC time series of the long-term PCA for the last 4000 years for two compilations of speleothem $\delta^{13}\text{C}$ time series. The dark line is the 1st PC time series that results from the PCA of the compilation $\delta^{13}\text{C}$ time series of stalagmites BU-4, C09-2, CC-3, GAR-01, K-1, SO-1 and SPA-12. The light green line is the 1st PC time series that results from the PCA of the compilation $\delta^{13}\text{C}$ time series of stalagmite BU-4, C09-2, CC-3, CC-26, GAR-01, K-1, SO-1 and SPA-12. The shading area depicts the 1-sigma standard deviation from the mean.

The 1st PCs time series that are computed from the two compilations of $\delta^{13}\text{C}$ time series show coeval variations (Fig. 14.3). However, between 3.6 and 3.3 ka BP the two curves show a different behaviour. The 1st PC time series for the 7 speleothem selection has a

minimum during this period, while the values of the 1st PC time series for the 8 speleothem selection are decreasing between 3.6 and 3.3 ka BP and reaches a minimum at c. 3.3 ka BP. Despite this time interval the overall evolution of the 1st PCs time series is similar with high values between 3.0 and 1.0 ka BP and a drop of the values at c. 1.0 ka BP. During this period of time the 1st PCs time series have local minima and maxima, with prominent peaks at c. 2.0, 1.75 and c. 1.6 ka BP. It is visible that between 3.0 and 2.0 ka BP the 1st PC time series of the 7 speleothem selection has a higher variability compared to the 8 speleothem selection. Furthermore, the 1st PC of the 7 speleothem selection has a minimum that is centred at c. 0.75 ka BP and it continuous for c. 300 years beginning at c. 0.9 ka BP. After this global minima the 1st PCs time series shows another maxima with a local minima at c. 0.2 ka BP.

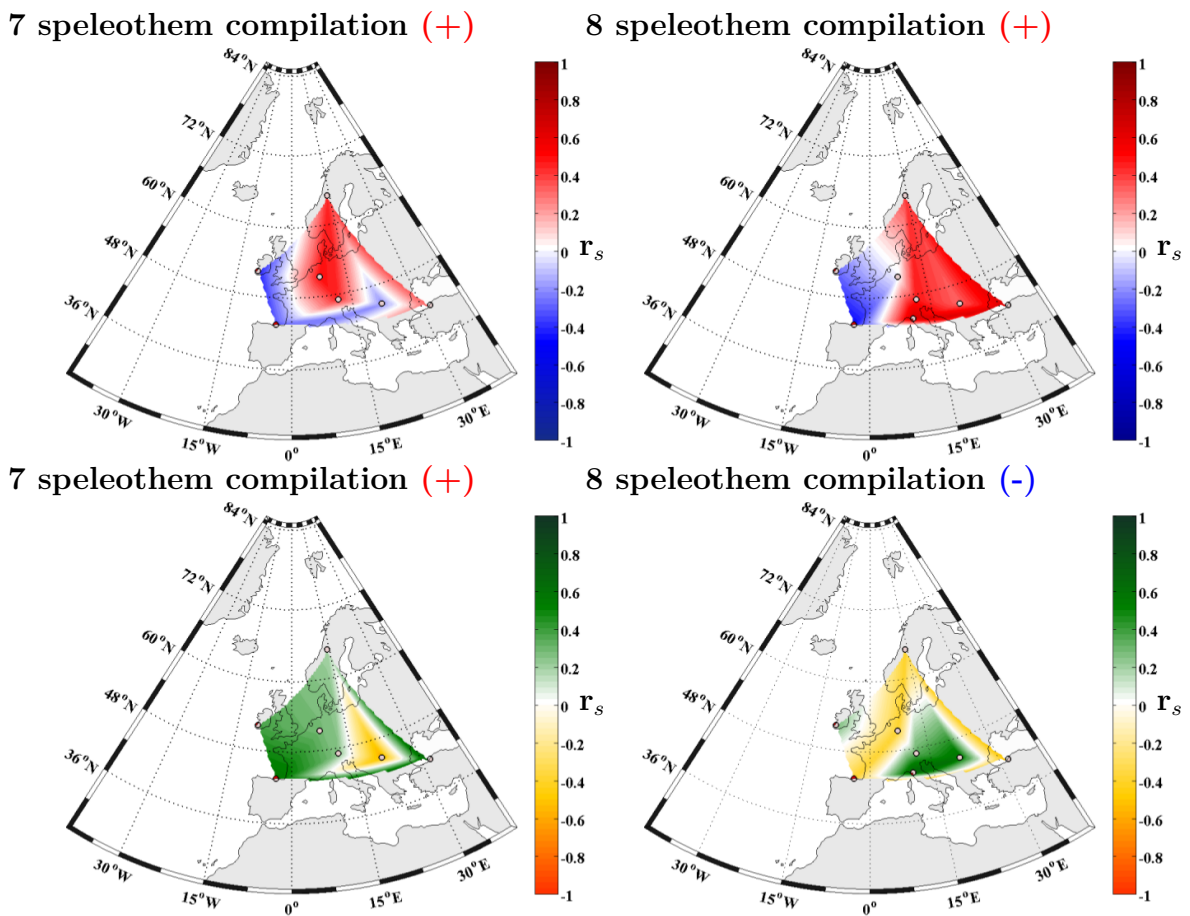


Fig. 14.4: Illustrated are the spatio-temporal coherence pattern expressed by the mean correlation between the 1st PC time series and the speleothem $\delta^{18}\text{O}$ (top panels) and $\delta^{13}\text{C}$ time series (bottom panels). The left panels are the results for the 7 speleothem compilation and the right panels for the 8 speleothem compilation. To compare the spatio-temporal coherence pattern for the compilations of $\delta^{13}\text{C}$ time series, the the r_s values for the 8 speleothem selection (right bottom panel) must be inverted (see text for detail).

The spatio-temporal coherence pattern for the computed 1st PC time series of the compilation of speleothem $\delta^{18}\text{O}$ and $\delta^{13}\text{C}$ time series are illustrated in Fig. 14.4. The Spearman's rank correlation coefficient, r_s is converted into a color scale indicated by the color bar on the left side of each map. If the 1st PC time series are illustrated in Fig. 14.2 and 14.3 not up-side-down, it is indicated by a red "plus" sign in Fig. 14.4. In case the 1st PC time series is pictured up-side-down, it is indicated by a blue "minus" sign in Fig. 14.4; in this case, the illustrated r_s must be inverted. Looking at the upper two panels, the long-term spatio-temporal coherence pattern for the two compilation of $\delta^{18}\text{O}$ time series is depicted. Hereby the 7 speleothem selection is positioned at the left side and the 8 speleothem selection on the right side. Positive values for r_s are indicated by the red shading area, whereas negative values for r_s are highlighted by blue values. The lower two maps show the long-term spatio-temporal coherence pattern for the two compilation of $\delta^{13}\text{C}$ time series. Again, the 7 speleothem selection is positioned on the left side and the 8 speleothem selection on the right side. The colour coding for the $\delta^{13}\text{C}$ time series is that positive values for r_s are illustrated in green and negative values for r_s are highlighted in yellow.

Comparing the two long-term spatio-temporal coherency patterns for the speleothem $\delta^{18}\text{O}$ time series (upper two maps) reveals a negative correlation between the speleothem $\delta^{18}\text{O}$ time series in Western Europe (CC-3, GAR-01) and the computed 1st PC time series (Fig. 14.2). A positive correlation between the $\delta^{18}\text{O}$ time series and the 1st PC time series is observed for speleothems from Central (BU-4, SPA-12), Northern Europe (K-1) and the stalagmite SO-1 from Northern Turkey. The observed East-West dipole of the correlation between the speleothem $\delta^{18}\text{O}$ time series and the 1st PC time persists for both compilation of speleothem $\delta^{18}\text{O}$ time series, although there are local differences. However, long-term correlation changes in Central Europe for the stalagmites BU-4 (Germany) and C09-2 (Romania). While the mean r_s value for stalagmite BU-4 for the 7 speleothem selection is positive (c. 0.5), the mean r_s value is c. 0 for the 8 speleothem selection. In contrast, for stalagmite C09-2 the mean r_s value changes it's sign. The mean r_s values is negative for the 7 speleothem selection and positive for the 8 speleothem selection. Stalagmite CC-26 has a positive mean r_s value indicated by a positive correlation between it's $\delta^{18}\text{O}$ time series and the 1st PC time series of the 8 speleothem selection. For the 8 speleothem selection, the dipole of r_s values between speleothems from Eastern and Western Europe is more pronounced than for the 7 speleothem selection. Furthermore, stalagmite BU-4 lies just in between the two patterns for positive and negative correlation.

The two long-term spatio-temporal coherence patterns between the speleothem $\delta^{13}\text{C}$ time series and the calculated 1st PC time series (Fig. 14.3) reveal that for the 7 speleothem selection all speleothem $\delta^{13}\text{C}$ time series, except that of stalagmite C09-2, have a positive correlation with the 1st PC time series (Fig. 14.3). The $\delta^{13}\text{C}$ time series of stalagmite C09-2 has a negative correlation with the 1st PC time series. For the 8 speleothem selection the speleothems BU-4, GAR-01, K-1 and SO-1 have a negative correlation with 1st PC time series, which is equivalent to the long-term correlation pattern of the 7 speleothem selection, because the 1st PC for the 8 speleothem selection is illustrated up-side-down in Fig. 14.3. Therefore negative values for r_s in map are positive and vice versa. For speleothem CC-3 and SPA-12 the sign of the mean r_s value is changed in comparison to the mean value of r_s

for the 7 speleothem selection. Stalagmite CC-26 has a positive correlation with the 1st PC, i.e., a negative correlation with the 1st that is illustrated in Fig. 14.3.

14.2 Short-term spatio-temporal coherent changes for the last 4,000 years

The mean long-term spatial correlation patterns illustrated in Fig. 14.4 are calculated for the complete coeval length of the proxy time series and are a superposition of different correlation patterns for different periods of time. They are addressed as "long-term". On smaller time scales, i.e., for shorter time window lengths, the spatial correlation patterns can change due to changing boundary conditions, whereas "boundary conditions" summarize all processes that could have changed the $\delta^{18}\text{O}$ and $\delta^{13}\text{C}$ values of speleothem's CaCO_3 . To visualize changing boundary conditions, PCA are performed on smaller time scales. This is conducted by a shifting time window along the speleothems proxy time series with varying starting points and a constant length of 300 years for the 7 speleothem selection. The computed 1st PC time series for the speleothem $\delta^{18}\text{O}$ and $\delta^{13}\text{C}$ time series are then compared with the 1st PC time series, which has been gained for the long-term analysis (Fig. 14.5 and 14.9). For the comparison of the long-term and short-term 1st PC time series, the short-term 1st PC time series are standardised to the mean value and the standard deviation of the long-term 1st PC time series of the corresponding period. The long-term 1st PC time series of the speleothem selection is used as the reference long-term 1st PC time series.

14.2.1 Results for $\delta^{18}\text{O}$ time series

The comparison between the long-term 1st PC time series and short-term 1st PC time series gained from the PCA of the compilation of speleothem $\delta^{18}\text{O}$ time series (7 speleothem selection) is illustrated in Fig. 14.5. The black line illustrates the mean value of the 1st PC for the 7 speleothem selection and dark-grey shading area the related 1-sigma error; the grey line depicts the mean value of the 1st PC of the 8 speleothem selection and the light-grey shading area the 1-sigma error of the mean value (cf. Sec. 14.1). The x-axis intercepts indicate the time windows, which were analysed for spatial and temporal coherent changes by PCA. The 1st PC time series are drawn in red and blue (Fig. 14.5).

The color of the short-term 1st PC time series indicates if the 1st PC time series is pictured up-side-down: if the 1st PC time series is not illustrated up-side-down it is marked by the color red; if it is pictured up-side-down it is highlighted by the color blue. For those 1st PC time series, which are illustrated up-side-down, the color scale in the spatial mean short-term correlation pattern must be inverted (Fig. 14.6, 14.7, 14.8). This is indicated by the red "+" or blue "-" at the top of each map. Although there are small differences between

the short-term and long-term 1st PC time series, especially regarding the amplitude of the time series, e.g., the local maximum during the global minimum, which is located at c. 1.7 ka BP. The overall comparison of the short-term and long-term 1st PC time series reveals that the stacked short-term 1st PC time series pictures the long-term 1st PC time series. This allows for detailed investigation of changes of the spatially and temporal coherent pattern by comparison of the derived pattern for each time window (Fig. 14.6, 14.7, 14.8). Hereby, the patterns are illustrated in chronological ordered in Fig. 14.6, 14.7, 14.8 starting with the first pattern (Fig. 14.6), which is derived for the time window 3.65 to 3.4 ka BP and ending with the last pattern for the time window from 0.35 to 0.05 ka BP (Fig. 14.8). The mean TEV including the 1-sigma error of each conducted time window is given in Tab. 14.1. Furthermore, the mean TEV for the $\delta^{18}\text{O}$ time series is in between 30.5 ± 3.1 and 41.4 ± 4.8 %.

run #	time window (ka BP)	TEV ($\delta^{18}\text{O}$) (%)	TEV ($\delta^{13}\text{C}$) (%)	Forktool $\delta^{18}\text{O}$ and $\delta^{13}\text{C}$
1	3.65-3.4	30.5 ± 3.1	31.8 ± 3.4	Fig. H.1 & H.29
2	3.4-3.1	31.6 ± 4.0	38.1 ± 4.1	Fig. H.3 & H.31
3	3.1-2.8	32.0 ± 3.9	37.6 ± 4.0	Fig. H.5 & H.33
4	2.8-2.5	36.3 ± 5.5	38.3 ± 4.3	Fig. H.7 & H.35
5	2.6-2.3	36.2 ± 4.5	45.9 ± 4.9	Fig. H.9 & H.37
6	2.3-2.0	34.8 ± 4.4	35.0 ± 4.4	Fig. H.11 & H.39
7	2.0-1.7	36.1 ± 4.5	38.3 ± 4.5	Fig. H.13 & H.41
8	1.7-1.4	32.7 ± 3.4	35.1 ± 4.1	Fig. H.15 & H.43
9	1.6-1.15	38.7 ± 4.7	40.3 ± 5.3	Fig. H.17 & H.47
10	1.4-1.1	34.7 ± 4.2	36.2 ± 4.8	Fig. H.19 & H.45
11	1.1-0.8	36.5 ± 4.5	34.3 ± 3.5	Fig. H.21 & H.49
12	0.8-0.5	36.8 ± 3.8	37.7 ± 3.9	Fig. H.23 & H.51
13	0.5-0.2	41.5 ± 4.8	41.5 ± 4.1	Fig. H.25 & H.53
14	0.35-0.05	37.7 ± 3.3	48.2 ± 2.4	Fig. H.27 & H.55

Tab. 14.1: Table of performed short-term PCA and the related total explained variance (TEV) of the 1st PC. In addition the related figure is linked for the results of the application of the Fork-tool on the distribution of r_s values. The results base on a total of 1,000 MC simulations.

In addition, the spatio-temporal coherence pattern that are derived for the collection of $\delta^{18}\text{O}$ time series picture a dipole (Fig. 14.6, 14.7, 14.8), except from run #6, #11 and #12, which show more complex pattern. Run #6 (Fig. 14.6) reveals that stalagmite SPA-12's $\delta^{18}\text{O}$ time series has a negative correlation with the derived 1st PC time series between 2.3 and 2.0 ka BP, whereas all others have a positive correlation. Run #11 (Fig. 14.7), which is the time window between 1.1-0.8 ka BP, shows a similar pattern compared with run #6, but stalagmite C09-2's $\delta^{18}\text{O}$ time series has a positive correlation with the computed 1st

PC time series pictured in Fig. 14.5. All other speleothem $\delta^{18}\text{O}$ time series have a negative correlation. Note that the derived 1st PC time series is illustrated up-side-down in Fig. 14.5. In the period from 0.8 to 0.5 ka BP (Run #11) the speleothem $\delta^{18}\text{O}$ time series in Central Europe and stalagmite SO-1 have a negative correlation with the 1st PC time series for this time (Fig. 14.7). All other speleothem $\delta^{18}\text{O}$ time series have a positive correlation. The pattern of run #11 shows that there is a positive spatial coherence pattern between stalagmite K-1 (Sweden) and C09-2 (Romania). However, this pattern could be also an artefact, which results from the linear interpolation applied. The pattern of run #9 and run #10 (Fig. 14.7) depicts that there is a negative correlation of stalagmite CC-3 (Ireland) and stalagmite SO-1 (Northern Turkey) and a positive correlation for stalagmite GAR-01, BU-4, SPA-12 and K-1, respectively. The sign of the correlation of stalagmite is different for the two runs; it is negative for run #9 and positive for run #10. However, this can be due to the fact that run #9 includes GAR-01's $\delta^{18}\text{O}$ time series, which has a hiatus between 1.1 and 1.3 ka BP.

Investigating the temporal change of the spatio-temporal coherence pattern, the figures (Fig. 14.6-14.8) illustrate that in the period from 3.65 and 2.3 ka BP (Fig. 14.6), 2.0 and 1.4 ka BP (Fig. 14.7) and 0.5 and 0.05 ka BP (Fig. 14.8) a dipole is the predominant coherence pattern, with a positive coherence pattern in Western Europe and a negative coherence pattern in Eastern Europe. The shape of the dipole is changing with time. In the time between 3.65 and 2.8 ka BP (run #1-#3; Fig. 14.6) the zone of zero correlation, which separates the pattern of positive and negative correlation, is located in Eastern Europe. The line then turns clock-wise and lies in Central Europe for the time window from 2.8 and 2.5 ka BP (run #4); in an inter-mediate between 2.6 and 2.3 ka BP state the pattern of positive correlation expands into Eastern Europe (run #5). The pattern is then changing for the next time window (see run #6, 2.3-2.0 ka BP). While the speleothem $\delta^{18}\text{O}$ time series in Western Europe have a strong positive correlation with the 1st PC, the correlations weakens for the speleothem $\delta^{18}\text{O}$ time series in Eastern Europe, i.e., for stalagmite C02-9; in comparison to run #5 the sign of the correlation is changing for stalagmite SPA-12 and SO-1. After this time window, between 2.0 and 1.4 ka BP a dipole, with negative correlation in Eastern Europe and a positive correlation in Western Europe (run #4 and #5; Fig. 14.7); the zone of zero correlation turns clock-wise between the two time windows of 2.0-1.7 and 1.7-1.4 ka BP. Between 1.4 and 1.1 ka BP and 1.6 and 1.15 ka BP, the coherence pattern pictures follow a negative-positive-negative pattern (run #9 and #10). For the next time window, 1.1-0.8 ka BP (run #11), the pattern depict a negative correlation for C09-2's time series and a positive correlation for the others. For the last 800 years run #12, #13 and #14 (Fig. 14.7 and 14.8) illustrate a dipole. The zone of zero correlation turns anti-clock-wise from run #12 to run #13 - note that the 1st PC of run #13 and #14 is plotted up-side-down and that the color code of the related map must be flipped to compare these maps with the color code of the map for run #12.

The overall comparison of the evolution of the spatial coherence pattern between the speleothem $\delta^{18}\text{O}$ time series and the 1st PC for the short-term investigations, illustrated in Fig. 14.6, 14.7 and 14.8, show that a dipole pattern is present for most of the time

windows (run #1, #2, #3, #4, #5, #7, #8, #12, #13, #14). This dipole pattern turns clock-wise and anti-clock wise with time. For run #6, and #11 the dipole like pattern is displaced, showing a synchronous variation of the speleothem $\delta^{18}\text{O}$ time series except for stalagmite SPA-12 for run #6 and stalagmite C09-2 for run #11 whose $\delta^{18}\text{O}$ time series are antiphase with the 1st PC. Run #9 and #10 picture a more complex pattern. The results are discussed in detail in Chapter 17, in particular the physical meaning of the 1st PC and the related coherence pattern.

14.2.2 Results for $\delta^{13}\text{C}$ time series

Like the comparison of the short-term and long-term 1stPC time series for the compilation $\delta^{18}\text{O}$ time series (Fig. 14.5), the comparison for the $\delta^{13}\text{C}$ time series is illustrated in Fig. 14.9. The derived mean long-term 1stPC time series for the 7 speleothem and 8 speleothem selection are shown in black and grey, respectively; the dark grey and light grey shaded area indicate the related 1-sigma standard deviation of the mean long-term 1stPC time series. The mean short-term 1stPC time series and the corresponding 1-sigma error are illustrated in green if the short-term 1stPC time series is pictured not up-side-down; if the short-term 1stPC time series is illustrated up-side-down it is marked by the color yellow (cf Fig. 14.9). The purple coloured 1stPC time series is derived from the selection, not including stalagmite GAR-01, i.e., only the $\delta^{13}\text{C}$ time series of BU-4, CC-3, C09-2, K-11, SO-1 and SPA-12 are included. With this selection of speleothem $\delta^{13}\text{C}$ time series the period between 1.4 and 1.1 ka BP can be investigated. All short-term time series are standardised to the mean value and 1-sigma error of the long-term time series of the 7 speleothem selection in the corresponding time window. The investigated time windows are listed in Tab. 14.1 including the TEV of each run. The related spatial coherence patterns are illustrated in Fig. 14.10, 14.11 and 14.12. The short-term 1stPC time series match the long-term 1stPC time series and all minima and maxima of the long-term 1stPC time series are captured by the stacked short-term 1stPC time series (Fig. 14.9). Hence, the computed spatio-temporal coherence pattern of Fig. 14.10, 14.11 and 14.12 can be used to suspend the super-position of different spatial pattern resulting in the spatio-temporal coherence pattern for the long-term PCA for the two collections of $\delta^{13}\text{C}$ time series (Fig. 14.4).

The resulting spatio-temporal coherence pattern picture the mean r_s value between the $\delta^{13}\text{C}$ time series and the derived 1st PC for each speleothem (Fig. 14.10, 14.11 and 14.12). Positive values are green and negative values are yellow. The mean r_s value is calculated by the average of the significant r_s values ($p < 0.05$) for each speleothem. For 1stPC time series that are shown up-side-down in Fig. 14.9. Consequently, the color code needs to be inverted to be comparable to the other spatial pattern. The spatio-temporal coherence pattern is marked with a blue "-" at the top of each map otherwise with a red "+". In the period between 3.65 and 2 ka BP (Fig. 14.10) the most prominent pattern is dipole like (run #1, #3, #4, #5). Run #2 and #6 picture and alternating sign of the correlation with positive-negative-positive and negative-positive-negative values for r_s , respectively. The

dipole like pattern with a positive for the southern speleothems and negative correlation for speleothems located in Central and Northern Europe, respectively, consist until 1.4 ka BP (run #7 and #8 in Fig. 14.10). In the period from 1.4 to 1.1 ka BP (run #10 and run #9 for completion) the correlation between the speleothem $\delta^{13}\text{C}$ time series with the 1st PC changes its sign compared to the dipole like pattern in run #7 and #8. There is a negative correlation for speleothems in Southern Europe and a positive one for those in Central and Northern Europe. In the time between 1.1 and 0.8 ka BP (run #11) dipole like pattern vanishes and is replaced by a pattern that shows a negative correlation at the location of stalagmite C09-2 (Romania) and positive correlations for all other locations. In the following period (0.8-0.5 ka BP, run #12) the $\delta^{13}\text{C}$ time series of stalagmite BU-4, SPA-12 and C09-2 are uncorrelated with the 1st PC time series; the remaining speleothems $\delta^{13}\text{C}$ time series have a positive correlation with the 1st PC time series. For the second to last time window covering the time between 0.5 and 0.2 ka BP (run #13) a dipole like pattern predominates, with a negative pattern in Southern Europe and the Alps and a positive pattern ranging from Central to Northern Europe and Turkey. The pattern of the last time window covering the period between 0.35 and 0.05 a more complex pattern appears. It shows a negative pattern over Ireland (stalagmite CC-3), the Alps (SPA-12) and Romania (C09-2) and positive pattern elsewhere.

The temporal dynamics of the coherence pattern reveal that a North-South dipole pattern is predominant. The dipole pattern turns clock-wise in the time between 3.4 and 3.1 ka BP (cf. Fig. 14.10, run #1, #3, #4, #5). Between these dipole patterns, an intermediate pattern occurs (3.4-3.1 ka BP). This pattern stands out due to its structure (Fig. 14.10, run #2). The North-South dipole pattern in the time between 3.1 and 2.3 ka BP is stable and not changing. Comparing the pattern of run #2 with that of run #1 gives reason for the assumption that the negative pattern of the dipole moves southwards while the negative pattern of the dipole remains. Furthermore, the negative correlation of K-1's $\delta^{13}\text{C}$ time series changes its sign and becomes positive. Subsequent to run #5 (2.6-2.3 ka BP) another intermediate states appears with an inverted pattern (run #6, 2.3-2.0 ka BP). After this a dipole like pattern is predominant that lasts until 1.4 ka BP (Fig. 14.11, run #7, #8). In contrast to the dipole like pattern between 3.1 and 2.3 ka BP this dipole like pattern pictures a positive r_s values for speleothems in Southern Europe and negative r_s values for those located in Central and Northern Europe. Run #9 covering the time between 1.65 and 1.15 ka BP and is a super position of run #8 and #10. It covers the temporal growth stop of stalagmite GAR-01 between c. 1.2 and 1.35 ka BP. This could be an explanation why the mean r_s value of stalagmite K-1 is c. 0 for run #9, because it is negative for run #8 and positive for run #10. Therefore, run #9 provides some additional information for run #10 at which stalagmite GAR-01 is not included allowing PCA between 1.4 and 1.1. ka BP. This time interval lacks the spatial information for the southern part of Western Europe, but bear resemblance with the pattern of run #9. A dipole like pattern. Neither a dipole like pattern nor an intermediate state pattern is present for the time between 1.1 and 0.5 ka BP. During this period the pattern is distinguished by an over regional pattern of positive r_s values that pictures negative values for stalagmite C09-2 $\delta^{13}\text{C}$ time series between 1.1 and

0.8 ka BP and no correlation for stalagmite BU-4, SPA-12 and C09-2 between 0.8 and 0.5 ka BP. Subsequently the dipole like pattern occurs again in the time between 0.5 and 0.05 ka BP (Fig. 14.12).

The overall comparison of the coherence patterns for the correlation between speleothems $\delta^{13}\text{C}$ time series and the 1st PC time series demonstrates that dipole like patterns are predominant. They can be found for the runs #1, #3, #4, #5, #7, #8, #10 and #13. More complex coherence patterns are present for run #2, #6, #9, #11, #12 and #14. They show an alternating spatial coherence of the $\delta^{13}\text{C}$ time series with respect to the 1st PC time series with positive-negative-positive and negative-positive-negative pattern, respectively orientated from Southern to Northern Europe (run #2, #6 and #9; however run #9 is only completing run #10); run #14 pictures a negative-positive-negative-positive pattern but in contrast to the others, is orientated from Western to Eastern Europe.

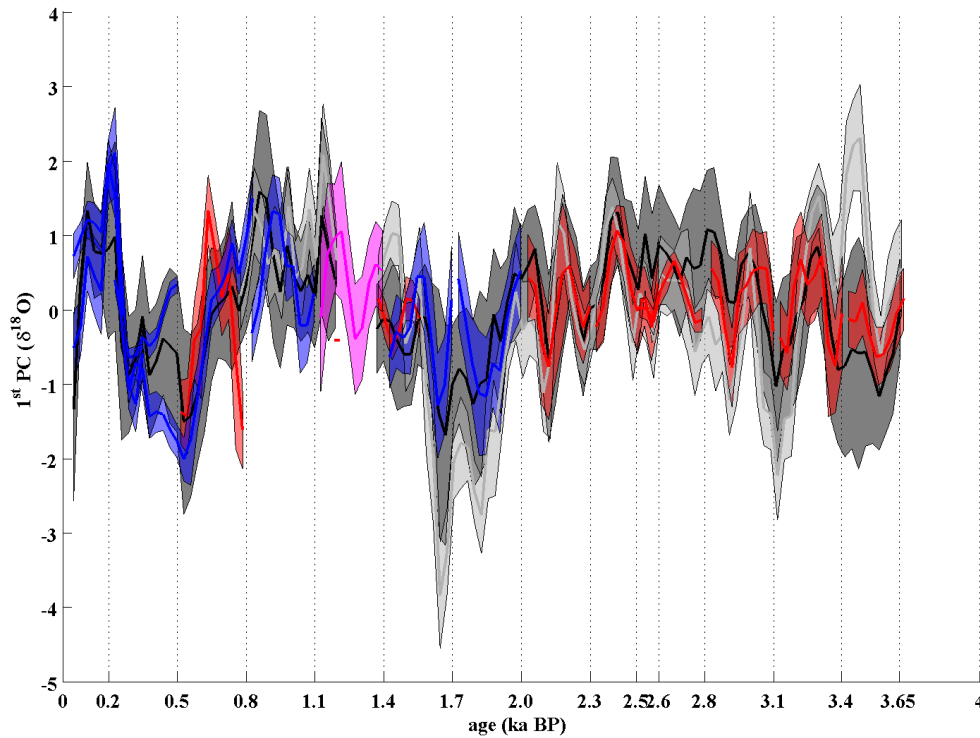


Fig. 14.5: Illustrated are the computed 1st PC time series for the short-term PCA of the compilation of $\delta^{18}\text{O}$ time series for the last 4000 years (blue and red lines). The 1st PC time series are pictured in red if no up-side-down effect was observed in comparison to the long-term 1st PC time series (grey lines) and in blue if an up-side-down effect was observed. The long-term 1st PC time series of the 7 speleothem selection is illustrated in dark grey and in light grey of the 8 speleothem selection. The shading area indicates the 1-sigma standard deviation.

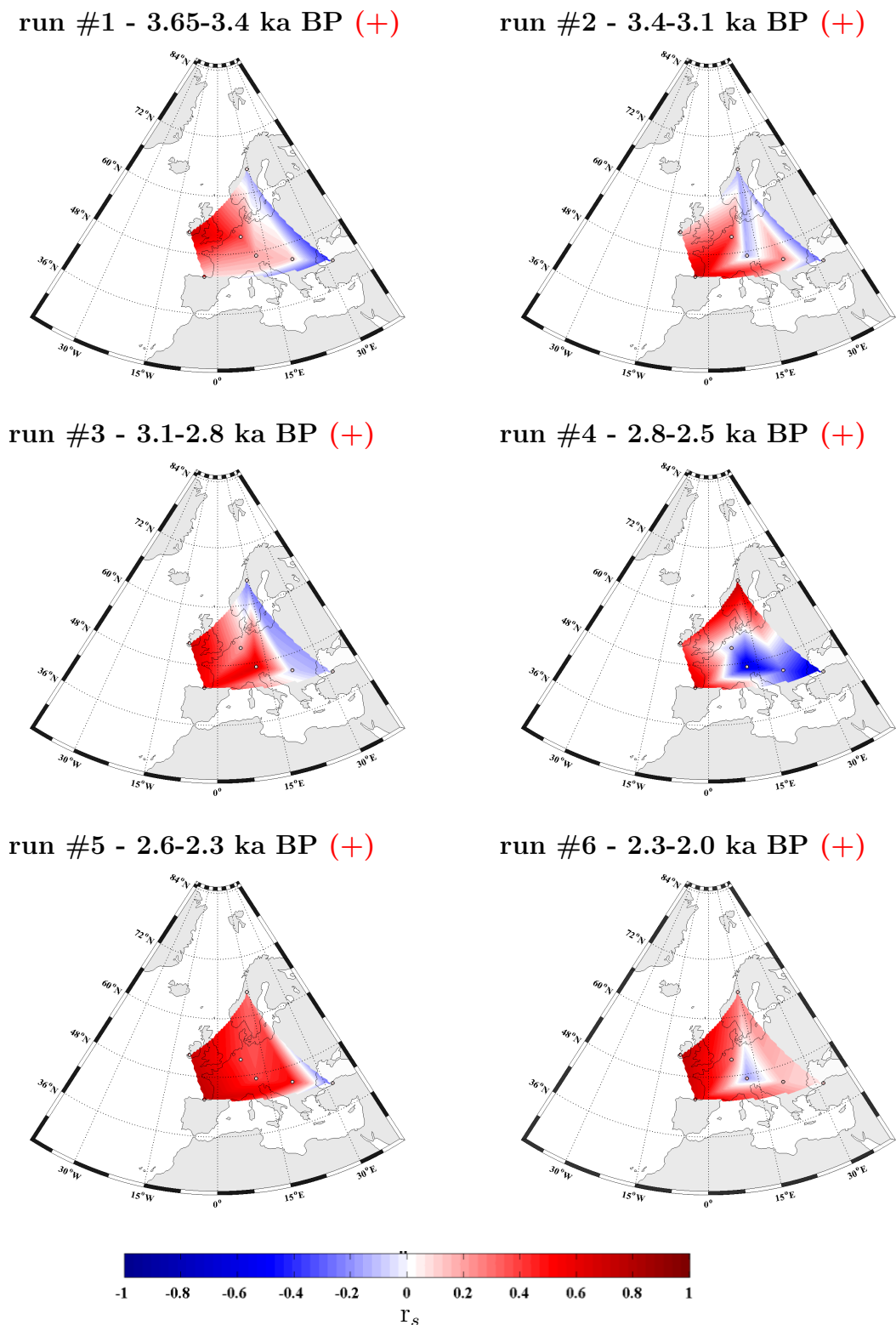
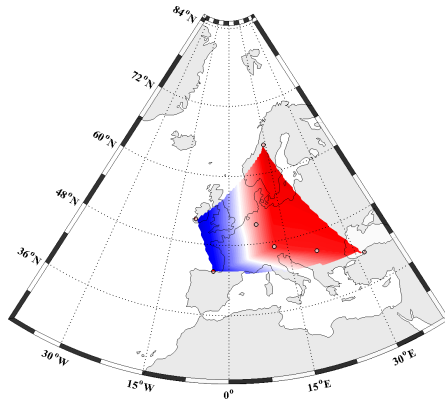
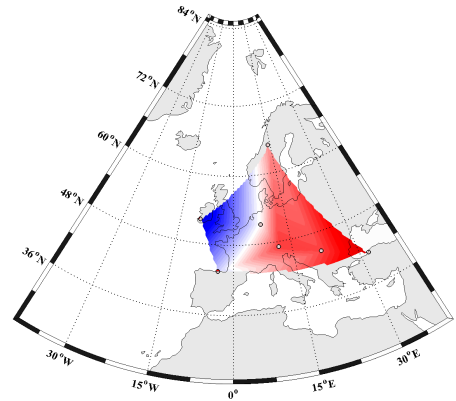


Fig. 14.6: Illustrated is the mean correlation between the short-term 1st PC time series and the speleothem $\delta^{18}\text{O}$ time series for several short-term runs.

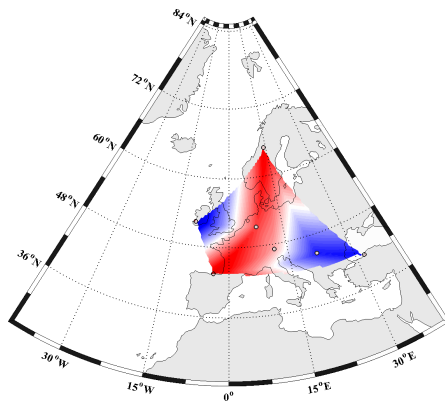
run #7 - 2.0-1.7 ka BP (-)



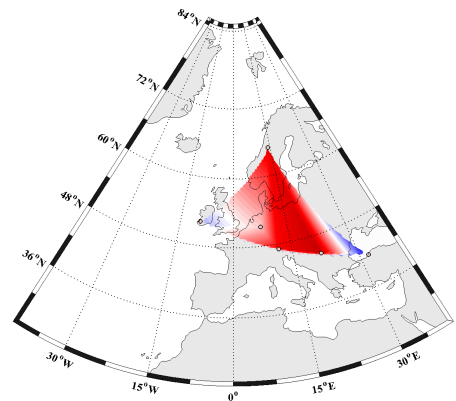
run #8 - 1.7-1.4 ka BP (-)



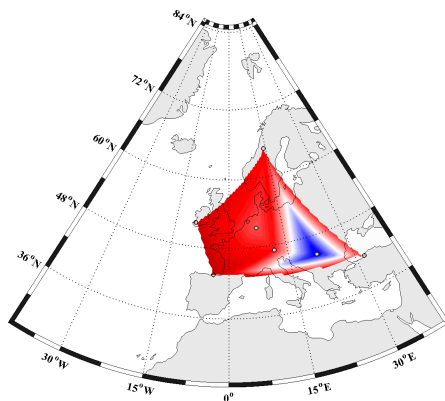
run #9 - 1.6-1.15 ka BP (+)



run #10 - 1.4-1.1 ka BP (+)



run #11 - 1.1-0.8 ka BP (-)



run #12 - 0.8-0.5 ka BP (+)

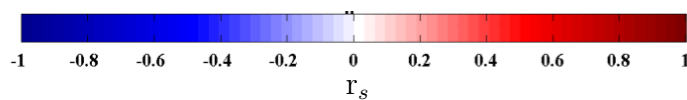
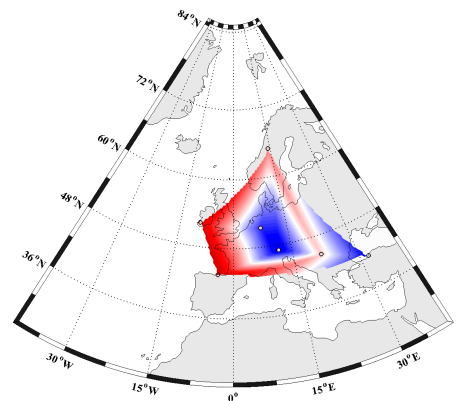


Fig. 14.7: Illustrated is the mean correlation between the short-term 1st PC time series and the speleothem $\delta^{18}\text{O}$ time series for several short-term runs.

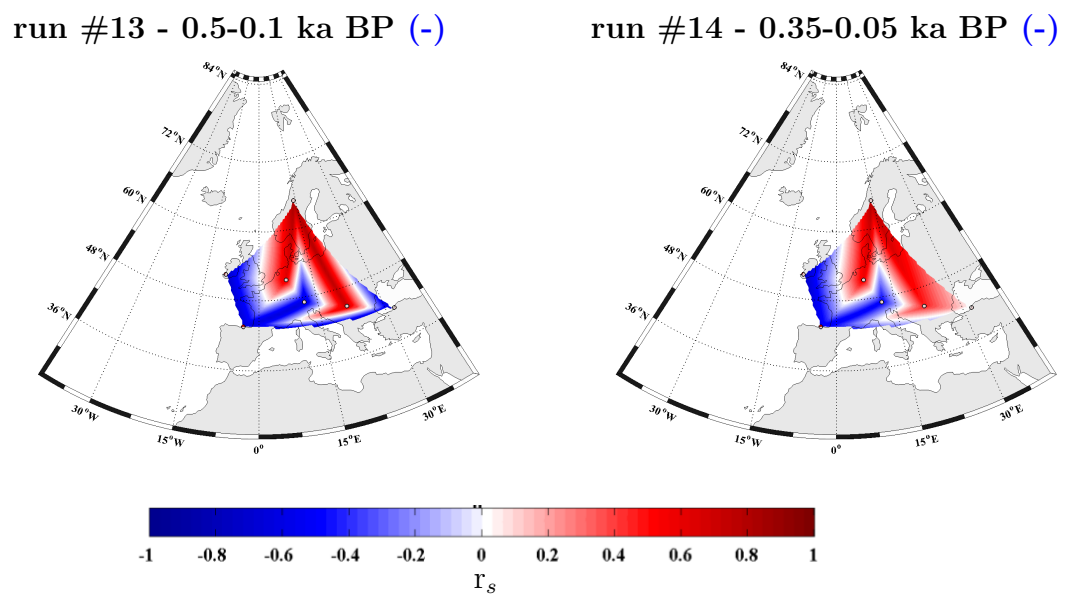


Fig. 14.8: Illustrated is the mean correlation between the short-term 1st PC time series and the speleothem $\delta^{18}\text{O}$ time series for several short-term runs.

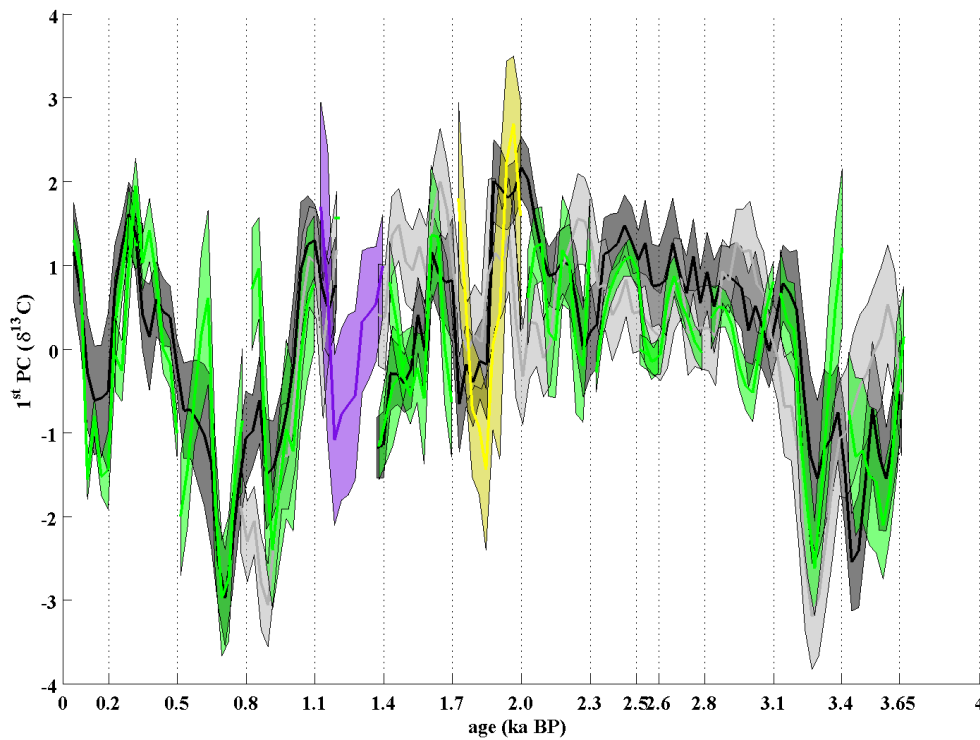


Fig. 14.9: Illustrated are the computed 1^{st} PC time series for the short-term PCA of the compilation of $\delta^{13}\text{C}$ time series for the last 4000 years (green and yellow lines). The 1^{st} PC time series are pictured in green if no up-side-down effect was observed in comparison to the long-term 1^{st} PC time series (grey lines) and in yellow if an up-side-down effect was observed. The long-term 1^{st} PC time series of the 7 speleothem selection is illustrated in dark grey and in light grey of the 8 speleothem selection. The shading area indicates the 1-sigma standard deviation.

14.2. Short-term spatio-temporal coherent changes for the last 4,000 years

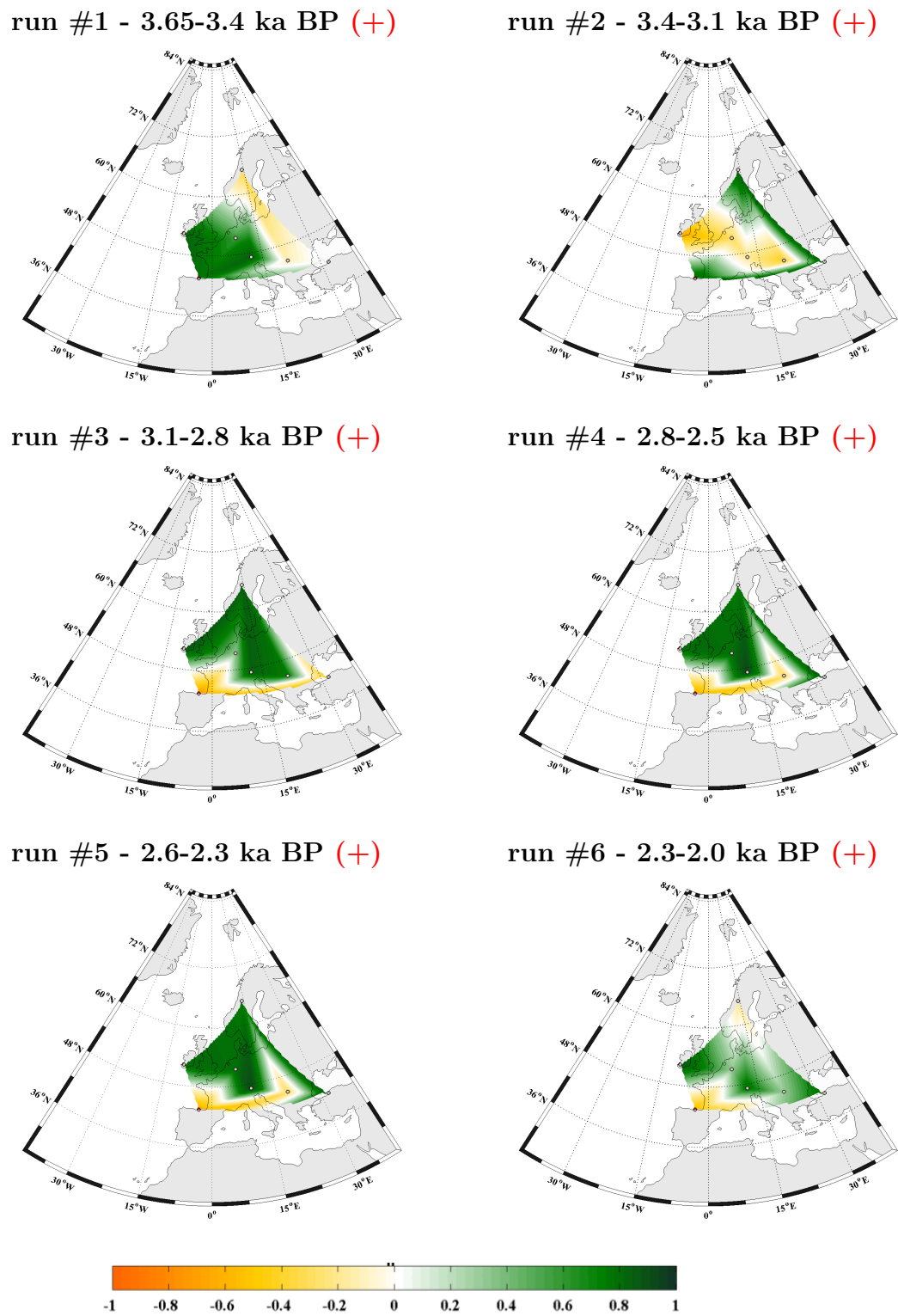
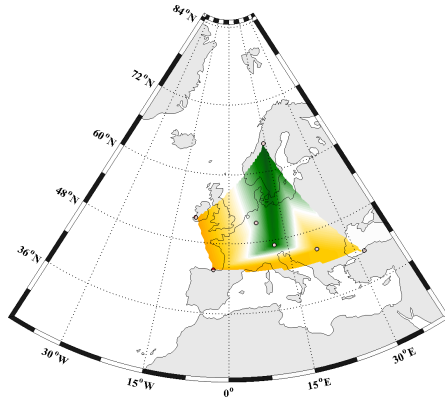


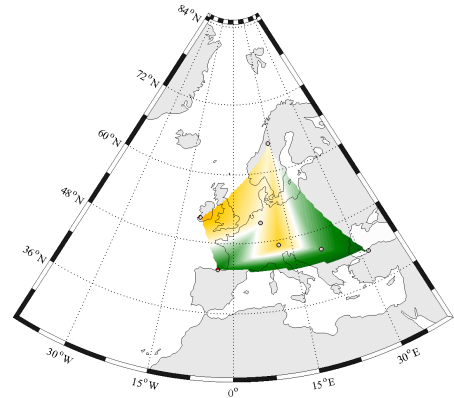
Fig. 14.10: Illustrated is the mean correlation between the short-term 1st PC time series and the speleothem $\delta^{13}\text{C}$ time series for several short-term runs.

14. Investigating spatio-temporal coherent changes for the last 4,000 years

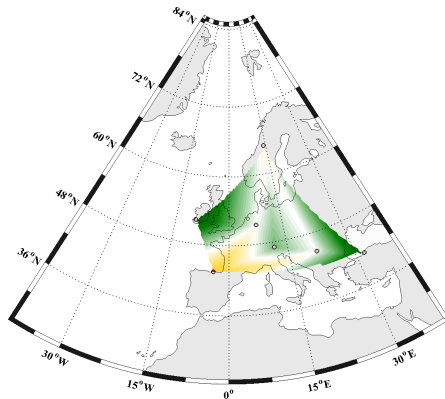
run #7 - 2.0-1.7 ka BP (-)



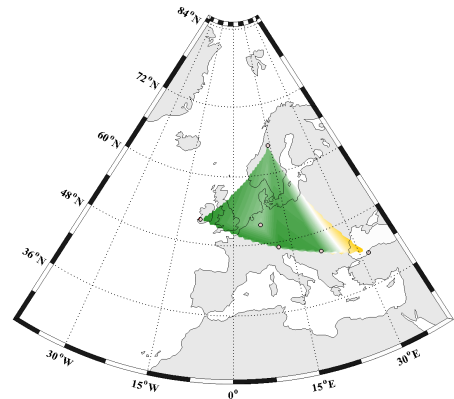
run #8 - 1.7-1.4 ka BP (+)



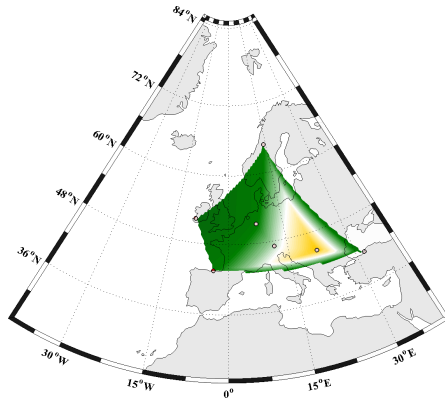
run #9 - 1.6-1.15 ka BP (+)



run #10 - 1.4-1.1 ka BP (+)



run #11 - 1.1-0.8 ka BP (+)



run #12 - 0.8-0.5 ka BP (+)

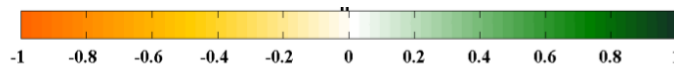
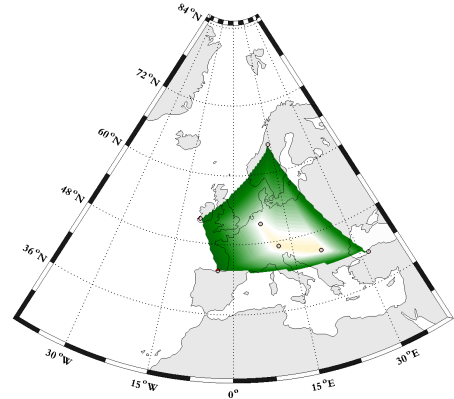


Fig. 14.11: Illustrated is the mean correlation between the short-term 1st PC time series and the speleothem $\delta^{13}\text{C}$ time series for several short-term runs.

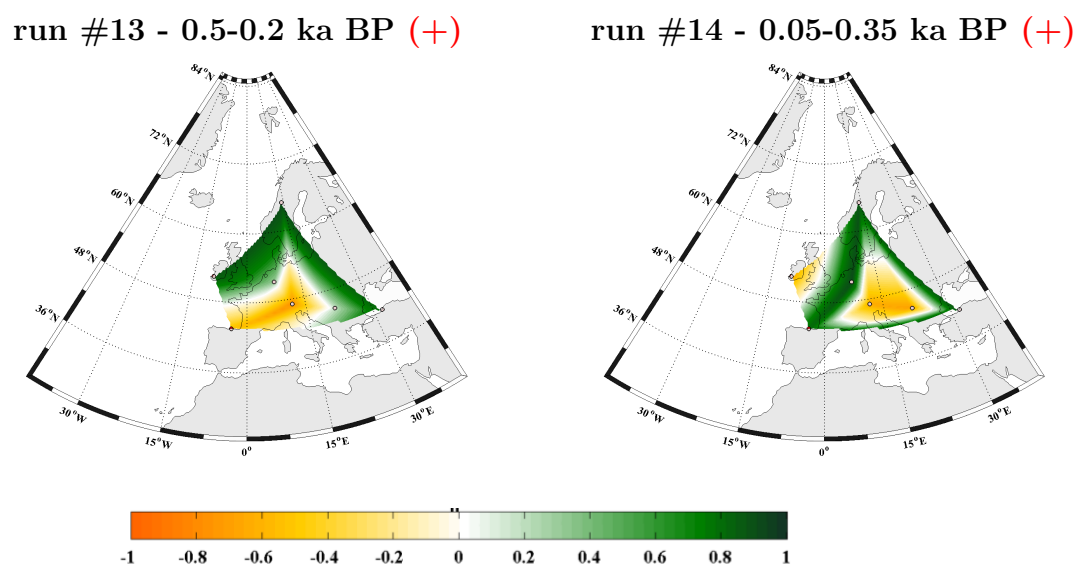


Fig. 14.12: Illustrated is the mean correlation between the short-term 1st PC time series and the speleothem $\delta^{13}\text{C}$ time series for several short-term runs.

15

Investigating spatio-temporal coherent changes for the last 8,000 years - PART II: Short-term analysis

In Chapter 13 the long-term spatio-temporal changes of the last 8,000 were investigated. In the preceding Chapter 14 the long-term as well as the short-term spatio-temporal changes of the last 4,000 years are analysed. In this chapter the short-term variability of spatio-temporal pattern are investigated in the time between 4,000 and 7,000 years BP. For this the same compilations of speleothem $\delta^{18}\text{O}$ and $\delta^{13}\text{C}$ time series are used as in Chapter 13 - speleothem BU-4, CC-26, CC-3, GAR-01, FM-3 and SO-1. The time interval is divided into 10 time windows with a length of 300 years. However, only 9 of them are investigated. The time window between 6.1 and 5.8 ka BP is not analysed, because of the temporal growth stop of stalagmite CC-3 in this period of time.

The mean eigenvalues for each time window are compared with the 95 % confidence interval of WN time series basing on the same properties as the original speleothem proxy time series (Fig. I.1 and I.2) - see also Chapter 10 for detail. The figures show that all mean eigenvalues are within the 95 % confidence interval of the WN time series and would be not significant according to Preisendorfer's Rule N. However, the eigenvalues of the long-term analysis show that only the 1st PC is significant in terms of Preisendorfer's Rule N (Fig. D.1 and D.2). Therefore, the short-term analysis are limited on the spatio-temporal pattern of the 1st PC time series with the compilations of $\delta^{18}\text{O}$ and $\delta^{13}\text{C}$ time series, respectively.

To demonstrate that the derived short-term 1st PC time series are similar with the long-term 1st PC time series they are compared with each other - in Fig. 15.1 for the compilation of $\delta^{18}\text{O}$ time series and in Fig. 15.2 for the compilation $\delta^{13}\text{C}$ time series. The long-term 1st PC time series are illustrated in different grey scales. The short-term 1st PC time series are normalised to the mean value of the long-term 1st PC time series of run #1 (black straight line) (see Chapter 13). The short-term 1st PC time series are pictured in red

and bright green if there was no up-side-down effect and blue and yellow if there was an up-side-down effect for the compilations of $\delta^{18}\text{O}$ and $\delta^{13}\text{C}$ time series, respectively. In addition to the short-term 1st PC time series for the time between 7,000 and 4,000 ka BP the short-term 1st PC time series of Chapter 14 are shown in Fig. 15.1 and 15.2. They are illustrated in purple and green if there was no up-side-down effect in comparison to the 8k long-term 1st PC time series and in cyan blue and orange if there was an up-side-down effect. The overall comparison of the stacked short-term 1st PC time series shows that the short-term 1st PC time series do cover the variability of the long-term 1st PC time series for the compilations of $\delta^{18}\text{O}$ time series as well as $\delta^{13}\text{C}$ time series. Thus, the short-term spatio-temporal coherence pattern can be investigated.

The application of the Fork-tool on the distribution of r_s values of the short-term analysis gives further information on the significance of the short-term 1st PC time series (Fig. J.1-J.36). The results show that before 5.5 ka BP, i.e. for run #5, #6, #7, #8 and #9, the application of the Fork-tool is positive for both, the $\delta^{18}\text{O}$ and $\delta^{13}\text{C}$ time series. Hence, for these time windows, the speleothem $\delta^{18}\text{O}$ and $\delta^{13}\text{C}$ time series have a signal in common. For run #2 and #3 the application of the Fork-tool is also positive, whereas it is negative for run #1 and #4. However, the application of the Fork-tool also shows that the behaviour of the r_s distributions is different for the time windows before and after 5.5 ka BP. Before 5.5 ka BP (run #1-#4) the application of the Fork-tool is resulting in minor changes of the distribution of r_s values whereas after it clearly cuts one half of the r_s distributions. The results of the Fork tool in combination with Preisendorfer's Rule N show that the short-term 1st PC time series are significant. However, run #1-#4 must be interpreted carefully.

The value of the TEV for the 1st PC for the investigated compilations of $\delta^{18}\text{O}$ and $\delta^{13}\text{C}$ time series is listed in Tab. 15.1 for each time window. The spatio-temporal coherence pattern for the investigated time windows are illustrated in Fig. 15.3 and 15.4 for the compilation of $\delta^{18}\text{O}$ time series and in Fig. 15.5 and 15.6 for the compilation of $\delta^{13}\text{C}$ time series. Note that if the short-term 1st PC time series are illustrated up-side-down in Fig. 15.1 or 15.2, respectively, the related maps are marked with a blue "-", otherwise with a red "+". The maps are illustrating the mean value for r_s between the speleothem proxy time series and the derived 1st PC time series.

For run #1, covering the time between 7.0 and 6.7 ka BP, the spatio-temporal coherence pattern for the compilation of $\delta^{18}\text{O}$ time series shows a small negative mean value for r_s for GAR-01's $\delta^{18}\text{O}$ time series and positive mean r_s values for the remaining $\delta^{18}\text{O}$ time series. However, except for stalagmite FM-3's $\delta^{18}\text{O}$ time series the mean correlation is weak. In comparison to the spatio-temporal coherence pattern of run #1 the pattern is picturing a more complex structure for run #2 (6.7-6.4 ka BP). It shows negative mean r_s values for stalagmite FM-3's and CC-26's $\delta^{18}\text{O}$ time series and positive values for the other speleothem $\delta^{18}\text{O}$ time series. This pattern structure appears also for run #3, #7 and #9 and can be a inter-mediate state between the dipole-like pattern structure of run #4,

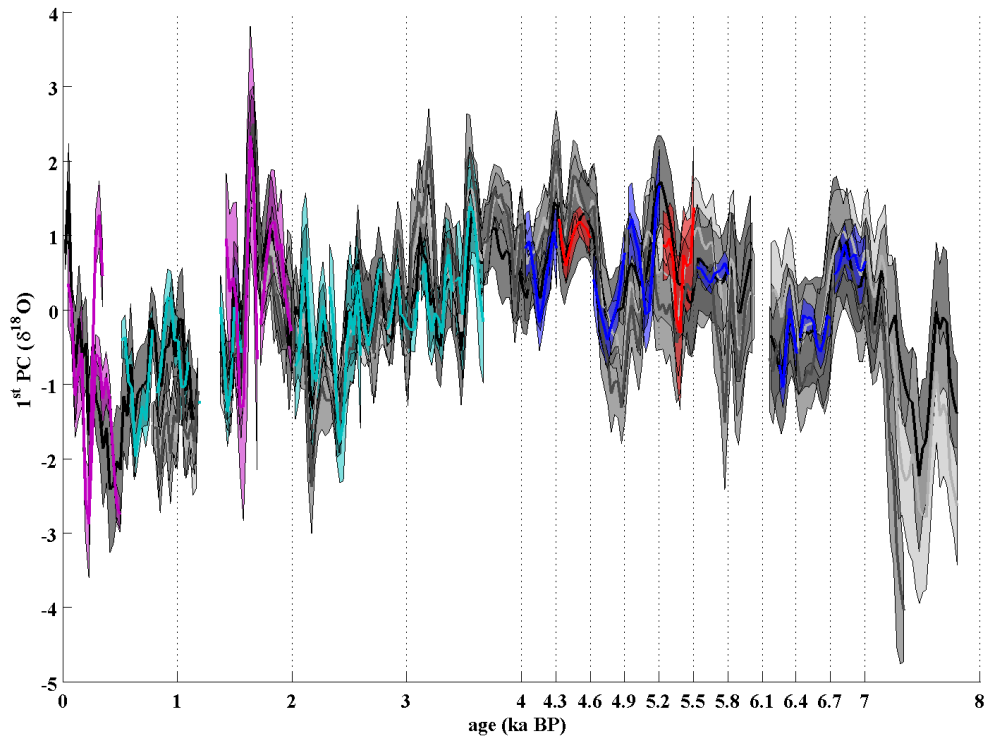


Fig. 15.1: Illustrated are the computed 1st PC time series for the short-term PCA of the compilation of $\delta^{18}\text{O}$ time series for the last 8000 years (blue and red lines). The 1st PC time series are pictured in red if no up-side-down effect was observed in comparison to the long-term 1st PC time series (grey lines) and in blue if an up-side-down effect was observed. In addition, the computed short-term 1st PC time series of the last 4000 years are illustrated. If no up-side-down effect is observed the 1st PC time series is illustrated in purple and in cyan if an up-side-down effect was observed. The long-term 1st PC time series for the 5 speleothem selection is illustrated in dark grey and in light grey for the 6 speleothem selection. The shaded area indicates the 1-sigma standard deviation.

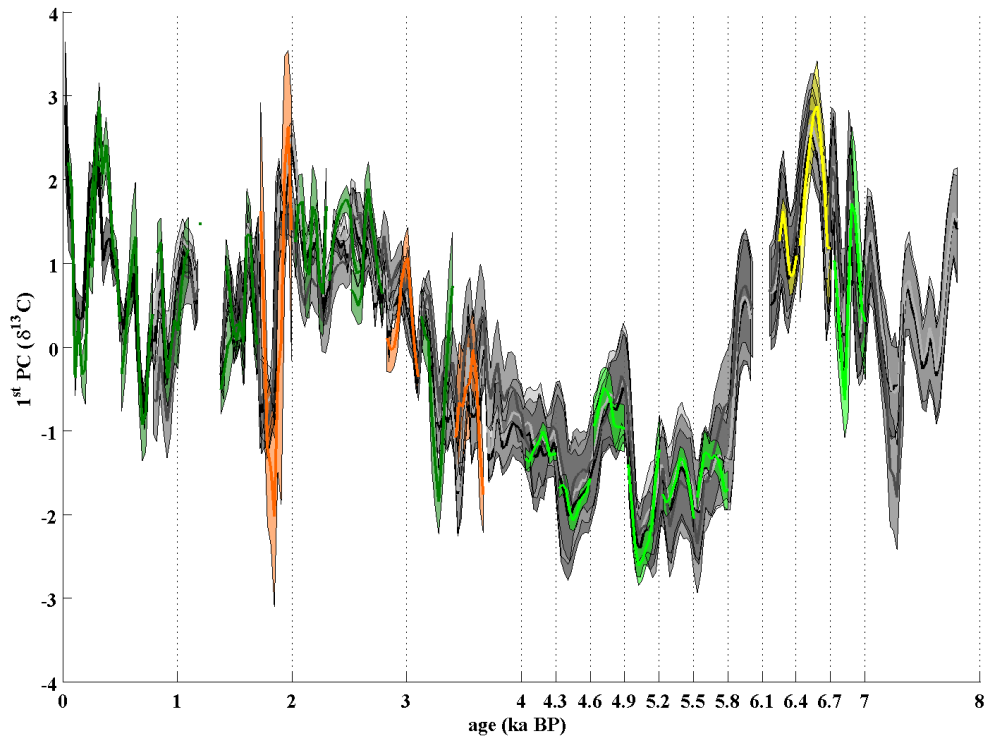


Fig. 15.2: Illustrated are the computed 1^{st} PC time series for the short-term PCA of the compilation of $\delta^{13}\text{C}$ time series for the last 8000 years (bright green and yellow lines). The 1^{st} PC time series are pictured in bright green if no up-side-down effect was observed in comparison to the long-term 1^{st} PC time series (grey lines) and in yellow if an up-side-down effect was observed. In addition, the computed short-term 1^{st} PC time series of the last 4000 years are illustrated. If no up-side-down effect is observed the 1^{st} PC time series is green in purple and in orange if an up-side-down effect was observed. The long-term 1^{st} PC time series for the 5 speleothem selection is illustrated in dark grey and in light grey for the 6 speleothem selection. The shaded area indicates the 1-sigma standard deviation.

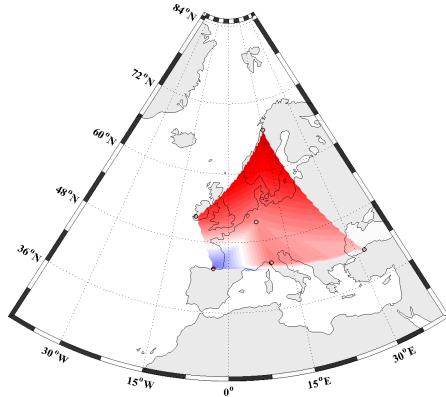
run #	time window (ka BP)	TEV ($\delta^{18}\text{O}$) (%)	TEV ($\delta^{13}\text{C}$) (%)	Fork tool $\delta^{18}\text{O}$ and $\delta^{13}\text{C}$
1	7.0-6.7	44.2 ± 6.2	35.7 ± 4.5	Fig. J.1 & J.19
2	6.7-6.4	37.7 ± 3.7	37.7 ± 5.1	Fig. J.3 & J.21
3	6.4-6.1	47.1 ± 7.2	47.7 ± 7.2	Fig. J.5 & J.23
4	5.8-5.5	35.4 ± 4.3	35.4 ± 4.0	Fig. J.7 & J.25
5	5.5-5.2	39.7 ± 5.8	41.6 ± 5.7	Fig. J.9 & J.27
6	5.2-4.9	42.5 ± 6.4	42.3 ± 5.2	Fig. J.11 & J.29
7	4.9-4.6	37.8 ± 4.6	35.7 ± 4.0	Fig. J.13 & J.31
8	4.6-4.3	36.5 ± 4.2	38.6 ± 4.6	Fig. J.15 & J.33
9	4.3-4.0	36.3 ± 4.3	36.4 ± 4.3	Fig. J.17 & J.35

Tab. 15.1: Table of performed short-term PCA and the related total explained variance of the 1st PC. In addition the related figure is linked for the results of the application of the Fork-tool on the distribution of r_s values. The results base on a total of 1,000 MC simulations.

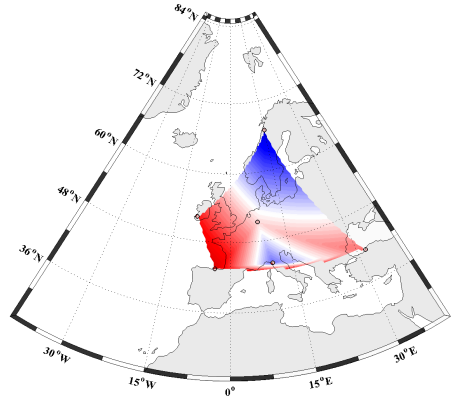
#5, #6 and #8. Note that also the spatio-temporal coherence pattern of run #1 of the 4k short-term analysis has a dipole-like structure similar to run #6. Hence, run #9 can be the inter-mediate state between 4.3 and 3.7 ka BP. Run #3 has the same pattern structure as run #2. Run #4, #5 and #6 have a dipole-like pattern. The dipole-like pattern is changing with time. In the time between 5.8 and 5.5 ka BP (run #4) stalagmite FM-3's $\delta^{18}\text{O}$ time series has a strong negative correlation and stalagmite CC-26's $\delta^{18}\text{O}$ time series a strong positive correlation. The other speleothems have a weak positive correlation resulting a north-south dipole. From run #4 to run #5 the dipole turns clock-wise into a west-east dipole with negative values in East and Central Europe and positive values in West Europe. The dipole then turn anti-clock-wise between run #5 and run #6. After this a inter-mediate pattern occurs but with opposite signs as for run #2. In the time between 4.6 and 4.3 ka BP (run #8) a dipole-like pattern is present with negative mean values for r_s in North (FM-3) and West Europe (CC-3) and positive mean r_s values for stalagmite GAR-01, BU-4 and CC-3. The mean r_s value for stalagmite CC-3's $\delta^{18}\text{O}$ time series with the 1st PC time series is 0. For the last run (run #9) the spatio-temporal coherence pattern has the same structure like for run #7.

The overall comparison of the spatio-temporal coherence pattern for the compilation of $\delta^{13}\text{C}$ time series shows that pattern are mostly monopole-like (run #1, #4, #6, #7, #8). Only for run #2, #3, #5 and #9 the spatio-temporal coherence pattern is dipole-like (Fig. 15.5 and 15.6). In the time between 7.0 and 6.7 ka BP the pattern shows high positive mean r_s values for the speleothem $\delta^{13}\text{C}$ time series of CC-3 and FM-3. Except from stalagmite GAR-01, whose $\delta^{13}\text{C}$ time series has a mean r_s values of c. 0 with the 1st PC time series, all remaining speleothem $\delta^{13}\text{C}$ time series have a positive mean r_s values. For run #2 and #3 (6.7-6.1 ka BP) the pattern changes from the monopole-like pattern of run #1 into

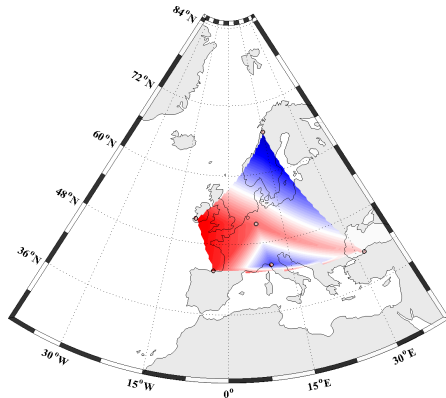
run #1 - 7.0-6.7 ka BP (-)



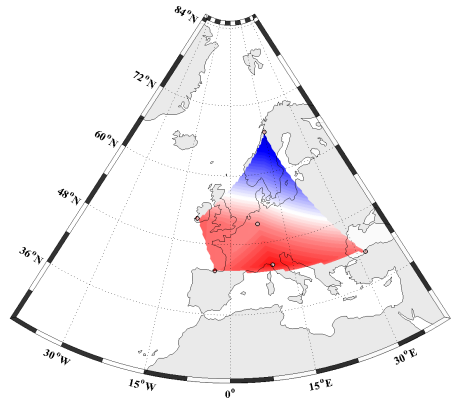
run #2 - 6.7-6.4 ka BP (-)



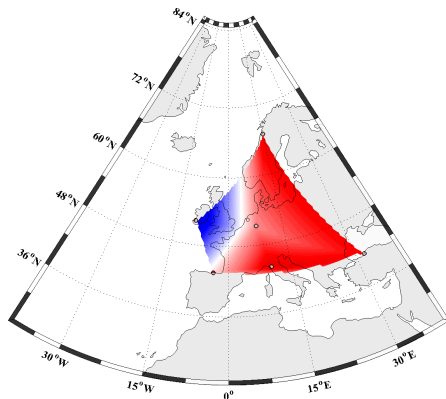
run #3 - 6.4-6.1 ka BP (-)



run #4 - 5.8-5.5 ka BP (-)



run #5 - 5.5-5.2 ka BP (+)



run #6 - 5.2-4.9 ka BP (-)

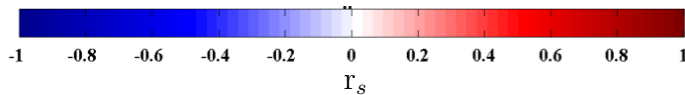
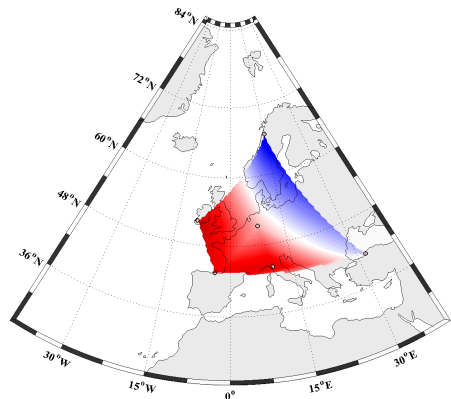
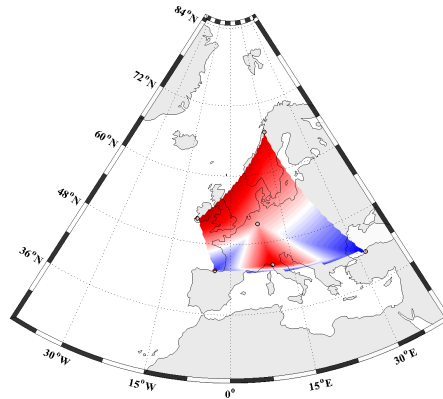
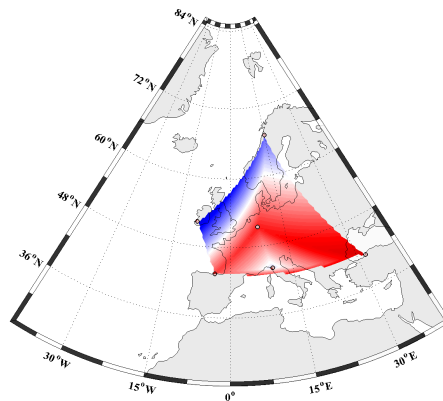


Fig. 15.3: Illustrated is the mean correlation between the short-term 1st PC time series and the speleothem $\delta^{18}\text{O}$ time series for several short-term runs. The "+" (no) and "-" (yes) indicate of the map corresponds to a 1st PC time series with an up-side-down effect.

run #7 - 4.9-4.6 ka BP (-)



run #8 - 4.6-4.3 ka BP (+)



run #9 - 4.3-4.0 ka BP (-)

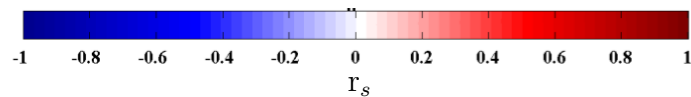
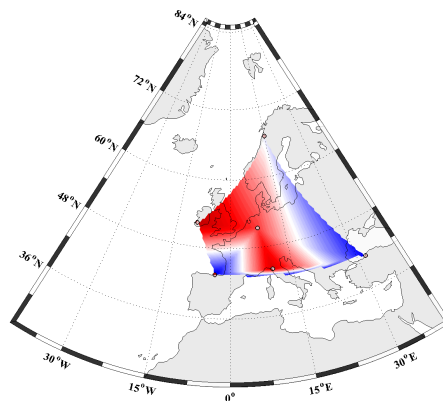
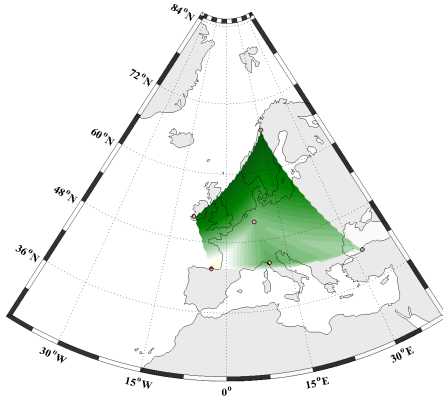


Fig. 15.4: Illustrated is the mean correlation between the short-term 1st PC time series and the speleothem $\delta^{18}\text{O}$ time series for several short-term runs. The "+" (no) and "-" (yes) indicate of the map corresponds to a 1st PC time series with an up-side-down effect.

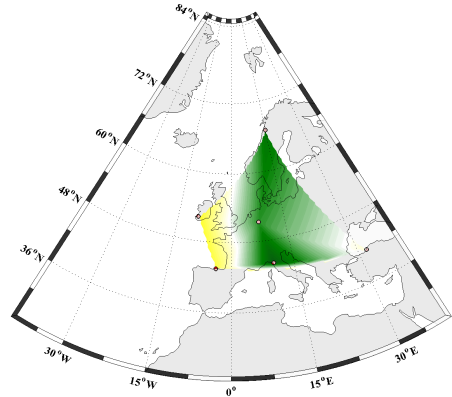
a dipole-like pattern with negative mean r_s values in West Europe and positive mean r_s values in Central and East Europe. For run #2 the mean r_s value between SO-1's $\delta^{13}\text{C}$ time series and the 1st PC time series is c. 0. Between 5.8 and 5.5 ka BP (run #4) the spatio-temporal coherence pattern shows again a monopole-like structure, although the mean r_s value between GAR-01's and FM-3's $\delta^{13}\text{C}$ time series and the 1st PC time series is c. 0. The time window between 5.5 and 5.2 ka BP (run #5) is picturing a dipole-like pattern with negative mean r_s values for FM-3's and SO-1's $\delta^{13}\text{C}$ time series. GAR-01's $\delta^{13}\text{C}$ time series has also a negative mean r_s value. The $\delta^{13}\text{C}$ time series of speleothem BU-4, CC-26 and CC-3 have a strong positive correlation with the 1st PC time series. After this time interval (run #6 - 5.2-4.9 ka BP) the spatio-temporal coherence pattern changes into a monopole-like pattern with a positive correlation to the 1st PC time series, though the mean r_s value for CC-26 is < 0.1 . The period between 4.9 and 4.6 ka BP (run #7) the picture clearly shows a monopole-like structure for the Western, Central and Northern European speleothems. Only stalagmites SO-1's $\delta^{13}\text{C}$ time series mean r_s value is c. 0 and have no correlation with the 1st PC time series during this time interval. In the next time window covering the time between 4.6 and 4.3 ka BP the monopole-like pattern is preserved, but the $\delta^{13}\text{C}$ time series of speleothem FM-3 and SO-1 have no correlation with 1st PC time series. For run #9 a dipole-like pattern occurs with negative mean r_s values for the Western and Northern speleothem $\delta^{13}\text{C}$ time series and positive mean r_s values for the Central and Eastern European $\delta^{13}\text{C}$ time series.

The short-term spatio-temporal coherence pattern of the 1st PC time series in the time between 7,000 and 4,000 ka BP for the two compilations of $\delta^{18}\text{O}$ and $\delta^{13}\text{C}$ time series are picturing two different modes, respectively. For the compilation of $\delta^{18}\text{O}$ time series, the short-term spatio-temporal coherence pattern of the 1st PC time series illustrate either a dipole-like structure or an inter-mediate mode with a more complex pattern structure (Fig. 15.3 and 15.4). The short-term spatio-temporal coherence pattern of the 1st PC time series for the compilation of $\delta^{13}\text{C}$ time series shows a monopole-like pattern or an intermediate-pattern that is dipole-like. For both, the compilations of $\delta^{18}\text{O}$ and $\delta^{13}\text{C}$ time series, the different pattern are alternating with time. Furthermore, the derived short-term 1st PC time series fit the calculated long-term 1st PC time series (Fig. 15.1 and 15.2).

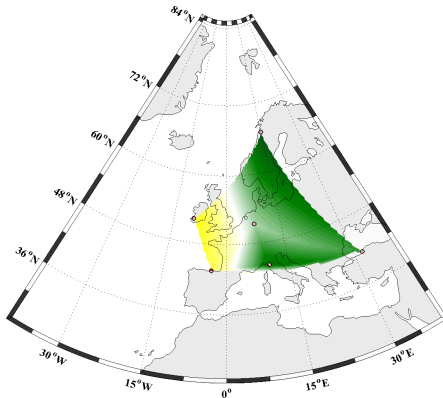
run #1 - 7.0-6.7 ka BP (+)



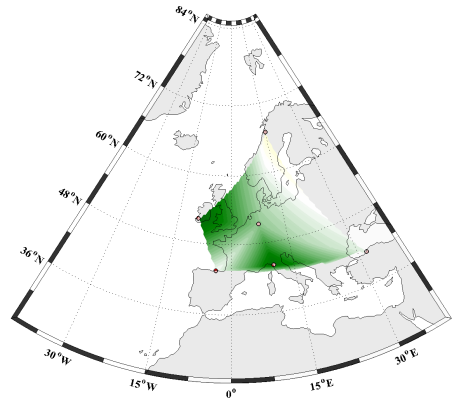
run #2 - 6.7-6.4 ka BP (-)



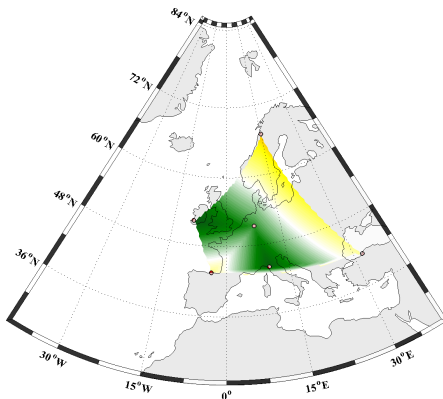
run #3 - 6.4-6.1 ka BP (-)



run #4 - 5.8-5.5 ka BP (+)



run #5 - 5.5-5.2 ka BP (+)



run #6 - 5.2-4.9 ka BP (+)

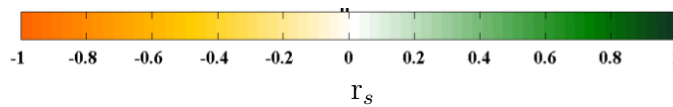
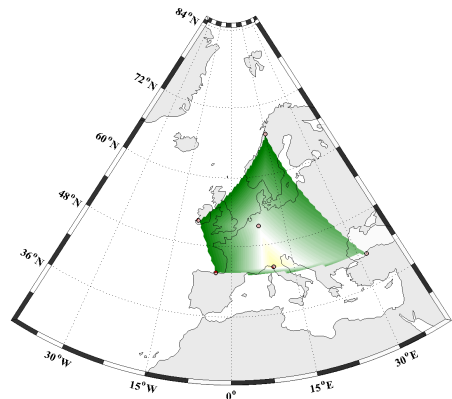
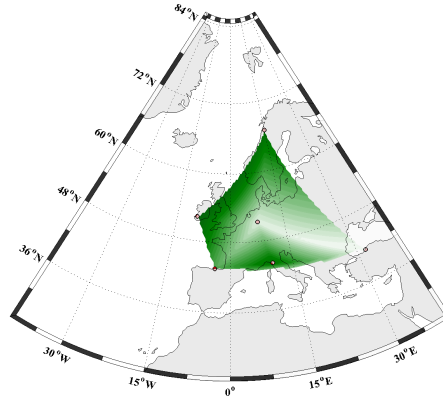
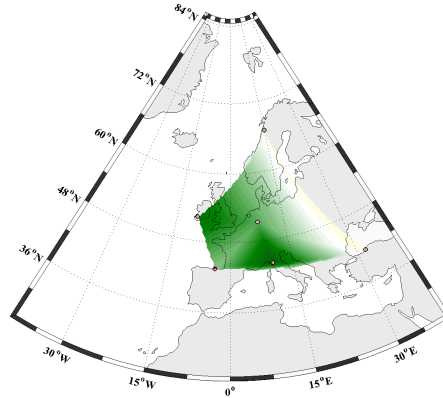


Fig. 15.5: Illustrated is the mean correlation between the short-term 1st PC time series and the speleothem $\delta^{13}\text{C}$ time series for several short-term runs. The "+" (no) and "-" (yes) indicate of the map corresponds to a 1st PC time series with an up-side-down effect.

run #7 - 4.9-4.6 ka BP (+)



run #8 - 4.6-4.3 ka BP (+)



run #9 - 4.3-4.0 ka BP (+)

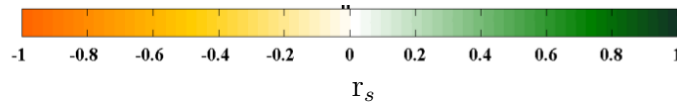
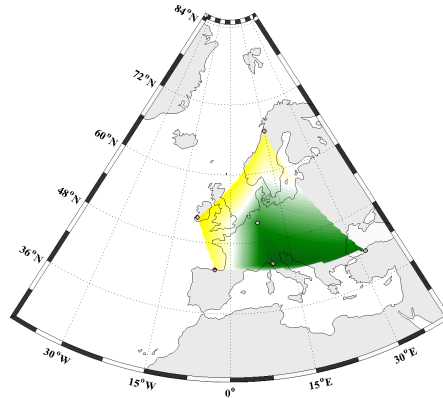


Fig. 15.6: Illustrated is the mean correlation between the short-term 1st PC time series and the speleothem $\delta^{13}\text{C}$ time series for several short-term runs. The "+" (no) and "-" (yes) indicate of the map corresponds to a 1st PC time series with an up-side-down effect.

16

Investigating spatio-temporal coherent changes for the last 10,000 years

In the previous chapters the long-term and short-term variability of period between 0 and 8,000 years BP has been analysed by PCA. In this chapter the long-term spatio-temporal coherency of four speleothems (CC-26, CC-3, GAR-01, SO-1) is analysed whose growth start was at 10 ka BP or even earlier and which grew simultaneously during the entire Holocene. The covered time interval is limited by the growth begin of CC-3 at c. 10.1 ka BP and by the growth stop of CC-26 at c. 0.8 ka BP. This allows for long-term PCA of the $\delta^{18}\text{O}$ and $\delta^{13}\text{C}$ time series of the four speleothems and closes the gap of spatio-temporal information in the time beyond 8.0 ka BP which was the limit of the forgoing PCA caused by the growth begin of BU-4 at 8.2 ka BP and of FM-3 at 7.5 ka BP. In total three PCA were performed at which each PCA base on a total of 1000 MC runs (Chapter 10). For the first two PCA the original $\delta^{18}\text{O}$ and $\delta^{13}\text{C}$ time series of stalagmite CC-26, CC-3, GAR-01 and SO-1 were used. For the third PCA the $\delta^{18}\text{O}$ time series of stalagmite SO-1 was corrected for the change in the $\delta^{18}\text{O}$ values of the Black Sea, which is the major water source of the region around SO-1 (Fleitmann et al., 2009). For this the original dataset of the $\delta^{18}\text{O}$ values (Bahr et al., 2008) were extrapolated with a linear function until 7 ka BP, which mark the end of the steep increase of SO-1 $\delta^{18}\text{O}$ time series.

To test the significance of the derived PCs of each ensemble, composed of the PCs of each MC run, Preisendorfer's Rule N is applied on the distribution of derived eigenvalues for each PC. For this the mean eigenvalues of the computed PCs are compared with an ensemble of eigenvalues resulting from PCA that are applied on a compilation of four artificial WN time series having the same properties as the investigated speleothem proxy time series (Chapter 10). The comparison shows that for three conducted PCA only the 1st PC is significant, because the mean eigenvalue of the 1st PC is above the 95 % level of the

eigenvalues derived for the white noise time series. The mean eigenvalue of the 2nd PC is below the 95 % level and above the 5 % level and all other PCs are below the 5 % level of the computed eigenvalues for the WN time series (Fig. K.1). In addition to Preisendorfer's Rule N the Fork-tool is applied on the distribution of r_s values to test the robustness of the significance of the derived 1st PCs for the three performed PCA. The results are illustrated in Fig. L.1 and Fig. L.2 for the compilation of speleothem $\delta^{18}\text{O}$ time series, whereas the latter is the result for the $\delta^{18}\text{O}$ time series of SO-1 corrected for the change of the $\delta^{18}\text{O}$ signal of the Black Sea. The results for the compilation of speleothem $\delta^{13}\text{C}$ time series is depicted in Fig. L.3. On the distribution for the compilation of speleothem $\delta^{18}\text{O}$ time series at which SO-1's $\delta^{18}\text{O}$ time series is uncorrected the distributions of r_s values of the four speleothems depicts a bimodal distribution but with distinct peaks. The application of the Fork-tool on the distributions of the r_s values however clearly shows that the 1st PC for these compilations is significant (Fig. L.1). The other two distributions picture a single peak of the unmodified distribution of r_s values being an explicit property of correlated time series (Fig. L.2 and L.3). Hence, the computed 1st PCs are significant. Therefore, the application of the Fork-tool confirms the significance of the derived 1st PCs and the corresponding 1st PCs time series. The 1stPC time series are pictured in Fig. 16.1 for the two compilation of $\delta^{18}\text{O}$ time series and in Fig. L.3 for the compilation of $\delta^{13}\text{C}$ time series. The 1st PC time series derived for the compilation of speleothem $\delta^{18}\text{O}$ time series, at which SO-1's is unchanged, explains 42.0 ± 0.9 % of their total variance; and 42.3 ± 1.0 % for the compilation at which SO-1's $\delta^{18}\text{O}$ time series is corrected for the source effect of the Black Sea. The 1st PC time series computed from the compilation of $\delta^{13}\text{C}$ time series explains 40.7 ± 1.3 % of their total variance (Tab. 16.1).

run #	time window (ka BP)	TEV ($\delta^{18}\text{O}$) (%)	TEV ($\delta^{13}\text{C}$) (%)	Fork-tool $\delta^{18}\text{O}$ and $\delta^{13}\text{C}$
1	0.77-10.0	42.0 ± 0.9	40.7 ± 1.3	Fig. L.1 & L.3
2	0.77-10.0	42.3 ± 1.0		Fig. L.2

Tab. 16.1: The table lists the results for the mean total explained variance and the related 1-sigma error of the 1st PC of run #1 and #2 that base on different compilations of speleothem $\delta^{18}\text{O}$ and $\delta^{13}\text{C}$ time series. In addition the related figure is linked for the results of the application of the Fork-tool on the distribution of r_s values. The results base on a total of 1,000 MC simulations.

From the 10 ka compilation of $\delta^{18}\text{O}$ time series derived mean of the 1st PC time series are illustrated in Fig. 16.1 showing the average of the calculated 1st PC time series at which the $\delta^{18}\text{O}$ time series of SO-1 is not corrected (blue line) including the 1-sigma standard deviation from the mean (blue shading area) and the mean of the 1st PC time series where the compilation of $\delta^{18}\text{O}$ records includes the corrected $\delta^{18}\text{O}$ time series of SO-1 (purple line) with the related 1-sigma standard deviation from the mean (purple shading area). For comparison, the long-term mean of the 1st PC time series is computed for the 8 ka

compilation of speleothem $\delta^{18}\text{O}$ time series (run #2, Tab. 13.1), including the $\delta^{18}\text{O}$ record of BU-4, CC-26, CC-3, GAR-01 and SO-1, is also illustrated in Fig. 16.1 (black line) with the related 1-sigma standard deviation from the mean (grey shading area).

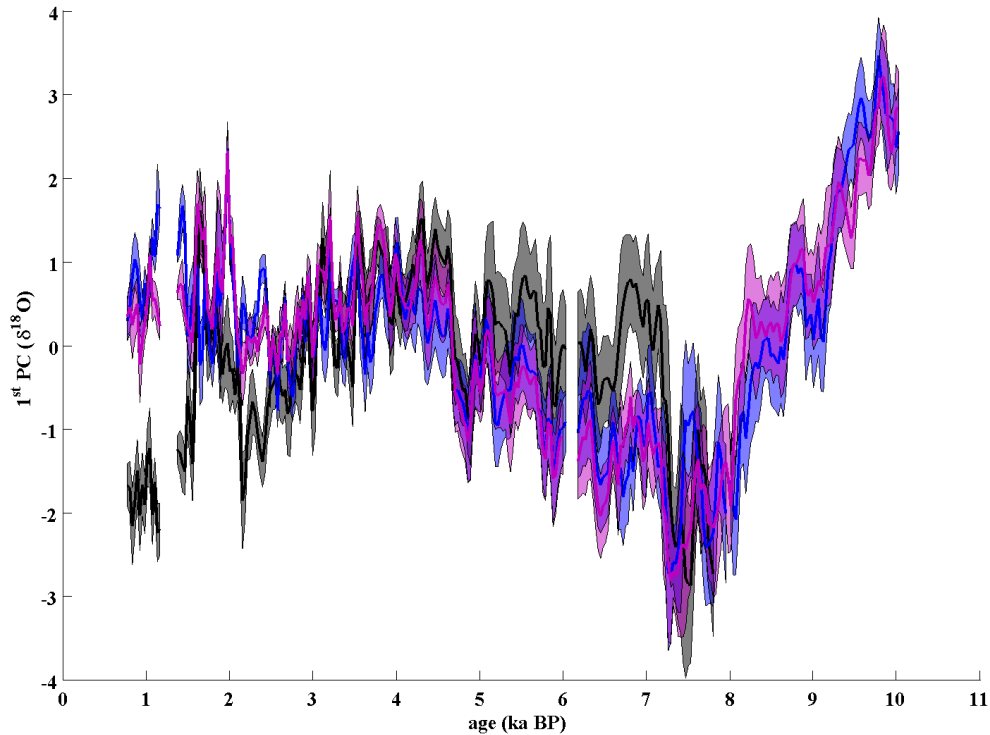


Fig. 16.1: The figure shows the derived average of the 1st PC time series of two compilations composed of the $\delta^{18}\text{O}$ time series of speleothem CC-26, CC-3, GAR-01 and SO-1. The blue line shows the average 1st PC time series of the original $\delta^{18}\text{O}$ time series. The second 1st PC time series (purple line) is derived for the same compilation of speleothems, but the $\delta^{18}\text{O}$ time series of stalagmite SO-1 is corrected for a local source effect (see text for detail). The black line is the average 1st PC time series of a compilation of speleothems covering the last 8,000 years (Chapter 13). All mean values are illustrated with their related 1-sigma standard deviation.

The long-term mean values of the two computed 10 ka 1st time series are in agreement within their 1-sigma error. The comparison of the two 10 ka 1st time series with the 8 ka 1st time series shows that all major features are shared, although there are differences in the absolute values resulting from the standardization of the 8 ka 1st time series to the same mean value and standard deviation as the 10 ka 1st time series during the coeval time period. The long-term trend of the derived 10 ka 1st time series pictures a progressive decrease in the time between 10 and 7.4 ka BP. After reaching a global minimum at 7.4 ka BP the

mean value of the 1st time series is increasing until c. 4 ka BP. Between c. 4.0 and 3.0 ka BP the evolution is rather constant in comparison with the forgoing long-term variability. At 3.0 ka BP another decrease of the trend is beginning reaching a local minimum between 2.5 and 2.0 ka BP. At 2.0 ka BP the values are again increasing. However, in the time between 2.0 and 0.8 ka BP, the hiatus of GAR-01 between 1.3 and 1.1 ka BP causing an interruption of the temporal evolution of the 1st time series. In summary the long-term variability in the early- and mid-Holocene, between 10 and 4 ka BP is greater than the variability between 4.0 and 0.8 ka BP, in particular the linear increase of the 1st time series between 7.0 and 4.0 ka BP with a change from c. -3 to 1.

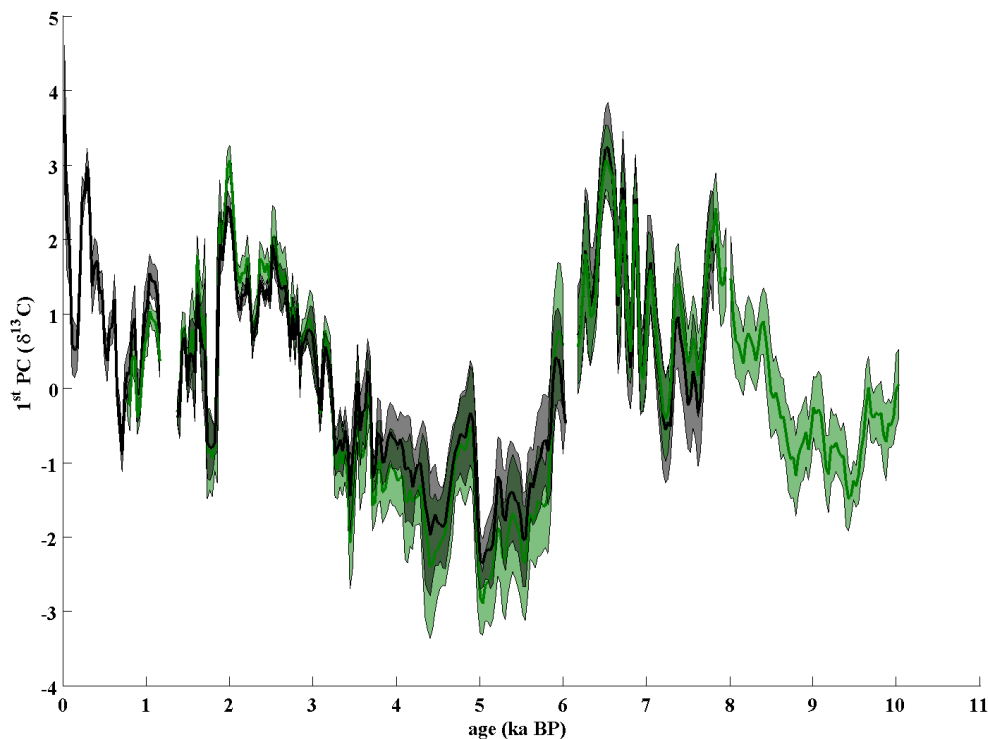


Fig. 16.2: The figure illustrates the temporal evolution of the average of derived 1st PC time series for the last 10,000 years (green line). The black line is picturing the average of computed 1st PC time series covering the last 8,000 years (see text for detail). All mean values are illustrated with their related 1-sigma standard deviation.

The calculated average of the 1st PC time series derived from the compilation of $\delta^{13}\text{C}$ time series is illustrated in Fig. 16.2 (green line) including its 1-sigma standard deviation (green shading area). In addition to the 10 ka 1st PC time series is the 8 ka 1st PC time series pictured in Fig. 16.2 (black line) based on the $\delta^{13}\text{C}$ time series of the speleothems BU-4, CC-3, GAR-01 and SO-1 and the related 1-sigma standard deviation (grey shading area)

(run #1, Tab 13.1). Within the 1-sigma error the derived 10 ka and 8 ka 1st PC time series are in agreement regarding the absolute values, the long- and short-term variability. The cyclicity of the computed 10 ka 1st PC time series shows phases of minima between c. 10 and 8.5 ka BP and c. 6.0 and 4.0 ka BP. The length of the first phase however can not be terminated in its duration because the 1st PC time series does not exceed 10 ka BP. The phases between c. 8.0 and 6.0 ka BP and from 2.5 until 0 ka BP are distinguished by local maxima in comparison to two minima. Both periods show a local minima. Until 0.14 ka BP the 1st PC time series show a progressive increase.

The long-term spatio-temporal coherency pattern for the compilations of $\delta^{18}\text{O}$ time series is pictured in Fig. 16.3. It illustrates the mean r_s values of the distribution of r_s values (Fig. L.1 and L.2) between the speleothem $\delta^{18}\text{O}$ time series and the 1st PC time series - illustrated in Fig. 16.1) - derived from the ensemble MC runs. The upper panel shows the pattern for the original $\delta^{18}\text{O}$ time series, whereas the lower panel shows the pattern for the source-corrected $\delta^{18}\text{O}$ time series of stalagmite SO-1. The difference between the two spatio-temporal coherency pattern is, that the mean correlation of stalagmite SO-1 changes its sign. In the upper panel at which the $\delta^{18}\text{O}$ time series is uncorrected the mean correlation with the 1st PC time series is negative whereas it is positive for source-corrected $\delta^{18}\text{O}$ time series. The mean correlation of the $\delta^{18}\text{O}$ time series of stalagmite CC-3 with the derived $\delta^{18}\text{O}$ time series is negative and positive the CC-26's and GAR-01's $\delta^{18}\text{O}$ time series for both compilation of $\delta^{18}\text{O}$ time series. Under consideration of the source-effect of the $\delta^{18}\text{O}$ time series of stalagmite SO-1 the long-term spatio-temporal coherency pattern pictures a dipole between North and South Europe.

For the mean correlation between the long-term 1st PC time series (Fig. 16.2) derived from the compilation of $\delta^{13}\text{C}$ time series and the $\delta^{13}\text{C}$ time series (Fig. L.3), illustrated in Fig. 16.4, the results picturing that the speleothem $\delta^{13}\text{C}$ time series of the stalagmites CC-3, GAR-01 and SO-1 are positively correlated with the 1st PC time series whereas the $\delta^{13}\text{C}$ time series of stalagmite CC-26 has a weak negative correlation.

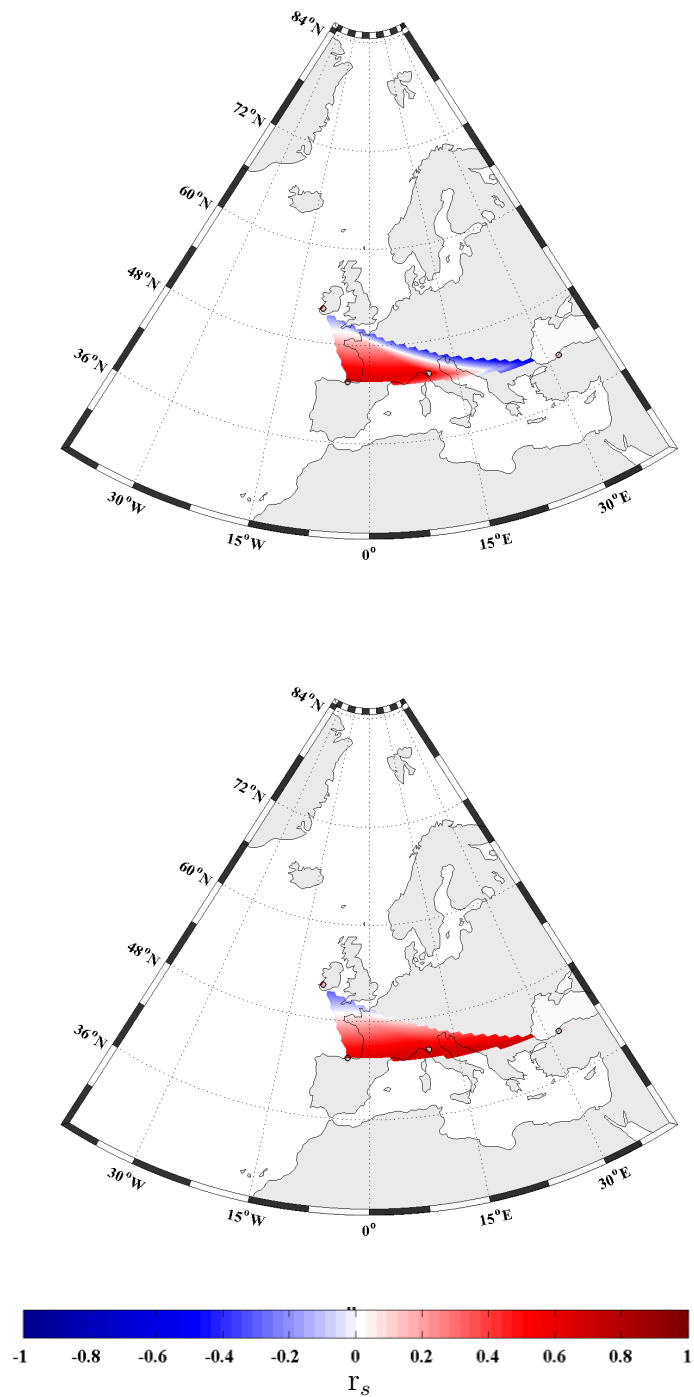


Fig. 16.3: The upper panel shows the long-term spatio-temporal coherency pattern between the 1st PC time series pictured in Fig. 16.1 and the original speleothem $\delta^{18}\text{O}$ time series. The lower panel shows the same as the upper but the $\delta^{18}\text{O}$ time series of stalagmite SO-1 is corrected for the source-effect of the Black Sea.

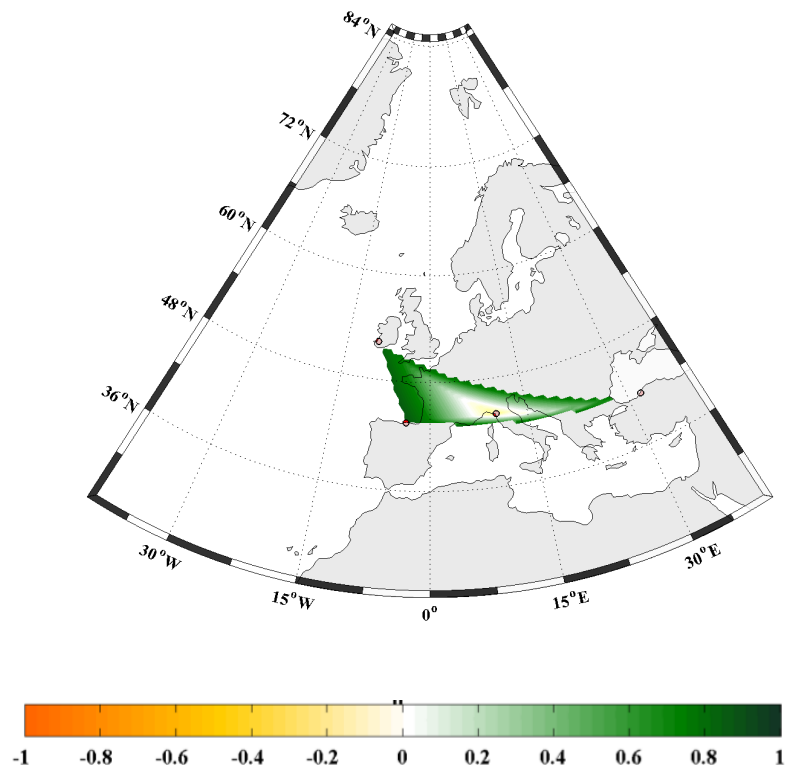


Fig. 16.4: Illustration of the mean correlation between the 1st PC time series for the long-term 10,000 year PCA and the $\delta^{13}\text{C}$ time series.



17

The European Holocene Climate from the speleothems view

17.1 Snapshots from the Holocene climate taken by speleothems

The progressive rainfall causes a depletion of stable isotopes of the continental European precipitation with increasing distance from the western margin (Fig. 11.3), resulting in a stable isotope gradient of the stable isotope values of precipitation (e.g. Dansgaard, 1964; Rozanski et al., 1982; McDermott et al., 2011). Dansgaard (1964) referred this effect as *continental effect* (Chapter 8.1). Rozanski et al. (1982) demonstrated this for δD . Within this framework the *continental effect* for European precipitation was demonstrated for $\delta^{18}O$ and re-examined for δD (Chapter 11). The *continental effect* is caused by the superimposed isotopes effects of the condensation of atmospheric moisture, i.e., the formation of precipitation, and the moisture recycling on the continental surface by evapo-transpiration. For this purpose both studies Rozanski et al. (1982) and this one apply a multi-box Rayleigh approach. Furthermore, it points out that the slope of the stable isotope gradient is steeper in the winter months (October-March) compared to the summer months (April-September). This effect is caused by the higher evapo-transpiration during the summer months and a partly recycling of winter precipitation (Rozanski et al., 1982). McDermott et al. (2011) demonstrated that the *continental effect* is also preserved in speleothems by analysing $\delta^{18}O$ values in a 100 year time slice every thousand years from selected European speleothems - speleothems were excluded when they fulfil one of the following conditions: (i) Alpine speleothems whose elevation is higher than 600 m, (ii) speleothems that are closer than 80 km to the coastline of the Mediterranean Sea and (iii) speleothems whose location lies above 56 °N. The derived gradients are robust and agree with independent results of groundwater samples (Rozanski, 1985; Darling, 2004) and tufa analysis (Andrews, 2006). Moreover,

McDermott et al. (2011) illustrates that the slope of the speleothem $\delta^{18}\text{O}$ gradient was changing during the entire Holocene. During the last 3000 years the slope had a mean value of $-0.1211 \text{ ‰}/^\circ\text{E}$ and seems more stable compared to rest of Holocene period (12,000-4000 years) (cf. Fig. 8 in McDermott et al., 2011). Independent investigations of fluid inclusions δD values of the last 4 ka suggest that the values are similar to present-day precipitation (Dennis et al., 2001). For the period between 12,000 and 4000 years the slope is constantly decreasing from $-0.2208 \text{ ‰}/^\circ\text{E}$ at 12 ka to $-0.1048 \text{ ‰}/^\circ\text{E}$ at 4 ka (Tab. 17.1). McDermott et al. (2011) state that "the temporal change in longitudinal isotope gradients thus reflect a combination of variations in the superimposed European $\delta^{18}\text{O}_{mw}$ and air temperature fields in Europe" - the subscript "mw" means meteoric water. McDermott et al. (2011) conclude that the steeper isotope gradients can cause a higher convective rainfall compared to modern conditions. Furthermore, the change of the slope between 4 ka and 3 ka is, perhaps, forced by a "shift in the atmospheric circulation in the late Holocene". In addition McDermott et al. (2011) shows that the $\delta^{18}\text{O}$ values at a 10°W intercept, i.e., on the western European margin, are decreasing throughout the Holocene. The $\delta^{18}\text{O}$ values are calculated from the extrapolation of the $\delta^{18}\text{O}$ gradients for each time slice. According to McDermott et al. (2011) the effect can be partly explained by the ice volume effect. Another argumentation of McDermott et al. (2011) is, that the different speleothem $\delta^{18}\text{O}$ at the 10°W intercept are caused by different $\delta^{18}\text{O}_{mw}$ values due to the differential early-Holocence warming. In the next section the different slopes of the speleothem $\delta^{18}\text{O}$ gradients shall be discussed in detail. For this purpose the SIP model is used to model the changes of the $\delta^{18}\text{O}$ gradients.

17.1.1 Investigating the temporal evolution of the $\delta^{18}\text{O}$ gradients by use of the SIP model

According to McDermott et al. (2011), the variability of the slopes of the speleothem $\delta^{18}\text{O}$ gradients during the Holocene can be explained by the change of the amount of rainfall during the passage from the Atlantic coast to the eastern part of Central Europe. Using a simplistic Rayleigh approach to calculate the isotopic composition of the atmospheric moisture and the precipitation, McDermott et al. (2011) found out that the amount of remaining moisture (F) is 0.8 at the western margin and 0.5 in the eastern part of Central Europe. The slopes that are more steeper or more shallower compared to the observed slope for recent speleothem $\delta^{18}\text{O}$ gradient explained by an increase or decrease of convective rainfall, respectively. The slope of the speleothem $\delta^{18}\text{O}$ gradients is non-sensitive to the selected oxygen isotope fractionation factor between calcite and water. This is due to the fact, that different oxygen isotope fractionation factors would only shift the absolute $\delta^{18}\text{O}$ values of the precipitated calcite (McDermott et al., 2011). However, this is only the case, if there is no cave air temperature gradient along the investigated transect. Under the assumption, that the cave air temperature varies parallel along the transect, then the slope of the speleothem $\delta^{18}\text{O}$ gradient is preserved by the speleothems (Sec. 11.3). Considering the simplistic Rayleigh approach of McDermott et al. (2011), there are several processes

not included, which would modify the isotopic composition of the precipitation. These key processes are: (i) the moisture recycling by evapo-transpiration and (ii) the temperature gradient between the Atlantic coast and the eastern part of Central Europe (Fig. B.1). In particular the second effect alters the slope of the precipitation $\delta^{18}\text{O}$ gradients when being preserved in speleothems, as a result of the temperature dependent oxygen isotope fractionation factor between water and calcite. The first effect might be negligible due to the small evapo-transpiration in the winter period and could have a minor influence on the slope. To consider these two effects a re-evaluation of the results of [McDermott et al. \(2011\)](#) is undertaken by applying the SIP model (Chapter 11).

To calculate the slopes for the Holocene time slices some assumptions must be made: (i) the temperature during the Holocene varied parallel along the investigated transect with the same variability. Hence, the present-day temperature gradient, for the years between 1901 and 2009, remains unchanged for the Holocene SIP model runs. (ii) The amount of winter evapo-transpiration is constant throughout the Holocene. Therefore the same values are used as for the present-day SIP model run. The mean values for temperature and evapo-transpiration are illustrated in Fig. B.1. (iii) The speleothems are only recording the isotopic fingerprint of the precipitation for the winter months (October-March), because the infiltration of water is the highest during this period of time - during the summer months (April-September) there is even a deficiency of water in the soil zone in Central Europe (Fig. B.1). Therefore, if any summer precipitation infiltrates into karst zone, the portion of it is negligible in comparison to the infiltration during the winter months. (iv) The change of the slopes is either caused by a change of the initial amount of moisture reaching the European Atlantic coastline, the change of the amount of precipitation or both at the same time. The initial amount of atmospheric moisture is expressed by the parameter γ (Sec. 11.1.4). The amount of precipitation is changing everywhere with the same portion. This means, if the amount of precipitation changes in Ireland by 10 % it also changes in all other locations by 10 %.

The reference scenario is the SIP model run for present-day (1901-2009) conditions based on CRU TS3.1 dataset (Sec. 11.1.2) along transect T1 starting in south-west Ireland and ending in Romania (Fig. 11.2). The results for the modern period are discussed in Sec. 11.2.1 for the period 1901 to 2009 and in Sec. 11.4 for the influence of the different NAO phases on the $\delta^{18}\text{O}$ gradient of precipitation and speleothems. The computed $\delta^{18}\text{O}$ gradient of the reference scenario is used to calculate the changed $\delta^{18}\text{O}$ gradient for the entire Holocene in accordance to the results of [McDermott et al. \(2011\)](#). The slopes of the $\delta^{18}\text{O}$ gradients of the reference scenario is listed in Tab. 17.1 (top row) including (from left to right) the related time slices, the slopes determined by [McDermott et al. \(2011\)](#), the computed slopes of the precipitation, the computed slopes of the speleothems, the values for γ and the multiplier ΔP for the amount of precipitation. In addition, the results listed for the two NAO scenarios are investigated in Sec. 11.4. The detailed results are listed in Tab. 11.3. It is noteworthy, that the mean winter NAO index varies between 1.9 and 1.7 for winter NAO plus phases and between -1.5 and -2.3 for winter NAO minus phases. The different ranges are due to the fact that winter NAO minus phases are sparsely covered by GNIP station

data, which are used to calibrate the SIP model. The computed slopes for the speleothem and precipitation $\delta^{18}\text{O}$ gradients of the reference scenario (quoted as "ref." in Tab. 17.1) show that the slope for the precipitation $\delta^{18}\text{O}$ gradient is c. 2.64 times steeper than the speleothem $\delta^{18}\text{O}$ gradient. This is a result of the winter temperature gradient along T1 (Fig. B.1). The temperature is constantly decreasing from the western European margin to the eastern parts of Central Europe. The constant temperature between 10 °W and 0 °E is caused by the balancing effect of the Atlantic and North Sea.

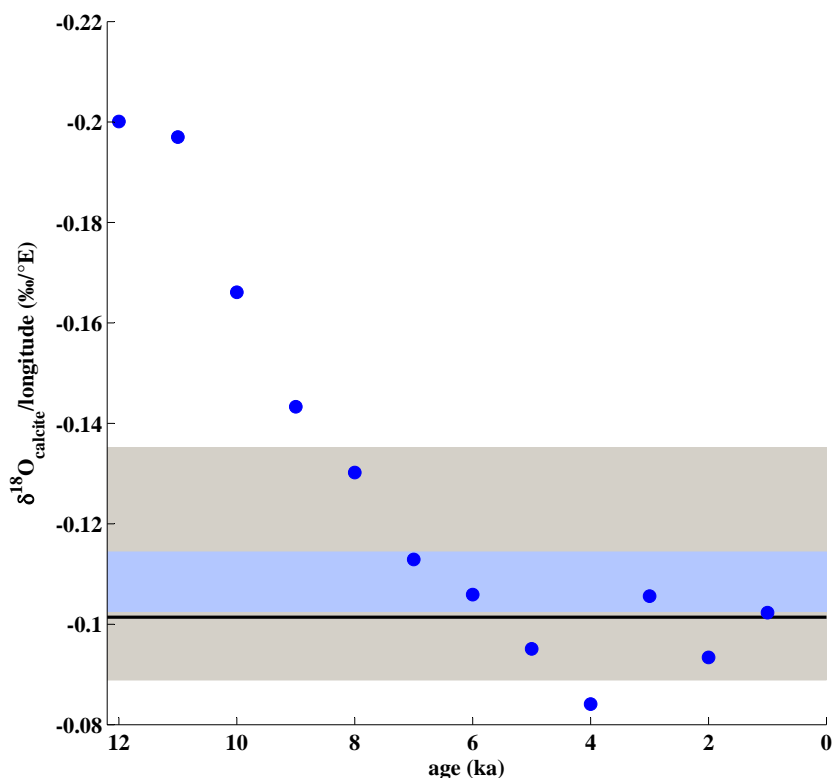


Fig. 17.1: Plot showing the temporal evolution of the slope of the speleothem $\delta^{18}\text{O}$ gradient for the time slices from 1ka to 12 ka (blue circles). The black line indicates the level of the slope computed for the reference scenario. The grey shading area is determined by the slopes that are computed for the winter NAO (wNAO) scenarios for a positive and negative wNAO phase. The upper level is determined by a negative wNAO phase whereas the lower level is computed for a positive wNAO phase. The azure shaded area indicates the slope of the $\delta^{18}\text{O}$ gradient for a wNAO index between 0.51 and -0.51 (see text for detail).

time window (ka BP)	intercept 10 °W ¹ (‰)	$\Delta\delta^{18}\text{O}_T$ (‰)	$\Delta\delta^{18}\text{O}_{SL}$ (‰)	slope speleothems ¹ (‰/ °E)	comp. slope precipitation (‰/ °E)	comp. slope speleothems (‰/ °E)	γ	ΔP
0 (ref.)	-3.6±0.2	0	0	-0.1221±0.0091	-0.268	-0.1014	1.40	1
0 (wNAO+)			-0.2435			-0.0889	1.50	1
0 (wNAO-)			-0.3552			-0.1352	1.20	1
1	-3.7±0.2	0.03	0.00	-0.123±0.0102	-0.2718 and -0.2701	-0.1023	1.39	1.0025
2	-3.8±0.2	0.04	0.00	-0.1141±0.0103	-0.2433 and -0.2563	-0.0934	1.49	0.9788
3	-3.5±0.3	0.06	-0.01	-0.1263±0.0143	-0.2826 and -0.2754	-0.1056	1.3574	1.0113
4	-4.0±0.2	0.05	-0.01	-0.1048±0.0088	-0.2152 and -0.2415	-0.0841	1.615	0.9525
5	-3.8±0.2	0.14	-0.02	-0.1158±0.0099	-0.2485 and -0.2588	-0.0951	1.47	0.9833
6	-3.5±0.2	0.07	-0.05	-0.1266±0.0099	-0.2838 and -0.2758	-0.1059	1.354	1.012
7	-3.4±0.2	0.03	-0.08	-0.1336±0.0104	-0.308 and -0.2869	-0.1129	1.29	1.0301
8	-3.1±0.2	-0.04	-0.17	-0.1509±0.0105	-0.3736 and -0.315	-0.1302	1.16	1.0735
9	-3.0±0.2	-0.21	-0.36	-0.1640±0.0106	-0.4306 and -0.3368	-0.1433	1.0812	1.1052
10	-2.7±0.2	-0.39	-0.64	-0.1868±0.0085	-0.3759	-0.1661	<1	1.1577
11	-2.0± 0.4	-0.84	-1.01	-0.2177±0.0199	-0.4317	-0.1970	<1	1.224
12	-2.4±0.4	-0.95	-1.38	-0.2208±0.0213	-0.4374	-0.2001	<1	1.2303

Tab. 17.1: The table lists the slopes of $\delta^{18}\text{O}$ gradients of Central European speleothems derived by [McDermott et al. \(2011\)](#). Furthermore the change of the initial amount of moisture and precipitation that is necessary to explain the changed slopes compared to the modern slopes calculated by SIP model. The reference period is the interval between 1901 and 2009 (see text for detail).

¹ data from [McDermott et al. \(2011\)](#)

The results for Holocene time slices are listed in Tab. 17.1. For the first nine time slices (1ka to 9 ka) speleothem (and precipitation) $\delta^{18}\text{O}$ gradients were calculated for both, a varying initial amount of atmospheric moisture (γ) and a changed amount of precipitation (ΔP). For the last three time slices (10 ka to 12 ka) only the amount of precipitation varies, because $\gamma < 1$. Hence, at the end of the transect there is no atmospheric moisture left. Note, that the scenarios for a changed initial amount of atmospheric moisture and a changed amount of precipitation are calculated independently from each other. Therefore, the obtained results are limits in which the Holocene values could have lied in. The values for γ and ΔP are estimated manually and are changed until the computed speleothem $\delta^{18}\text{O}$ slope fits to the calculated $\delta^{18}\text{O}$ slope based on the results of [McDermott et al. \(2011\)](#) and of the reference scenario. Because the sensitivity of the precipitation $\delta^{18}\text{O}$ gradients is different for changes in γ or ΔP , both computed slopes for the two scenarios are listed in Tab. 17.1 under the label "*comp. slope precipitation*". The first value is the slope derived by modifying γ and the second for changed ΔP . For the last three late-Holocene scenarios (10 ka to 12 ka), the listed value only refers to a changed ΔP .

The computed values for the Holocene slopes of the speleothem $\delta^{18}\text{O}$ gradient are illustrated in Fig. 17.2 (blue circles). The black line indicates the level of the slope computed for the reference scenario; it is -0.1014 ‰/°E . The grey shading area is picturing the values that are in between the computed slopes for the speleothem $\delta^{18}\text{O}$ gradient derived for the scenario of a positive and negative wNAO phase. It is therefore highlighting the variability of the slope for different wNAO phases. However, the GNIP station values used to calibrate the SIP model are only representative for a well defined period of time. Furthermore, the number of GNIP station values is limited due to the fact that GNIP stations have been running since 1961. Thus, the time range is limited. For this reason the GNIP stations Wallingford, Koblenz and Neuherberg have only recorded one year with a negative wNAO phase, that means a wNAO index smaller than 0.8. All other derived $\delta^{18}\text{O}$ and $\delta^{18}\text{O}$ values come from stations which have data from at least 3 years for positive and negative wNAO phase. The GNIP station Vienna Hohe Varte has the greatest data pool. Records from 16 years exist there for during which the wNAO index was greater than 0.8. Therefore, the grey shading area indicates a great variability of the wNAO index. The upper level that is determined by the minus wNAO phase scenario, represents a NAO index that is c. -2.3 . The lower level is determined by the positive wNAO phase scenario and is representing a wNAO index of c. 1.8 . For the last hundred years (1901-2000), however, the mean NAO index was 0.51 ± 1.09 . Therefore, the mean wNAO index between 1901-2000 CE is smaller (centennial time scale) is smaller than the minimum and maximum of the observed wNAO indices (annual scale). Hence, the centennial variability of the slope of the speleothem $\delta^{18}\text{O}$ gradient might be smaller than indicated by the grey shading area. Although the available slope-NAO dataset is restricted to only three data points, a lot of information can be gained from it. The three data points can be fitted with a linear regression (Fig. M.1) and can be used to indicate the wNAO variability of the slope of the $\delta^{18}\text{O}$ gradient on a centennial time scale. Defining the mean wNAO index of 0.51 of the last century as the "usual" wNAO variability on a centennial time scale and the equation of linear regression (Fig. M.1) the slope of the $\delta^{18}\text{O}$

gradient can be calculated for a NAO index of ± 0.51 . The calculated range of slopes is indicated by the azure shading area in Fig. 17.1 and is limited by the slope of the $\delta^{18}\text{O}$ gradient for a wNAO index of 0.51 resulting in a slope of $-0.1027 \text{ ‰}/^\circ\text{E}$ (lower level) and for a wNAO index of -0.51 resulting in a slope of $-0.1143 \text{ ‰}/^\circ\text{E}$ (upper level). The figure is illustrating that the slope of the speleothem $\delta^{18}\text{O}$ gradient is constantly decreasing from 12 ka to 4 ka. Between 4 ka and 3 ka the slope rapidly increases and is, in comparison with the period before 3 ka, highly variable - the pictures results are identical with that of Fig. 8 in McDermott et al. (2011) and only differ in the absolute values of the slope.

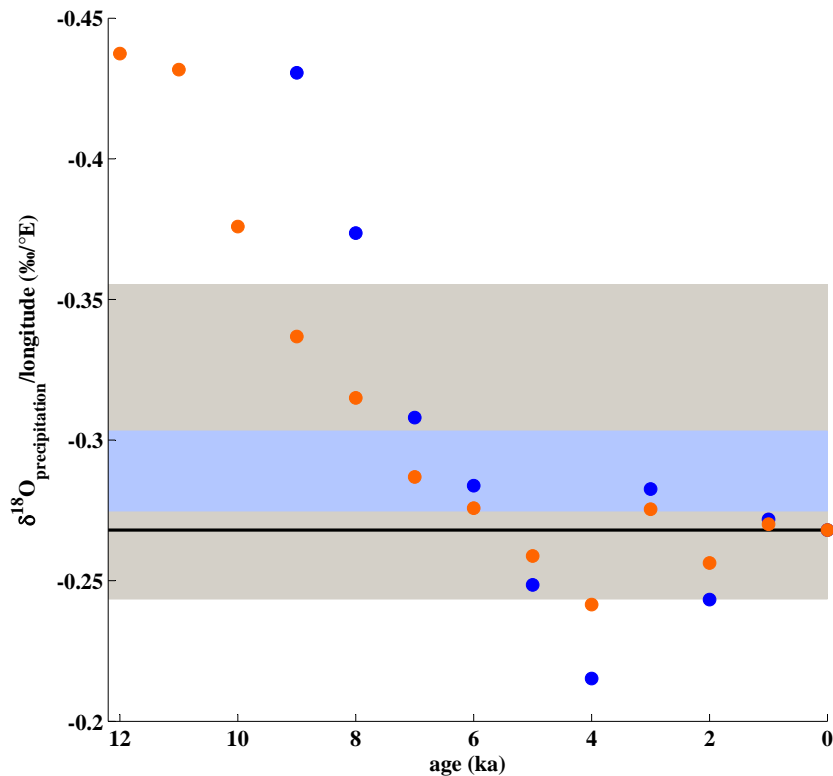


Fig. 17.2: The figure illustrates the temporal evolution of the slopes of the precipitation $\delta^{18}\text{O}$ gradients during the Holocene computed with the SIP model. The blue circles picture the results, if only the initial amount of moisture (γ) is changed. The orange circles are the computed results for the scenario, if only the amount of precipitation has changed (ΔP). The black line is indicating the slope of the precipitation $\delta^{18}\text{O}$ gradient for the reference scenario. The grey shading area indicates the variability of the slope for the two NAO scenarios. All values are listed in Tab. 17.1. The azure shading area is highlighting the variability of the slope for wNAO indexes between between -0.51 and 0.51 (see text for detail).

For each set of γ and ΔP explaining the temporal change of the slope of the speleothem $\delta^{18}\text{O}$

gradient two different slopes of the precipitation $\delta^{18}\text{O}$ gradients are obtained (Tab. 17.1). The Holocene evolution of the computed slopes of the precipitation $\delta^{18}\text{O}$ gradients are illustrated in Fig. 17.2. The blue circles indicate the temporal change of the slope if the initial amount of atmospheric moisture (γ) changes. The orange circles are picturing the evolution of slopes through the Holocene, if the amount of precipitation changes (ΔP). The black line in Fig. 17.2 depicts the level of the computed slope for the reference scenario. The reference scenario covers the period between 1901 and 2009 CE (see above). The grey shading area is highlighting the variability of the computed slopes for the two wNAO scenarios (Sec. 11.4) with a mean wNAO index of c. -2.3 and c. -1.8 for the two NAO scenarios with a negative and positive NAO phase (Tab. 11.3). In an analogous manner, as for the slopes of the speleothem $\delta^{18}\text{O}$ gradient, the variability of the wNAO index on a centennial scale can be calculated from a linear regression of the slopes for the two wNAO scenarios and the reference scenarios (pictured in Fig. M.2). The centennial variability of the wNAO index is ± 0.51 . The results are illustrated by the azure shading area in Fig. 17.2. Note that only the values of the γ -scenarios can be compared with it, because for the NAO scenarios only γ changes. The results for the slope of the precipitation $\delta^{18}\text{O}$ gradients point out that the sensitivity of the computed slope on changes of γ and ΔP is different. This is due to the fact, that the isotopy of the atmospheric moisture is proportional to γ^{-1} , whereas it is proportional to ΔP (see Eq. 11.10). This leads to steeper gradient for the temporal evolution of the slope of the precipitation $\delta^{18}\text{O}$ gradient in the time between 9 ka and 4 ka for the change of γ compared to the slopes derived for changes in ΔP . Between 3 ka and 0 ka the computed slopes are varying around the slope of the reference scenario. In the following part the computed slopes of the speleothem and precipitation $\delta^{18}\text{O}$ gradient illustrated in Fig. 17.1 and 17.2 are discussed.

The late-Holocene period - 3 ka-0 ka: In the last 3000 years the slope of the computed speleothem $\delta^{18}\text{O}$ has varied between 1.49 and 1.36 ‰/°E. The value of the slope of the 1 ka time slice (-0.1023 ‰/°E) is close to that of the reference scenario (-0.1014 ‰/°E) whereas the value for the 2 ka time slice is less negative (-0.0934 ‰/°E). The slope for the 3 ka time slice is -0.1056 ‰/°E and is steeper compared to the reference scenario (Fig. 17.1). To compute the changed slopes γ is varied between 1.49 and 1.3574 and ΔP between 0.9788 and 1.0113 (Tab. 17.1). Only the slope of the speleothem $\delta^{18}\text{O}$ gradient for the 3 ka time slice is within the variability of the slope for the centennial wNAO variability. The slopes for 1 ka and 2 ka time slices are below the level calculated for the centennial wNAO variability. Thus, if the changed slopes would be caused by the wNAO variability the wNAO index would be c. 0.51 for the 1 ka time slice and c. 1.3 for the 2 ka time slice. The computed slopes for the precipitation $\delta^{18}\text{O}$ gradient varies between -0.2433 and -0.2826 ‰/°E if γ is changed and between -0.2563 and -0.2754 ‰/°E for the case when ΔP is changed (Fig. 17.2). Caused by the higher sensitivity of the precipitation $\delta^{18}\text{O}$ gradient on changes of γ the computed slopes for the ΔP -scenarios are closer to the level of the reference scenario than to the γ -scenarios.

Results of the SIP model suggest that the climate conditions of the 1 ka time slice were similar compared to the reference scenario. For the 2 ka and 3 ka time slice, however, the

climate in Central Europe was warmer and/or drier and colder and/or wetter, respectively. Assuming that the NAO is the major climate process determining the climate in Central Europe during the winter months, the 1 ka time slice had a similar mean wNAO phase compared to present-day with mean wNAO index of 0.51. The 2 ka time slice would have an even greater wNAO index of c. 1.3. Hence, the climate during this time interval was very warm and/or dry compared to the last 100 years. The wNAO index for the 3 ka time slice would be compared to other two time slices (1 ka and 2 ka) and the reference scenario smaller, with a mean wNAO index of 0.25. Therefore, the climate was colder and/or wetter compared to present-day.

The early- and mid-Holocene period - 12 ka-4 ka: The temporal evolution in the period between 12 ka and 4 ka differentiates from late-Holocene period (3 ka to 0 ka) on the basis of two main characteristics: (i) in the time between 11 ka and 4 ka the slope of the speleothem $\delta^{18}\text{O}$ gradient is monotonically decreasing having a value of $-0.1970 \text{‰}/^\circ\text{E}$ at 11 ka and $-0.0841 \text{‰}/^\circ\text{E}$ at 4 ka (Fig. 17.1); (ii) the slope of the speleothem $\delta^{18}\text{O}$ gradient for two time slices at 12 ka and 11 ka is c. twice as high as the slope of the reference scenario and constant compared to the period 11-4 ka. Furthermore, the two periods between 12 ka and 11 ka seems less variable and more constant than the time between 11 ka and 4 ka. However, this is speculative, because there is no data available for period later than 12 ka yet. To compute the temporal change in slopes of the speleothem $\delta^{18}\text{O}$ gradient between 9 ka and 4 ka γ changed from 1.0812 to 1.615. Before 9 ka γ is smaller than 1 and there is a deficiency of the amount of moisture, because the total amount of precipitation is not changed for the γ -scenarios. For the ΔP -scenarios the amount of precipitation decreases from the 1.2303-times (+23 %) at 12 ka to the 0.9525-times (-4.75 %) at 4 ka compared to the present-day amount of precipitation. Furthermore, the beginning of the monotonically change of the $\delta^{18}\text{O}$ gradient at 11 ka and the ending at 4 ka are either higher or lower than expected for a NAO variability on a centennial time scale (wNAO index = ± 0.51) and even for the limited time period investigated for the NAO-scenarios in Sec. 11.4 (wNAO index = 1.8 and -2.3).

The temporal change of the slope of the precipitation $\delta^{18}\text{O}$ gradient for the time period between 12 ka and 4 ka illustrated in Fig. 17.2 pictures that the slope between 9 ka and 4 ka changes stronger for the γ -scenario (from -0.4306 to $-0.2152 \text{‰}/^\circ\text{E}$) than for the ΔP -scenario (from -0.3368 to $-0.2415 \text{‰}/^\circ\text{E}$). This is due to the fact that the sensitivity of the isotopic evolution of the atmospheric moisture is higher for changes in γ than for ΔP (see above).

To discuss whether the change of γ or ΔP or of both parameters has forced the temporal change of the speleothem (blue circles) and precipitation (red circles) $\delta^{18}\text{O}$ gradient the sensitivity of the $\delta^{18}\text{O}$ gradients on γ and ΔP are illustrated in Fig. 17.3 and 17.4. The change of the slope is calculated from the difference between the actual slope and the slope of the reference scenario. The change of γ and ΔP is given in % and refers to the difference of the actual value of the parameter to that of the reference scenario. The used values base on the computed scenarios for the different time slices summarised in Tab. 17.1.

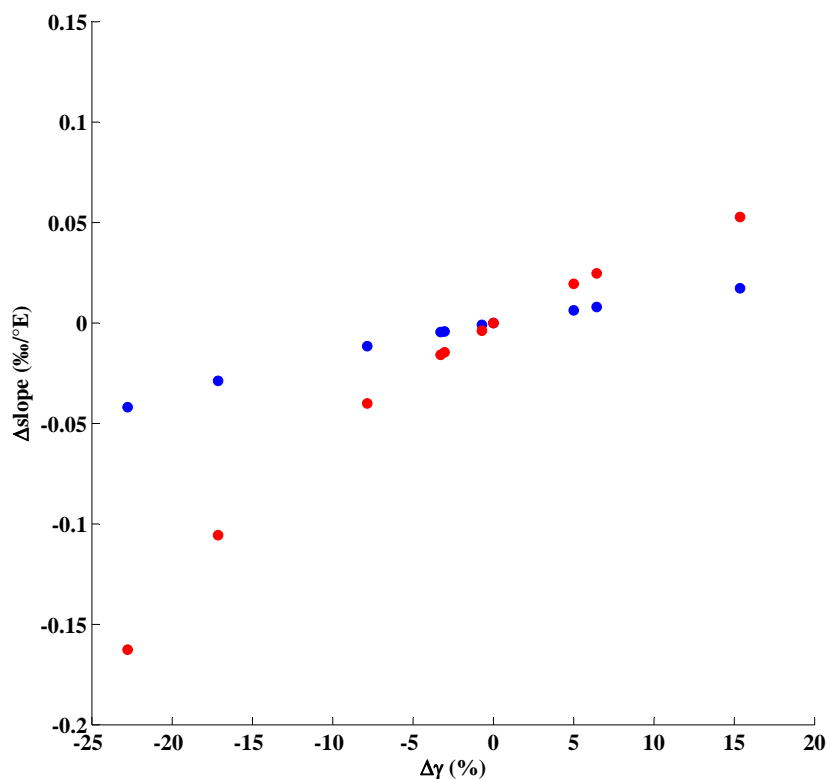


Fig. 17.3: Computed sensitivity of the slope of the precipitation (red circles) and calcite (blue circles) $\delta^{18}\text{O}$ gradient on changes of γ . The changes of γ are expressed by the difference between the actual γ and the γ value of the reference scenario ($\gamma_{ref}=1.4$) and is given in %. The illustrated values base on the computed time slice scenarios summarised in Tab. 17.1.

The $\delta^{18}\text{O}$ gradient of the precipitation is more sensitive on changes of γ and ΔP than the $\delta^{18}\text{O}$ gradient of the precipitated calcite (Fig. 17.3 and 17.4). This is due to the facts that (i) a gradient of the mean annual temperature between Western and the eastern parts of Central Europe is present (Fig. B.1), with warmer temperature in Western Europe ($\approx 10^\circ\text{C}$) and colder temperatures in the eastern parts of Central Europe ($\approx 6.3^\circ\text{C}$ at 14°E) and (ii) that one assumption for the time slice-scenarios is that, if a temperature variation occurred, then the temperature varied parallel along the investigated transect and is, therefore, only shift the present-day temperature gradient by a constant value. Hence, the difference of the temperature between Western Europe (here Ireland) and the eastern part of Central Europe (here Romania) is preserved. This temperature gradient is balancing the $\delta^{18}\text{O}$ gradient of the precipitation that is transferred into the cave by seepage, as a result of the oxygen isotope fractionation effects during the precipitation of calcite. The main process here is the oxygen isotope fractionation factor between water and calcite, $\alpha_{calcite/H_2O}$. Because the sign of $\alpha_{calcite/H_2O}$ is negative a decrease of the temperature causes an increase of the

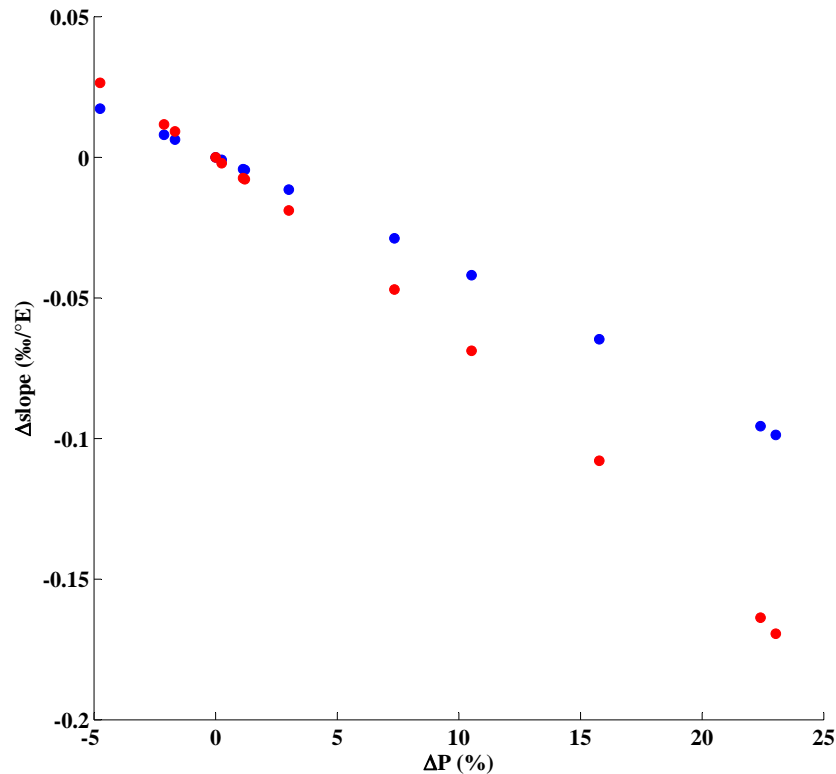


Fig. 17.4: Computed sensitivity of the slope of the precipitation (red circles) and calcite (blue circles) $\delta^{18}\text{O}$ gradient on changes of ΔP . The changes of ΔP are expressed by the difference between the actual ΔP and ΔP value of the reference scenario ($\Delta\text{P}_{ref}=1$) and is given in $\%$. The illustrated values base on the computed time slice scenarios summarised in Tab. 17.1.

$\delta^{18}\text{O}$ values of the precipitated calcite (Chapter 7). Hence, the steeper $\delta^{18}\text{O}$ gradients of the precipitation are transformed into shallower $\delta^{18}\text{O}$ gradients for speleothems by the temperature dependent effect of the oxygen isotope fractionation between water and calcite. Hence, in addition to the change of the initial amount of precipitation (γ) and the amount of precipitation (ΔP), a change of the temperature gradient could have occurred too, that changes the slope of the speleothem $\delta^{18}\text{O}$ gradients. To explain the speleothem $\delta^{18}\text{O}$ gradient for the 11 ka time slice under present-day meteorological conditions (precipitation and evapo-transpiration) there must be a temperature gradient between Western and the eastern part of Central Europe of about 9.725 °C. However, the temperature gradient of the mean annual temperature between Western and the eastern part of Central Europe at 11 ka is between 2 °C and 3 °C, with warmer conditions in the eastern part of Central Europe, according to regional temperature reconstructions for the northern part of Western Europe, the western part of Central Europe and the eastern part Central Europe derived

from pollen records (Davis et al., 2003). In the time between 8000 years BP and c. 0 ka BP the mean annual air temperature in the eastern part of Central Europe was approximately 1 °C warmer than in the northern part of Western Europe and the eastern part of Central Europe and, therefore, the mean annual air temperature gradient would be even more shallow compared to the 11 ka time slice (Davis et al., 2003). Hence, the temperature gradient through the Holocene is either comparable to present-day conditions or is shallower, resulting in the same speleothem $\delta^{18}\text{O}$ gradient as for present-day or a shallower speleothem $\delta^{18}\text{O}$ gradient. Consequently, only changes in the meteorology can be responsible for the temporal change of the speleothem $\delta^{18}\text{O}$ gradient between 11 ka and 4 ka - therefore, only changes in γ and ΔP are responsible for the early- and mid-Holocene evolution of the speleothem $\delta^{18}\text{O}$ gradient. This agrees with the interpretation of McDermott et al. (2011), but here it is demonstrated, in addition, that a possible temperature gradient during this period of time is not responsible for the temporal evolution of the speleothem $\delta^{18}\text{O}$ gradient. However, it is not clear if only a change in the initial amount of precipitation (γ) or the amount of precipitation (ΔP) or both are account for the variability of the $\delta^{18}\text{O}$ gradient in the period between 11 ka and 4 ka.

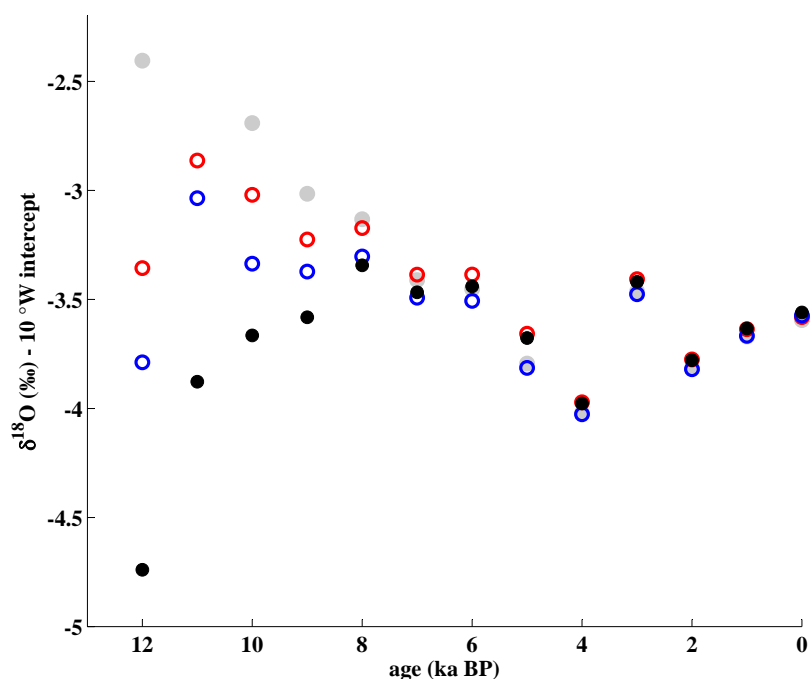


Fig. 17.5: Uncorrected $\delta^{18}\text{O}$ values at a 10 °W intercept (grey full circles) are corrected for varying temperatures during the Holocene (red open circles), for the effect of fresh water input in the Atlantic ocean (blue open circles) and for both effects (black closed circles).

To answer this question, the speleothem $\delta^{18}\text{O}$ values at the 10 °W intercept are investigated for each time slice. The values are calculated from the regression lines of each time slice

(McDermott et al., 2011) and are listed in Tab. 17.1 and illustrated in Fig. 17.5 (grey closed circles). The temporal evolution of the speleothem $\delta^{18}\text{O}$ values at the 10 °W intercept were also discussed by McDermott et al. (2011). By using the sea level curve of Wanner et al. (2008) and a scaling factor of 0.011 ‰/m (Fairbanks, 1989), McDermott et al. (2011) calculated that the $\delta^{18}\text{O}$ value of the surface Atlantic ocean water was approximately 0.6-0.7 ‰ higher at 11 ka and 0.33 ‰ at 9 ka, compared to present-day. The later value is also reported by LeGrande and Schmidt (2009), which are stating a value of 0.34 ‰ at 9 ka. To explain the decrease of about 2 ‰ between 11 ka and 4 ka of the speleothem $\delta^{18}\text{O}$ values at the 10 °W intercept, McDermott et al. (2011) supposed two effects: the first is the ice volume effect (i.e., the increase of the sea level) causing a shift towards more positive values in the early- and mid-Holocene (0.6-0.7 ‰ at 11 ka and 0.33 ‰ at 9 ka). However, the ice volume effect alone can not explain the observation of the speleothem $\delta^{18}\text{O}$ values at the 10 °W intercept. Therefore, McDermott et al. (2011) mention as a second effect, that the atmospheric moisture at the 10 °W intercept has more proximal sources in the early- and mid-Holocene and as a consequence higher $\delta^{18}\text{O}$ values. This is due to the fact, that less precipitation has formed over the ocean and therefore, the atmospheric moisture is not that depleted in ^{18}O as it would be for sources in further distance.

However, to deduce the oxygen isotopic composition of the palaeo precipitation from the speleothem $\delta^{18}\text{O}$ values at the 10 °W intercept, the speleothem $\delta^{18}\text{O}$ values must be corrected for temporal evolution of the European Holocene temperature. This is due to the fact, that the absolute values of the speleothem $\delta^{18}\text{O}$ values calculated from the regression lines of each time slice are depending on the temperature. The slope of the regression lines does also depend on the temperature, if the palaeo temperature gradient changed compared to the present day temperature gradient. However, the latter has been excluded (see above). Thus, the ice volume effect and the temperature effect can account for the Holocene evolution of the $\delta^{18}\text{O}$ values at the 10 °W intercept. The temperature effect is calculated from mean annual temperature reconstructed for the western part of Central Europe from pollen records (Davis et al., 2003) and $^{18}\alpha_{\text{calcite}/\text{H}_2\text{O}}$ (Kim and O'Neil, 1997). A present day mean annual temperature of 10.7 °C is assumed that is based on the long-term mean temperature recorded at the Valentine GNIP station (south-west Ireland). The speleothem $\delta^{18}\text{O}$ values of the 10 °W intercept that are corrected for the temperature effect are illustrated in Fig. 17.5 (red open circles) - a continuous time series is illustrated in Fig. N.1 (red curve). It demonstrates that the speleothem $\delta^{18}\text{O}$ values were substantially higher during the early-Holocene (12 ka to 9 ka), due to colder mean annual temperatures. The shift of the ice volume effect is in analogy to McDermott et al. (2011) calculated from the sea level curve of Wanner et al. (2008) and a scaling factor of 0.011 ‰/m Fairbanks (1989). Since the sea level curve of Wanner et al. (2008) lasting only until c. 10,000 years BP a linear interpolation is used to calculate the sea level change until 12,000 years BP. The corrected speleothem $\delta^{18}\text{O}$ values of the 10 °W intercept are illustrated in Fig. 17.5 (blue open circles) - a continuous curve of the ice volume effect is pictured in Fig. N.1 (blue curve). It pictures that the early- and mid-Holocene $\delta^{18}\text{O}$ values of the surface ocean waters were higher compared to the present-day surface ocean waters. If the temperature effect and the ice volume effect are accounted for the effect on the corrected speleothem $\delta^{18}\text{O}$ values is

larger in the early- and mid-Holocene and subordinated in the late-Holocene (Fig. N.1). The speleothem $\delta^{18}\text{O}$ values of the 10°W intercept that are corrected for the temperature effect and for the ice volume effect are illustrated in Fig. 17.5 (black closed circles). The figure pictures that the corrected $\delta^{18}\text{O}$ values of the 10°W intercept were substantially smaller in the time between 12 ka and 8 ka than the uncorrected values whereas the difference between the original and the corrected is monotonously decreasing with time. During this period the ice volume effect and the temperature effect are contributing equally to the correction of the $\delta^{18}\text{O}$ values at the 10°W intercept. The corrected $\delta^{18}\text{O}$ values of the 10°W intercept during the mid- and late-Holocene (7 ka - 0 ka) are only changed by $\pm 0.05\text{‰}$. The corrected $\delta^{18}\text{O}$ values (black closed circles) deviate from the values published by McDermott et al. (2011) (Fig. 8b in McDermott et al., 2011) mainly in the early-Holocene (12 ka - 8 ka) and picturing a different trend; the results of McDermott et al. (2011) are picturing decreasing $\delta^{18}\text{O}$ values whereas the corrected $\delta^{18}\text{O}$ values are depicting an increasing until 8 ka and a constant values between 8 ka and 6 ka. Hence, the $\delta^{18}\text{O}$ values must be reinterpreted for the early-Holocene to explain the difference of 0.54 (1.42) ‰ of the $\delta^{18}\text{O}$ values of the 10°W intercept between 11 (12) ka and 8 ka. The change in the $\delta^{18}\text{O}$ values at the 10°C West intercept can have several causes: (i) *A changed Ocean sea surface temperature.* A possible reason can be an warming of the surface of the Atlantic Ocean in time between 1 ka and 6 ka BP, because the evaporated moisture is more enriched in ^{18}O with increasing sea surface temperature (Fig. O.1). Assuming a relative humidity of 76 % above the surface of the Atlantic Ocean (Broecker, 1995) the sensitivity of the $\delta^{18}\text{O}$ value on sea surface temperature changes calculated with Eq. (11.1) is 0.0878 ‰/°C. Hence the sea surface temperature must have increases by approximately 6.15 °C in the time between 11 ka BP and 6 ka BP. However, this is an upper limit, because an increase in the relative humidity would also result in an enrichment of ^{18}O in the evaporated moisture from the Ocean (Fig. O.1). For instance, the sensitivity of the $\delta^{18}\text{O}$ value of the evaporated moisture on changes of the relative humidity above the sea surface calculated with Eq. (11.1) is 0.0602 ‰/% at a temperature of 10 °C. Note that an increase in the sea surface temperature is accompanied by an increase of the evaporation rate.

(ii) *The origin of the precipitated water has changed.* An increase of the $\delta^{18}\text{O}$ value at the 10°W intercept can be also caused if either the amount of precipitation over the Atlantic Ocean has increased or the source of the water is more distal from the western margin of the European continent. The latter effect has been assumed by McDermott et al. (2011) to explain the decrease of the $\delta^{18}\text{O}$ values at the 10°W intercept and thus suggesting a more proximal source.

17.1.2 A revisited interpretation of the results observed by McDermott et al. (2011)

The collective interpretation of the evolution of the $\delta^{18}\text{O}$ gradient and the corrected $\delta^{18}\text{O}$ values at the 10 °W intercept suggests that the change of the $\delta^{18}\text{O}$ gradient is caused by an increase of the sea surface temperature in the time between 11 ka BP and 8 ka BP caused by the early-Holocene warming, which results on one hand in an increase in the amount of moisture in the atmosphere and on the other hand a coeval increase of the $\delta^{18}\text{O}$ value of the evaporated moisture. The decrease of the $\delta^{18}\text{O}$ values by about 0.5 ‰ at the 10 °W intercept between 6 ka BP and 4 ka BP is likely not caused by a change of the sea surface temperature, because then the sea surface temperature should have cooled approximately by 5 °C. Such dramatic temperature changes of the sea surface temperature in the mid-Holocene are not reported. Hence, a possible reason for the change in the $\delta^{18}\text{O}$ value at the 10 °W intercept is a change of the source of atmospheric moisture. As suggested by McDermott et al. (2011) this would be a more proximal source to the western margin of the European continent, because less precipitation has been formed over the Atlantic Ocean and thus the atmospheric moisture is more enriched in ^{18}O . This can originate by change and/or movement in the atmospheric circulation, also mentioned by McDermott et al. (2011). Coeval with the change of a more proximal source would be an increased amount of precipitation, which is consistent with results of the SIP model for this period of time.

Furthermore, the time between 3 ka BP and 0 ka BP is predominantly determined by the North Atlantic Oscillation (NAO) during the winter months (October-March), which is indicated by the comparison of the variability of the slope of the speleothem $\delta^{18}\text{O}$ gradient (blue circles) for a variability of the NAO on a centennial time scale (azure shading area) (Fig. 17.1 and Fig. 17.2). Moreover, the comparison of the temporal evolution of the speleothem $\delta^{18}\text{O}$ gradient in the period between 11 ka BP and 4 ka BP with the variance of the $\delta^{18}\text{O}$ gradient caused by the centennial variability of the NAO (during the winter month) reveals that the change of the speleothem $\delta^{18}\text{O}$ gradient can not be explained by the NAO. Taking into account that the change of the speleothem $\delta^{18}\text{O}$ gradient in the time between 11 ka BP and 8 ka BP is possibly changed by an increase of the sea surface temperatures in the Atlantic Ocean, then the change of the speleothem $\delta^{18}\text{O}$ gradient is induced by a change in the atmospheric circulation, suggesting a transition mode of the atmospheric circulation from 8 ka BP to 4 ka BP. It is noticeable that the state of the atmosphere at 8 ka BP is comparable to a negative mode of the NAO with a NAO index of c. -2.3 and the state of the atmosphere at 4 ka BP is comparable to a positive mode of the NAO with a NAO index of c. 2.3. Furthermore, the comparison of the speleothem $\delta^{18}\text{O}$ gradient with the NAO variance of the slope (azure shading area) suggests that the state of the atmosphere was then comparable to present day conditions with a mean NAO index for the last 100 years of about 0.51 (see above). This is also observed by Wackerbarth et al. (2012) indicating a positive NAO mode at 6 ka by comparing speleothem $\delta^{18}\text{O}$ values with computed values of the ECHAM5-wiso model (Werner et al., 2011). However, the

speleothem $\delta^{18}\text{O}$ gradient suggest that the atmospheric circulation is still in a transition state at 6 ka. The present day atmospheric circulation might only start between 4 ka BP and 3 ka BP as suggested by the speleothem $\delta^{18}\text{O}$ gradient and the variance of the slope of the speleothem $\delta^{18}\text{O}$ gradient for a centennial NAO variability (wNAO index = ± 0.51).

17.2 Interpretation of the long-term and short-term 1st PC time series

In the Chapters 13, 14, 15 and 16 a compilation of speleothem $\delta^{18}\text{O}$ and $\delta^{13}\text{C}$ time series were investigated with PCA for spatio-temporal coherent changes on a long-term and a short-term scale. The investigated speleothems are listed in Tab. 12.1 and indicated by the blue color of the speleothem name. It has been demonstrated for the investigated speleothem $\delta^{18}\text{O}$ and $\delta^{13}\text{C}$ time series compilations that the 1st PC and the related 1st PC time series is significant for the long-term and for the short-term analysis. In the following sections, the physical interpretability of the long- and short-term 1st PC time series shall be discussed.

17.2.1 The physical interpretation of the long-term 1st PC time series

To interpret the computed long-term 1st PC time series for their physical meaning it must be considered (*i*) which proxy was investigated and (*ii*) which speleothem proxy time series are contributed to the 1st PC time series. The first point will be very important, in particular, if proxy time series from different regions are compared. This is due to the reason, that physical parameters must be selected before the interpretation of the 1st PC time series, that can explain a variation(s) of speleothem proxy time series from different regions. With focus on speleothem $\delta^{18}\text{O}$ and $\delta^{13}\text{C}$ time series the parameter can be (*a*) a change of the isotopic composition of the source of the isotopes; for the oxygen isotopes this is the ocean (Sec. 8.1) and the vegetation of the carbon isotopes (Sec. 8.2). (*b*) Another parameter is the mean annual temperature that changes the oxygen and the carbon isotope composition of the precipitated calcite (Sec. 7.4). (*c*) the supraregional change of the amount of precipitation: this could affect the $\delta^{13}\text{C}$ value of the drip water by changing the configuration of the karst system (open or closed system) (Sec. 8.2), but also the drip interval can be changed (if the drip interval is sensitive to precipitation changes) which would increase (longer drip interval) or decrease (shorter drip interval) the disequilibrium effects during the precipitation of calcite (Sec. 7.4). The second point, which speleothem proxy time series contribute to the 1st PC time series is important, because speleothems from different regions can be influenced by different climatic zones. For instance, stalagmite CR-1 which is growing on Sicily is mostly influenced by the Mediterranean climate whereas

stalagmite BU-4 which has been formed in Central Europe might be mainly influenced by a Central European climate. It is therefore essential for the interpretation of computed PC time series to know which speleothems contribute to PC time series.

17.2.1.1 The physical interpretation of the 8000 year long-term 1st PC time series for the compilation of $\delta^{18}\text{O}$ time series

The PCA was applied on the compilation of $\delta^{18}\text{O}$ time series from stalagmite BU-4, CC-3, CC-26, FM-3, GAR-01 and SO-1 for the 8000 year long-term run. The computed 1st PC time series is illustrated with the standardised $\delta^{18}\text{O}$ time series in Fig. P.1 (for BU-4), Fig. P.3 (for CC-3), Fig. P.4 (for CC-26), Fig. P.7 (for FM-3), Fig. P.8 (for GAR-01) and Fig. P.12 (for SO-1). The figures illustrate that the computed 1st PC time series is mainly determined by the variability of the stalagmites CC-3, CC-26 and SO-1. The stalagmites FM-3 and GAR-01 do also contribute to the 1st PC time series, but with less similarities as stalagmite CC-3, CC-26 and SO-1. Stalagmite BU-4 has no common pattern with the computed 1st PC time series, except the time between 0.8 ka BP and 0 ka BP. This is also pictured by the spatio-temporal coherency pattern of the 8000 year long-term analysis illustrated in Fig. 13.4 (run #3) - note that the spatio-temporal coherency pattern is based on the mean correlation between the 1st PC time series and the individual $\delta^{18}\text{O}$ time series. Therefore, the 1st PC time series must be mostly influenced by the $\delta^{18}\text{O}$ time series from the Western Margin (CC-3 and GAR-01), from the Mediterranean (CC-26) and Northern Turkey (SO-1). This is also supported by the comparison with the computed 1st PC time series with Mediterranean speleothem $\delta^{18}\text{O}$ time series that has not been included in the interpretation. These speleothems are CL-26 (Fig. P.5), CR-1 (Fig. P.6), GP-2 (Fig. P.9) and SV-1 (Fig. P.14). Furthermore, stalagmite C09-2 has a similar trend like the computed 1st PC time series, but is anti-correlated in the time between 3.5 and 2 ka BP. The $\delta^{18}\text{O}$ time series of stalagmite MB-3 (Fig. P.11) has also common pattern with the derived 1st PC time series as well as stalagmite SPA-12 (Fig. P.13). The Scandinavian stalagmite K-1 (Fig. P.10) has also similar variations like the 1st PC time series but is anti-correlated to it. Hence, the spatio-temporal pattern of Fig. 13.4 (run #3) is supported by independent speleothem $\delta^{18}\text{O}$ time series.

With focus on the long-term trend of the 1st time series (Fig. 13.2) possible reason for this behaviour can be a synchronous change of the $\delta^{18}\text{O}$ value of the precipitation, which must be anti-correlated between Northwest Europe and Southern Europe. However, in the time between 7 ka BP and 4.5 ka BP stalagmite FM-3 is in phase with the derived 1st PC time series and the $\delta^{18}\text{O}$ values are also increasing. The increase in the $\delta^{18}\text{O}$ values of the Mediterranean stalagmites and the increase in the $\delta^{18}\text{O}$ value of stalagmite FM-3, however, can have different origins. In general, possible reasons for a increase in the $\delta^{18}\text{O}$ values can be a decrease of the mean annual temperature (due to the negative temperature sensitivity of precipitated calcite; Sec. 7.4) or the increase of the sea surface temperature (Fig. O.1). [Linge et al. \(2009\)](#) interpreted the stalagmite $\delta^{18}\text{O}$ data as a temperature proxy, that have a negative correlation with the surface temperature. For the Mediterranean speleothem $\delta^{18}\text{O}$

values it is not clear if the annual air temperature has cooled or the sea surface temperature of the water source has increased. Hence, the 1st PC time series can be interpreted as a temperature proxy on the long-term scale.

17.2.1.2 The physical interpretation of the 4000 year long-term 1st PC time series for the compilation of $\delta^{18}\text{O}$ time series

The long-term analysis of $\delta^{18}\text{O}$ time series during the last 4000 years is based on the time series of stalagmite BU-4, C09-2, CC-3, CC-26, GAR-01, K-1 SO-1 and SPA-12. The results of the PCA on the first compilation (including BU-4, C09-2, CC-3, GAR-01, K-1 SO-1 and SPA-12) (blue line) and the second compilation (first compilation plus CC-26) (magenta line) is illustrated in Fig. 17.6. The black curves in Fig. 17.6 are picturing the long-term 1st PC time series of the long-term analysis of the last 8000 years of run #1 and #2 (see Fig. 13.2 for the complete time series). All curves are depicted with the corresponding 1-sigma standard deviation from the mean value. The spatio-temporal coherency pattern is illustrated in Fig. 14.4 for the 1st PC time series illustrated in Fig. 17.6. The comparison between the computed 1st PC time series of the first compilation and the speleothem $\delta^{18}\text{O}$ time series is illustrated in Fig. P.15 for BU-4, Fig. P.16 for C09-2, Fig. P.17 for CC-3, Fig. P.18 for CC-26, Fig. P.21 for GAR-01, Fig. P.22 for K-1, Fig. P.23 for SO-1 and Fig. P.24 for SPA-12. Note that in comparison to Fig. 17.6, the 1st PC time series are pictured up-side-down in the Figs. P.15-P.24. Therefore, the mean values for r_s between the 1st PC time series and the speleothem $\delta^{18}\text{O}$ time series have the opposite sign as illustrated. In addition, the computed 1st PC time series is compared with stalagmite CL-26 (Fig. P.19) and SV-1 (Fig. P.25). The $\delta^{18}\text{O}$ time series of stalagmite CL-26 is inphase with the 1st PC time series in the time between 3.6 ka BP and c. 2 ka BP and is approximately in antiphase with the 1st PC time series for the last 2000 years. Stalagmite SV-1 has a negative correlation with the computed 1st PC time series. The comparison between the $\delta^{18}\text{O}$ time series of stalagmite FM-3 and the 1st PC time series is pictured in Fig. P.20. It illustrates that the $\delta^{18}\text{O}$ time series is in phase with the 1st PC time series, except for the time between 3.0-2.5 ka BP and 1.5-0.9 ka BP. Hence, the comparison between $\delta^{18}\text{O}$ time series of CL-26 and SV-1 and the computed 1st PC time series confirm the spatio-temporal coherence pattern illustrated in Fig. 14.4.

The comparison of the derived long-term 1st PC time series for the 8000 (black lines) and 4000 (blue and magenta line) years' analysis reveal that they agree to each other (Fig. 17.6). The only prominent difference is the evolution of the 1st PC time series in the time between 0.9 ka BP and 0 ka BP, during which the 1st PC time series of the 4000 years analysis depicts a maximum and the 1st PC time series of the 8000 years analysis a minimum. However, this is a result of the concept behind PCA that the 1st PC time series should explain the most variance. This results in the difference of the 1st PC time series for the last 900 years. Moreover, this does not limit the interpretability of the 1st PC time series, because the physical meaning of the 1st PC time series is based on the evolution of the

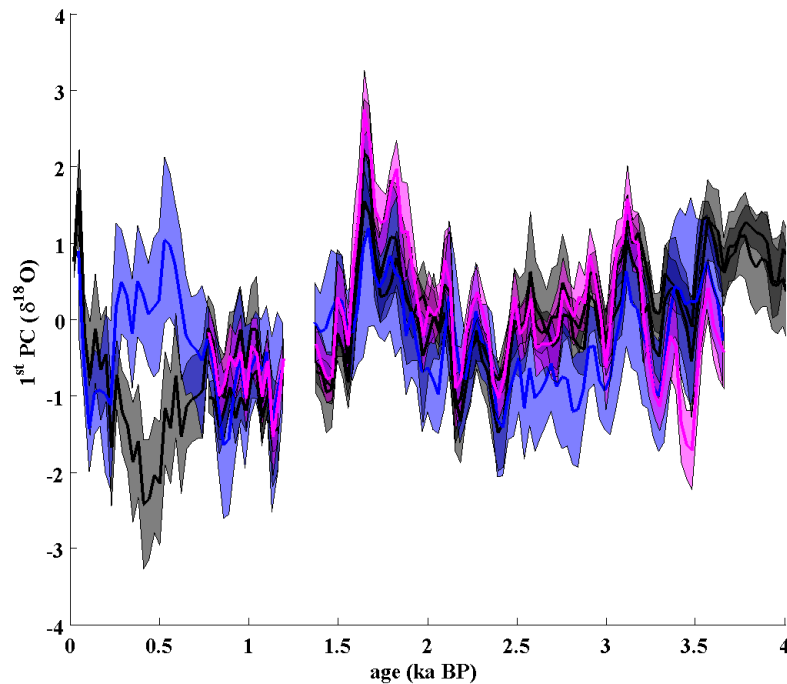


Fig. 17.6: The figure illustrates the 1st PC time series for the 8 ka long-term analysis of the compilation of $\delta^{18}\text{O}$ time series for run #1 and #2 in the time between 4 ka BP and 0 ka BP (black lines) in comparison to the 1st PC time series for the 4 ka long-term analysis for the $\delta^{18}\text{O}$ time series. The blue line is based on the speleothem compilation of BU-4, C09-2, CC-3, GAR-01, K-1 SO-1 and SPA-12. The magenta line is based on the same compilation and includes in addition CC-26. The 1-sigma standard deviation of the mean value is indicated by the shading area for all curves. The difference between the 1st PC time series in the time between c. 0.9 ka BP and 0 ka BP is a consequence of the concept of PCA.

$\delta^{18}\text{O}$ time series during this time.

The $\delta^{18}\text{O}$ values of the speleothems can be determined by the mean annual temperature (Sec. 7.4), the oxygen isotopic composition of the source, the sea surface temperature (Sec. 8.1) and the drip interval (Sec. 7.4). For speleothems in Central European, the main source of drip water is the Atlantic ocean. For speleothems from Mediterranean regions the sources of the drip water can be the Atlantic ocean and the Mediterranean Sea. An influence of the source can be excluded in this case here. This is due to the reason that for such a scenario the changes in the evaporated moisture from the Atlantic Ocean and the Mediterranean Sea must occur synchronously. Furthermore, the observed East-West dipole of the spatio-temporal coherence pattern would not occur, if the changes are caused by the changes of the evaporated moisture from the Atlantic Ocean, as the Atlantic Ocean is main water source for the Central European stalagmites. Consequently, if changes in the

isotope composition of the Atlantic Ocean would have occurred and are accounting for the variance of the speleothem $\delta^{18}\text{O}$ time series, then the stalagmites of Central Europe should be inphase with the speleothem $\delta^{18}\text{O}$ time series from Western Europe. However, this is not observed (Fig. 14.4). Therefore, only the mean annual temperature and the hydrology of the karst system might have changed.

By comparing the $\delta^{18}\text{O}$ time series (Fig. P.15-P.25) with the computed 1st PC time series, it indicates that the 1st PC time series are either a temperature signal, a hydrology signal or both. The scale of the 1st PC time series shows, that positive temperature and precipitation (under the assumption that an increasing amount of precipitation results in shorter drip intervals) changes are equating negative 1st PC time series values. The calibration is due to the fact that the 1st PC time series must explain the observed $\delta^{18}\text{O}$ values. Hence, decreasing speleothem $\delta^{18}\text{O}$ values can be only caused by an increasing temperature and/or shorter drip intervals and vice versa (cf. Fig. P.17). Therefore, the mean annual temperature and the hydrology during the winter months in Western Europe was warmer and/or wetter during the last 4000 years whereas in Central and the eastern part of Central Europe it was colder and/or drier. Note that this climate relationship is also observed for temperature and precipitation along the Central European transect (cf. Fig. B.1).

17.2.1.3 The physical interpretation of the 8000 year long-term 1st PC time series for the compilation of $\delta^{13}\text{C}$ time series

The long-term analysis of $\delta^{13}\text{C}$ time series of the last 8000 years is based on the $\delta^{13}\text{C}$ time series of stalagmite BU-4, CC-3, CC-26, FM-3, GAR-01 and SO-1. The computed 1st PC time series are illustrated in Fig. 13.3. The spatio-temporal coherency pattern between the computed 1st PC time series and the stalagmite $\delta^{13}\text{C}$ time series indicates, that the speleothem $\delta^{13}\text{C}$ time series of stalagmite BU-4, CC-3, GAR-01 and SO-1 are inphase with the 1st PC time series whereas the stalagmite $\delta^{13}\text{C}$ time series of stalagmite CC-26 and FM-3 are not correlated with the computed 1st PC time series. This is also depicted by the comparison of the computed 1st PC time series (of run #1) and the individual $\delta^{13}\text{C}$ time series in Fig. P.26 for stalagmite BU-4, Fig. P.28 for stalagmite CC-3, Fig. P.29 for stalagmite CC-26, Fig. P.33 for stalagmite GAR-01 and Fig. P.36 for stalagmite SO-1. Moreover, the $\delta^{13}\text{C}$ time series of stalagmite C09-2 (Fig. P.27), CL-26 (Fig. P.30), CR-1 (Fig. P.31), K-1 (Fig. P.34), MB-3 (Fig. P.34) and SPA-12 (Fig. P.37) are compared with the derived 1st PC time series. Note that these records were not included in the PCA. The Mediterranean speleothems CL-26 and CR-1 depict no common variance with the 1st PC time series. The $\delta^{13}\text{C}$ time series of CL-26 however has a similar trend as stalagmite CC-26 which could suggest that the Mediterranean speleothems could have had a Mediterranean temporal $\delta^{13}\text{C}$ evolution on the long-term scale. The $\delta^{13}\text{C}$ time series of stalagmite C09-2 is in antiphase with the 1st PC time series during it's growth period which covers approximately the last 4500 years. Also the $\delta^{13}\text{C}$ time series of stalagmite MB-3 fits the computed 1st PC time series and is therefore in coherence with the $\delta^{13}\text{C}$ time series of stalagmite CC-3, GAR-01 and SO-1. Another outstanding feature is the increase of the 1st PC time series beginning

at c. 4 ka BP and ending at c. 2 ka BP, because in comparison to the stalagmites GAR-01, MB-3, SPA-12 and SO-1 whose increase in the $\delta^{13}\text{C}$ time series coincide with the increase of 1st PC time series at 4 ka BP, the increase in the $\delta^{13}\text{C}$ value of stalagmite CC-3 beings 1000 years earlier compared to the 1st PC time series. Apart from the earlier increase, the $\delta^{13}\text{C}$ time series is inphase with the computed 1st PC time series. Therefore, on the long-term scale, the computed 1st PC time series can be interpreted as a common variance in the $\delta^{13}\text{C}$ time series of the stalagmites BU-4, CC-3, GAR-01, MB-3, SO-1 (inphase) and SPA-12, C09-2 (antiphase).

The change of the $\delta^{13}\text{C}$ value on an European-scale can be caused by a vegetation change (Sec. 8.2), a change of the dissolution system (open or closed system; Sec. 8.2), or by a change of the amount of precipitation above the caves in combination with a changed cave hydrology (if the drip interval is sensitive on precipitation changes). A possible coherent temperature change can be excluded because the temperature sensitivity of the $\delta^{13}\text{C}$ value of the precipitated calcite (Sec. 7.4) is negligible in comparison to the sensitivity of the soilwater/drip water $\delta^{13}\text{C}$ value on the other environmental changes (vegetation/precipitation). One difficulty for the interpretation of the 1st PC time series is, that under the assumption that an increased amount of precipitation changes the dissolution of CaCO_3 , that the system is "more" closed, then the $\delta^{13}\text{C}$ value of the solution increases (Hendy, 1971; Salomons and Mook, 1986) (Sec. 8.2). If a higher amount of precipitation causes also an increased input of water into the cave, the drip interval becomes smaller and therefore, possible disequilibrium effects during the calcite precipitation are eased, resulting in a decrease of the $\delta^{13}\text{C}$ value (Sec. 7.4). If the sharp decrease of the 1st PC time series at approximately 6 ka BP (present in the $\delta^{13}\text{C}$ time series of BU-4, $\Delta\delta^{13}\text{C} = \text{c. } -1.3 \text{ ‰}$; CC-3, $\Delta\delta^{13}\text{C} = \text{c. } -6 \text{ ‰}$; GAR-01, $\Delta\delta^{13}\text{C} = \text{c. } -2.3 \text{ ‰}$; MB-3, $\Delta\delta^{13}\text{C} = \text{c. } -3 \text{ ‰}$; SO-1, $\Delta\delta^{13}\text{C} = \text{c. } -1 \text{ ‰}$) is caused by a change in the amount of precipitation, then it must have been a dramatic change. Assuming a mean annual temperature of 10 °C, then the sensitivity of the speleothem $\delta^{13}\text{C}$ values on the drip interval is c. 0.003 ‰/s at a drip interval of 0 s and decreases with increasing drip interval. For a decrease in the $\delta^{13}\text{C}$ value of 1 ‰ the drip interval must become shorter by between 333 s and 1000 s if the sensitivity of the $\delta^{13}\text{C}$ value is in the range between 0.003 ‰/s-0.001 ‰/s. Note, the changes in the $\delta^{13}\text{C}$ values of CC-3, GAR-01 and MB-3 are even higher than 1 ‰. In addition, another cause could be the change of the configuration of the karst zone from a closed system to an open system. The change from an open to a closed system is in range between -4 ‰ and -7 ‰ for soil pCO_2 values between 100,000 ppm and 1000 ppm for a C4 vegetation and -2 ‰ and -3 ‰ for a C3 vegetation (Salomons and Mook, 1986). However, this would imply a significant decrease of the amount of precipitation all over Europe with the strongest effect in Western Europe. The effect decreases with further distance from the western margin. Moreover, the vegetation could have changed accompanied by a change of the amount of precipitation. The increase in the $\delta^{13}\text{C}$ values can have the same origins as the decrease of the values but with the opposite direction.

17.2.1.4 The physical interpretation of the 4000 year 1st long-term PC time series for the compilation of $\delta^{13}\text{C}$ time series

The long-term analysis of the $\delta^{13}\text{C}$ time series for the last 4000 years is based on the speleothem $\delta^{13}\text{C}$ time series of stalagmites BU-4, C09-2, CC-3, CC-26, GAR-01, K-1, SO-1 and SPA-12. The standardised $\delta^{13}\text{C}$ time series are illustrated together with the derived 1st PC time series (derived from the compilation of the last 4000 years) in Fig. P.38 for BU-4, Fig. P.39 for C09-2, Fig. P.40 for CC-3, Fig. P.41 for CC-26, Fig. P.44 for GAR-01, Fig. P.45 for K-1, Fig. P.47 for SO-1 and Fig. P.48 for SPA-12. The spatio-temporal coherence pattern between the computed 1st PC time series and the $\delta^{13}\text{C}$ time series is illustrated in Fig. 14.4. Furthermore, the 1st PC time series is compared to the $\delta^{13}\text{C}$ time series of stalagmite CL-26 (Fig. P.42), FM-3 (Fig. P.43), MB-3 (Fig. P.46). From these stalagmite $\delta^{13}\text{C}$ time series only that of stalagmite MB-3 has a common variance with the computed 1st PC time series. The $\delta^{13}\text{C}$ time series of stalagmite CL-26 and FM-3 have no signal in common with the 1st PC time series.

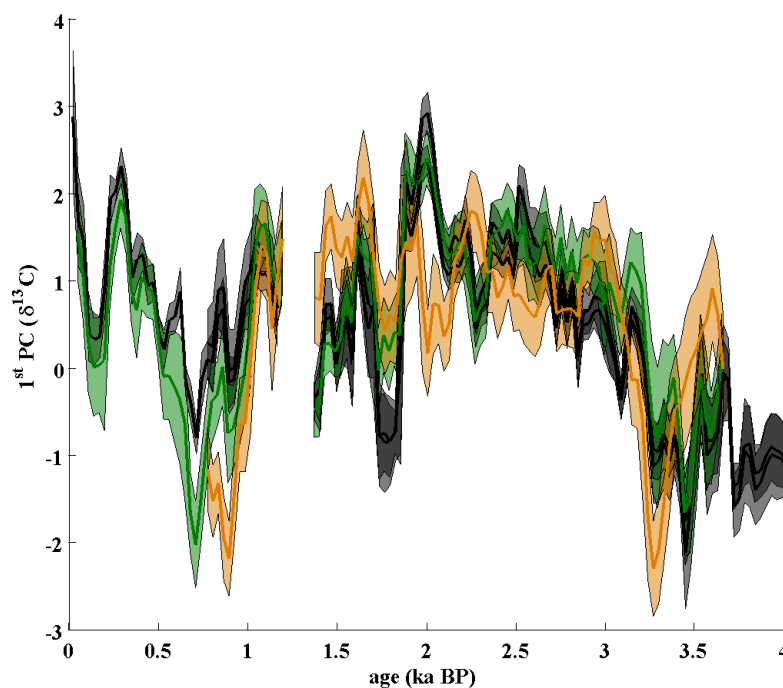


Fig. 17.7: The figure illustrates the 1st PC time series for the 8 ka long-term analysis of the compilation of $\delta^{13}\text{C}$ time series for run #1 and #2 between 4 ka BP and 0 ka BP (black lines) in comparison to the 1st PC time series for the 4 ka long-term analysis for the $\delta^{13}\text{C}$ time series. The green line is based on the speleothem compilation of BU-4, C09-2, CC-3, GAR-01, K-1, SO-1 and SPA-12. The orange line is based on the same compilation plus includes CC-26.

The computed 1st PC time series of the 8000 year long-term analysis of run #1 and run #2 are illustrated in Fig. 17.7 (black lines). The comparison with the derived 1st PC time series of the 4000 year long-term analysis (green line, compilation of BU-4, C09-2, CC-3, GAR-01, K-1, SO-1 and SPA-12; orange line, first compilation plus CC-26) reveals that the derived 1st PC time series for the 4000 year long-term analysis agrees with the 8000 year long-term analysis. In respect to the discussion of the 8000 year long-term analysis, a change of the vegetation, variations in the amount of precipitation and the implied change in the karst configuration (open or closed system with respect to the CaCO₃ dissolution) and the drip interval can cause changes in the observed $\delta^{13}\text{C}$ values of speleothems. Under the assumption that the vegetation did not change significantly during the last 4000 years, the 1st PC time series can be used as a precipitation proxy. This is due to the fact, that the $\delta^{13}\text{C}$ value of stalagmites is mainly determined by the configuration of the karst system during the dissolution of CaCO₃ and the drip interval. Considering spatio-temporal changes in the $\delta^{13}\text{C}$ values a change of the configuration of the karst system during the dissolution of CaCO₃ is more reasonable than continuous changes in the drip interval. This is due to the fact that every karst matrix is unique and for this reason the response of the drip interval on changes of the amount of precipitation is different for every drip site above a stalagmite. Hence, the 1st PC time series is interpreted as a change of the configuration of the karst system regarding an open or a closed system. Increasing $\delta^{13}\text{C}$ values are therefore associated with an increase of the amount of precipitation and vice versa. Positive values of the 1st PC time series are thus interpreted as an increased amount of precipitation, whereas negative values are interpreted as a decrease of the amount of precipitation (cf. Fig. P.44). This interpretation implies an increase of the amount of precipitation from 3.5 ka BP to 2.0 ka BP in Europe. In the period between 2.0 ka BP and 1.0 ka BP the values of the 1st PC time series are constant with variations of higher order. During the first half of the last 1000 years the amount of precipitation has rapidly decreased and reaches a minimum at c. 0.75 ka BP. After that period, the amount of precipitation increases again. Since all speleothem $\delta^{13}\text{C}$ time series, except stalagmite C09-2, have a positive correlation with the derived 1st PC time series, this means that the amount of precipitation has varied on a long-time scale in coherence for most parts of Europe. An exception representing the stalagmites from Southern Europe and the $\delta^{13}\text{C}$ time series of stalagmite C09-2. However, if the stalagmite CC-26 is included in the compilation of speleothems, it reveals that the $\delta^{13}\text{C}$ time series of stalagmite CC-26 and C09-2 have both a similar correlation with the computed 1st PC time series (Fig. 14.4). This may indicate that the amount of precipitation on the 4000 year long-term scale is a dipole between the Mediterranean region and Western-, Central- and the eastern part of Central Europe. However, this is speculative, because of the absence of data from the Mediterranean region, which does not allow for a quantitative analysis.

17.2.2 The physical interpretation of the short-term PC time series

In Sec. 14.2 and 15 the short-term analysis were presented. The analysed datasets are based on the same compilations as the long-term 8000 year and 4000 year PCA. The short-term PCA for the time between 7000 and 4000 years BP were performed on the compilation of the $\delta^{18}\text{O}$ and $\delta^{13}\text{C}$ time series of stalagmites BU-4, CC-3, CC-26, FM-3, GAR-01 and SO-1. For the short-term PCA between 3600 years BP and 0 years BP the dataset was composed of the $\delta^{18}\text{O}$ and $\delta^{13}\text{C}$ time series of stalagmites BU-4, C09-2, CC-3, CC-26, GAR-01, K-1, SO-1 and SPA-12. The comparison of the computed short-term 1st PC time series with the respective long-term 1st PC time series is illustrated in Fig. 15.1 and Fig. 14.5 for the compilations of $\delta^{18}\text{O}$ time series between 7000 and 0 years BP and 4000 and 0 years BP, respectively, and for the compilations of $\delta^{13}\text{C}$ time series in Fig. 15.2 and Fig. 14.9. The comparison reveals that the computed short-term 1st PC time series are consistent with the long-term 1st PC time series. In the foregoing sections the long-term 8000 year and 4000 year 1st PC time series derived from the compilations of speleothem $\delta^{18}\text{O}$ and $\delta^{13}\text{C}$ time series were interpreted as a proxy for temperature and a hydrology, respectively. Hence, the results of short-term PCA of the compilation of $\delta^{18}\text{O}$ and $\delta^{13}\text{C}$ time series will be interpreted as a proxy for temperature and hydrology as well.

It is noteworthy that the occurrence of the spatio-temporal coherence pattern for the compilation of $\delta^{18}\text{O}$ and $\delta^{13}\text{C}$ time series pattern is changing: for the compilation of $\delta^{18}\text{O}$ time series that spatio-temporal coherence pattern is changing from a predominantly North-South dipole in the time between 7000 and 4000 years BP into an East-West dipole during the last 3700 years. The spatio-temporal coherence pattern for the compilation of $\delta^{13}\text{C}$ time series also pictures a change in the predominant structure of the pattern. During the late early- and mid-Holocene the spatio-temporal coherence pattern illustrates mostly a coeval change of the $\delta^{13}\text{C}$ time series, though also a dipole pattern occurs. However, the spatio-temporal coherence patterns that depict a dipole, show that the dipole is mainly formed by a combination of a strong and a weak correlation between the 1st PC time series and the $\delta^{13}\text{C}$ time series. Hence, the predominant mode is still a coherent variation of the $\delta^{13}\text{C}$ time series at which speleothem $\delta^{13}\text{C}$ time series do not correspond to the common variance of the computed 1st PC time series during particular intervals (cf. Fig. 15.1 and Fig. 14.5). During the last 3700 years the spatio-temporal coherence pattern computed from the compilation of $\delta^{13}\text{C}$ time series pictures a North-South dipole predominantly.

The short-term changes of the computed 1st PC time series can be interpreted in terms of warmer/colder or wetter/drier climate by comparing the short-term 1st PC time series to the respective long-term 1st PC time series and the original $\delta^{18}\text{O}$ and $\delta^{13}\text{C}$ time series, respectively. For instance, the example of the 4000 year long-term 1st PC time series pictures an increase of the 1st PC time series in the time between 1.5 ka BP and c. 0.8 ka BP. After 0.8 ka BP the 1st PC time series decreases and reaches a minimum at c. 0.5 ka BP. During the last 500 years the 1st PC time series illustrates increasing values (cf. Fig. 14.5). The evolution of the 1st time series for the compilation of $\delta^{18}\text{O}$ time series is

interpreted in a way that increasing values correspond to a cooling and decreasing values to a warming. In combination with the spatio-temporal coherence pattern (Fig. 14.7 and 14.8) (considering the up-side-down effect, denoted by the "+" and "-" in the figures) a warming was present in the time between 1.5 and 0.8 ka BP in Central and Northern Europe. Between 0.8 and 0.5 ka BP a warming occurred in Western Europe, whereas the temperatures in Central and Eastern Europe were cooling. During the last 500 years a warming happen in Northern-, Central and the eastern part of Central Europe, whereas the temperatures Western Europe and Northern Turkey were cooling.

18

Summary

1) The adaptability of Principal Component Analysis on speleothem proxy time series (Chapter 10):

Within this framework a method has been developed that allows to apply Principal Component Analysis on speleothem proxy time series. The method is based on a Monte Carlo approach and accounts for the speleothem age uncertainty and the different temporal resolutions of speleothem proxy time series. Furthermore, beside the Preisendorfer's Rule N significance criteria (Preisendorfer and Mobley, 1988) for Principal Components a new significance criteria is established and is called "Fork-took". The Fork-took is based on the sensitivity of the correlation between the PC time series and the original speleothem proxy time series. It indicates if the speleothem proxy time series are correlated with PC time series.

2) The big debate on the oxygen isotope fractionation factor $^{18}\alpha_{\text{calcite}/\text{H}_2\text{O}}$ of Kim and O'Neil (1997) (Chapter 9):

Since Coplen (2007) questioned the applicableness of the oxygen isotope fractionation factor $^{18}\alpha_{\text{calcite}/\text{H}_2\text{O}}$ of Kim and O'Neil (1997) for cave deposits a big debate stated on whether $^{18}\alpha_{\text{calcite}/\text{H}_2\text{O}}$ describes the speleothem oxygen isotope fractionation between water and calcite inside caves or not. It is demonstrated here that the observed offset between theoretical equilibrium $\delta^{18}\text{O}$ values and observed $\delta^{18}\text{O}$ values can be an artefact caused by the sampling method. The theoretical equilibrium $\delta^{18}\text{O}$ values are calculated from water samples inside the cave and the cave air temperature by using the oxygen isotope fractionation factor $^{18}\alpha_{\text{calcite}/\text{H}_2\text{O}}$ of Kim and O'Neil (1997) (Tremaine et al., 2011; McDermott et al., 2011; Johnston et al., 2013). The artefact is caused by the occurrence of Prior Calcite Precipitation either within the karst zone and/or on the cave ceiling. The Prior Calcite Precipitation induces an enrichment of ^{18}O in the oxygen isotope composition of HCO_3^- . This change of the oxygen isotope composition of HCO_3^- can not be detected with the usual sampling procedure of cave drip waters. The calculated oxygen isotope fractionation

factor $^{18}\alpha_{\text{calcite}/\text{H}_2\text{O}}$ from the calcite and cave drip water is higher due to Prior Calcite Precipitation. This can be a reason for the observed offset between the observed shift between the oxygen isotope fractionation factor $^{18}\alpha_{\text{calcite}/\text{H}_2\text{O}}$ of [Kim and O'Neil \(1997\)](#) and that calculated from calcite and cave drip waters.

3) The relationship between the precipitation winter $\delta^{18}\text{O}$ (δD) gradient and the North Atlantic Oscillation (Chapter 11):

In analogy to [Rozanski et al. \(1982\)](#) a multi-box Rayleigh approach model has been developed, the "Stable Isotopes in Precipitation" model, that allows to calculate the stable isotope composition of the precipitation, the infiltrated water and of calcite (for equilibrium isotope fractionation). It is demonstrated that the results of the Stable Isotopes in Precipitation model agree with observed stable isotope values of the precipitation for a Central European Transect and a Northern European transect. The observed stable isotope values of the precipitation are data from the GNIP dataset. The separation of the precipitation stable isotope values from the GNIP dataset (observed values) for positive and negative NAO phases has revealed that the observed $\delta^{18}\text{O}$ gradient in precipitation along a West-East transect is a function of the NAO - those years where the winter NAO index is either >0.8 or <0.8 are analysed. This relationship is interpreted as a change of the amount of moisture in the atmosphere. During a positive NAO phase more moisture is in atmosphere in Central Europe whereas during a negative NAO phase less moisture is in the atmosphere.

4) The interpretation of the speleothem $\delta^{18}\text{O}$ gradient during the Holocene (Sec. 17.1):

[McDermott et al. \(2011\)](#) observed for 100 year time slices taken in 1000 year intervals of European speleothem $\delta^{18}\text{O}$ time series a linear relationship. Furthermore, [McDermott et al. \(2011\)](#) demonstrated that the $\delta^{18}\text{O}$ gradients along a West-East transect are changing during the Holocene with steeper $\delta^{18}\text{O}$ gradients in the early-Holocene. The Stable Isotopes in Precipitation model is used to make a quantitative analysis of the $\delta^{18}\text{O}$ gradients. The results suggest that there was less moisture in the atmosphere arriving at the western margin of the European Continent during the early-Holocene and that the amount of moisture increases until 4 ka BP. Furthermore, a change of the atmospheric circulation occurred during the early- and mid-Holocene (11 ka until 4 ka). The transition is from a possibly very weak NAO like pattern (11 ka) to a very strong NAO like pattern (4 ka). After 4 ka a reorganisation of the atmospheric circulation happened and the present-day North Atlantic Oscillation pattern established.

5) The interpretation of the spatio-temporal coherence pattern between 1st PC and speleothem proxy time series (Sec. 17.2):

Principal Component Analysis was applied on several compilations of European speleothem $\delta^{18}\text{O}$ and $\delta^{13}\text{C}$ time series. The compilations were analysed for their long-term and short-term spatio-temporal coherency. It is demonstrated that for most cases only the 1st PC is significant. The related 1st PC time series can be interpreted as a temperature proxy for the compilation of $\delta^{18}\text{O}$ time series and as precipitation/hydrological proxy for the compilation

of $\delta^{13}\text{C}$ time series. The short-term analysis allow to uncover the spatio-temporal change of the coherence of the investigated speleothem $\delta^{18}\text{O}$ and $\delta^{13}\text{C}$ time series and demonstrate that the pattern are changing with time. Moreover, the spatio-temporal coherence pattern have different predominant patterns between 8.0 ka BP and 4 ka BP and 4.0 ka BP and 0 ka BP suggesting a possible change of (latent) heat transfer and consequently of the temperature (for the $\delta^{18}\text{O}$ time series) and the precipitation pattern (for the $\delta^{13}\text{C}$ time series). This can be also interpreted as a change in the atmospheric circulation and is supported by the finding of Sec. 17.1.



19

Outlook

Aim a): An independent interpretation of the spatio-temporal coherence pattern

The computed and physically interpreted spatio-temporal coherence pattern must be validated by independent palaeo climate proxies (e.g. pollen) to proof whether the recorded changes are only observed by speleothem proxy time series or by other palaeo climate archives, too.

Aim b): Expansion of the spatial and temporal coverage:

The speleothems used for the Principal Component Analysis are only covering central parts of Europe (Austria, Germany, Ireland, Italy, Romania, Sweden, Spain, Turkey) . However, to test if the computed PC time series are also valid for other parts of Europe (Eastern Europe, Mediterranean) further records must be analysed.

Aim c): Down-scaling of the spatial coverage:

PCA allows spatio-temporal coherence analysis of particular regions which are influenced by different hydrological cycles. One possible region are the Alps that might be influenced by the hydrological cycle of the Mediterranean as well as that of Central Europe.

Aim d): Up-scaling of the spatial coverage:

PCA allows also spatio-temporal coherence analysis of *(i)* other continents but *(ii)* also for the interconnection of different regions.

Aim e): Independent validation of the atmospheric circulation transition and reorganisation:

The suggested transition and reorganisation of the atmospheric circulation must be proofed with *(i)* independent palaeo climate proxies on the continent (e.g. pollen, lake sediments)

and of the Atlantic ocean (e.g. deep sea corals) and (ii) should be tested applying General Circulation Models.

Appendices

A

Distribution of r_s values for analysed $\delta^{18}\text{O}$ time series for the PCA chapter

time window: 0.7-7.8 ka BP - Part I

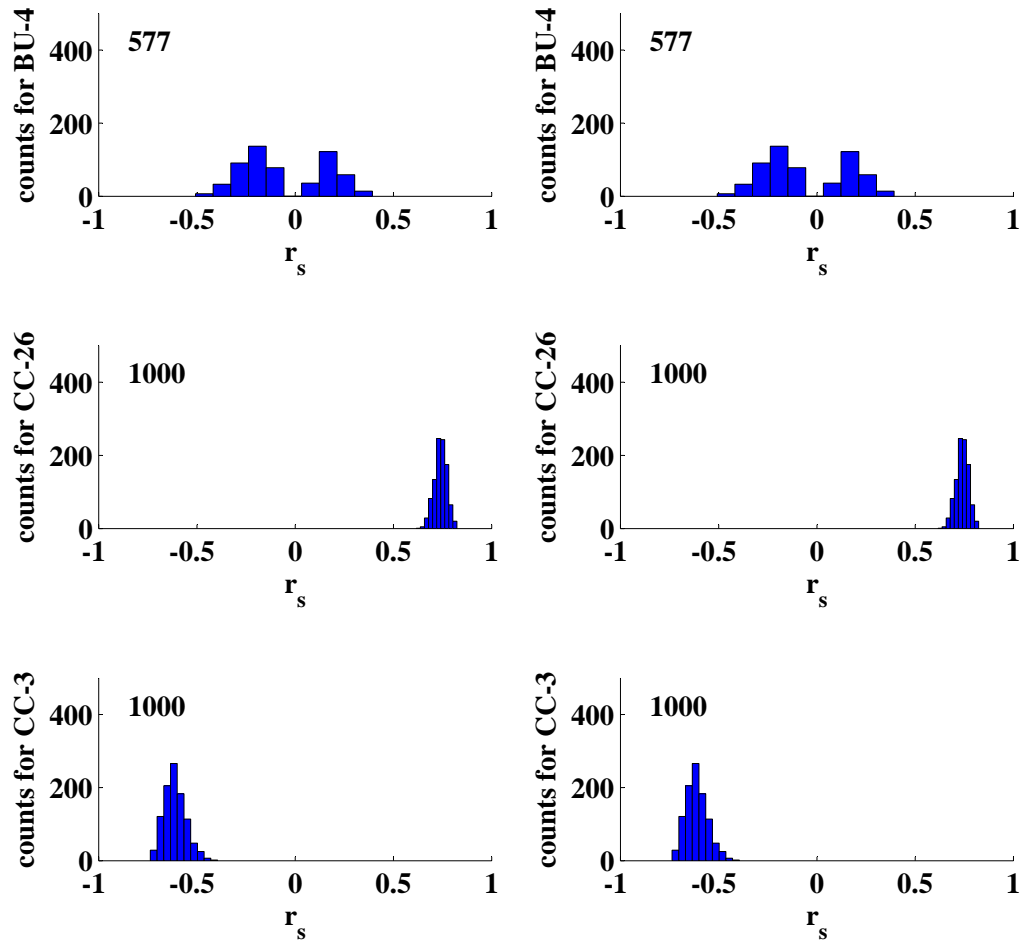


Fig. A.1: Illustrated is the distribution of speleothem r_s values for the time window between 0.7 ka BP and 7.8 ka BP. The left panels illustrates the distribution of r_s values before the application of the Fork-tool and the right panels after the application of the Fork-tool.

time window: 0.7-7.8 ka BP - Part II

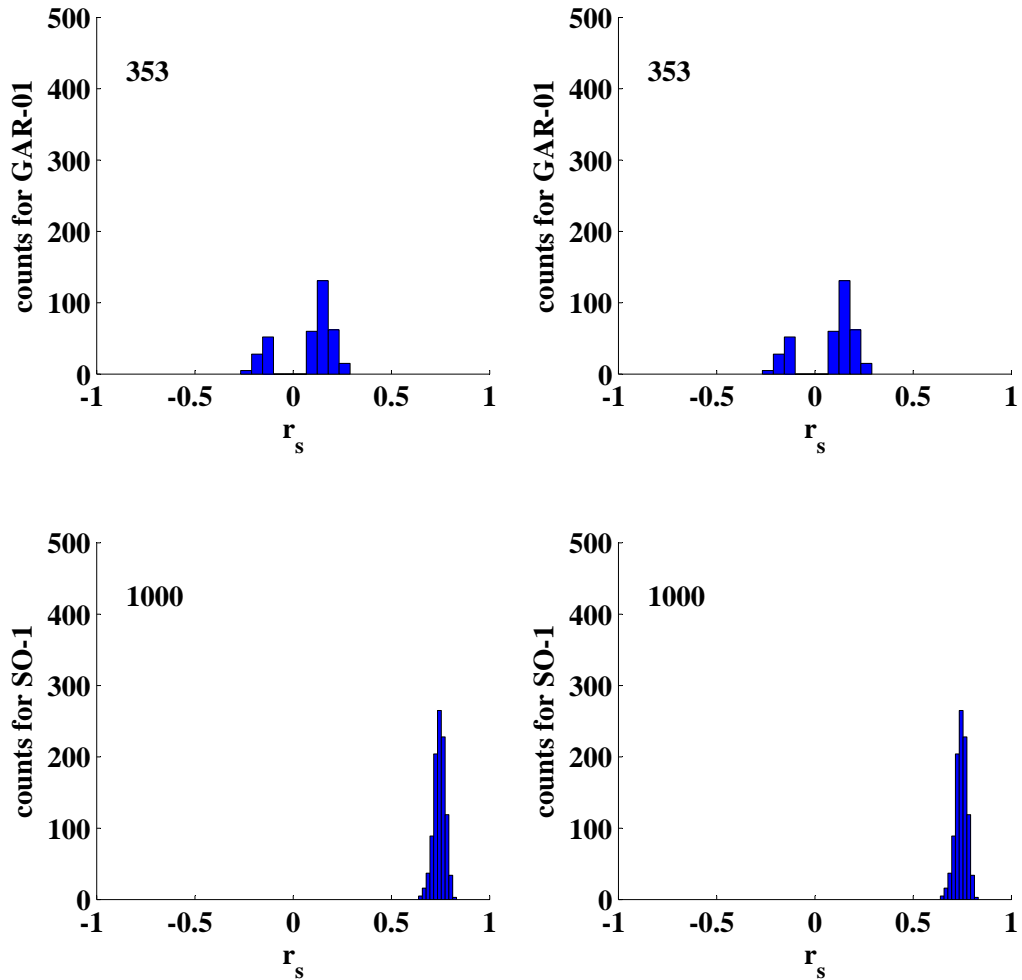


Fig. A.2: Illustrated is the distribution of speleothem r_s values for the time window between 0.7 ka BP and 7.8 ka BP. The left panels illustrates the distribution of r_s values before the application of the Fork-tool and the right panels after the application of the Fork-tool.

time window: 4-7.8 ka BP - Part I

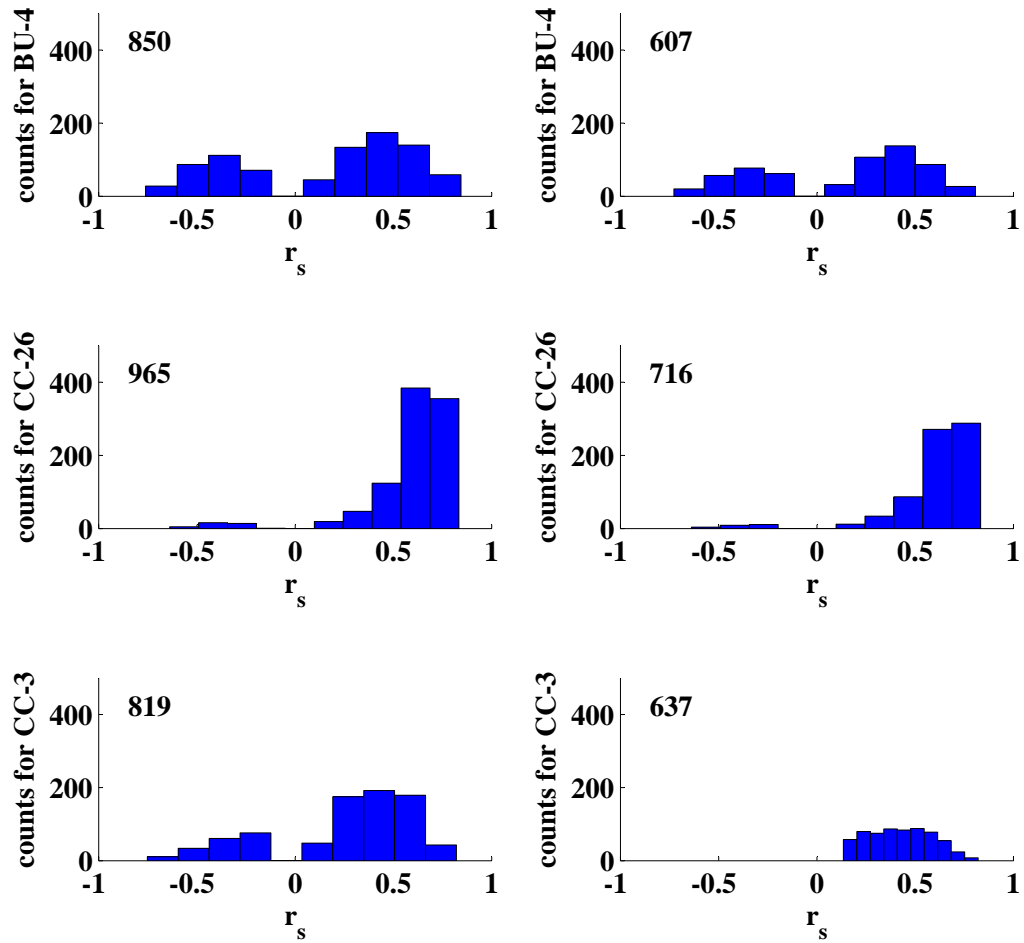


Fig. A.3: Illustrated is the distribution of speleothem r_s values for the time window between 4.0 ka BP and 7.8 ka BP. The left panels illustrates the distribution of r_s values before the application of the Fork-tool and the right panels after the application of the Fork-tool.

time window: 4-7.8 ka BP - Part II

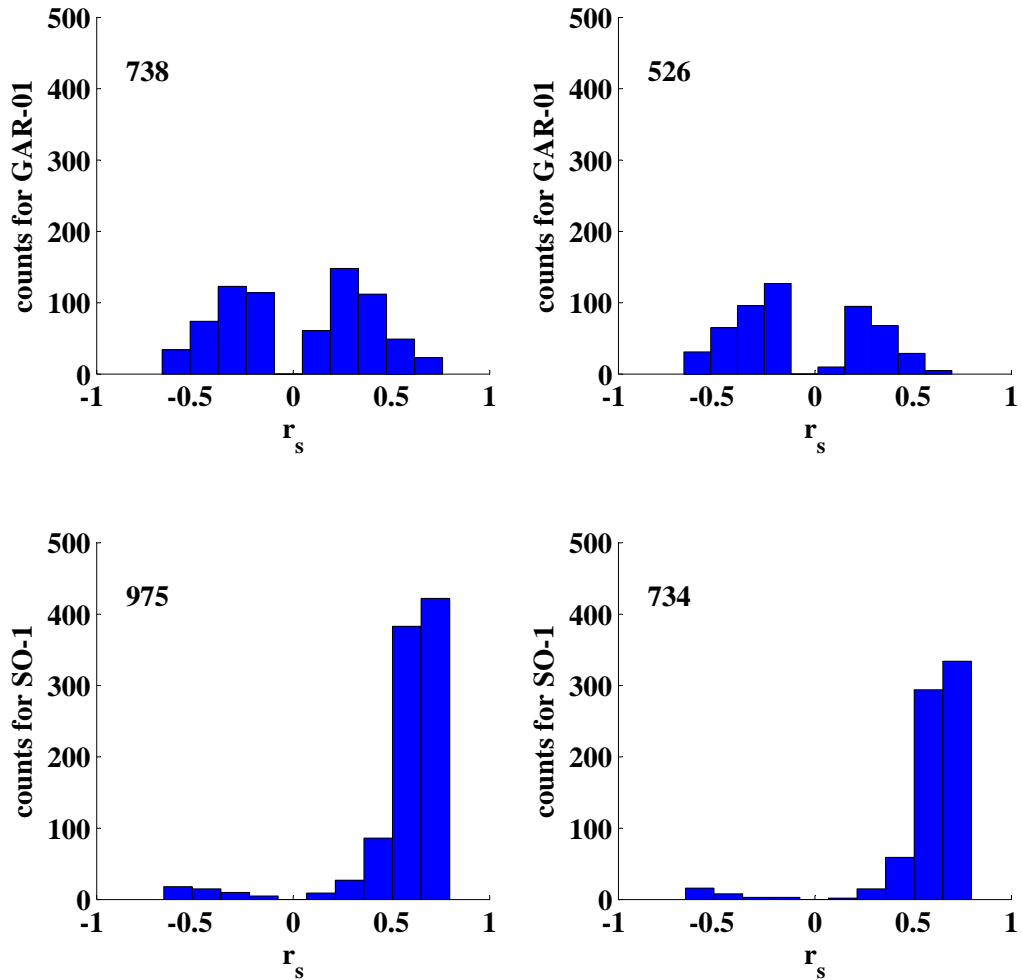


Fig. A.4: Illustrated is the distribution of speleothem r_s values for the time window between 4.0 ka BP and 7.8 ka BP. The left panels illustrates the distribution of r_s values before the application of the Fork-tool and the right panels after the application of the Fork-tool.

time window: 4-5 ka BP - Part I

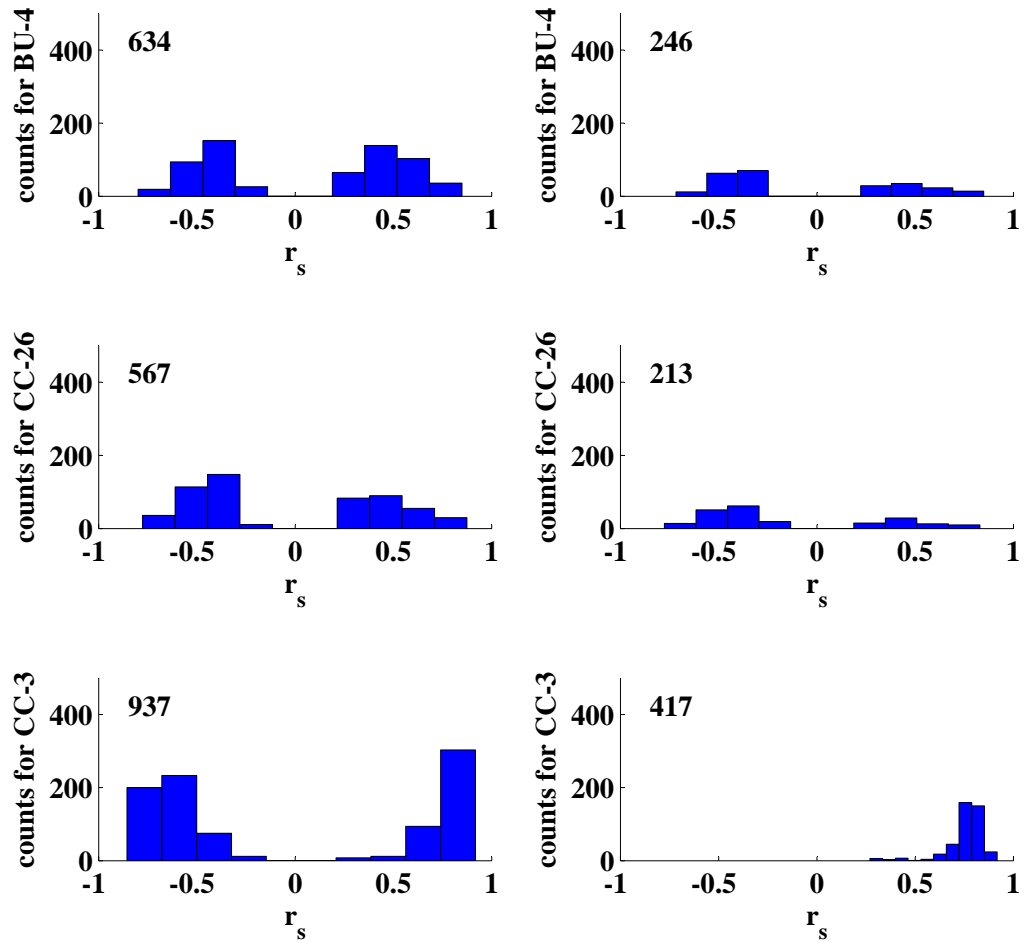


Fig. A.5: Illustrated is the distribution of speleothem r_s values for the time window between 4.0 ka BP and 5.0 ka BP. The left panels illustrates the distribution of r_s values before the application of the Fork-tool and the right panels after the application of the Fork-tool.

time window: 4-5 ka BP - Part II

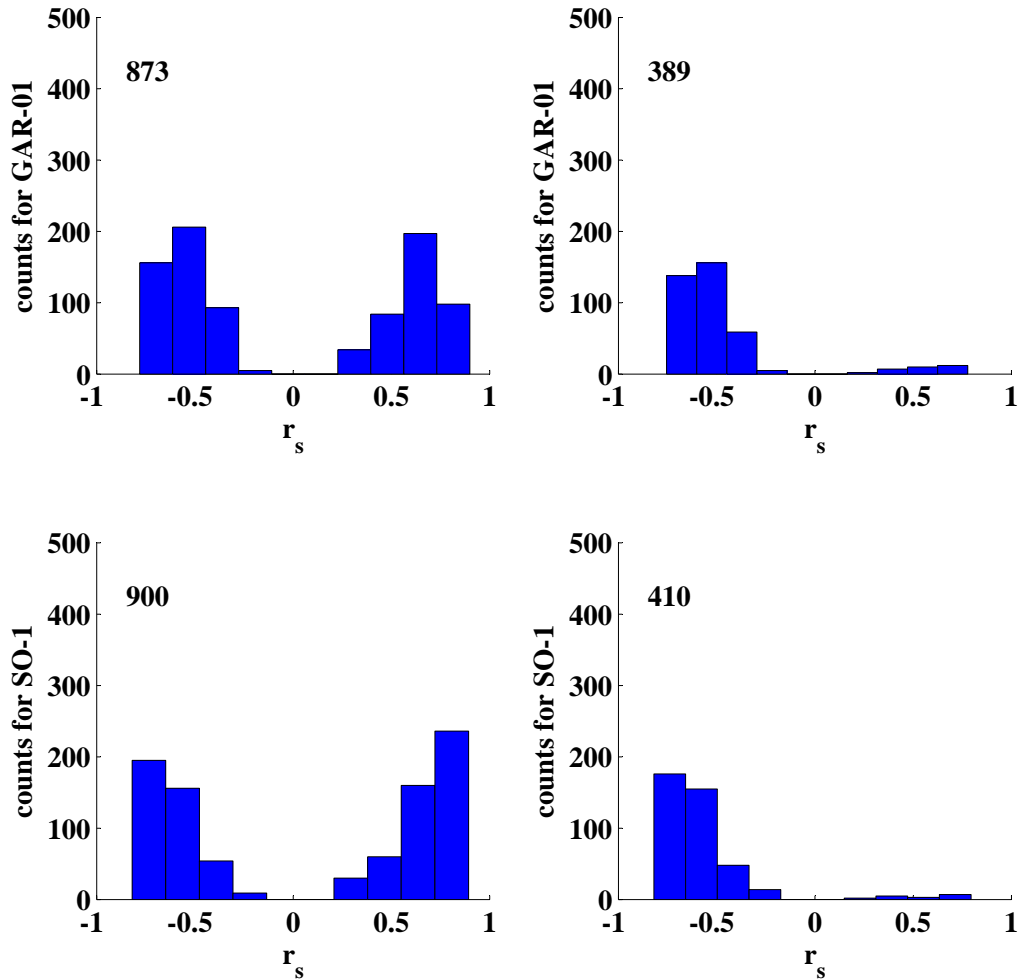


Fig. A.6: Illustrated is the distribution of speleothem r_s values for the time window between 4.0 ka BP and 5.0 ka BP. The left panels illustrates the distribution of r_s values before the application of the Fork-tool and the right panels after the application of the Fork-tool.

time window: 4-4.33 ka BP - Part I

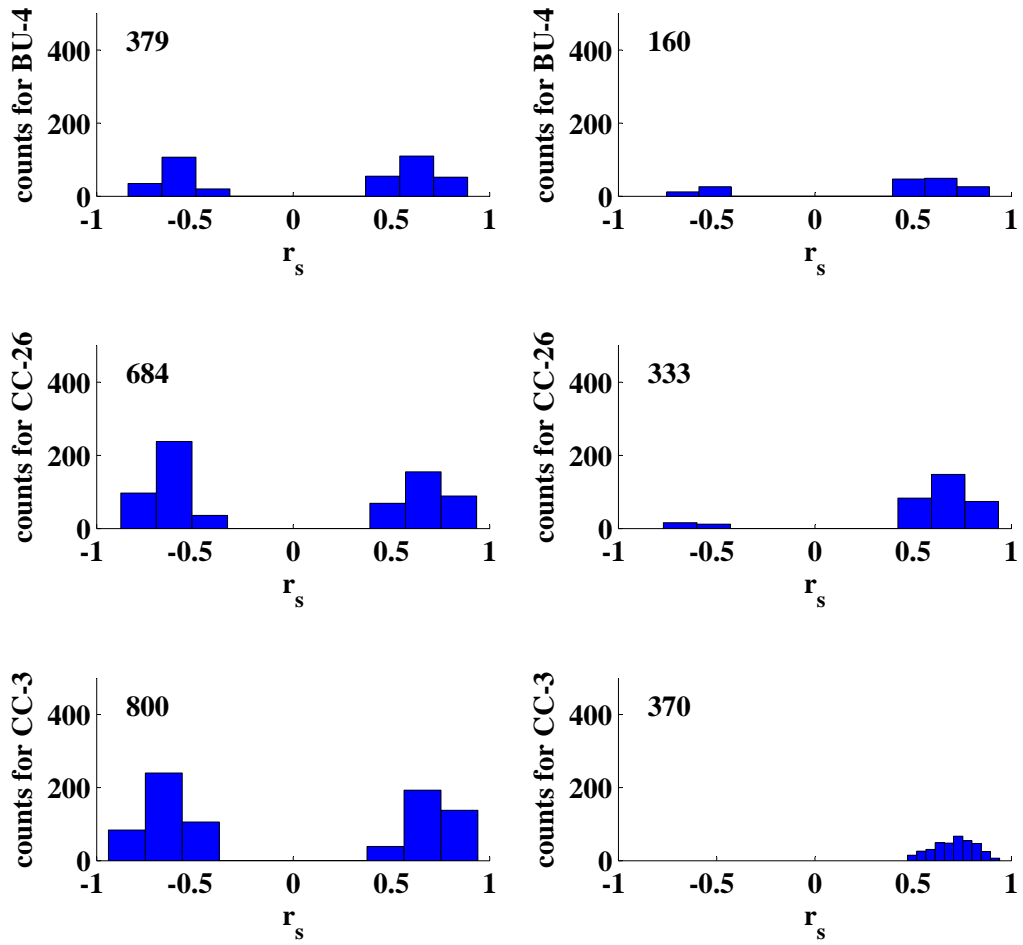


Fig. A.7: Illustrated is the distribution of speleothem r_s values for the time window between 4.0 ka BP and 4.33 ka BP. The left panels illustrates the distribution of r_s values before the application of the Fork-tool and the right panels after the application of the Fork-tool.

time window: 4-4.33 ka BP - Part II

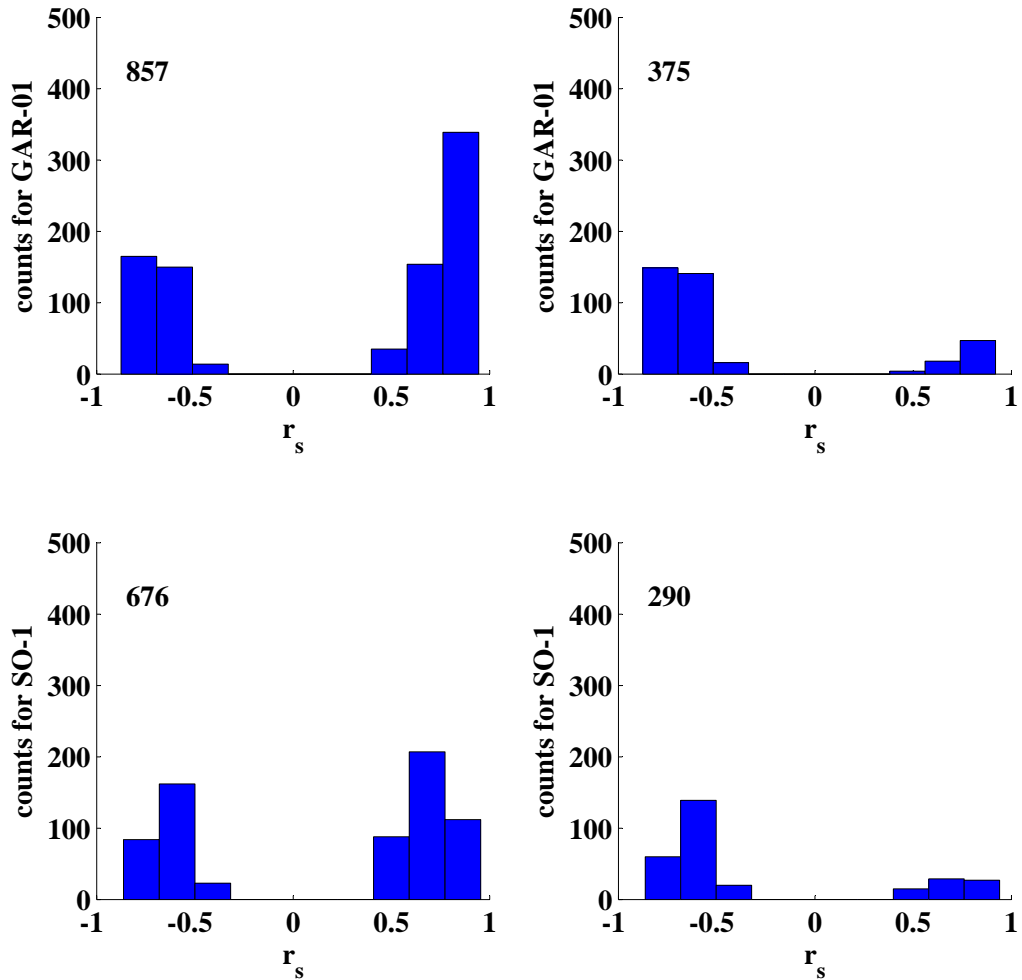


Fig. A.8: Illustrated is the distribution of speleothem r_s values for the time window between 4.0 ka BP and 4.33 ka BP. The left panels illustrates the distribution of r_s values before the application of the Fork-tool and the right panels after the application of the Fork-tool.

time window: 4.33-4.66 ka BP - Part I

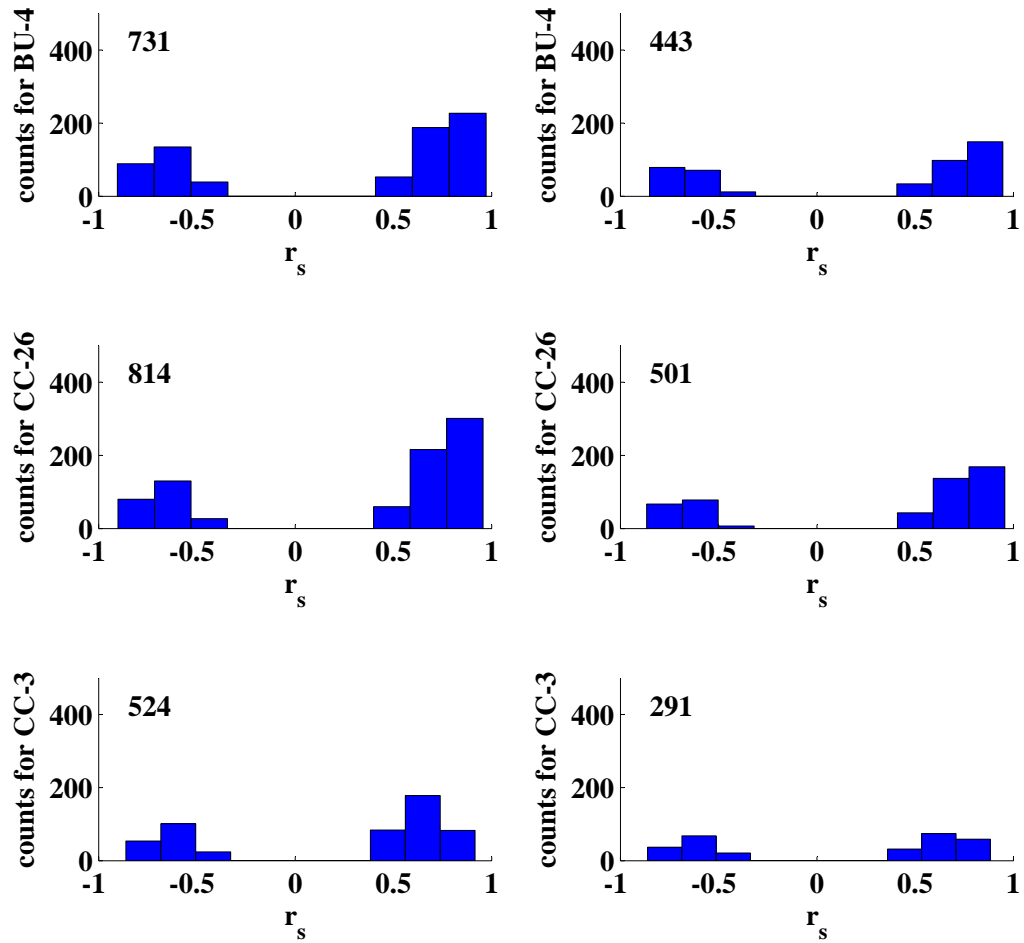


Fig. A.9: Illustrated is the distribution of speleothem r_s values for the time window between 4.33 ka BP and 4.66 ka BP. The left panels illustrates the distribution of r_s values before the application of the Fork-tool and the right panels after the application of the Fork-tool.

time window: 4.33-4.66 ka BP - Part II

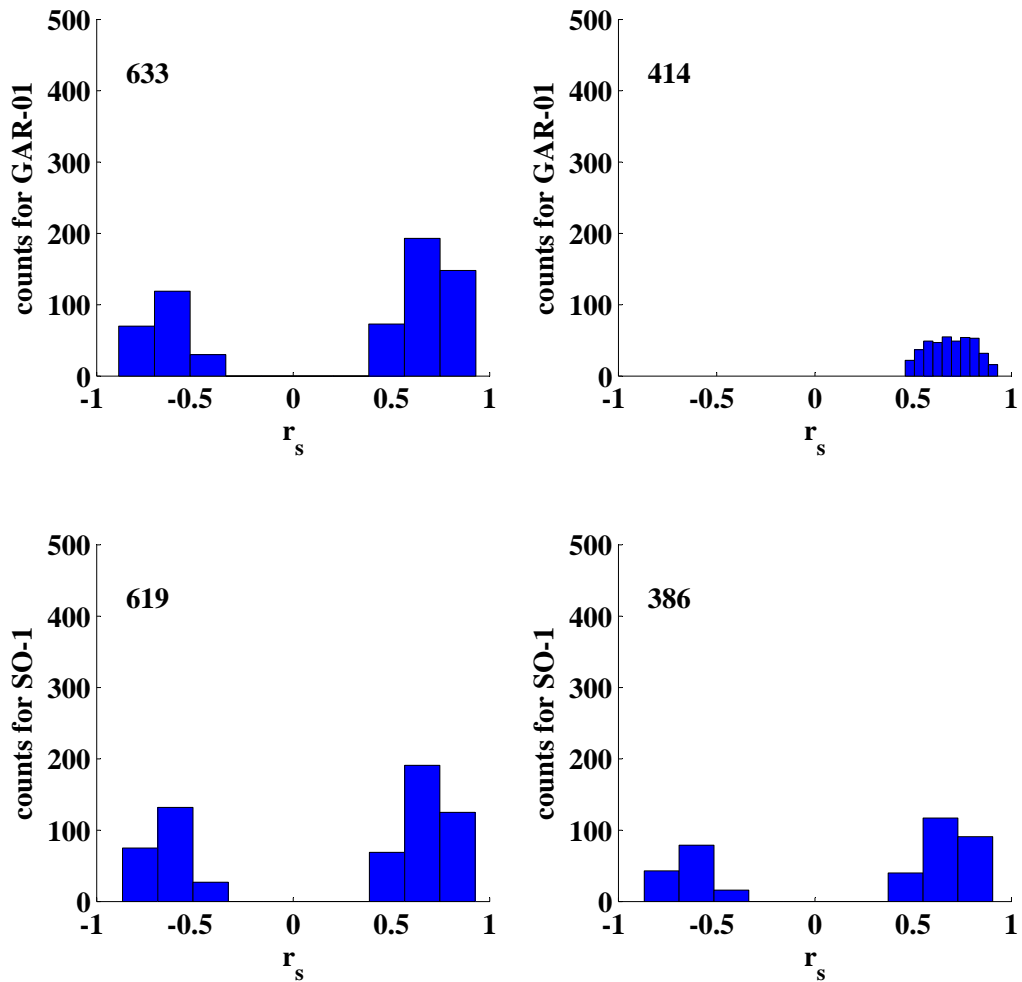


Fig. A.10: Illustrated is the distribution of speleothem r_s values for the time window between 4.33 ka BP and 4.66 ka BP. The left panels illustrates the distribution of r_s values before the application of the Fork-tool and the right panels after the application of the Fork-tool.

time window: 4.66-5.0 ka BP - Part I

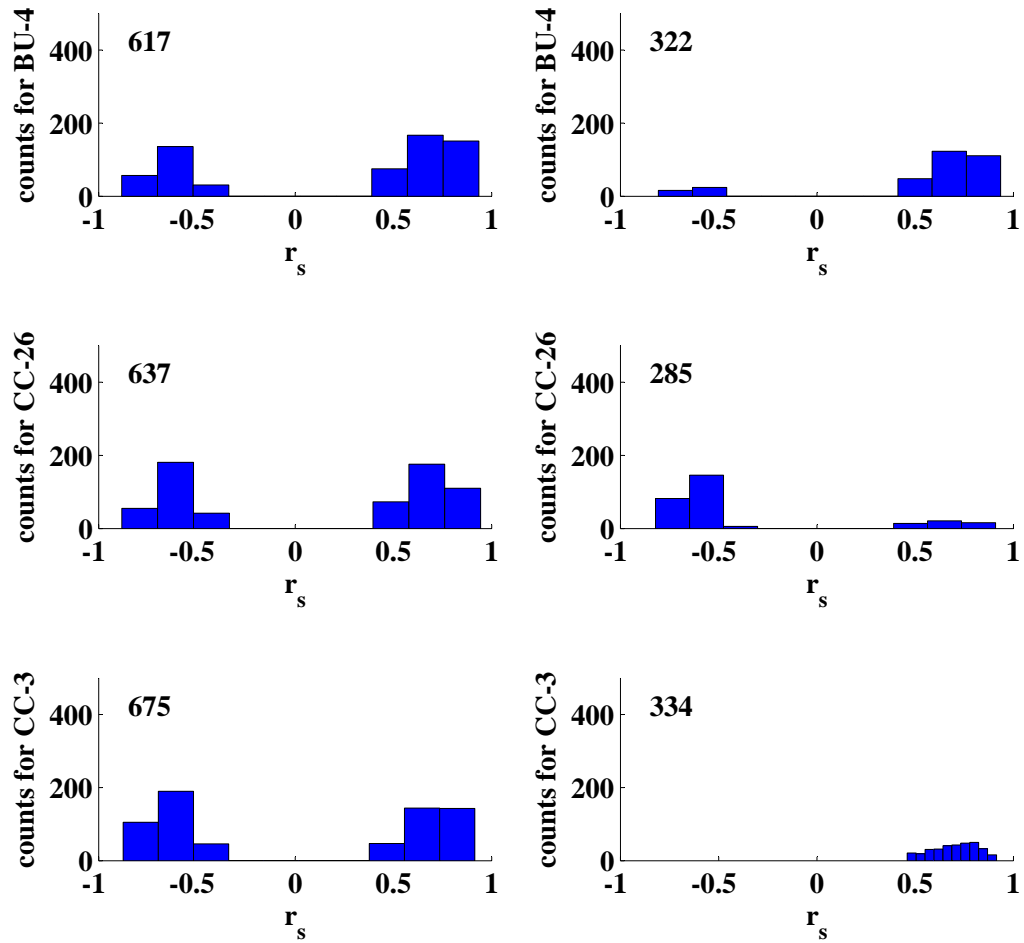


Fig. A.11: Illustrated is the distribution of speleothem r_s values for the time window between 4.66 ka BP and 5.0 ka BP. The left panels illustrates the distribution of r_s values before the application of the Fork-tool and the right panels after the application of the Fork-tool.

time window: 4.66-5.0 ka BP - Part II

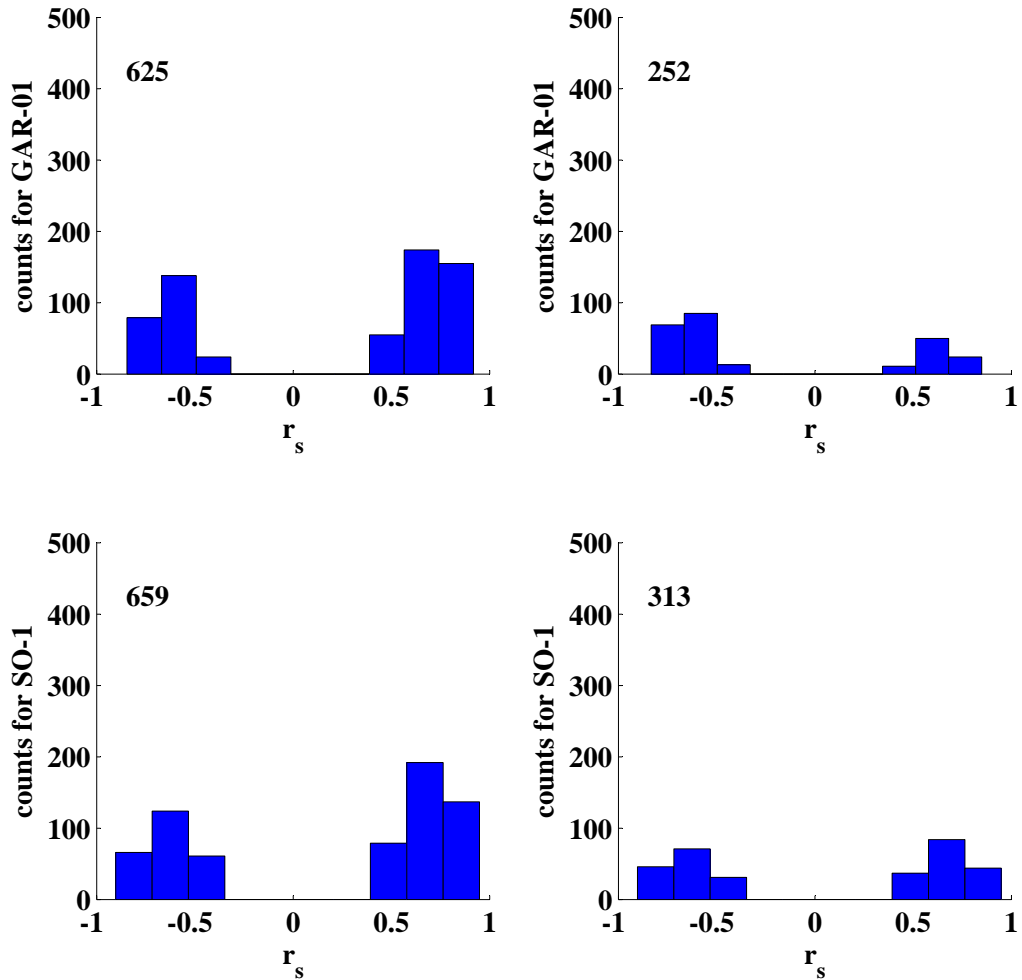


Fig. A.12: Illustrated is the distribution of speleothem r_s values for the time window between 4.66 ka BP and 5.0 ka BP. The left panels illustrates the distribution of r_s values before the application of the Fork-tool and the right panels after the application of the Fork-tool.

B

Model parameters for the SIP model for the transects T1 and T2

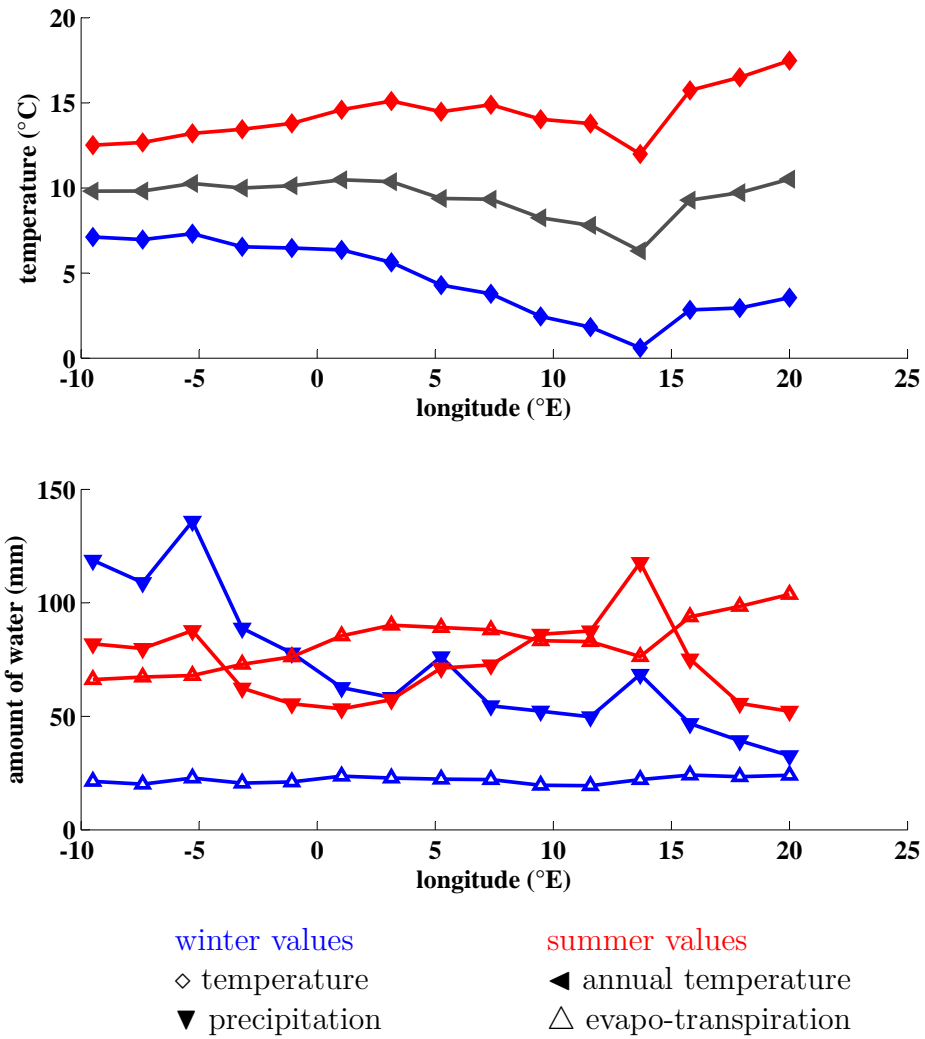


Fig. B.1: The figure shows the winter (blue) and summer (red) for the temperature (diamond) (upper panel), the precipitation (up-side-down triangle) and evaporation (triangle) (lower panel) for the transect T1. The black line in the upper panel pictures the mean annual air temperature.

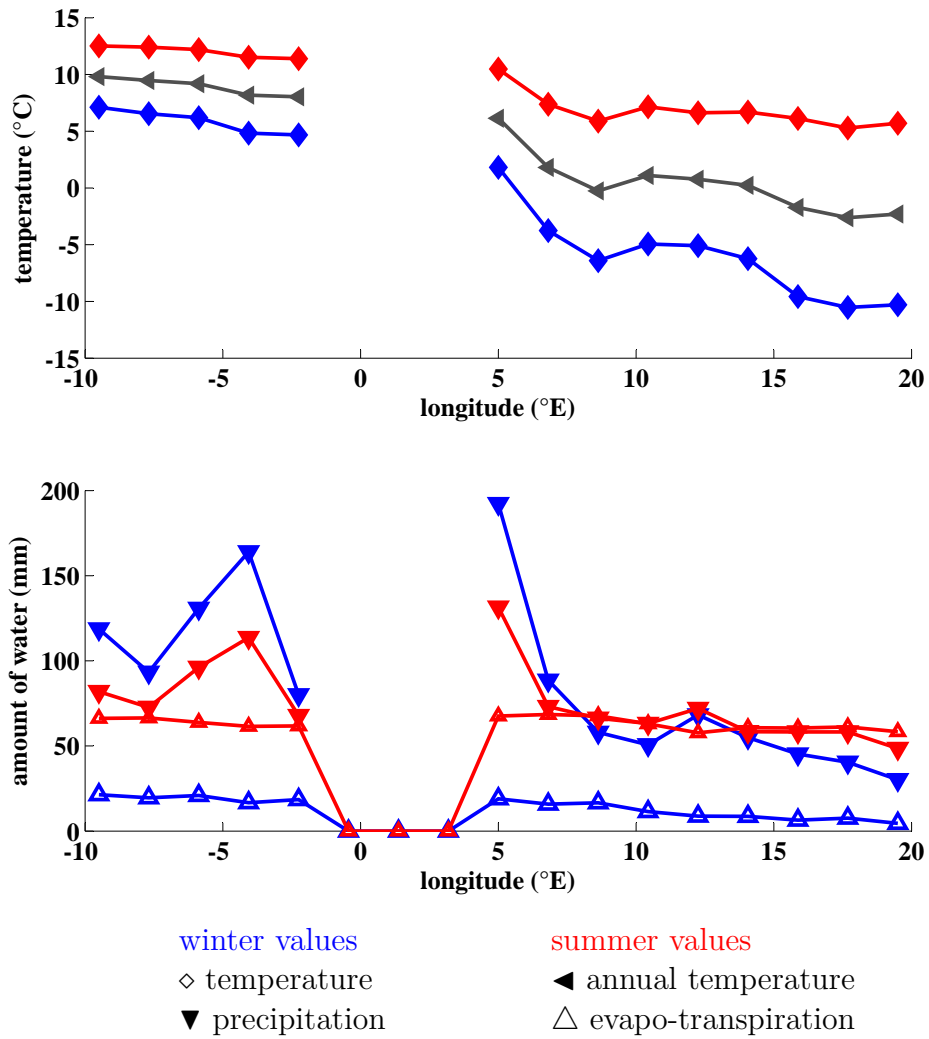


Fig. B.2: The figure shows the winter (blue) and summer (red) for the temperature (diamond) (upper panel), the precipitation (up-side-down triangle) and evaporation (triangle) (lower panel) for the transect T2. The black line in the upper panel pictures the mean annual air temperature.

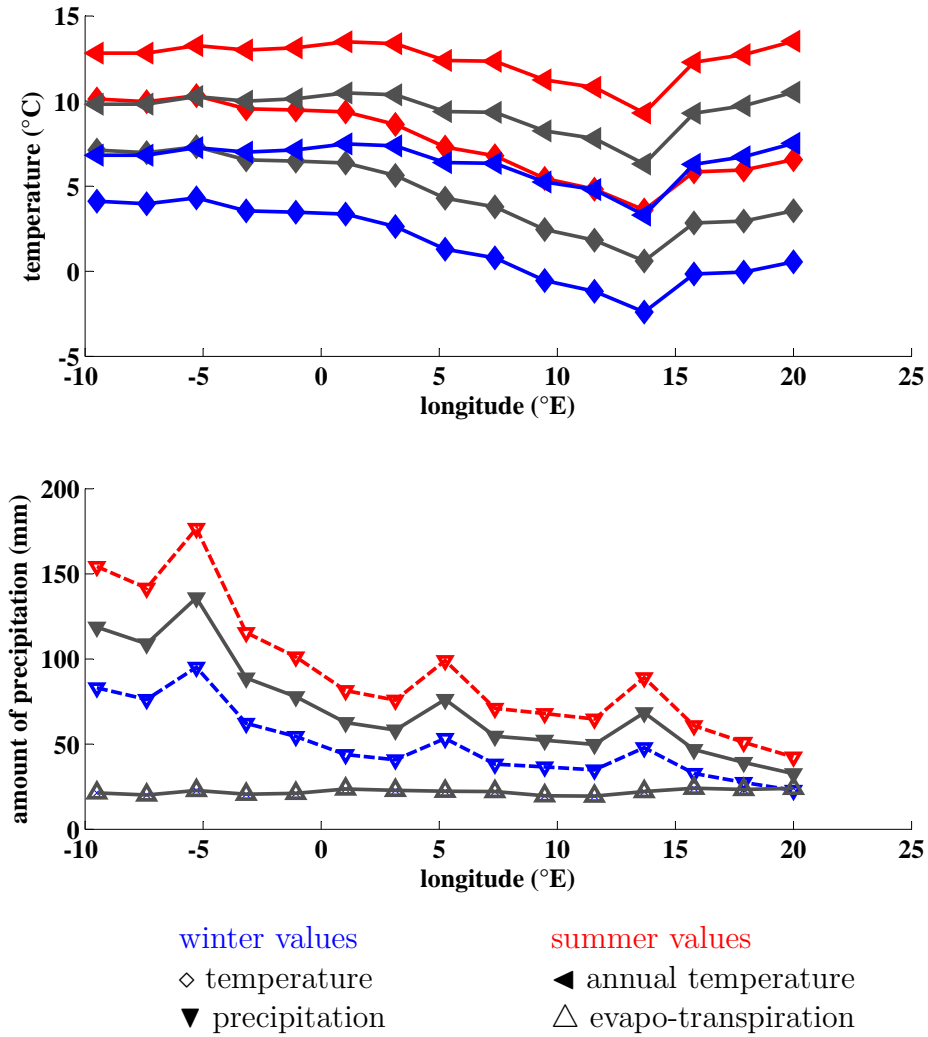


Fig. B.3: (upper panel) Illustrated are the winter temperature triangle and the mean annual temperature (diamond) for the reference scenario (black), the +3 °C scenario (red) and the -3 °C scenario (blue) with respect to the reference scenario. (lower panel) Illustrated is the precipitation (up-side-down triangle) and evapo-transpiration (triangle) for the reference scenario (black). The blue curve is picturing the amount of precipitation for the -30 % scenario; the red curve depicts the amount of precipitation for the +30 % scenario.

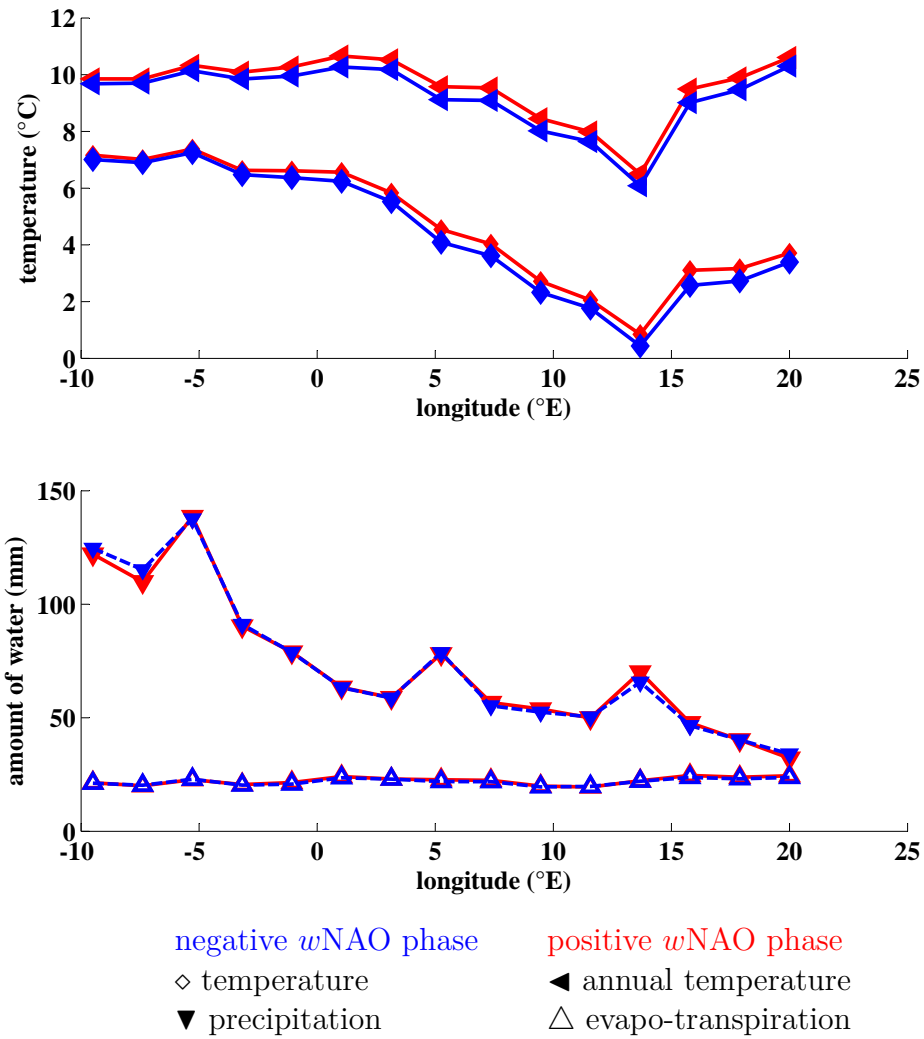


Fig. B.4: (upper panel) Illustrated is the temperature along the transect T1 for positive (red) and negative (blue) NAO phases. Diamonds are winter temperatures (October-March) whereas the triangles depict the mean annual temperatures in the period from October-September for the selected years. (lower panel) Depict is the precipitation (up-side-down triangle) and the evapo-transpiration (triangle) for the transect T1 for positive (red) and negative (blue) NAO phases. Only those years were selected during which the winter NAO index is either > 0.8 or < 0.8 .

C

Holocene European speleothems

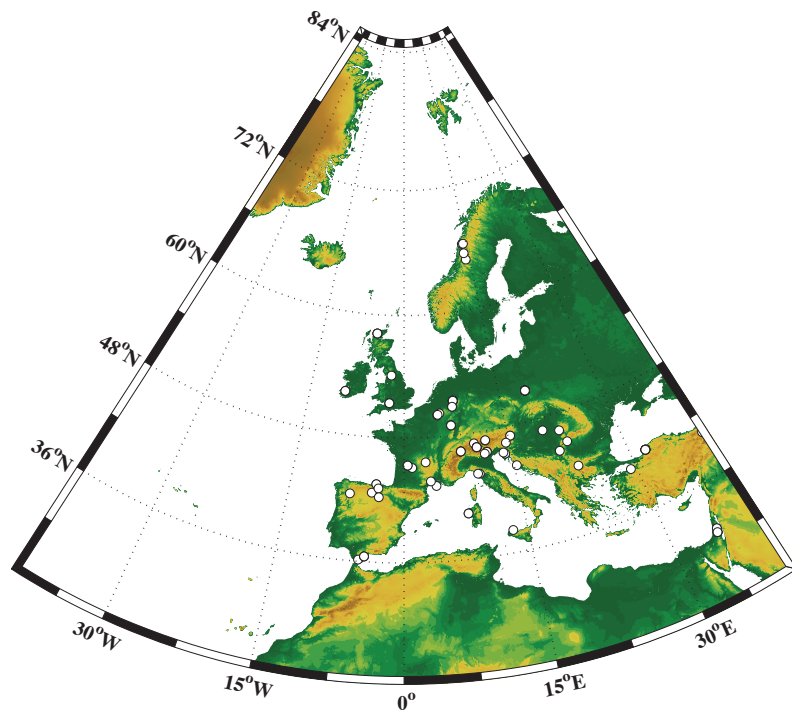


Fig. C.1: Map of speleothems studies that are investigating speleothems in Europe since 1995 based on the data compilation of (Dambach, 2012). The investigated studies are listed in Tab. C.1-C.4.

name	cave	longitude	latitude	altitude	actual cave	growth	growth	dating	proxies	reference
					air temperature	stop	begin			
		°E	°N	(m)	(°C)	(ka BP)	(ka BP)	method		
2p	Akcakale Cave	40,26	39,32	1530		0,244	0,244	Laminae counting/TIMS	$\delta^{18}\text{O}$, $\delta^{13}\text{C}$	
AH-1	Atta Cave	50,8	7,44	308	9,4	0,86	8,43	TIMS	$\delta^{18}\text{O}$	
BFM-9	Browns Folly Mine	51,39	-2,29	180	10	-0,048	0,022	Laminae counting/MS	$\delta^{18}\text{O}$, $\delta^{13}\text{C}$	
BFM-Boss	Browns Folly Mine	51,39	-2,29		10	-0,046	0,034	visual stratigraphy/Laminae counting/MS	$\delta^{18}\text{O}$, $\delta^{13}\text{C}$	
BU-1	Bunker Cave	51,37	7,67	184	10,8	0,137	6,645	TIMS	$\delta^{18}\text{O}$, $\delta^{13}\text{C}$	
BU-11	Bunker Cave	51,37	7,67	184	10,8	0,16	1,59 (120)	TIMS	$\delta^{18}\text{O}$, $\delta^{13}\text{C}$	
BU-12	Bunker Cave	51,37	7,666	184	10,8	4,72 (0,18)	6,7 (120)	TIMS	$\delta^{18}\text{O}$, $\delta^{13}\text{C}$	
BU-2	Bunker Cave	51,37	7,666	184	10,8	7,49	10,71	TIMS	$\delta^{18}\text{O}$, $\delta^{13}\text{C}$	
BU-4	Bunker Cave	51,37	7,666	184	10,8	-0,6	8,16	TIMS	$\delta^{18}\text{O}$, $\delta^{13}\text{C}$	
BU-6	Bunker Cave	51,37	7,666	184	10,8	8,74	10,25	TIMS	$\delta^{18}\text{O}$, $\delta^{13}\text{C}$	
C-1-10	Mt Cornadore Cave	45,58	2,98			0,0065	0,087	$^{226}\text{Ra}/^{210}\text{Pb}$		
C-11	Cueva del Cobre	42,59	-4,22	1640	5,5	-0,05	3,899	MC-ICP-MS	$\delta^{13}\text{C}$	
C.1	Ciemnea	51,01	19,09			0,65	9	14C	$\delta^{13}\text{C}$	
C.2	Ciemnea	51,01	19,09			0,63	5,86	14C	$\delta^{13}\text{C}$	
C09-2	Closani Cave	45,07	22,79	80	11	-0,30	c. 4	TIMS	$\delta^{18}\text{O}$, $\delta^{13}\text{C}$	
Candela	El Pindal Cave	43,23	4,3	24	12	8,663	15,394	14C	$\delta^{13}\text{C}$	
CC-26	Corchia Cave	44,00	10,22	1300	7,5	0,75	11,26	MC-ICP-MS	$\delta^{18}\text{O}$, $\delta^{13}\text{C}$	
CC-3	Crag Cave	52,23	-9,44	60	10,4	-0,05	10,1	TIMS/MC-ICP-MS?	$\delta^{18}\text{O}$, $\delta^{13}\text{C}$	
CC-Bil	Crag Cave	52,23	-9,44	60	10,4	-0,052	0,198	visual stratigraphy/MC-ICP-MS		
CL-26	Clamouse Cave	43,70	3,6	75	14,5	0,282	11,127	TIMS	$\delta^{18}\text{O}$, $\delta^{13}\text{C}$	
COM-BU	Bunker Cave	51,37	7,67		c. 10	-0,6	10,72	TIMS/Correlation	$\delta^{18}\text{O}$	
COMNISPA2	Spannagel Cave	47,08	11,67	2165	2,4	-0,014	9,93	TIMS/Correlation	$\delta^{18}\text{O}$	
CPV-B-6	Cova des Pas de Vallgornera	43,57	48,91	2,6		0,1206	0,1206	TIMS		
CPV-B-9	Cova des Pas de Vallgornera	43,57	48,91	2,6		0,1162	0,1162	TIMS		
CR-1	Carburangeli Cave	38,15	13,2	22	19,4	1,115	9,87	Laminae counting/TIMS?	$\delta^{18}\text{O}$, $\delta^{13}\text{C}$	
D.1	Dziewicza Cave	51,01	19,09			1,74	3,98	14C	$\delta^{13}\text{C}$	
DI-D1-2	Cova del Dimoni	43,77	53	2,5		0,1184	0,1184	MC-ICP-MS		
DiI-D3	Cova del Dimoni	43,77	53	2,5		0,1142	0,1142	MC-ICP-MS		

Tab. C.1: The table is a compilation of European speleothem studies that are illustrated in Fig. C.1.

name	cave	longitude °E	latitude °N	altitude (m)	actual cave	growth	growth	dating method	proxies	reference
					air temperature	stop	begin			
					(°C)	(ka BP)	(ka BP)			
ER-76	Grotta di Ernesto	45,97	11,65	1167	6,6	0	8,06	visual stratigraphy/TIMS	$\delta^{18}O$, $\delta^{13}C$	
ER-77	Grotta di Ernesto	45,97	11,65	1167	6,6	-0,042	0,563	visual stratigraphy		
ER-78	Grotta di Ernesto	45,97	11,65	1167	6,6	-0,05	0,049	visual stratigraphy		
ESP-03	Cova da Arcoia	42,36	-7,05	1240		-0,01	9,29	MC-ICP-MS	$\delta^{18}O$, $\delta^{13}C$	
F-2	Browns Folly Mine	51,39	-2,29		10	-0,048	0,019	Laminae counting/MS	$\delta^{18}O$, $\delta^{13}C$	
Fau-stm-14	La Faurie	45,08	1,11	225	12,9	-0,046	0,031	14C	$\delta^{13}C$	
GAR-01	Garma Cave	43,43	-3,66	75	12,1	-0,026	13,91		$\delta^{18}O$, $\delta^{13}C$	
GAR-02	Garma Cave	43,43	-3,66	75	12,1	-0,055	1,009		$\delta^{18}O$, $\delta^{13}C$	
GIB-04-a	New St Michae's Cave	36,15	-5,35	400	18,3	-0,054	-0,001		$\delta^{18}O$, $\delta^{13}C$	
GN-D3-2	Grotta di Nettuno	40,34	8,09	4,3		0,117	0,117	TIMS		
GN-D4	Grotta di Nettuno	40,34	8,09	4,3		0,120	0,120	TIMS		
GZ-1	Cogola di Giazzeria	45,85	11,33	1025		-0,044	4,434		$\delta^{18}O$, $\delta^{13}C$	
Ham-85-2	Hamarnes Cave	66,42	14,02	220	3,5	4,510	123	TIMS	$\delta^{18}O$, $\delta^{13}C$	
HAN-STM-5b	Han-sur-Lesse	50,08	5,1	180	8,9	-0,045	0	14C	$\delta^{18}O$, $\delta^{13}C$	
HLK-2	Herbstlabyrinth-Advent Cave					-0,06	ca. 13	TIMS	$\delta^{18}O$, $\delta^{13}C$	
K-11	Korallgrottan	64,88	14,15	570	2,7	-0,055	3,792	TIMS	$\delta^{18}O$, $\delta^{13}C$	
K.1	W. Kroczycach	51,01	19,09			2,56	3,69	14C	$\delta^{13}C$	
K1	Katerloch Cave	47,08	15,33	900	8	6,97	10,23	MC-ICP-MS	$\delta^{18}O$, $\delta^{13}C$	
K1 (2)	Karaca Cave	40,32	29,24	1536	12,7	5,96	77,33	MC-ICP-MS/TIMS?	$\delta^{18}O$, $\delta^{13}C$	
K3	Katerloch Cave	47,08	15,33	900	8	7,93	9,75	MC-ICP-MS	$\delta^{18}O$, $\delta^{13}C$	
L-03	Larshullet Cave	66,41	14,25	400	1,4	0,204	3,56	TIMS	$\delta^{18}O$, $\delta^{13}C$	
L.1	Lokietka Cave	51,01	19,09			0,84	20,5	14C	$\delta^{13}C$	
LH-70	Lancaster Hole	54,10	-2,1	294	10	3,572	12,78		$\delta^{18}O$, $\delta^{13}C$	
LV-5	Kaite Cave	43,02	-3,39	860	10,4	-0,05	3,899	MC-ICP-MS	$\delta^{13}C$	
MB-2	Milchbach Cave	46,37	8,05	1840	2,5	3,3	6,75	MC-ICP-MS	$\delta^{18}O$, $\delta^{13}C$	
MB-3	Milchbach Cave	46,37	8,05	1840	2,5	2,15	9,15	MC-ICP-MS	$\delta^{18}O$, $\delta^{13}C$	
MB-5	Milchbach Cave	46,37	8,05	1840	2,5	2,23	7,25	MC-ICP-MS	$\delta^{18}O$, $\delta^{13}C$	
MB-6	Milchbach Cave	46,37	8,05	1840	2,5	5,52	6,05	MC-ICP-MS	$\delta^{18}O$, $\delta^{13}C$	

Tab. C.2: The table is a compilation of European speleothem studies that are illustrated in Fig. C.1.

name	cave	longitude	latitude	altitude	actual cave air temperature	growth stop	growth begin	dating method	proxies	reference
		°E	°N	(m)	(°C)	(ka BP)	(ka BP)			
MOD-22	Modric Cave	44,15	15,32	32	12,9	0,37	1,619	14C/MC-ICP-MS	$\delta^{18}\text{O}$, $\delta^{13}\text{C}$	
N.1	Nietoperzowa Cave	51,01	19,09			4,71	6,57	14C	$\delta^{13}\text{C}$	
N.2	Nietoperzowa Cave	51,01	19,09			3,29	5,10	14C	$\delta^{13}\text{C}$	
Noname-1	Duhlata Cave	42,48	23,18	ca. 940		0	243,533	TIMS		
Noname-10	Pere Noel Cave	50,13	5,16	180	9,6	1,75	12,85	TIMS/MC-ICP-MS/14C	$\delta^{18}\text{O}$, $\delta^{13}\text{C}$	
Noname-11	Hotton Cave	50,25	5,45			2,75	11,15	TIMS/MC-ICP-MS/14C	$\delta^{18}\text{O}$, $\delta^{13}\text{C}$	
Noname-12	Höllach Cave	47	10	1440	3,5	1,38	12,69	TIMS	$\delta^{18}\text{O}$, $\delta^{13}\text{C}$	
O-1	Ovacik Cave	41,46	32,02			0,055	0,17	MC-ICP-MS	$\delta^{18}\text{O}$, $\delta^{13}\text{C}$	
Obi-84	Obir Cave	46,51	14,54	1100	5,7	-0,052	0,035	Laminae counting		
PFU-6	Klapferloch Cave	46,57	10,33	1140	ca. 4,8	-0,047	2,943	MC-ICP-MS	$\delta^{18}\text{O}$, $\delta^{13}\text{C}$	
PFU-7	Klapferloch Cave	46,57	10,33	1140	ca. 4,8	-0,047	2,943	MC-ICP-MS	$\delta^{18}\text{O}$, $\delta^{13}\text{C}$	
PFU-8	Klapferloch Cave	46,57	10,33	1140	ca. 4,8	-0,047	2,943	MC-ICP-MS	$\delta^{18}\text{O}$, $\delta^{13}\text{C}$	
PFU-9	Klapferloch Cave	46,57	10,33	1140	ca. 4,8	-0,047	2,943	MC-ICP-MS	$\delta^{18}\text{O}$, $\delta^{13}\text{C}$	
PN-75	Pere Noel Cave	50,13	5,16	180	9,6	2,41	13,22		$\delta^{18}\text{O}$, $\delta^{13}\text{C}$	
POS-STM-4	Postojna Cave	45,46	14,12	529	8	-0,046	0,008	14C	$\delta^{18}\text{O}$, $\delta^{13}\text{C}$	
PP-10	Poleva Cave	44,42	21,44	390	10,5	2,41	74,13	TIMS	$\delta^{18}\text{O}$, $\delta^{13}\text{C}$	
PU-2	Ursilor Cave	46,32	22,25	482	9,81	1,085	6,42	TIMS	$\delta^{18}\text{O}$, $\delta^{13}\text{C}$	
REF-01	Refugio Cave	36,50	-4,67	625	17,5	0,04	2,41		$\delta^{18}\text{O}$, $\delta^{13}\text{C}$	
REF-02	Refugio Cave	36,50	-4,67	625	17,5	3,66	4,876		$\delta^{18}\text{O}$, $\delta^{13}\text{C}$	
REF-04	Refugio Cave	36,50	-4,67	625	17,5	0,674	4,89		$\delta^{18}\text{O}$, $\delta^{13}\text{C}$	
RL-4	Buca della Renella	44,00	10	300		1,27	7		$\delta^{18}\text{O}$	
S.1	W. Straszkykowej Gorze	51,01	19,09			4,12	9,02	14C	$\delta^{13}\text{C}$	
SG-95	Soylegrotta	65,5	14	280	2,8	0,216	3,825	TIMS	$\delta^{18}\text{O}$, $\delta^{13}\text{C}$	
SLX-1	Cueva Mayor	42,2	-3,3	1020	10,6	-0,05	3,899	MC-ICP-MS	$\delta^{13}\text{C}$	
SO-1	Sofular Cave	41,42	31,93	442	12	-0,056	50,27	MC-ICP-MS	$\delta^{18}\text{O}$, $\delta^{13}\text{C}$	
SO-10	Sofular Cave	41,42	31,93	442	12	ca. 0	ca. 2,5	MC-ICP-MS	$\delta^{18}\text{O}$, $\delta^{13}\text{C}$	

Tab. C.3: The table is a compilation of European speleothem studies that are illustrated in Fig. C.1.

name	cave	longitude	latitude	altitude	actual cave	growth	growth	dating	proxies	reference
					air temperature	stop	begin			
					(°C)	(ka BP)	(ka BP)			
		°E	°N	(m)				method		
SO-2	Sofular Cave	41,42	31,93	442	12	0,092	39	MC-ICP-MS	$\delta^{18}\text{O}$, $\delta^{13}\text{C}$	
SO-3	Sofular Cave	41,42	31,93	442	12	0,1	1	MC-ICP-MS?		
SO-4	Sofular Cave	41,42	31,93	442	12	2	3	MC-ICP-MS?		
SPA-12	Spannagel Cave	47,12	11,67	2531	1,8	0,015	7,12	TIMS	$\delta^{18}\text{O}$, $\delta^{13}\text{C}$	
STAL-AH-1	Atta Cave	50,8	7,44	308	9,4	1,9	2,88	TIMS	$\delta^{18}\text{O}$, $\delta^{13}\text{C}$	
STAL-B7-1	B7-Cave	49	7	185	9,4	6,2	12,41	TIMS	$\delta^{18}\text{O}$, $\delta^{13}\text{C}$	
STAL-B7-5	B7-Cave	49	7	185	9,4	5,85	8,81	TIMS	$\delta^{18}\text{O}$, $\delta^{13}\text{C}$	
STAL-B7-7	B7-Cave	49	7	185	9,4	0,54	17,23	TIMS	$\delta^{18}\text{O}$, $\delta^{13}\text{C}$	
SU 96-7	Uamh an Tartair	58,15	-4,98	220	7,1	-0,041	0,946	TIMS/Laminae counting		
SU-2	Uamh an Tartair	58,15	-4,98	220	7,1	1,204	2,567	TIMS		
SU-96-1-2	Uamh an Tartair	58,15	-4,98	220	7,1	2,533	3,77	TIMS		
SV-1	Grotta Savi	45,61	13,88	441	12,3	-0,04	17,64	MC-ICP-MS	$\delta^{18}\text{O}$, $\delta^{13}\text{C}$	
T.1	Towarna Cave	51,01	19,09			1,02	2,47	14C	$\delta^{13}\text{C}$	
Trio	Trio Cave	46,79	19,98	275		3,205	4,822	MC-ICP-MS	$\delta^{18}\text{O}$, $\delta^{13}\text{C}$	
Vil-car-1	Villars Cave	45,3	0,5	175	11,6	10,952	177,88	MC-ICP-MS	$\delta^{18}\text{O}$, $\delta^{13}\text{C}$	
Vil-stm11	Villars Cave	45,3	0,5	175	12,4	5,671	15,28	TIMS	$\delta^{18}\text{O}$, $\delta^{13}\text{C}$	
W.1	Wierzchowska Gorna Cave	51,01	19,09			1,85	1,85	14C	$\delta^{13}\text{C}$	
Z.1	Zegar Cave	51,01	19,09			6,41	6,41	14C	$\delta^{13}\text{C}$	
Z.2	Zegar Cave	51,01	19,09			6,5	6,5	14C	$\delta^{13}\text{C}$	

Tab. C.4: The table is a compilation of European speleothem studies that are illustrated in Fig. C.1.

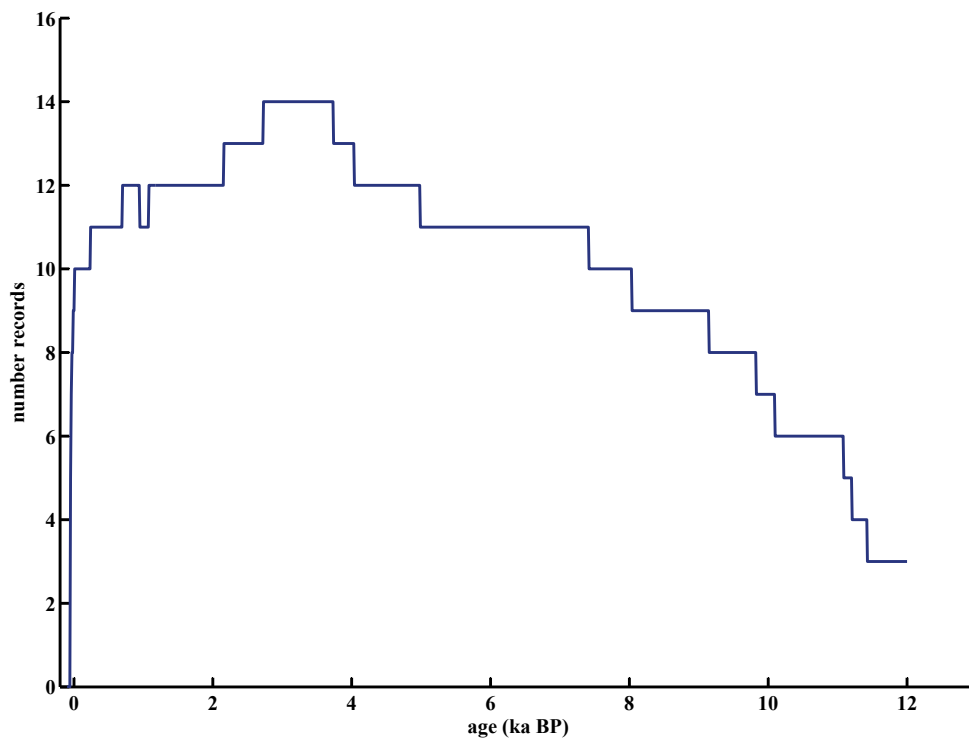


Fig. C.2: Illustrated is the number of records against time that are usable for PCA.

D

Eigenvalues of the 8,000 year PCA - PART I: Long-term analysis

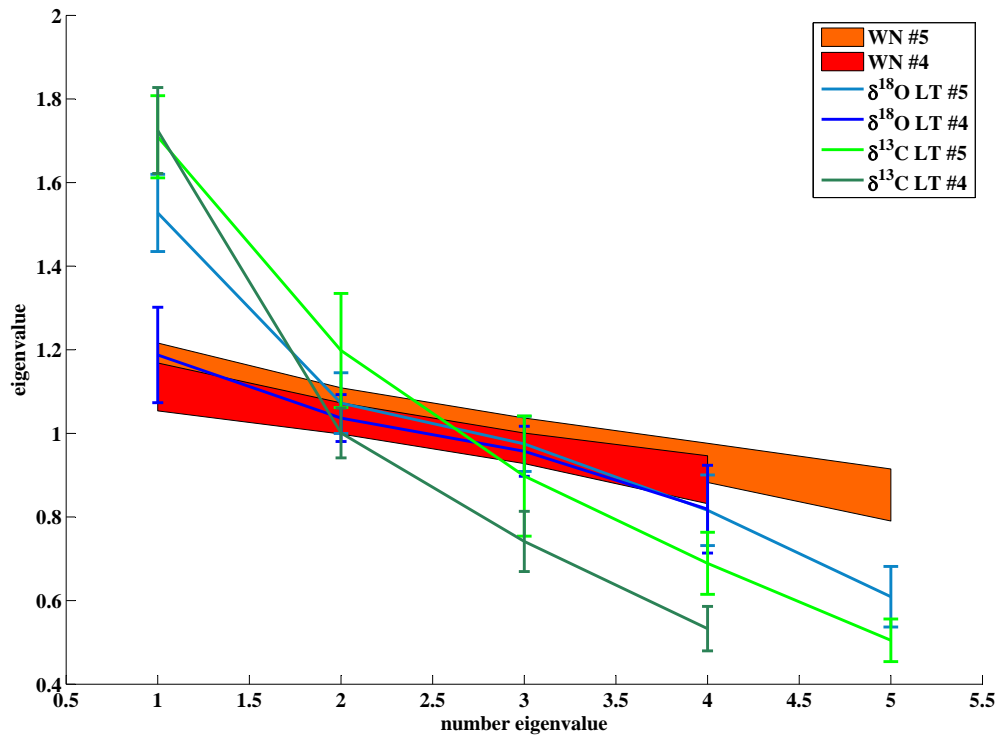


Fig. D.1: Illustrated are the mean eigenvalues for the long-term PCA for each PC. For the compilation of $\delta^{18}\text{O}$ time series run #1 is illustrated in dark blue and run #2 in light blue. For the compilation of $\delta^{13}\text{C}$ time series run #1 is illustrated in dark green and run #2 in light green. Moreover, the 95 % and 5 % confidence level is pictures for 4 (red shading area) and 5 (orange shading area) white noise time series indicated by the upper and lower line of the shading areas.

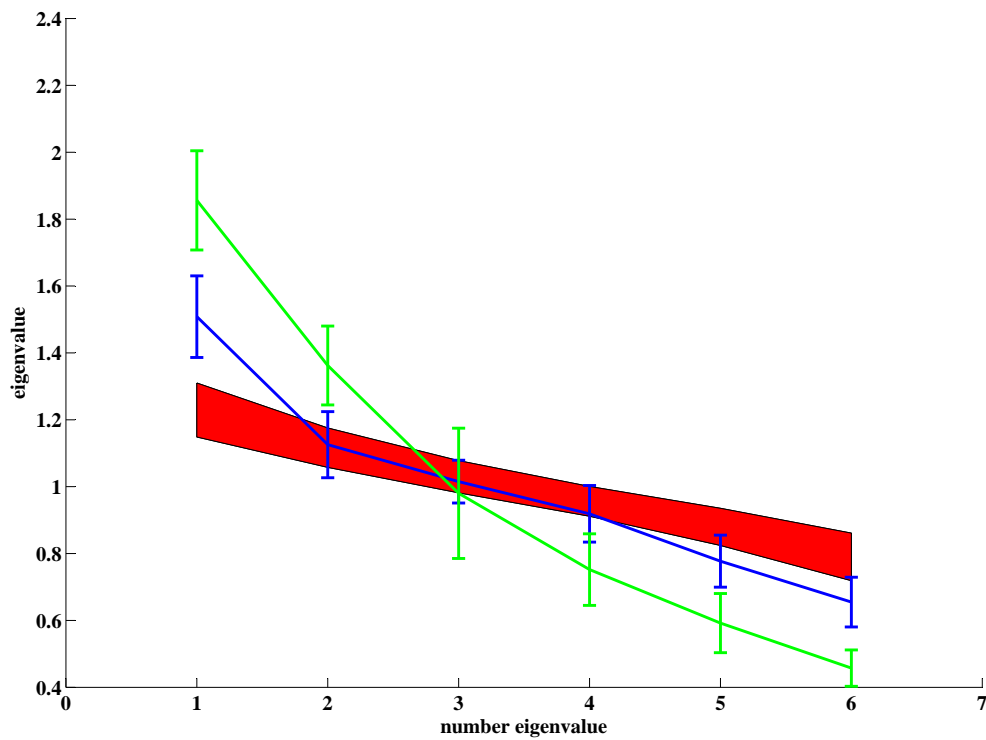


Fig. D.2: Illustrated are the mean eigenvalues for run #3 for the compilation of $\delta^{18}\text{O}$ (blue) and $\delta^{13}\text{C}$ (green) time series. Furthermore, the 95 % and 5 % confidence level of the eigenvalues is illustrated, computed from 6 white noise time series (red shading area).

E

Results of the application of the Fork-tool onto the 8,000 year runs - PART I: Long-term analysis

E.1 Distribution of r_s for short-term coherence pattern for $\delta^{18}O$ time series

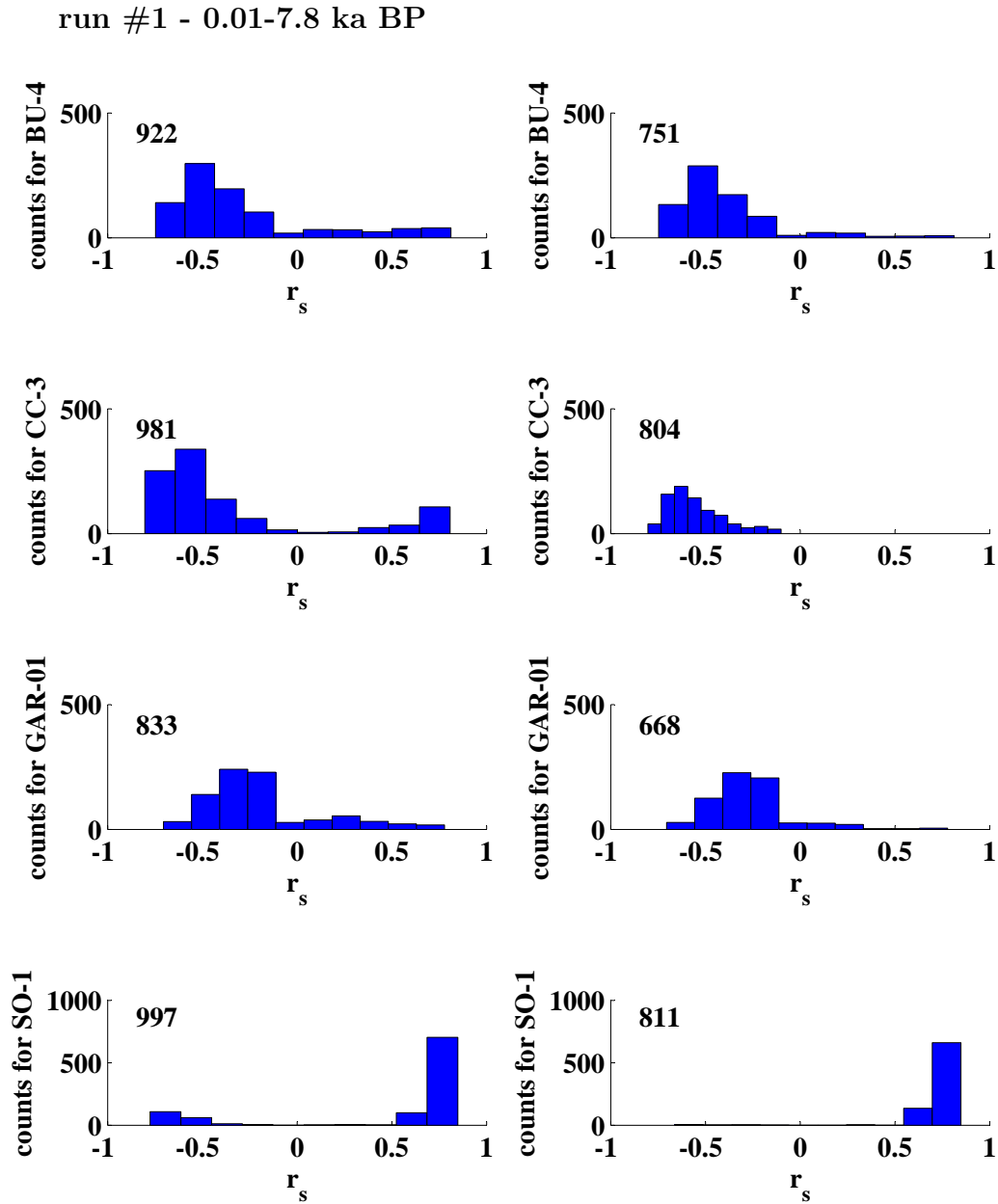


Fig. E.1: Illustrated is the distribution of speleothem r_s for run #1 of the 8000 years long-term PCA on $\delta^{18}\text{O}$ time series before (left panels) and after (right panels) the application of the Fork-tool.

run #2 - 0.75-7.8 ka BP - Part I

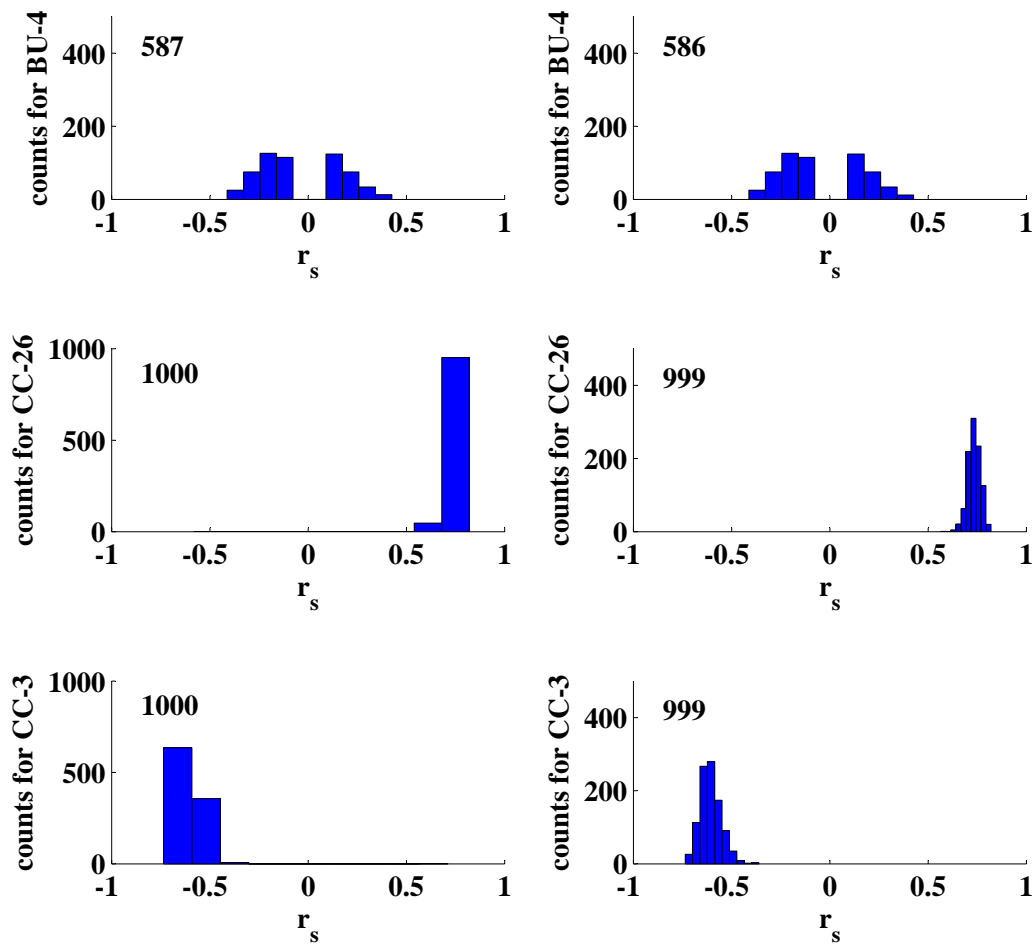


Fig. E.2: Illustrated is the distribution of speleothem r_s for run #2 of the 8000 years long-term PCA on $\delta^{18}O$ time series before (left panels) and after (right panels) the application of the Fork-tool.

run #2 - 0.75-7.8 ka BP - Part II

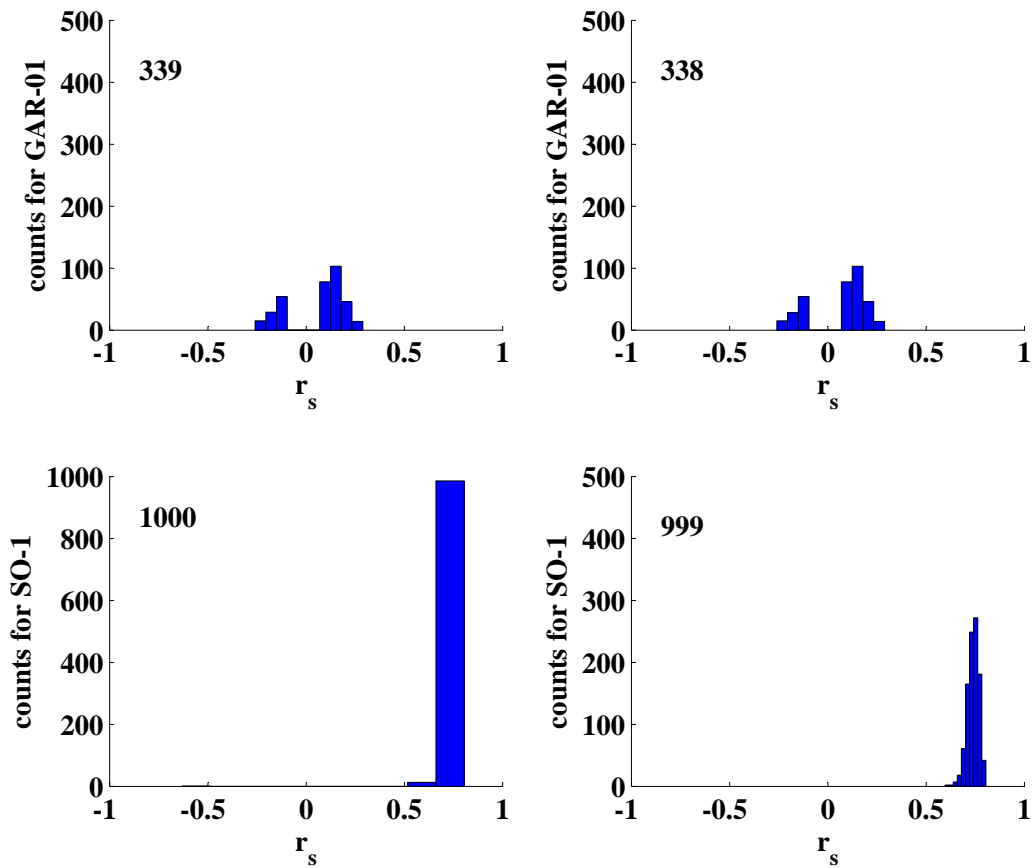


Fig. E.3: Illustrated is the distribution of speleothem r_s for run #2 of the 8000 years long-term PCA on $\delta^{18}\text{O}$ time series before (left panels) and after (right panels) the application of the Fork-tool.

run #3 - 0.75-7.3 ka BP - Part I

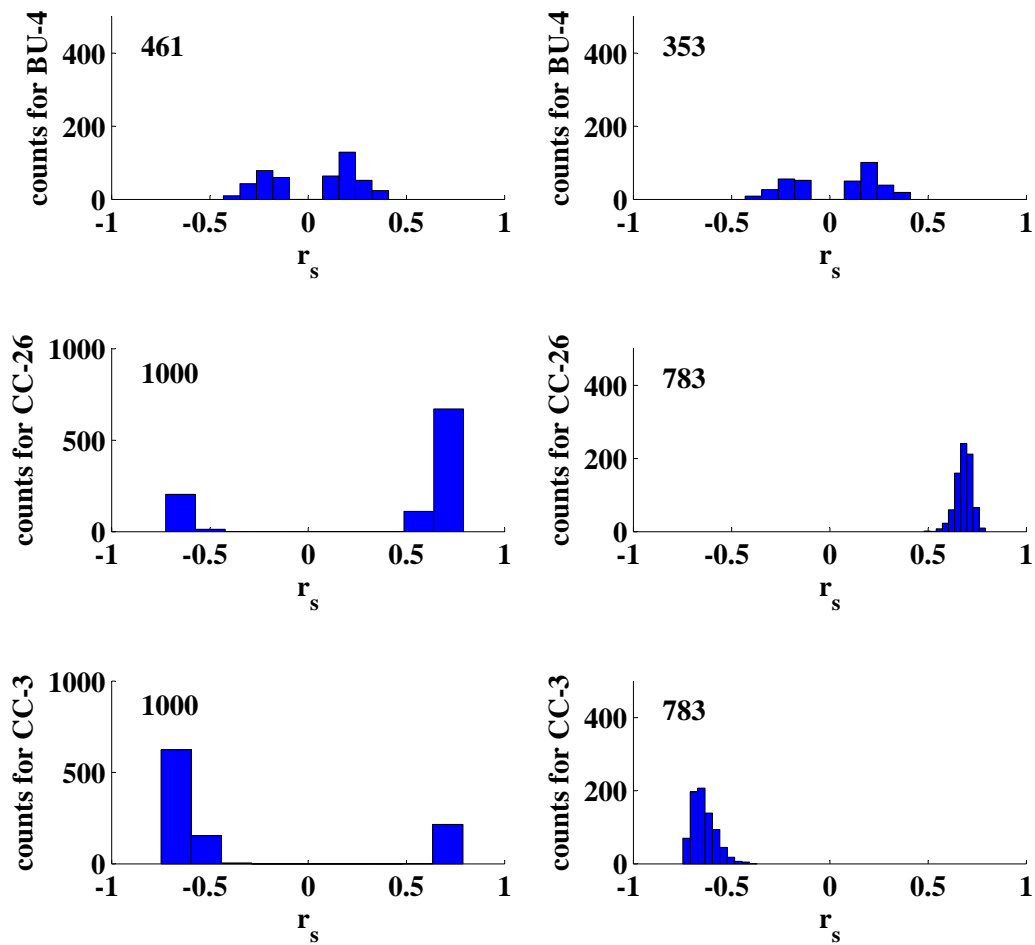


Fig. E.4: Illustrated is the distribution of speleothem r_s for run #3 of the 8000 years long-term PCA on $\delta^{18}O$ time series before (left panels) and after (right panels) the application of the Fork-tool.

run #3 - 0.75-7.3 ka BP - Part II

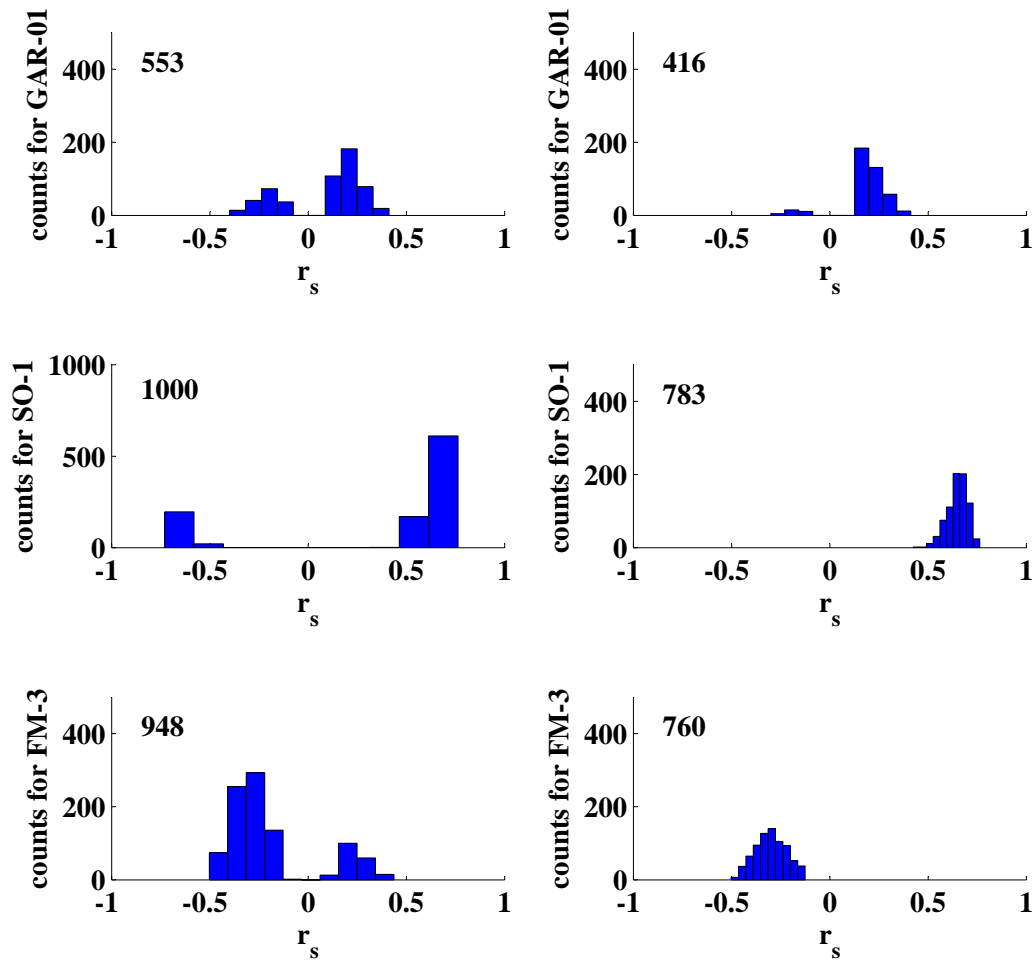


Fig. E.5: Illustrated is the distribution of speleothem r_s for run #3 of the 8000 years long-term PCA on $\delta^{18}\text{O}$ time series before (left panels) and after (right panels) the application of the Fork-tool.

E.2 Distribution of r_s for short-term coherence pattern for $\delta^{13}C$ time series

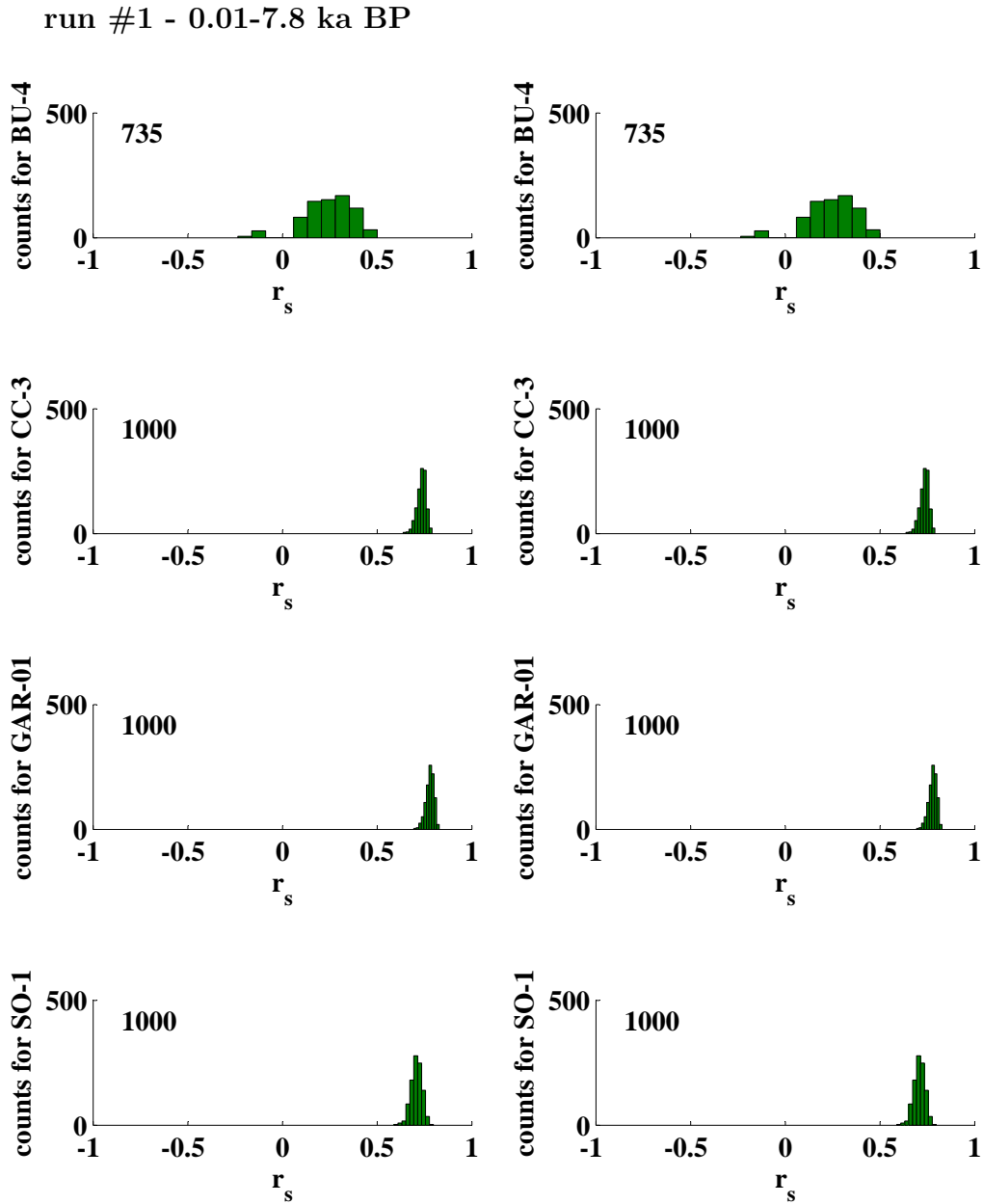


Fig. E.6: Illustrated is the distribution of speleothem r_s for run #1 of the 8000 years long-term PCA on $\delta^{13}\text{C}$ time series before (left panels) and after (right panels) the application of the Fork-tool.

run #2 - 0.75-7.8 ka BP - Part I

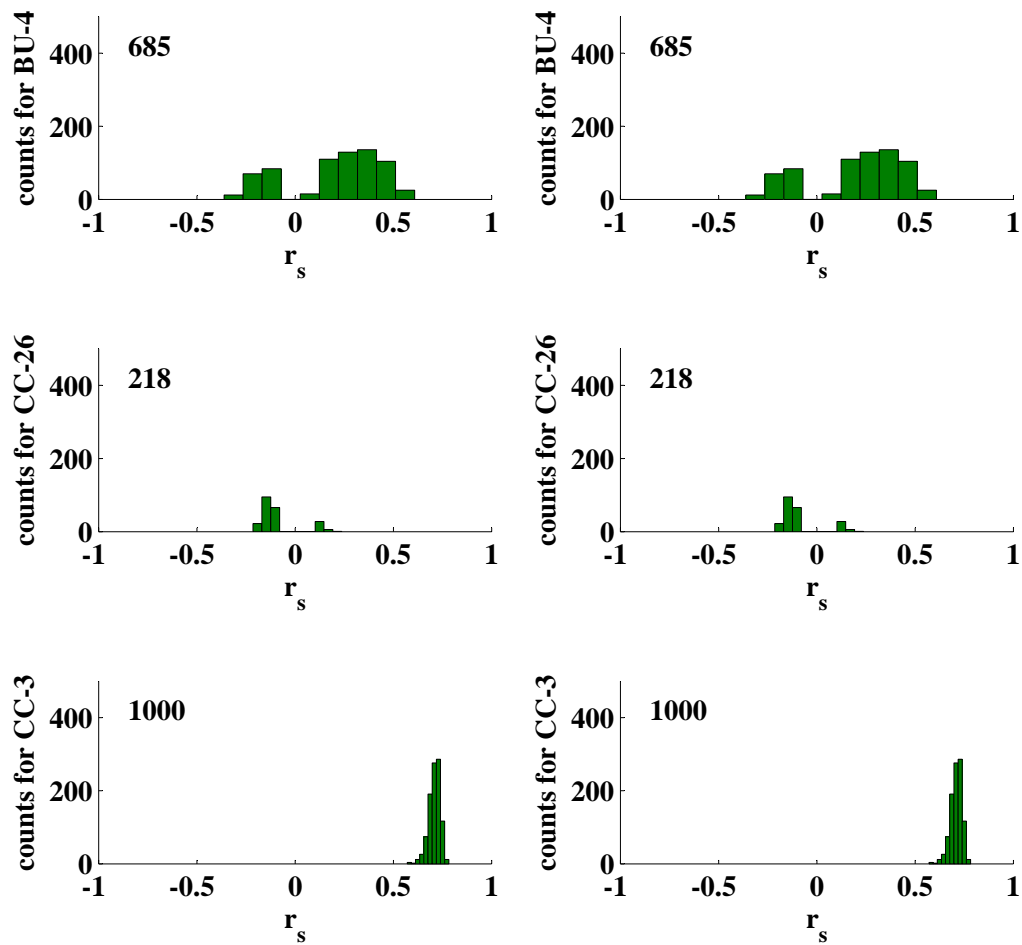


Fig. E.7: Illustrated is the distribution of speleothem r_s for run #2 of the 8000 years long-term PCA on $\delta^{13}C$ time series before (left panels) and after (right panels) the application of the Fork-tool.

run #2 - 0.75-7.8 ka BP - Part II

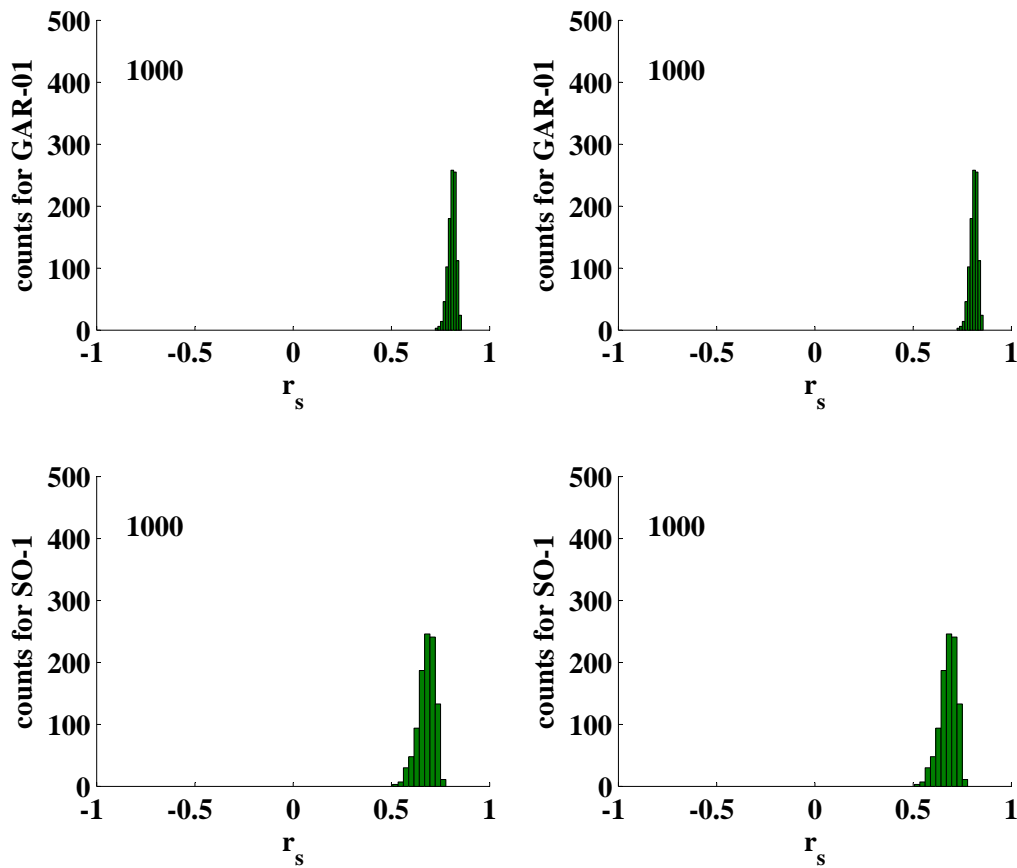


Fig. E.8: Illustrated is the distribution of speleothem r_s for run #2 of the 8000 years long-term PCA on $\delta^{13}\text{C}$ time series before (left panels) and after (right panels) the application of the Fork-tool.

run #3 - 0.75-7.3 ka BP - Part I

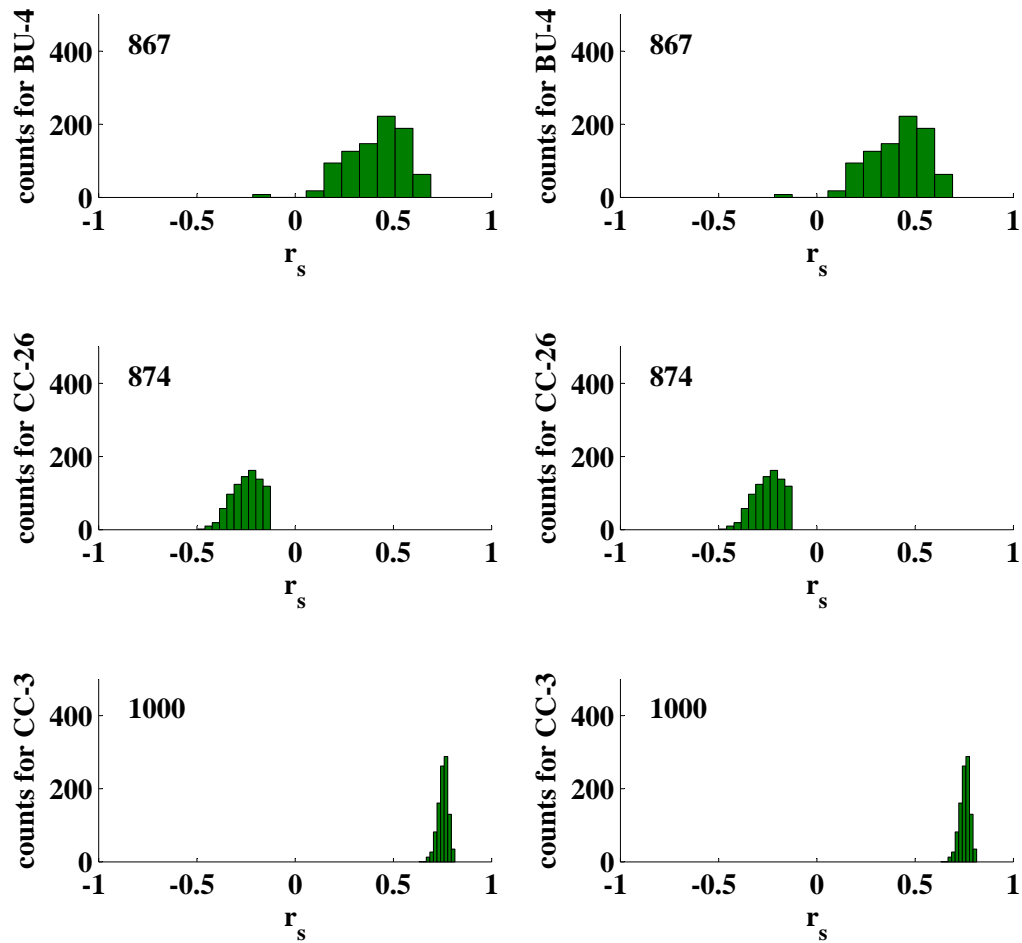


Fig. E.9: Illustrated is the distribution of speleothem r_s for run #3 of the 8000 years long-term PCA on $\delta^{13}C$ time series before (left panels) and after (right panels) the application of the Fork-tool.

run #3 - 0.75-7.3 ka BP - Part II

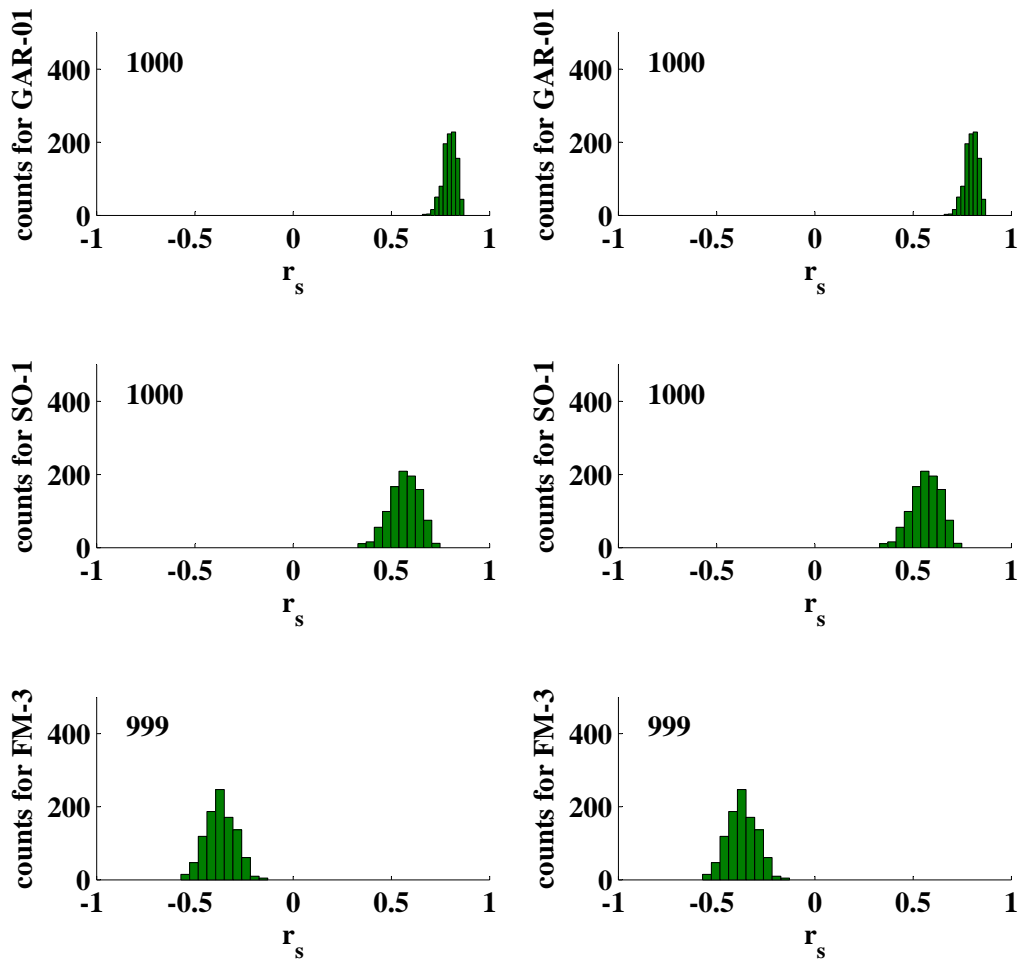


Fig. E.10: Illustrated is the distribution of speleothem r_s for run #3 of the 8000 years long-term PCA on $\delta^{13}\text{C}$ time series before (left panels) and after (right panels) the application of the Fork-tool.

F

Eigenvalues of the 4,000 years runs

F.1 4,000 years Long-term runs

F.1.1 Eigenvalues of the short-term coherence pattern

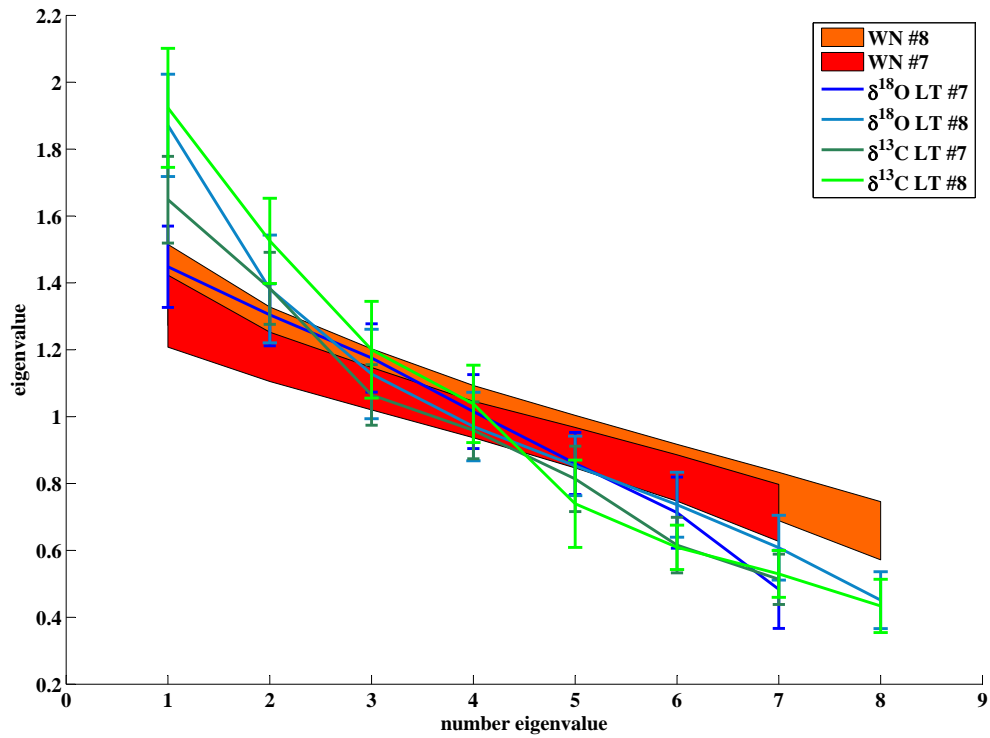


Fig. F.1: Illustrated are the mean eigenvalues for the long-term PCA for each PC. For the compilation of $\delta^{18}\text{O}$ time series run #1 is illustrated in dark blue and run #2 in light blue. For the compilation of $\delta^{13}\text{C}$ time series run #1 is illustrated in dark green and run #2 in light green. Moreover, the 95 % and 5 % confidence level is pictures for 7 (red shading area) and 8 (orange shading area) white noise time series indicated by the upper and lower line of the shading areas.

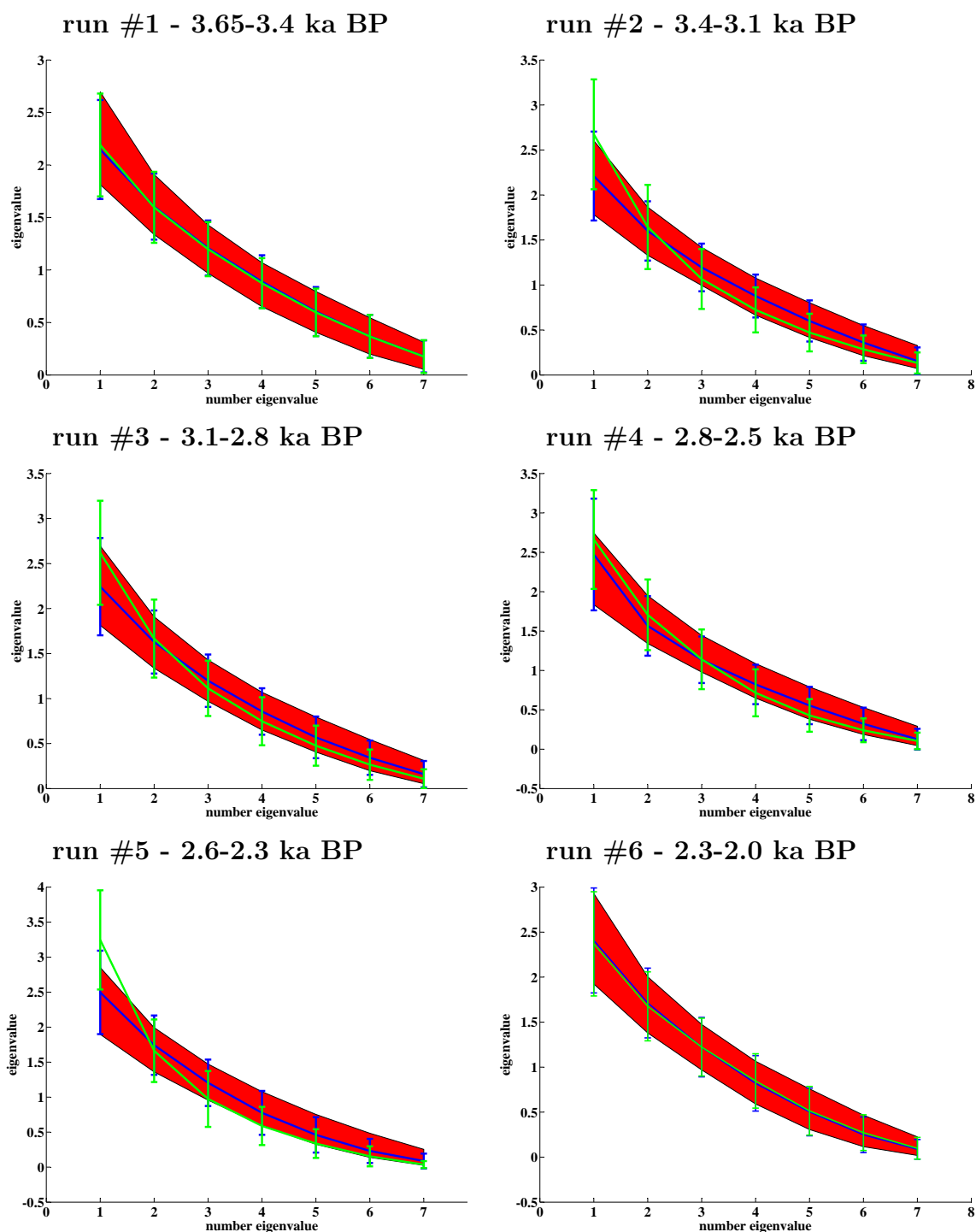


Fig. F.2: Illustrated are the mean eigenvalues for the indicated short-term PCA runs for the compilation of $\delta^{18}\text{O}$ (blue) and $\delta^{13}\text{C}$ (green) time series. Furthermore, the 95 % and 5 % confidence level of the eigenvalues is illustrated, computed from white noise time series (red shading area).

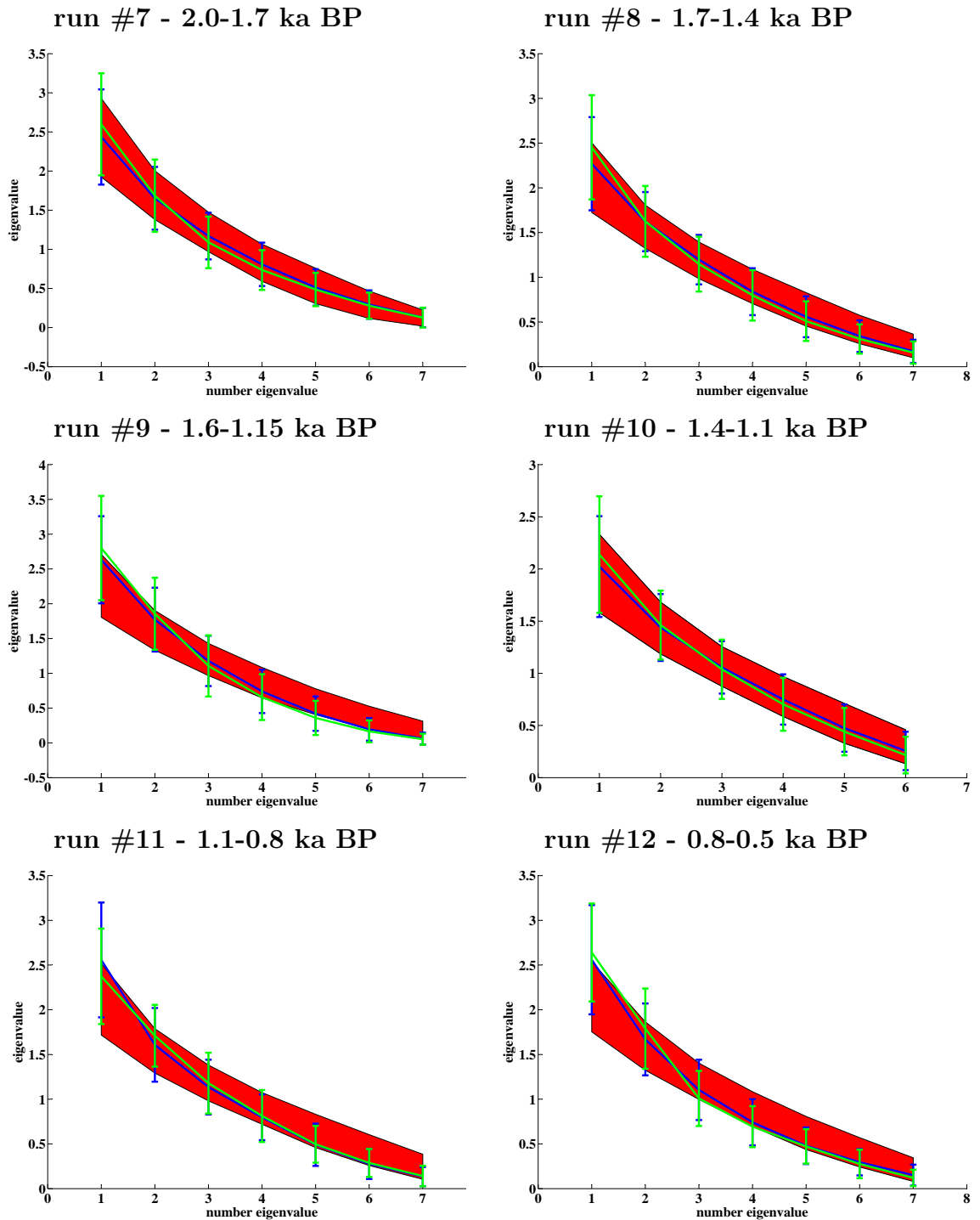


Fig. F.3: Illustrated are the mean eigenvalues for the indicated short-term PCA runs for the compilation of $\delta^{18}\text{O}$ (blue) and $\delta^{13}\text{C}$ (green) time series. Furthermore, the 95 % and 5 % confidence level of the eigenvalues is illustrated, computed from white noise time series (red shading area).

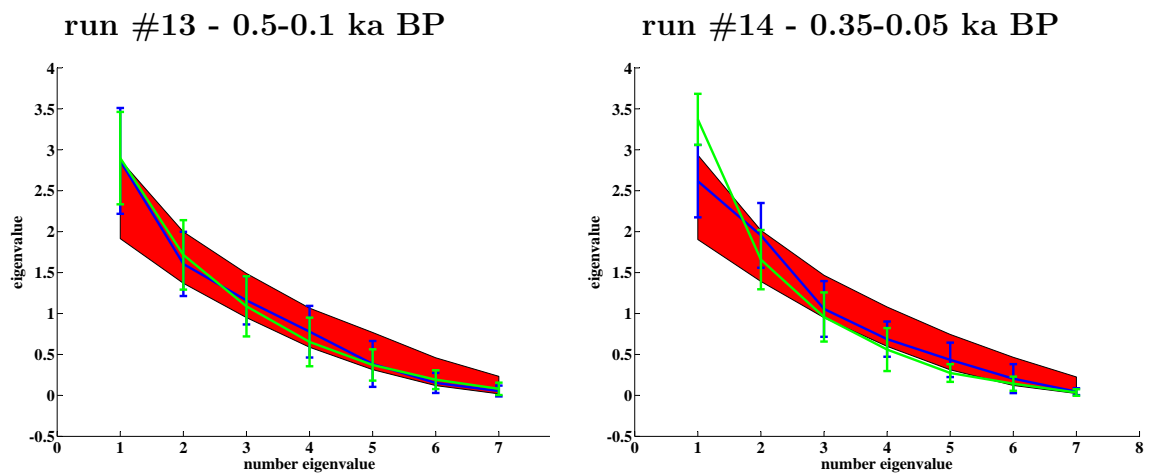


Fig. F.4: Illustrated are the mean eigenvalues for the indicated short-term PCA runs for the compilation of $\delta^{18}\text{O}$ (blue) and $\delta^{13}\text{C}$ (green) time series. Furthermore, the 95 % and 5 % confidence level of the eigenvalues is illustrated, computed from white noise time series (red shading area).

G

**Results of the application of the
Fork-tool onto the 4000 year
long-term runs**

run #1 - 3.65-0.0 ka BP - Part I

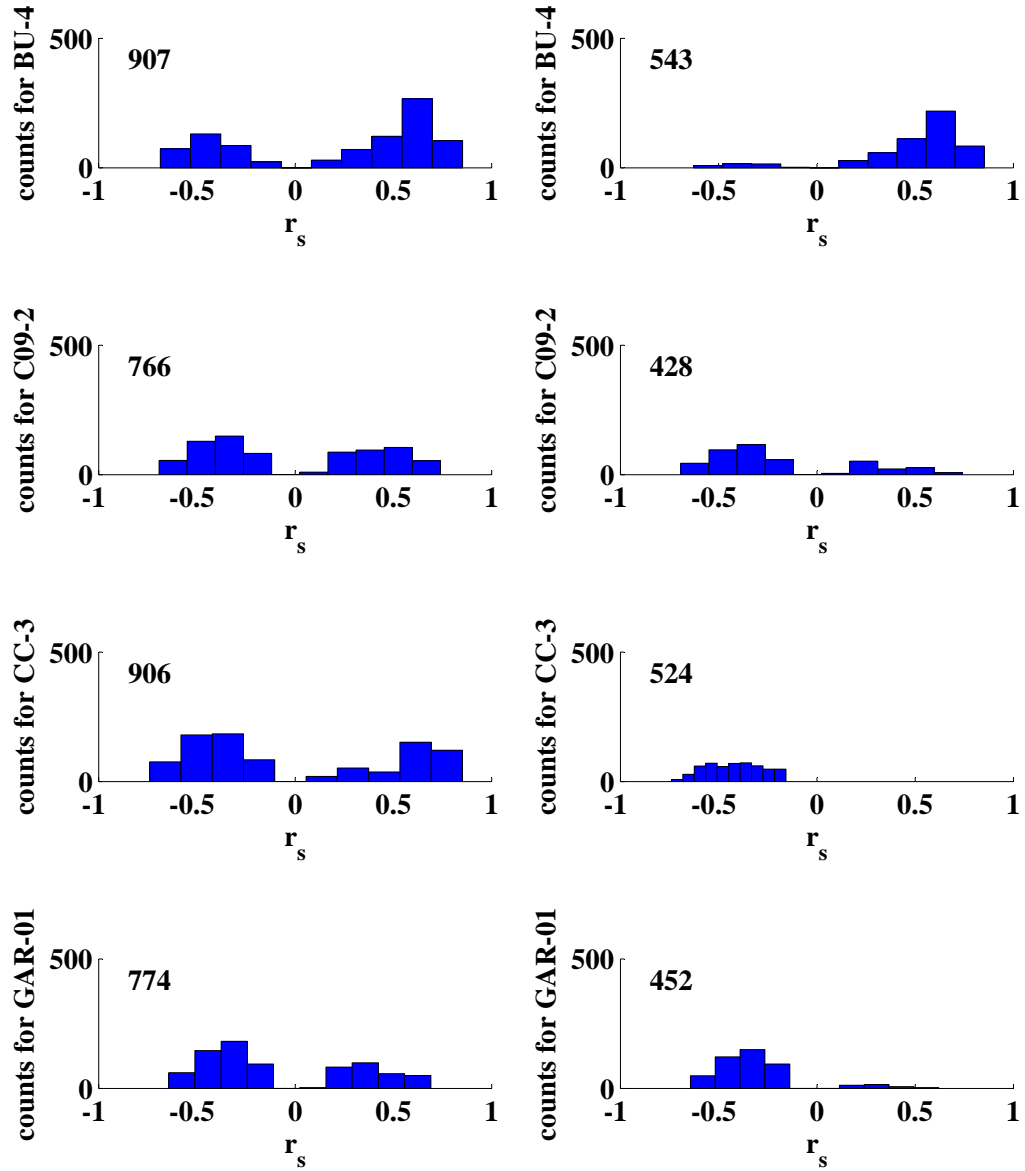


Fig. G.1: Illustrated is the distribution of speleothem r_s for the indicated runs of the 4000 years long-term PCA on $\delta^{18}\text{O}$ time series before (left panels) and after (right panels) the application of the Fork-tool.

run #1 - 3.65-0.0 ka BP - Part II

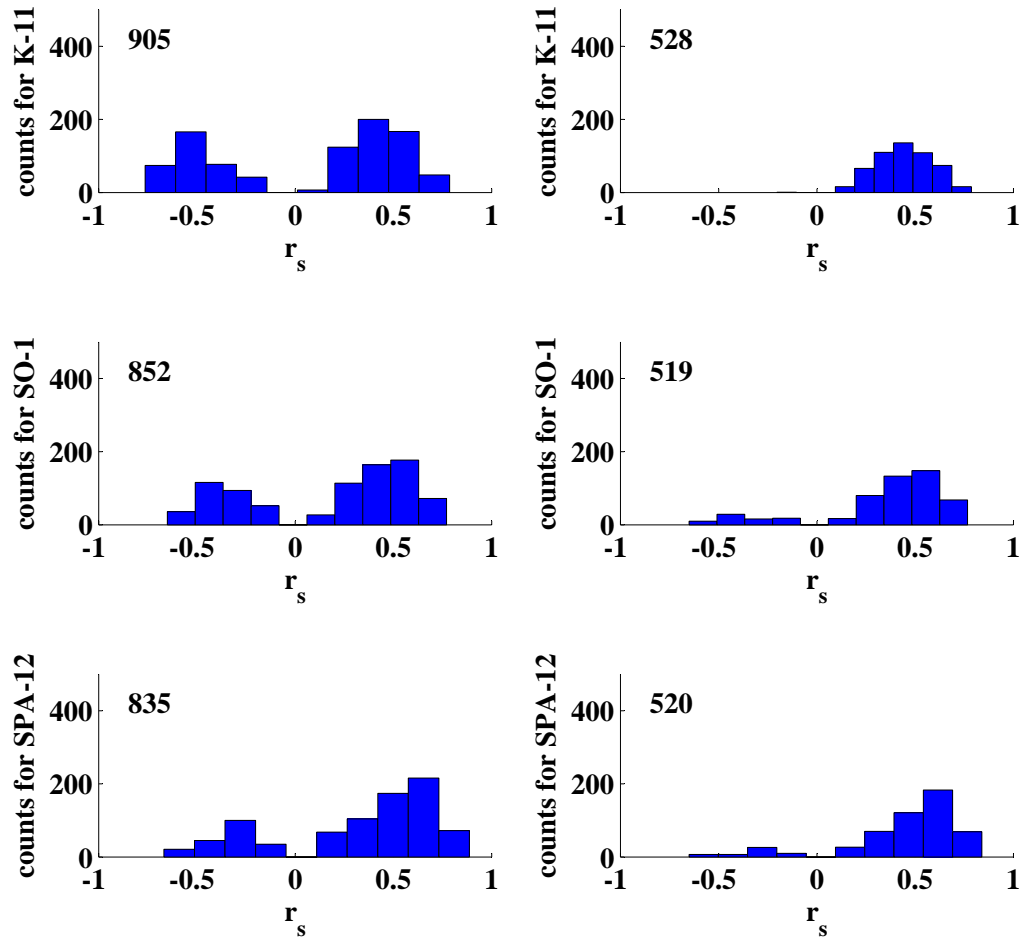


Fig. G.2: Illustrated is the distribution of speleothem r_s for the indicated runs of the 4000 years long-term PCA on $\delta^{18}\text{O}$ time series before (left panels) and after (right panels) the application of the Fork-tool.

run #2 - 3.65-0.33 ka BP - Part I

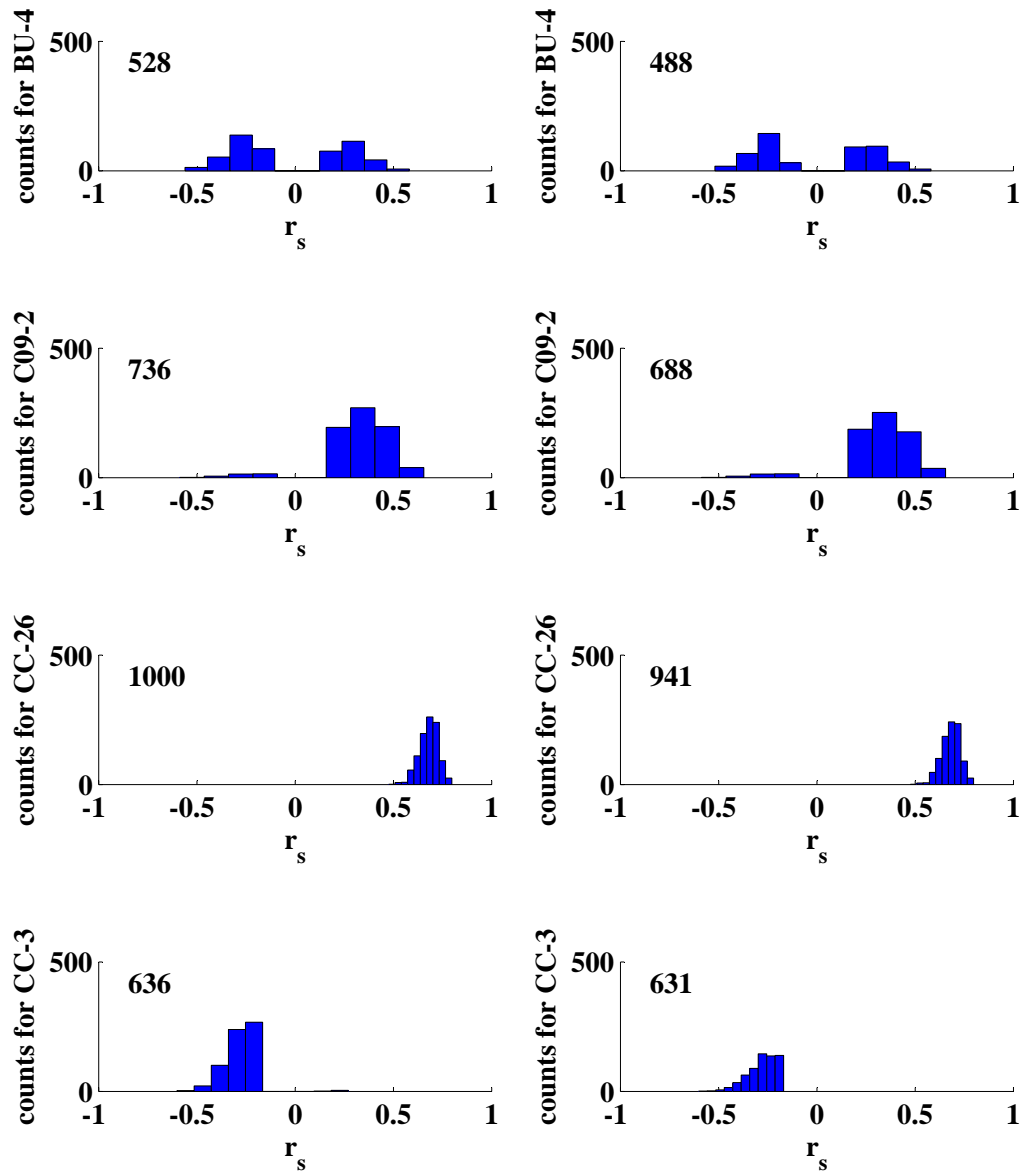


Fig. G.3: Illustrated is the distribution of speleothem r_s for the indicated runs of the 4000 years long-term PCA on $\delta^{18}\text{O}$ time series before (left panels) and after (right panels) the application of the Fork-tool.

run #2 - 3.65-0.33 ka BP - Part II

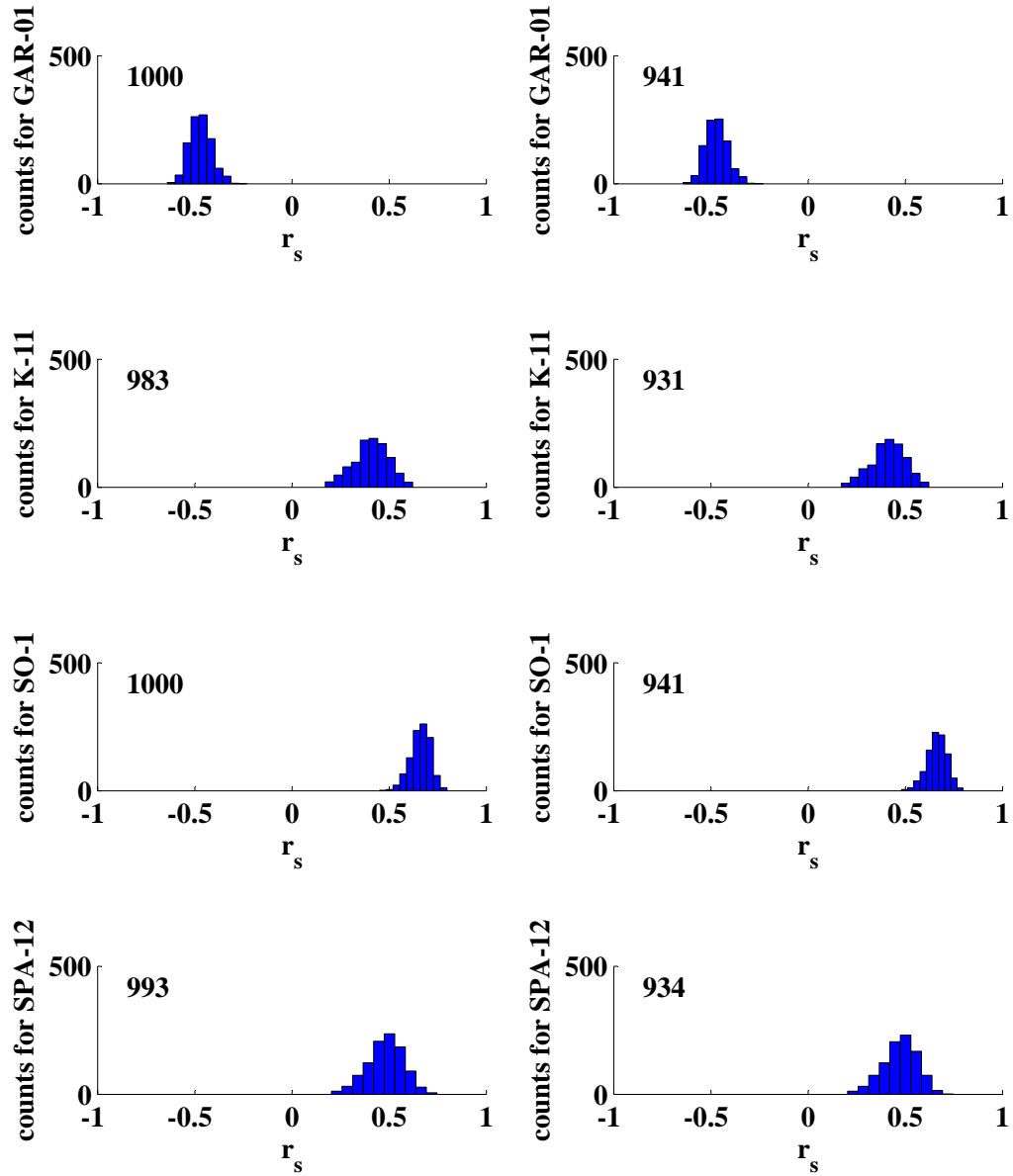


Fig. G.4: Illustrated is the distribution of speleothem r_s for the indicated runs of the 4000 years long-term PCA on $\delta^{18}\text{O}$ time series before (left panels) and after (right panels) the application of the Fork-tool.

run #1 - 3.65-0.0 ka BP - Part I

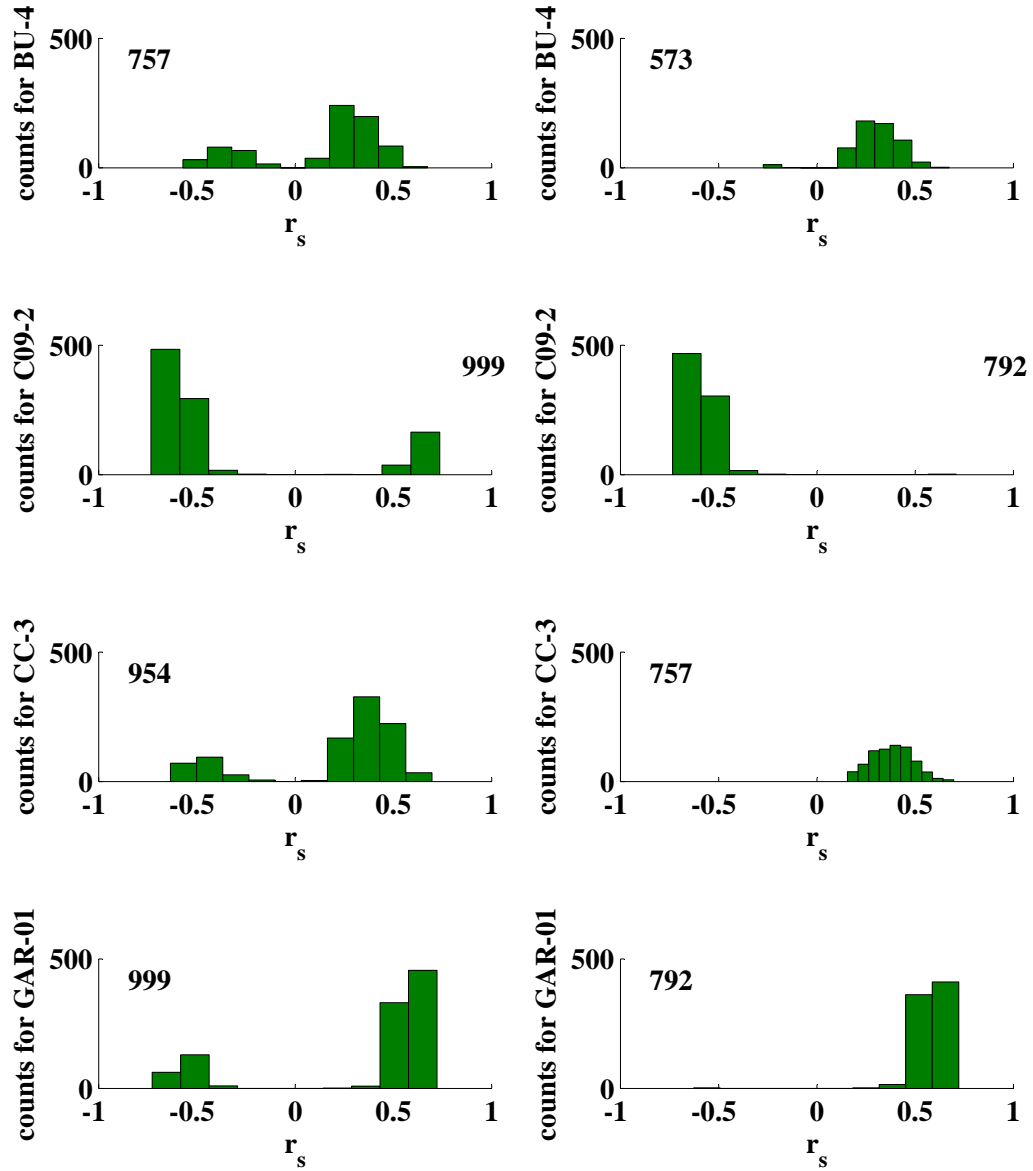


Fig. G.5: Illustrated is the distribution of speleothem r_s for the indicated runs of the 4000 years long-term PCA on $\delta^{13}\text{C}$ time series before (left panels) and after (right panels) the application of the Fork-tool.

run #1 - 3.65-0.0 ka BP - Part II

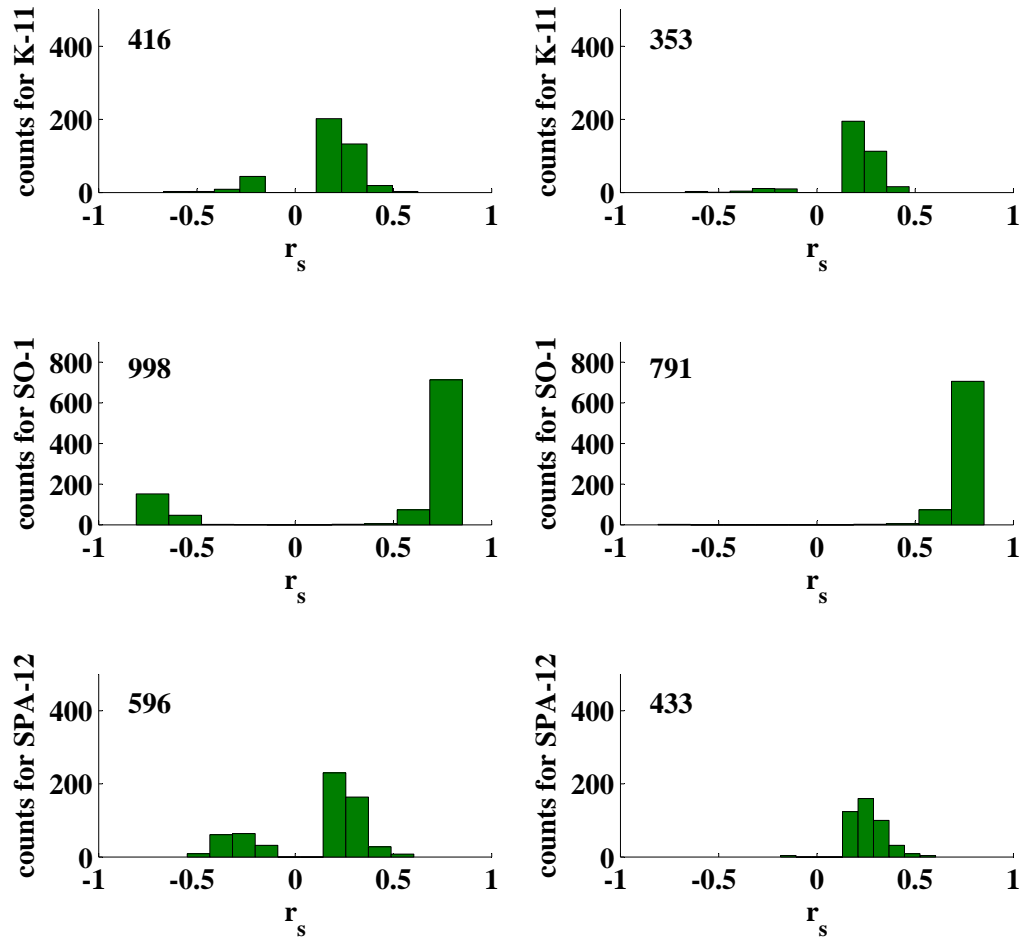


Fig. G.6: Illustrated is the distribution of speleothem r_s for the indicated runs of the 4000 years long-term PCA on $\delta^{13}\text{C}$ time series before (left panels) and after (right panels) the application of the Fork-tool.

run #2 - 3.65-0.33 ka BP - Part I

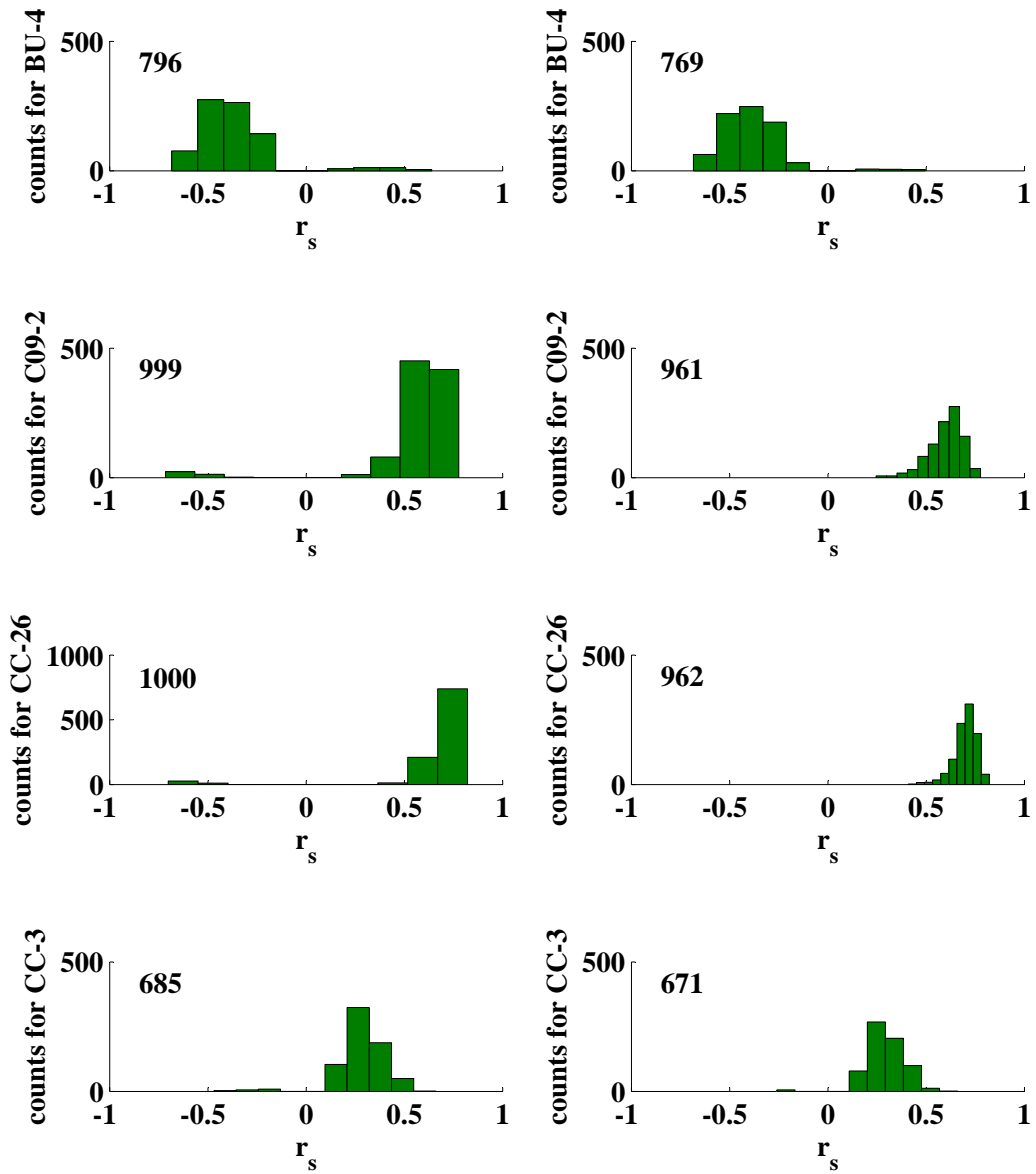


Fig. G.7: Illustrated is the distribution of speleothem r_s for the indicated runs of the 4000 years long-term PCA on $\delta^{13}\text{C}$ time series before (left panels) and after (right panels) the application of the Fork-tool.

run #2 - 3.65-0.33 ka BP - Part II

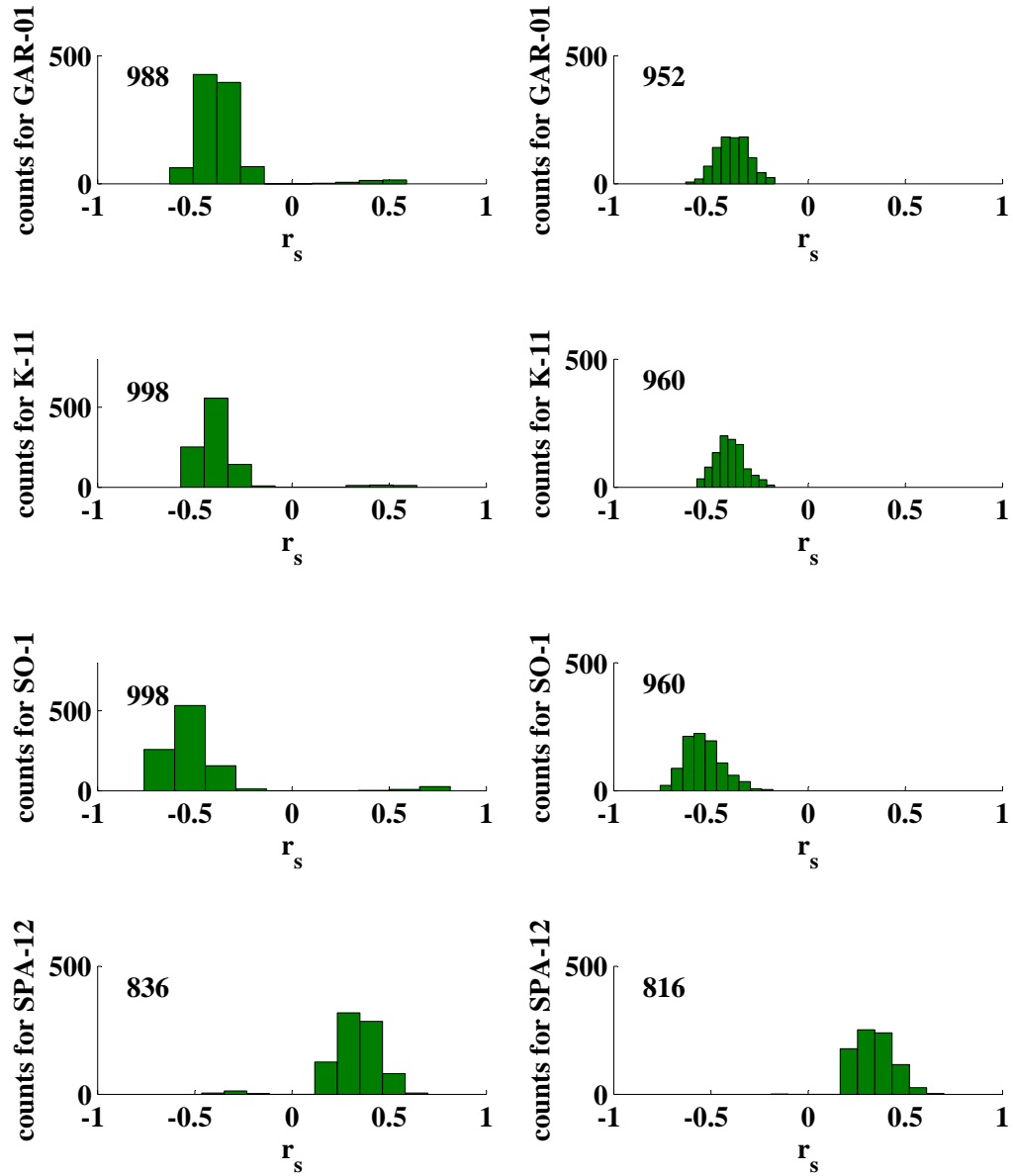


Fig. G.8: Illustrated is the distribution of speleothem r_s for the indicated runs of the 4000 years long-term PCA on $\delta^{13}\text{C}$ time series before (left panels) and after (right panels) the application of the Fork-tool.

H

Results of the application of the Fork-tool onto the 4000 year short-term runs

H.1 Distribution of r_s for short-term coherence pattern for $\delta^{18}O$ time series

run #1 - 3.65-3.4 ka BP - Part I

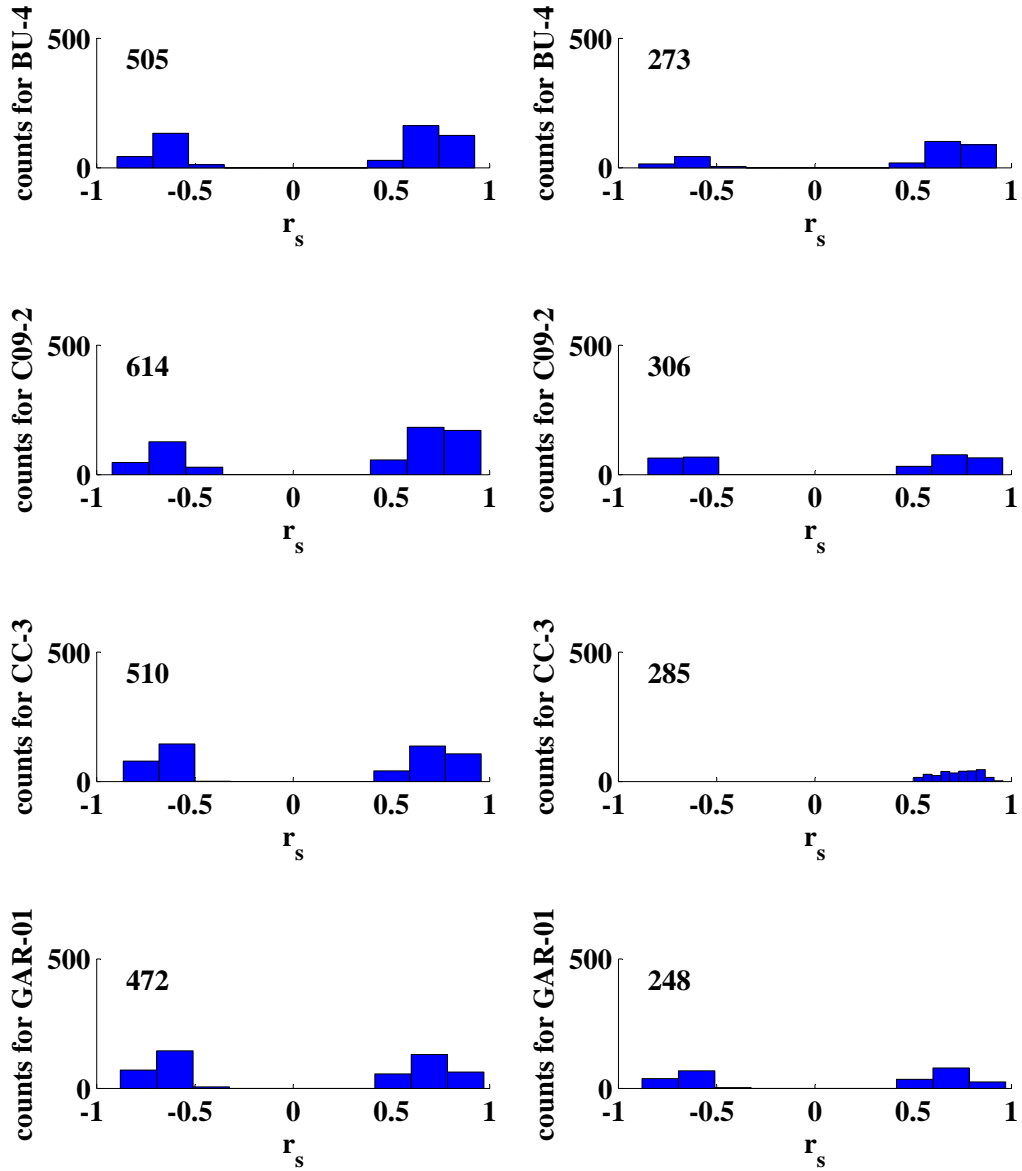


Fig. H.1: Illustrated is the distribution of speleothem r_s for the indicated runs of the 4000 years short-term PCA on $\delta^{18}\text{O}$ time series before (left panels) and after (right panels) the application of the Fork-tool.

run #1 - 3.65-3.4 ka BP - Part II

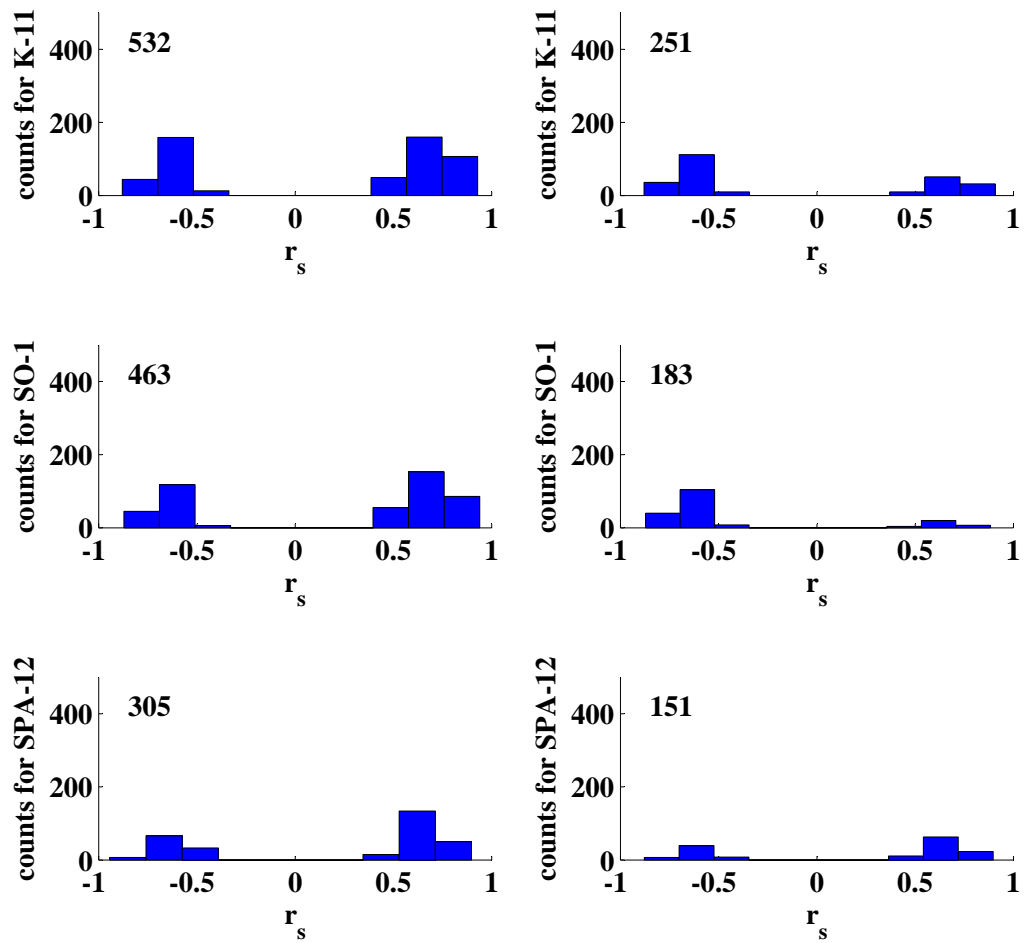


Fig. H.2: Illustrated is the distribution of speleothem r_s for the indicated runs of the 4000 years short-term PCA on $\delta^{18}O$ time series before (left panels) and after (right panels) the application of the Fork-tool.

run #2 - 3.4-3.1 ka BP - Part I

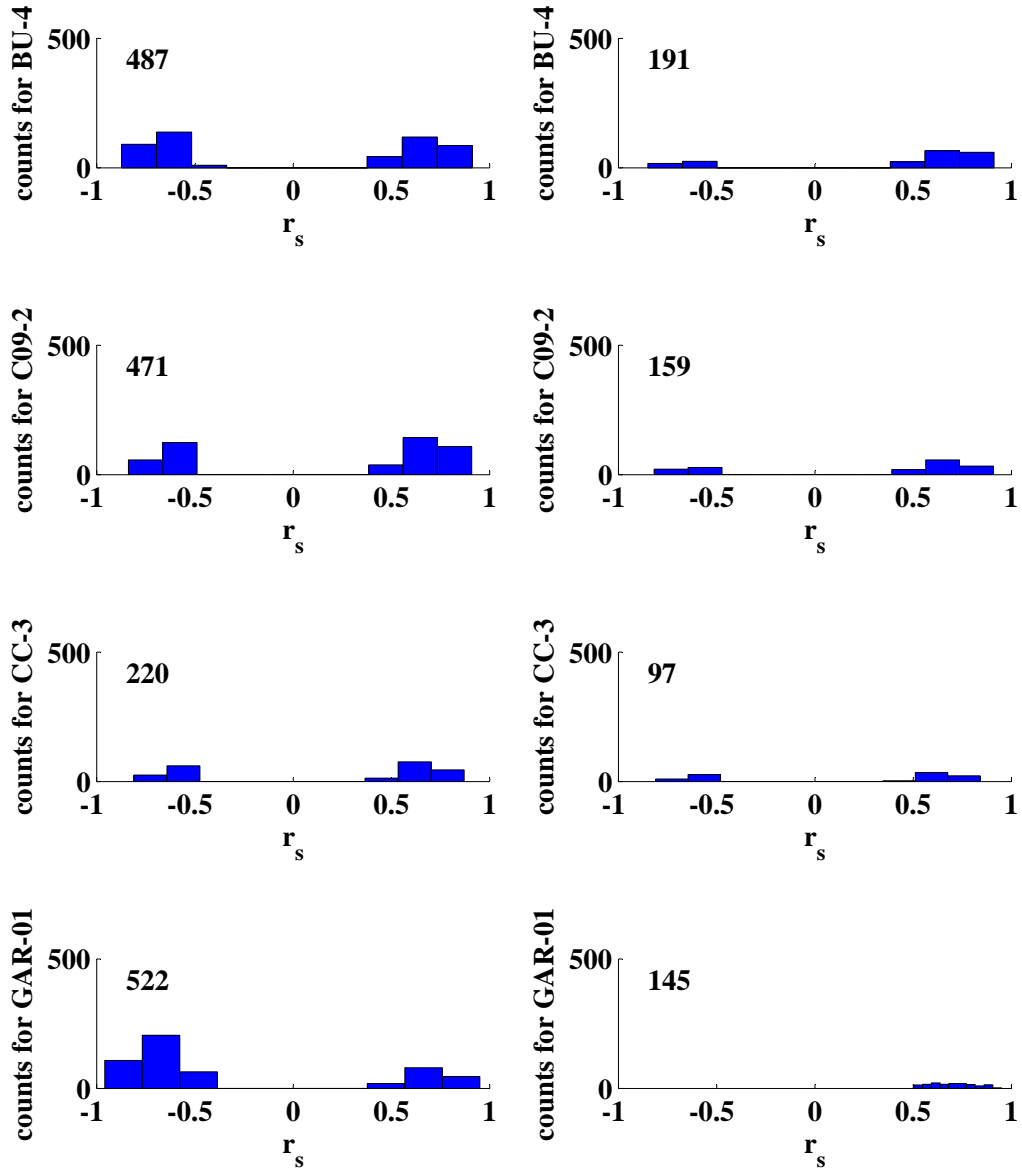


Fig. H.3: Illustrated is the distribution of speleothem r_s for the indicated runs of the 4000 years short-term PCA on $\delta^{18}\text{O}$ time series before (left panels) and after (right panels) the application of the Fork-tool.

run #2 - 3.4-3.1 ka BP - Part II

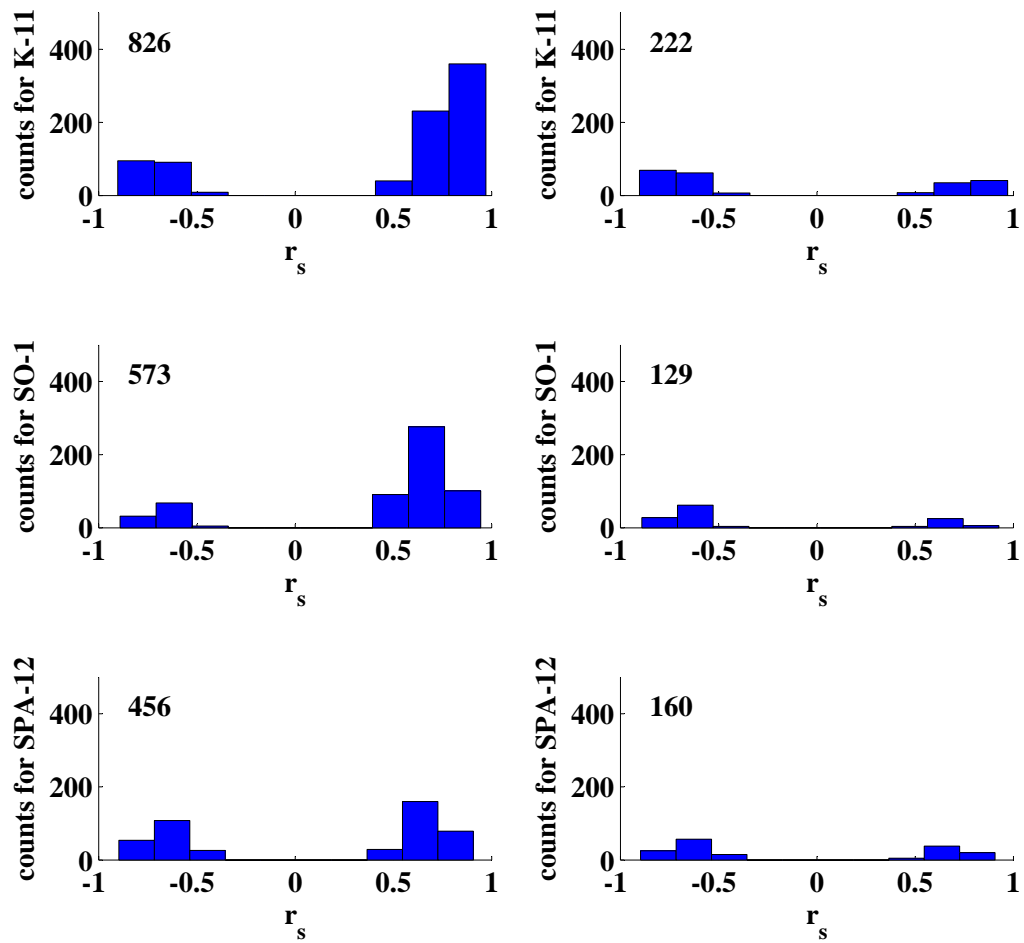


Fig. H.4: Illustrated is the distribution of speleothem r_s for the indicated runs of the 4000 years short-term PCA on $\delta^{18}O$ time series before (left panels) and after (right panels) the application of the Fork-tool.

run #3 - 3.1-2.8 ka BP - Part I

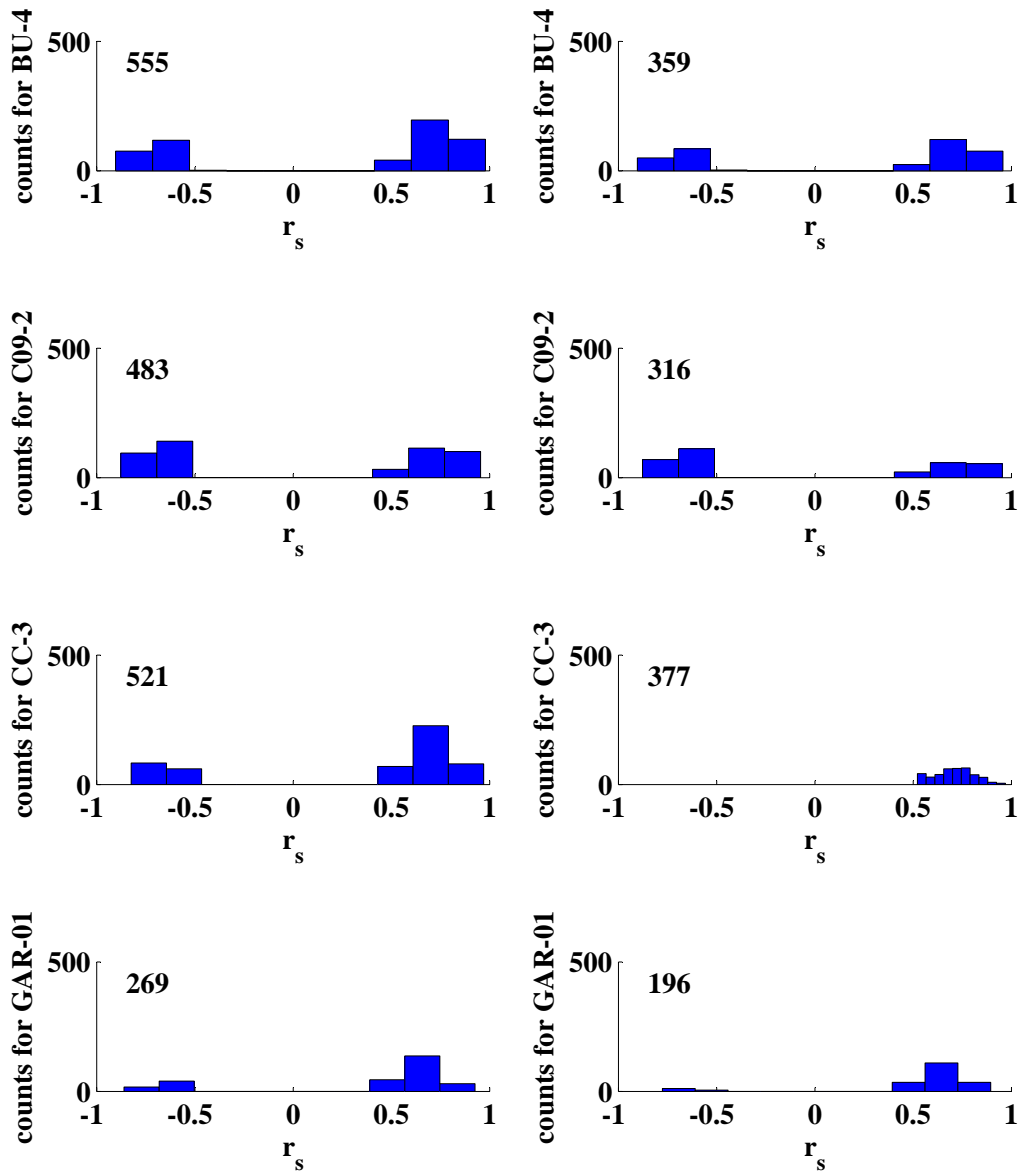


Fig. H.5: Illustrated is the distribution of speleothem r_s for the indicated runs of the 4000 years short-term PCA on $\delta^{18}\text{O}$ time series before (left panels) and after (right panels) the application of the Fork-tool.

run #3 - 3.1-2.8 ka BP - Part II

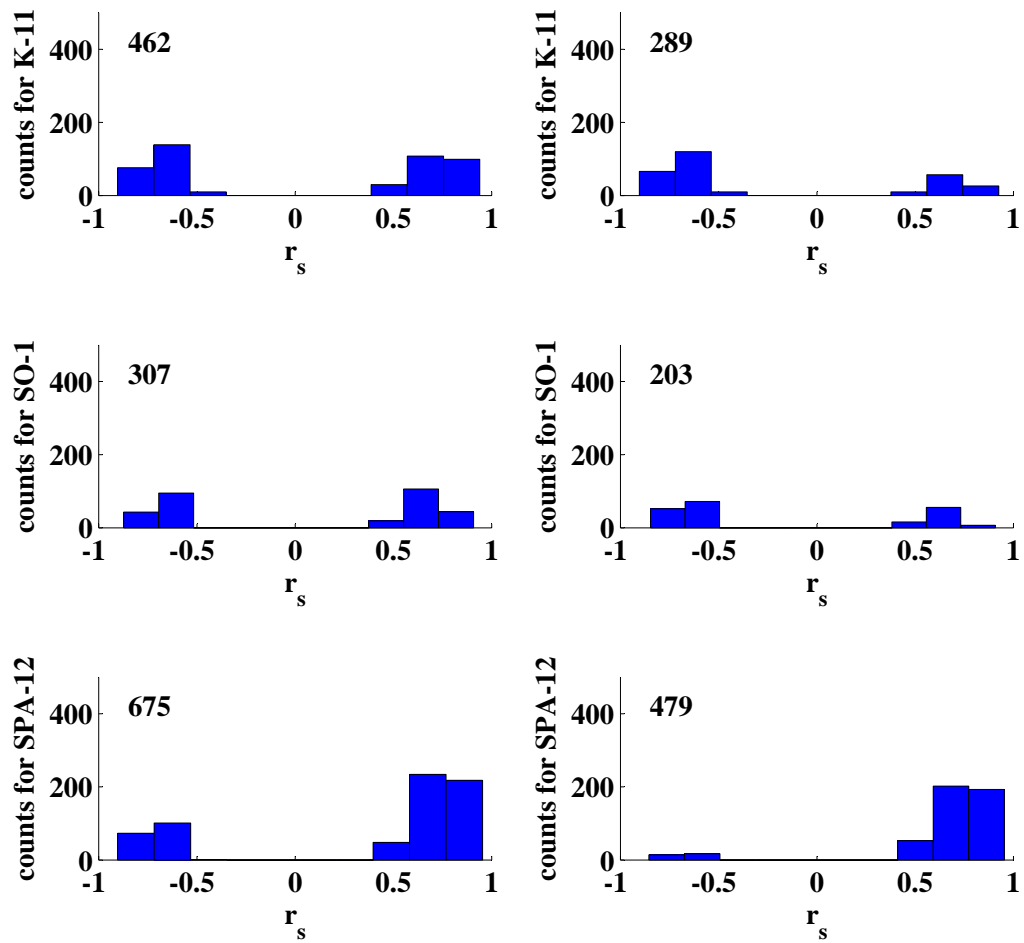


Fig. H.6: Illustrated is the distribution of speleothem r_s for the indicated runs of the 4000 years short-term PCA on $\delta^{18}O$ time series before (left panels) and after (right panels) the application of the Fork-tool.

run #4 - 2.8-2.5 ka BP - Part I

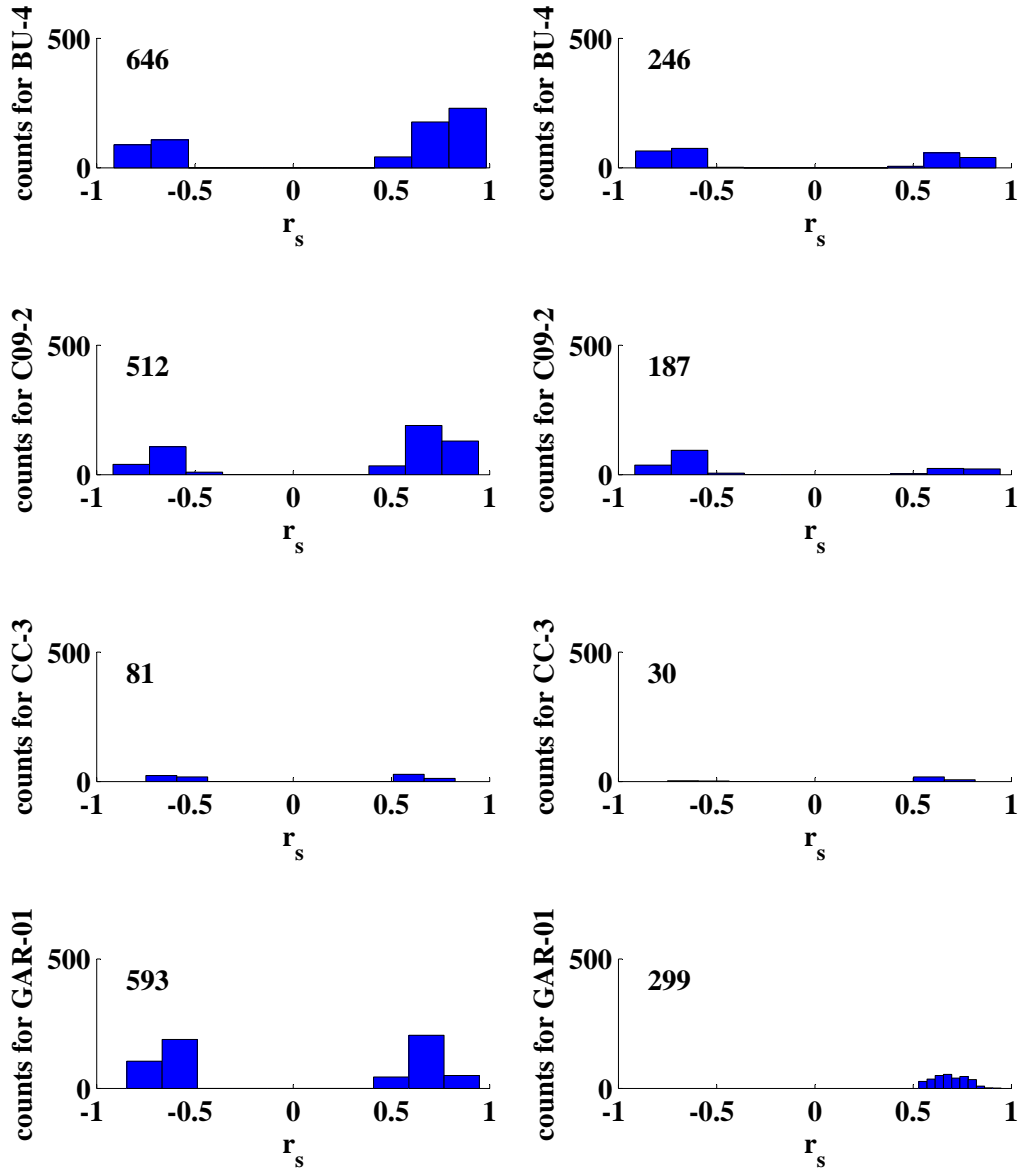


Fig. H.7: Illustrated is the distribution of speleothem r_s for the indicated runs of the 4000 years short-term PCA on $\delta^{18}\text{O}$ time series before (left panels) and after (right panels) the application of the Fork-tool.

run #4 - 2.8-2.5 ka BP - Part II

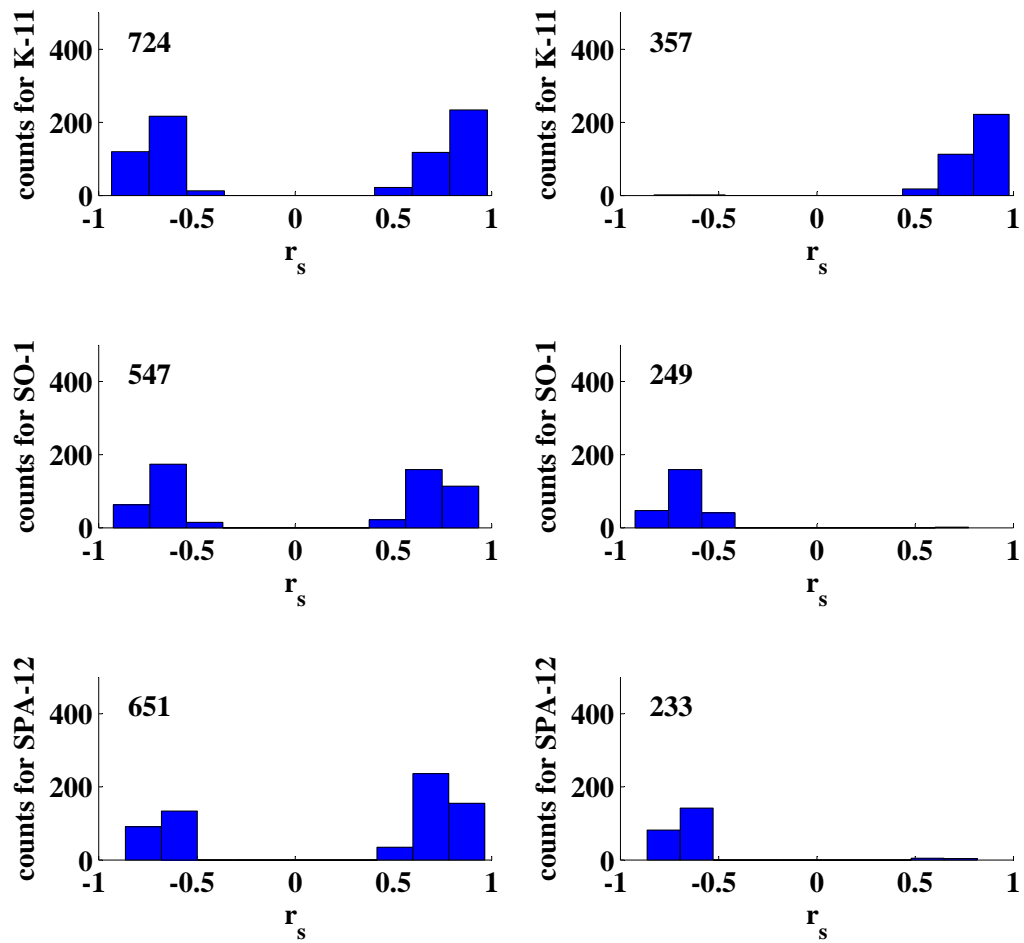


Fig. H.8: Illustrated is the distribution of speleothem r_s for the indicated runs of the 4000 years short-term PCA on $\delta^{18}O$ time series before (left panels) and after (right panels) the application of the Fork-tool.

run #5 - 2.6-2.3 ka BP - Part I

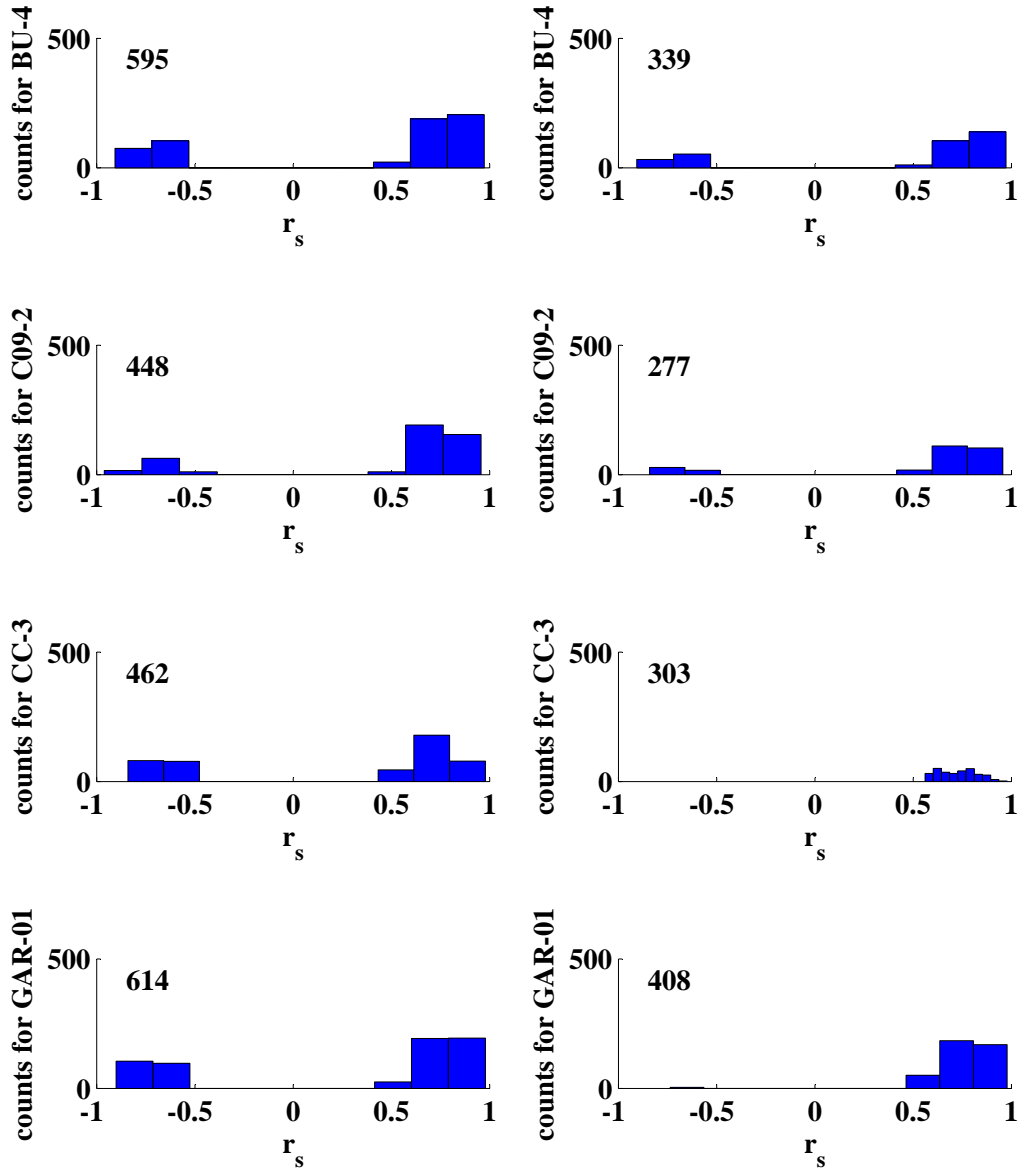


Fig. H.9: Illustrated is the distribution of speleothem r_s for the indicated runs of the 4000 years short-term PCA on $\delta^{18}\text{O}$ time series before (left panels) and after (right panels) the application of the Fork-tool.

run #5 - 2.6-2.3 ka BP - Part II

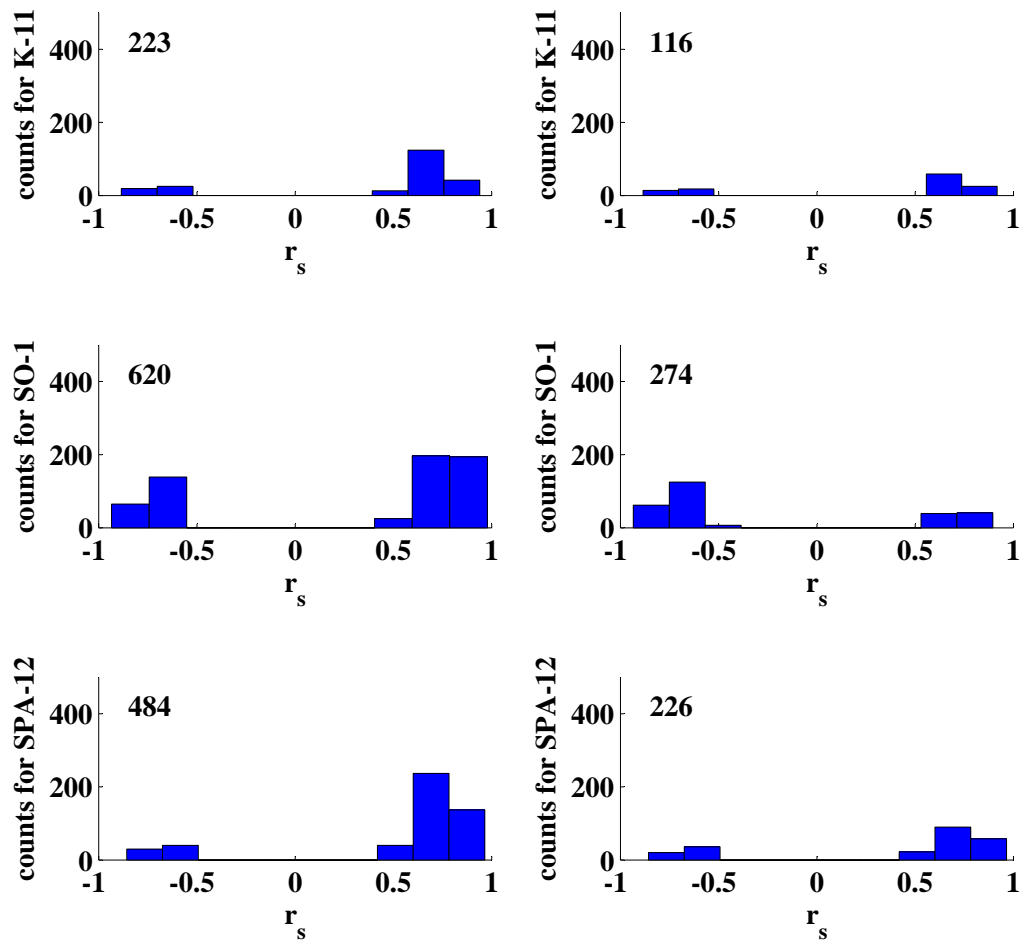


Fig. H.10: Illustrated is the distribution of speleothem r_s for the indicated runs of the 4000 years short-term PCA on $\delta^{18}O$ time series before (left panels) and after (right panels) the application of the Fork-tool.

run #6 - 2.3-2.0 ka BP - Part I

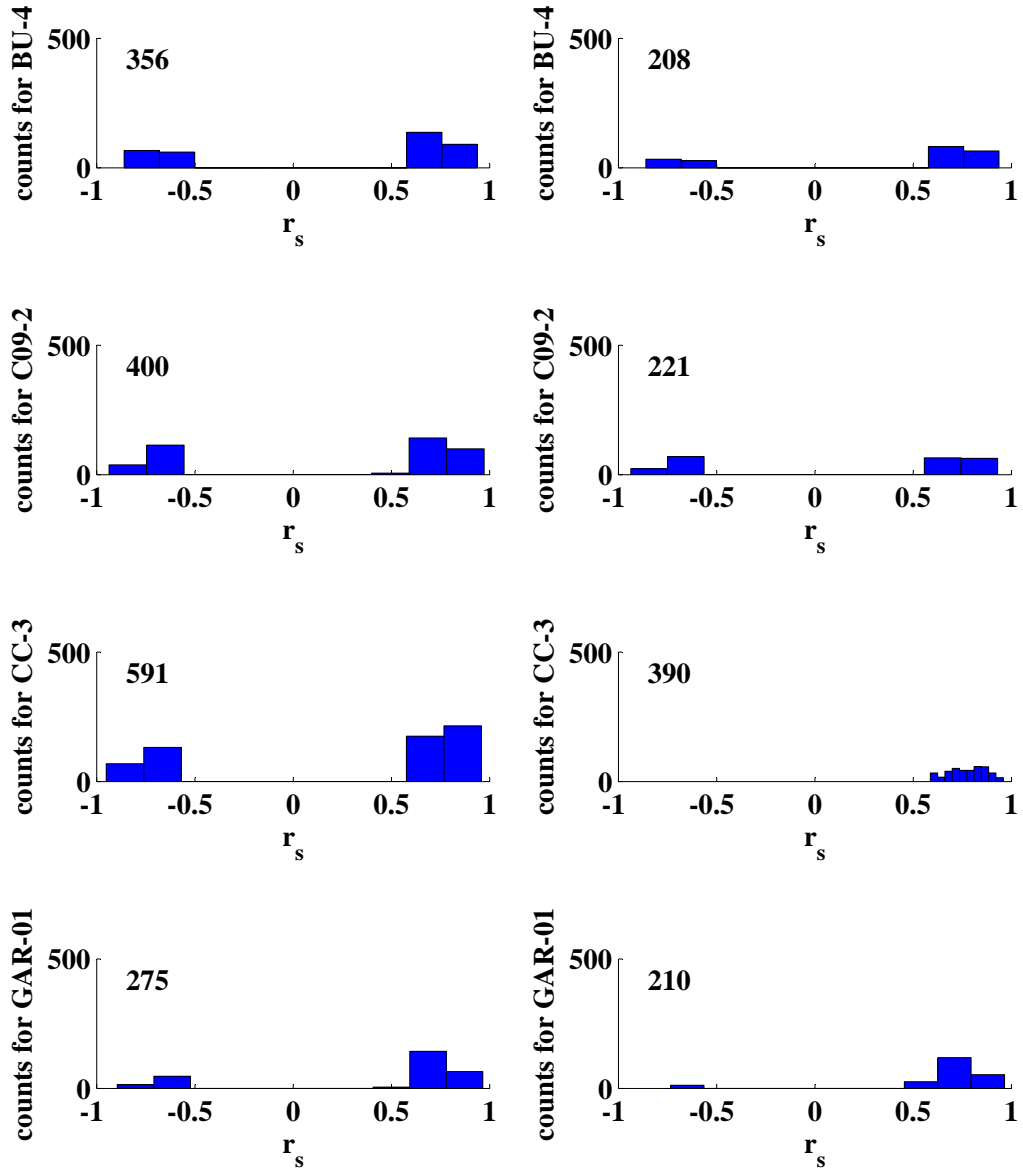


Fig. H.11: Illustrated is the distribution of speleothem r_s for the indicated runs of the 4000 years short-term PCA on $\delta^{18}\text{O}$ time series before (left panels) and after (right panels) the application of the Fork-tool.

run #6 - 2.3-2.0 ka BP - Part II

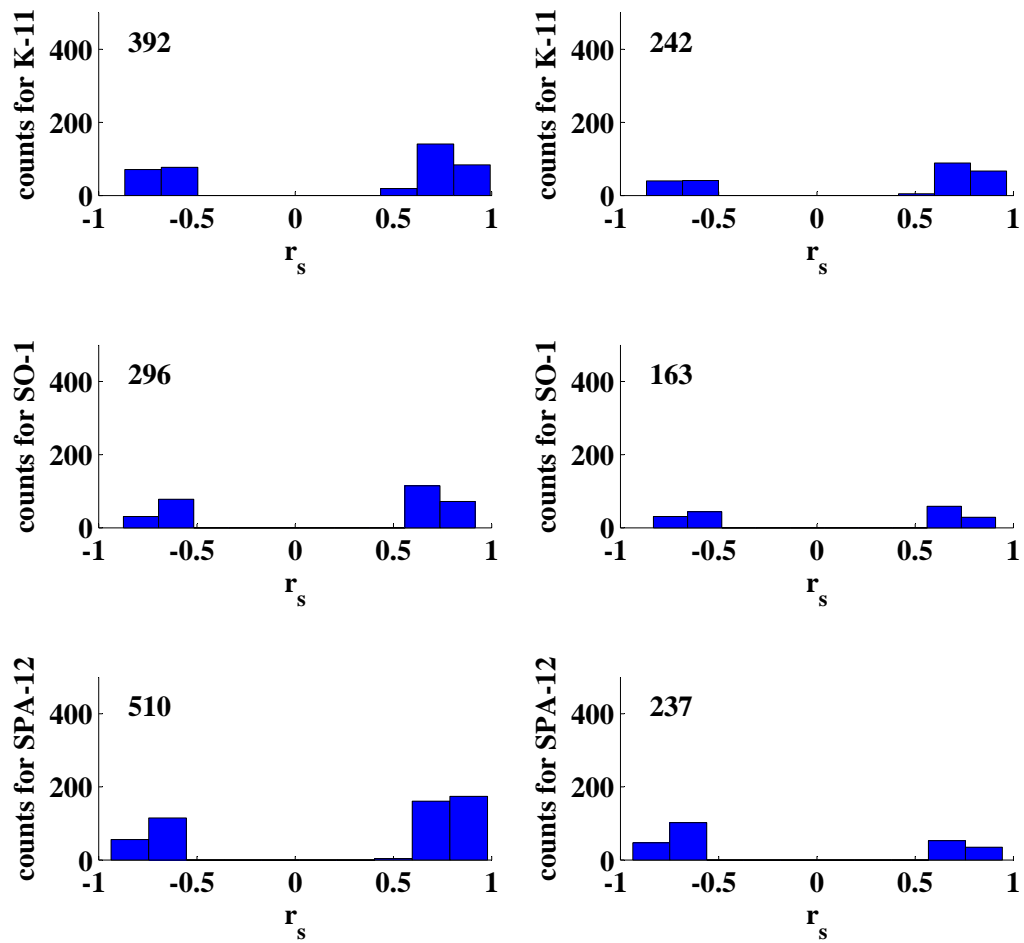


Fig. H.12: Illustrated is the distribution of speleothem r_s for the indicated runs of the 4000 years short-term PCA on $\delta^{18}O$ time series before (left panels) and after (right panels) the application of the Fork-tool.

run #7 - 2.0-1.7 ka BP - Part I

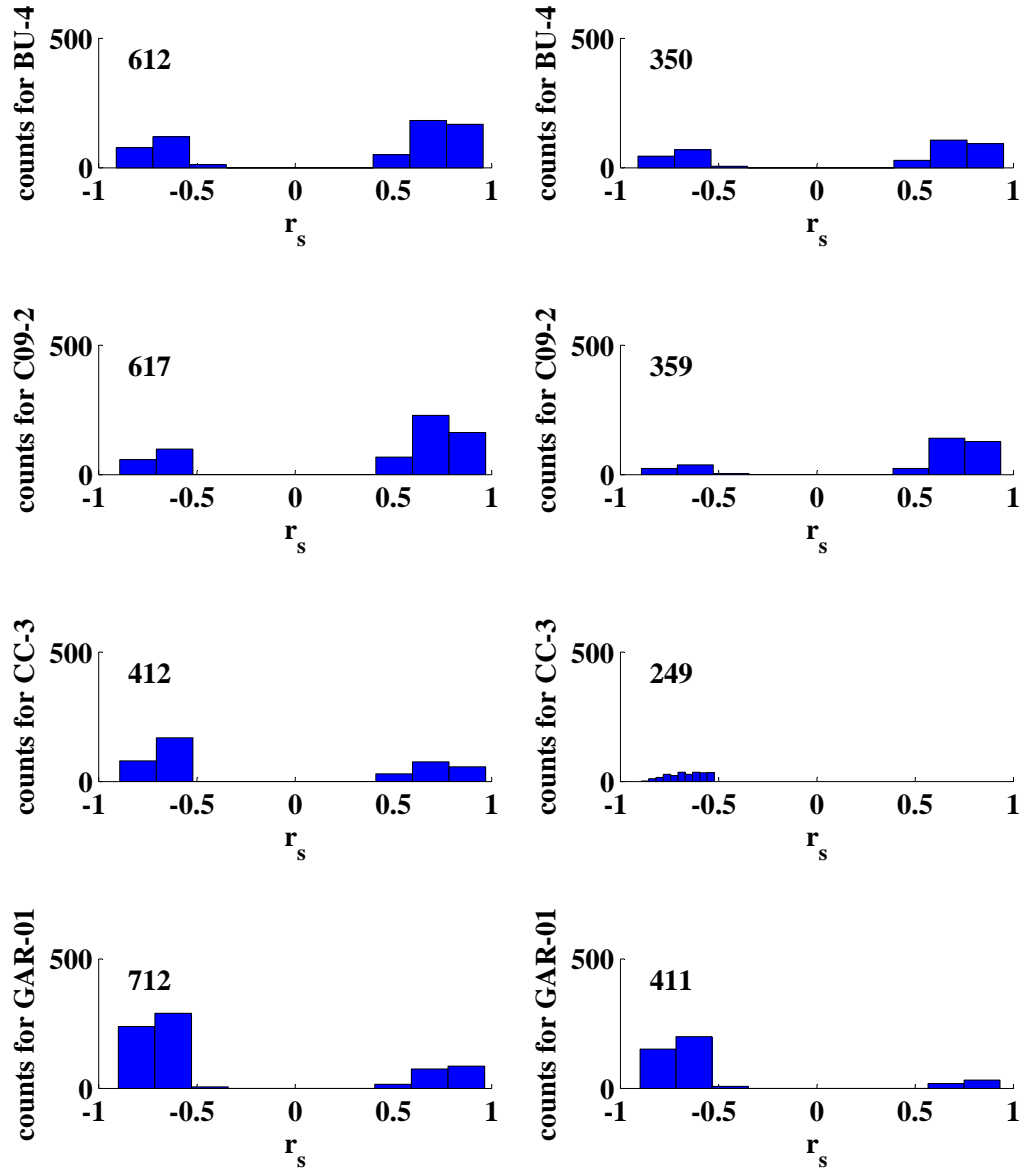


Fig. H.13: Illustrated is the distribution of speleothem r_s for the indicated runs of the 4000 years short-term PCA on $\delta^{18}\text{O}$ time series before (left panels) and after (right panels) the application of the Fork-tool.

run #7 - 2.0-1.7 ka BP - Part II

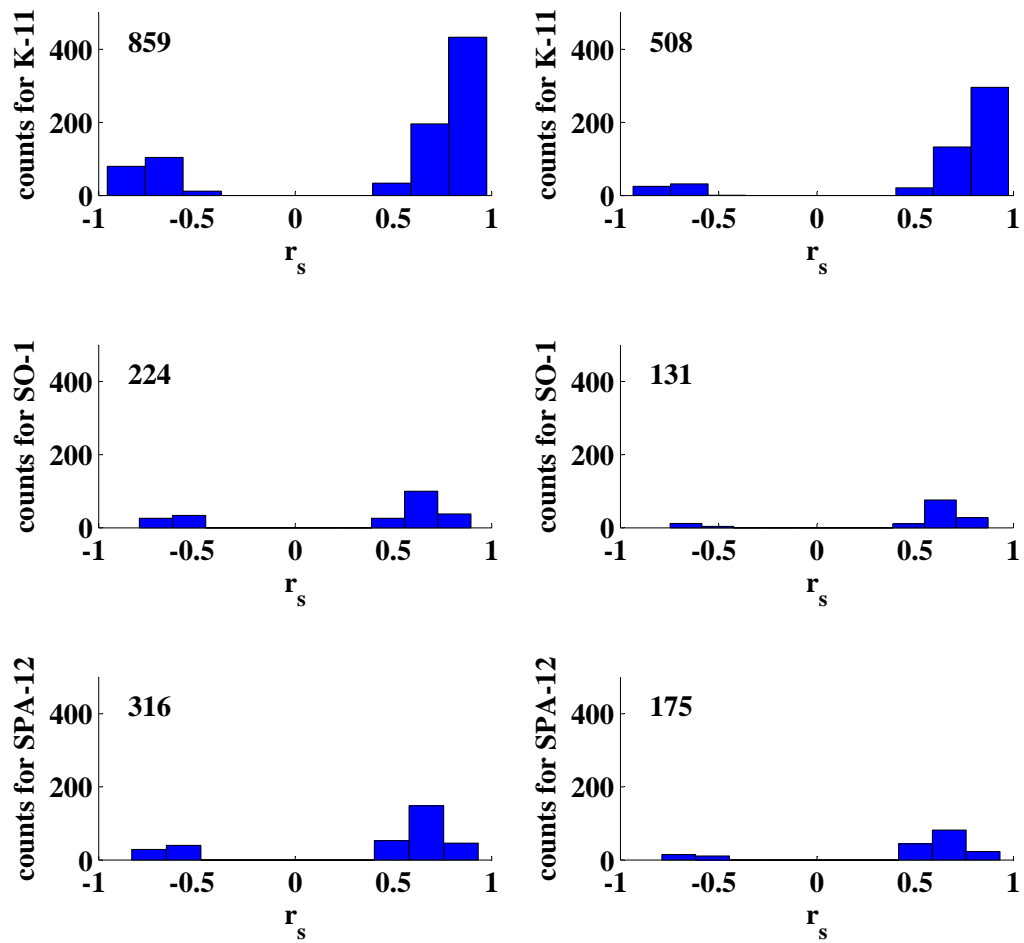


Fig. H.14: Illustrated is the distribution of speleothem r_s for the indicated runs of the 4000 years short-term PCA on $\delta^{18}O$ time series before (left panels) and after (right panels) the application of the Fork-tool.

run #8 - 1.7-1.4 ka BP - Part I

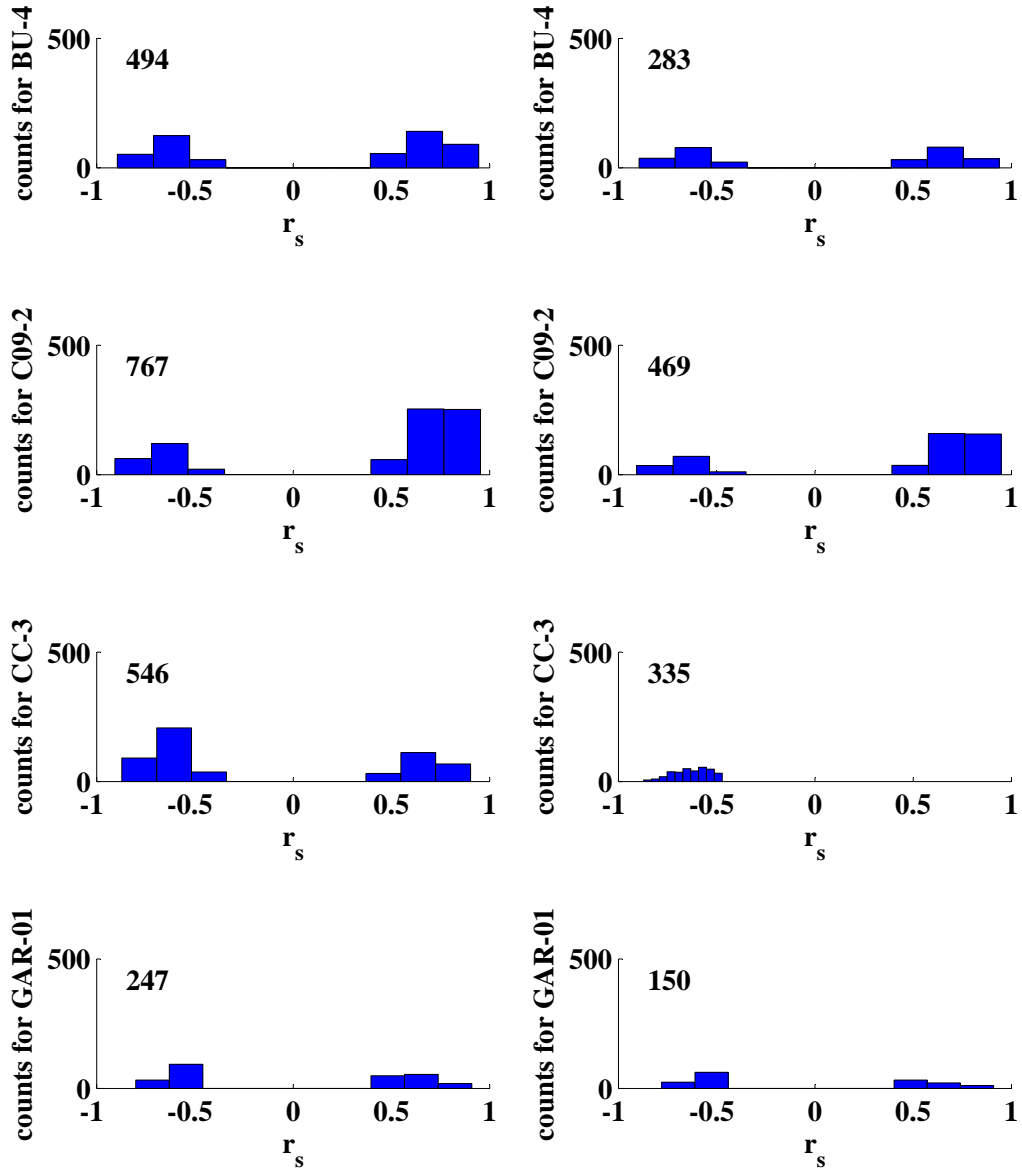


Fig. H.15: Illustrated is the distribution of speleothem r_s for the indicated runs of the 4000 years short-term PCA on $\delta^{18}\text{O}$ time series before (left panels) and after (right panels) the application of the Fork-tool.

run #8 - 1.7-1.4 ka BP - Part II

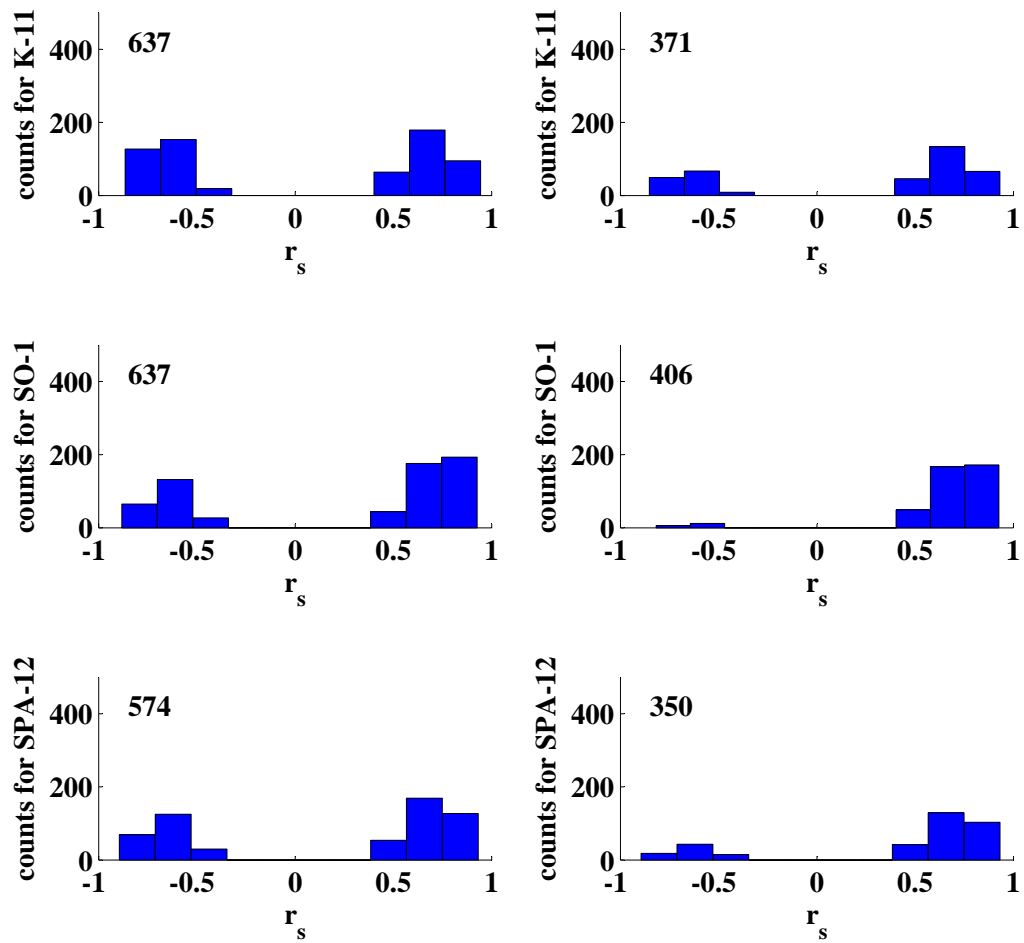


Fig. H.16: Illustrated is the distribution of speleothem r_s for the indicated runs of the 4000 years short-term PCA on $\delta^{18}O$ time series before (left panels) and after (right panels) the application of the Fork-tool.

run #9 - 1.4-1.1 ka BP - Part I

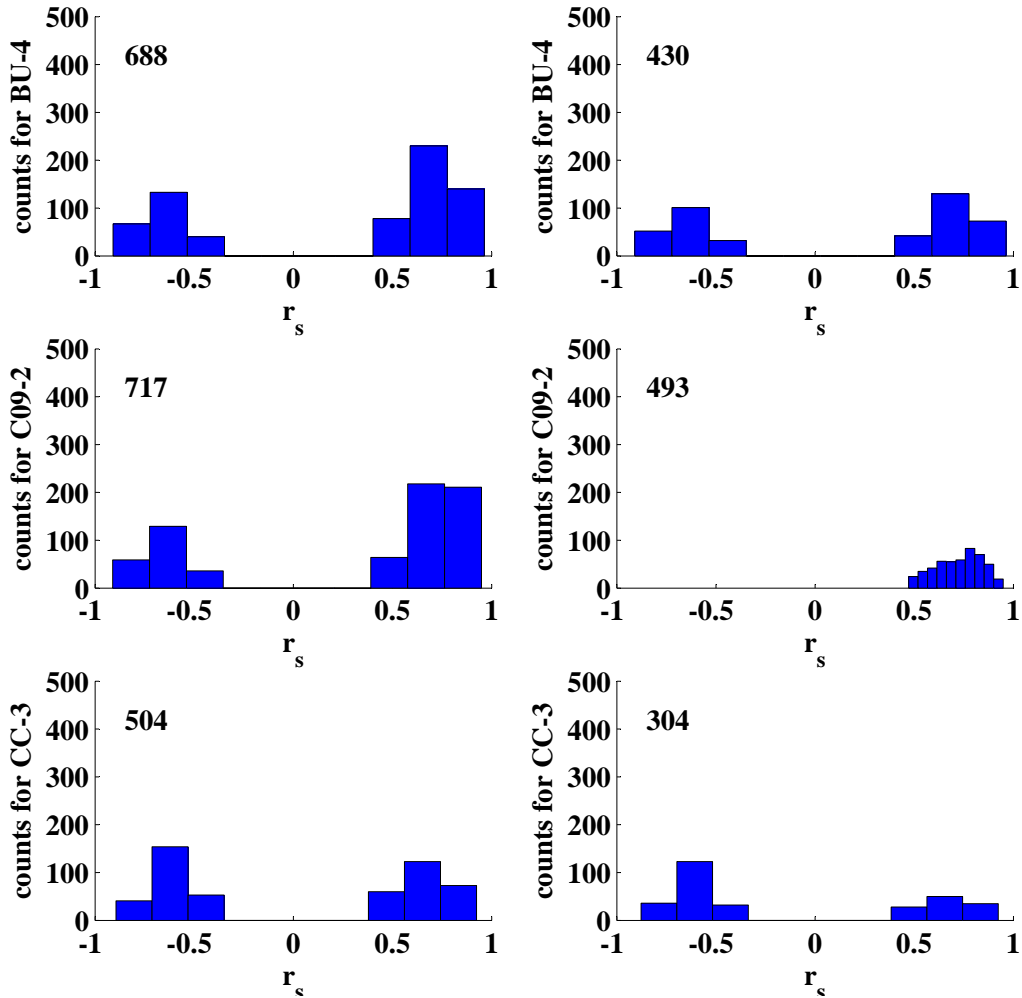


Fig. H.17: Illustrated is the distribution of speleothem r_s for the indicated runs of the 4000 years short-term PCA on $\delta^{18}\text{O}$ time series before (left panels) and after (right panels) the application of the Fork-tool.

run #9 - 1.4-1.1 ka BP - Part II

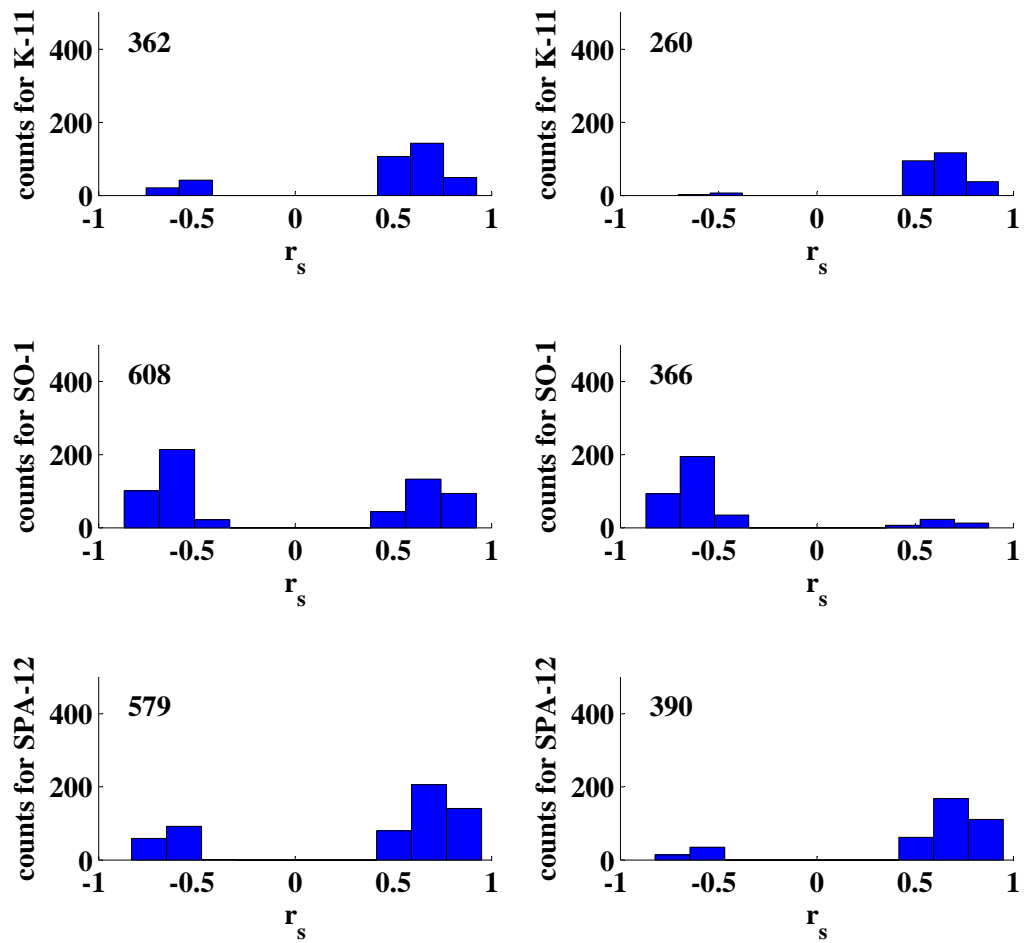


Fig. H.18: Illustrated is the distribution of speleothem r_s for the indicated runs of the 4000 years short-term PCA on $\delta^{18}O$ time series before (left panels) and after (right panels) the application of the Fork-tool.

run #10 - 1.6-1.15 ka BP - Part I

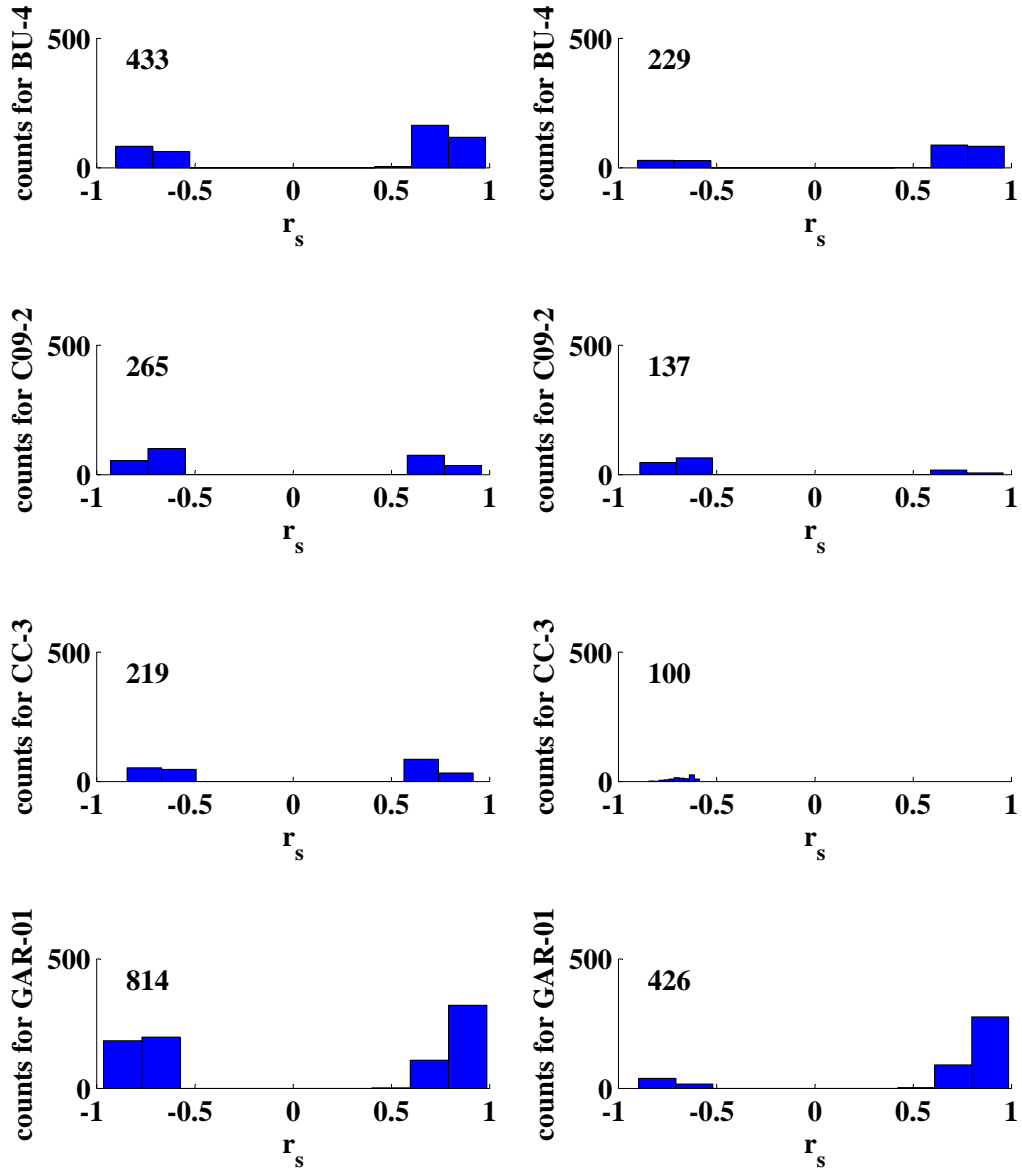


Fig. H.19: Illustrated is the distribution of speleothem r_s for the indicated runs of the 4000 years short-term PCA on $\delta^{18}\text{O}$ time series before (left panels) and after (right panels) the application of the Fork-tool.

run #10 - 1.6-1.15 ka BP - Part II

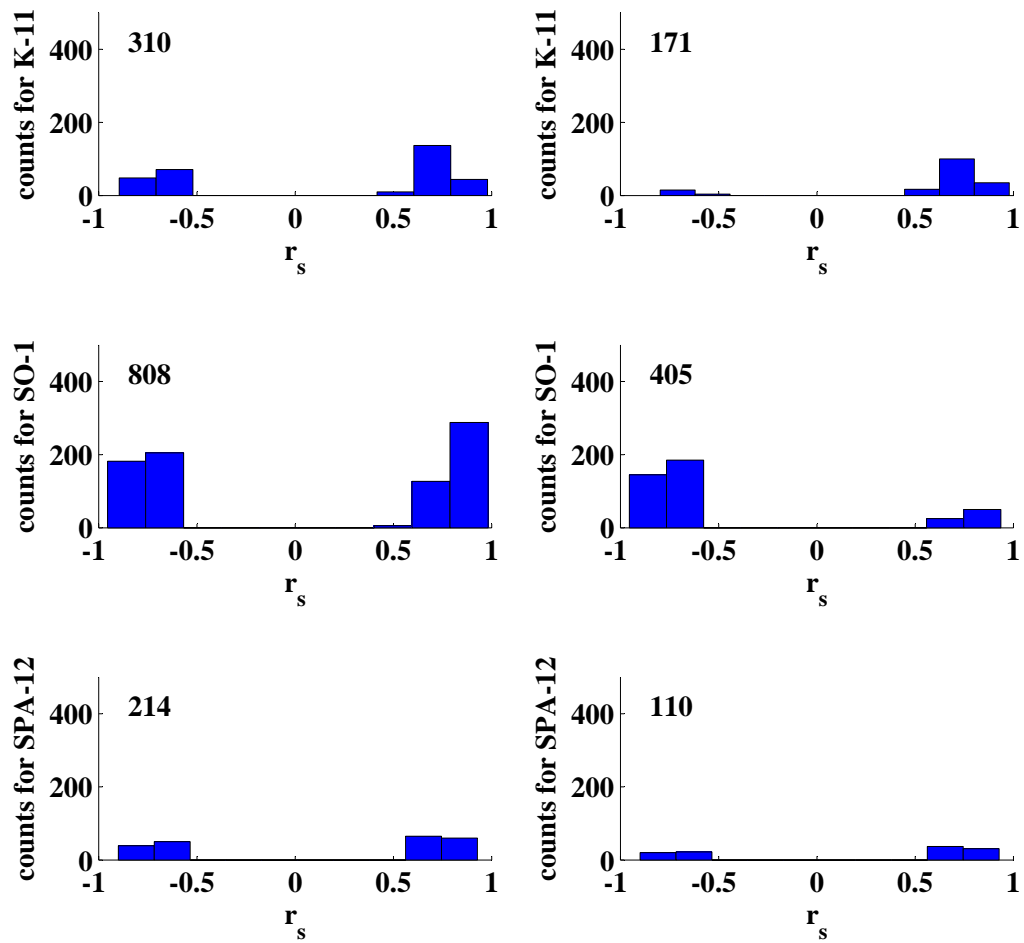


Fig. H.20: Illustrated is the distribution of speleothem r_s for the indicated runs of the 4000 years short-term PCA on $\delta^{18}O$ time series before (left panels) and after (right panels) the application of the Fork-tool.

run #11 - 1.1-0.8 ka BP - Part I

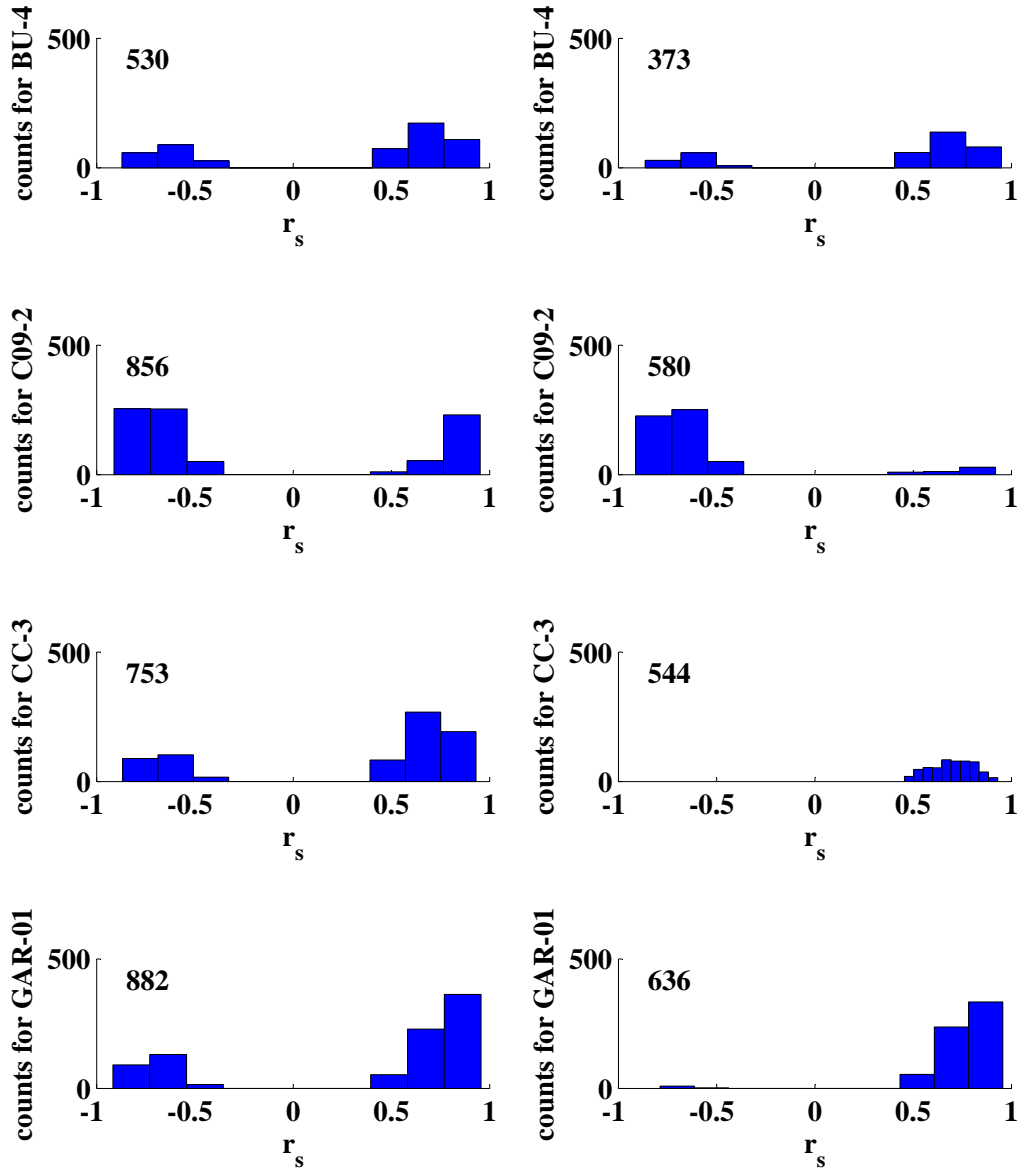


Fig. H.21: Illustrated is the distribution of speleothem r_s for the indicated runs of the 4000 years short-term PCA on $\delta^{18}\text{O}$ time series before (left panels) and after (right panels) the application of the Fork-tool.

run #11 - 1.1-0.8 ka BP - Part II

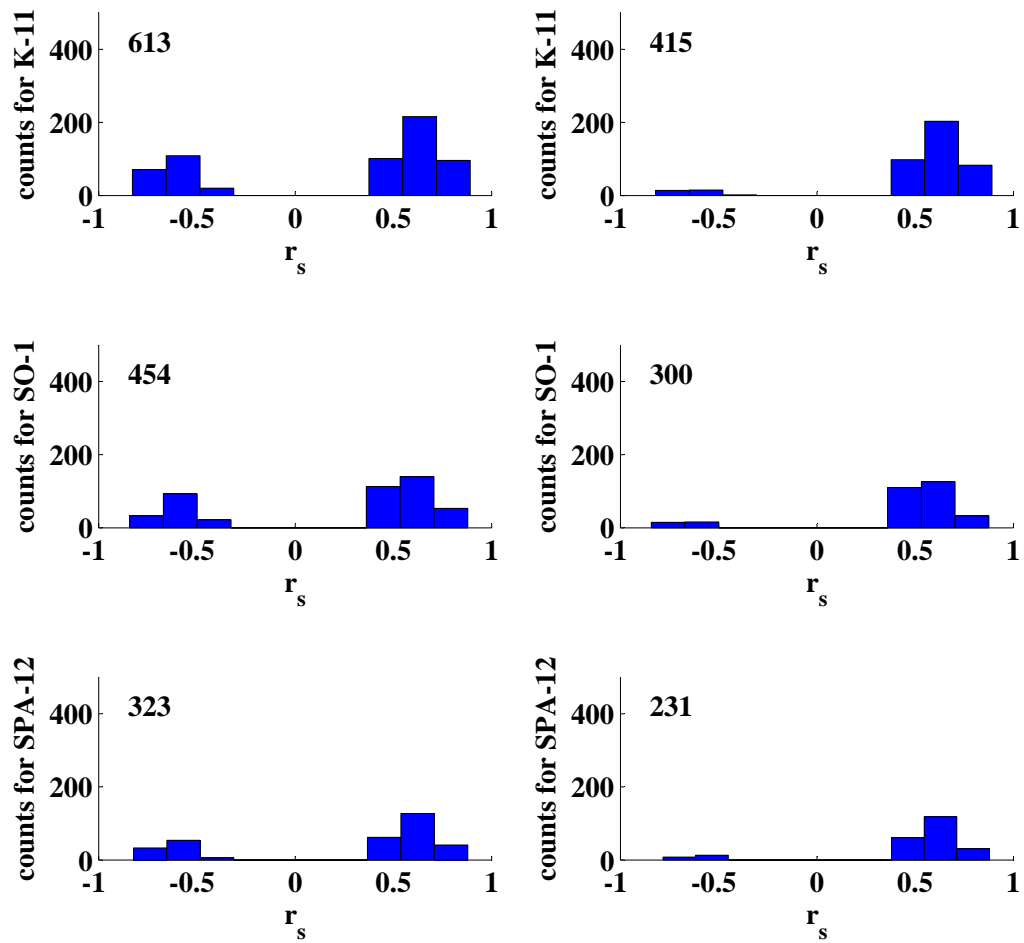


Fig. H.22: Illustrated is the distribution of speleothem r_s for the indicated runs of the 4000 years short-term PCA on $\delta^{18}O$ time series before (left panels) and after (right panels) the application of the Fork-tool.

run #12 - 0.8-0.5 ka BP - Part I

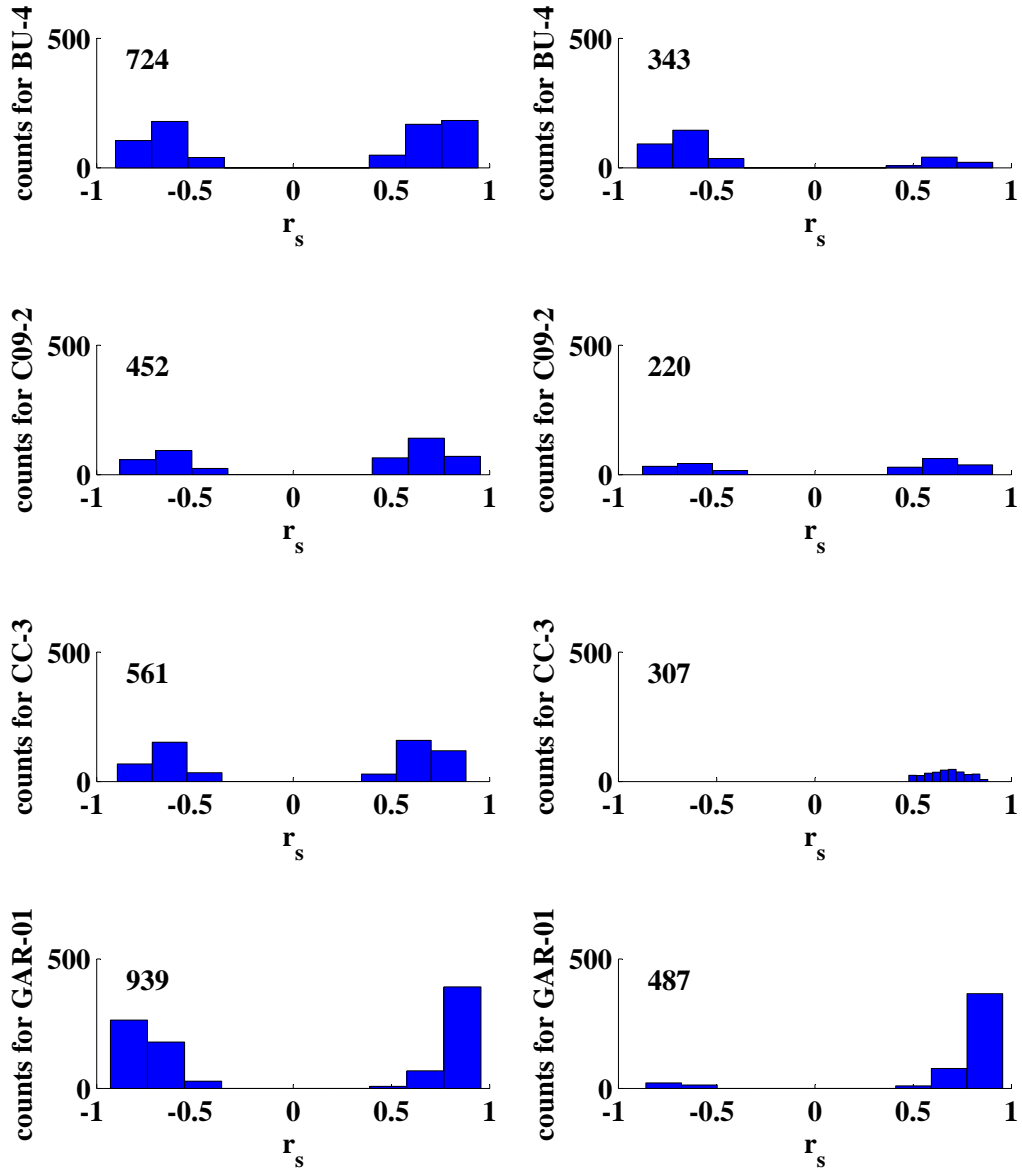


Fig. H.23: Illustrated is the distribution of speleothem r_s for the indicated runs of the 4000 years short-term PCA on $\delta^{18}\text{O}$ time series before (left panels) and after (right panels) the application of the Fork-tool.

run #12 - 0.8-0.5 ka BP - Part II

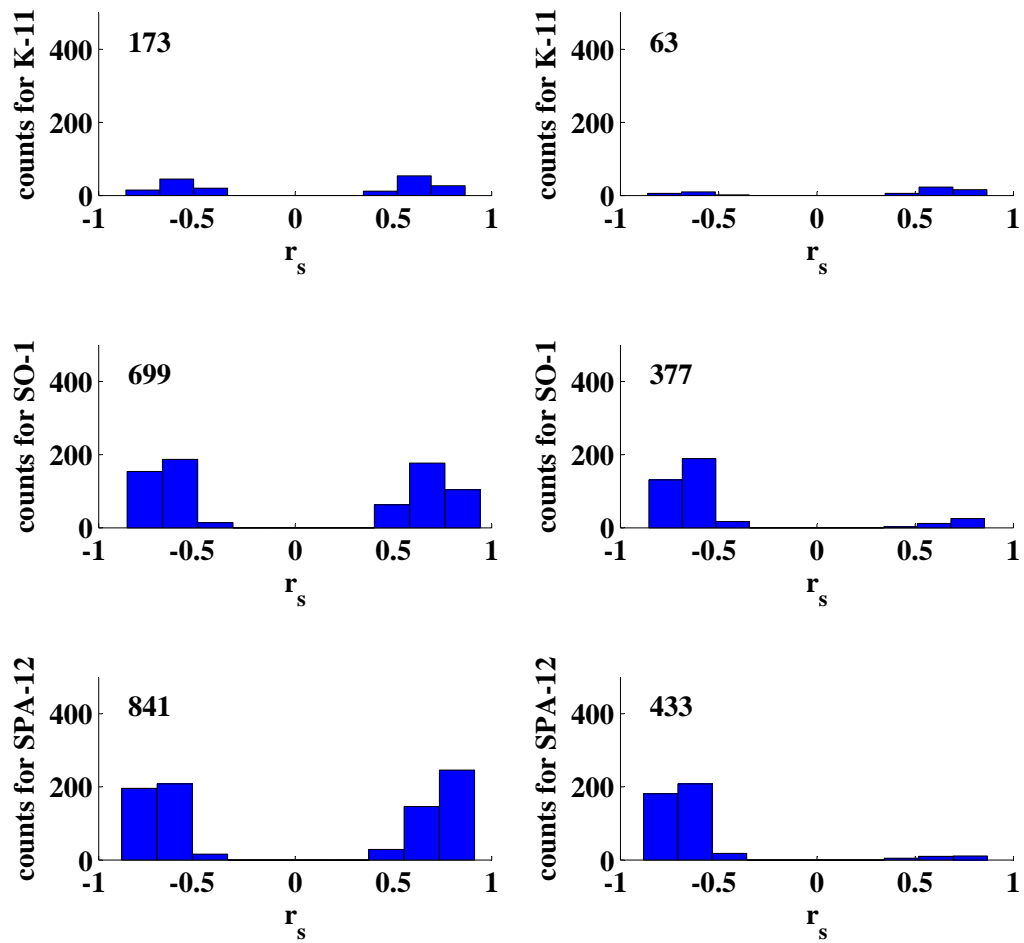


Fig. H.24: Illustrated is the distribution of speleothem r_s for the indicated runs of the 4000 years short-term PCA on $\delta^{18}O$ time series before (left panels) and after (right panels) the application of the Fork-tool.

run #13 - 0.5-0.2 ka BP - Part I

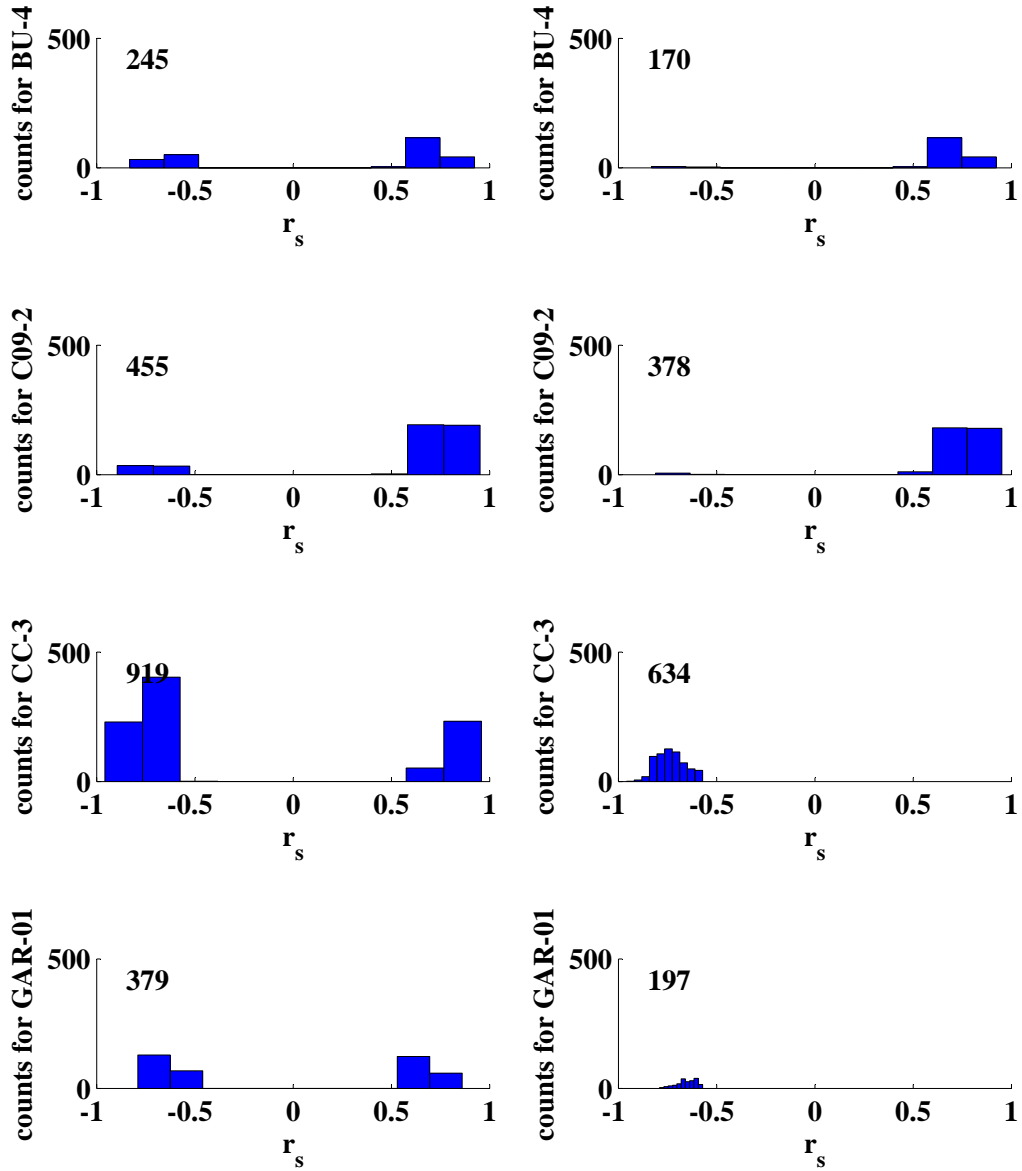


Fig. H.25: Illustrated is the distribution of speleothem r_s for the indicated runs of the 4000 years short-term PCA on $\delta^{18}\text{O}$ time series before (left panels) and after (right panels) the application of the Fork-tool.

run #13 - 0.5-0.2 ka BP - Part II

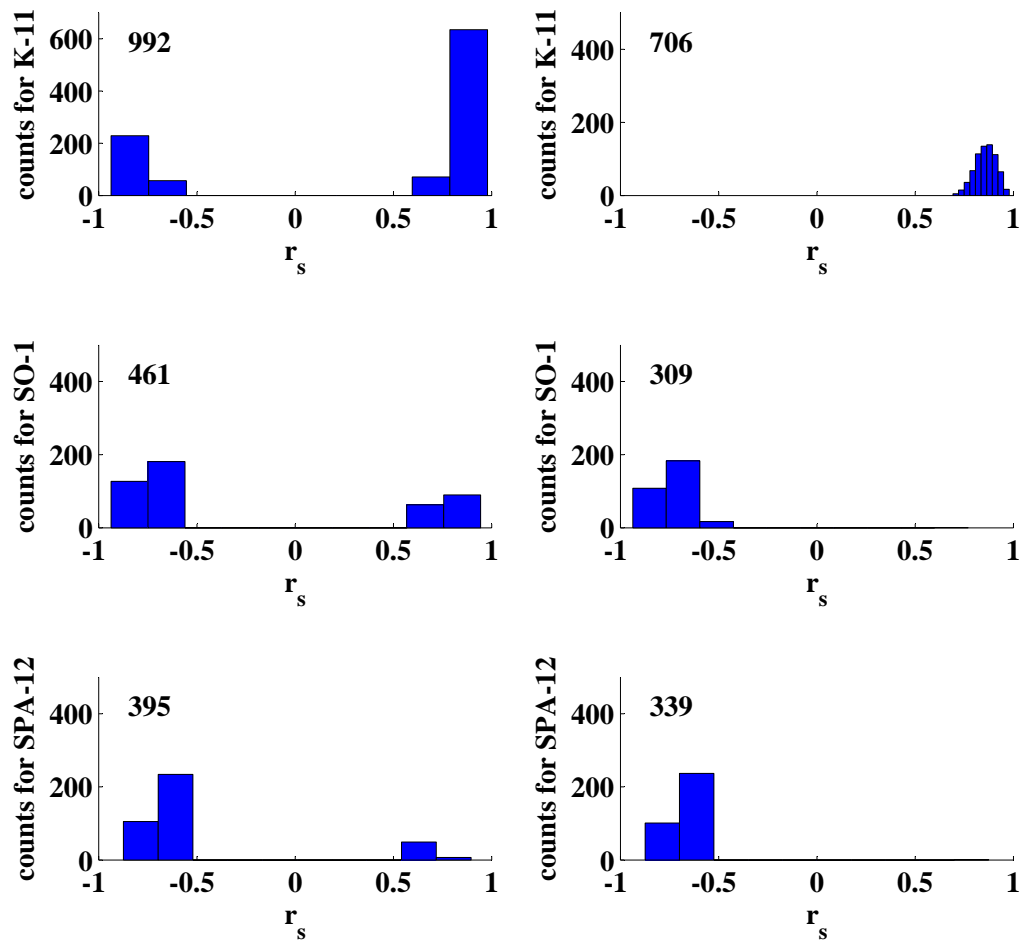


Fig. H.26: Illustrated is the distribution of speleothem r_s for the indicated runs of the 4000 years short-term PCA on $\delta^{18}O$ time series before (left panels) and after (right panels) the application of the Fork-tool.

run #14 - 0.35-0.05 ka BP - Part I

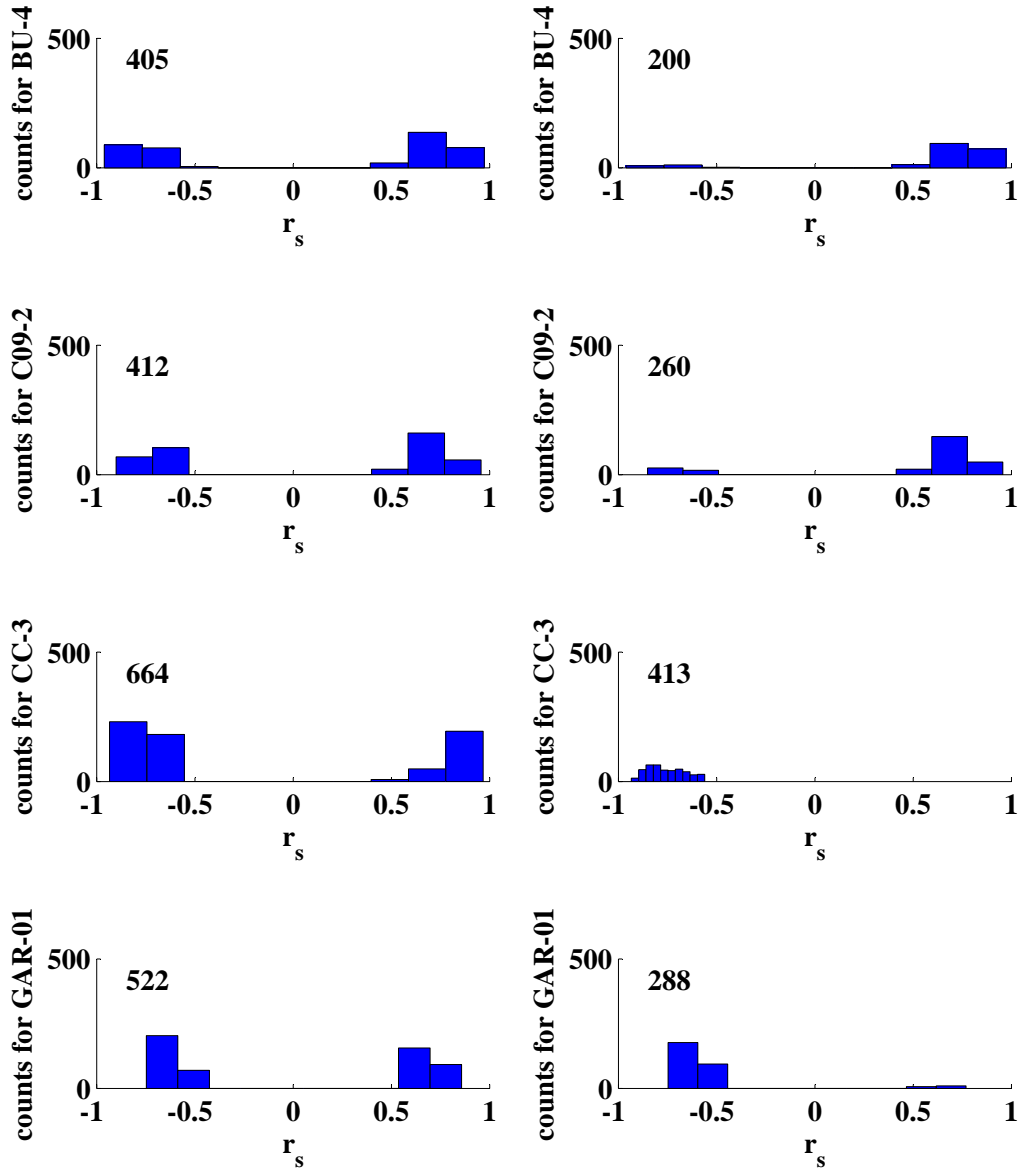


Fig. H.27: Illustrated is the distribution of speleothem r_s for the indicated runs of the 4000 years short-term PCA on $\delta^{18}\text{O}$ time series before (left panels) and after (right panels) the application of the Fork-tool.

run #14 - 0.35-0.05 ka BP - Part II

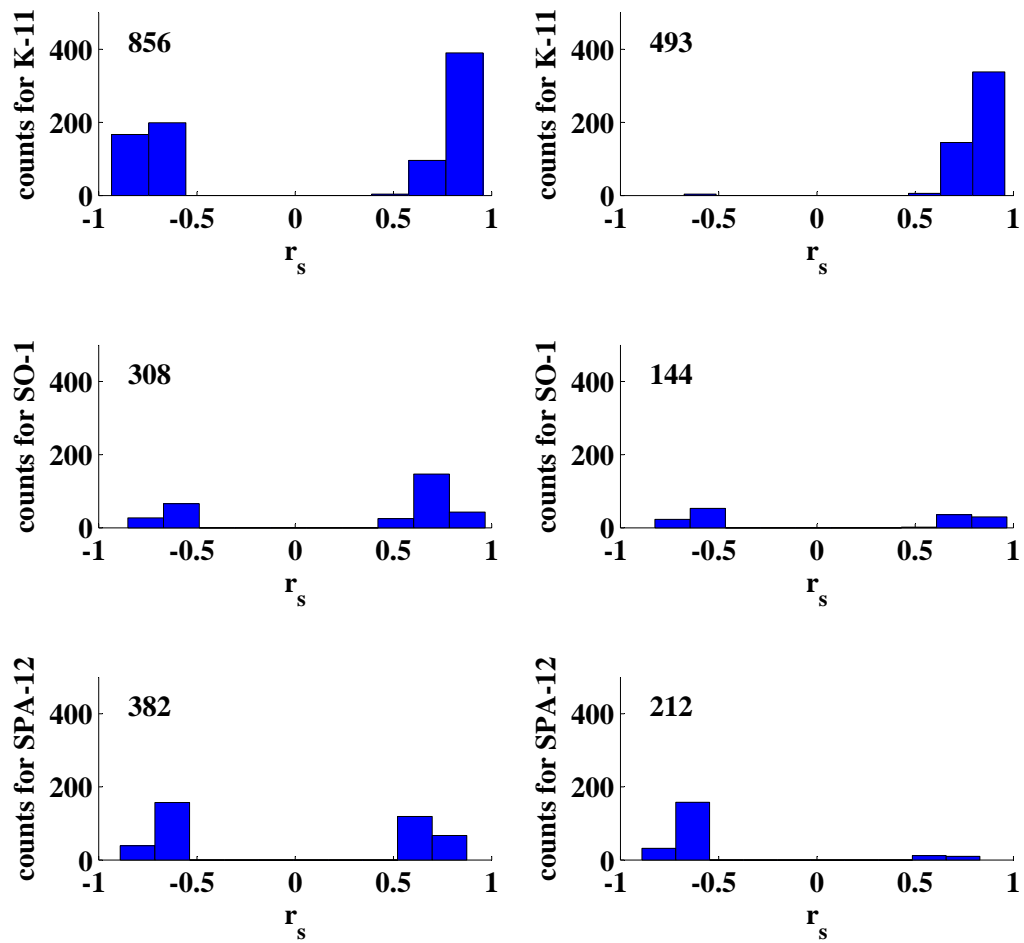


Fig. H.28: Illustrated is the distribution of speleothem r_s for the indicated runs of the 4000 years short-term PCA on $\delta^{18}O$ time series before (left panels) and after (right panels) the application of the Fork-tool.

H.2 Distribution of r_s for short-term coherence pattern for $\delta^{13}C$ time series

run #1 - 3.65-3.4 ka BP - Part I

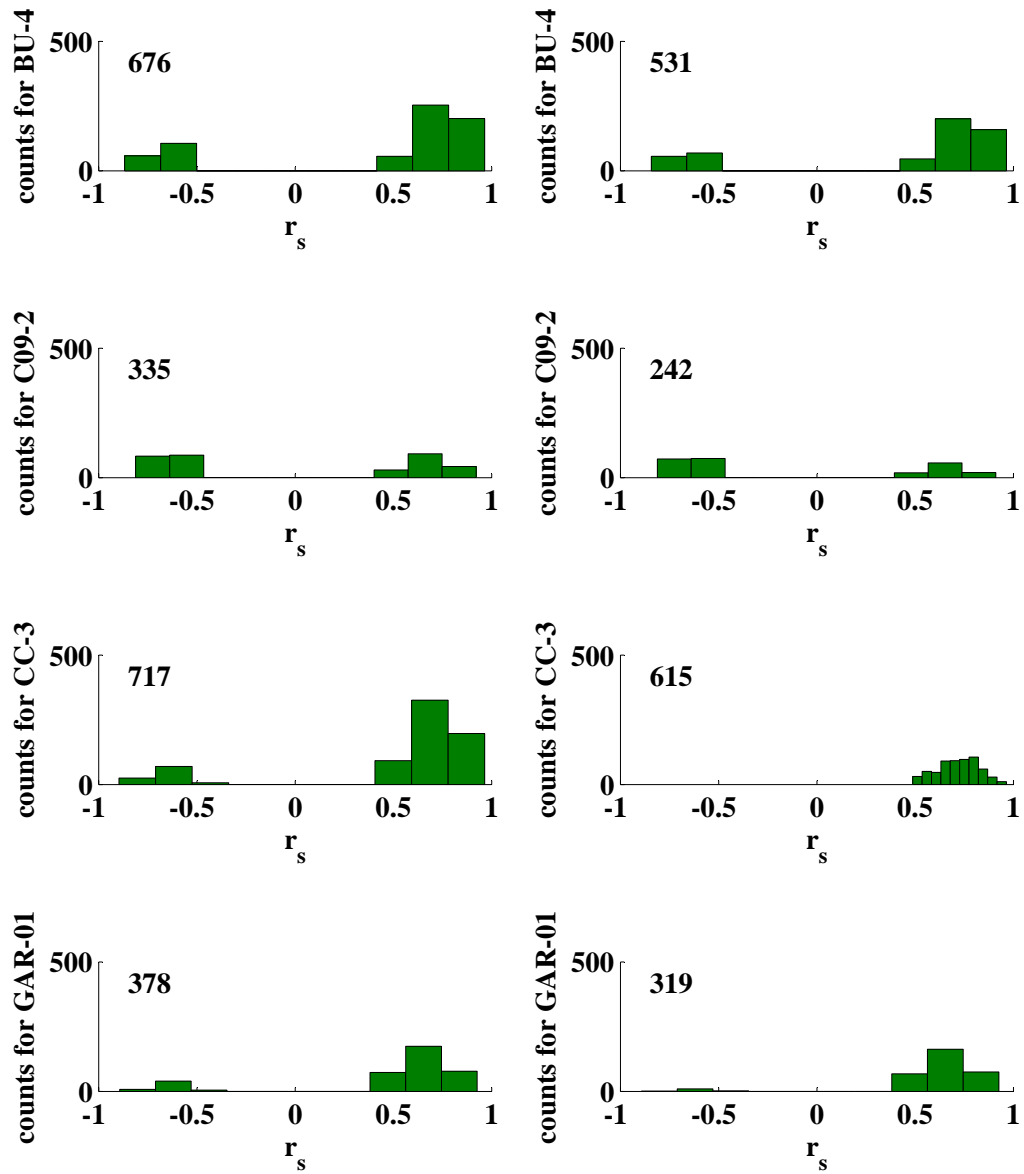


Fig. H.29: Illustrated is the distribution of speleothem r_s for the indicated runs of the 4000 years short-term PCA on $\delta^{13}C$ time series before (left panels) and after (right panels) the application of the Fork-tool.

run #1 - 3.65-3.4 ka BP - Part II

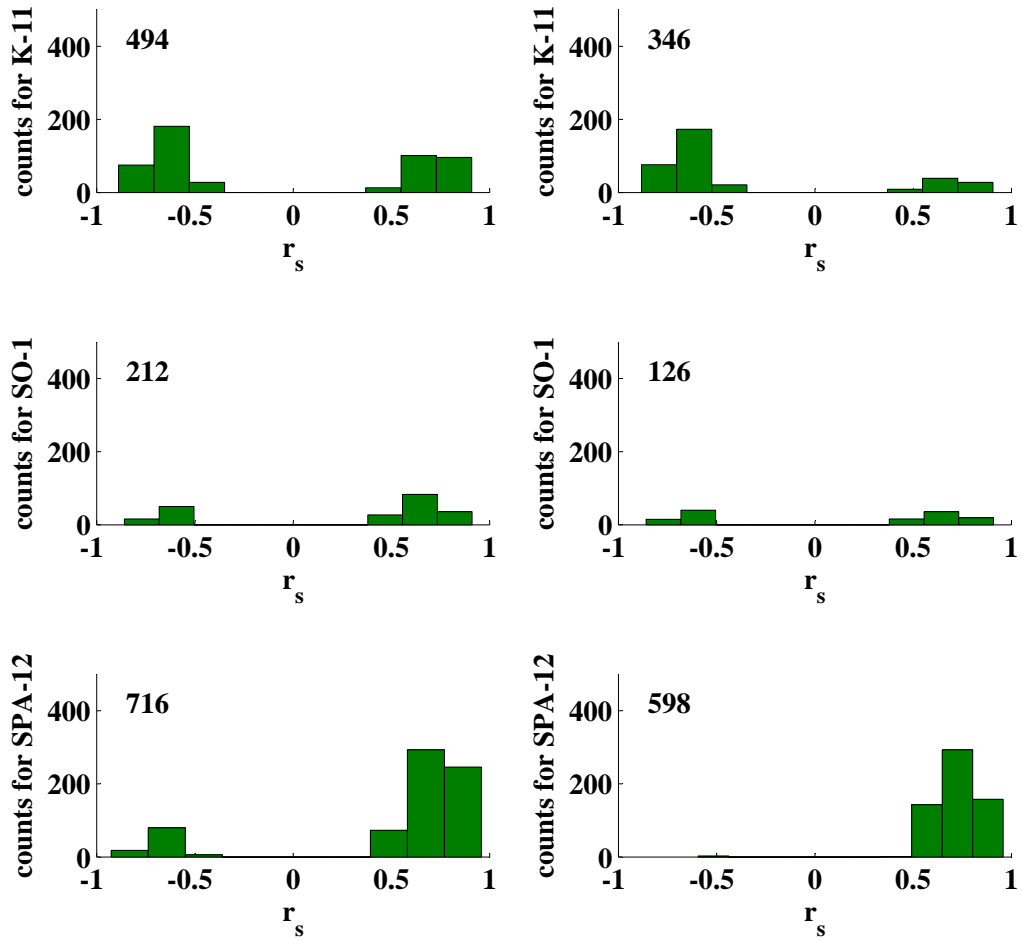


Fig. H.30: Illustrated is the distribution of speleothem r_s for the indicated runs of the 4000 years short-term PCA on $\delta^{13}\text{C}$ time series before (left panels) and after (right panels) the application of the Fork-tool.

run #2 - 3.4-3.1 ka BP - Part I

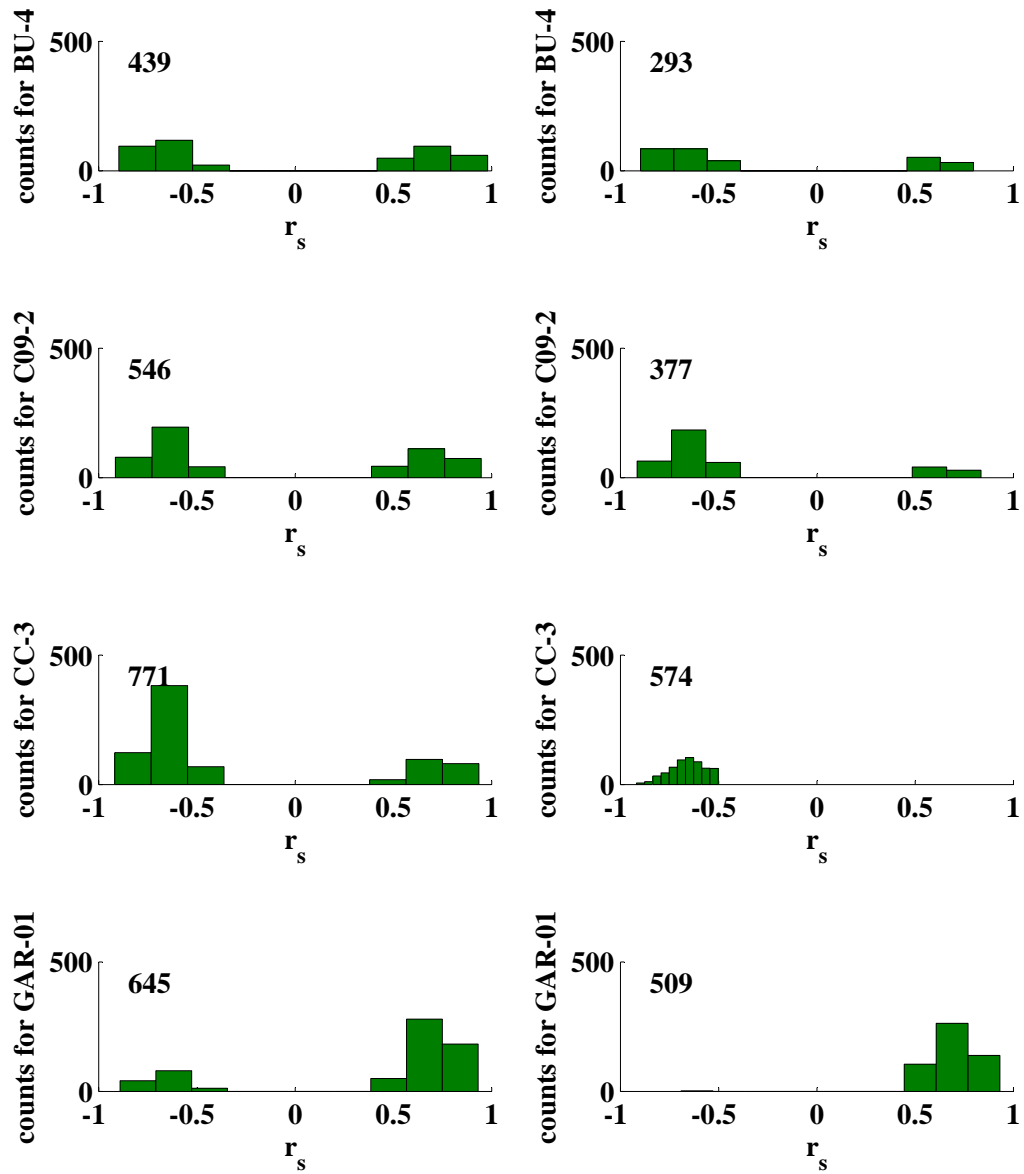


Fig. H.31: Illustrated is the distribution of speleothem r_s for the indicated runs of the 4000 years short-term PCA on $\delta^{13}C$ time series before (left panels) and after (right panels) the application of the Fork-tool.

run #2 - 3.4-3.1 ka BP - Part II

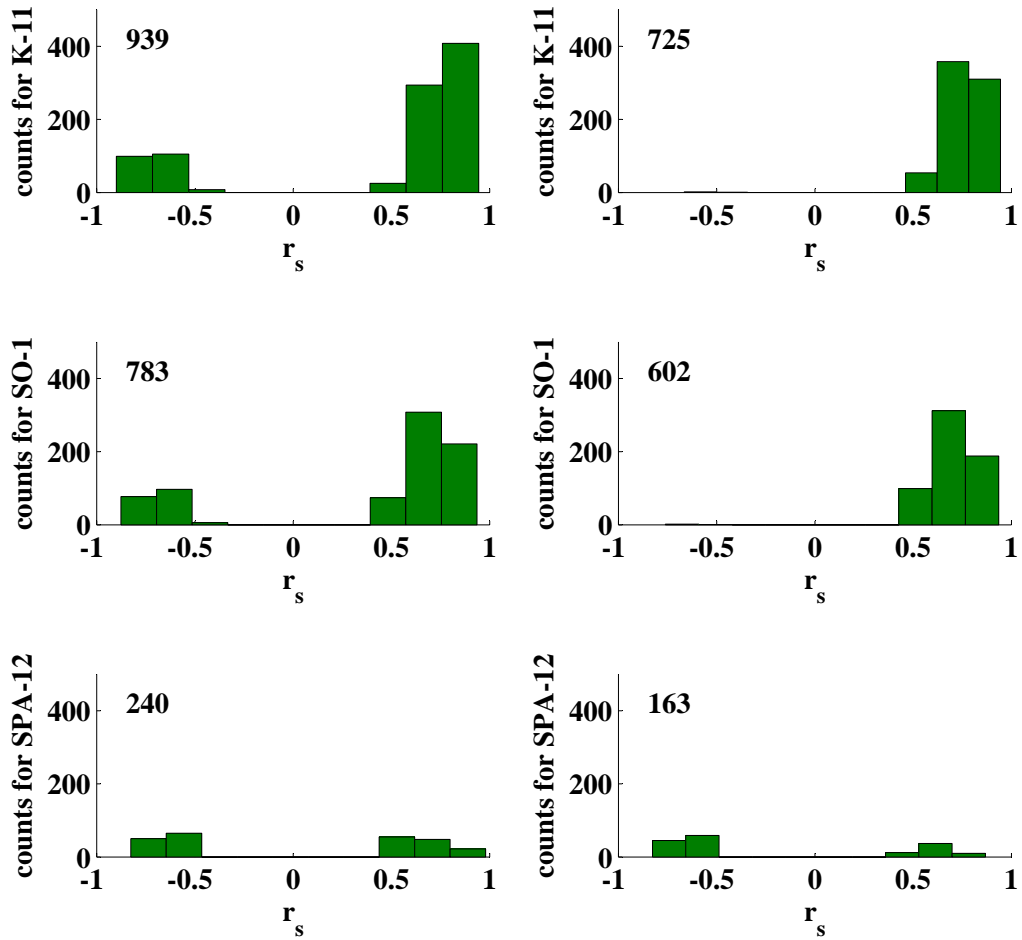


Fig. H.32: Illustrated is the distribution of speleothem r_s for the indicated runs of the 4000 years short-term PCA on $\delta^{13}\text{C}$ time series before (left panels) and after (right panels) the application of the Fork-tool.

run #3 - 3.1-2.8 ka BP - Part I

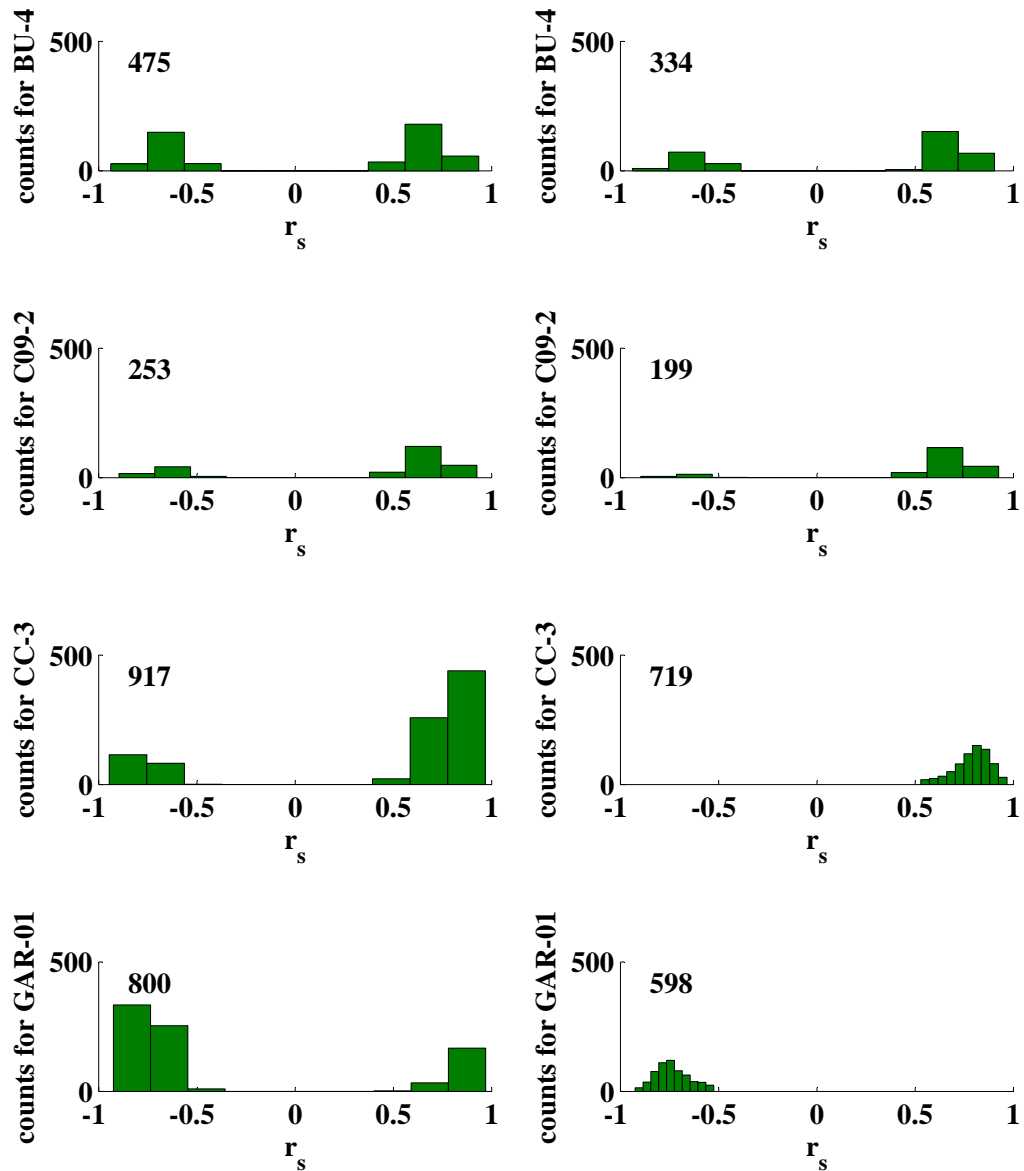


Fig. H.33: Illustrated is the distribution of speleothem r_s for the indicated runs of the 4000 years short-term PCA on $\delta^{13}C$ time series before (left panels) and after (right panels) the application of the Fork-tool.

run #3 - 3.1-2.8 ka BP - Part II

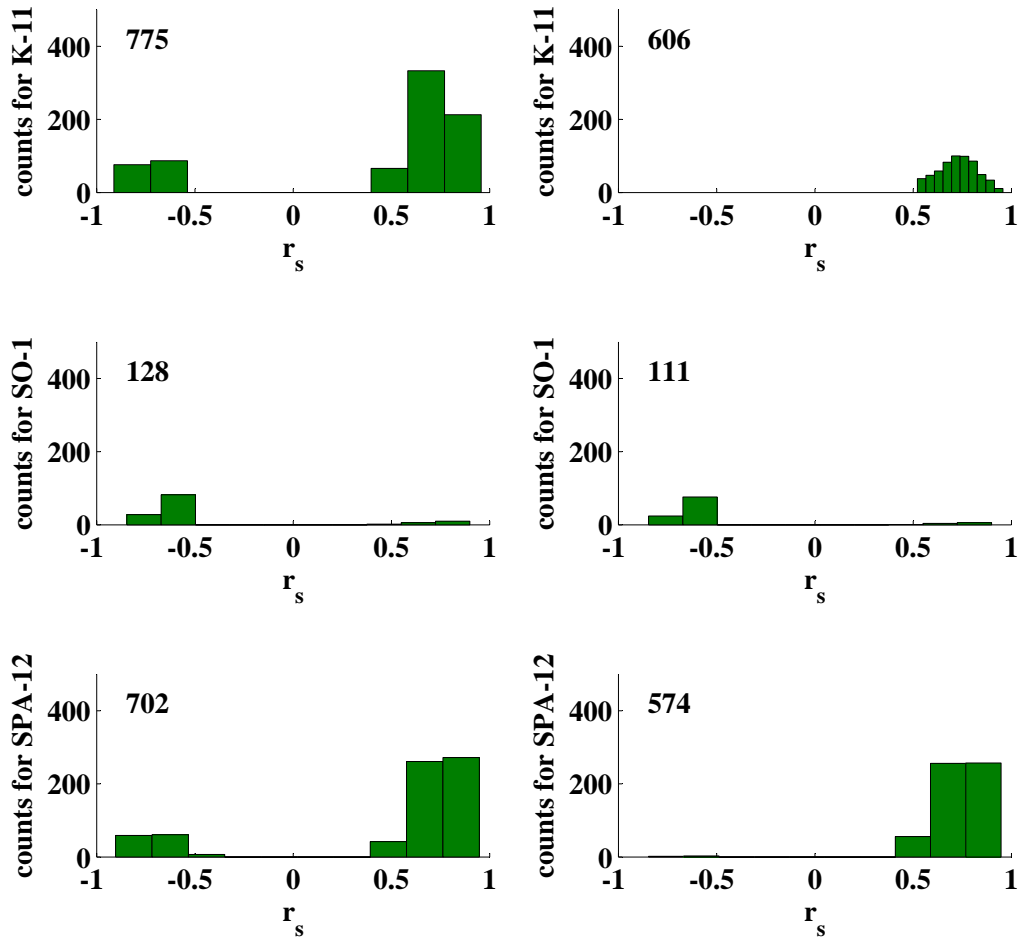


Fig. H.34: Illustrated is the distribution of speleothem r_s for the indicated runs of the 4000 years short-term PCA on $\delta^{13}\text{C}$ time series before (left panels) and after (right panels) the application of the Fork-tool.

run #4 - 2.8-2.5 ka BP - Part I

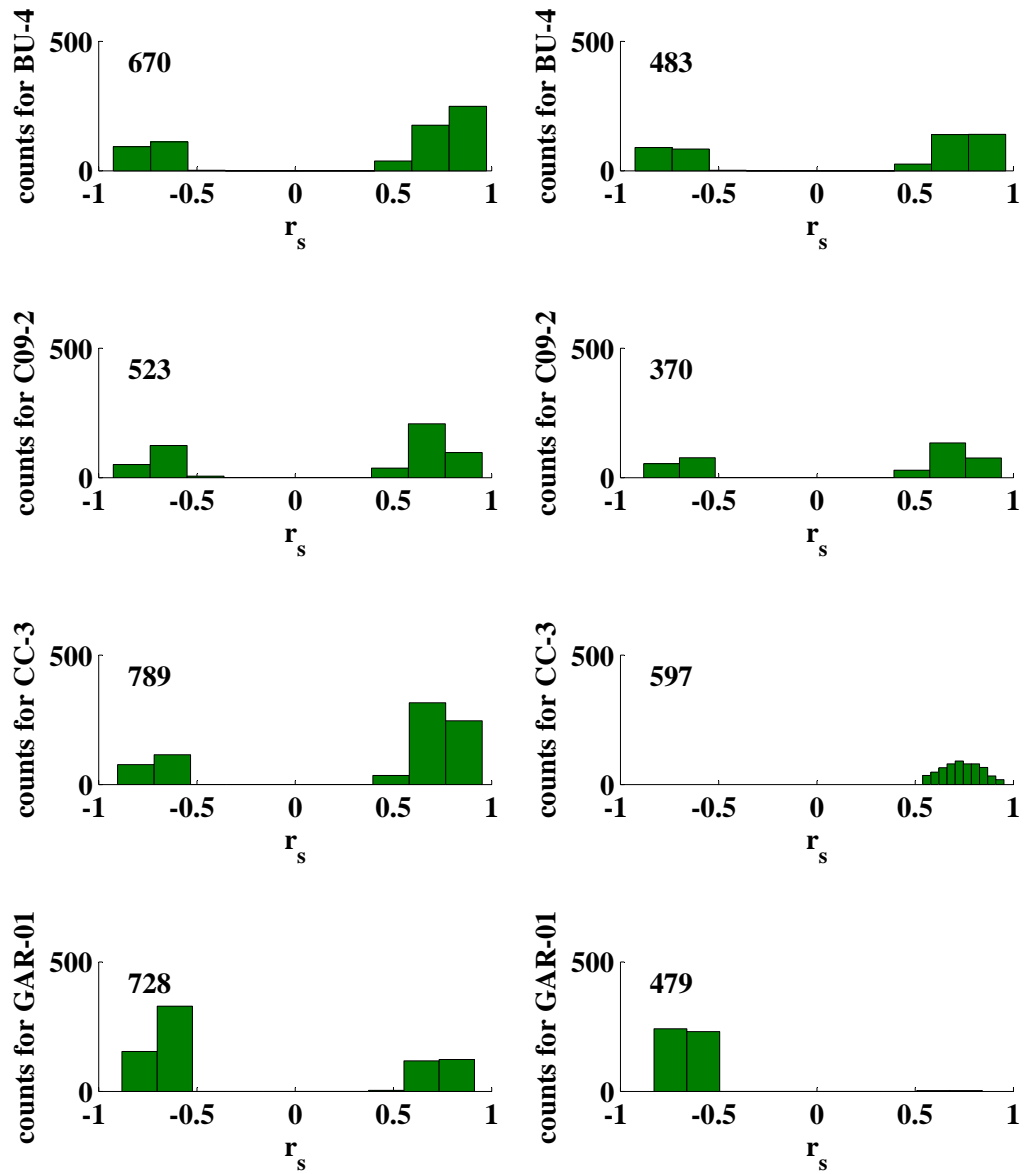


Fig. H.35: Illustrated is the distribution of speleothem r_s for the indicated runs of the 4000 years short-term PCA on $\delta^{13}C$ time series before (left panels) and after (right panels) the application of the Fork-tool.

run #4 - 2.8-2.5 ka BP - Part II

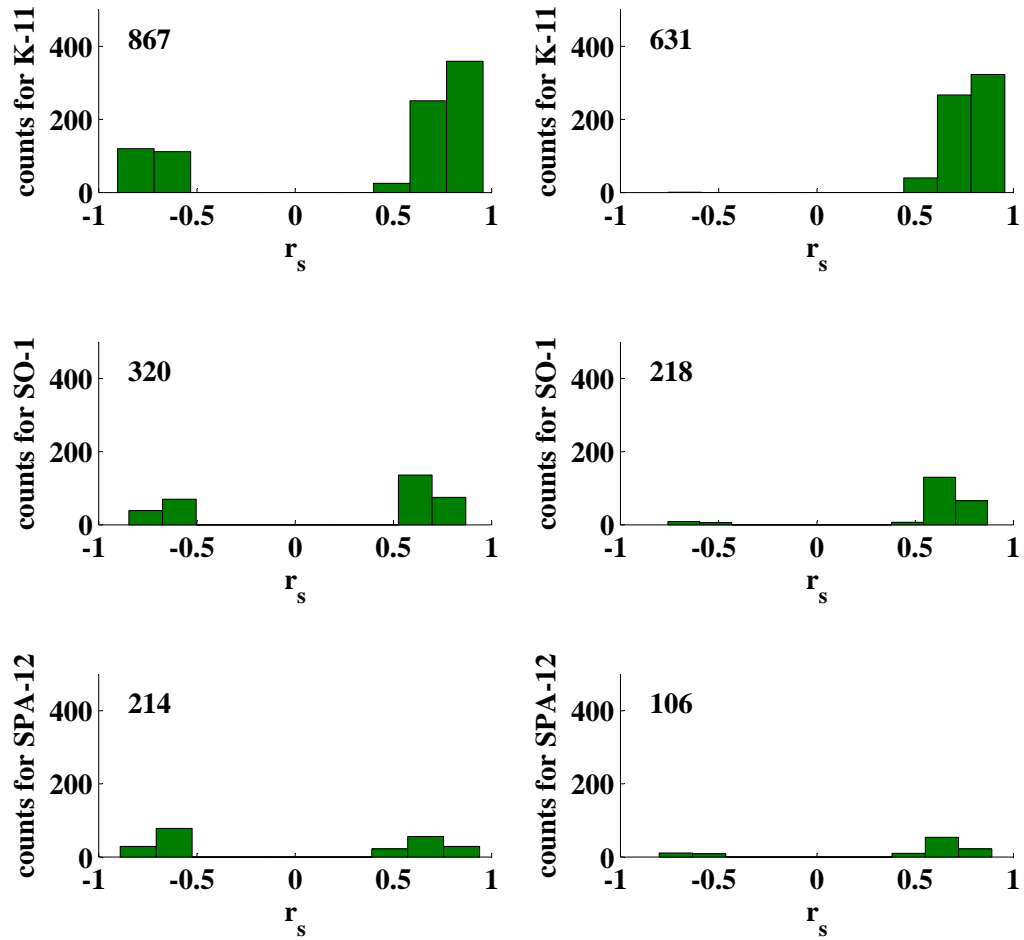


Fig. H.36: Illustrated is the distribution of speleothem r_s for the indicated runs of the 4000 years short-term PCA on $\delta^{13}\text{C}$ time series before (left panels) and after (right panels) the application of the Fork-tool.

run #5 - 2.6-2.3 ka BP - Part I

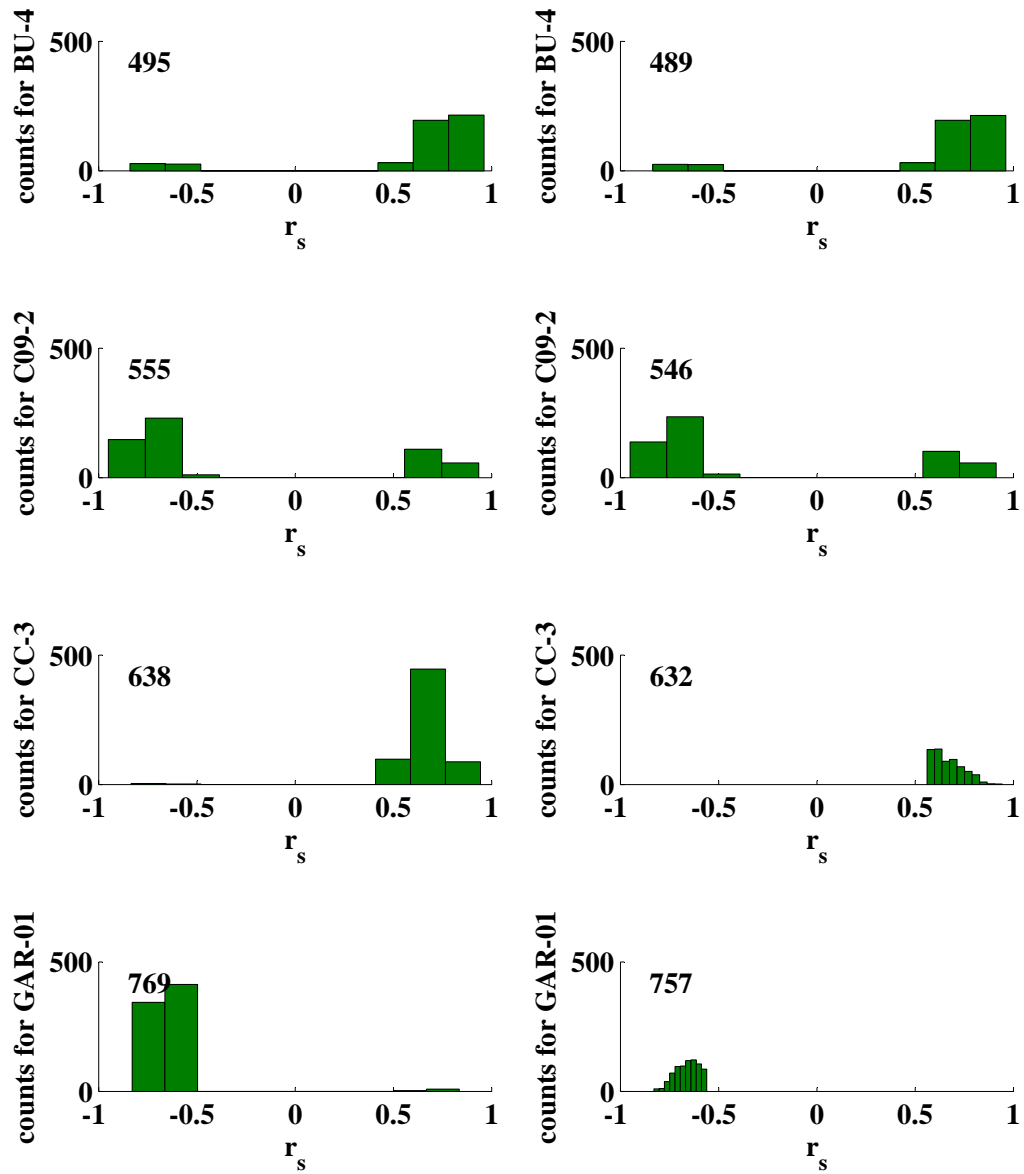


Fig. H.37: Illustrated is the distribution of speleothem r_s for the indicated runs of the 4000 years short-term PCA on $\delta^{13}C$ time series before (left panels) and after (right panels) the application of the Fork-tool.

run #5 - 2.6-2.3 ka BP - Part II

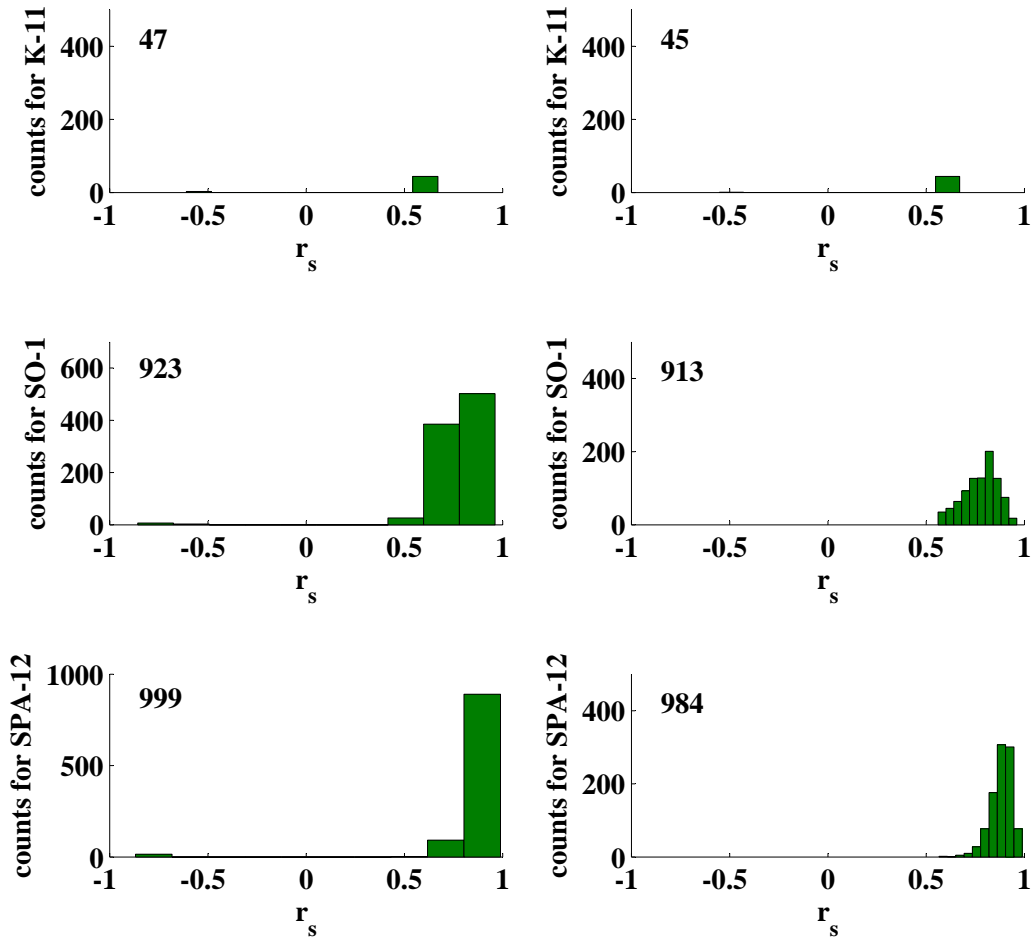


Fig. H.38: Illustrated is the distribution of speleothem r_s for the indicated runs of the 4000 years short-term PCA on $\delta^{13}\text{C}$ time series before (left panels) and after (right panels) the application of the Fork-tool.

run #6 - 2.3-2.0 ka BP - Part I

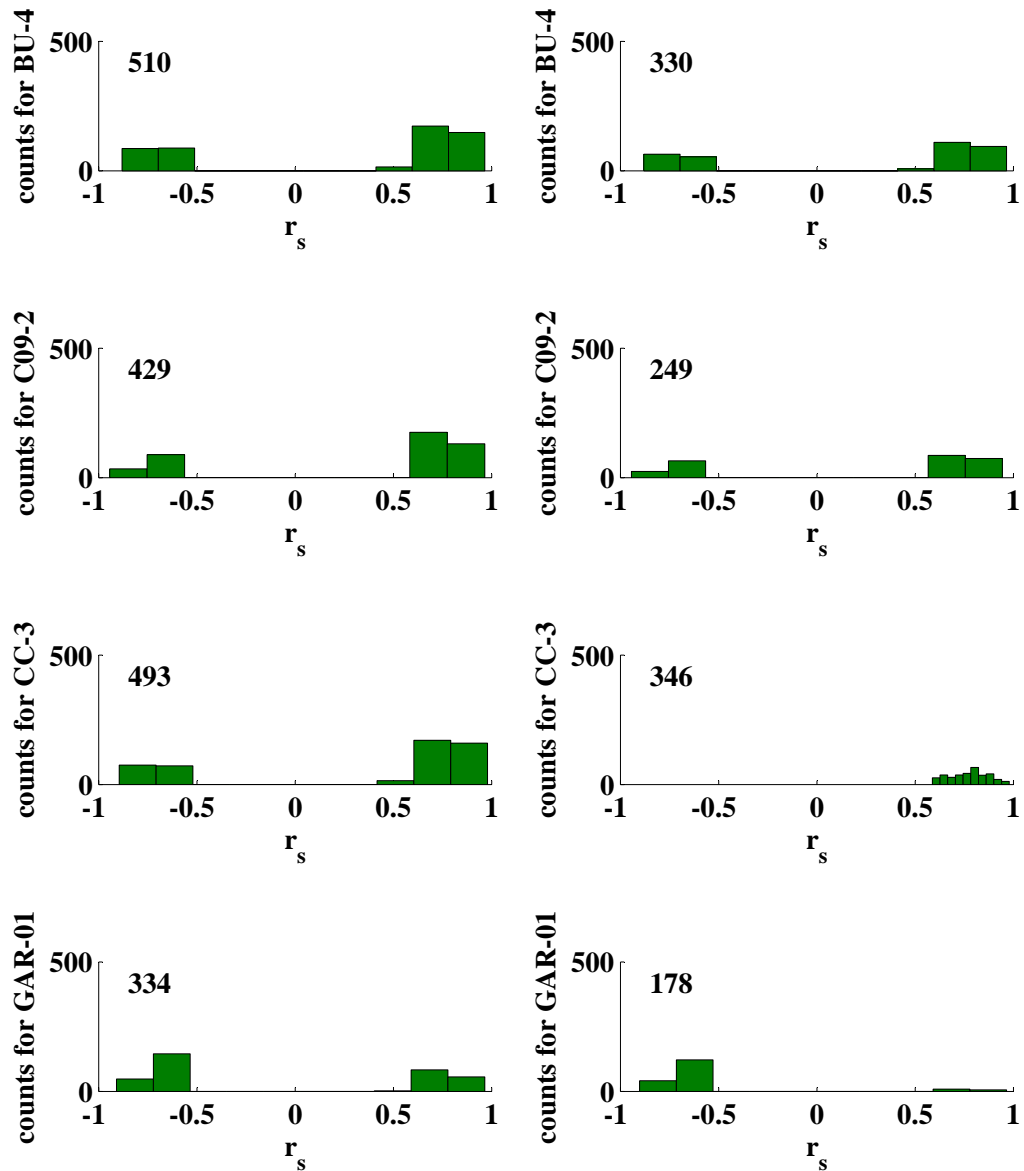


Fig. H.39: Illustrated is the distribution of speleothem r_s for the indicated runs of the 4000 years short-term PCA on $\delta^{13}C$ time series before (left panels) and after (right panels) the application of the Fork-tool.

run #6 - 2.3-2.0 ka BP - Part II

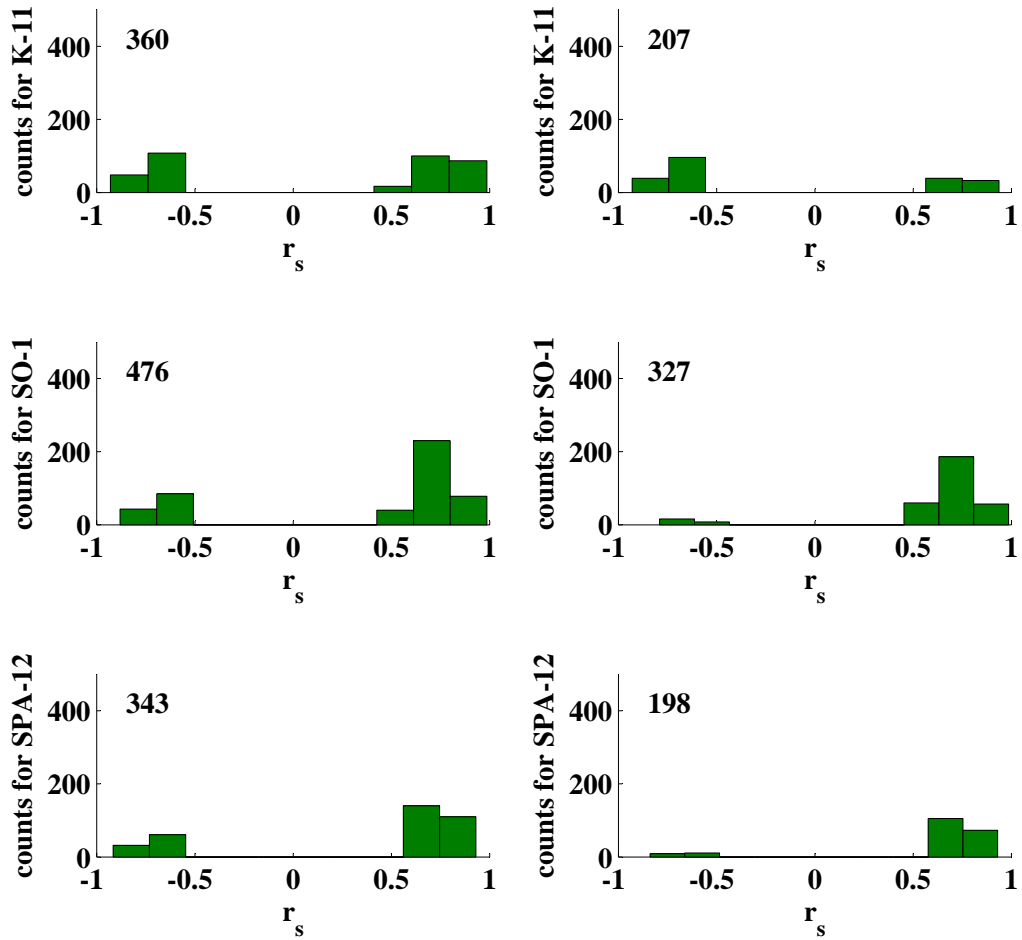


Fig. H.40: Illustrated is the distribution of speleothem r_s for the indicated runs of the 4000 years short-term PCA on $\delta^{13}\text{C}$ time series before (left panels) and after (right panels) the application of the Fork-tool.

run #7 - 2.0-1.7 ka BP - Part I

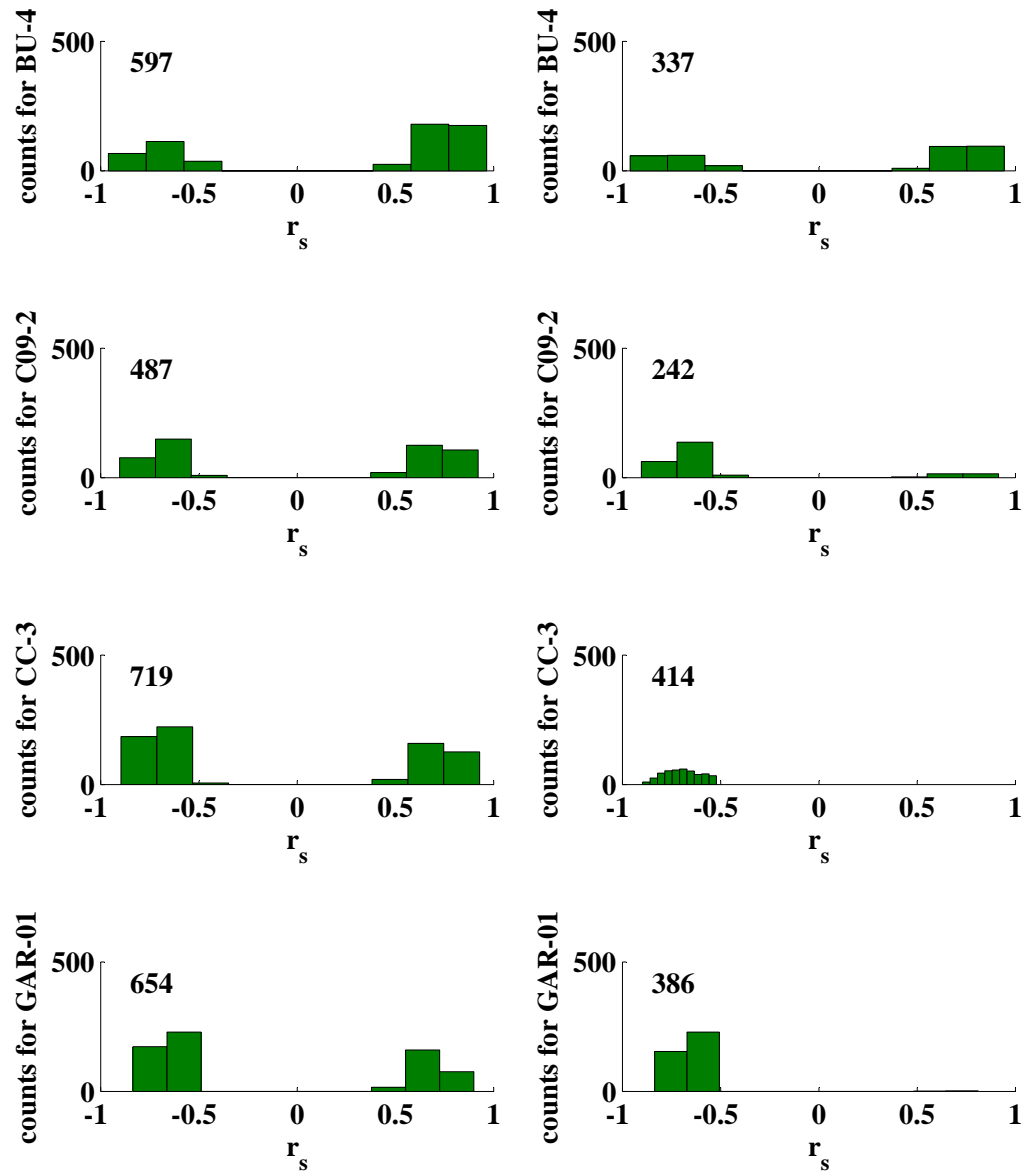


Fig. H.41: Illustrated is the distribution of speleothem r_s for the indicated runs of the 4000 years short-term PCA on $\delta^{13}C$ time series before (left panels) and after (right panels) the application of the Fork-tool.

run #7 - 2.0-1.7 ka BP - Part II

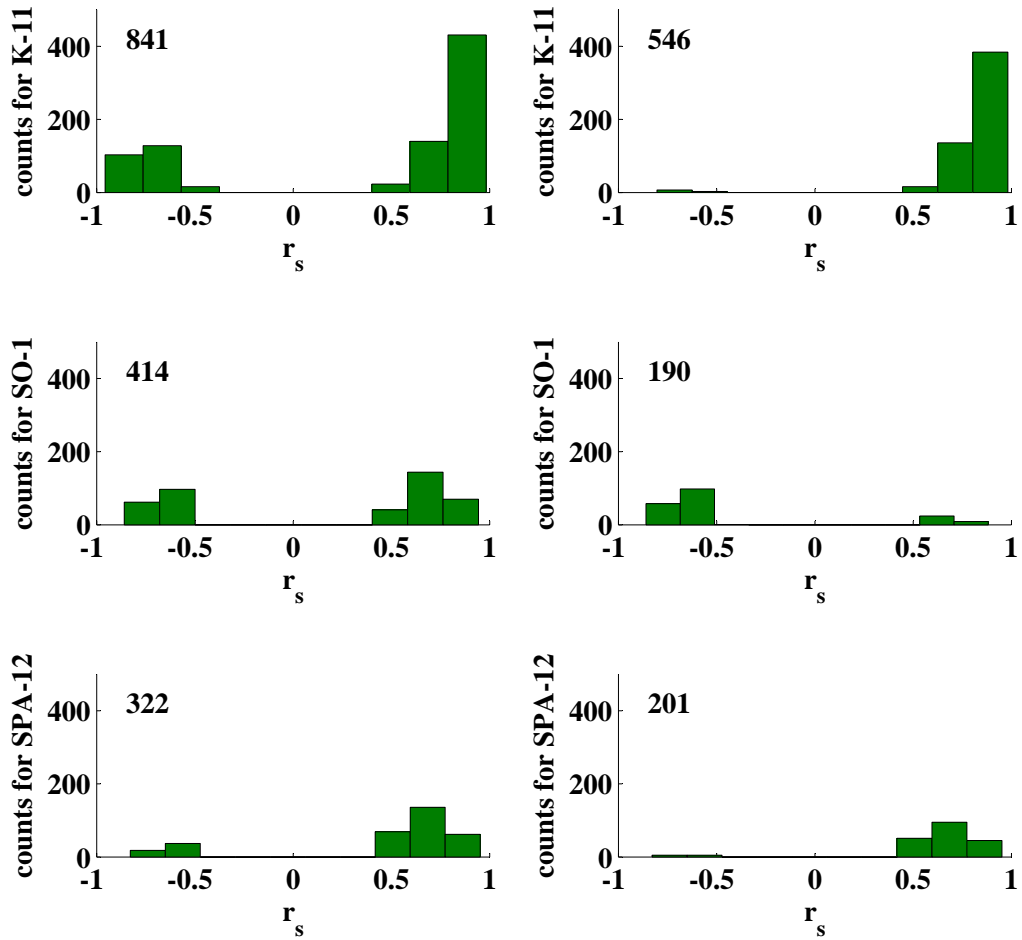


Fig. H.42: Illustrated is the distribution of speleothem r_s for the indicated runs of the 4000 years short-term PCA on $\delta^{13}\text{C}$ time series before (left panels) and after (right panels) the application of the Fork-tool.

run #8 - 1.7-1.4 ka BP - Part I

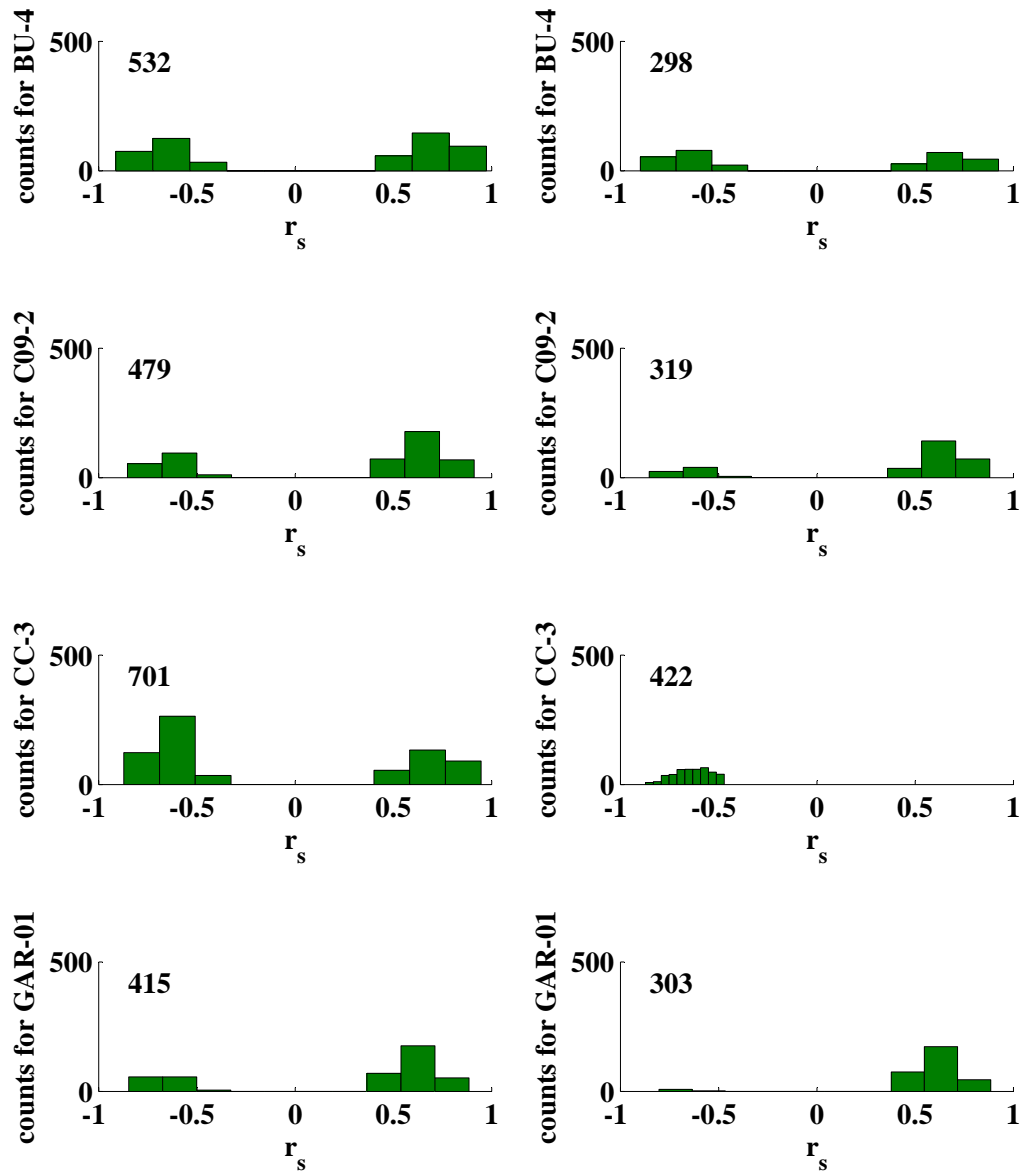


Fig. H.43: Illustrated is the distribution of speleothem r_s for the indicated runs of the 4000 years short-term PCA on $\delta^{13}C$ time series before (left panels) and after (right panels) the application of the Fork-tool.

run #8 - 1.7-1.4 ka BP - Part II

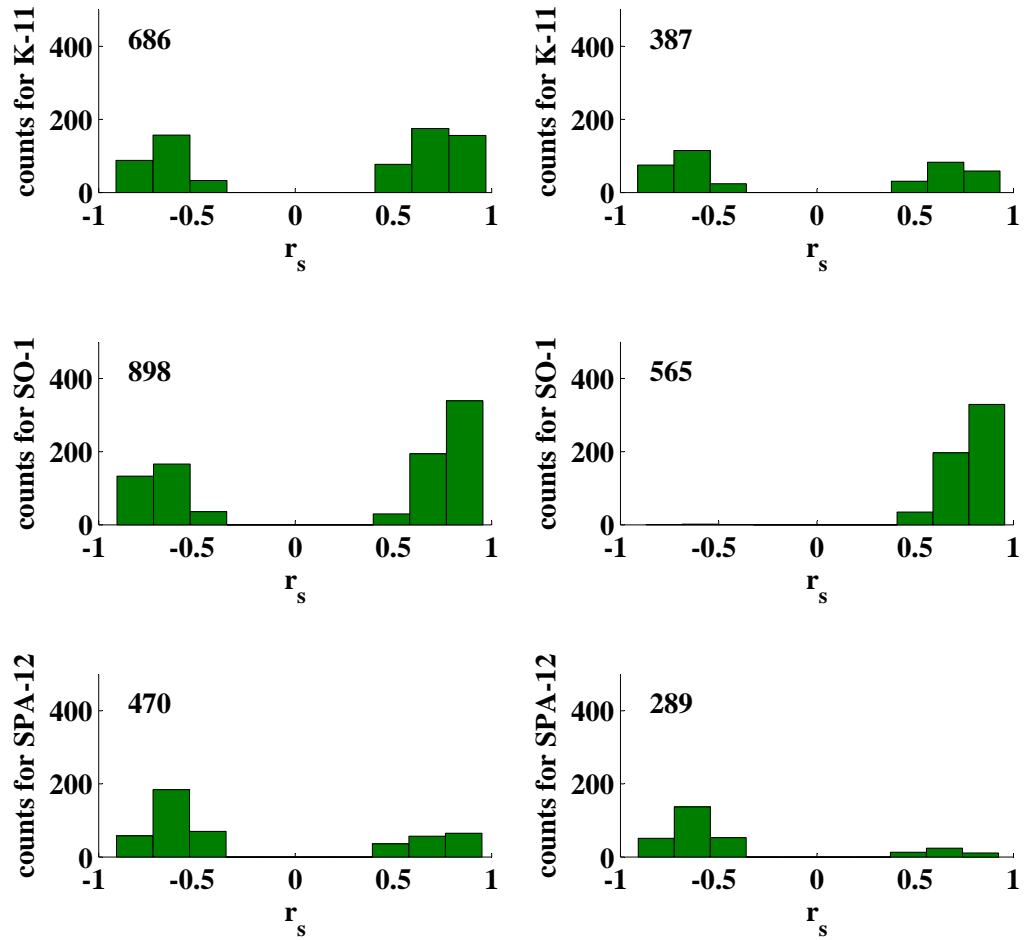


Fig. H.44: Illustrated is the distribution of speleothem r_s for the indicated runs of the 4000 years short-term PCA on $\delta^{13}\text{C}$ time series before (left panels) and after (right panels) the application of the Fork-tool.

run #9 - 1.6-1.15 ka BP - Part I

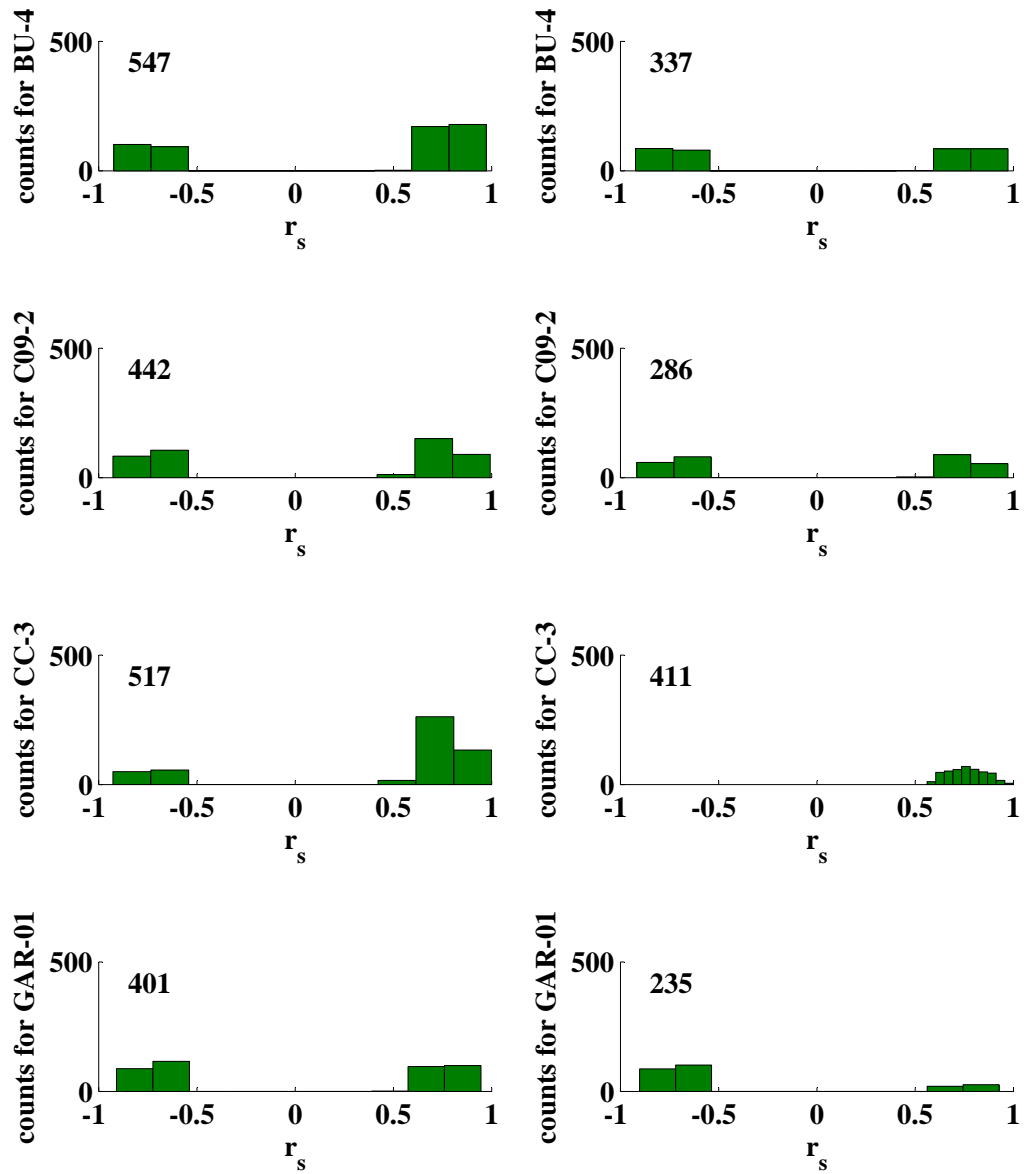


Fig. H.45: Illustrated is the distribution of speleothem r_s for the indicated runs of the 4000 years short-term PCA on $\delta^{13}C$ time series before (left panels) and after (right panels) the application of the Fork-tool.

run #9 - 1.6-1.15 ka BP - Part II

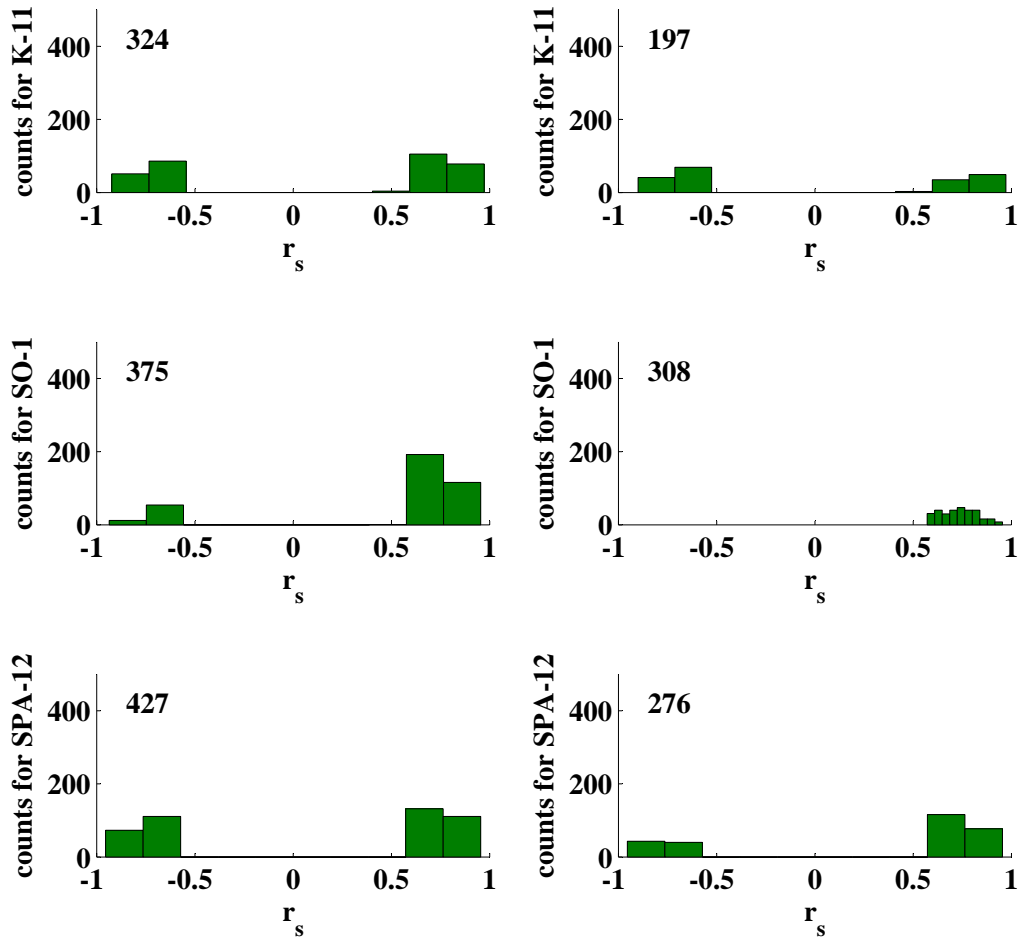


Fig. H.46: Illustrated is the distribution of speleothem r_s for the indicated runs of the 4000 years short-term PCA on $\delta^{13}\text{C}$ time series before (left panels) and after (right panels) the application of the Fork-tool.

run #10 - 1.4-1.1 ka BP - Part I

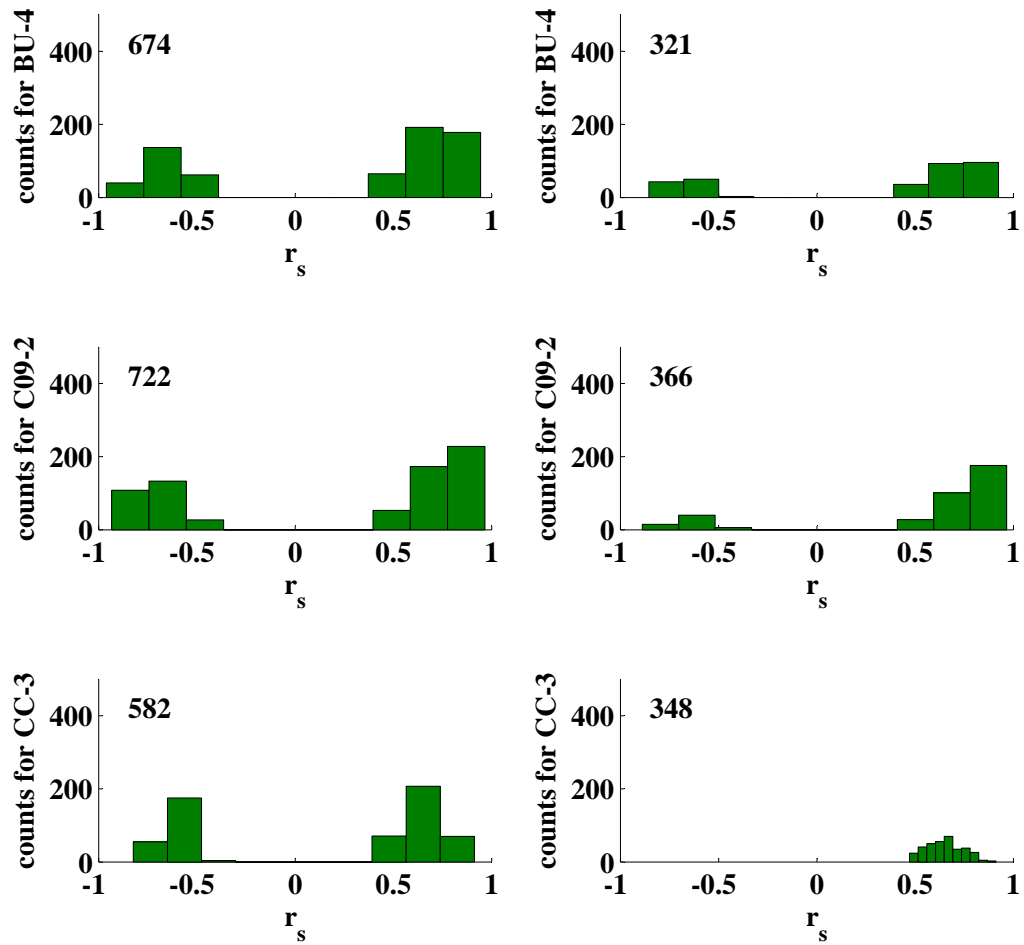


Fig. H.47: Illustrated is the distribution of speleothem r_s for the indicated runs of the 4000 years short-term PCA on $\delta^{13}C$ time series before (left panels) and after (right panels) the application of the Fork-tool.

run #10 - 1.4-1.1 ka BP - Part II

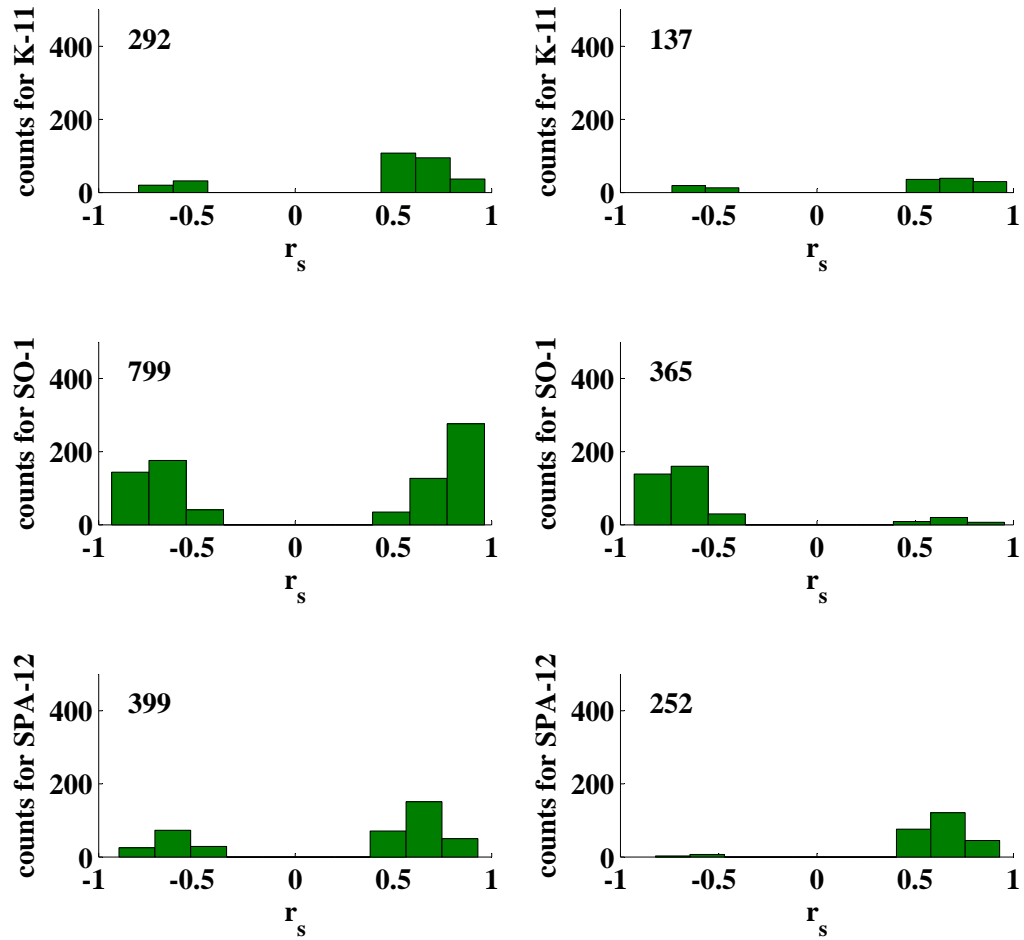


Fig. H.48: Illustrated is the distribution of speleothem r_s for the indicated runs of the 4000 years short-term PCA on $\delta^{13}\text{C}$ time series before (left panels) and after (right panels) the application of the Fork-tool.

run #11 - 1.1-0.8 ka BP - Part I

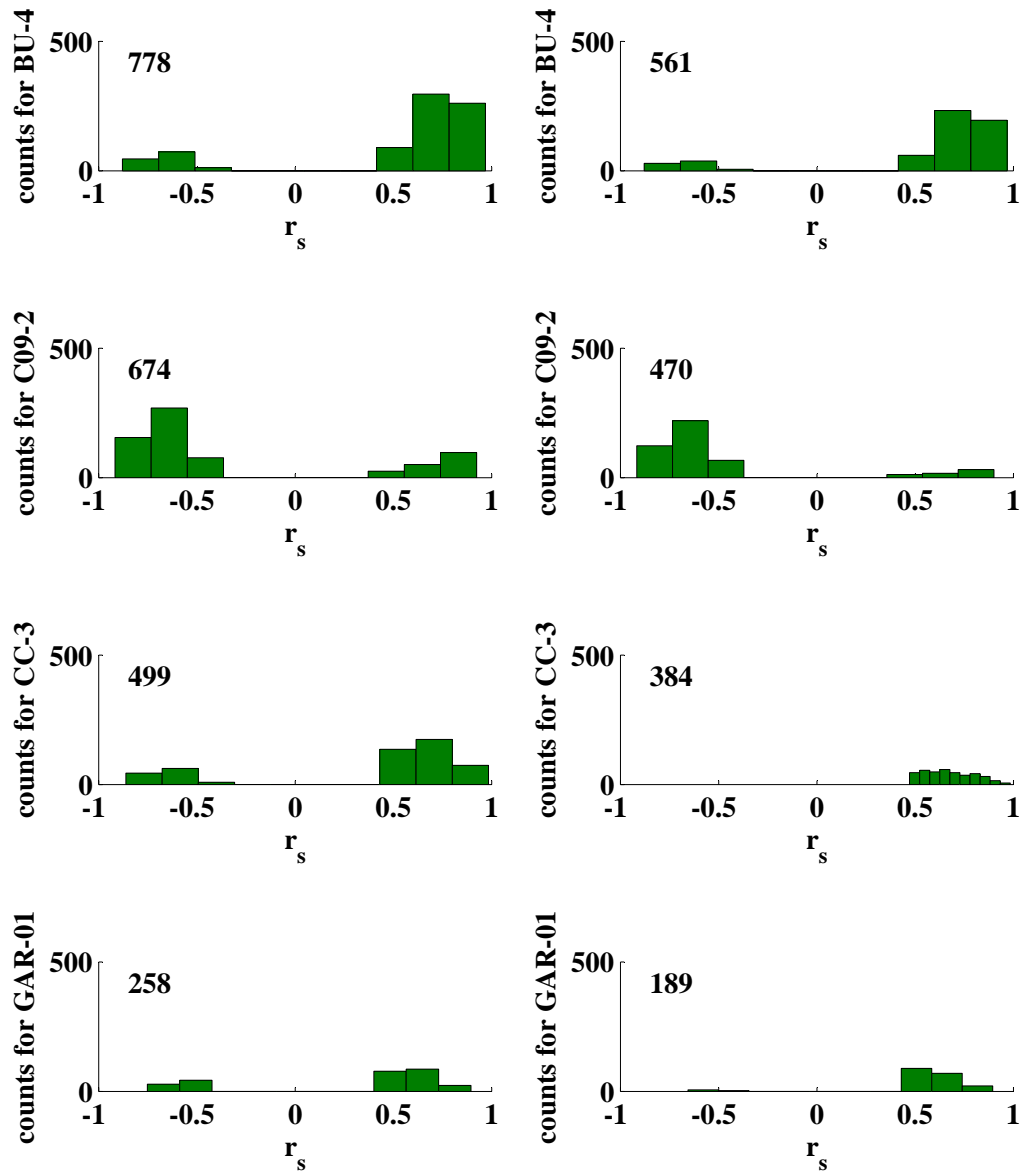


Fig. H.49: Illustrated is the distribution of speleothem r_s for the indicated runs of the 4000 years short-term PCA on $\delta^{13}C$ time series before (left panels) and after (right panels) the application of the Fork-tool.

run #11 - 1.1-0.8 ka BP - Part II

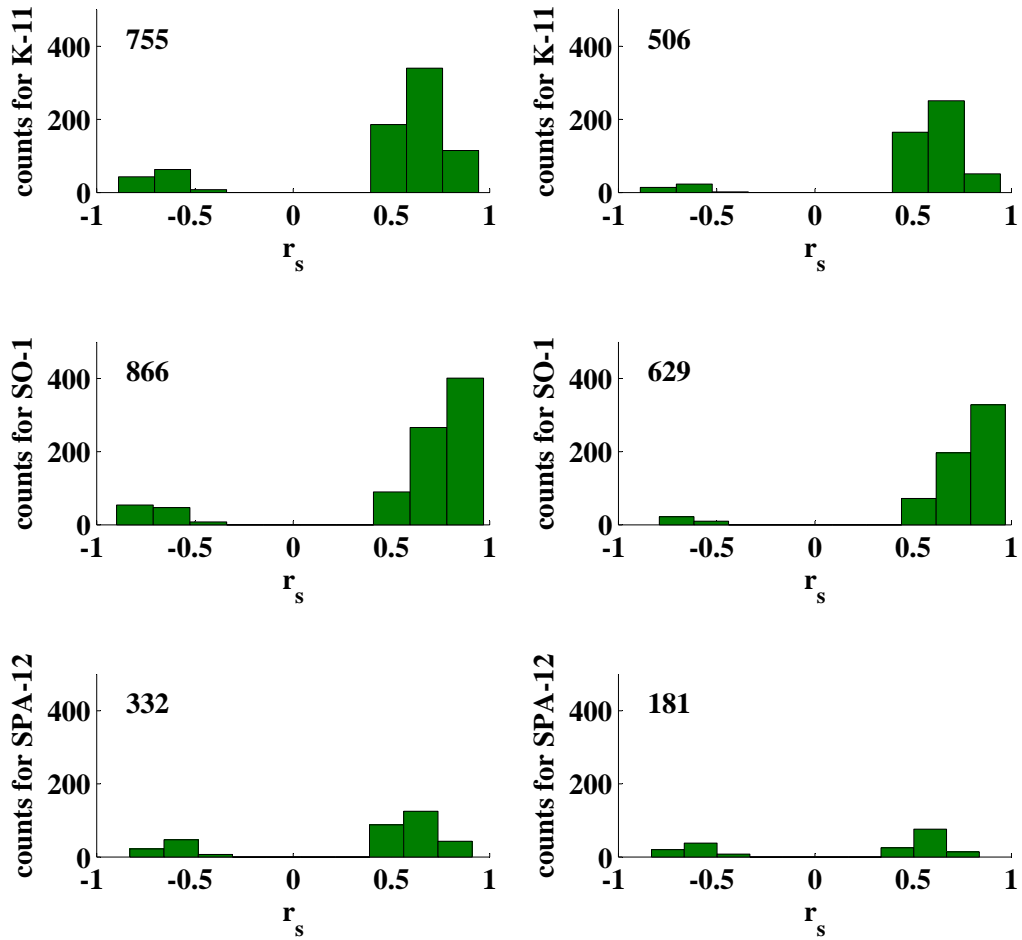


Fig. H.50: Illustrated is the distribution of speleothem r_s for the indicated runs of the 4000 years short-term PCA on $\delta^{13}\text{C}$ time series before (left panels) and after (right panels) the application of the Fork-tool.

run #12 - 0.8-0.5 ka BP - Part I

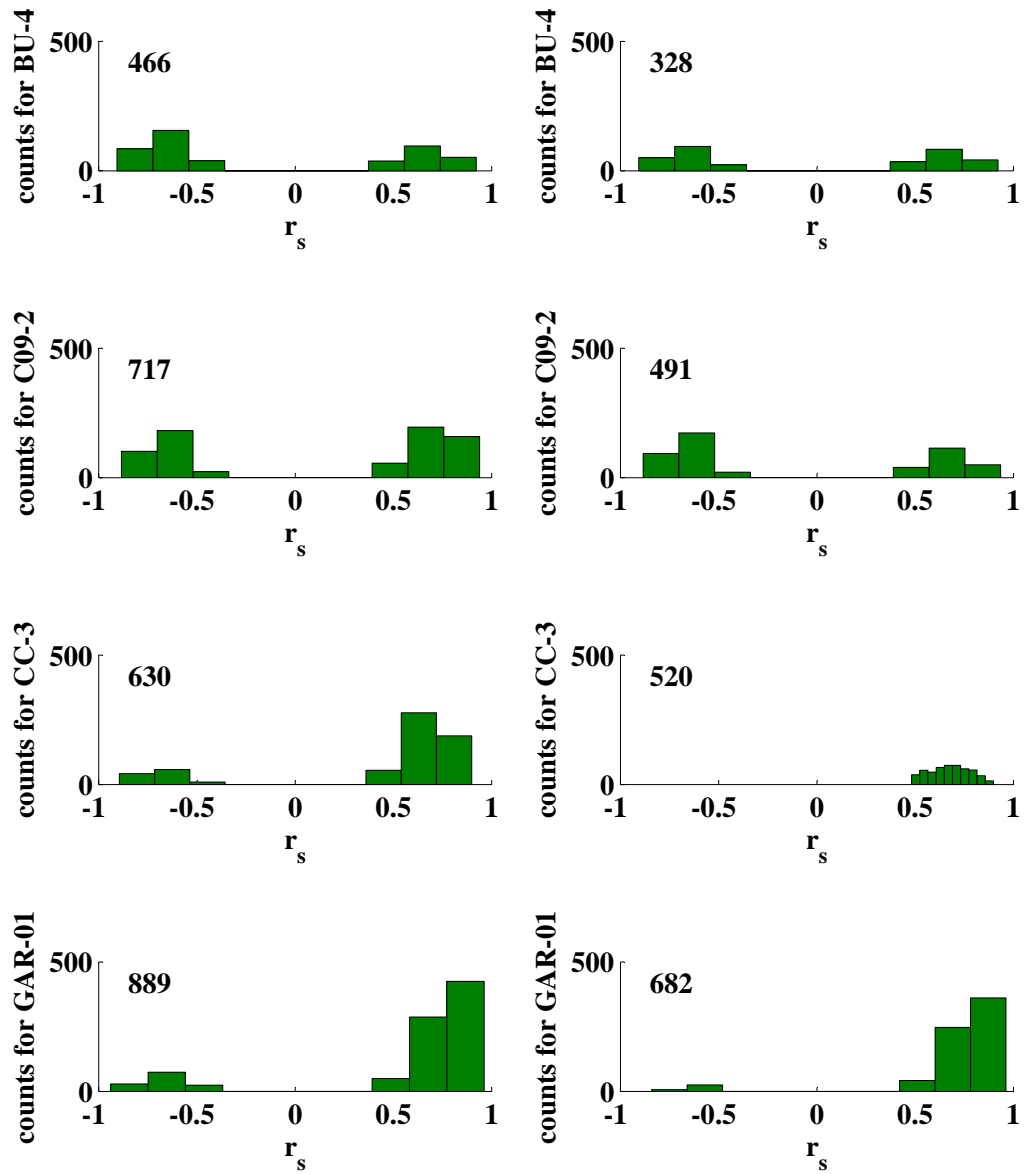


Fig. H.51: Illustrated is the distribution of speleothem r_s for the indicated runs of the 4000 years short-term PCA on $\delta^{13}C$ time series before (left panels) and after (right panels) the application of the Fork-tool.

run #12 - 0.8-0.5 ka BP - Part II

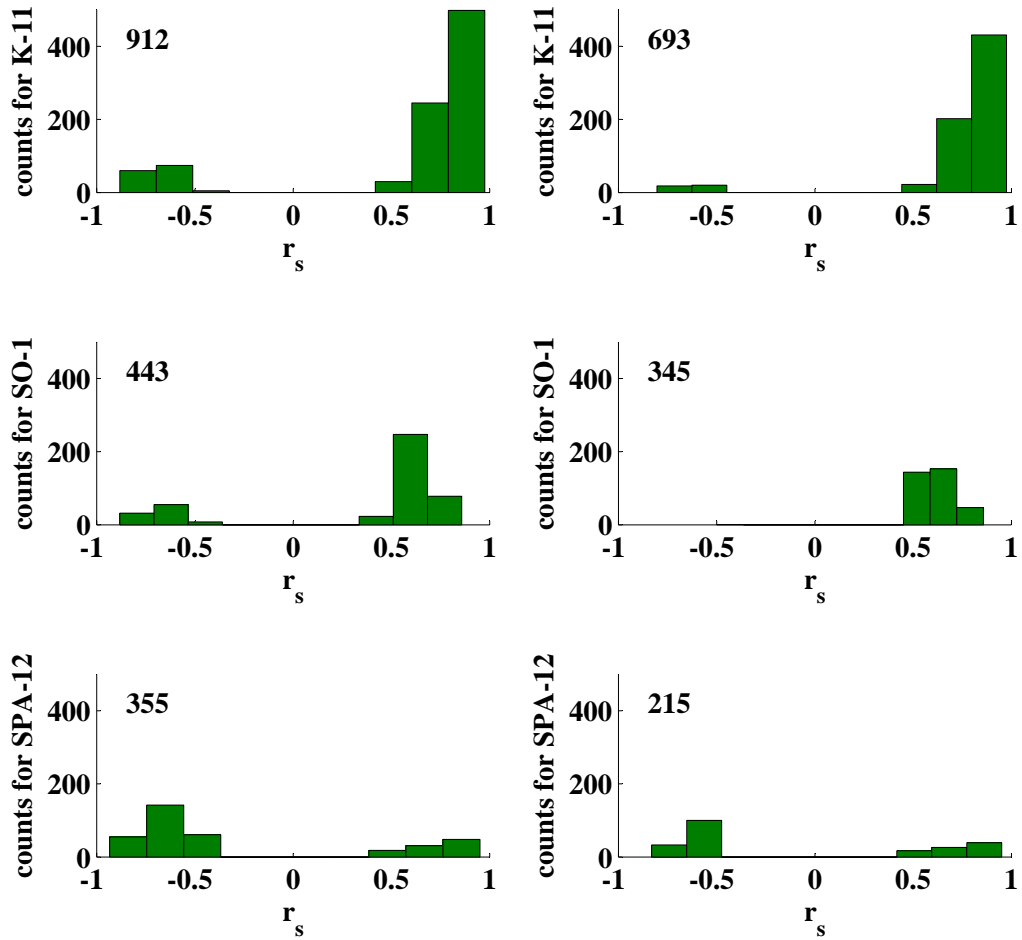


Fig. H.52: Illustrated is the distribution of speleothem r_s for the indicated runs of the 4000 years short-term PCA on $\delta^{13}\text{C}$ time series before (left panels) and after (right panels) the application of the Fork-tool.

run #13 - 0.5-0.2 ka BP - Part I

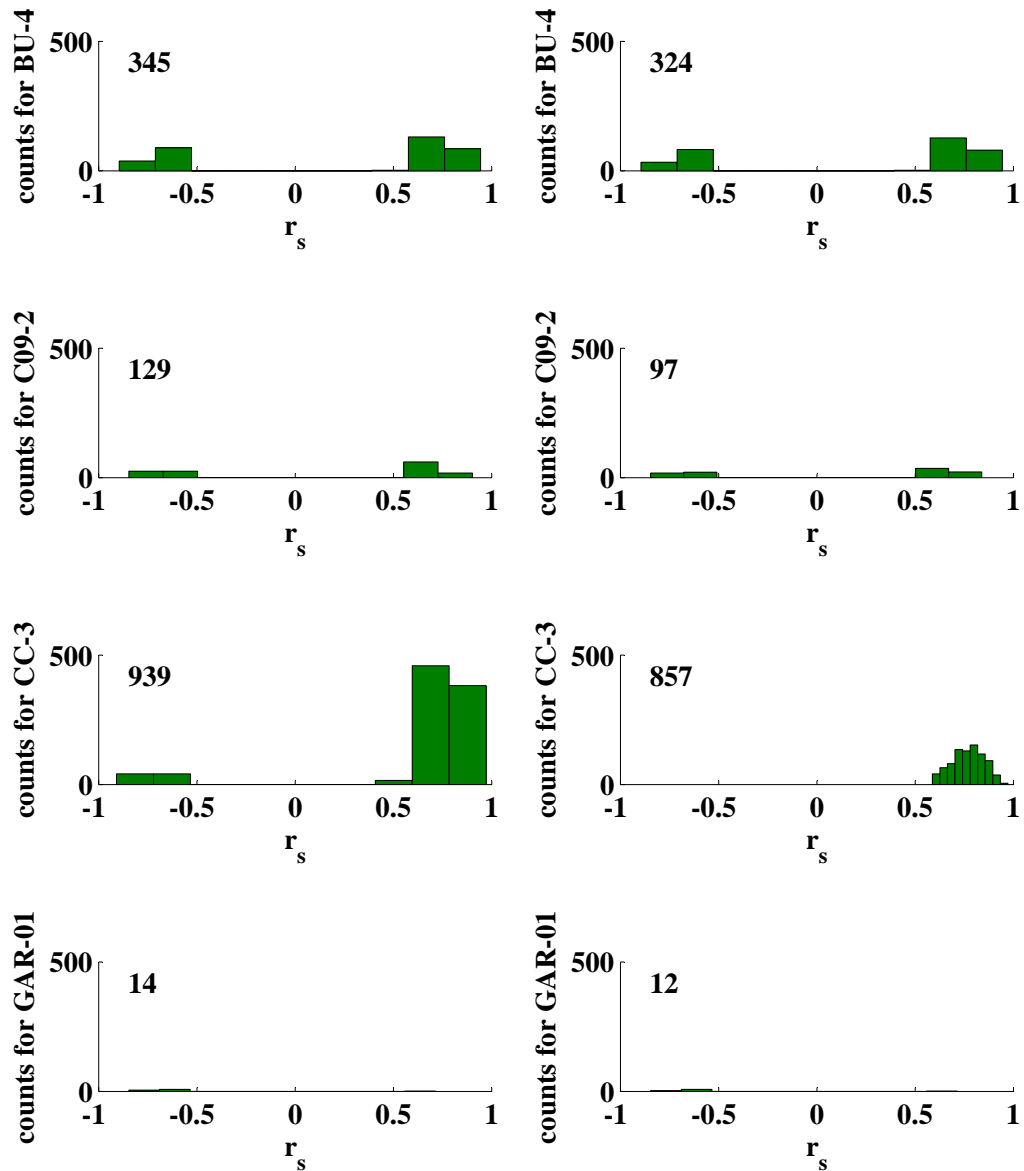


Fig. H.53: Illustrated is the distribution of speleothem r_s for the indicated runs of the 4000 years short-term PCA on $\delta^{13}C$ time series before (left panels) and after (right panels) the application of the Fork-tool.

run #13 - 0.5-0.2 ka BP - Part II

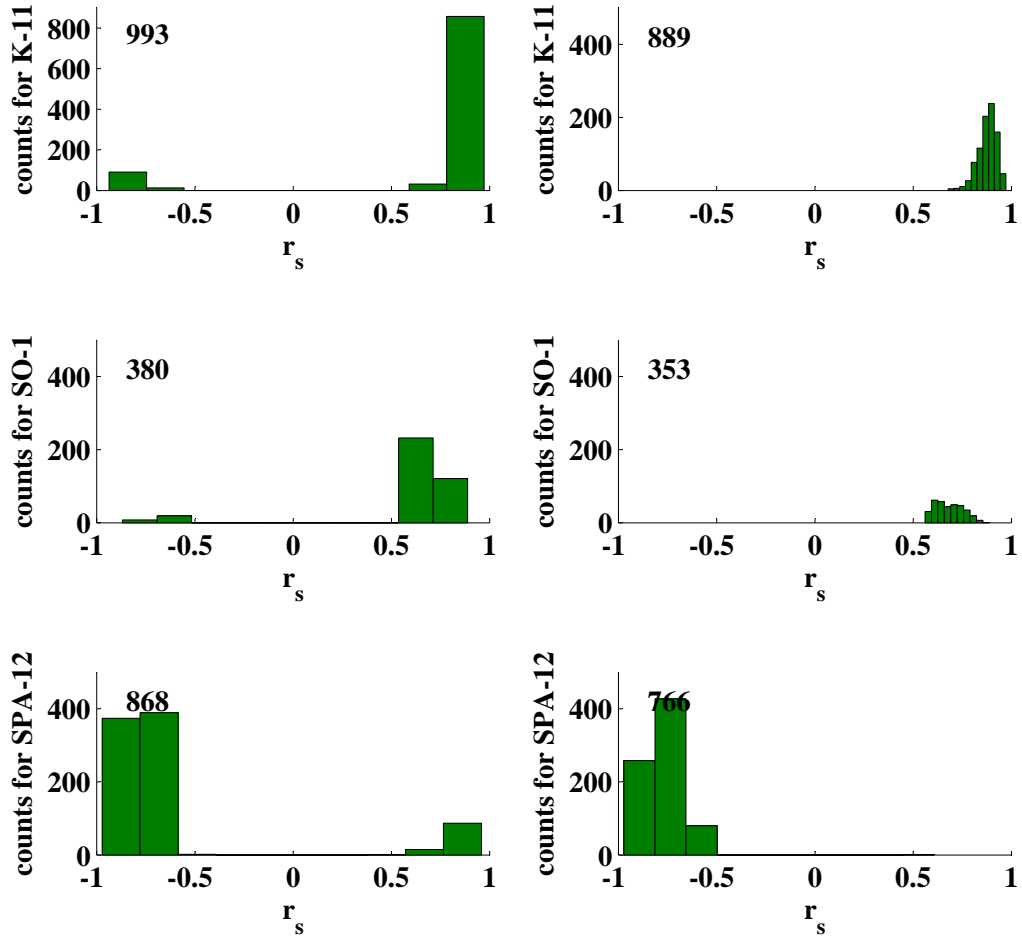


Fig. H.54: Illustrated is the distribution of speleothem r_s for the indicated runs of the 4000 years short-term PCA on $\delta^{13}\text{C}$ time series before (left panels) and after (right panels) the application of the Fork-tool.

run #14 - 0.35-0.05 ka BP - Part I

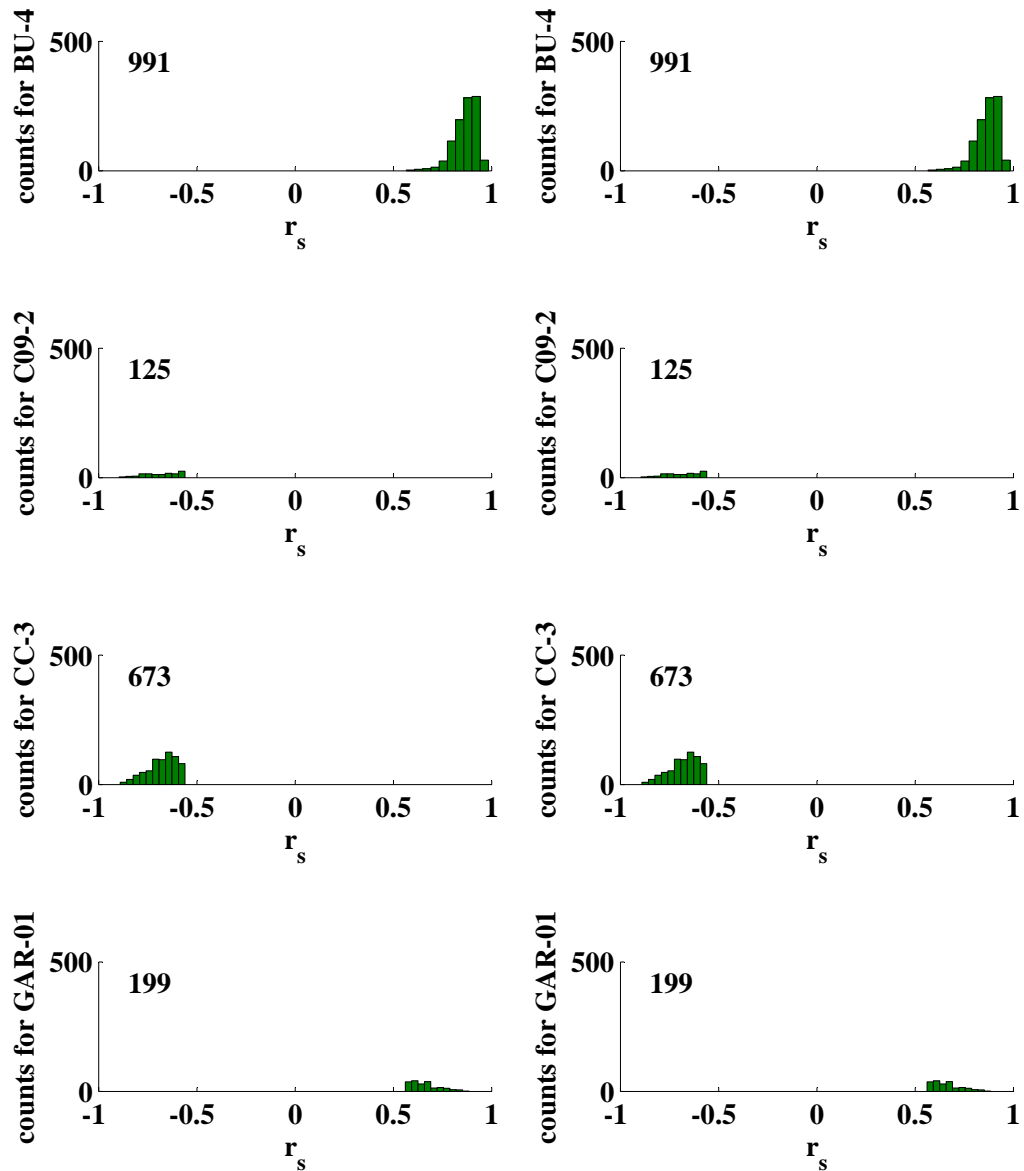


Fig. H.55: Illustrated is the distribution of speleothem r_s for the indicated runs of the 4000 years short-term PCA on $\delta^{13}C$ time series before (left panels) and after (right panels) the application of the Fork-tool.

run #14 - 0.35-0.05 ka BP - Part II

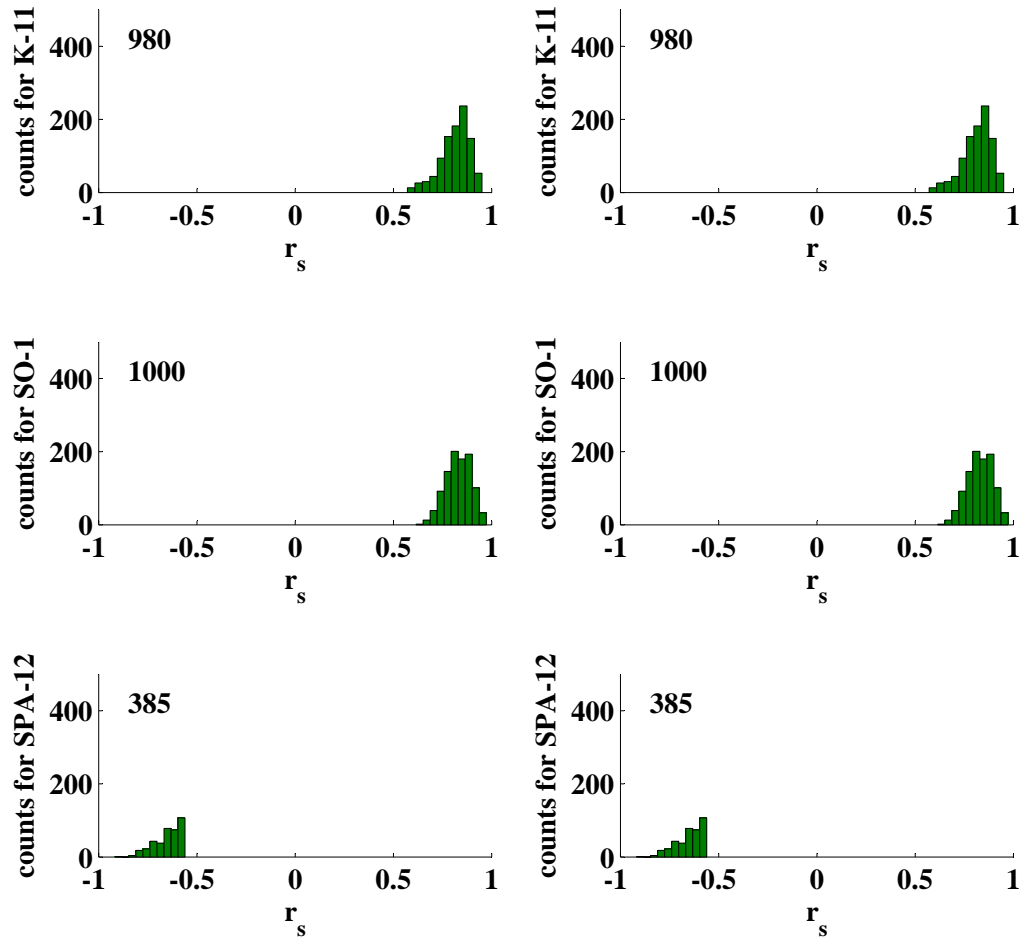


Fig. H.56: Illustrated is the distribution of speleothem r_s for the indicated runs of the 4000 years short-term PCA on $\delta^{13}\text{C}$ time series before (left panels) and after (right panels) the application of the Fork-tool.

I

Eigenvalues of the 8,000 years runs - PART II: Short-term analysis

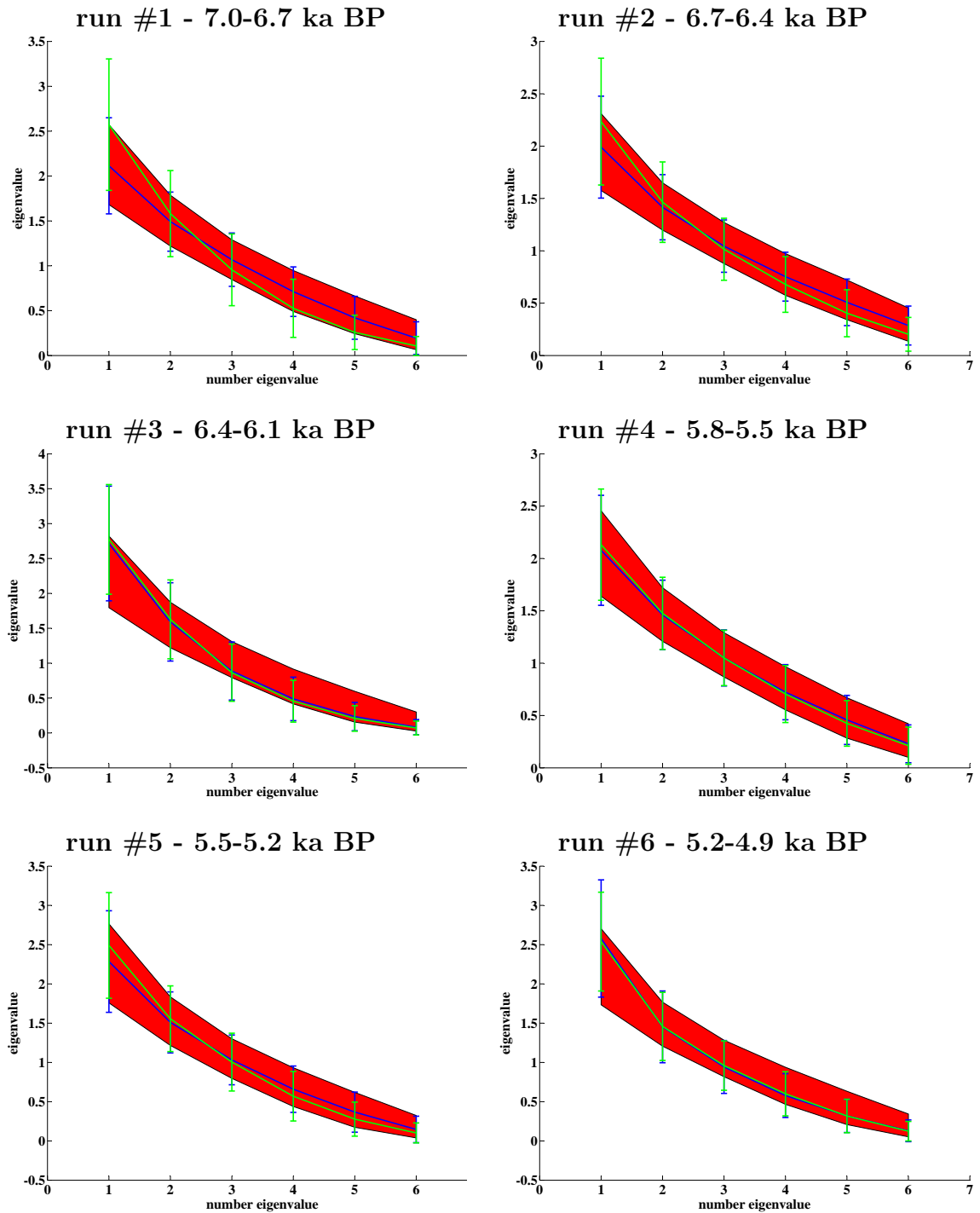


Fig. I.1: Illustrated are the mean eigenvalues for the indicated short-term PCA runs for the compilation of $\delta^{18}\text{O}$ (blue) and $\delta^{13}\text{C}$ (green) time series. Furthermore, the 95 % and 5 % confidence level of the eigenvalues is illustrated, computed from white noise time series (red shading area).

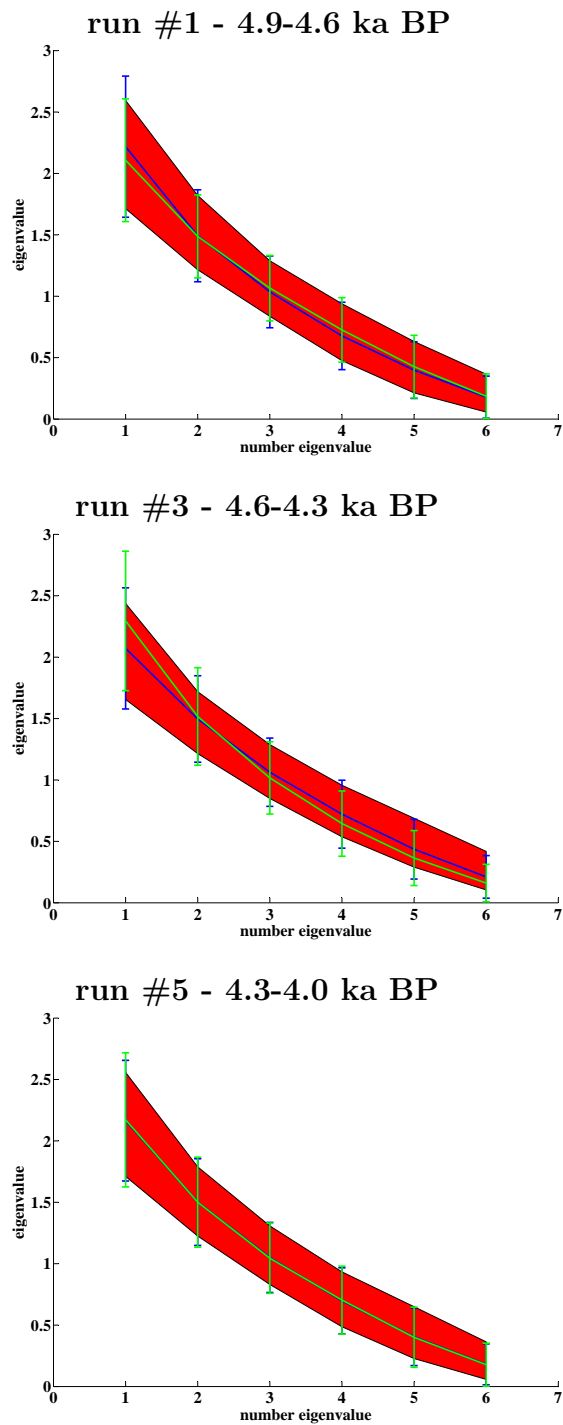


Fig. I.2: Illustrated are the mean eigenvalues for the indicated short-term PCA runs for the compilation of $\delta^{18}\text{O}$ (blue) and $\delta^{13}\text{C}$ (green) time series. Furthermore, the 95 % and 5 % confidence level of the eigenvalues is illustrated, computed from white noise time series (red shading area).

J

Results of the application of the Fork-tool onto the 8,000 ka runs - PART II: Short-term analysis

J.1 Distribution of r_s for short-term coherence pattern for $\delta^{18}O$ time series

run #1 - 7.0-6.7 ka BP - Part I

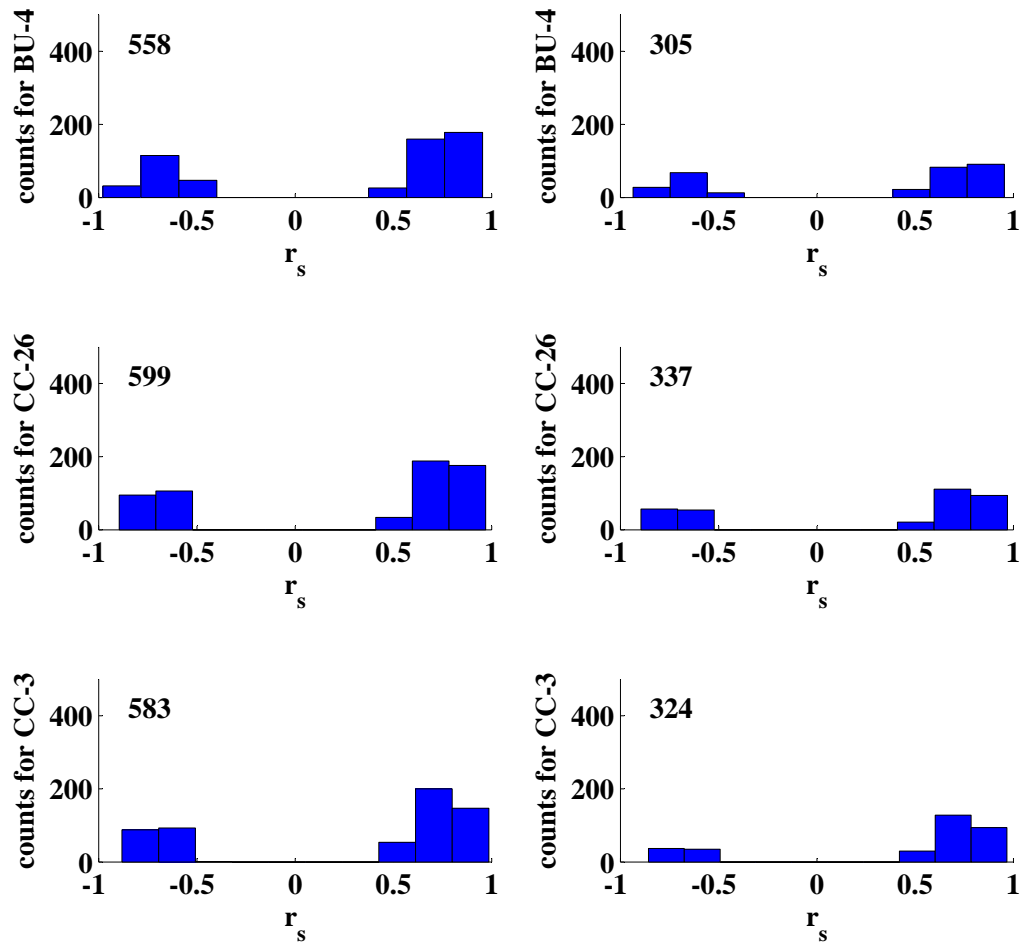


Fig. J.1: Illustrated is the distribution of speleothem r_s for the indicated runs of the 4000 years short-term PCA on $\delta^{18}O$ time series before (left panels) and after (right panels) the application of the Fork-tool.

run #1 - 7.0-6.7 ka BP - Part II

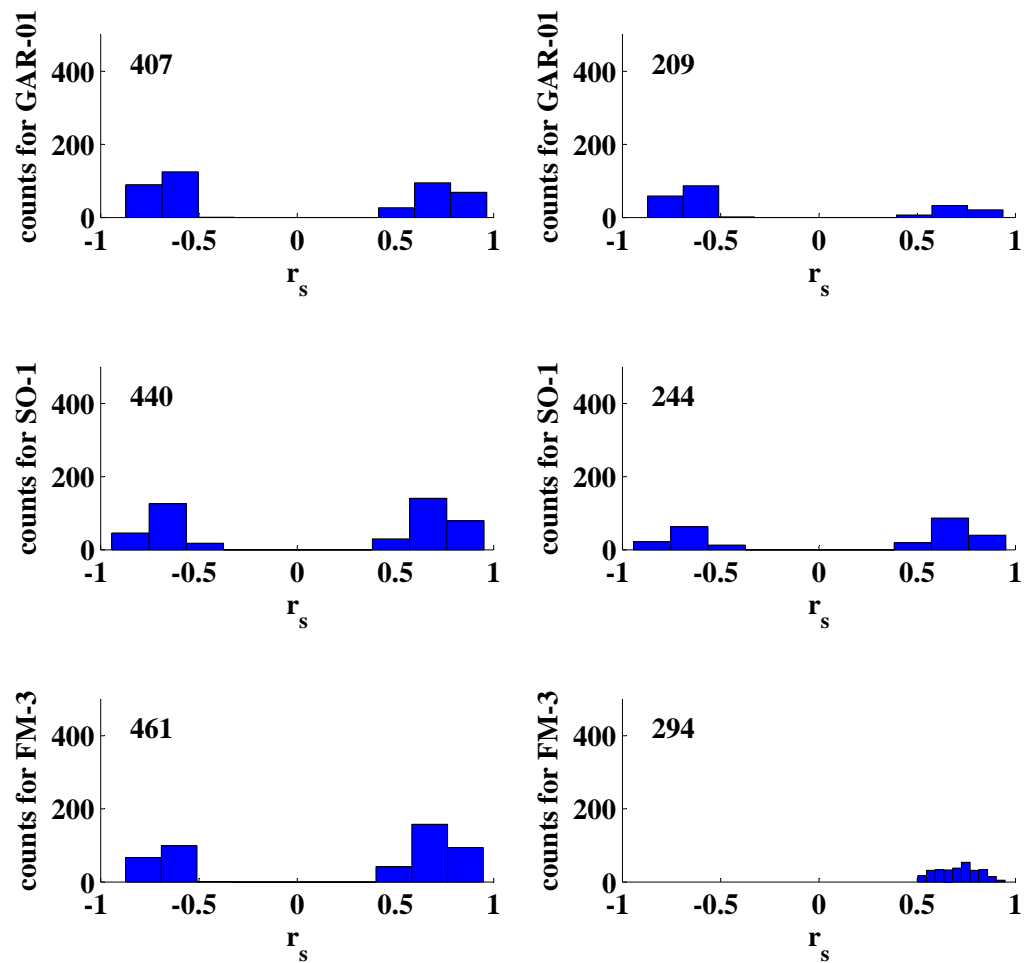


Fig. J.2: Illustrated is the distribution of speleothem r_s for the indicated runs of the 4000 years short-term PCA on $\delta^{18}\text{O}$ time series before (left panels) and after (right panels) the application of the Fork-tool.

run #2 - 6.7-6.4 ka BP - Part I

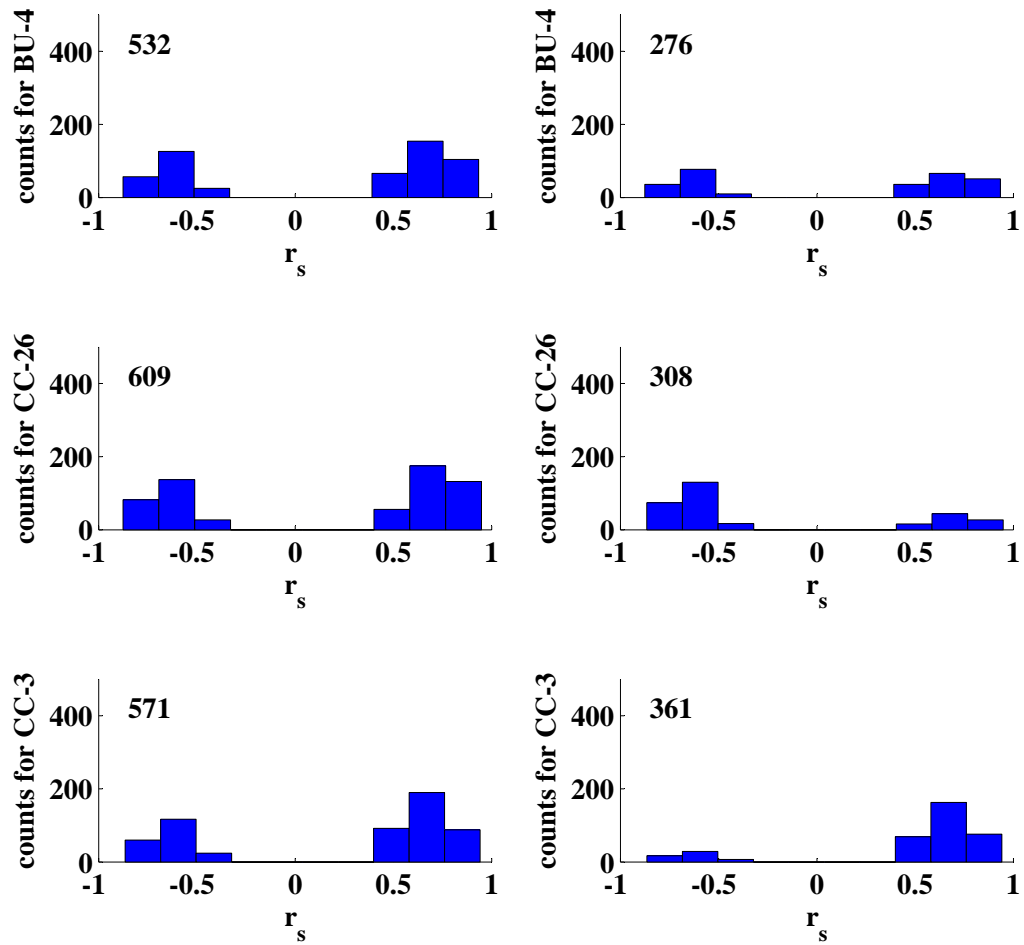


Fig. J.3: Illustrated is the distribution of speleothem r_s for the indicated runs of the 4000 years short-term PCA on $\delta^{18}O$ time series before (left panels) and after (right panels) the application of the Fork-tool.

run #2 - 6.7-6.4 ka BP - Part II

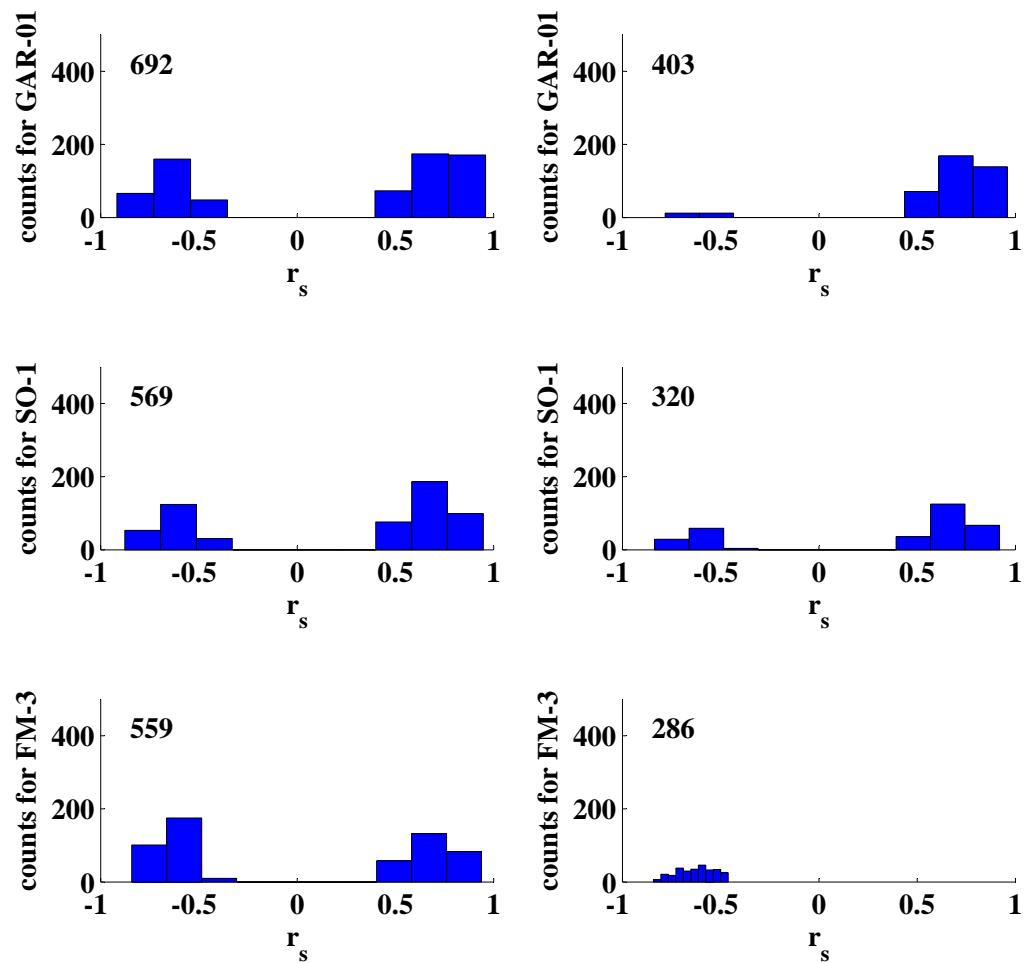


Fig. J.4: Illustrated is the distribution of speleothem r_s for the indicated runs of the 4000 years short-term PCA on $\delta^{18}\text{O}$ time series before (left panels) and after (right panels) the application of the Fork-tool.

run #3 - 6.4-6.1 ka BP - Part I

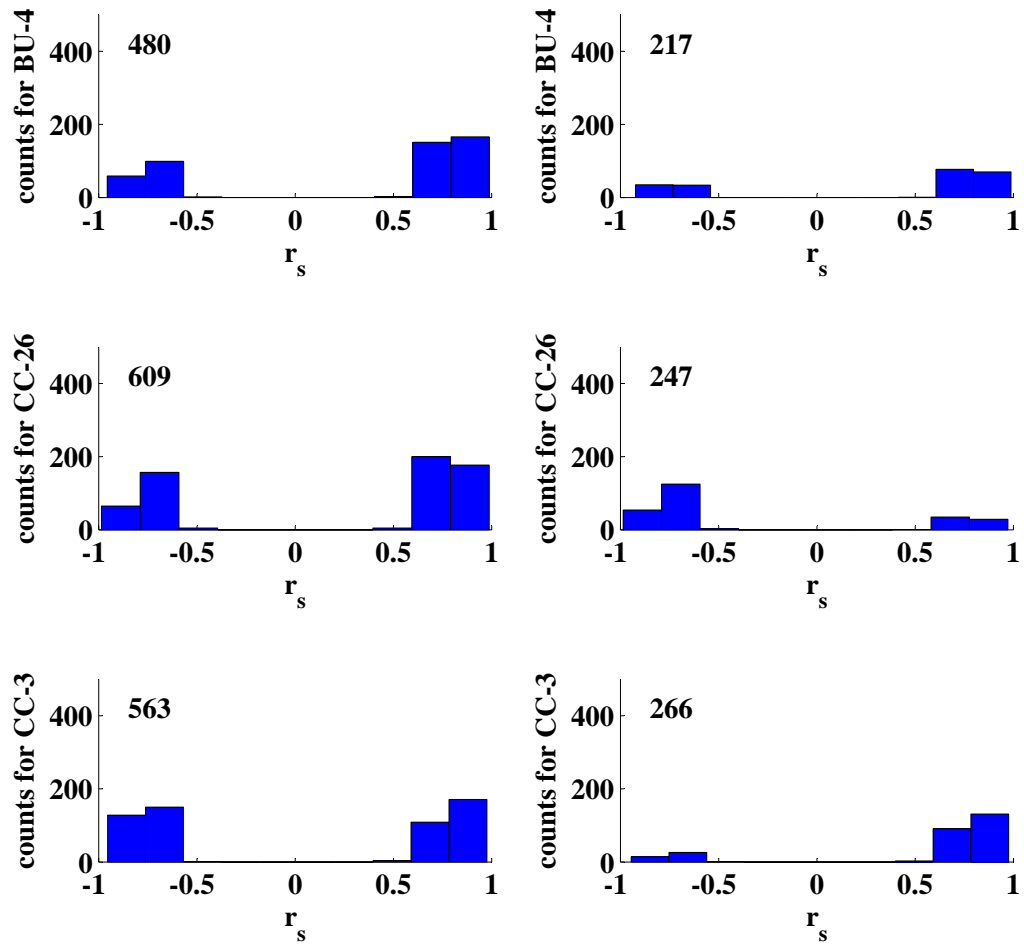


Fig. J.5: Illustrated is the distribution of speleothem r_s for the indicated runs of the 4000 years short-term PCA on $\delta^{18}O$ time series before (left panels) and after (right panels) the application of the Fork-tool.

run #3 - 6.4-6.1 ka BP - Part II

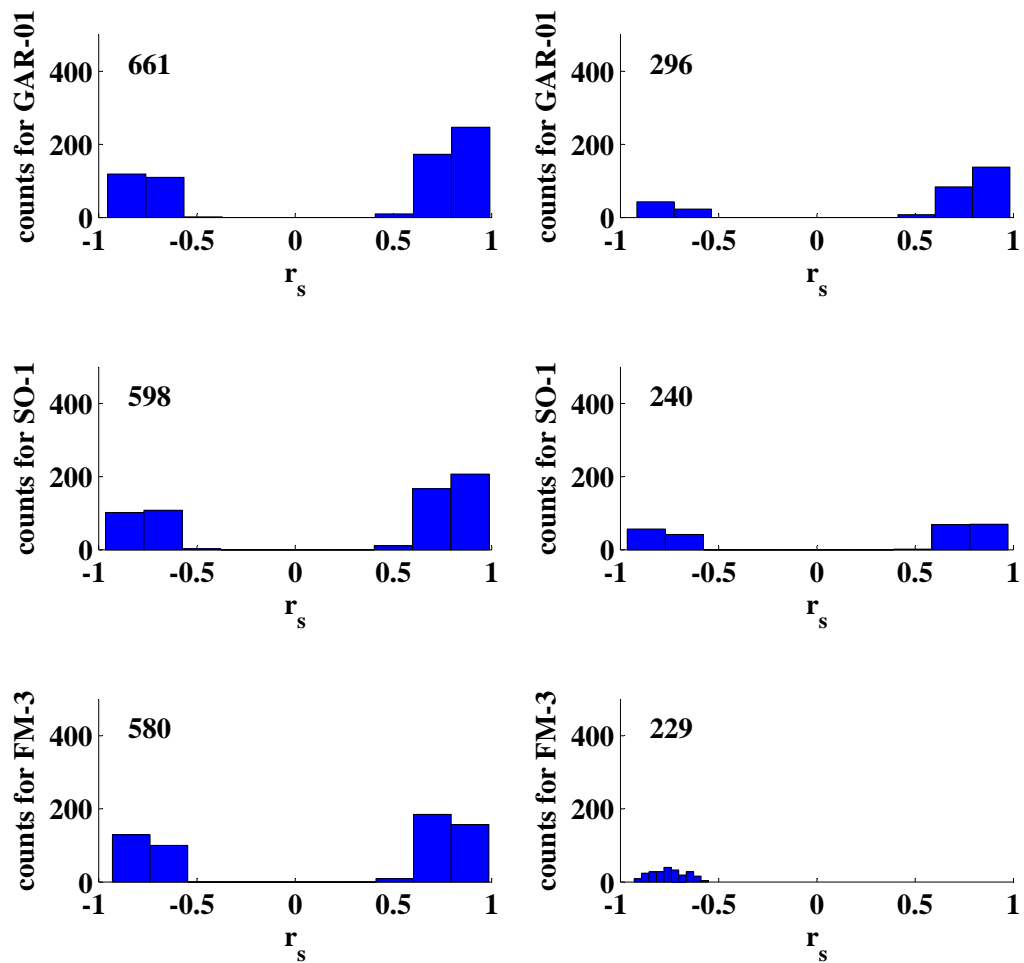


Fig. J.6: Illustrated is the distribution of speleothem r_s for the indicated runs of the 4000 years short-term PCA on $\delta^{18}\text{O}$ time series before (left panels) and after (right panels) the application of the Fork-tool.

run #4 - 5.8-5.5 ka BP - Part I

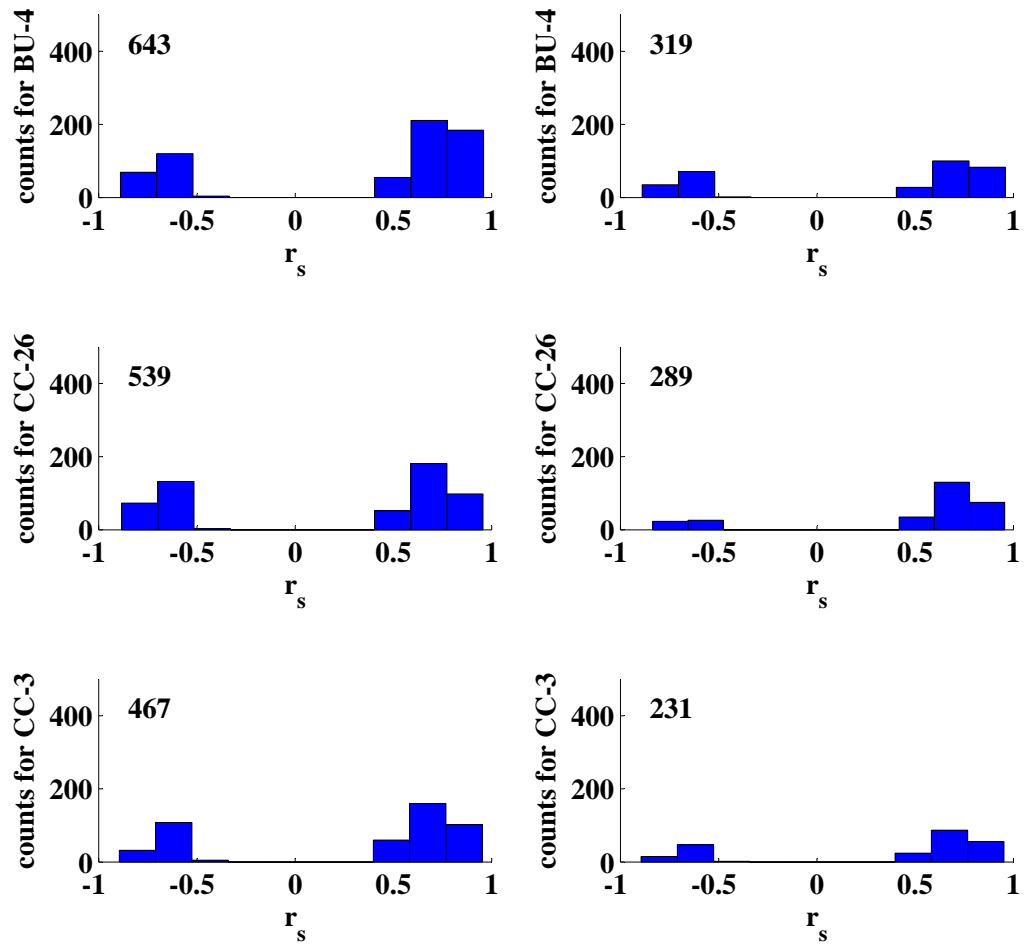


Fig. J.7: Illustrated is the distribution of speleothem r_s for the indicated runs of the 4000 years short-term PCA on $\delta^{18}O$ time series before (left panels) and after (right panels) the application of the Fork-tool.

run #4 - 5.8-5.5 ka BP - Part II

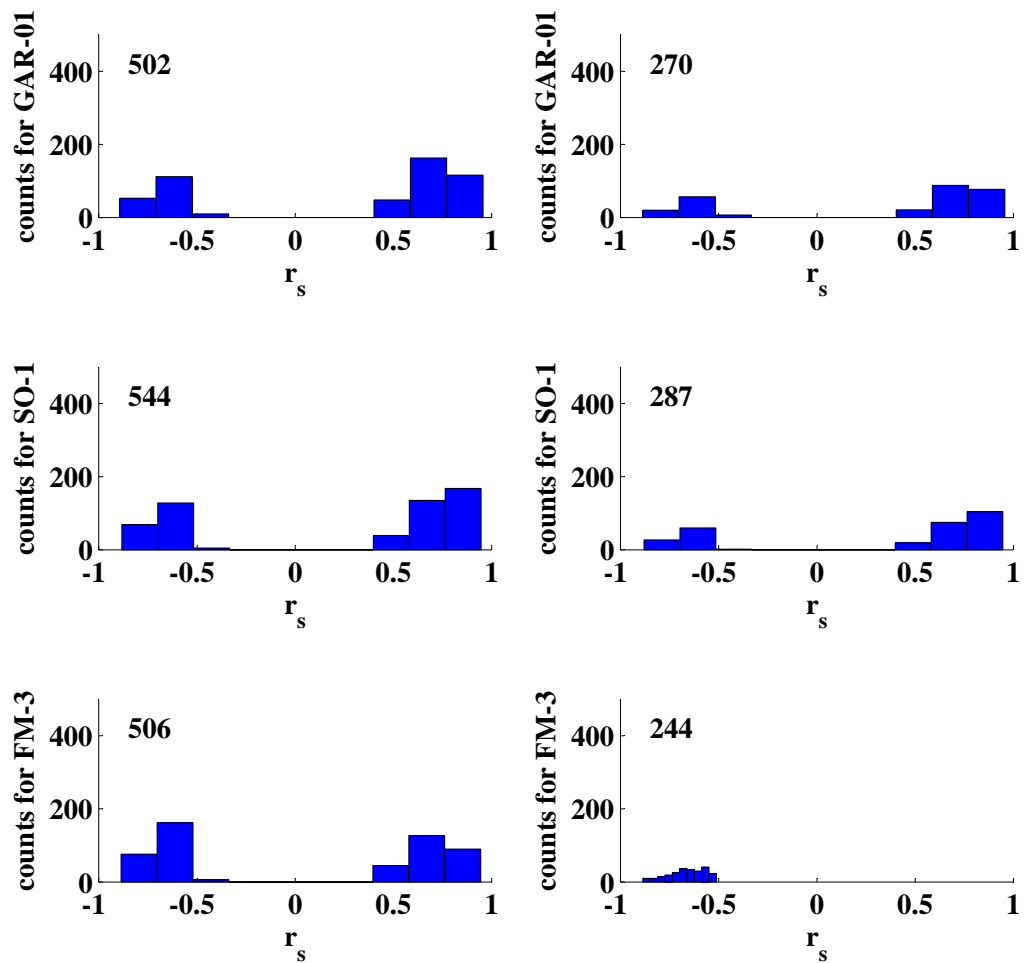


Fig. J.8: Illustrated is the distribution of speleothem r_s for the indicated runs of the 4000 years short-term PCA on $\delta^{18}\text{O}$ time series before (left panels) and after (right panels) the application of the Fork-tool.

run #5 - 5.5-5.2 ka BP - Part I

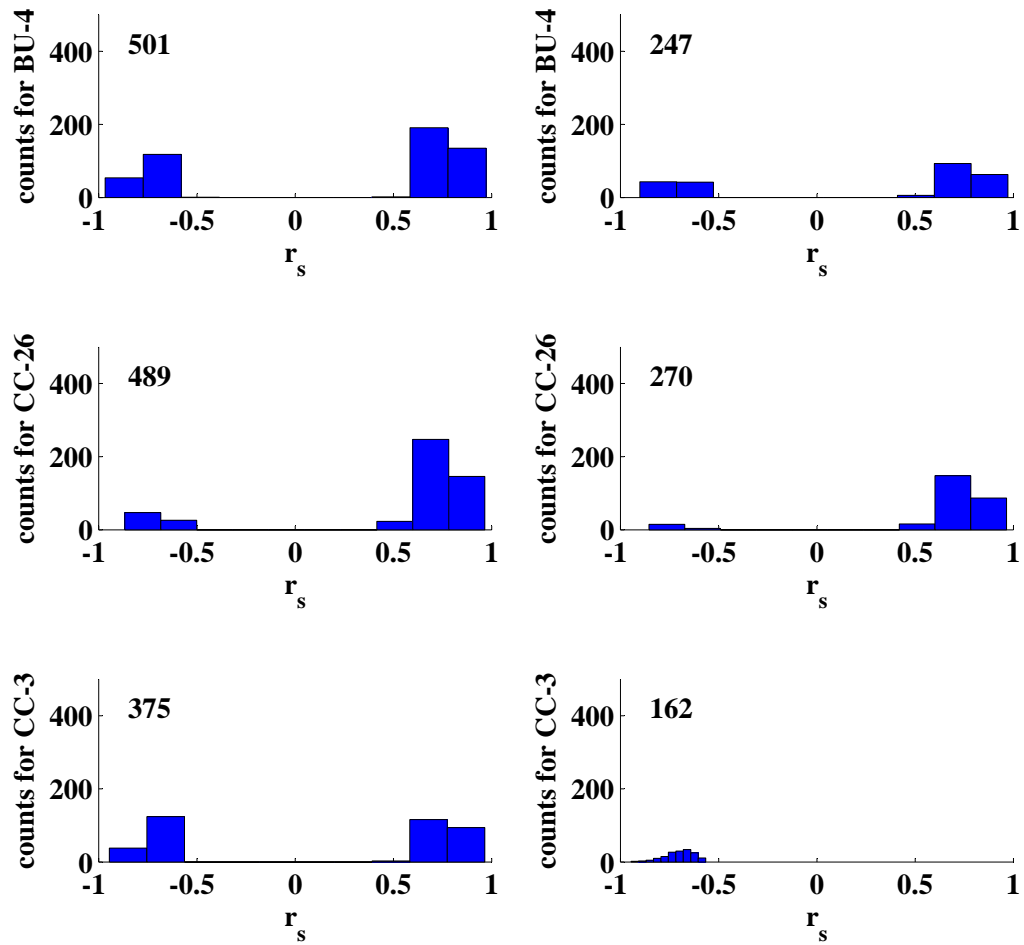


Fig. J.9: Illustrated is the distribution of speleothem r_s for the indicated runs of the 4000 years short-term PCA on $\delta^{18}O$ time series before (left panels) and after (right panels) the application of the Fork-tool.

run #5 - 5.5-5.2 ka BP - Part II

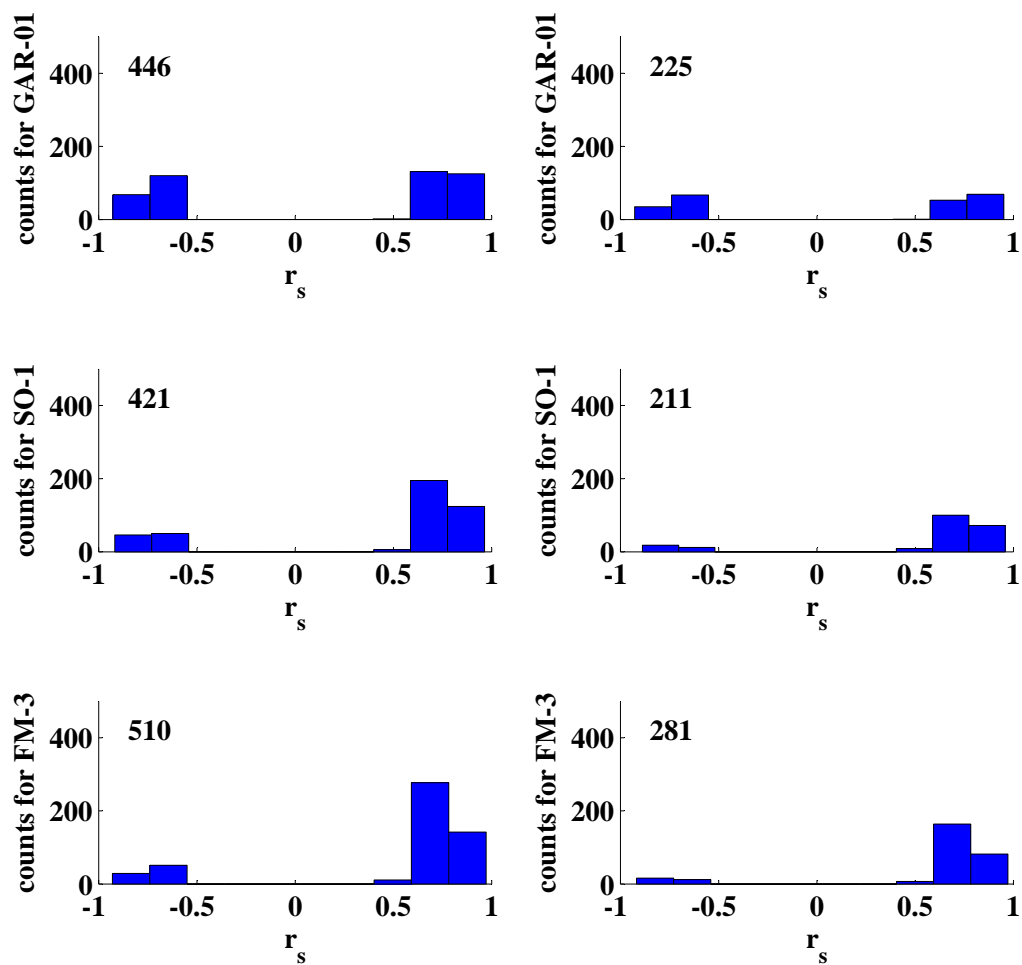


Fig. J.10: Illustrated is the distribution of speleothem r_s for the indicated runs of the 4000 years short-term PCA on $\delta^{18}\text{O}$ time series before (left panels) and after (right panels) the application of the Fork-tool.

run #6 - 5.2-4.9 ka BP - Part I

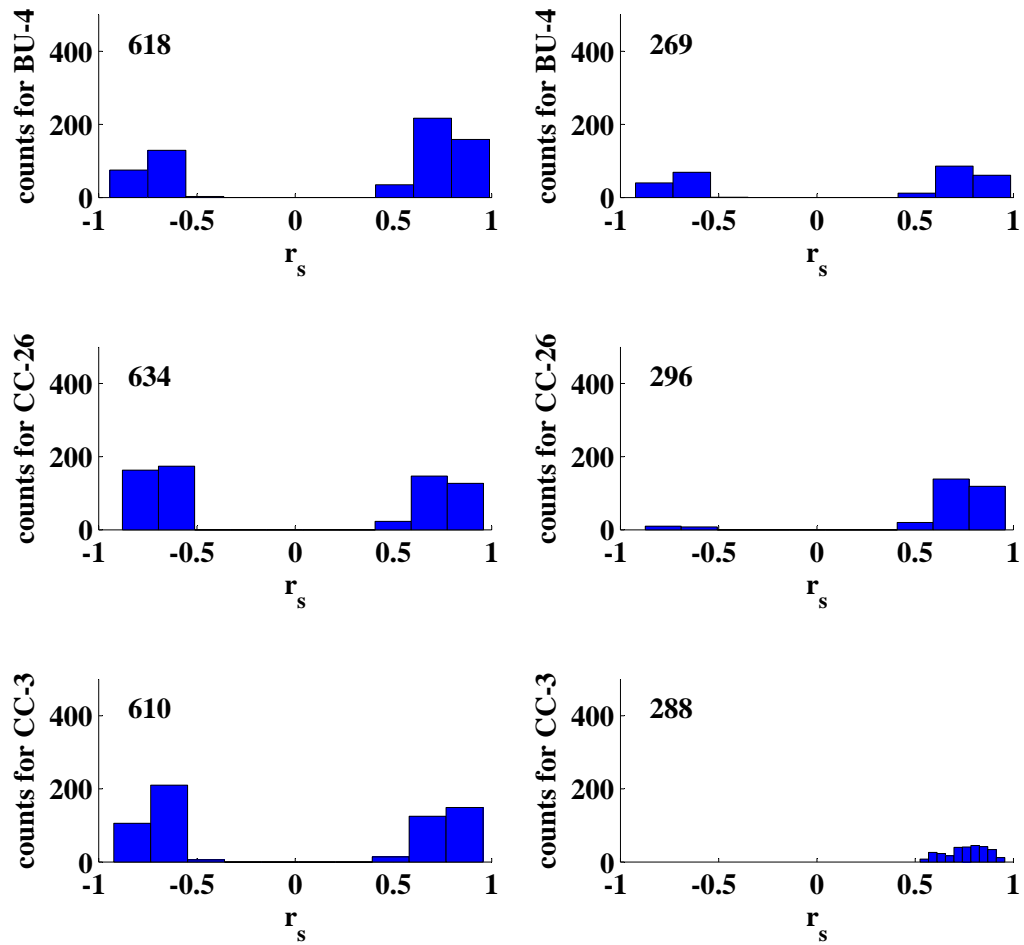


Fig. J.11: Illustrated is the distribution of speleothem r_s for the indicated runs of the 4000 years short-term PCA on $\delta^{18}O$ time series before (left panels) and after (right panels) the application of the Fork-tool.

run #6 - 5.2-4.9 ka BP - Part II

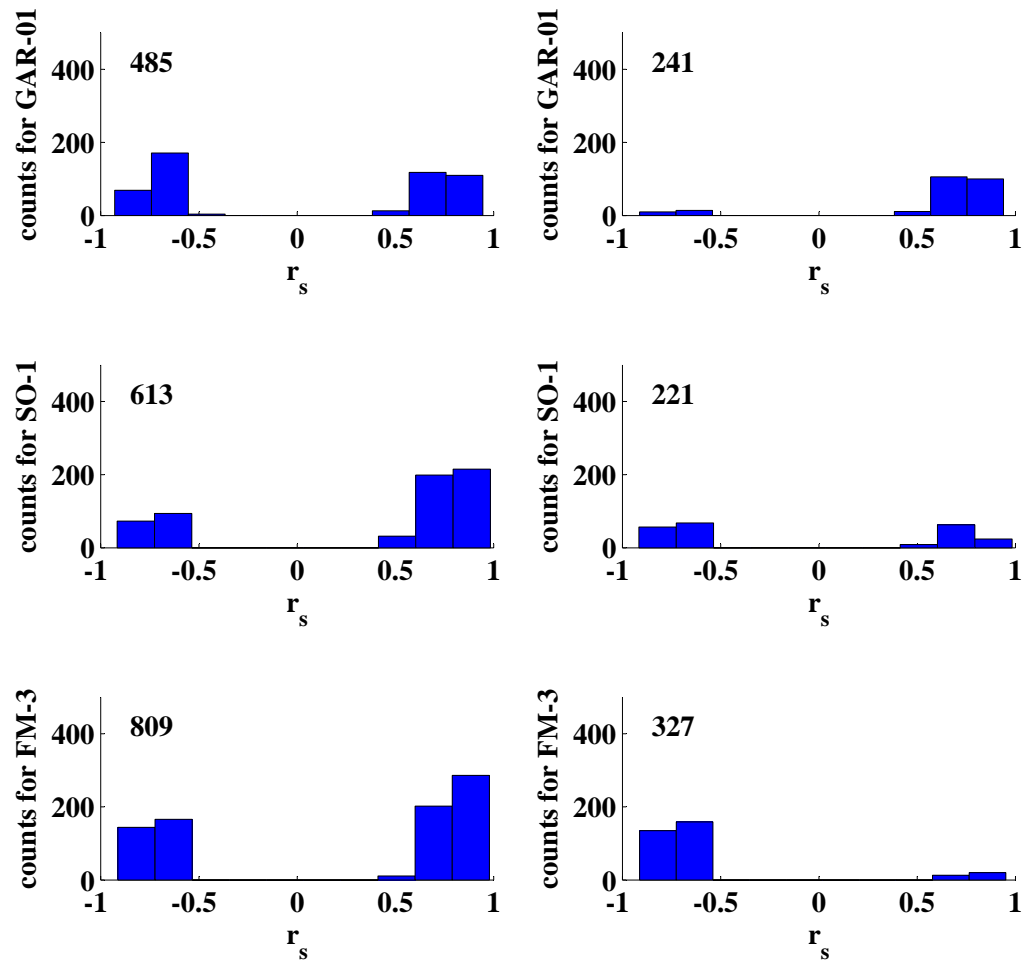


Fig. J.12: Illustrated is the distribution of speleothem r_s for the indicated runs of the 4000 years short-term PCA on $\delta^{18}\text{O}$ time series before (left panels) and after (right panels) the application of the Fork-tool.

run #7 - 4.9-4.6 ka BP - Part I

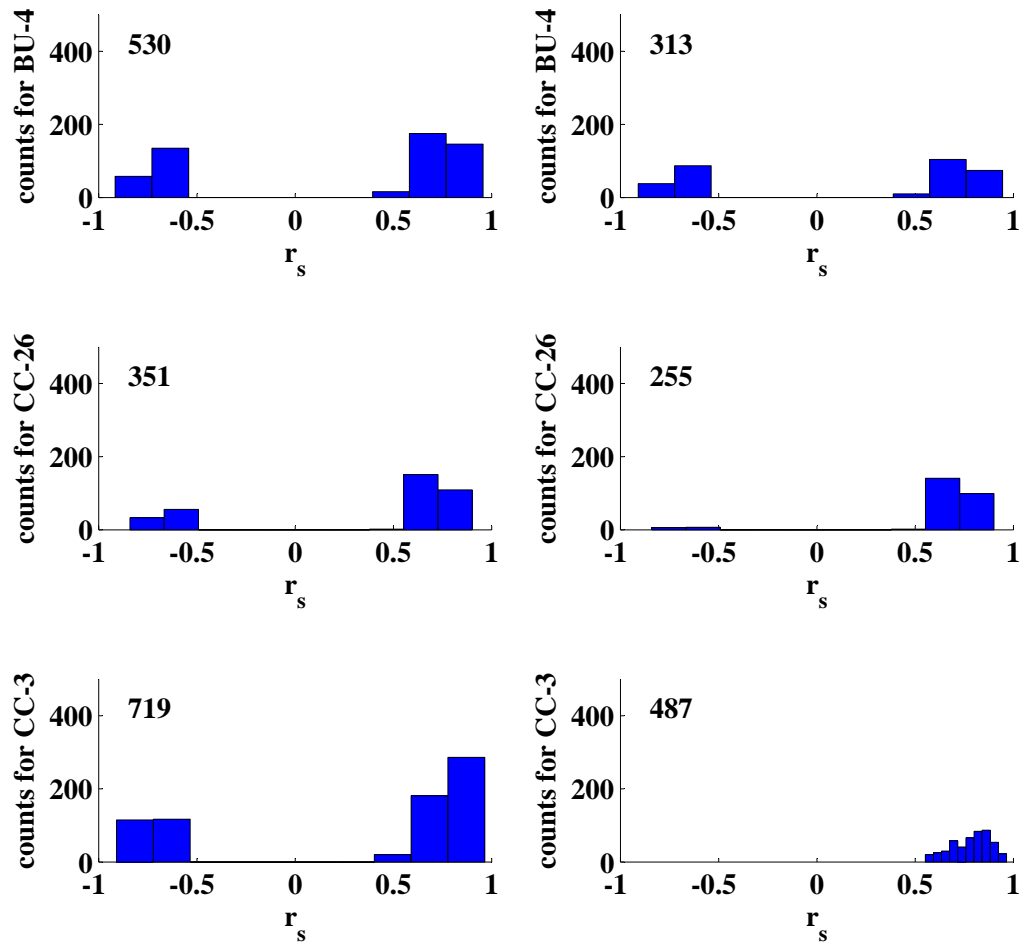


Fig. J.13: Illustrated is the distribution of speleothem r_s for the indicated runs of the 4000 years short-term PCA on $\delta^{18}O$ time series before (left panels) and after (right panels) the application of the Fork-tool.

run #7 - 4.9-4.6 ka BP - Part II

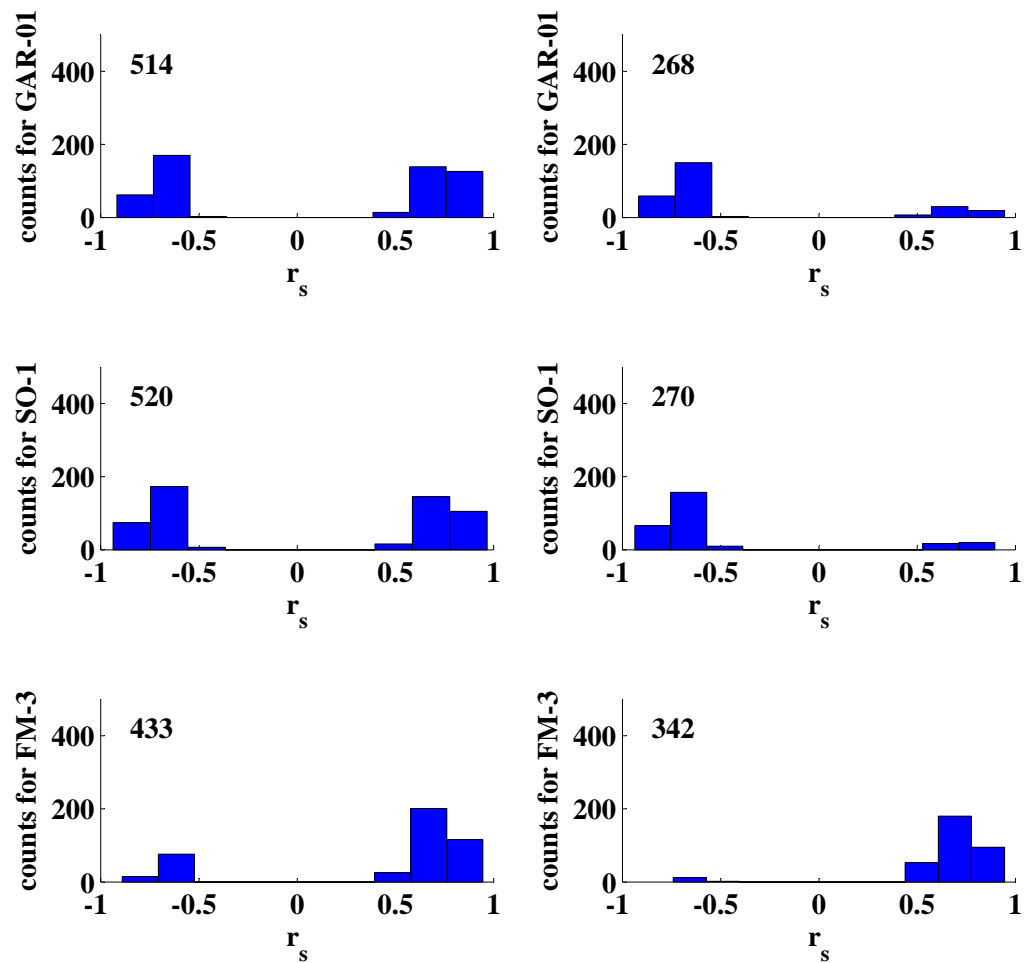


Fig. J.14: Illustrated is the distribution of speleothem r_s for the indicated runs of the 4000 years short-term PCA on $\delta^{18}\text{O}$ time series before (left panels) and after (right panels) the application of the Fork-tool.

run #8 - 4.6-4.3 ka BP - Part I

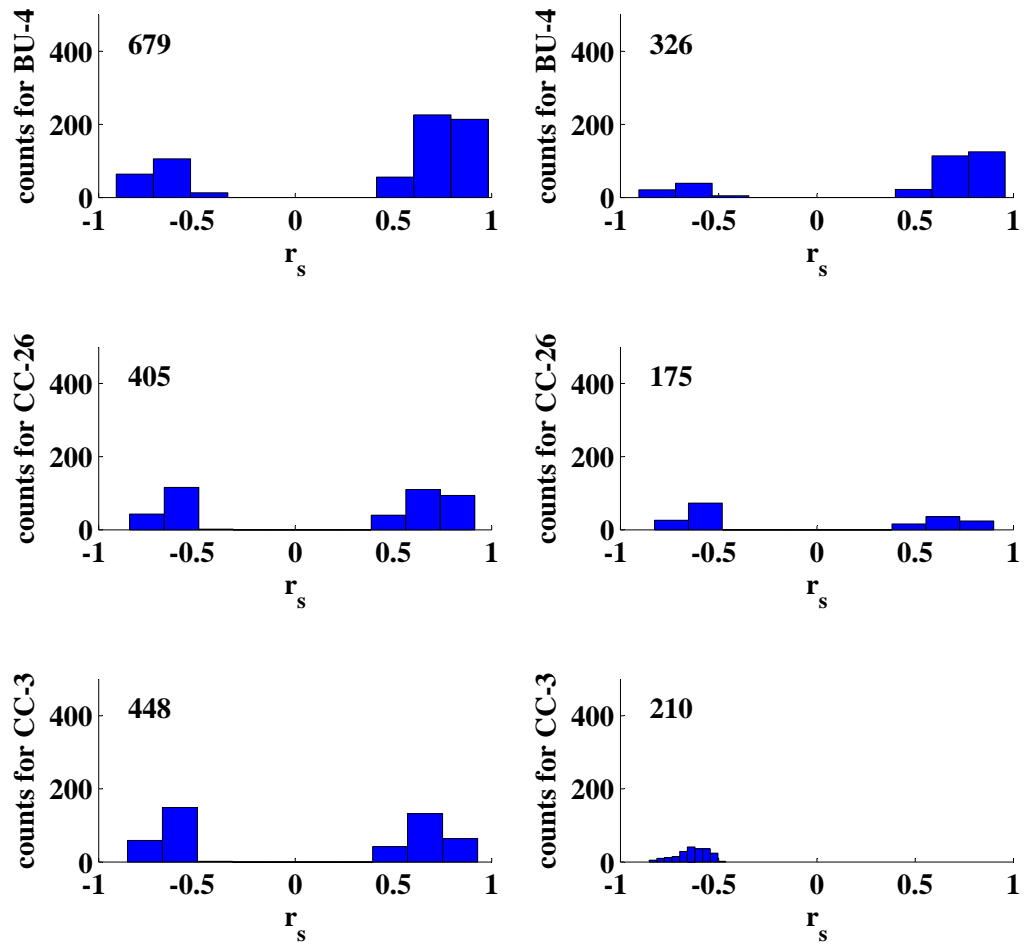


Fig. J.15: Illustrated is the distribution of speleothem r_s for the indicated runs of the 4000 years short-term PCA on $\delta^{18}O$ time series before (left panels) and after (right panels) the application of the Fork-tool.

run #8 - 4.6-4.3 ka BP - Part II

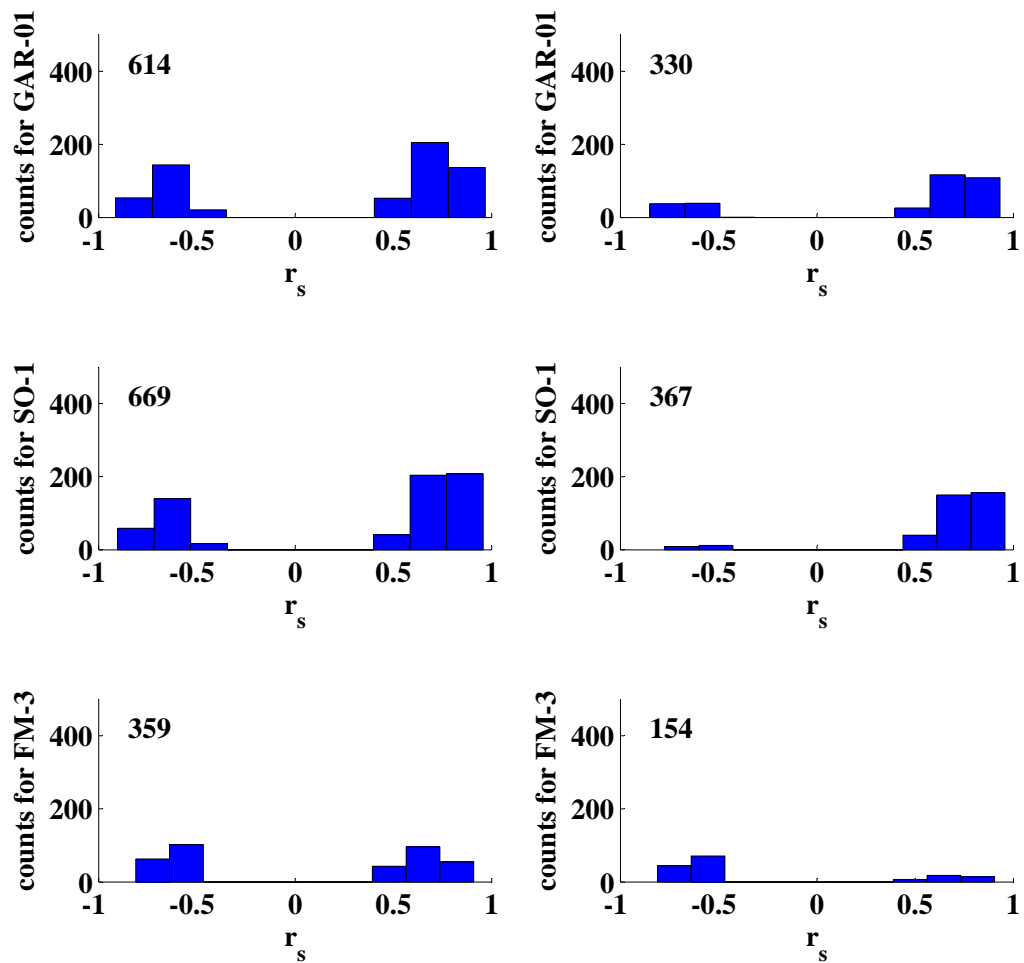


Fig. J.16: Illustrated is the distribution of speleothem r_s for the indicated runs of the 4000 years short-term PCA on $\delta^{18}\text{O}$ time series before (left panels) and after (right panels) the application of the Fork-tool.

run #9 - 4.3-4.0 ka BP - Part I

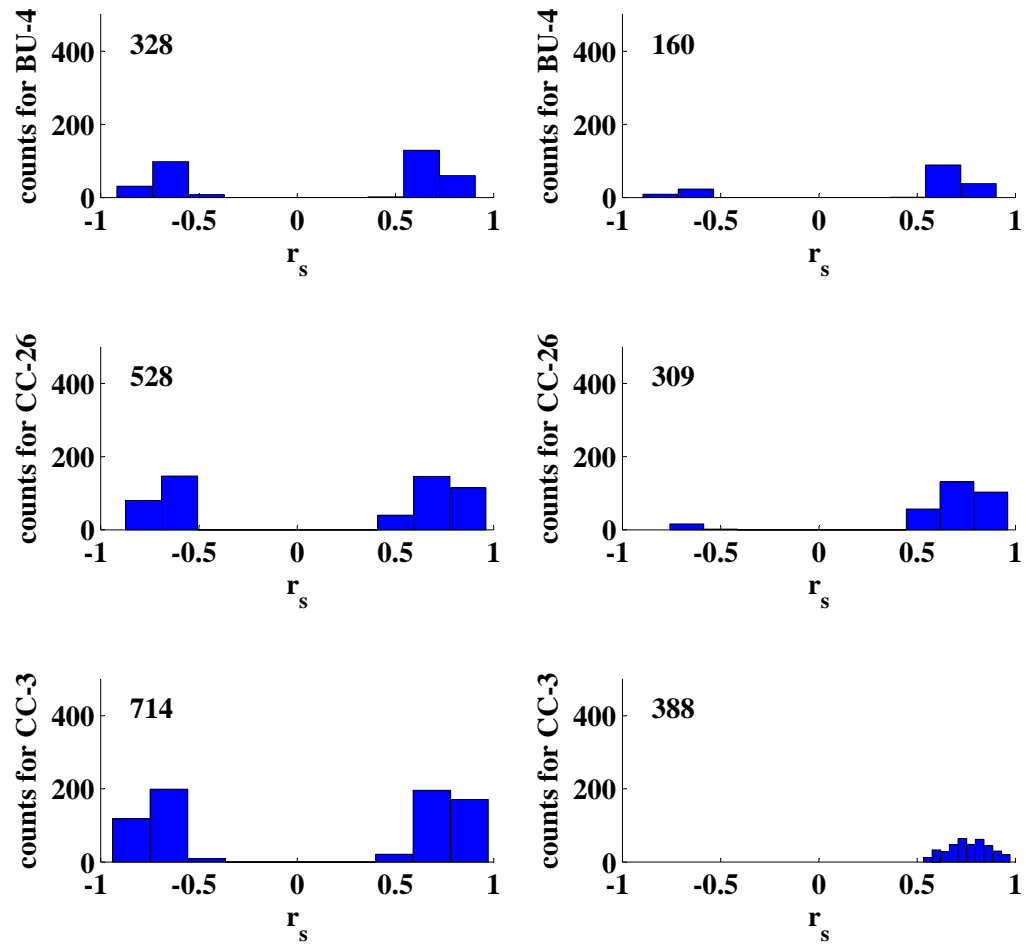


Fig. J.17: Illustrated is the distribution of speleothem r_s for the indicated runs of the 4000 years short-term PCA on $\delta^{18}O$ time series before (left panels) and after (right panels) the application of the Fork-tool.

run #9 - 4.3-4.0 ka BP - Part I

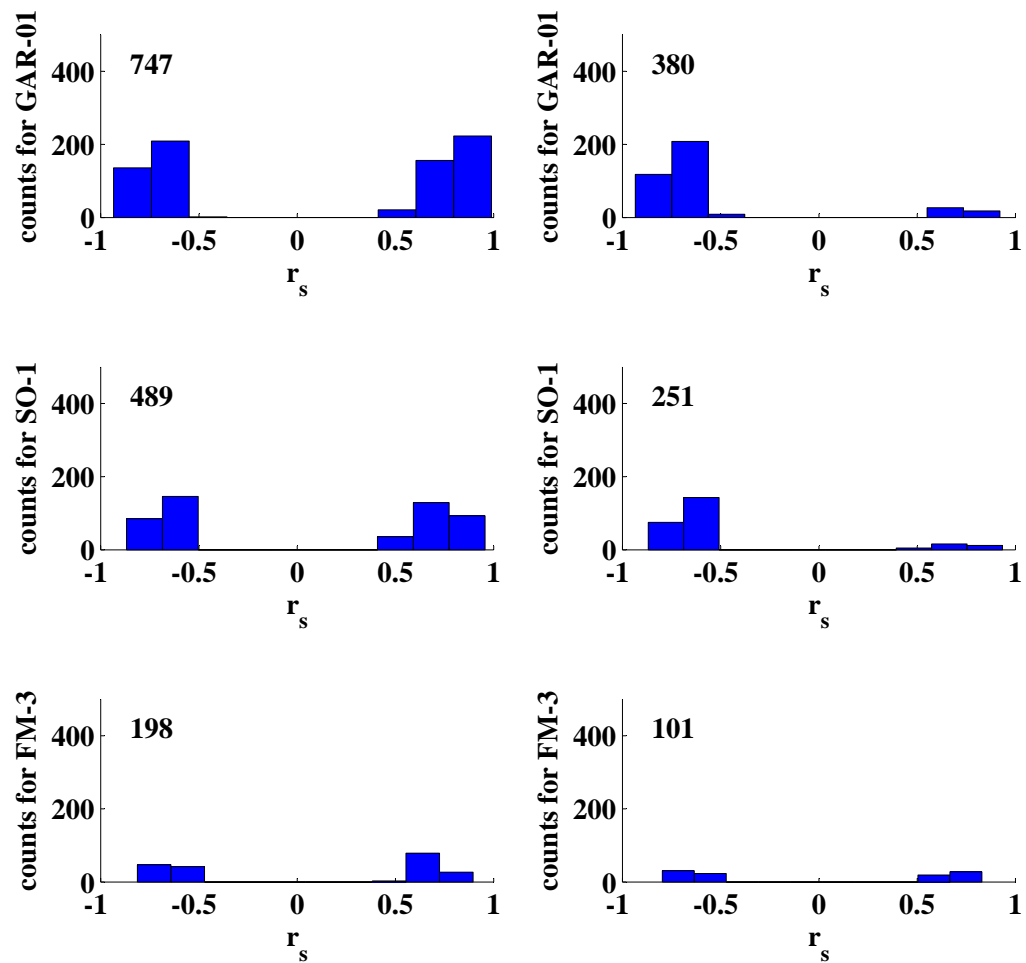


Fig. J.18: Illustrated is the distribution of speleothem r_s for the indicated runs of the 4000 years short-term PCA on $\delta^{18}\text{O}$ time series before (left panels) and after (right panels) the application of the Fork-tool.

J.2 Distribution of r_s for short-term coherence pattern for $\delta^{13}C$ time series

run #1 - 7.0-6.7 ka BP - Part I

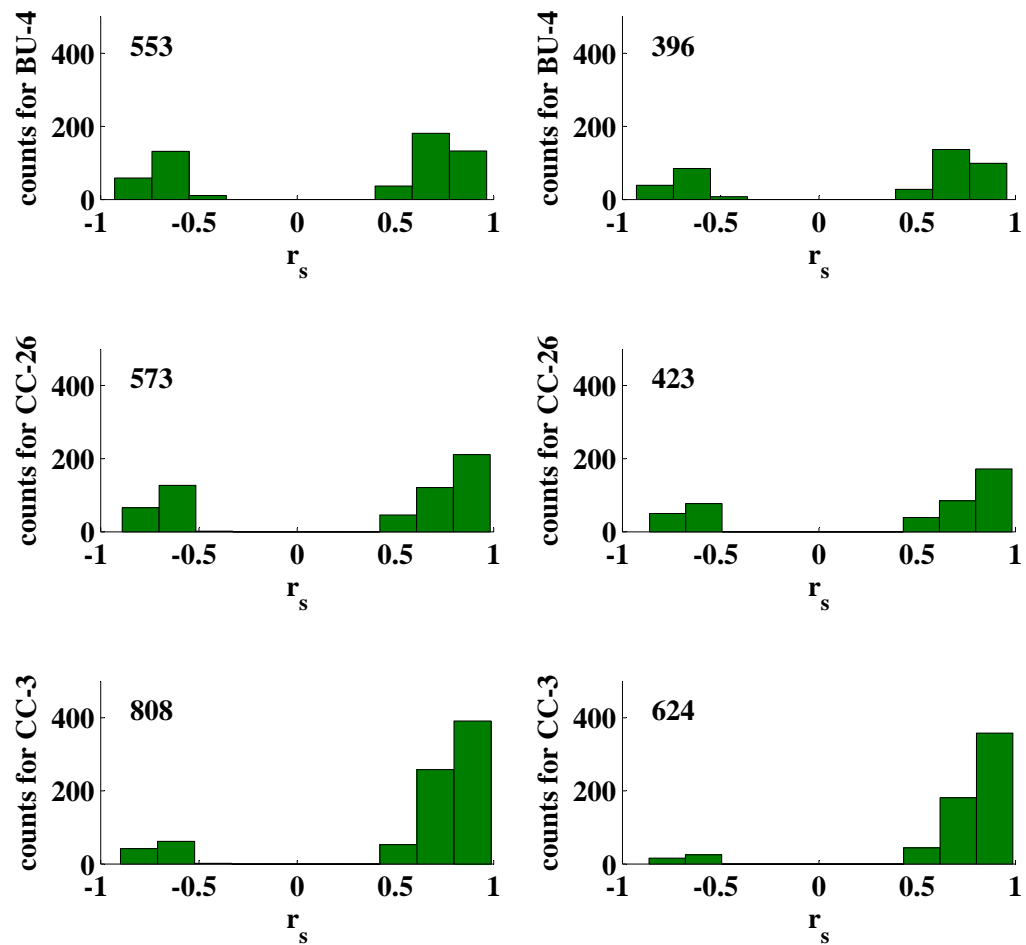


Fig. J.19: Illustrated is the distribution of speleothem r_s for the indicated runs of the 4000 years short-term PCA on $\delta^{13}\text{C}$ time series before (left panels) and after (right panels) the application of the Fork-tool.

run #1 - 7.0-6.7 ka BP - Part II

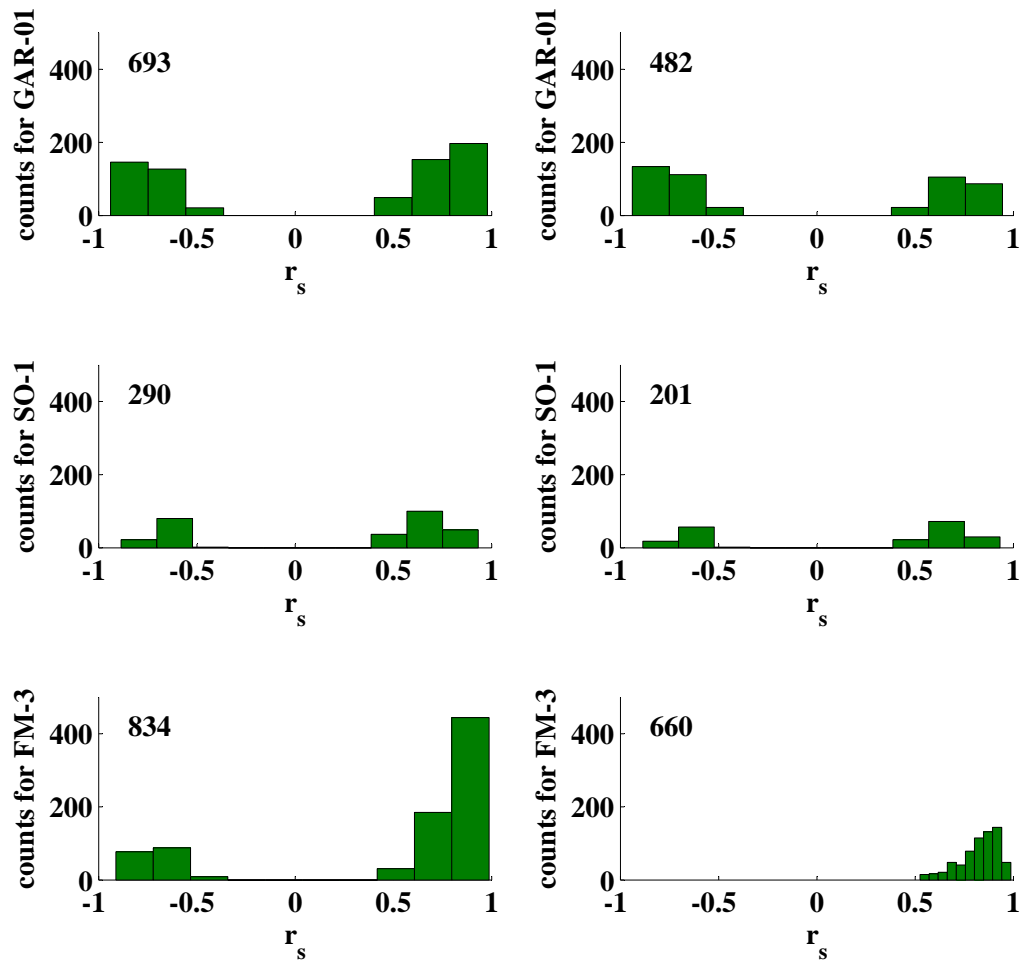


Fig. J.20: Illustrated is the distribution of speleothem r_s for the indicated runs of the 4000 years short-term PCA on $\delta^{13}C$ time series before (left panels) and after (right panels) the application of the Fork-tool.

run #2 - 6.7-6.4 ka BP - Part I

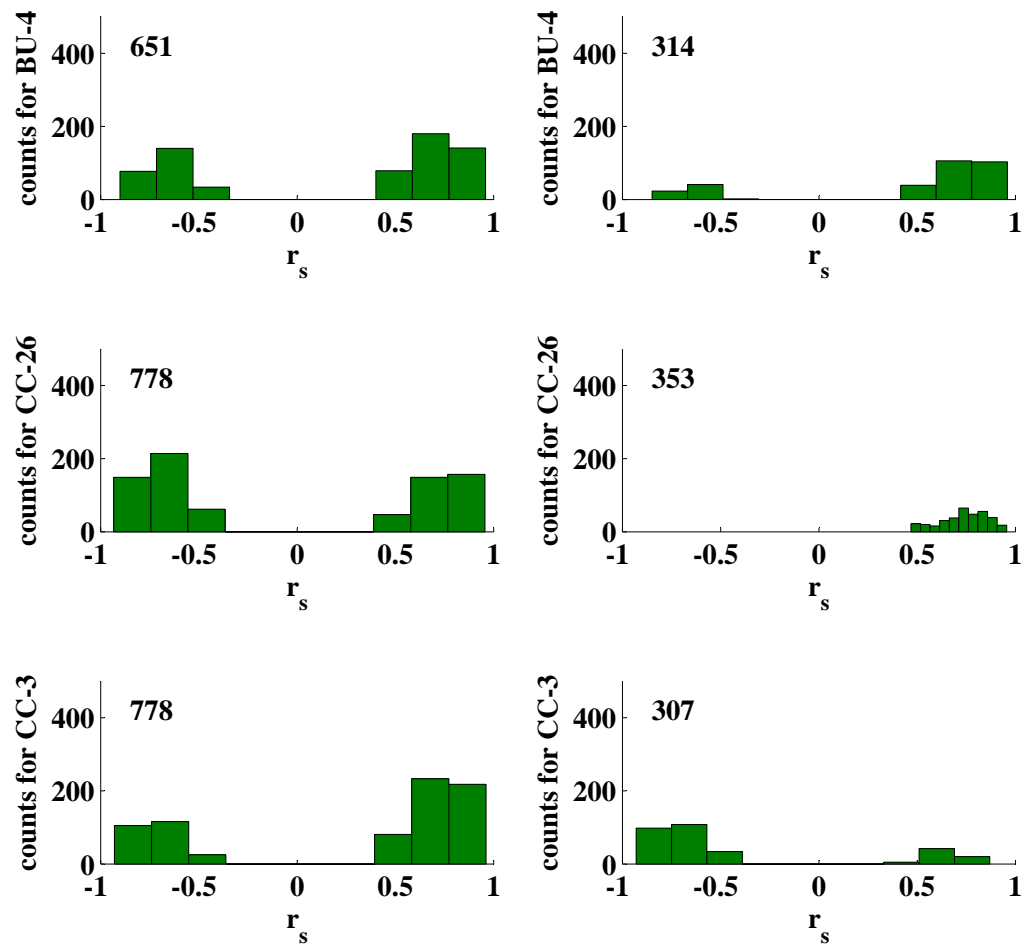


Fig. J.21: Illustrated is the distribution of speleothem r_s for the indicated runs of the 4000 years short-term PCA on $\delta^{13}\text{C}$ time series before (left panels) and after (right panels) the application of the Fork-tool.

run #2 - 6.7-6.4 ka BP - Part II

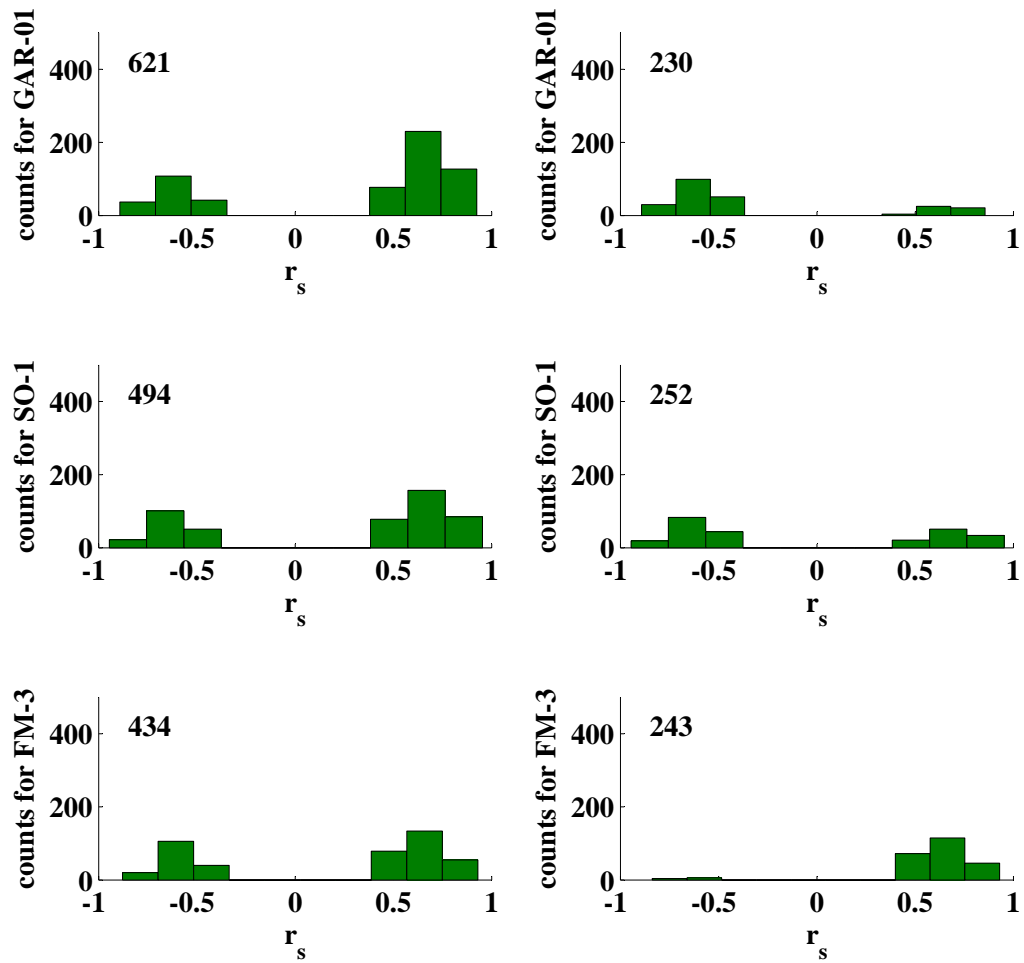


Fig. J.22: Illustrated is the distribution of speleothem r_s for the indicated runs of the 4000 years short-term PCA on $\delta^{13}C$ time series before (left panels) and after (right panels) the application of the Fork-tool.

run #3 - 6.4-6.1 ka BP - Part I

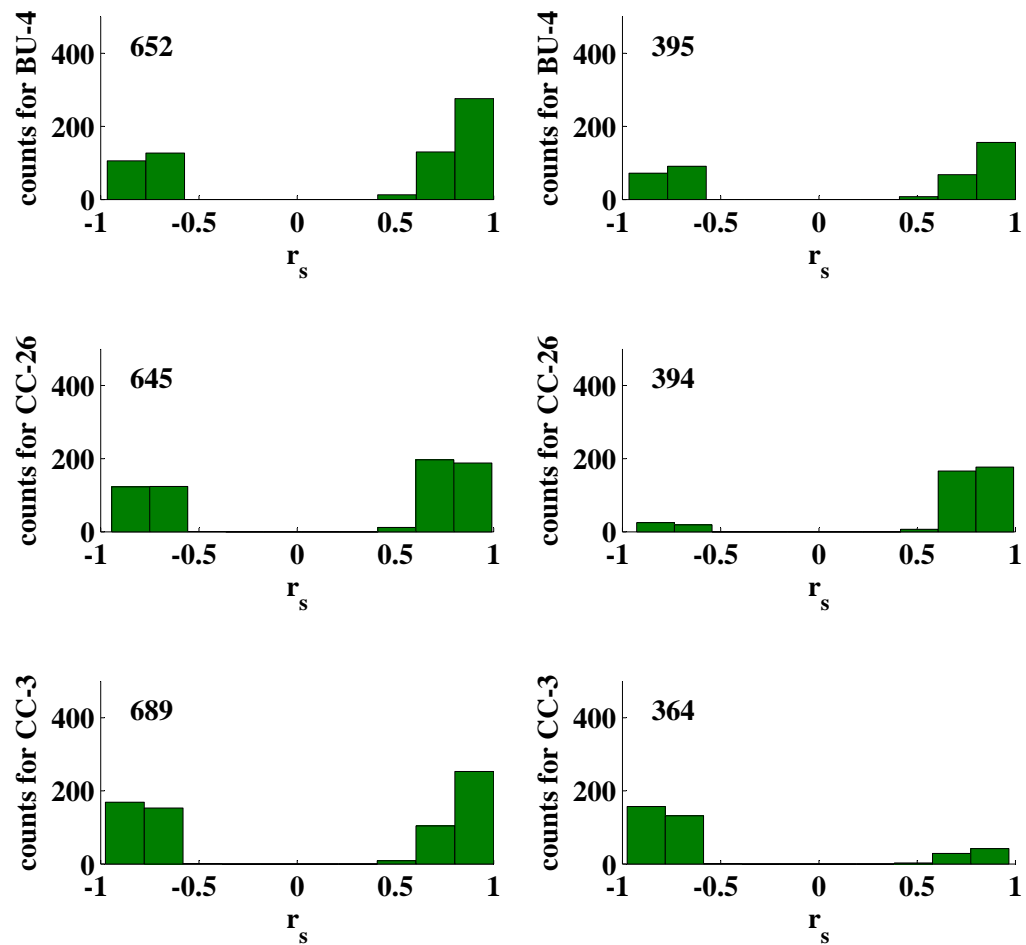


Fig. J.23: Illustrated is the distribution of speleothem r_s for the indicated runs of the 4000 years short-term PCA on $\delta^{13}\text{C}$ time series before (left panels) and after (right panels) the application of the Fork-tool.

run #3 - 6.4-6.1 ka BP - Part II

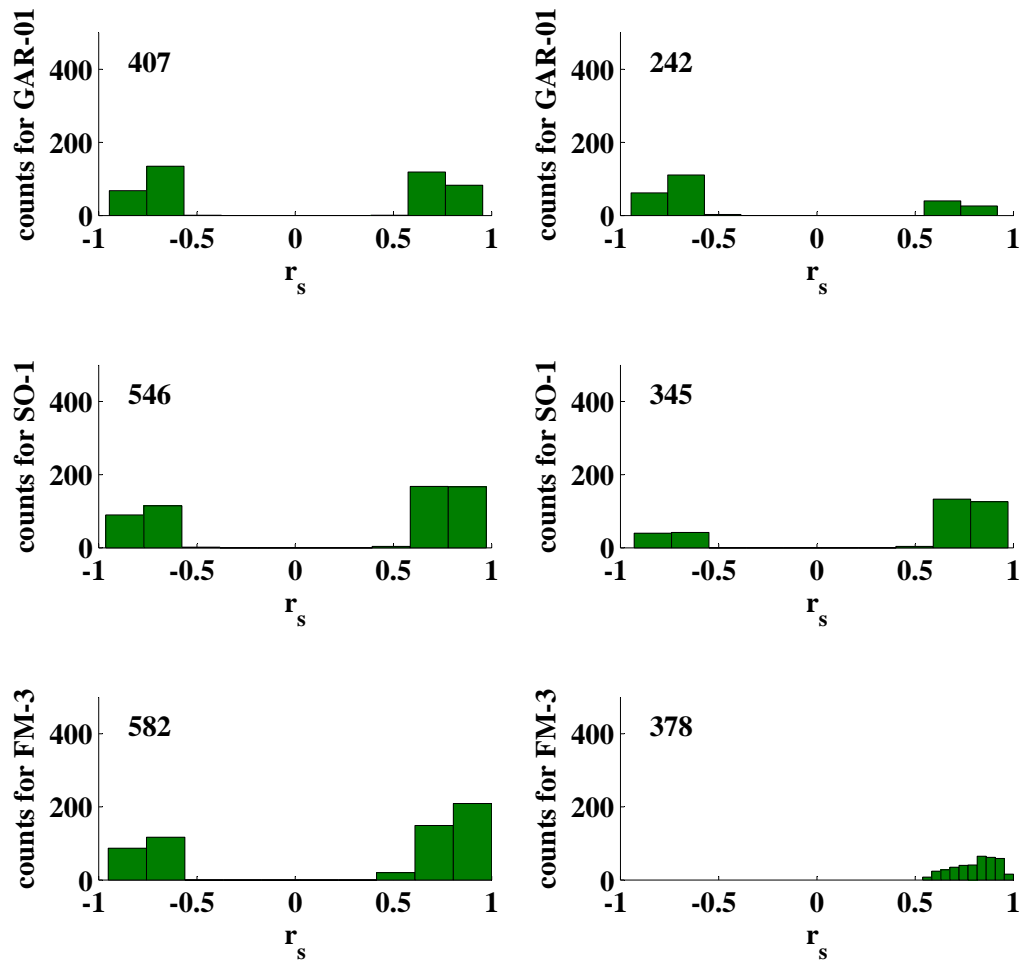


Fig. J.24: Illustrated is the distribution of speleothem r_s for the indicated runs of the 4000 years short-term PCA on $\delta^{13}C$ time series before (left panels) and after (right panels) the application of the Fork-tool.

run #4 - 5.8-5.5 ka BP - Part I

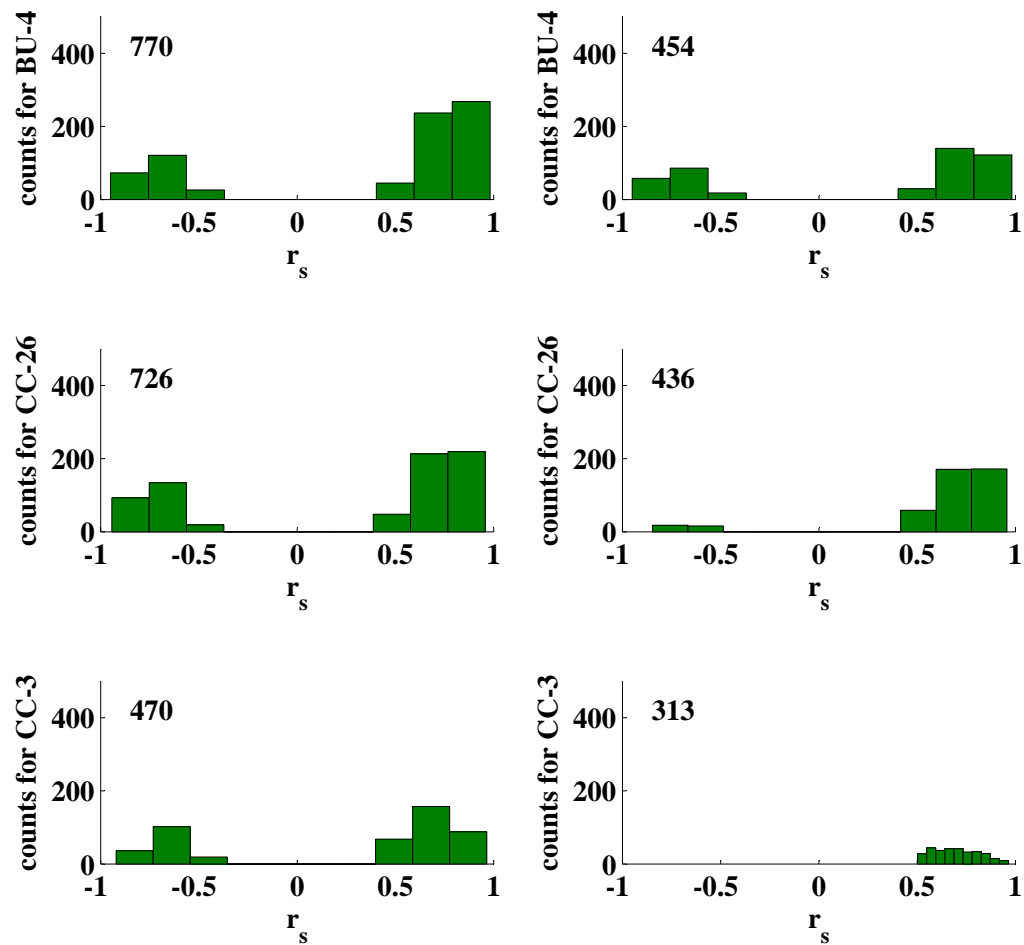


Fig. J.25: Illustrated is the distribution of speleothem r_s for the indicated runs of the 4000 years short-term PCA on $\delta^{13}\text{C}$ time series before (left panels) and after (right panels) the application of the Fork-tool.

run #4 - 5.8-5.5 ka BP - Part II

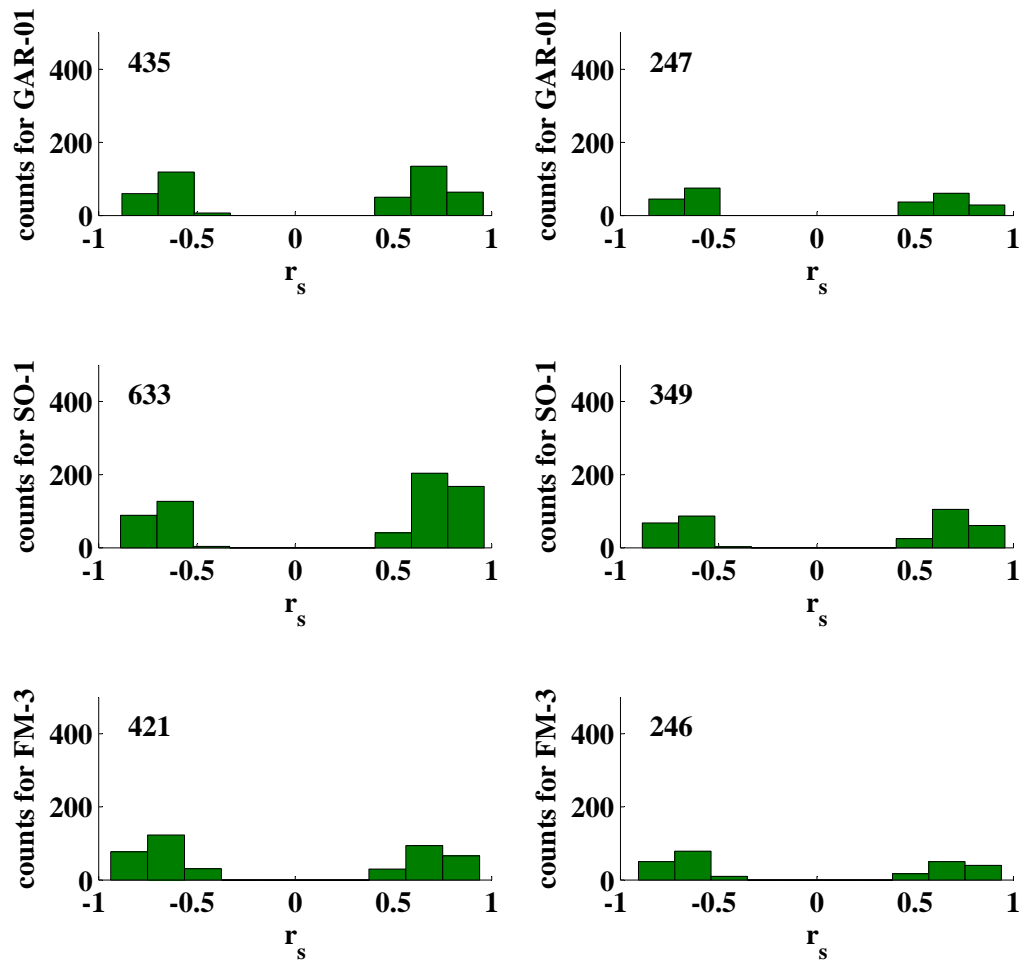


Fig. J.26: Illustrated is the distribution of speleothem r_s for the indicated runs of the 4000 years short-term PCA on $\delta^{13}C$ time series before (left panels) and after (right panels) the application of the Fork-tool.

run #5 - 5.5-5.2 ka BP - Part I

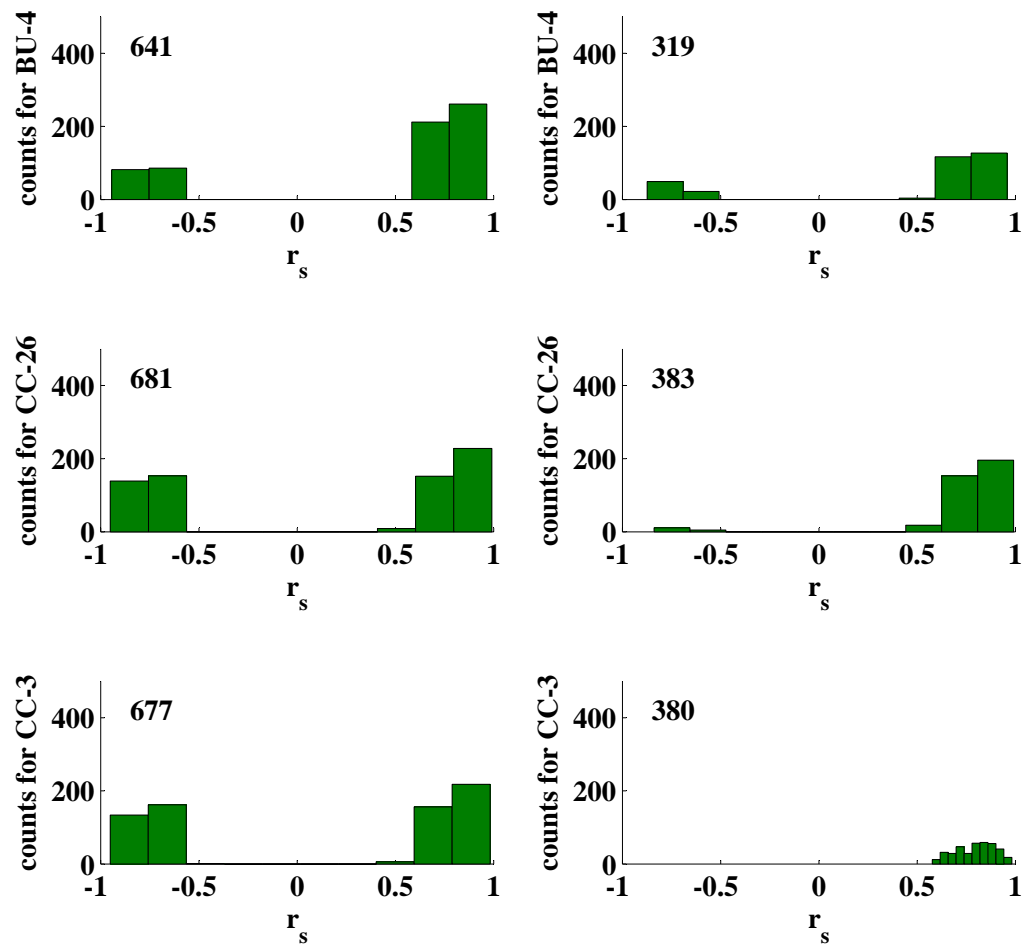


Fig. J.27: Illustrated is the distribution of speleothem r_s for the indicated runs of the 4000 years short-term PCA on $\delta^{13}\text{C}$ time series before (left panels) and after (right panels) the application of the Fork-tool.

run #5 - 5.5-5.2 ka BP - Part II

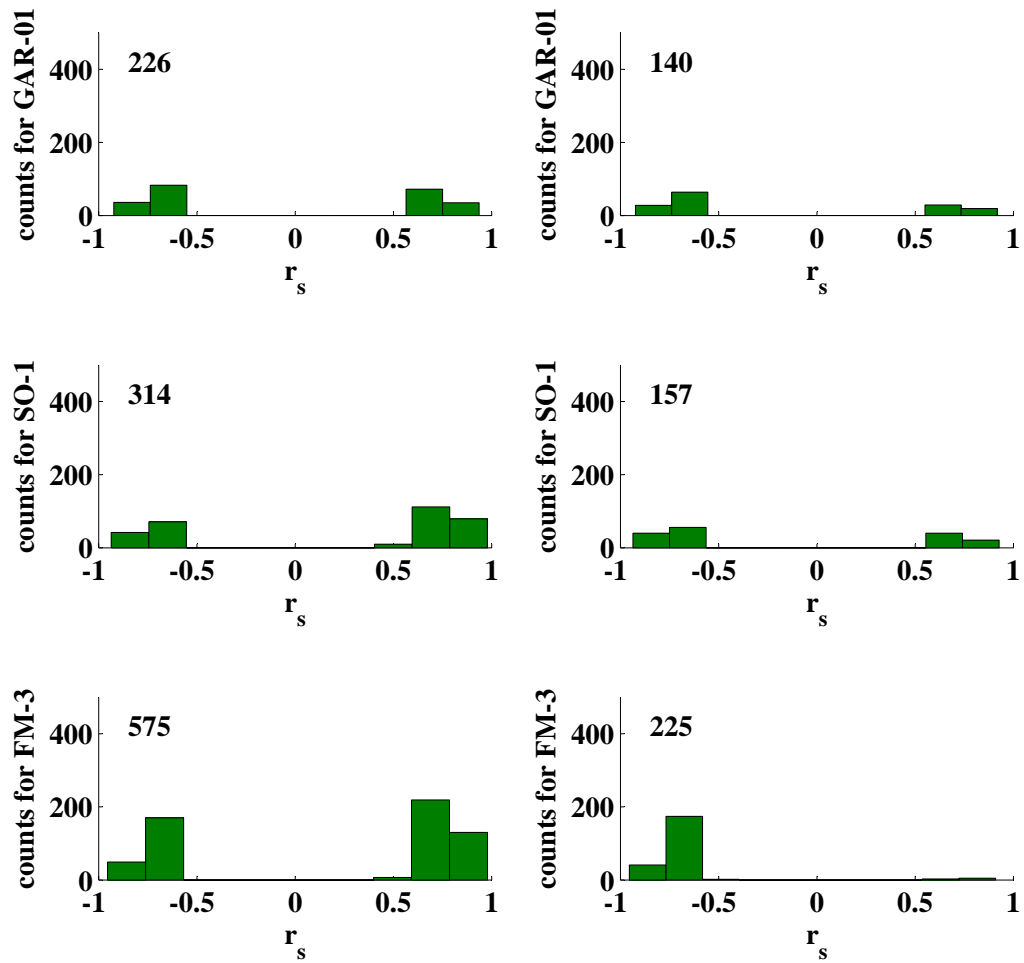


Fig. J.28: Illustrated is the distribution of speleothem r_s for the indicated runs of the 4000 years short-term PCA on $\delta^{13}C$ time series before (left panels) and after (right panels) the application of the Fork-tool.

run #6 - 5.2-4.9 ka BP - Part I

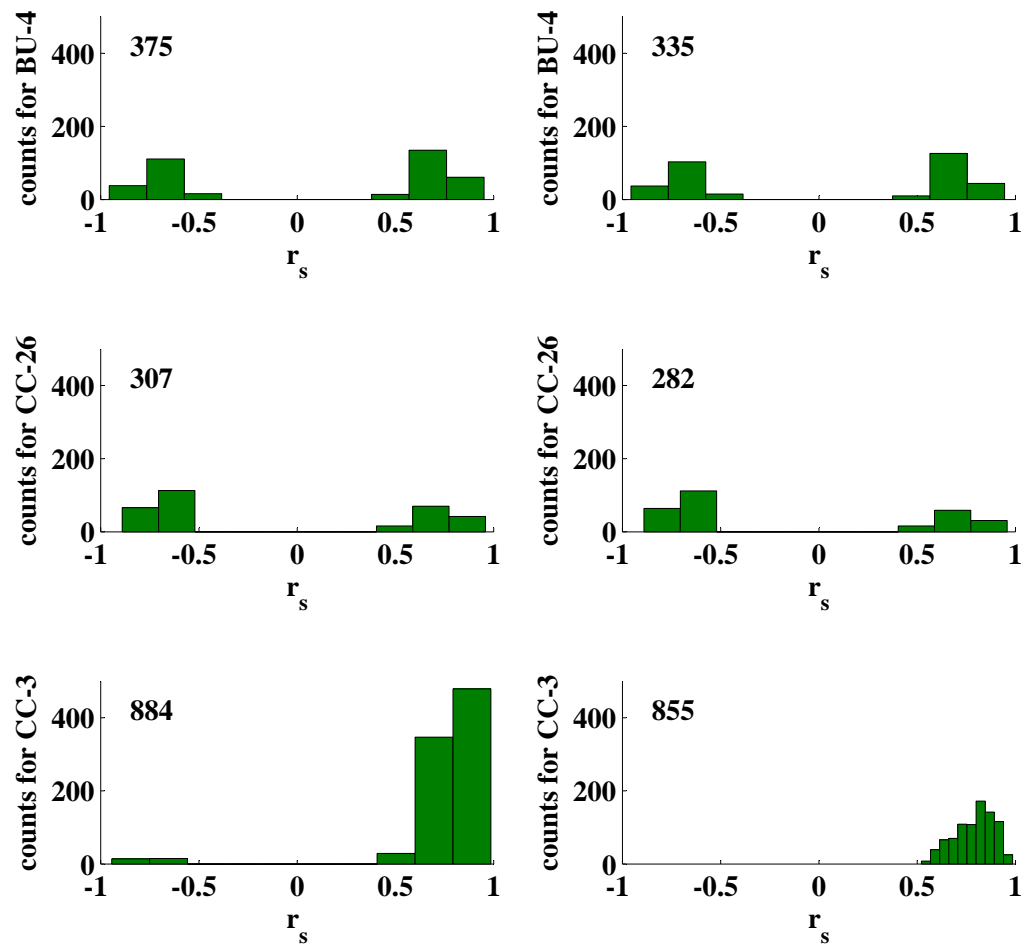


Fig. J.29: Illustrated is the distribution of speleothem r_s for the indicated runs of the 4000 years short-term PCA on $\delta^{13}\text{C}$ time series before (left panels) and after (right panels) the application of the Fork-tool.

run #6 - 5.2-4.9 ka BP - Part II

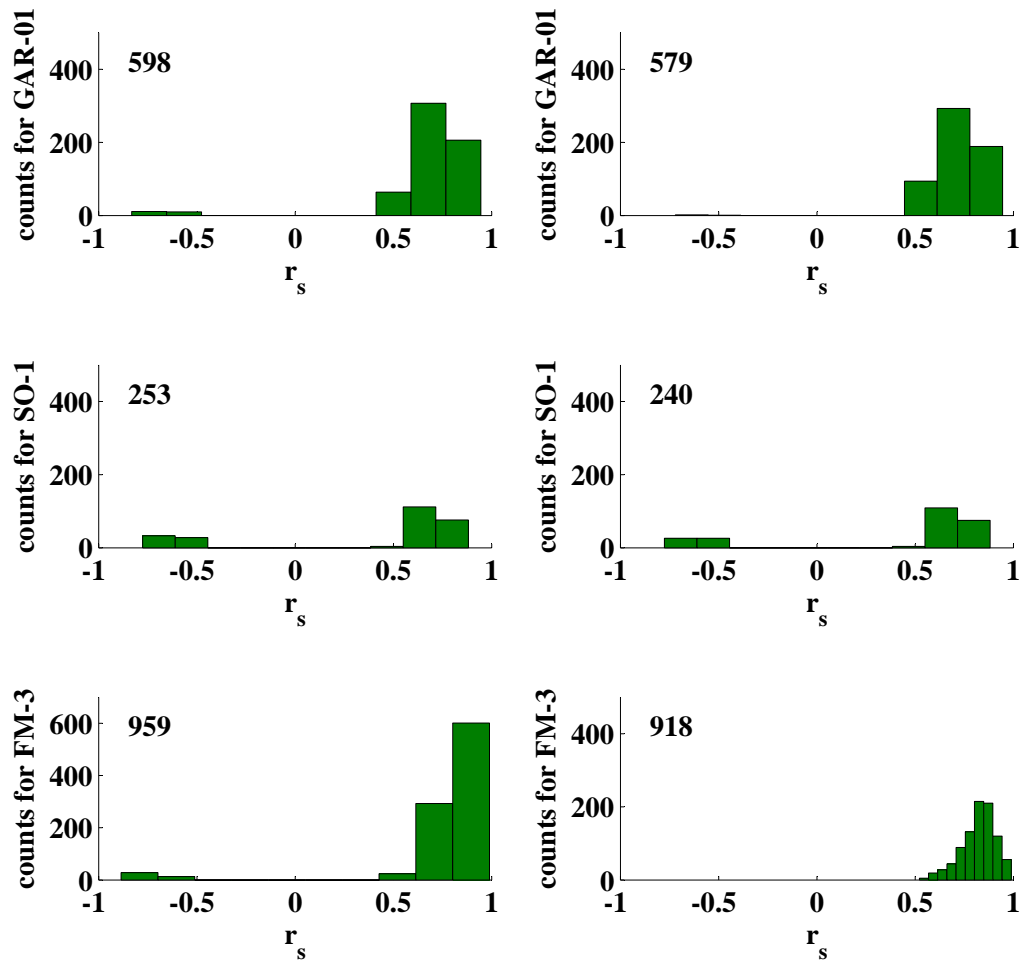


Fig. J.30: Illustrated is the distribution of speleothem r_s for the indicated runs of the 4000 years short-term PCA on $\delta^{13}C$ time series before (left panels) and after (right panels) the application of the Fork-tool.

run #7 - 4.9-4.6 ka BP - Part I

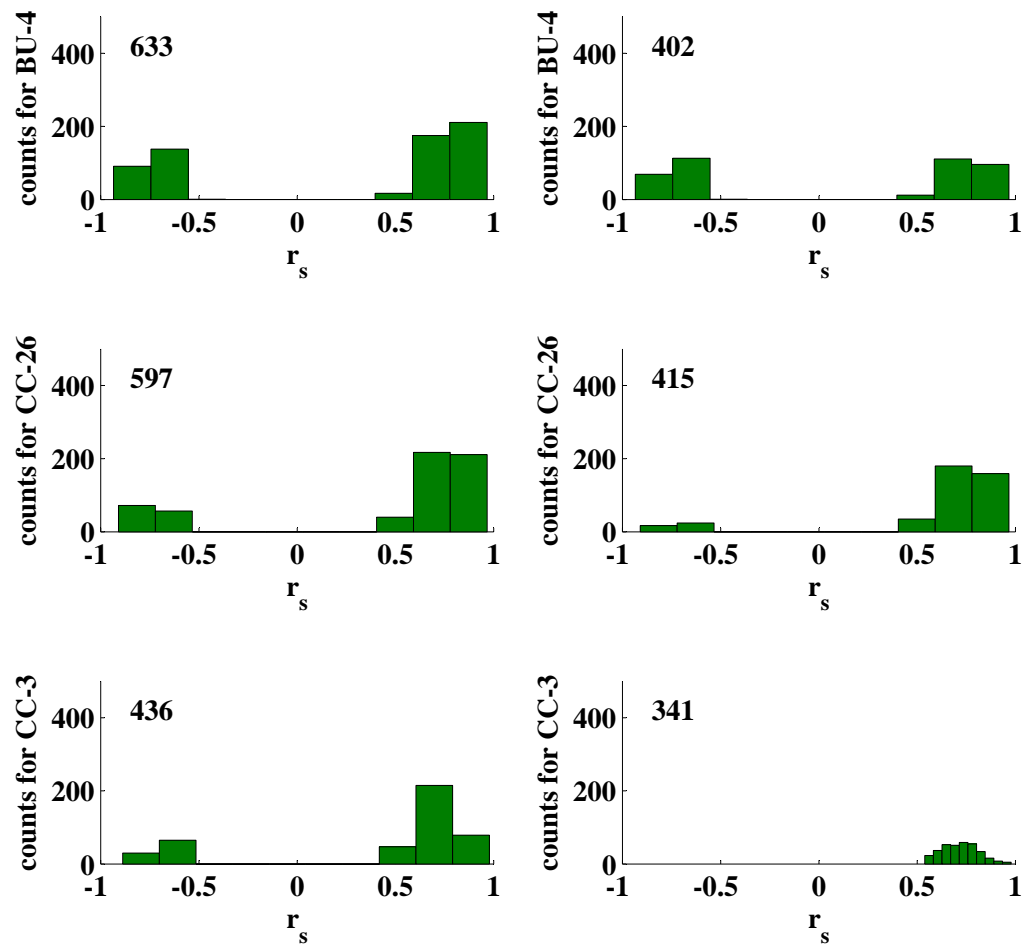


Fig. J.31: Illustrated is the distribution of speleothem r_s for the indicated runs of the 4000 years short-term PCA on $\delta^{13}\text{C}$ time series before (left panels) and after (right panels) the application of the Fork-tool.

run #7 - 4.9-4.6 ka BP - Part II

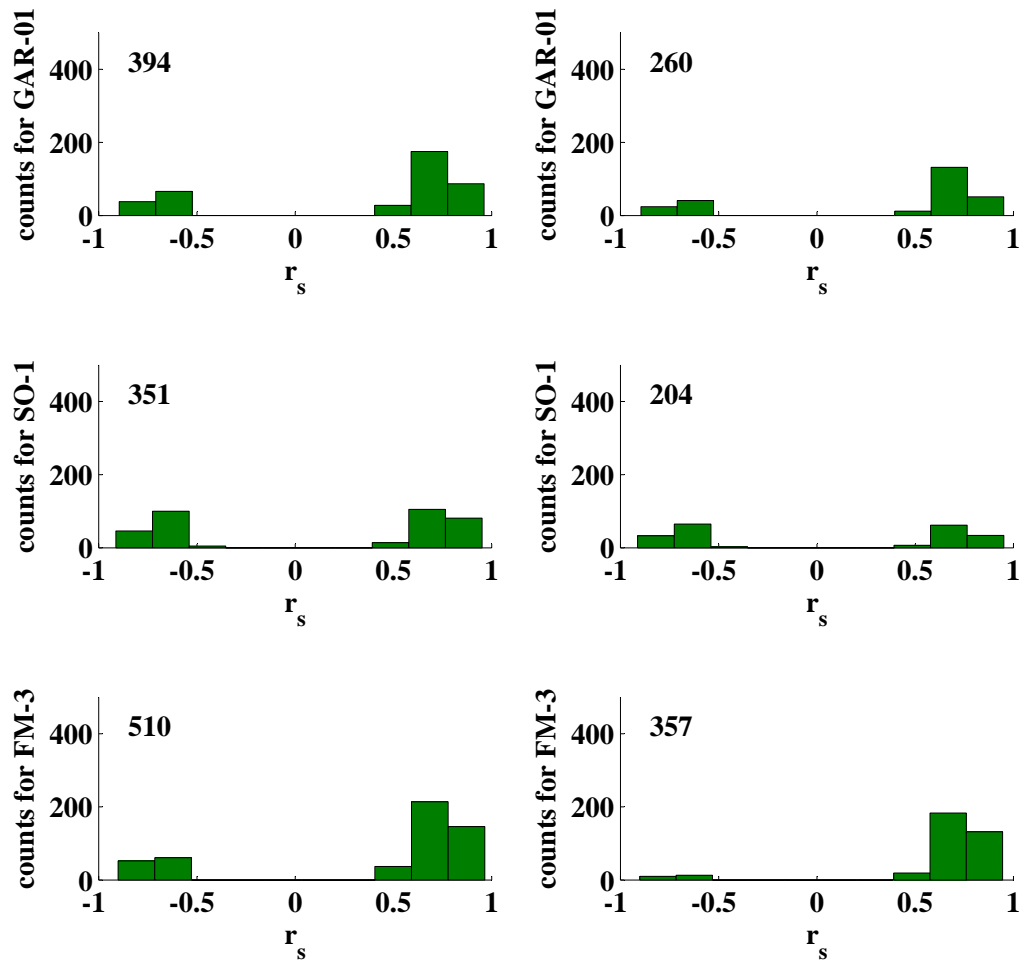


Fig. J.32: Illustrated is the distribution of speleothem r_s for the indicated runs of the 4000 years short-term PCA on $\delta^{13}C$ time series before (left panels) and after (right panels) the application of the Fork-tool.

run #8 - 4.6-4.3 ka BP - Part I

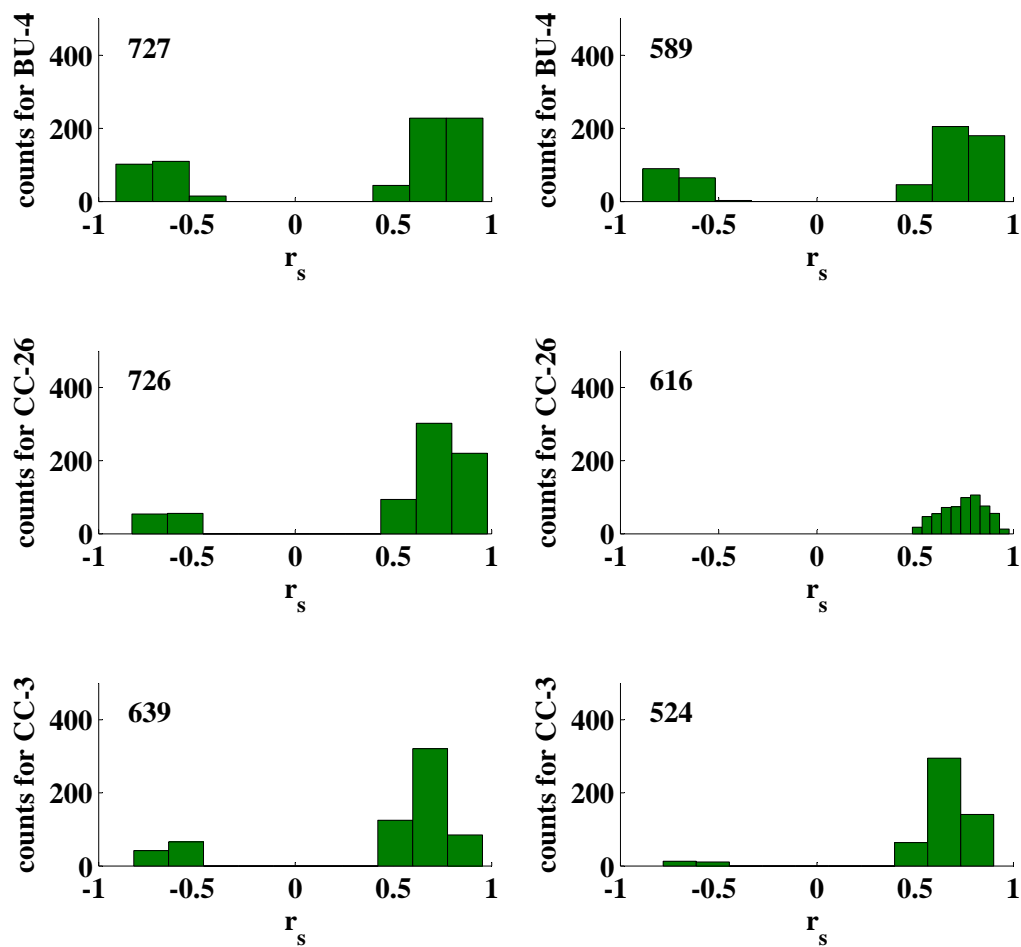


Fig. J.33: Illustrated is the distribution of speleothem r_s for the indicated runs of the 4000 years short-term PCA on $\delta^{13}\text{C}$ time series before (left panels) and after (right panels) the application of the Fork-tool.

run #8 - 4.6-4.3 ka BP - Part II

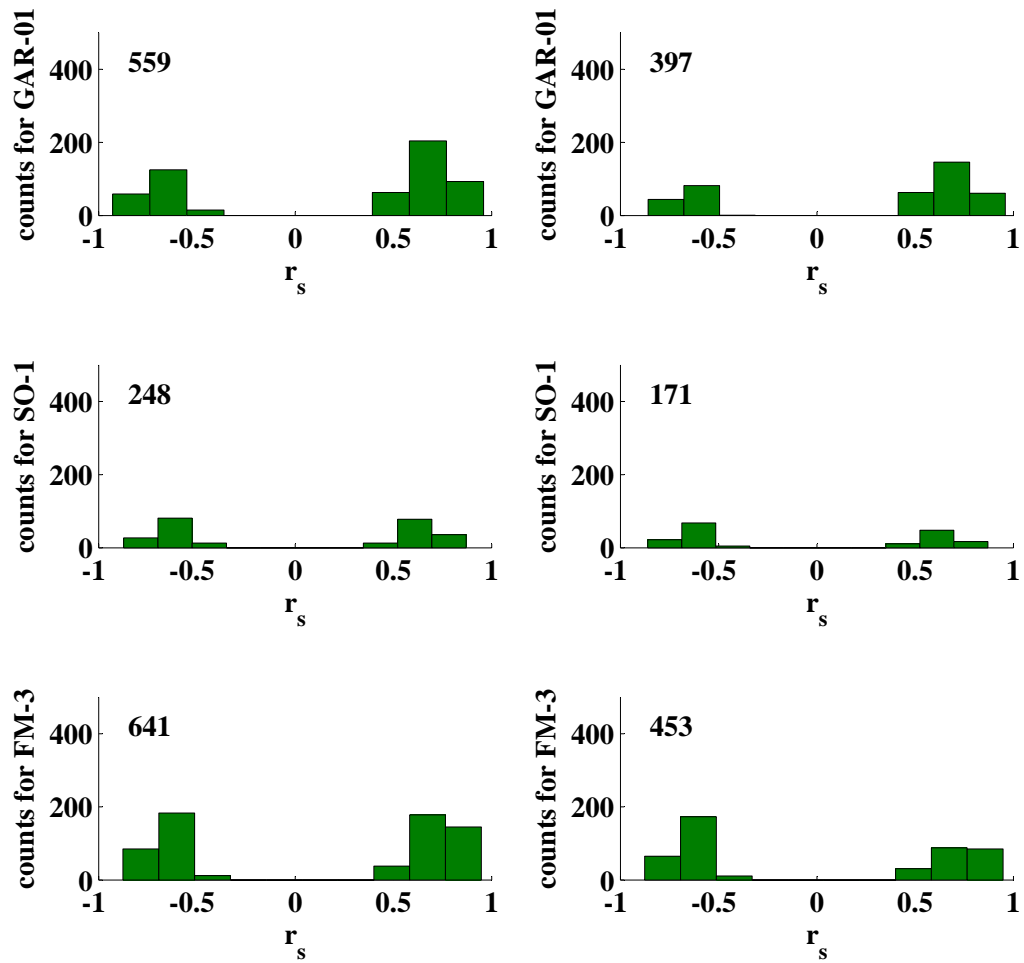


Fig. J.34: Illustrated is the distribution of speleothem r_s for the indicated runs of the 4000 years short-term PCA on $\delta^{13}C$ time series before (left panels) and after (right panels) the application of the Fork-tool.

run #9 - 4.3-4.0 ka BP - Part I

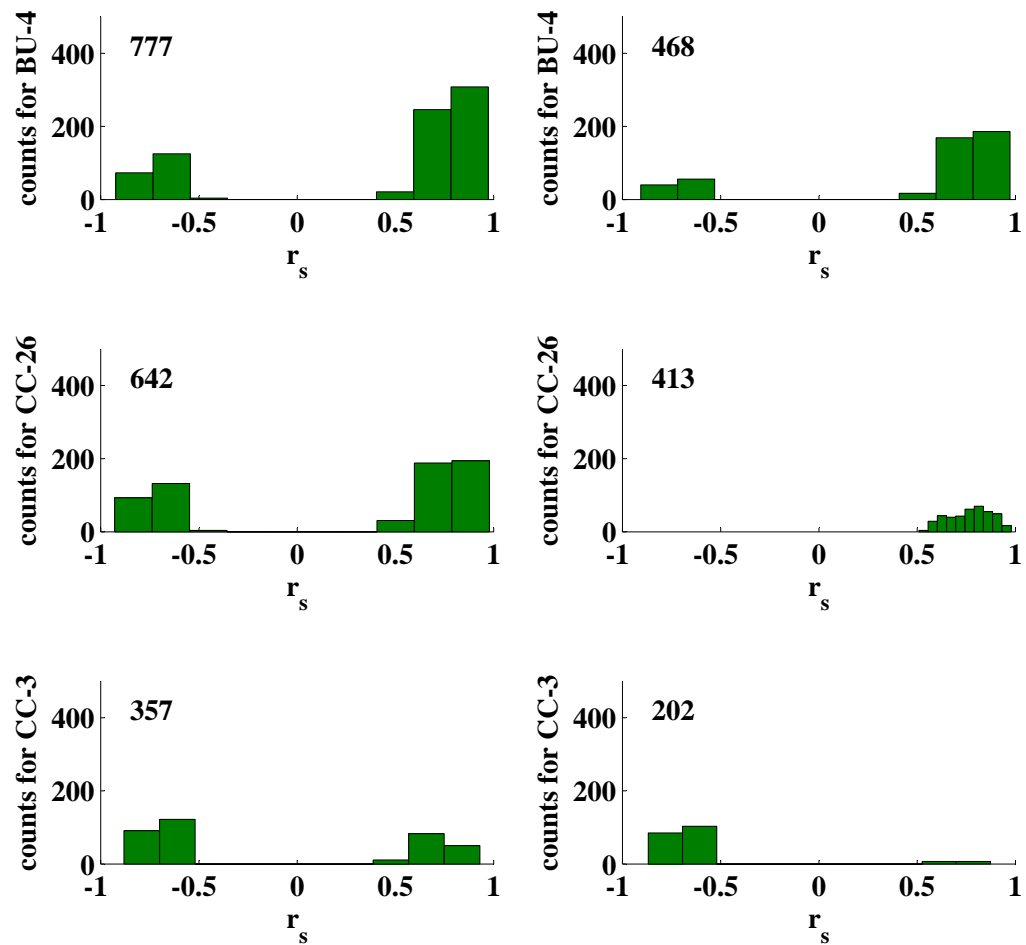


Fig. J.35: Illustrated is the distribution of speleothem r_s for the indicated runs of the 4000 years short-term PCA on $\delta^{13}\text{C}$ time series before (left panels) and after (right panels) the application of the Fork-tool.

run #9 - 4.3-4.0 ka BP - Part II

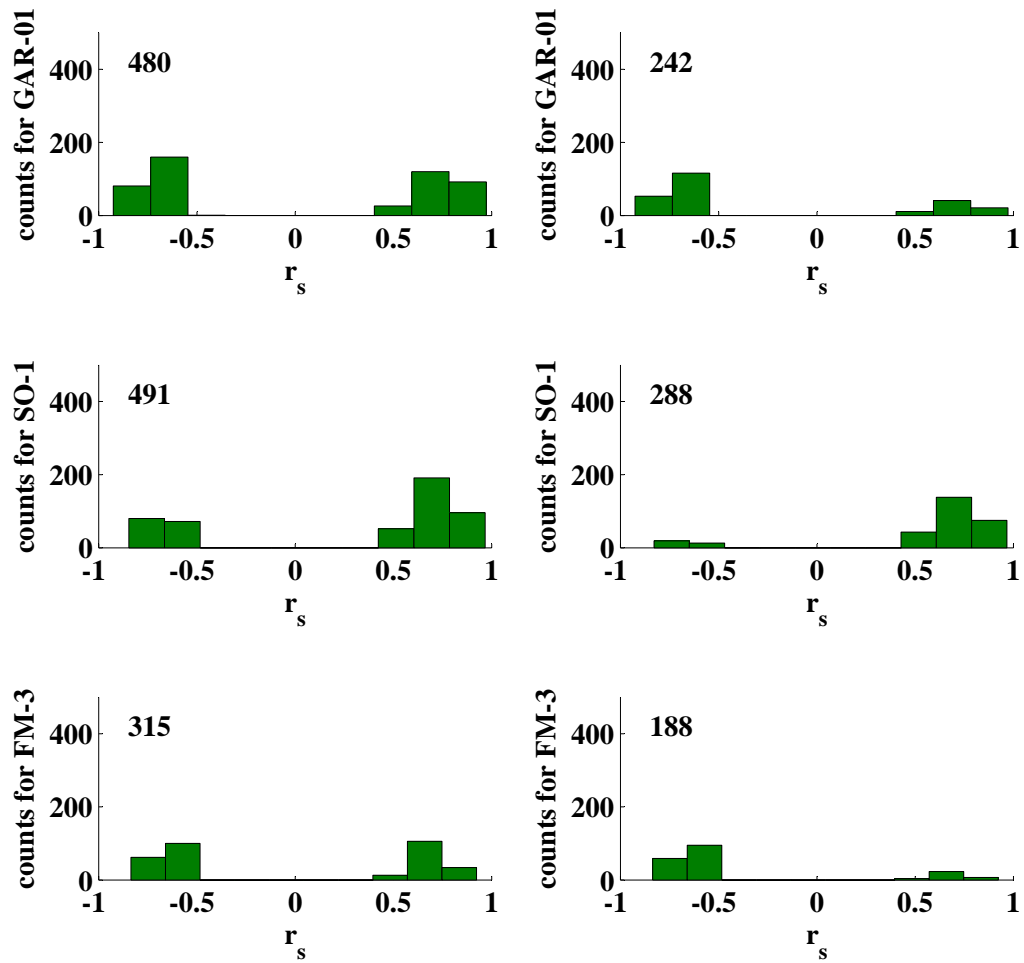


Fig. J.36: Illustrated is the distribution of speleothem r_s for the indicated runs of the 4000 years short-term PCA on $\delta^{13}C$ time series before (left panels) and after (right panels) the application of the Fork-tool.

K

**Eigenvalues of the 10,000 years runs -
Long-term analysis**

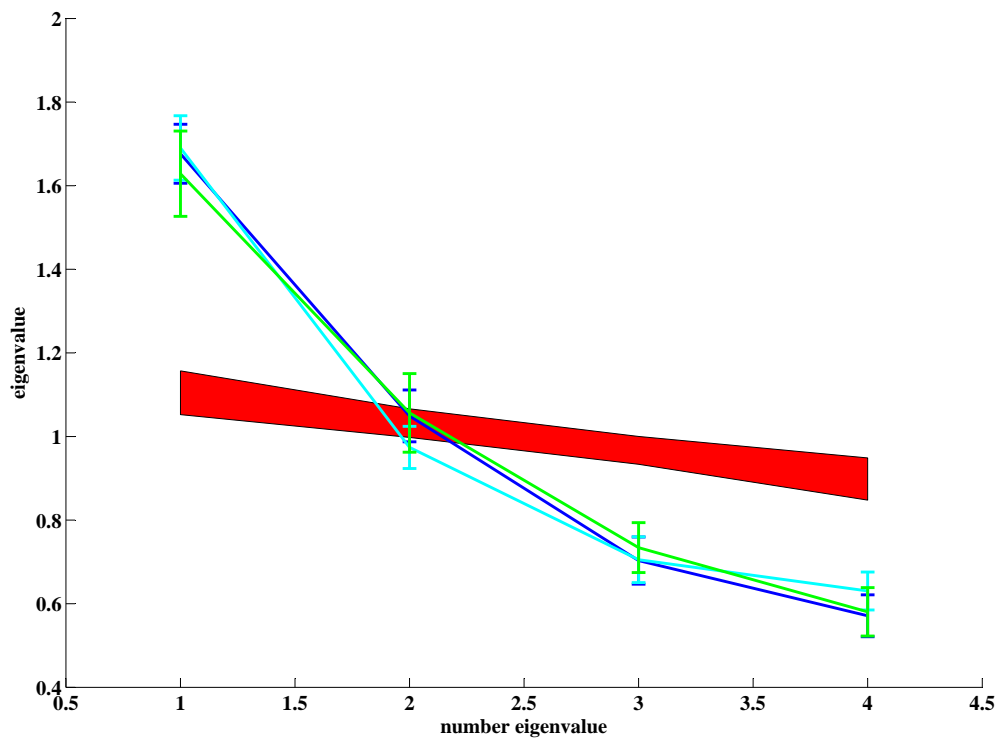


Fig. K.1: Illustrated are the mean eigenvalues of the 10,000 year long-term PCA for the compilation of $\delta^{18}\text{O}$ (blue) and $\delta^{13}\text{C}$ (green) time series. Furthermore, the 95 % and 5 % confidence level of the eigenvalues is illustrated, computed from 6 white noise time series (red shading area).

L

**Results of the application of the
Fork-tool onto the 10,000 year runs -
Long-term analysis**

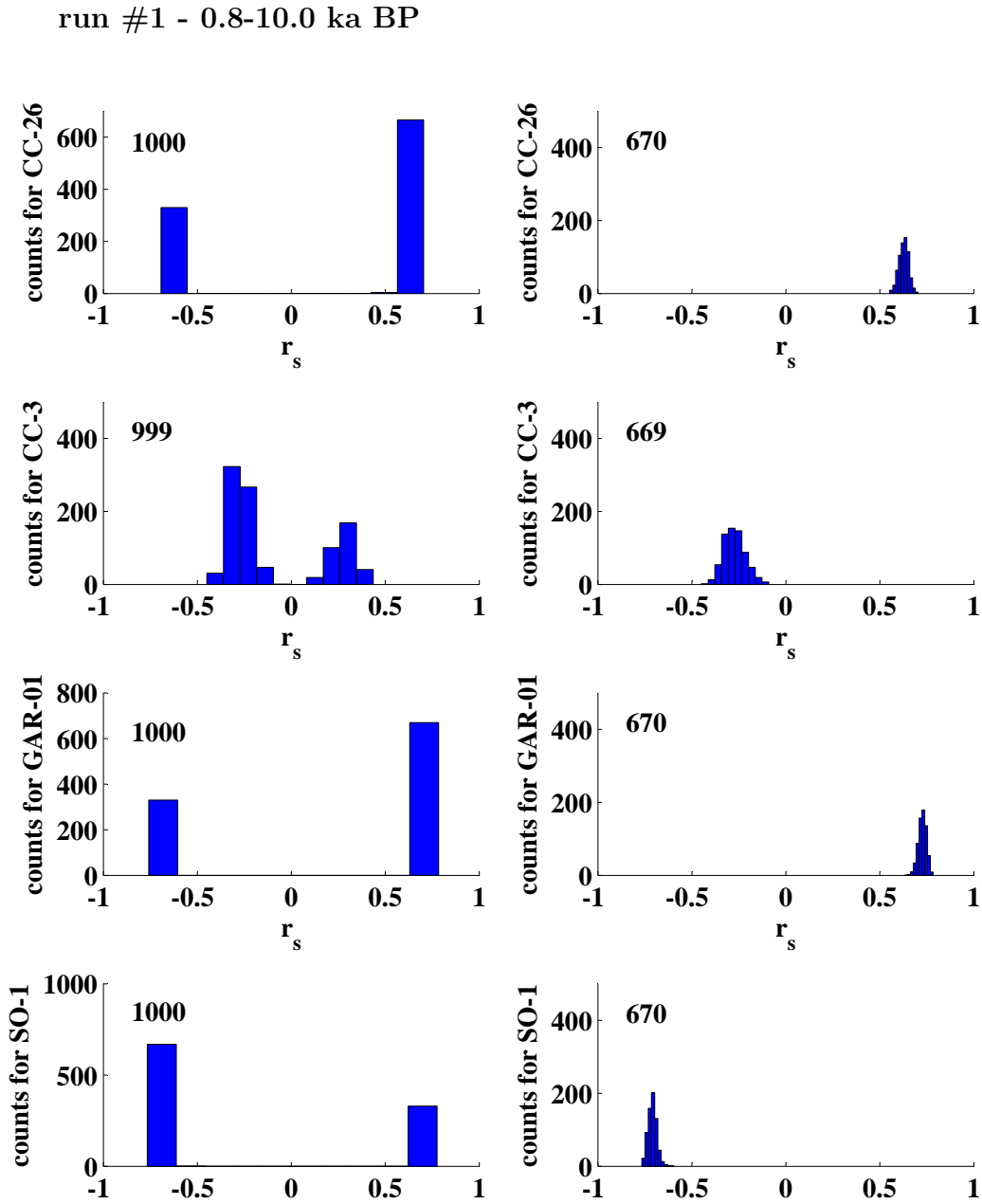


Fig. L.1: Illustrated is the distribution of speleothem r_s for the indicated runs of the 10,000 years long-term PCA on $\delta^{18}\text{O}$ time series before (left panels) and after (right panels) the application of the Fork-tool.

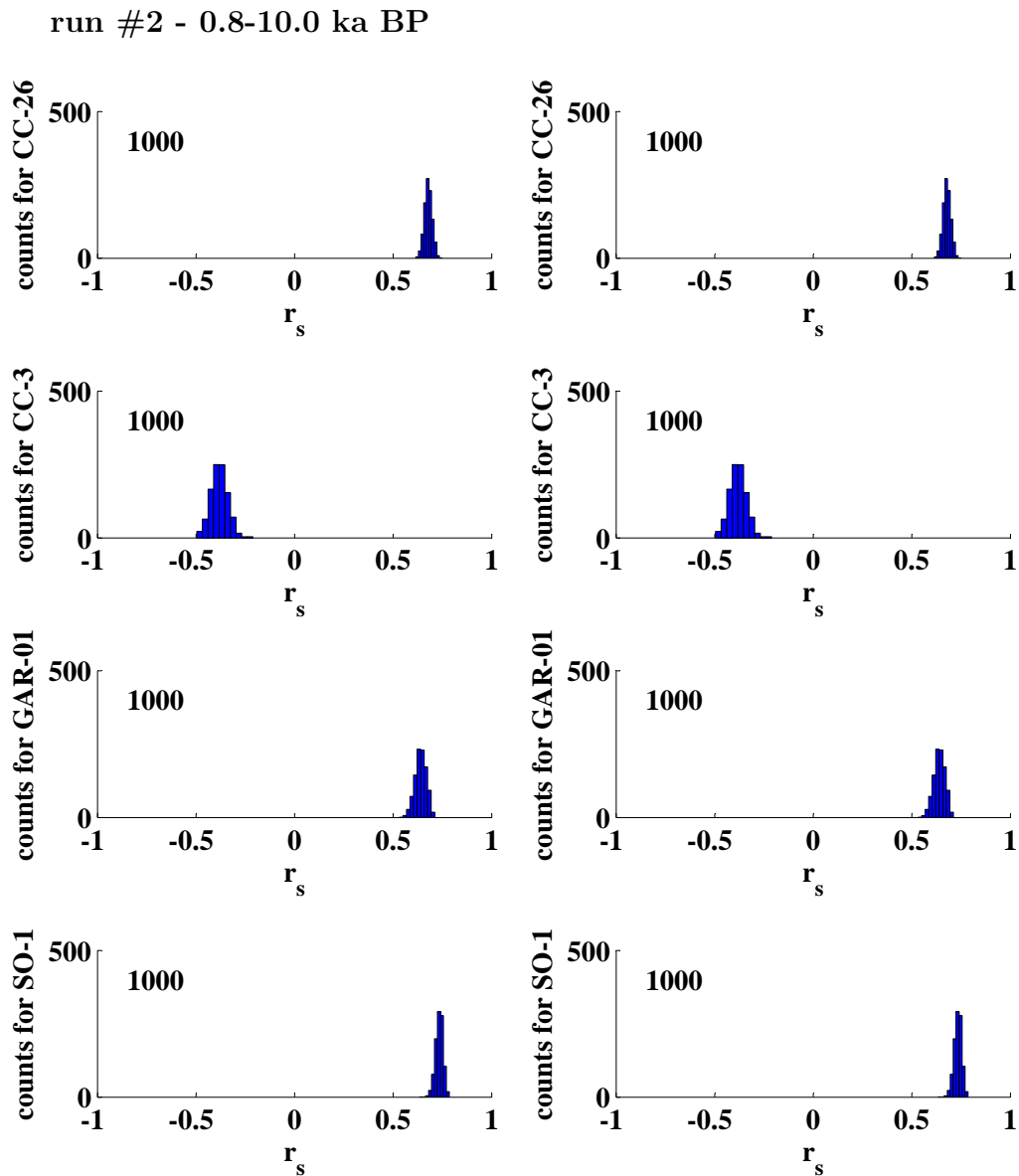


Fig. L.2: Illustrated is the distribution of speleothem r_s for the indicated runs of the 10,000 years long-term PCA on $\delta^{18}\text{O}$ time series before (left panels) and after (right panels) the application of the Fork-tool. Here, the $\delta^{18}\text{O}$ times series is corrected for the source effect of the Black Sea.

run #2 - 0.8-10.0 ka BP

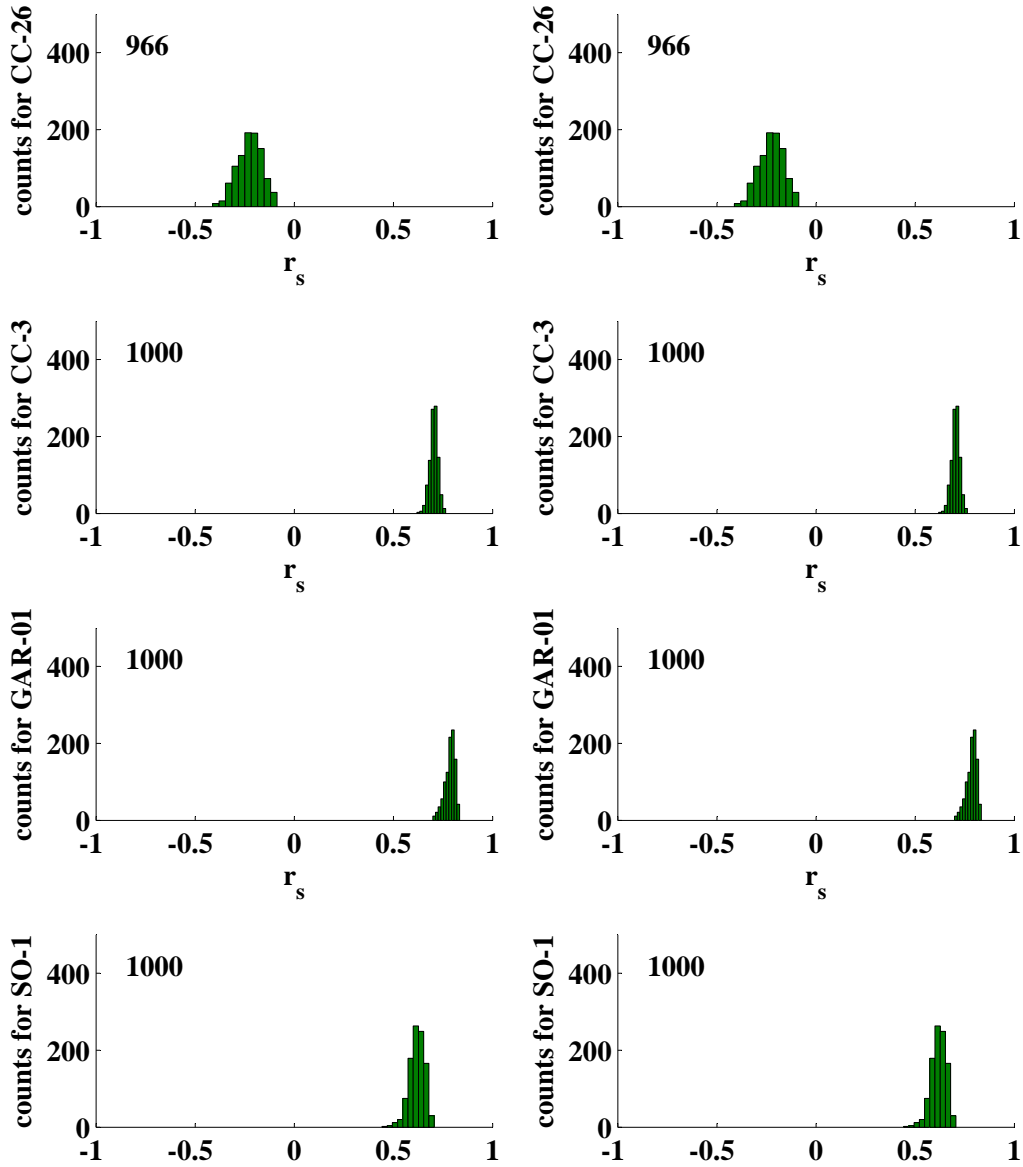


Fig. L.3: Illustrated is the distribution of speleothem r_s for the indicated runs of the 10,000 years long-term PCA on $\delta^{13}\text{C}$ time series before (left panels) and after (right panels) the application of the Fork-tool.

M

**Dependence of the slope of the
speleothem and precipitation $\delta^{18}\text{O}$
gradient on the wNAO index**

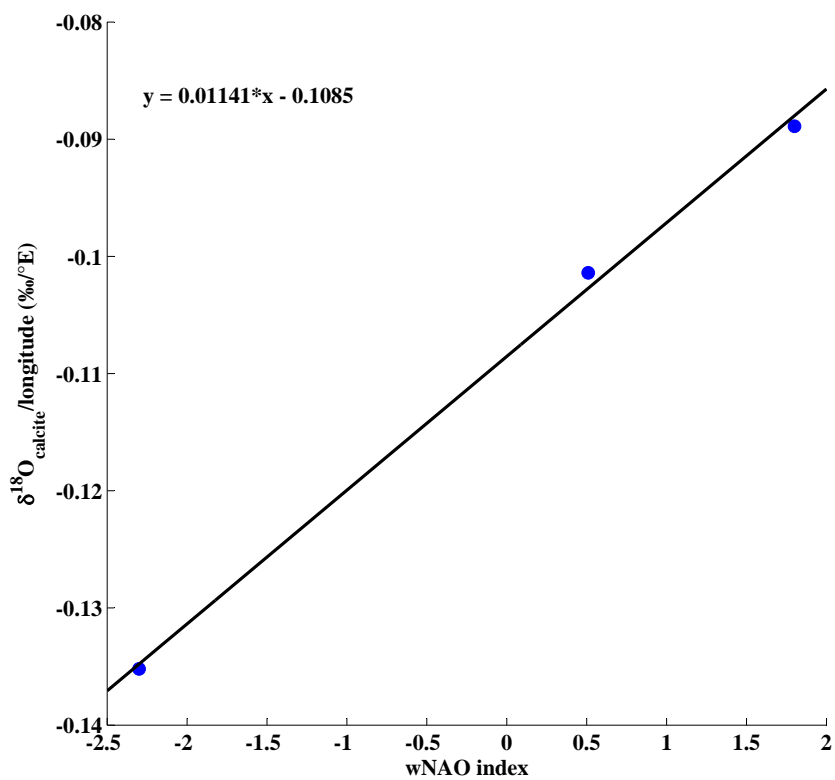


Fig. M.1: Slope of the speleothem $\delta^{18}\text{O}$ gradient against the NAO index (blue circles). The calculated slopes base on the two wNAO scenarios and the reference scenario (Tab. 17.1). The line results from a linear regression described in the equation in the top left corner (see Chapter 17.1 for detail).

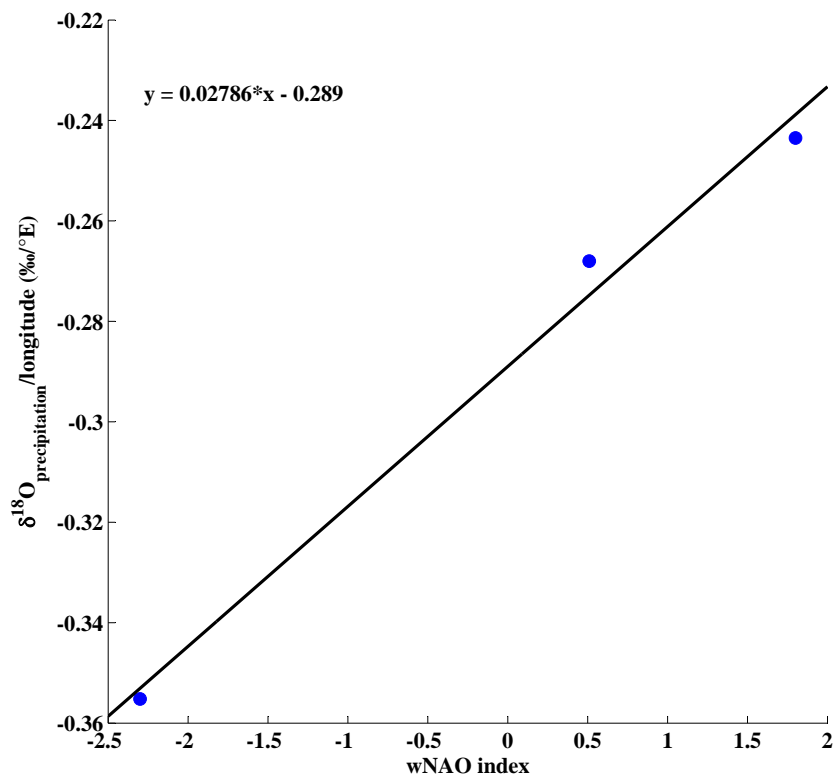


Fig. M.2: Slope of the precipitation $\delta^{18}\text{O}$ gradient against the NAO index (blue circles). The calculated slopes base on the two wNAO scenarios and the reference scenario (Tab. 17.1). The line results from a linear regression described in the equation in the top left corner (see Chapter 17.1 for detail).

N

Correction of the speleothem $\delta^{18}\text{O}$
values at the 10 °W intercept

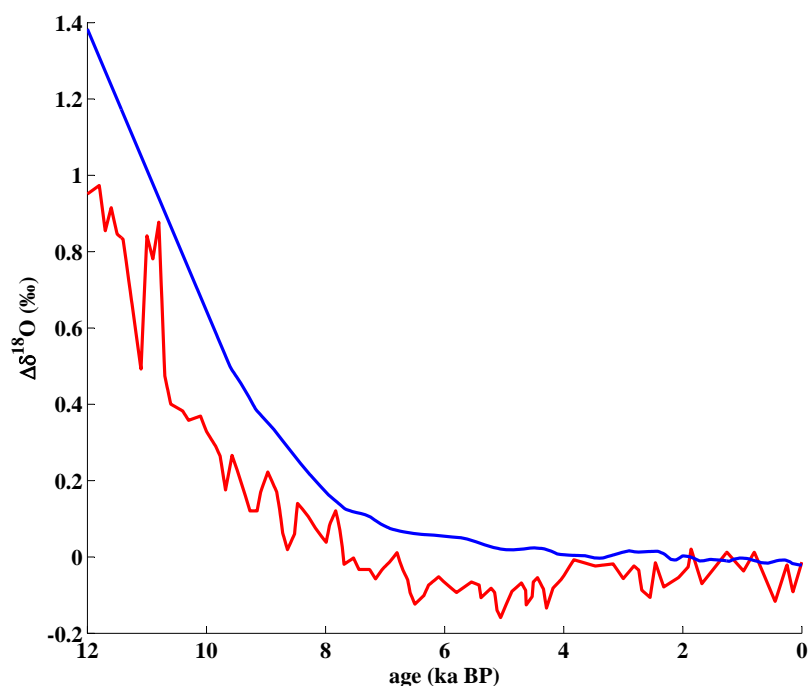


Fig. N.1: The figure is illustrating the effect of the sea level change during the Holocene on the $\delta^{18}\text{O}$ value of the ocean surface water (blue line). The curve is calculated from the sea level curve of [Wanner et al. \(2008\)](#) using scaling factor of 0.011 ‰/m ([Fairbanks, 1989](#)). The red line is picturing the change in the speleothem $\delta^{18}\text{O}$ value due to Holocene temperature for west Central Europe. The red curve is calculated from the temperature reconstruction of [Davis et al. \(2003\)](#) using the isotope fractionation factor between calcite and water of [Kim and O’Neil \(1997\)](#).

O

**Oxygen isotopic composition of
evaporative moisture from the ocean**

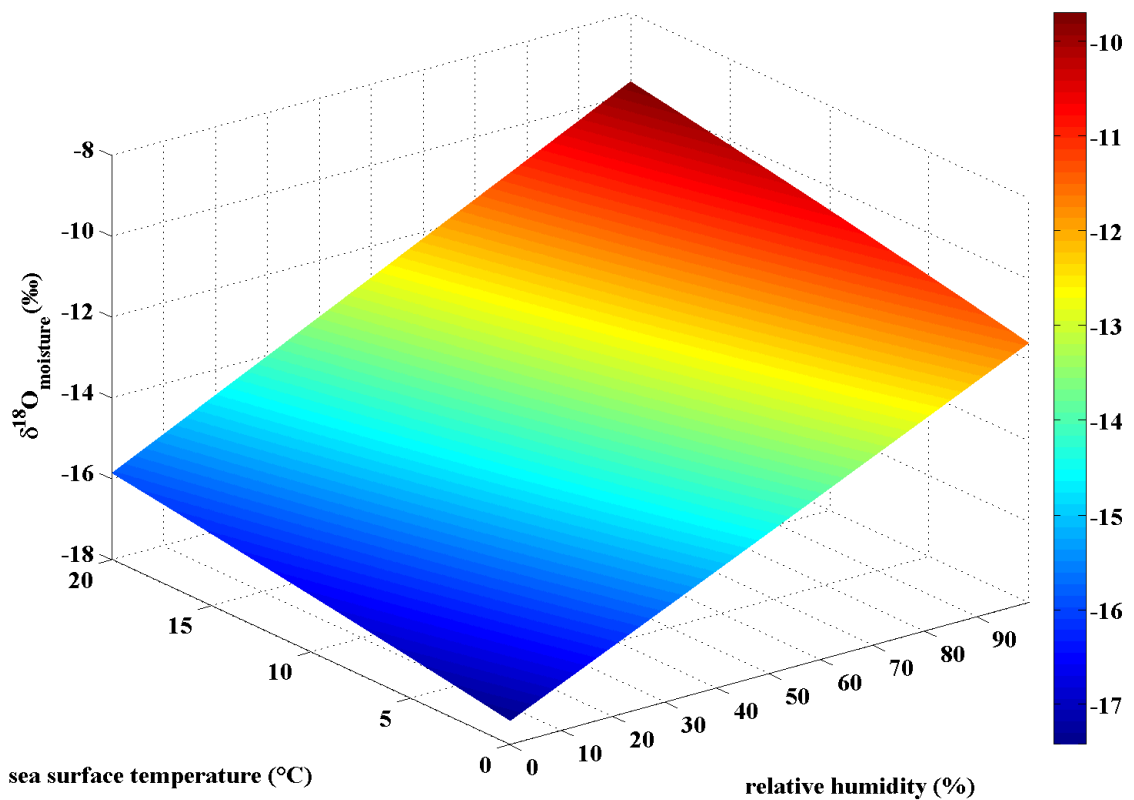


Fig. O.1: The figure is illustrating the dependence of the $\delta^{18}\text{O}$ value of evaporative moisture from the ocean in dependence the sea surface temperature (°C) and the relative humidity above the sea surface (%). The values are calculated in accordance with the equations of Sec. 11.1.3 and a wind velocity of 4 m/s (smooth regime).

P

Comparison of computed 1st PC time series with the original speleothem $\delta^{18}\text{O}$ and $\delta^{13}\text{C}$ time series for the last 8000 years

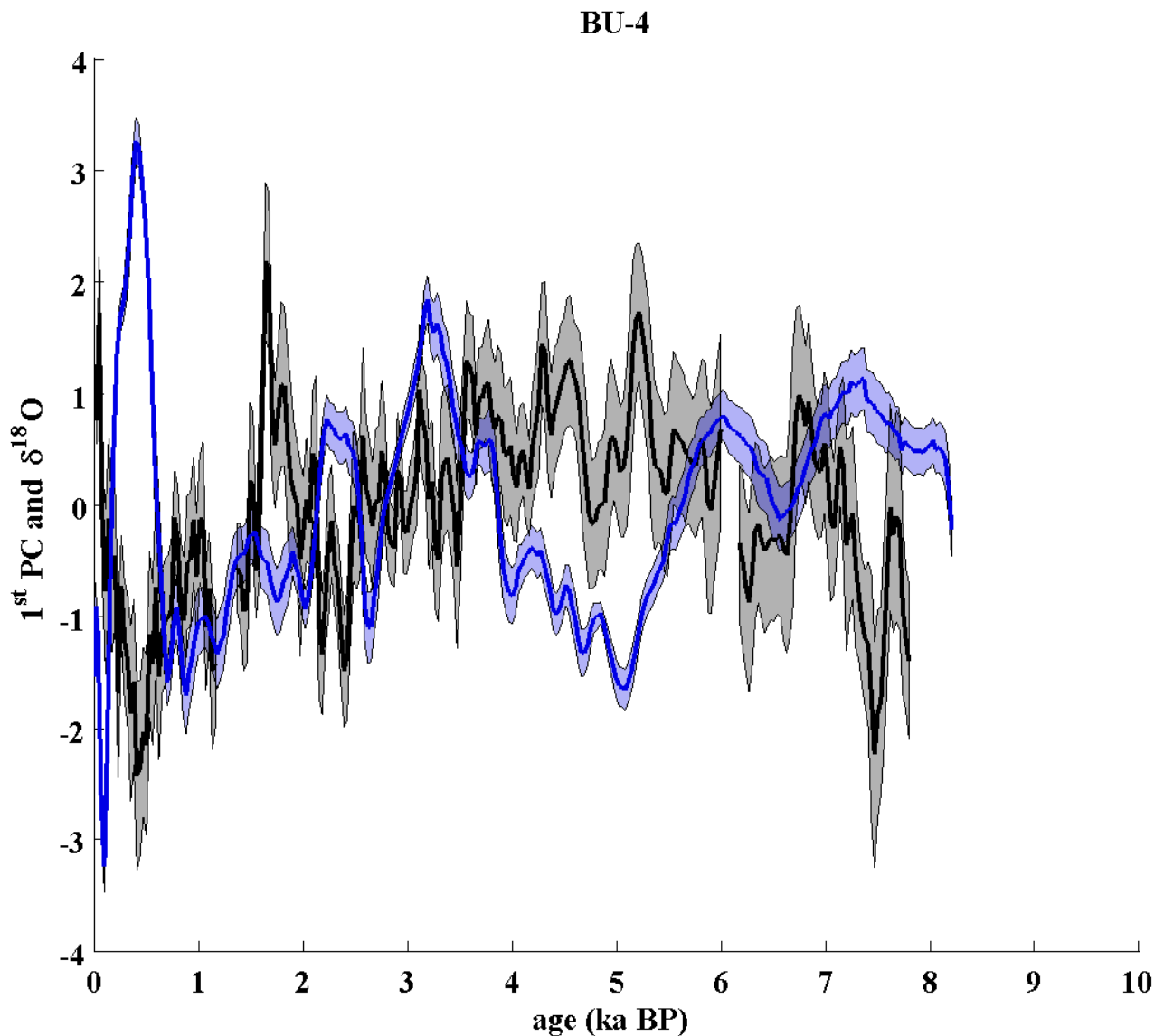


Fig. P.1: The figure is illustrating the computed 1st PC time series for the 8 ka long-term PCA (black line) including its 1-sigma confidence interval (grey shading area). Moreover, the figure pictures the standardised $\delta^{18}\text{O}$ time series of stalagmite BU-4 (blue line) with its 1-sigma confidence interval (blue shading area). The 1-sigma confidence interval is computed by using PCA.

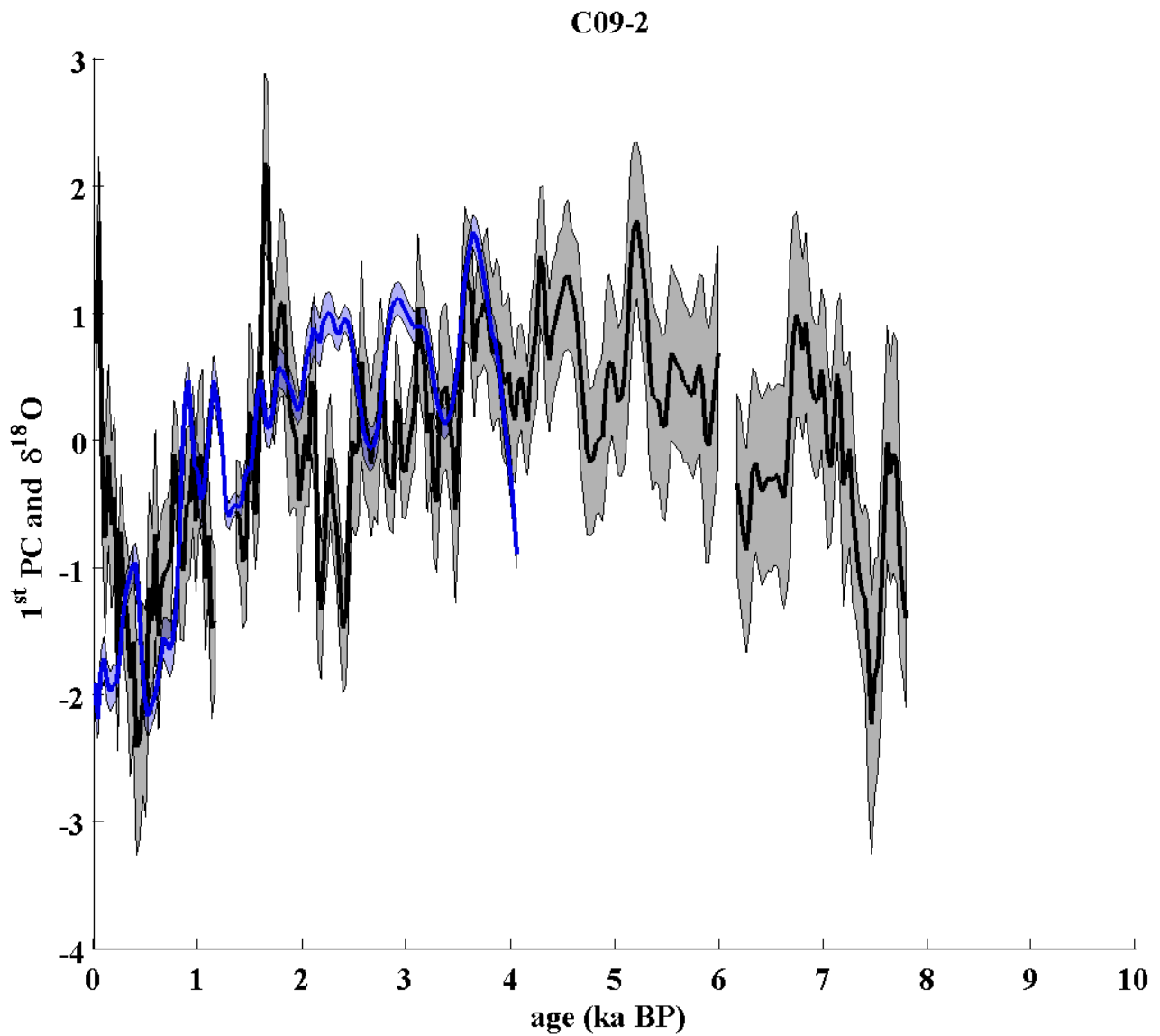


Fig. P.2: The figure is illustrating the computed 1st PC time series for the 8 ka long-term PCA (black line) including its 1-sigma confidence interval (grey shading area). Moreover, the figure pictures the standardised $\delta^{18}\text{O}$ time series of stalagmite C09-2 (blue line) with its 1-sigma confidence interval (blue shading area). The 1-sigma confidence interval is computed by using PCA.

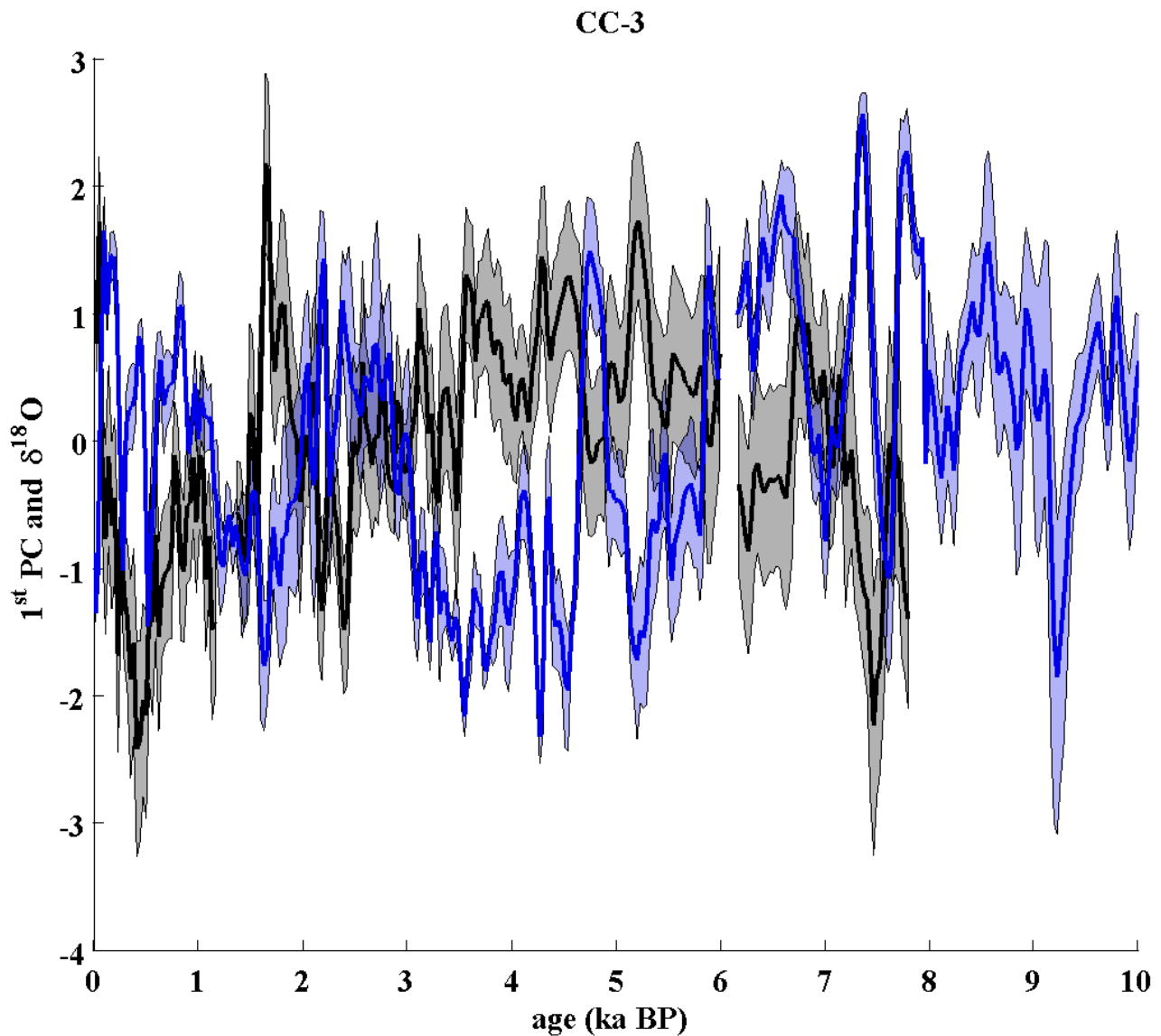


Fig. P.3: The figure is illustrating the computed 1st PC time series for the 8 ka long-term PCA (black line) including its 1-sigma confidence interval (grey shading area). Moreover, the figure pictures the standardised $\delta^{18}\text{O}$ time series of stalagmite CC-3 (blue line) with its 1-sigma confidence interval (blue shading area). The 1-sigma confidence interval is computed by using PCA.

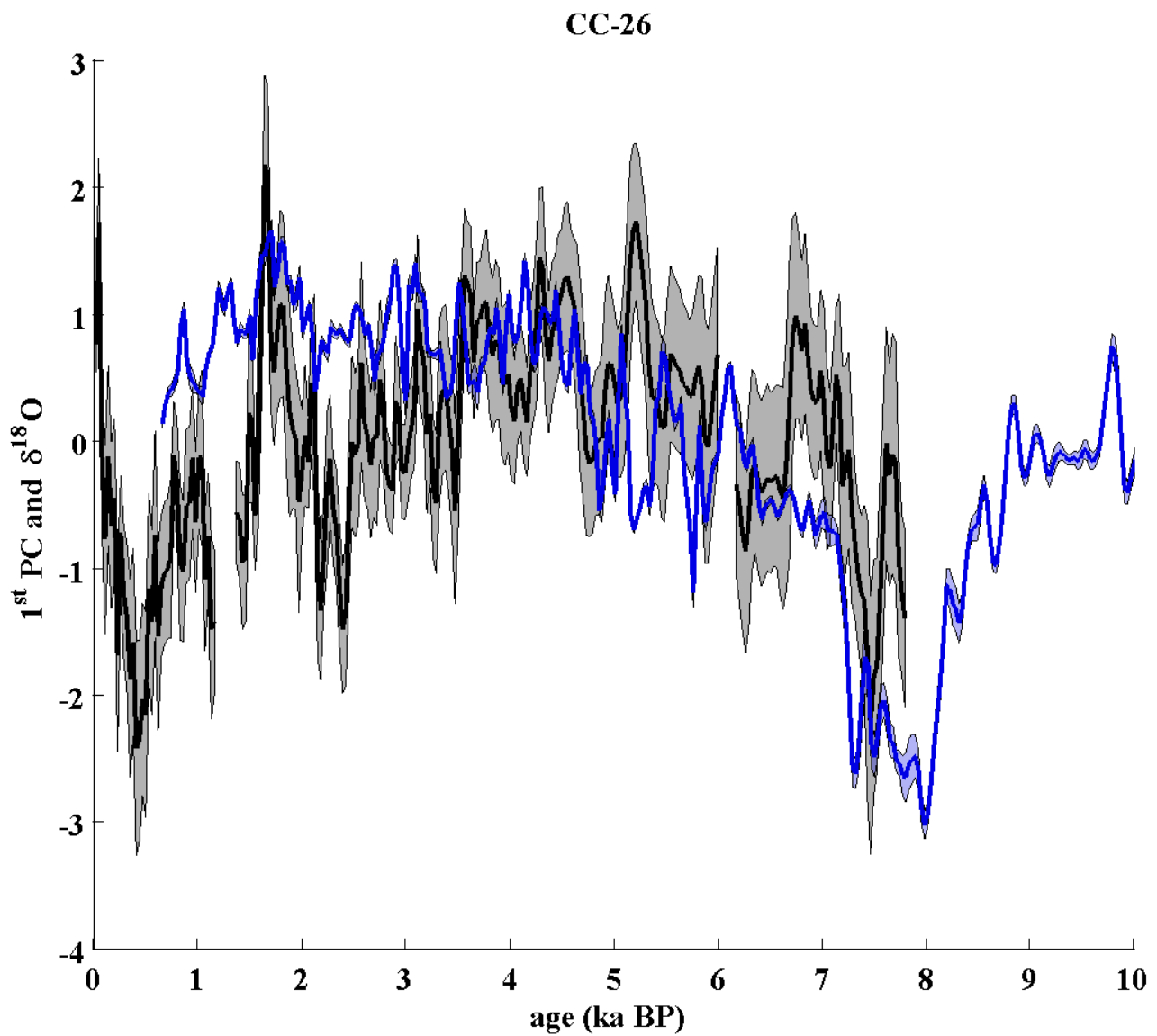


Fig. P.4: The figure is illustrating the computed 1st PC time series for the 8 ka long-term PCA (black line) including its 1-sigma confidence interval (grey shading area). Moreover, the figure pictures the standardised δ¹⁸O time series of stalagmite CC-26 (blue line) with its 1-sigma confidence interval (blue shading area). The 1-sigma confidence interval is computed by using PCA.

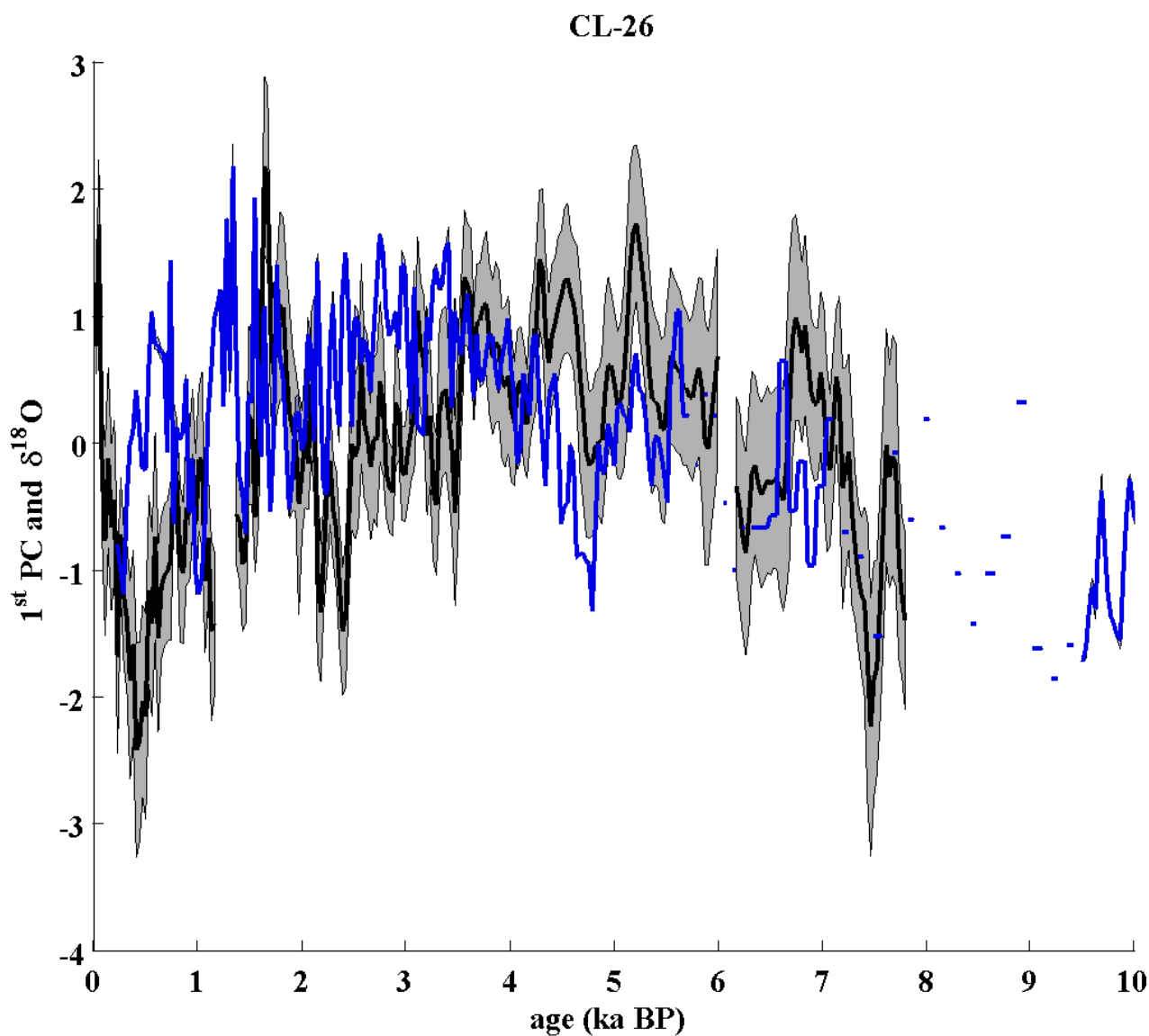


Fig. P.5: The figure is illustrating the computed 1st PC time series for the 8 ka long-term PCA (black line) including its 1-sigma confidence interval (grey shading area). Moreover, the figure pictures the standardised $\delta^{18}\text{O}$ time series of stalagmite CL-26 (blue line) with its 1-sigma confidence interval (blue shading area). The 1-sigma confidence interval is computed by using PCA.

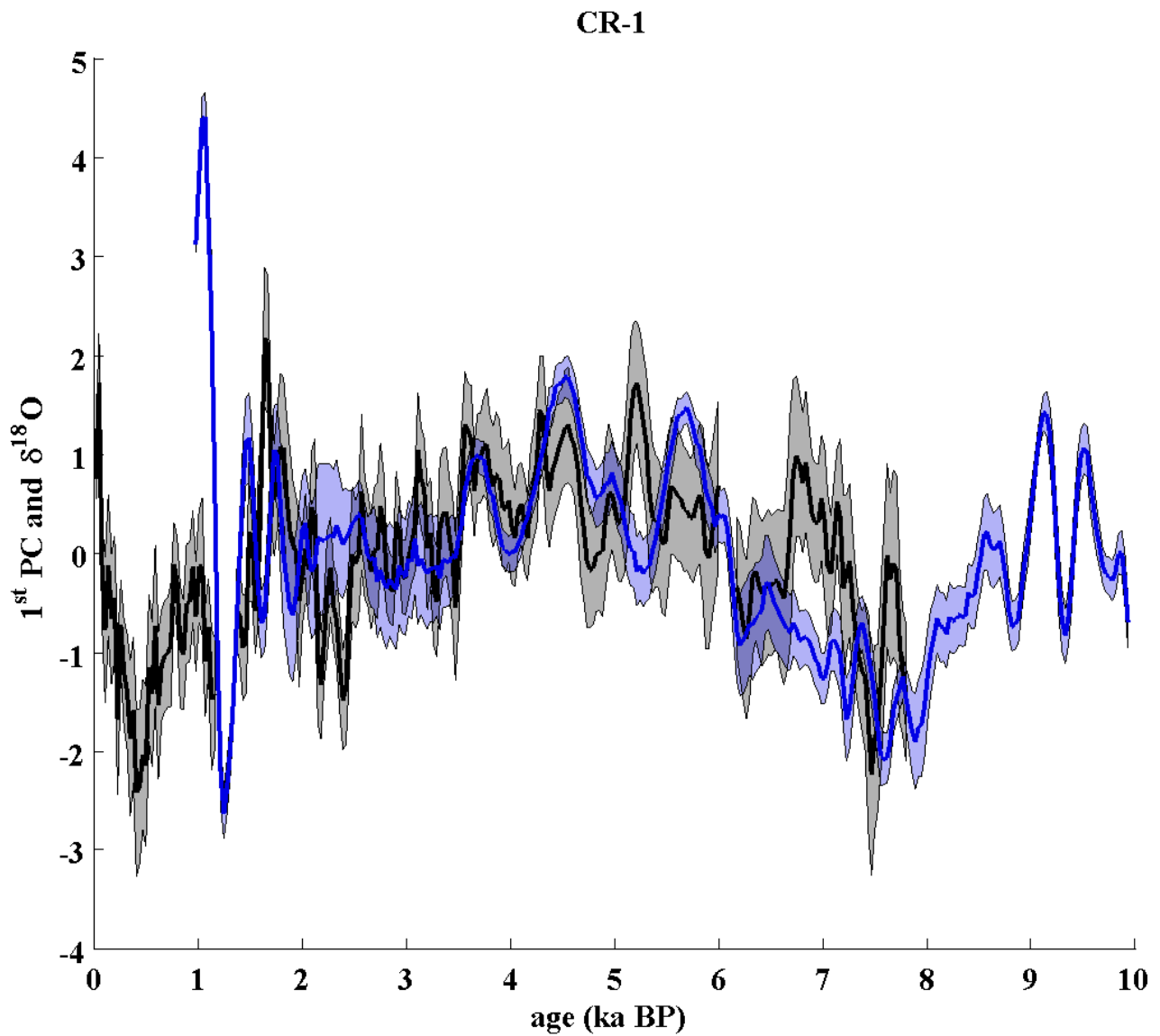


Fig. P.6: The figure is illustrating the computed 1st PC time series for the 8 ka long-term PCA (black line) including its 1-sigma confidence interval (grey shading area). Moreover, the figure pictures the standardised $\delta^{18}\text{O}$ time series of stalagmite CR-1 (blue line) with its 1-sigma confidence interval (blue shading area). The 1-sigma confidence interval is computed by using PCA.

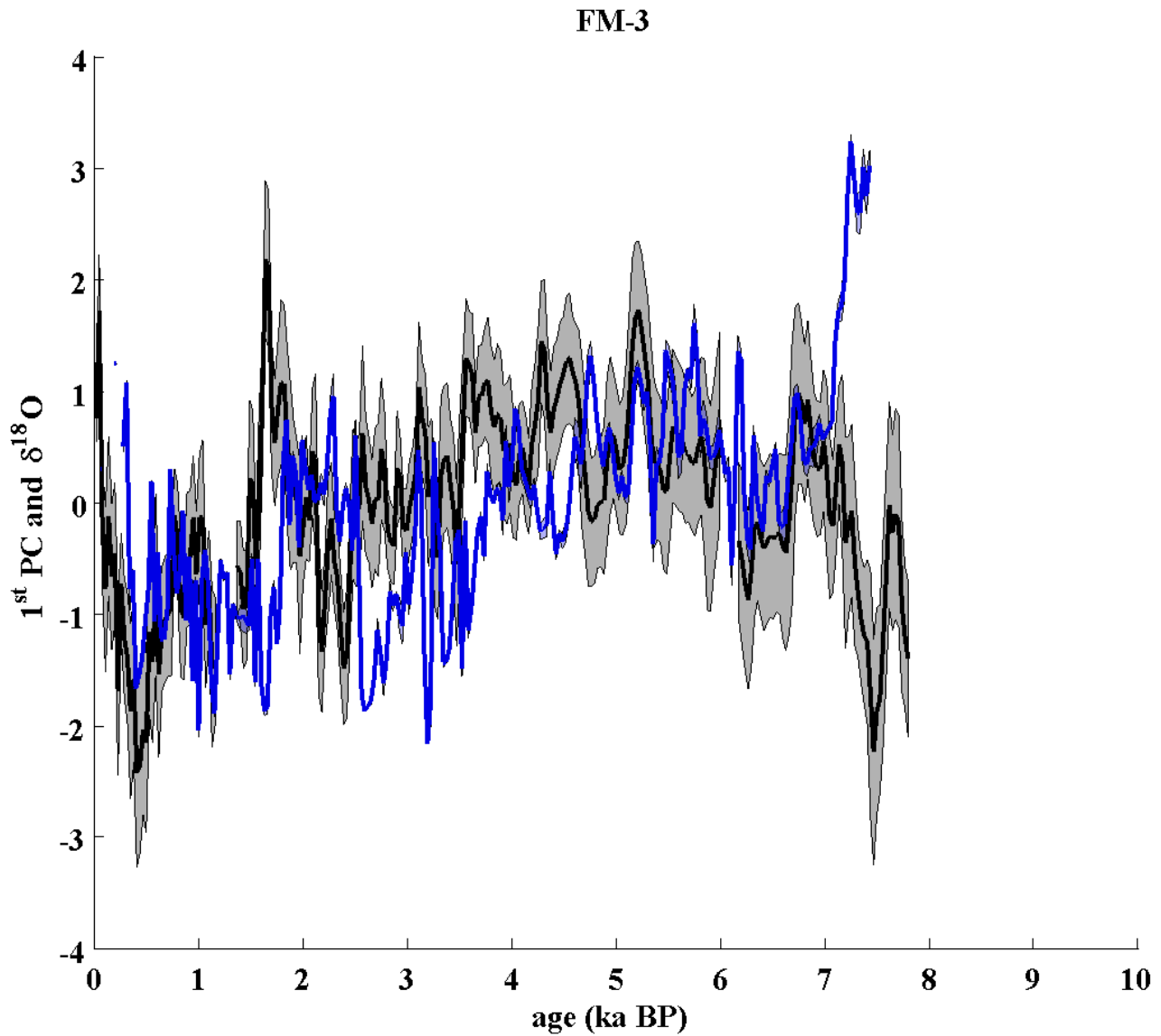


Fig. P.7: The figure is illustrating the computed 1st PC time series for the 8 ka long-term PCA (black line) including its 1-sigma confidence interval (grey shading area). Moreover, the figure pictures the standardised $\delta^{18}\text{O}$ time series of stalagmite FM-3 (blue line) with its 1-sigma confidence interval (blue shading area). The 1-sigma confidence interval is computed by using PCA.

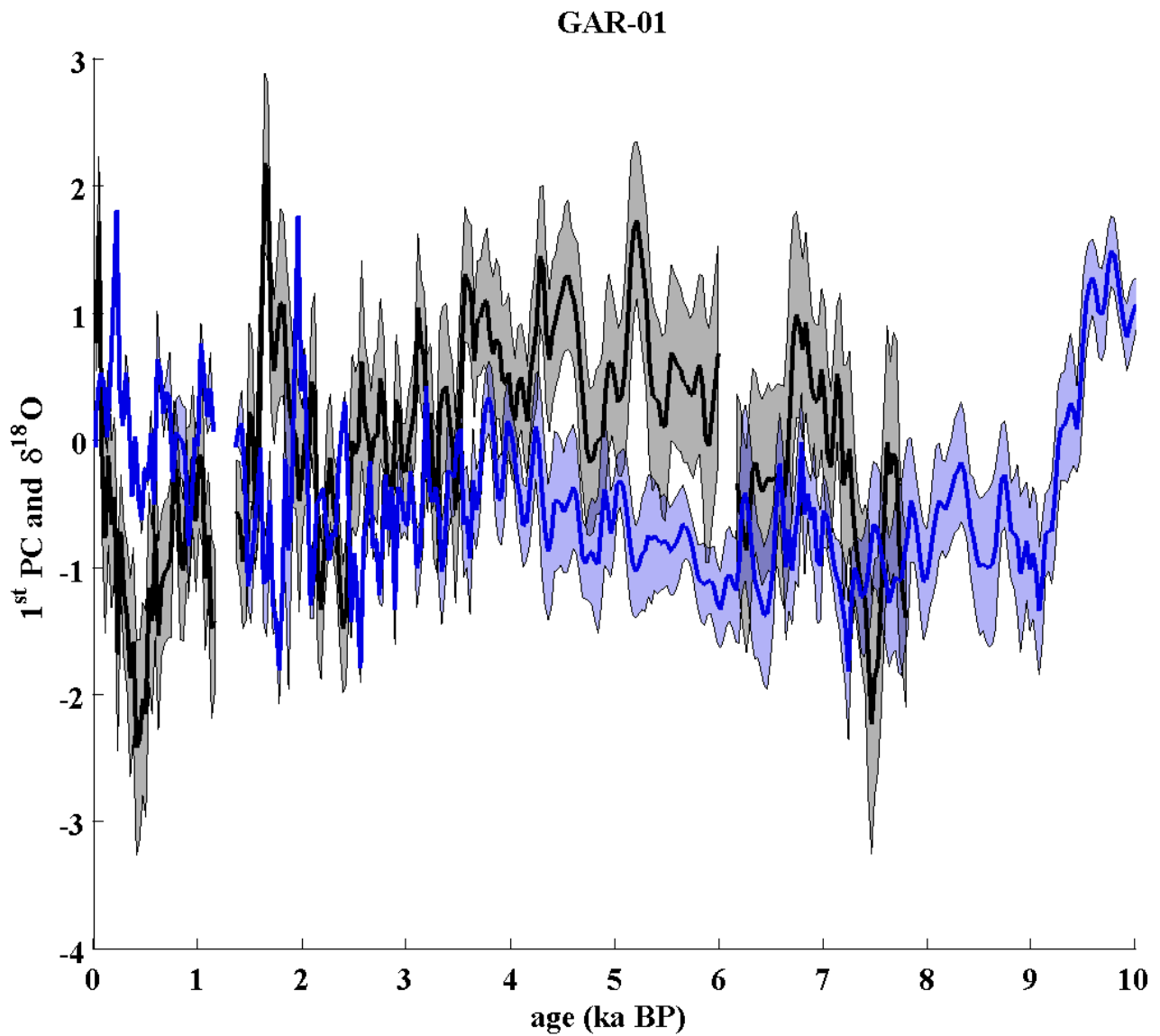


Fig. P.8: The figure is illustrating the computed 1st PC time series for the 8 ka long-term PCA (black line) including its 1-sigma confidence interval (grey shading area). Moreover, the figure pictures the standardised $\delta^{18}\text{O}$ time series of stalagmite GAR-01 (blue line) with its 1-sigma confidence interval (blue shading area). The 1-sigma confidence interval is computed by using PCA.

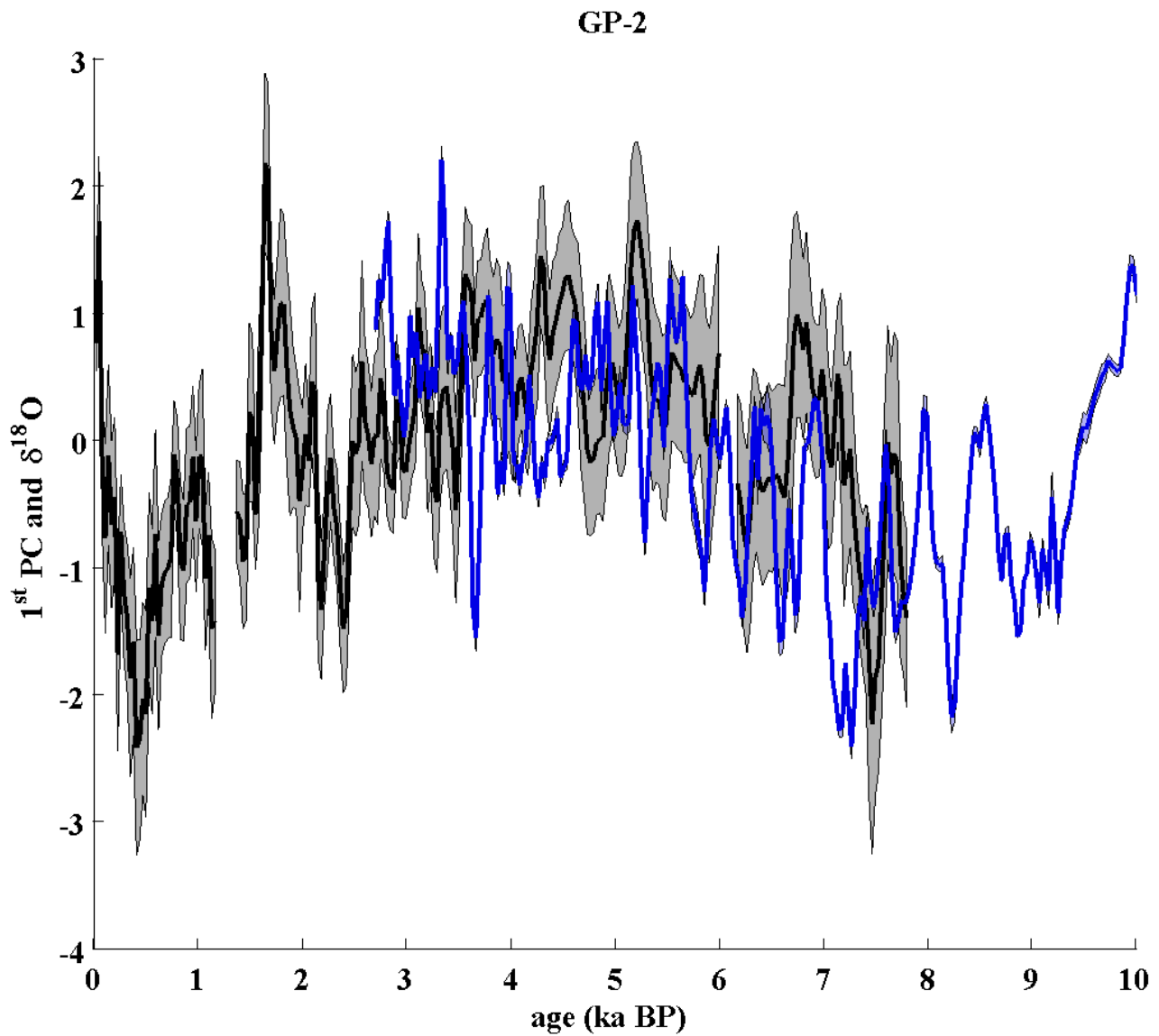


Fig. P.9: The figure is illustrating the computed 1st PC time series for the 8 ka long-term PCA (black line) including its 1-sigma confidence interval (grey shading area). Moreover, the figure pictures the standardised $\delta^{18}\text{O}$ time series of stalagmite GP-2 (blue line) with its 1-sigma confidence interval (blue shading area). The 1-sigma confidence interval is computed by using PCA.

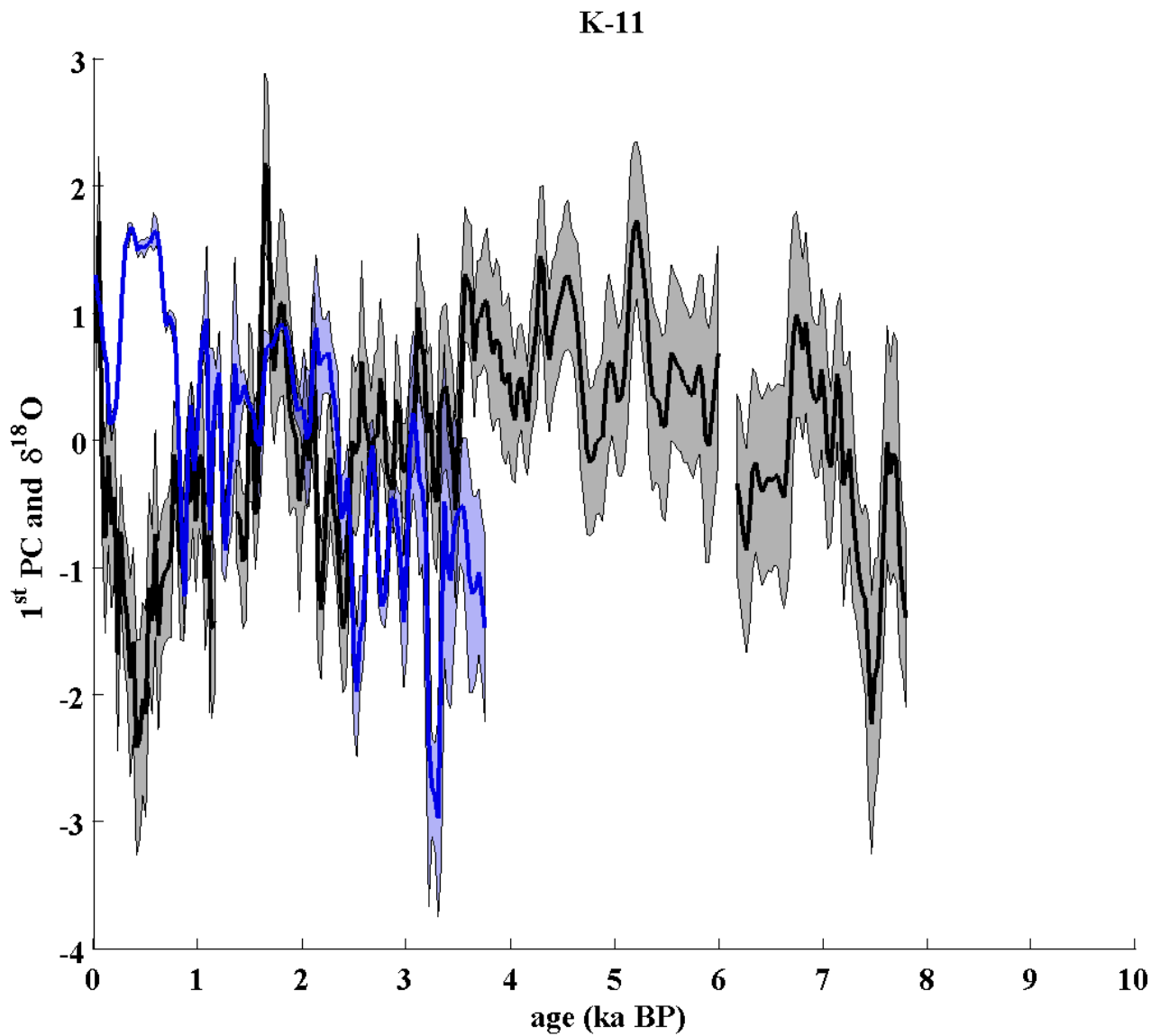


Fig. P.10: The figure is illustrating the computed 1st PC time series for the 8 ka long-term PCA (black line) including its 1-sigma confidence interval (grey shading area). Moreover, the figure pictures the standardised δ¹⁸O time series of stalagmite K-1 (blue line) with its 1-sigma confidence interval (blue shading area). The 1-sigma confidence interval is computed by using PCA.

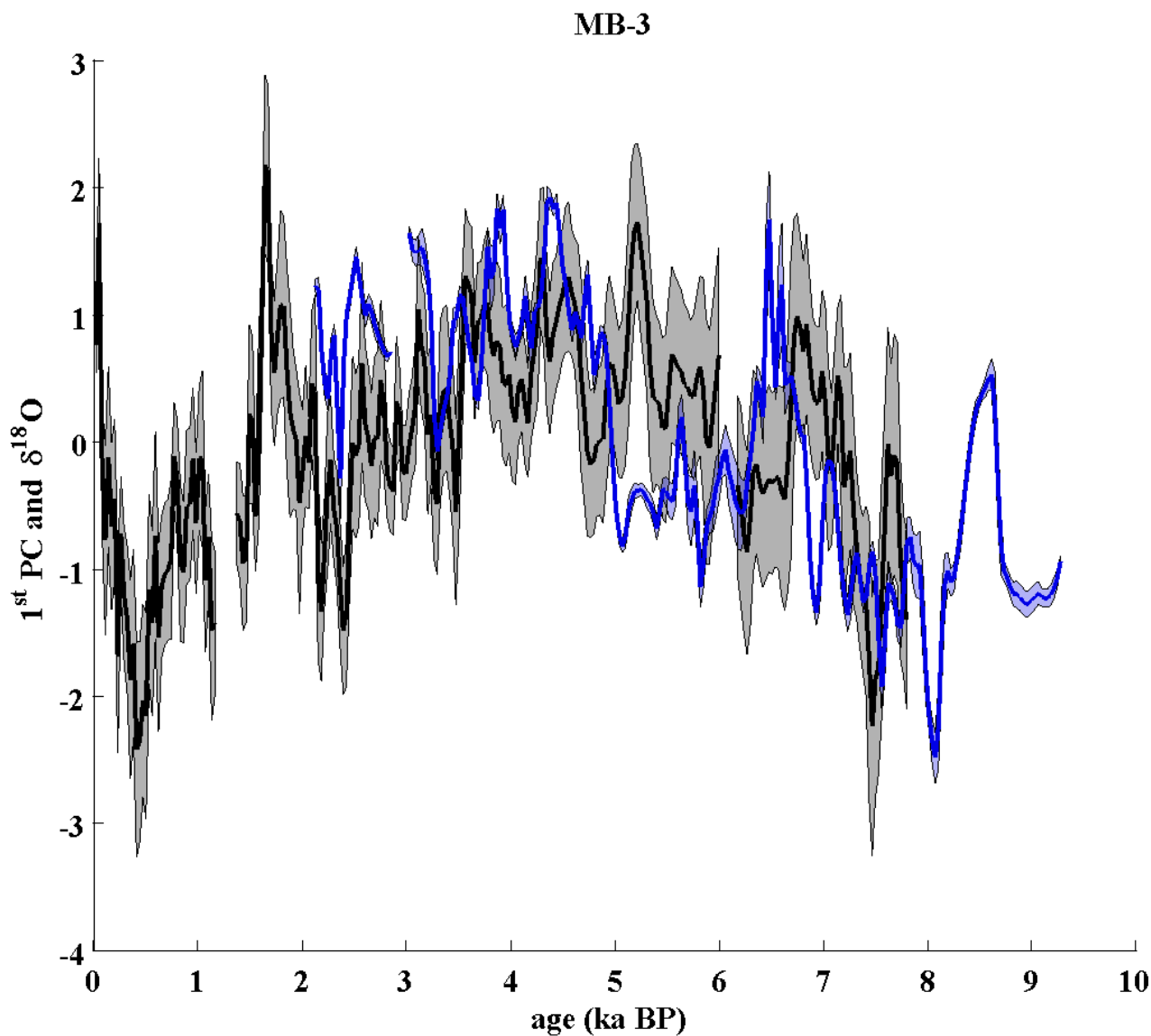


Fig. P.11: The figure is illustrating the computed 1st PC time series for the 8 ka long-term PCA (black line) including its 1-sigma confidence interval (grey shading area). Moreover, the figure pictures the standardised $\delta^{18}\text{O}$ time series of stalagmite MB-3 (blue line) with its 1-sigma confidence interval (blue shading area). The 1-sigma confidence interval is computed by using PCA.

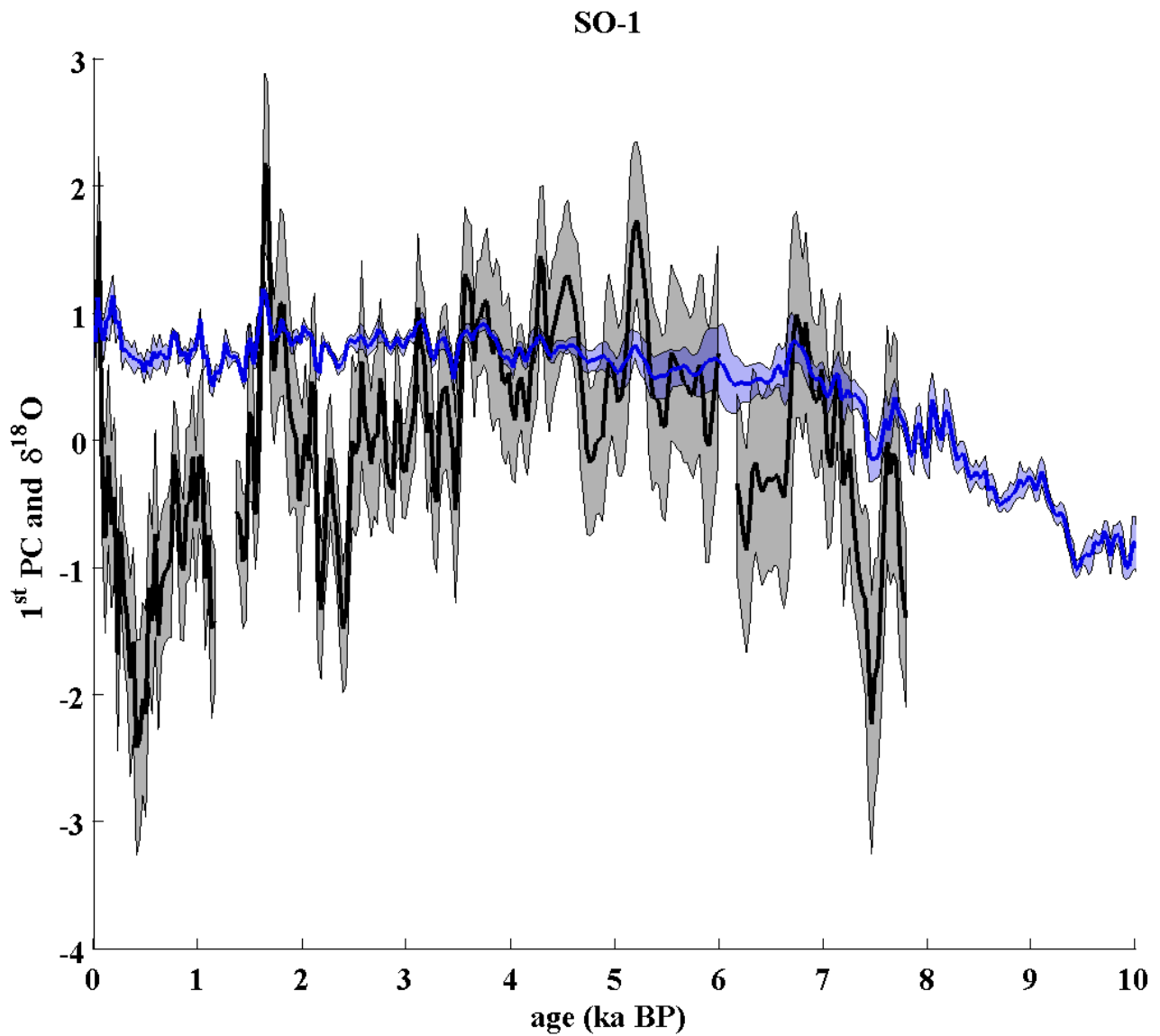


Fig. P.12: The figure is illustrating the computed 1st PC time series for the 8 ka long-term PCA (black line) including its 1-sigma confidence interval (grey shading area). Moreover, the figure pictures the standardised $\delta^{18}\text{O}$ time series of stalagmite SO-1 (blue line) with its 1-sigma confidence interval (blue shading area). The 1-sigma confidence interval is computed by using PCA.

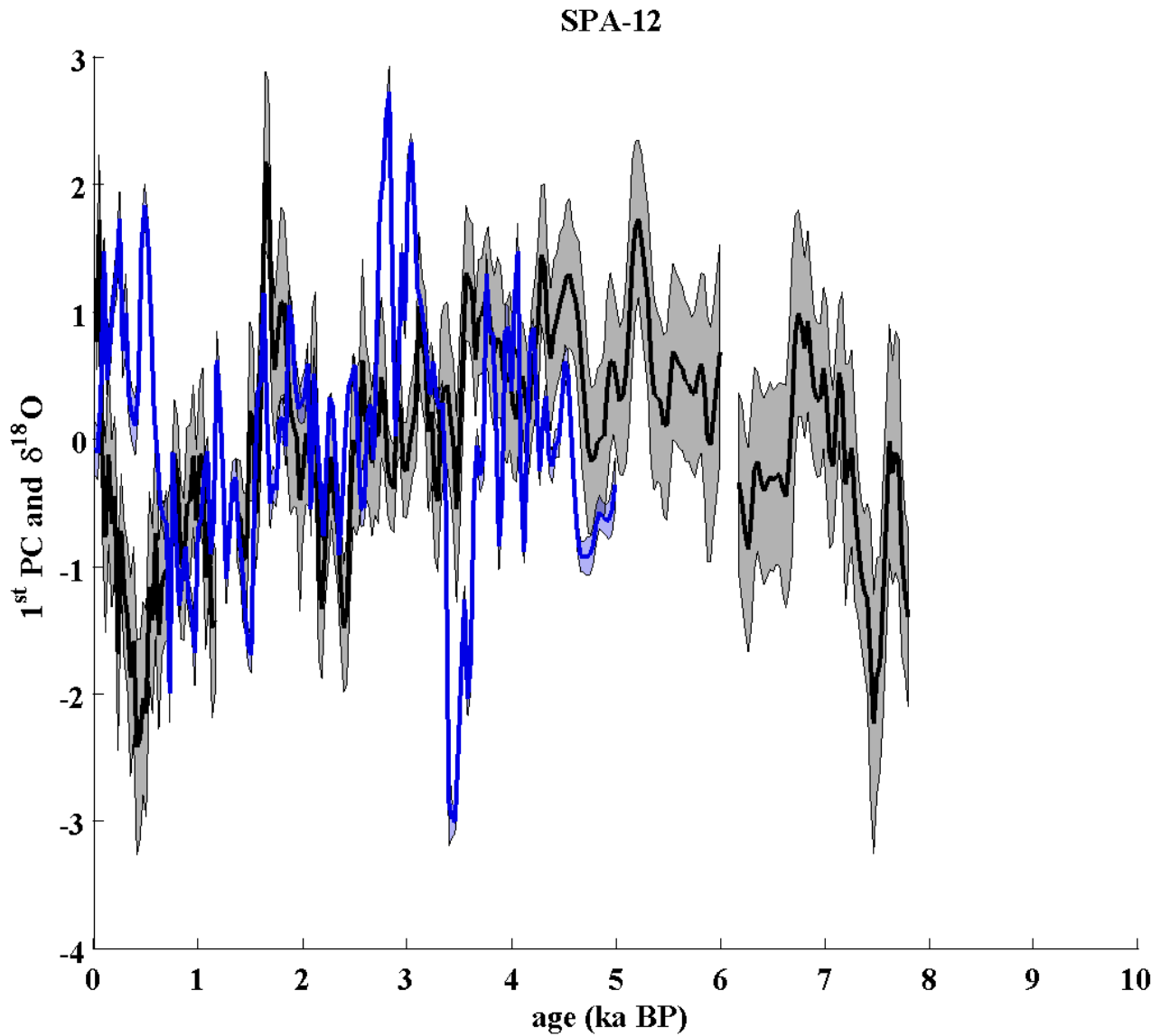


Fig. P.13: The figure is illustrating the computed 1st PC time series for the 8 ka long-term PCA (black line) including its 1-sigma confidence interval (grey shading area). Moreover, the figure pictures the standardised $\delta^{18}\text{O}$ time series of stalagmite SPA-12 (blue line) with its 1-sigma confidence interval (blue shading area). The 1-sigma confidence interval is computed by using PCA.

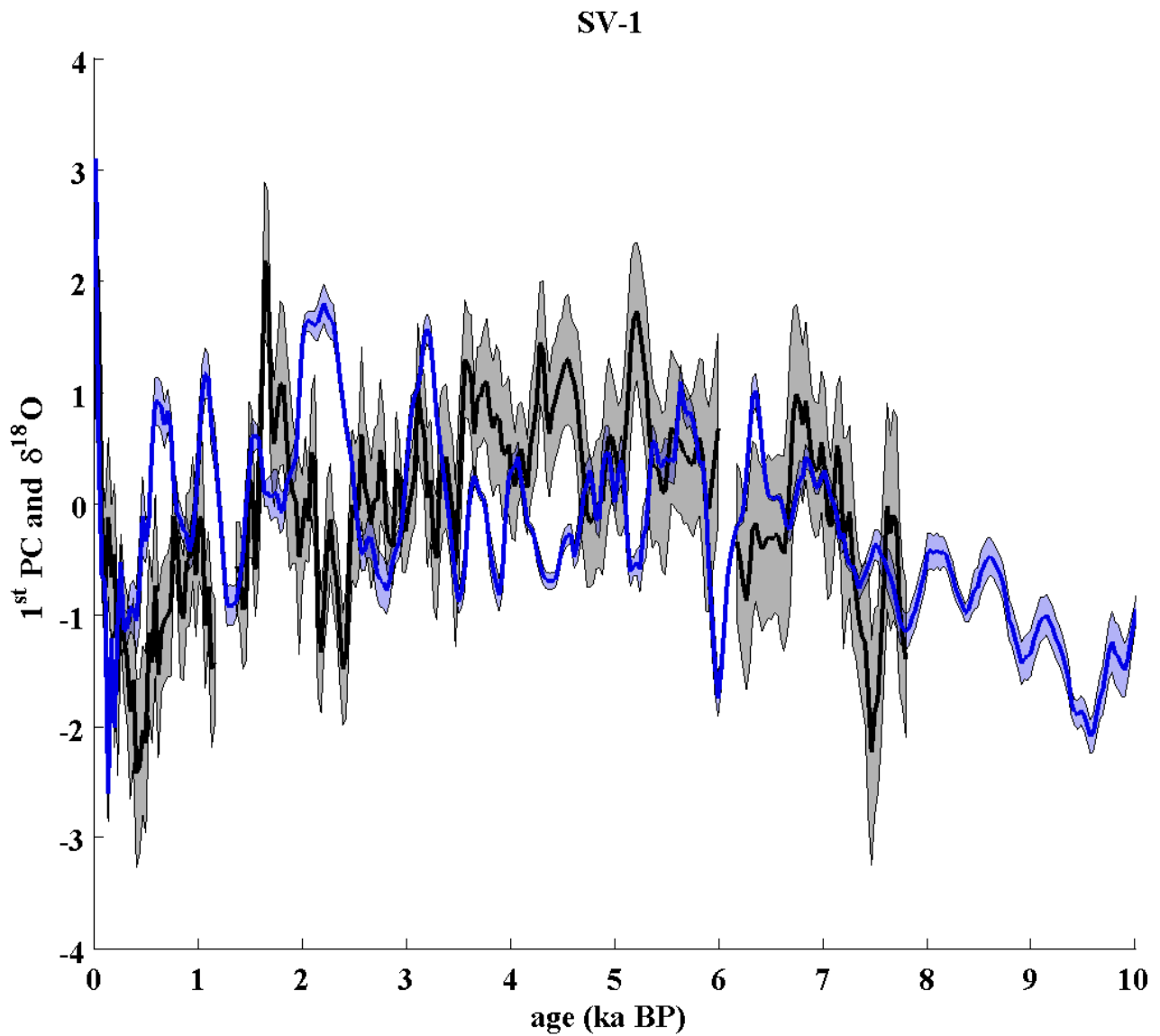


Fig. P.14: The figure is illustrating the computed 1st PC time series for the 8 ka long-term PCA (black line) including its 1-sigma confidence interval (grey shading area). Moreover, the figure pictures the standardised $\delta^{18}\text{O}$ time series of stalagmite SV-1 (blue line) with its 1-sigma confidence interval (blue shading area). The 1-sigma confidence interval is computed by using PCA.

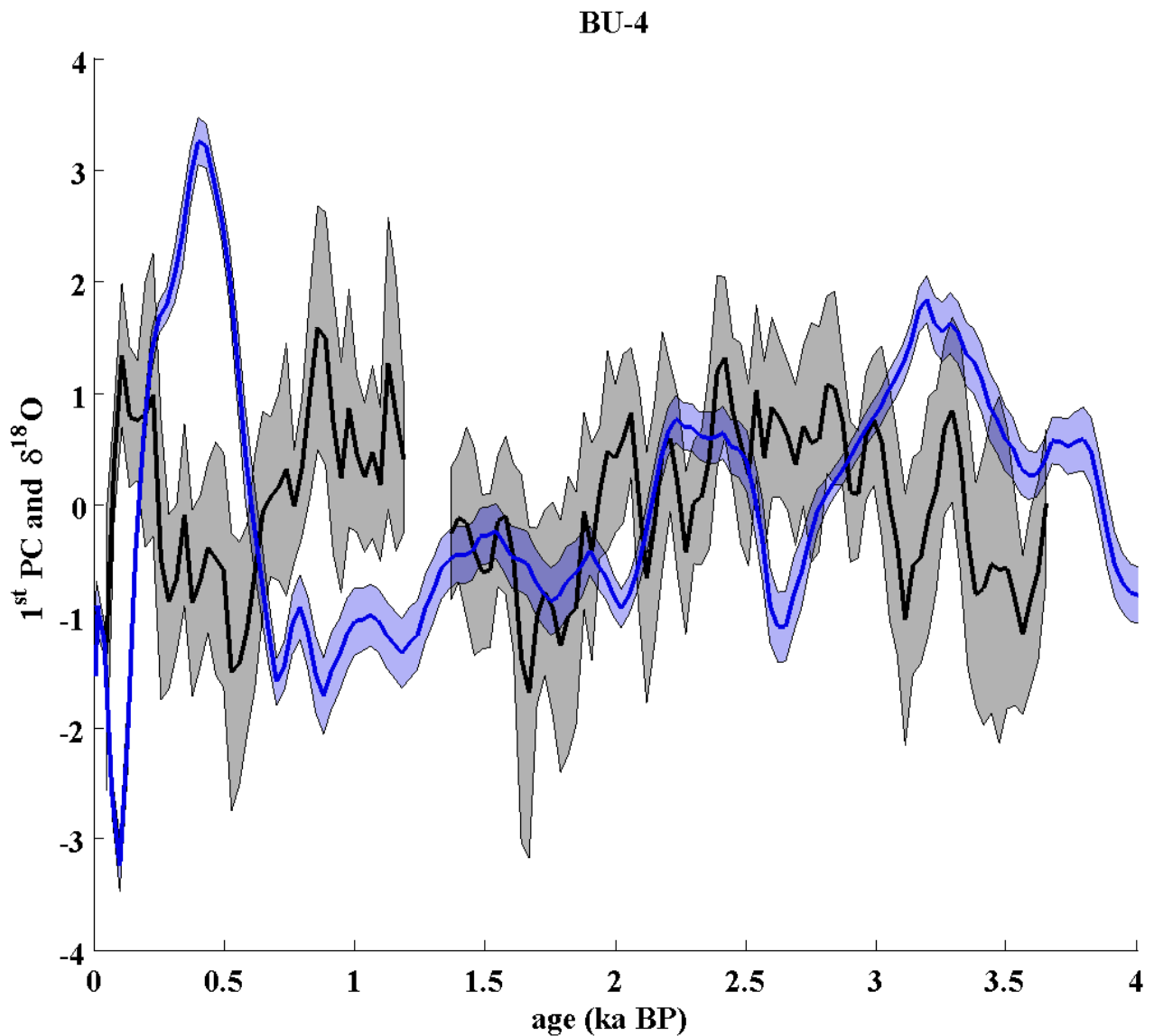


Fig. P.15: The figure is illustrating the computed 1st PC time series for the 4 ka long-term PCA (black line) including its 1-sigma confidence interval (grey shading area). Moreover, the figure pictures the standardised $\delta^{18}\text{O}$ time series of stalagmite BU-4 (blue line) with its 1-sigma confidence interval (blue shading area). The 1-sigma confidence interval is computed by using PCA.

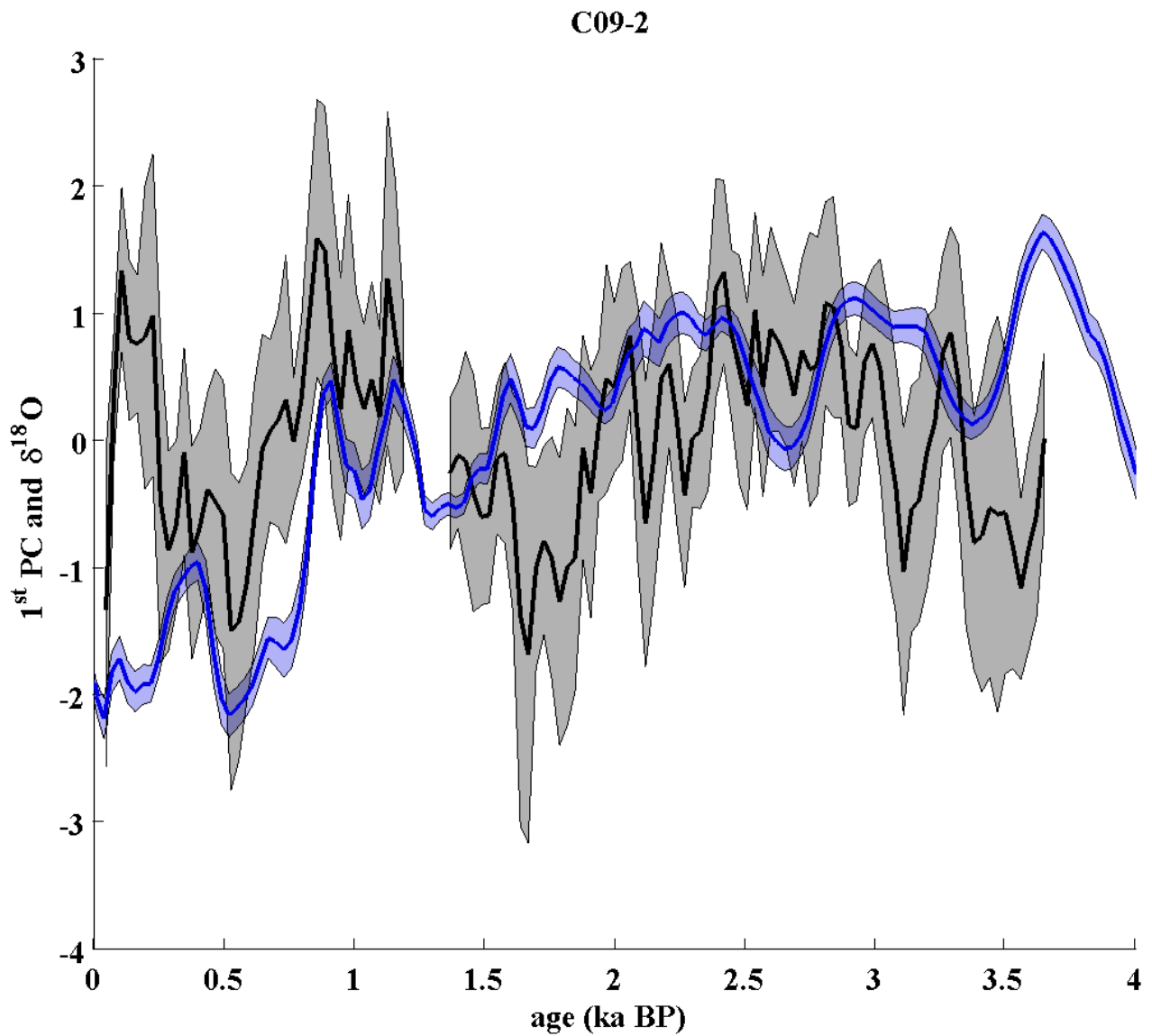


Fig. P.16: The figure is illustrating the computed 1st PC time series for the 4 ka long-term PCA (black line) including its 1-sigma confidence interval (grey shading area). Moreover, the figure pictures the standardised $\delta^{18}\text{O}$ time series of stalagmite C09-2 (blue line) with its 1-sigma confidence interval (blue shading area). The 1-sigma confidence interval is computed by using PCA.

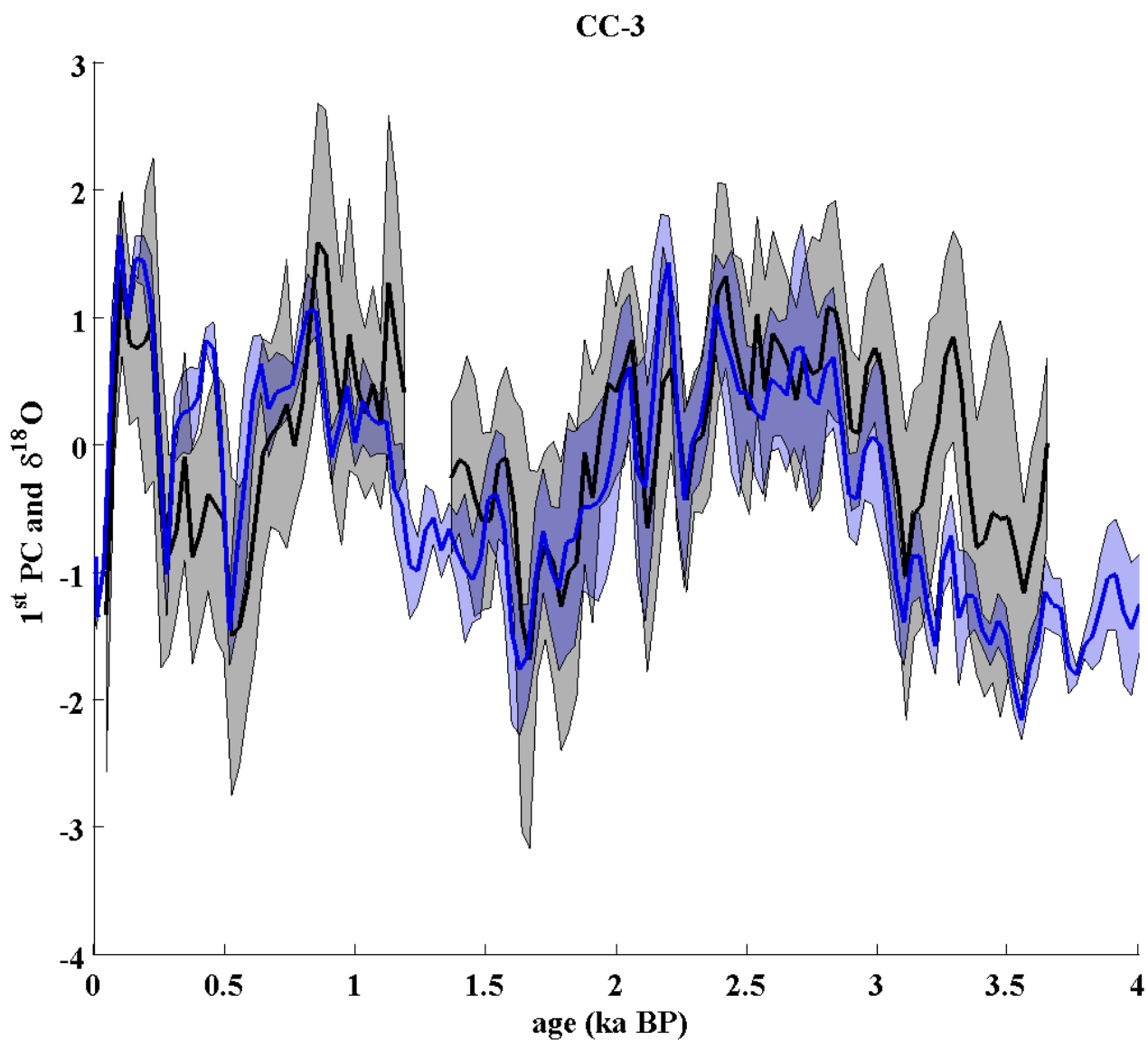


Fig. P.17: The figure is illustrating the computed 1st PC time series for the 4 ka long-term PCA (black line) including its 1-sigma confidence interval (grey shading area). Moreover, the figure pictures the standardised $\delta^{18}\text{O}$ time series of stalagmite CC-3 (blue line) with its 1-sigma confidence interval (blue shading area). The 1-sigma confidence interval is computed by using PCA.

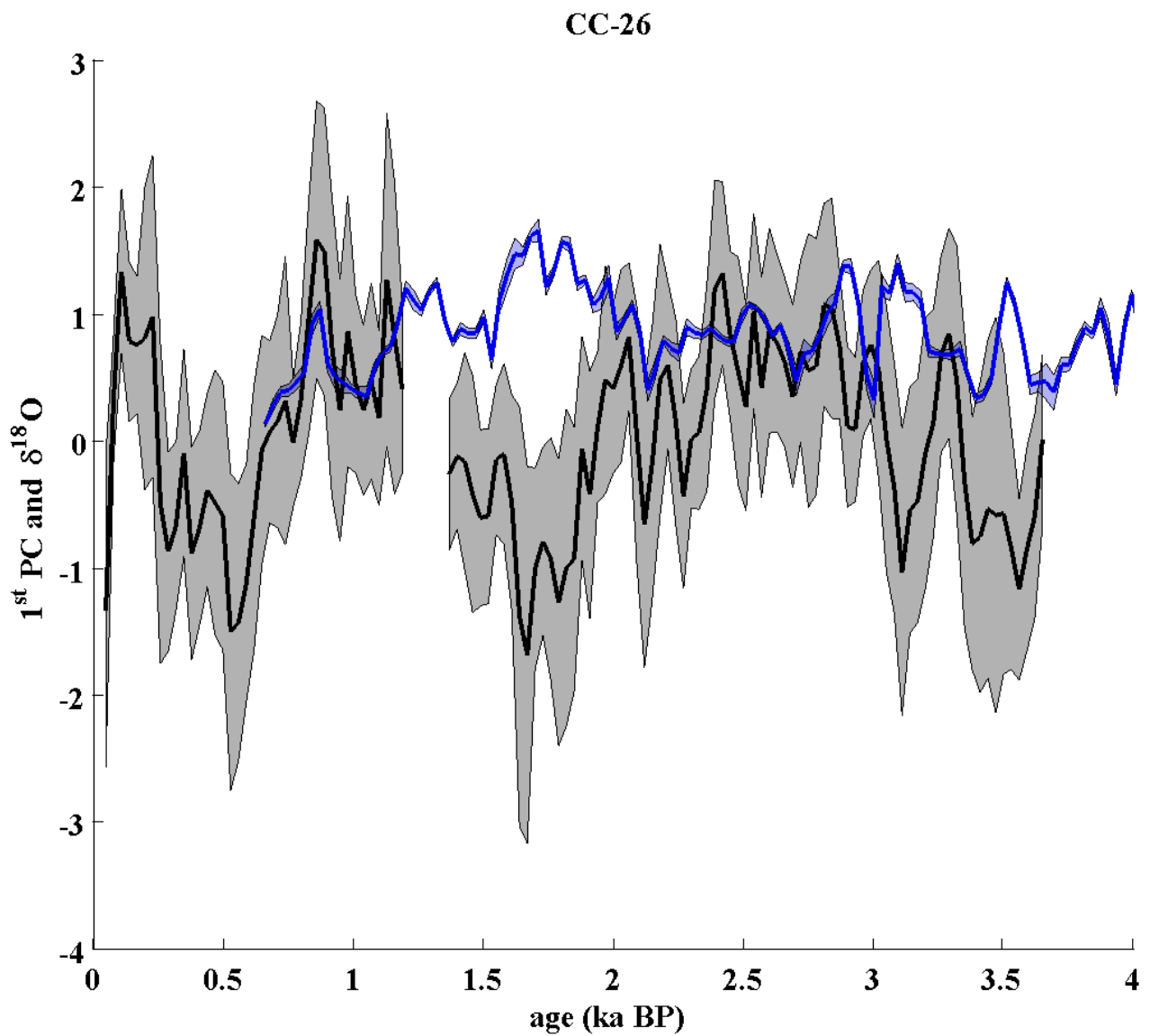


Fig. P.18: The figure is illustrating the computed 1st PC time series for the 4 ka long-term PCA (black line) including its 1-sigma confidence interval (grey shading area). Moreover, the figure pictures the standardised δ¹⁸O time series of stalagmite CC-26 (blue line) with its 1-sigma confidence interval (blue shading area). The 1-sigma confidence interval is computed by using PCA.

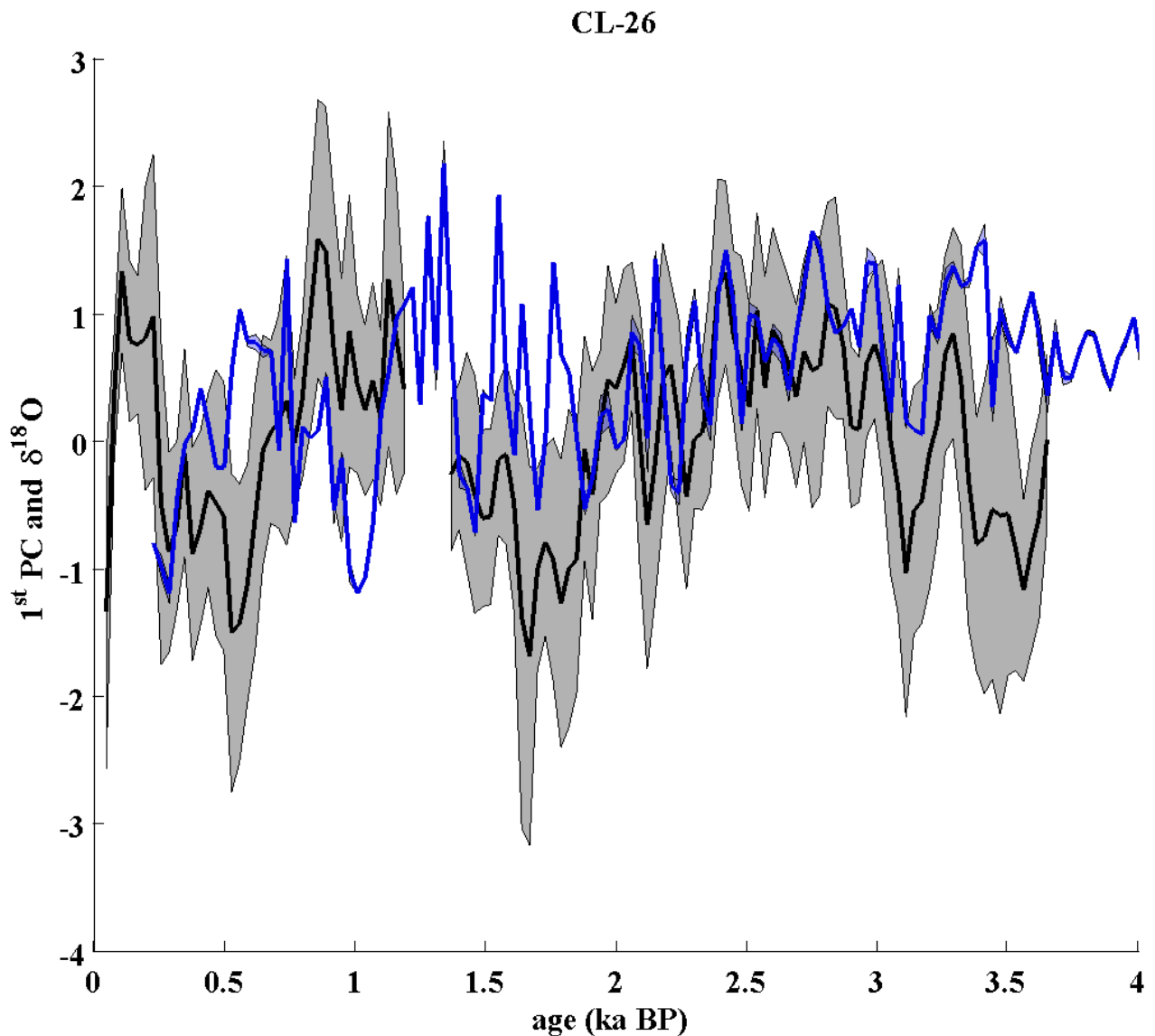


Fig. P.19: The figure is illustrating the computed 1st PC time series for the 4 ka long-term PCA (black line) including its 1-sigma confidence interval (grey shading area). Moreover, the figure pictures the standardised $\delta^{18}\text{O}$ time series of stalagmite CL-26 (blue line) with its 1-sigma confidence interval (blue shading area). The 1-sigma confidence interval is computed by using PCA.

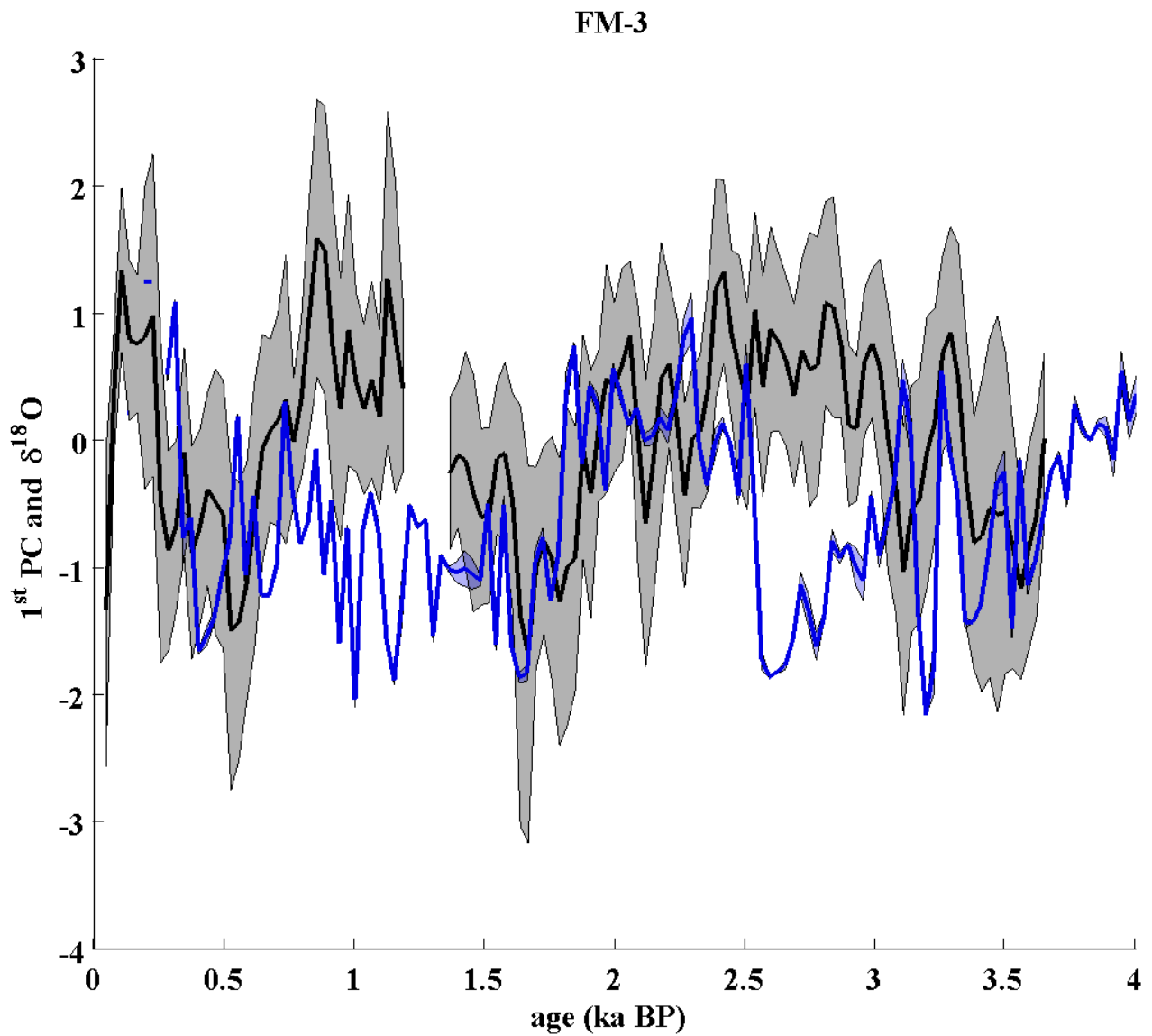


Fig. P.20: The figure is illustrating the computed 1st PC time series for the 4 ka long-term PCA (black line) including its 1-sigma confidence interval (grey shading area). Moreover, the figure pictures the standardised $\delta^{18}\text{O}$ time series of stalagmite FM-3 (blue line) with its 1-sigma confidence interval (blue shading area). The 1-sigma confidence interval is computed by using PCA.

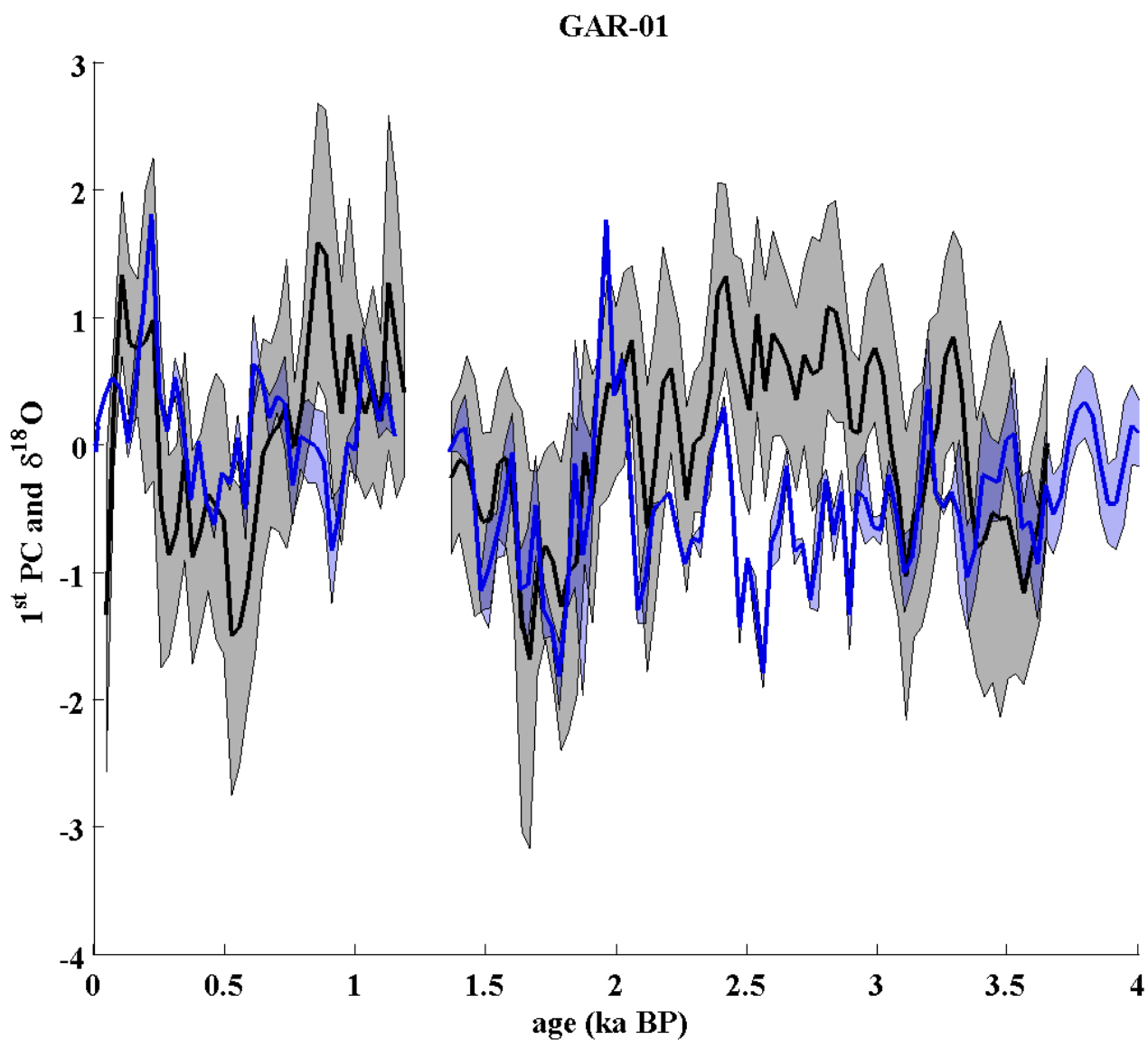


Fig. P.21: The figure is illustrating the computed 1st PC time series for the 4 ka long-term PCA (black line) including its 1-sigma confidence interval (grey shading area). Moreover, the figure pictures the standardised $\delta^{18}\text{O}$ time series of stalagmite GAR-01 (blue line) with its 1-sigma confidence interval (blue shading area). The 1-sigma confidence interval is computed by using PCA.

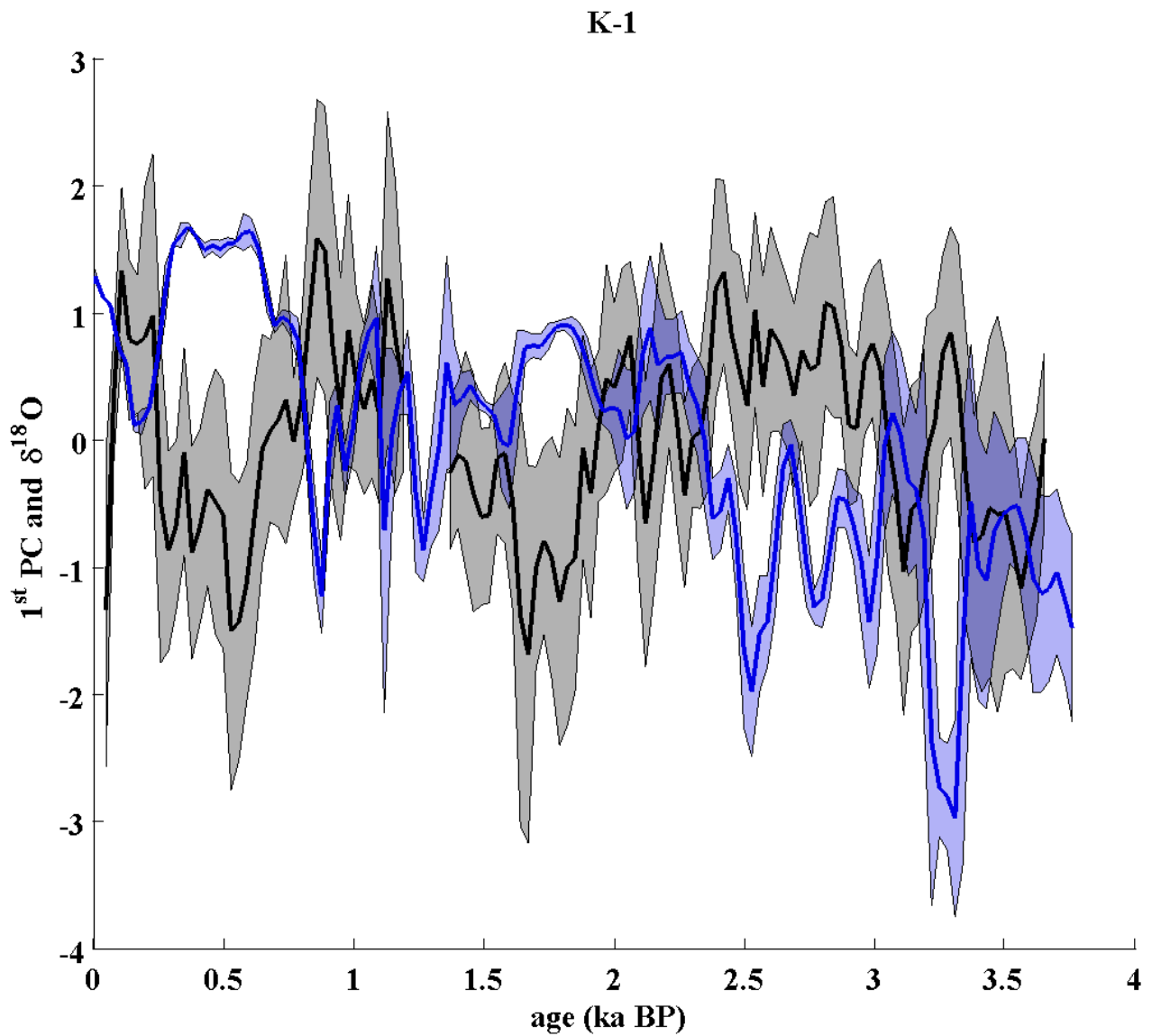


Fig. P.22: The figure is illustrating the computed 1st PC time series for the 4 ka long-term PCA (black line) including its 1-sigma confidence interval (grey shading area). Moreover, the figure pictures the standardised $\delta^{18}\text{O}$ time series of stalagmite K-1 (blue line) with its 1-sigma confidence interval (blue shading area). The 1-sigma confidence interval is computed by using PCA.

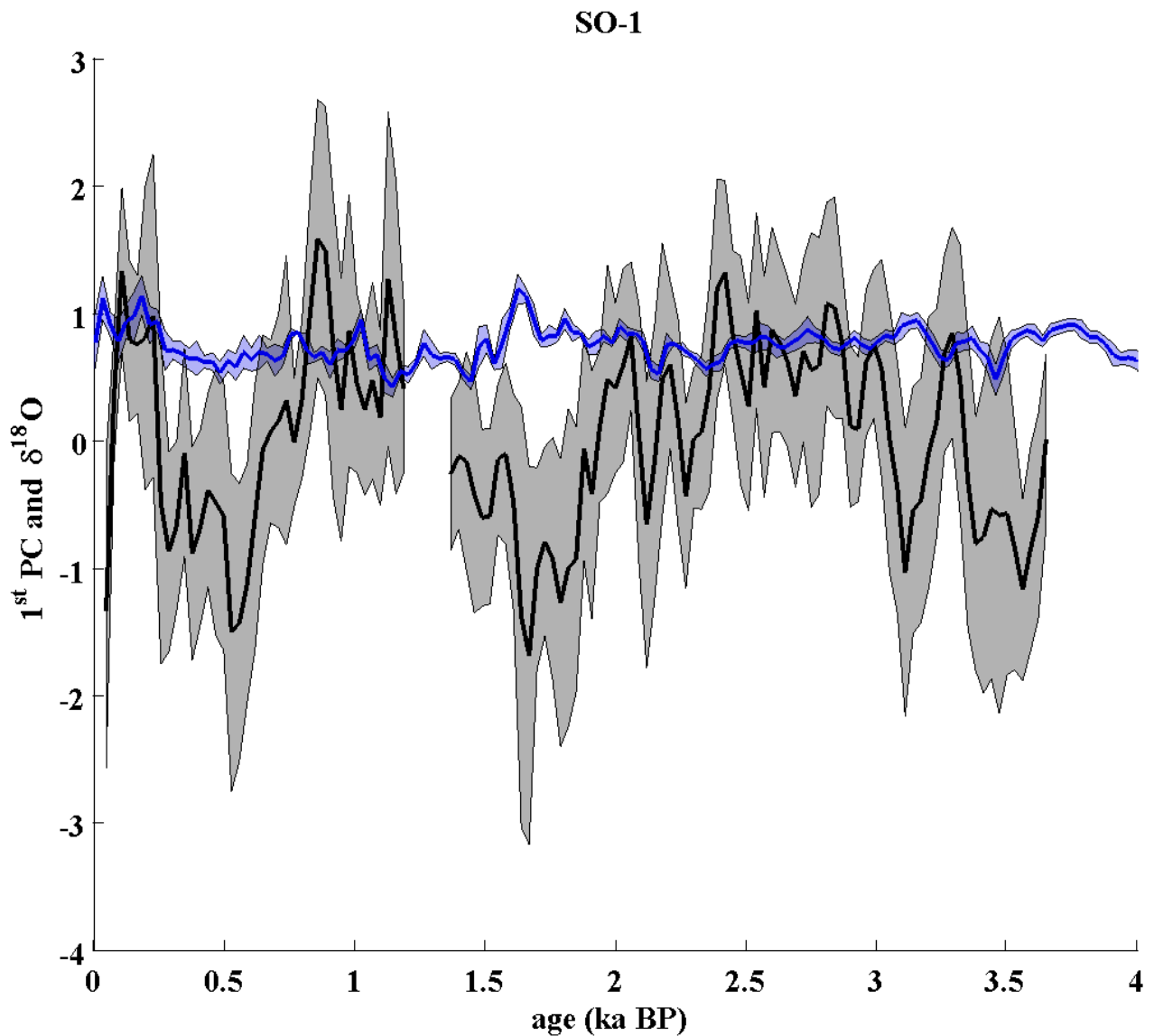


Fig. P.23: The figure is illustrating the computed 1st PC time series for the 4 ka long-term PCA (black line) including its 1-sigma confidence interval (grey shading area). Moreover, the figure pictures the standardised $\delta^{18}\text{O}$ time series of stalagmite SO-1 (blue line) with its 1-sigma confidence interval (blue shading area). The 1-sigma confidence interval is computed by using PCA.

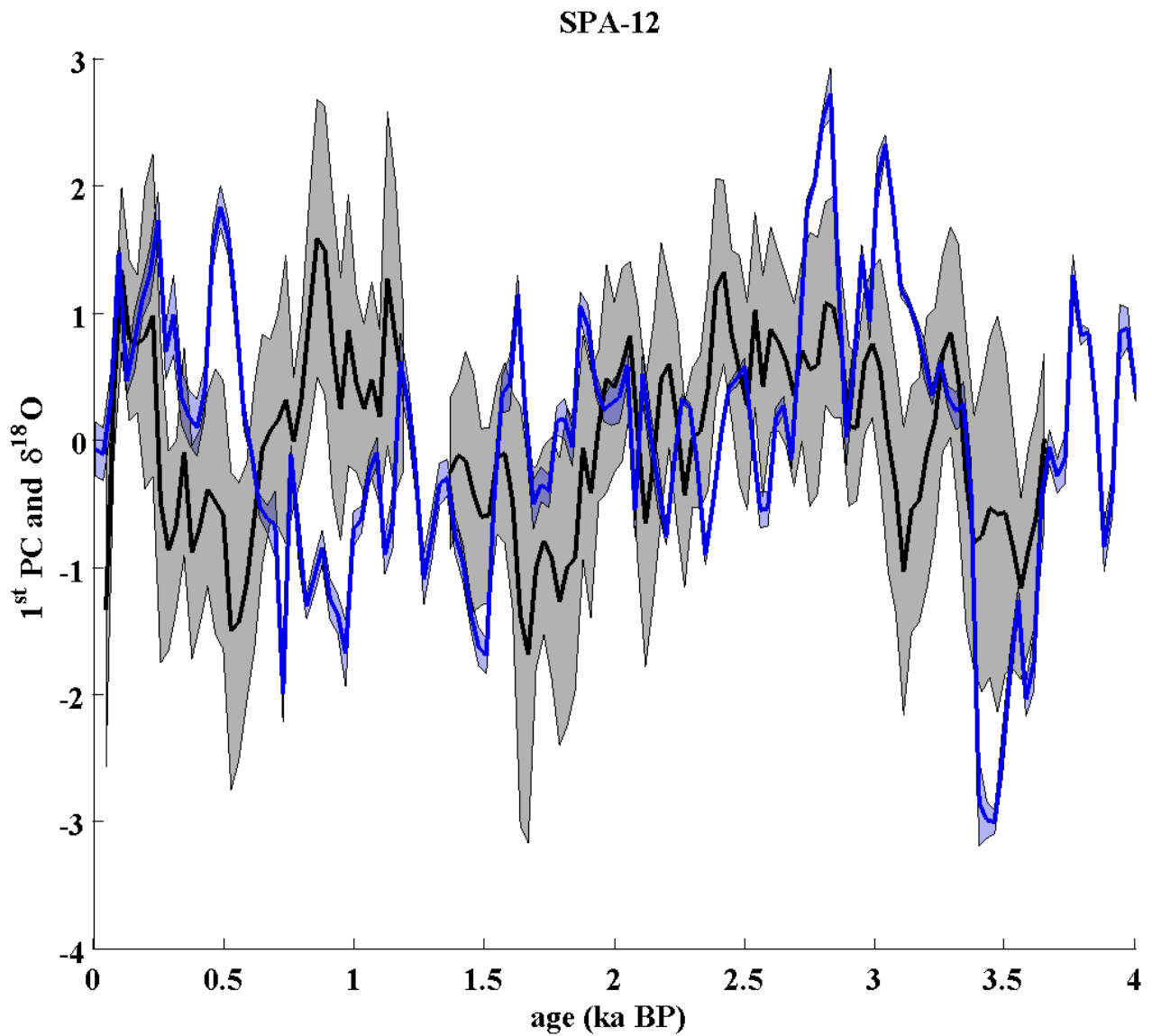


Fig. P.24: The figure is illustrating the computed 1st PC time series for the 4 ka long-term PCA (black line) including its 1-sigma confidence interval (grey shading area). Moreover, the figure pictures the standardised $\delta^{18}\text{O}$ time series of stalagmite SPA-12 (blue line) with its 1-sigma confidence interval (blue shading area). The 1-sigma confidence interval is computed by using PCA.

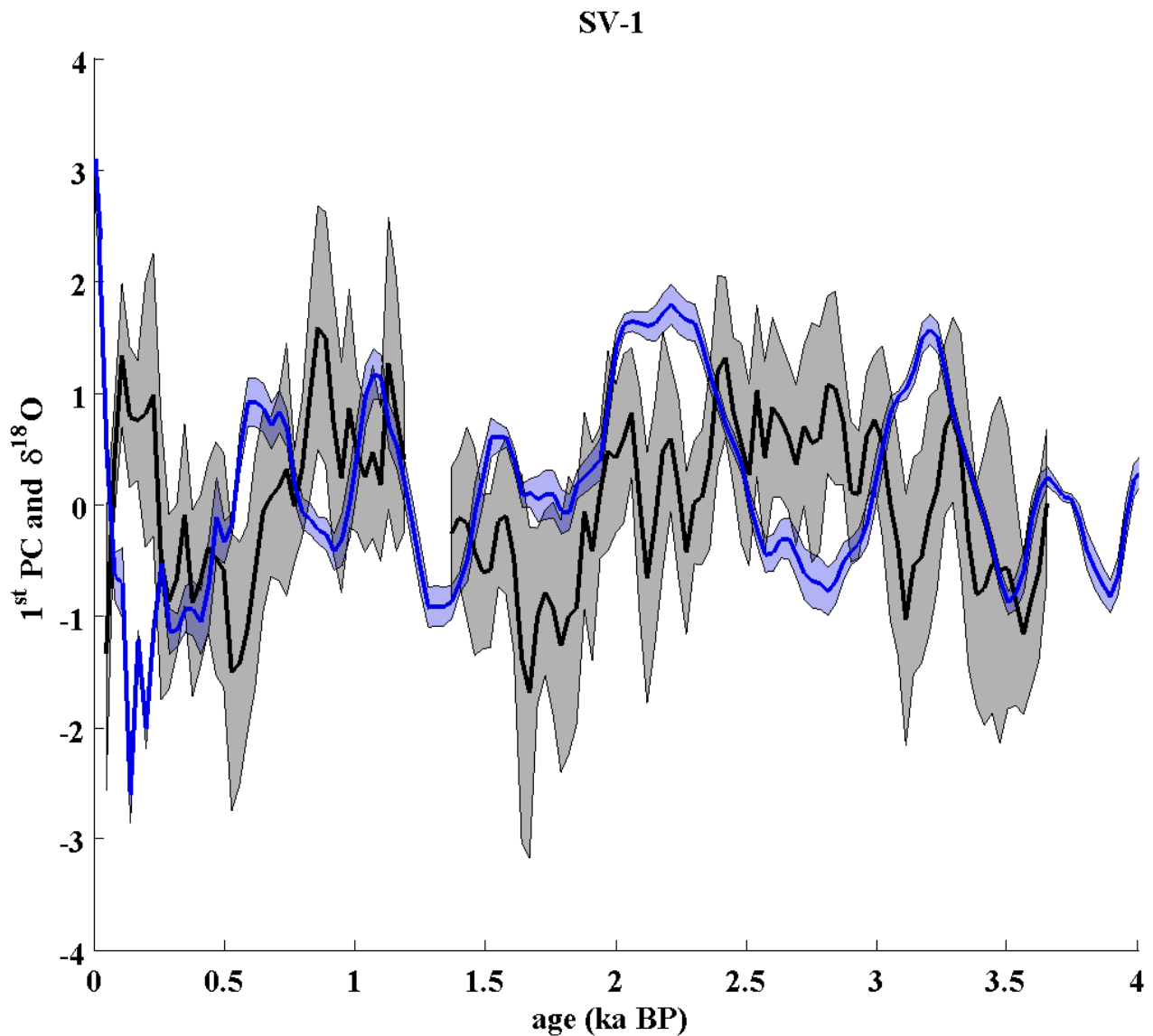


Fig. P.25: The figure is illustrating the computed 1st PC time series for the 4 ka long-term PCA (black line) including its 1-sigma confidence interval (grey shading area). Moreover, the figure pictures the standardised $\delta^{18}\text{O}$ time series of stalagmite SV-1 (blue line) with its 1-sigma confidence interval (blue shading area). The 1-sigma confidence interval is computed by using PCA.

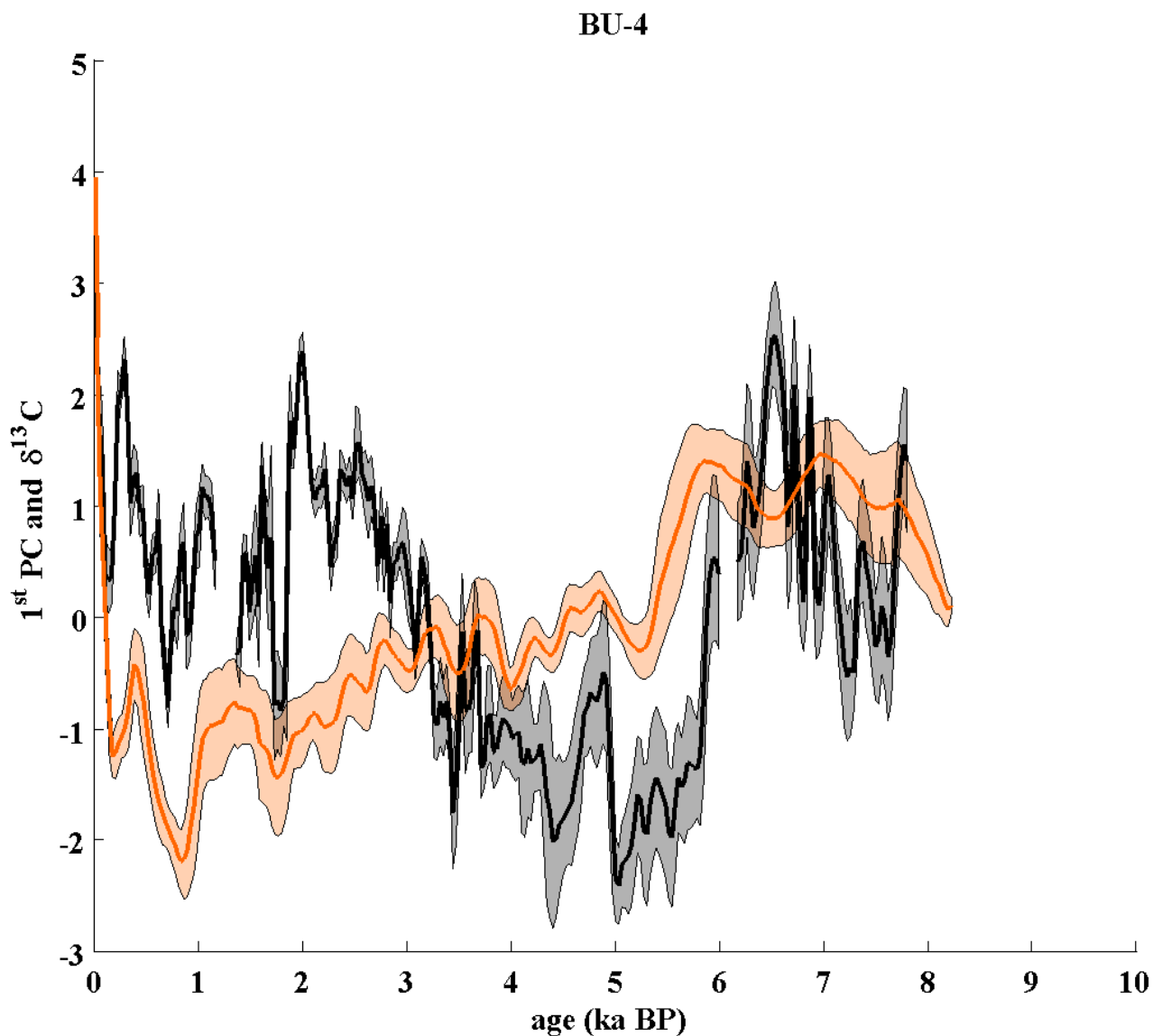


Fig. P.26: The figure is illustrating the computed 1st PC time series for the 8 ka long-term PCA (black line) including it's 1-sigma confidence interval (grey shading area). Moreover, the figure pictures the standardised $\delta^{13}\text{C}$ time series of stalagmite BU-4 (orange line) with it's 1-sigma confidence interval (orange shading area). The 1-sigma confidence interval is computed by using PCA.

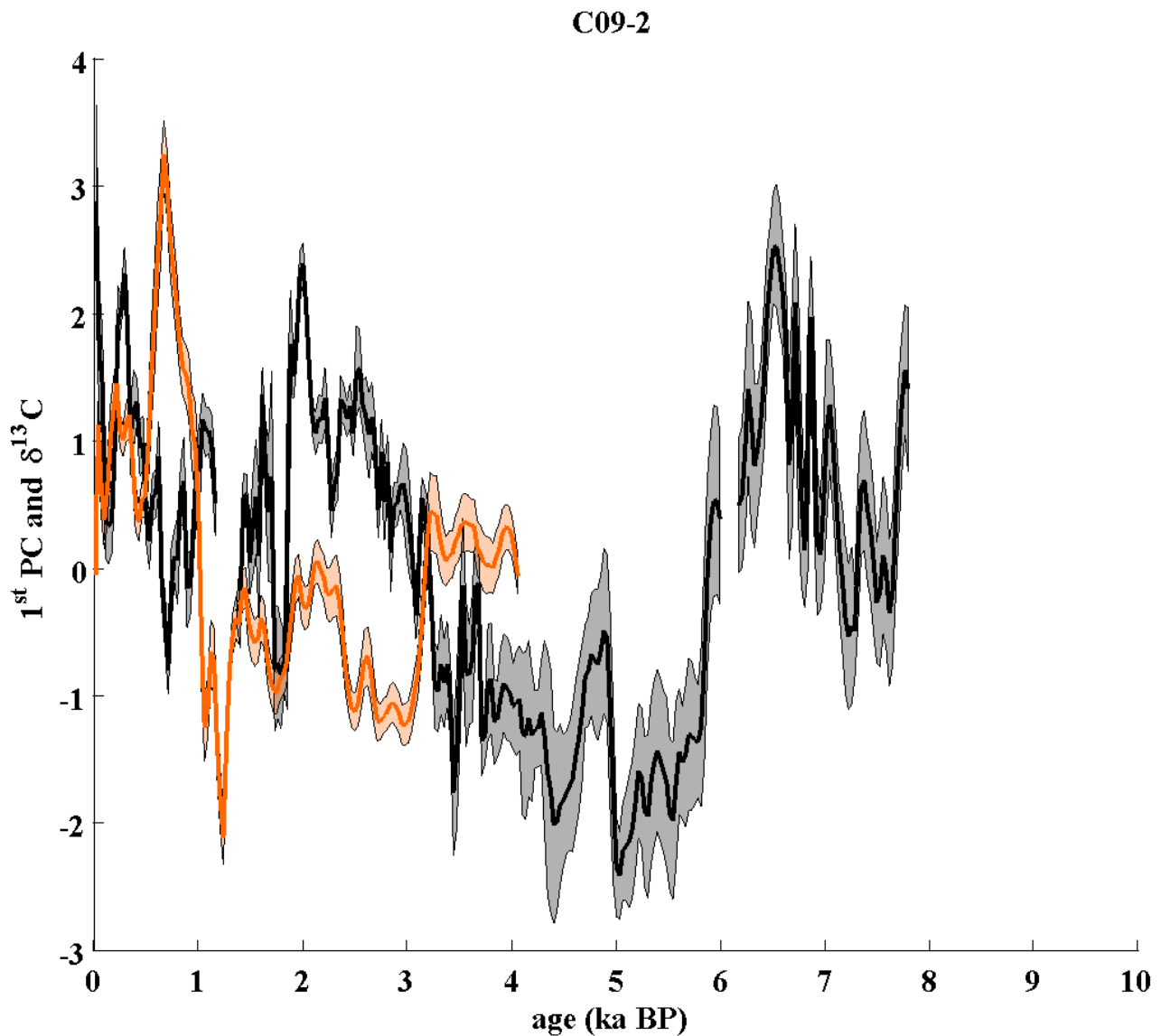


Fig. P.27: The figure is illustrating the computed 1st PC time series for the 8 ka long-term PCA (black line) including its 1-sigma confidence interval (grey shading area). Moreover, the figure pictures the standardised $\delta^{13}\text{C}$ time series of stalagmite C09-2 (orange line) with its 1-sigma confidence interval (orange shading area). The 1-sigma confidence interval is computed by using PCA.

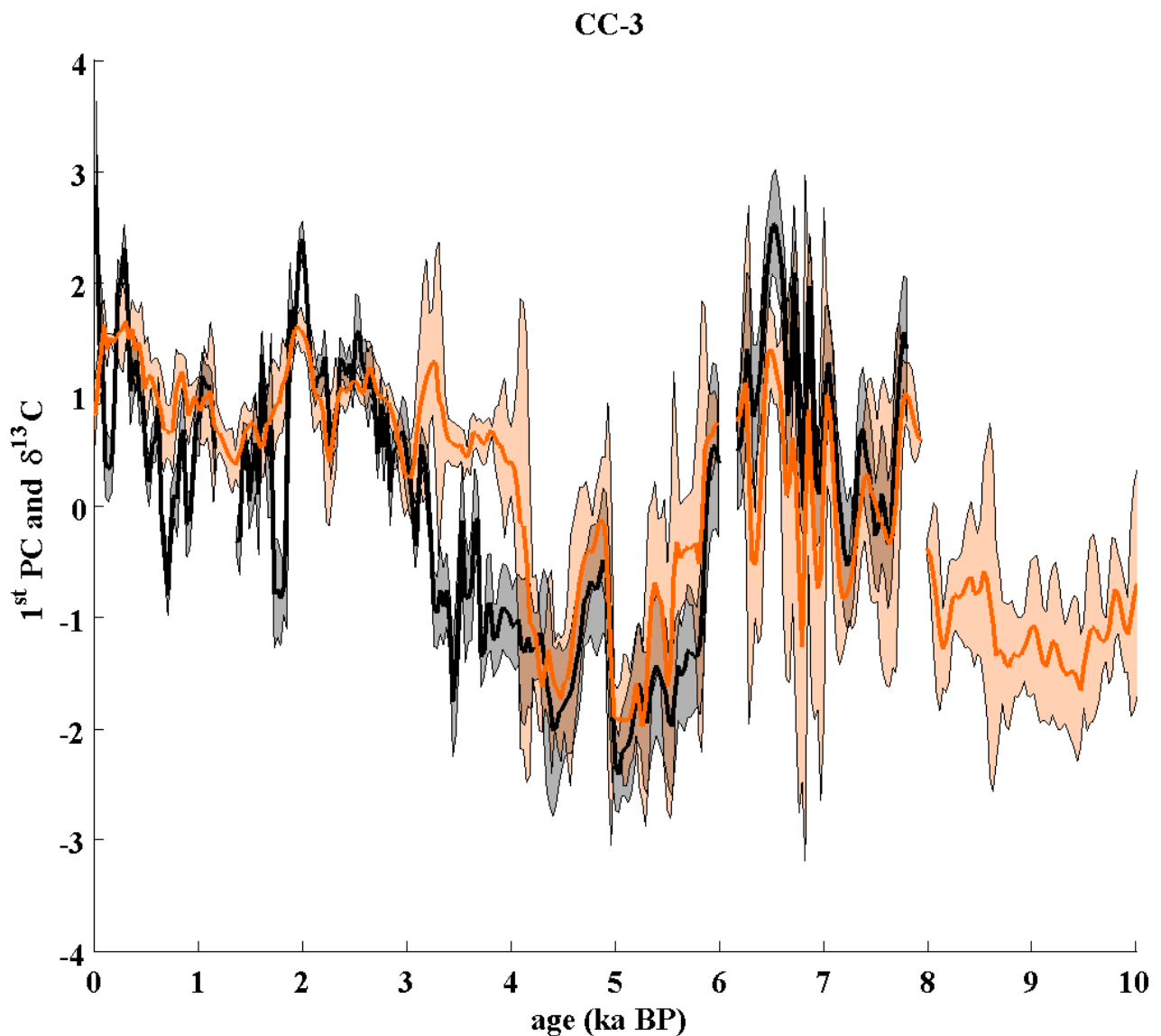


Fig. P.28: The figure is illustrating the computed 1st PC time series for the 8 ka long-term PCA (black line) including its 1-sigma confidence interval (grey shading area). Moreover, the figure pictures the standardised $\delta^{13}\text{C}$ time series of stalagmite CC-3 (orange line) with its 1-sigma confidence interval (orange shading area). The 1-sigma confidence interval is computed by using PCA.

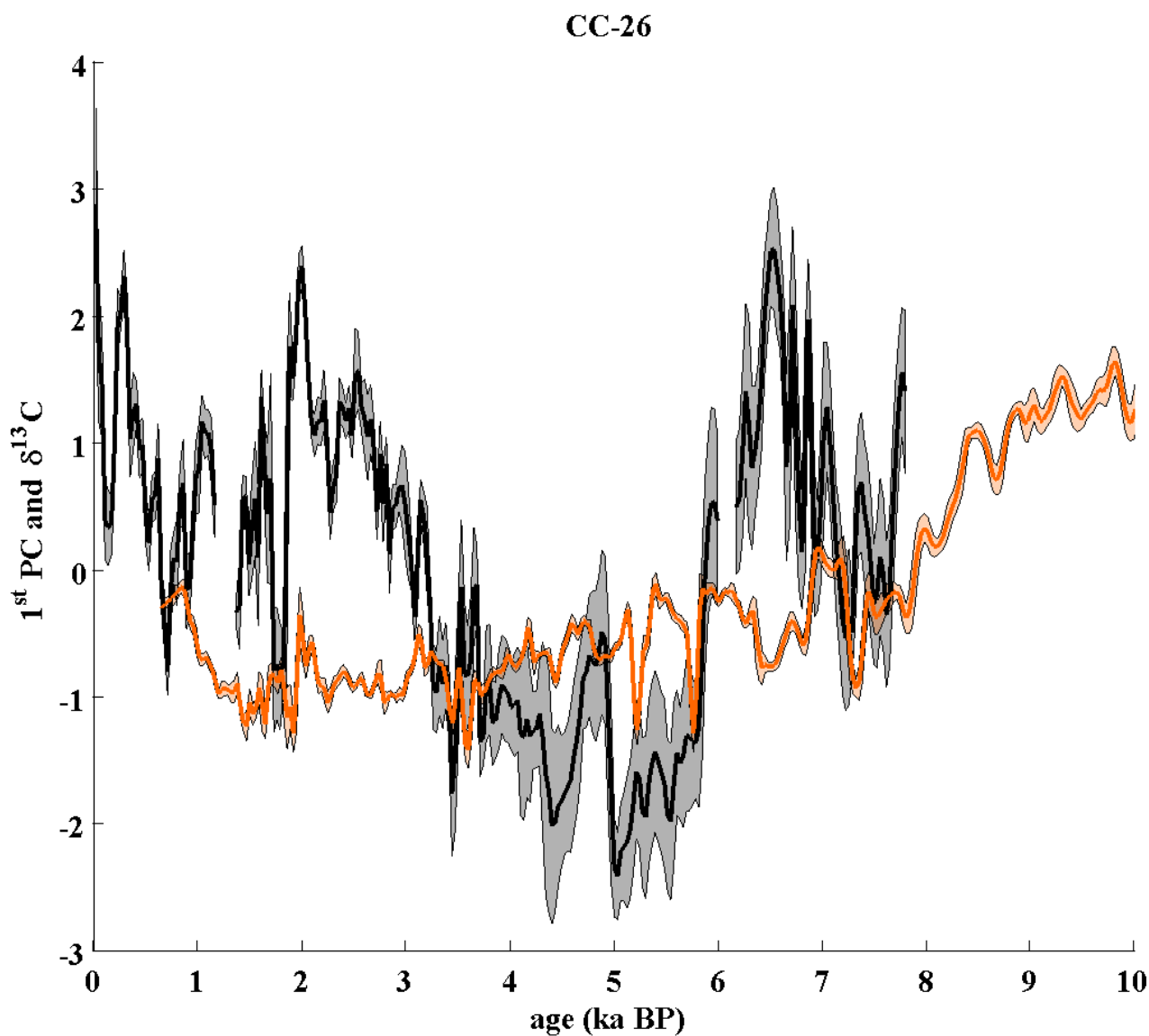


Fig. P.29: The figure is illustrating the computed 1st PC time series for the 8 ka long-term PCA (black line) including its 1-sigma confidence interval (grey shading area). Moreover, the figure pictures the standardised $\delta^{13}\text{C}$ time series of stalagmite CC-26 (orange line) with its 1-sigma confidence interval (orange shading area). The 1-sigma confidence interval is computed by using PCA.

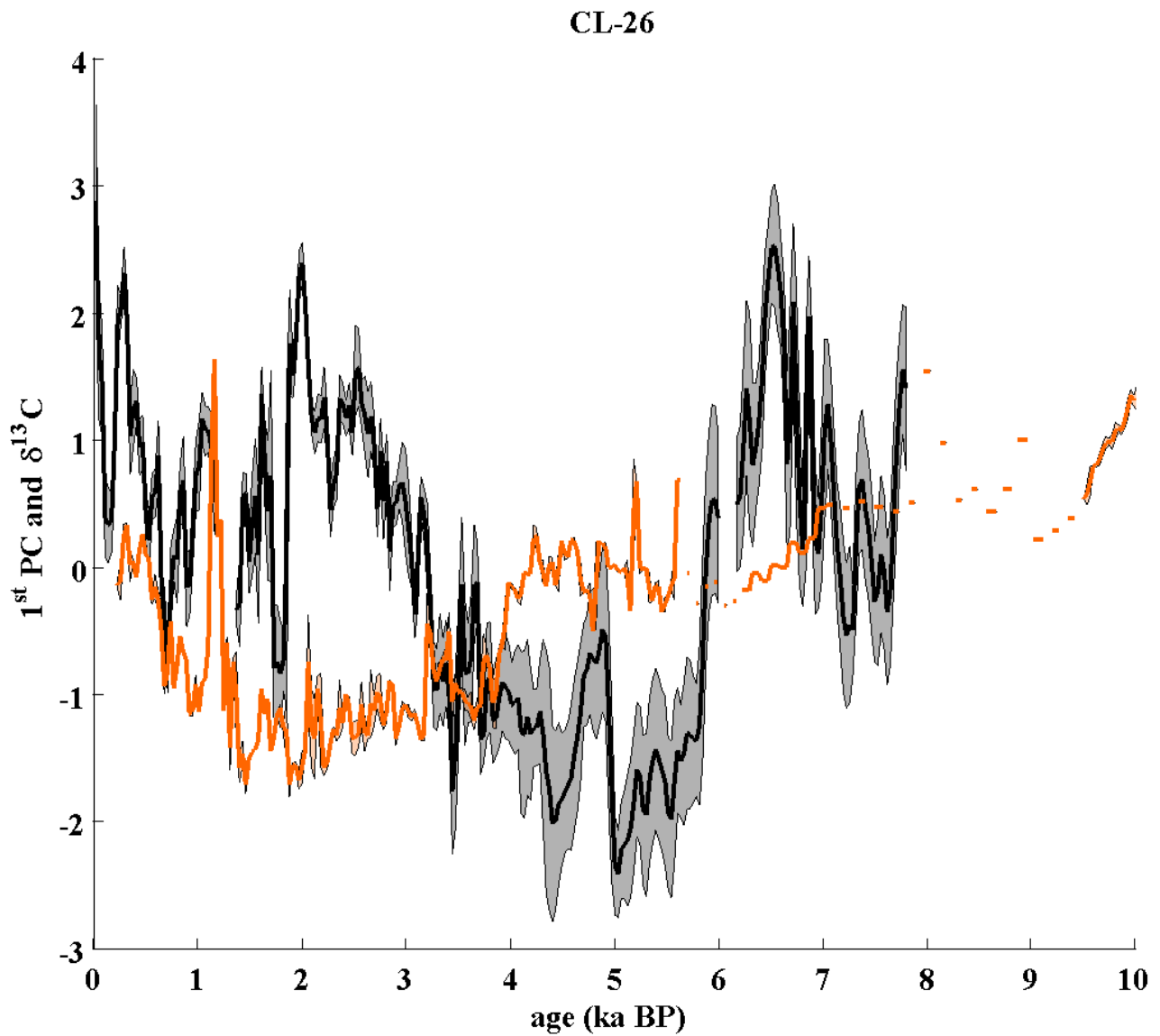


Fig. P.30: The figure is illustrating the computed 1st PC time series for the 8 ka long-term PCA (black line) including its 1-sigma confidence interval (grey shading area). Moreover, the figure pictures the standardised $\delta^{13}\text{C}$ time series of stalagmite CL-26 (orange line) with its 1-sigma confidence interval (orange shading area). The 1-sigma confidence interval is computed by using PCA.

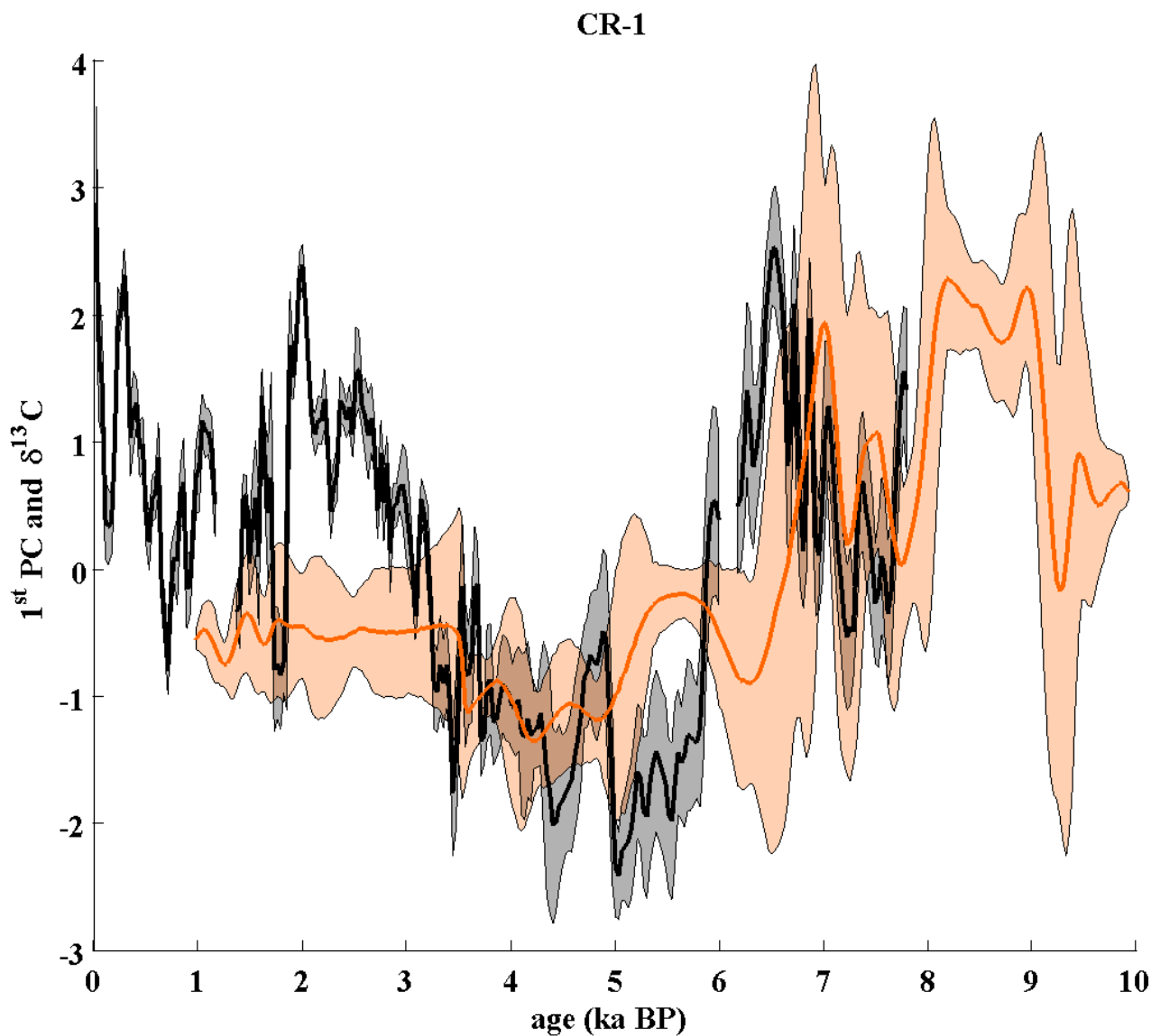


Fig. P.31: The figure is illustrating the computed 1st PC time series for the 8 ka long-term PCA (black line) including its 1-sigma confidence interval (grey shading area). Moreover, the figure pictures the standardised $\delta^{13}\text{C}$ time series of stalagmite CR-1 (orange line) with its 1-sigma confidence interval (orange shading area). The 1-sigma confidence interval is computed by using PCA.

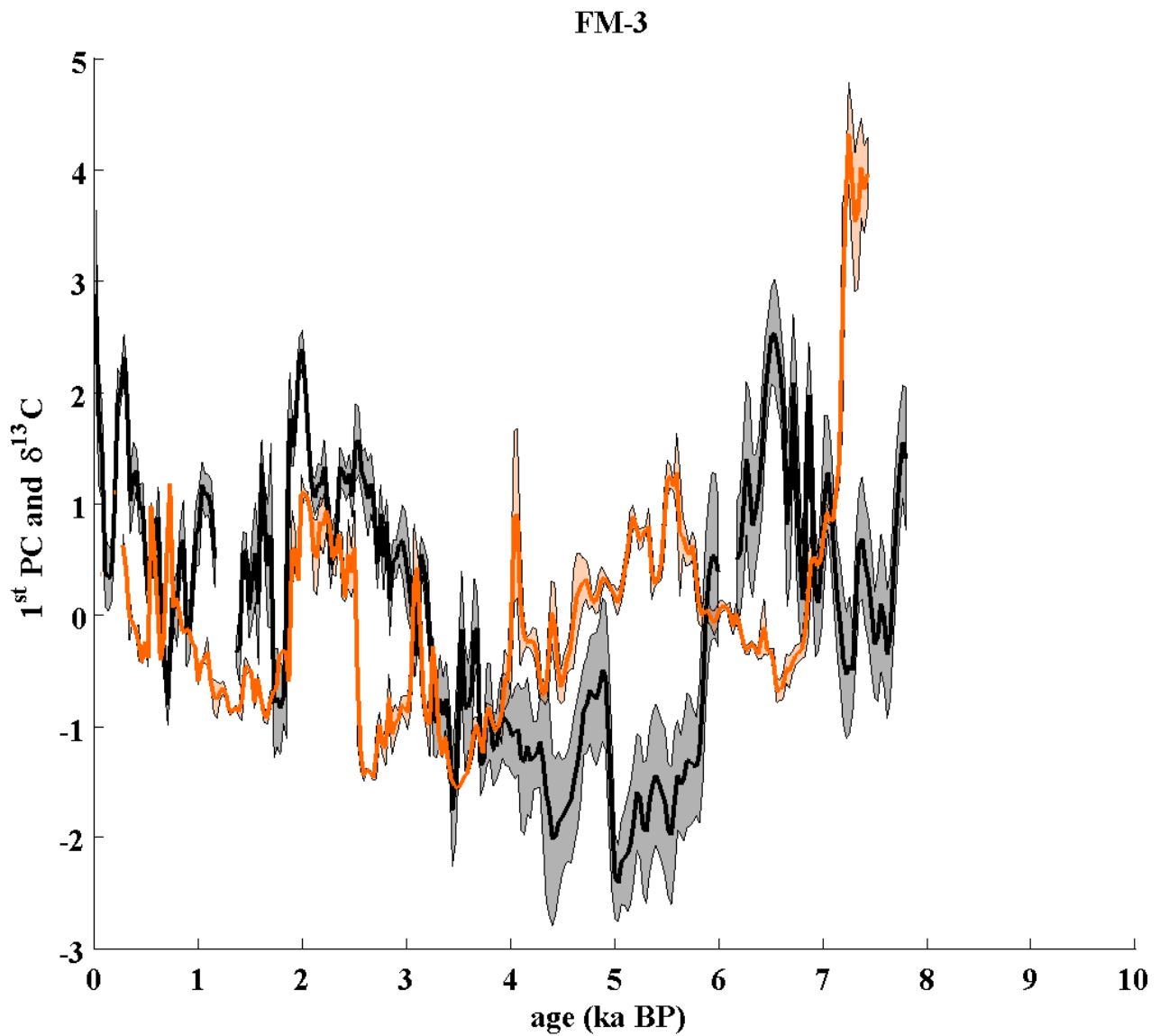


Fig. P.32: The figure is illustrating the computed 1st PC time series for the 8 ka long-term PCA (black line) including its 1-sigma confidence interval (grey shading area). Moreover, the figure pictures the standardised $\delta^{13}\text{C}$ time series of stalagmite FM-3 (orange line) with its 1-sigma confidence interval (orange shading area). The 1-sigma confidence interval is computed by using PCA.

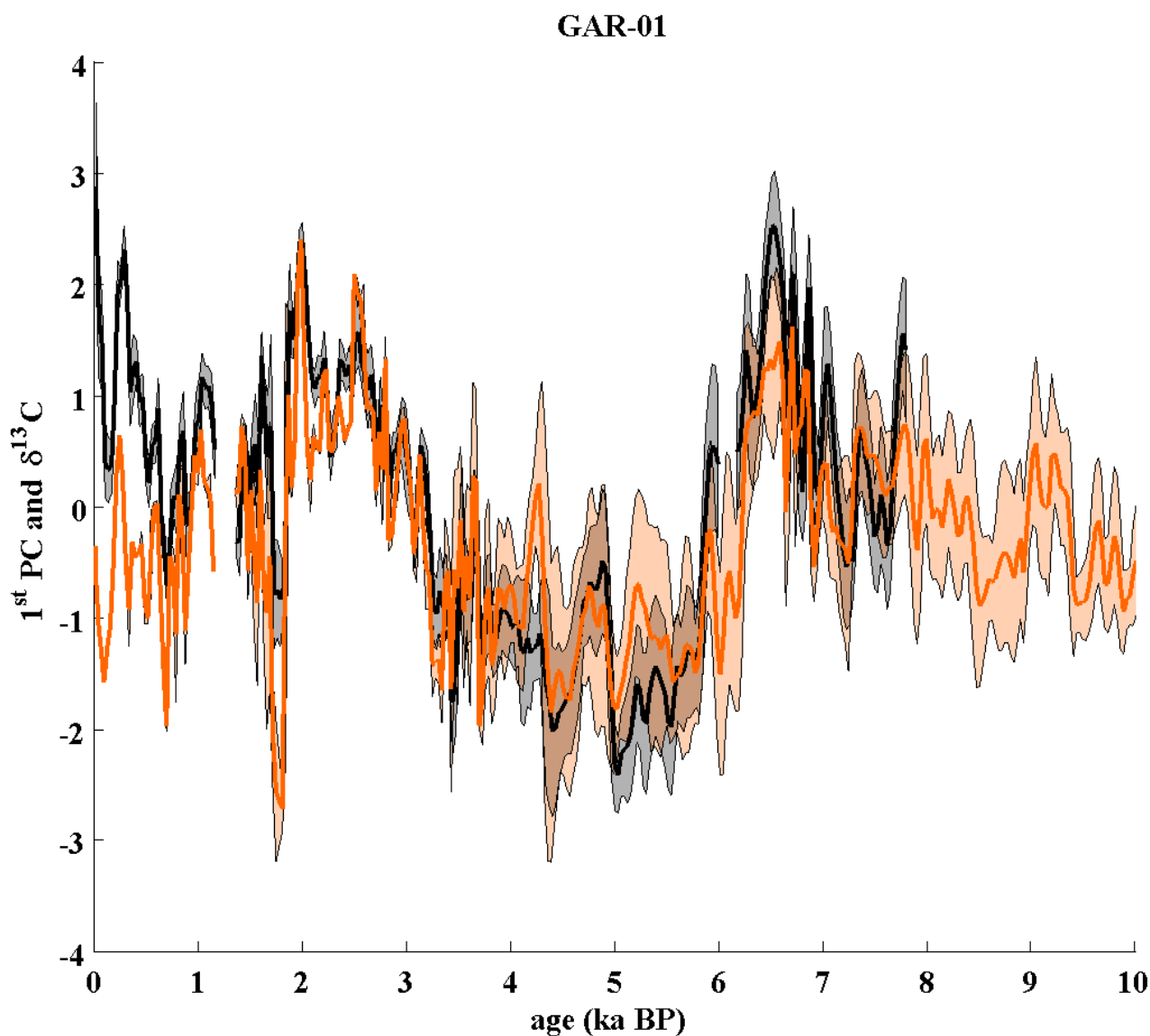


Fig. P.33: The figure is illustrating the computed 1st PC time series for the 8 ka long-term PCA (black line) including its 1-sigma confidence interval (grey shading area). Moreover, the figure pictures the standardised $\delta^{13}\text{C}$ time series of stalagmite FM-3 (orange line) with its 1-sigma confidence interval (orange shading area). The 1-sigma confidence interval is computed by using PCA.

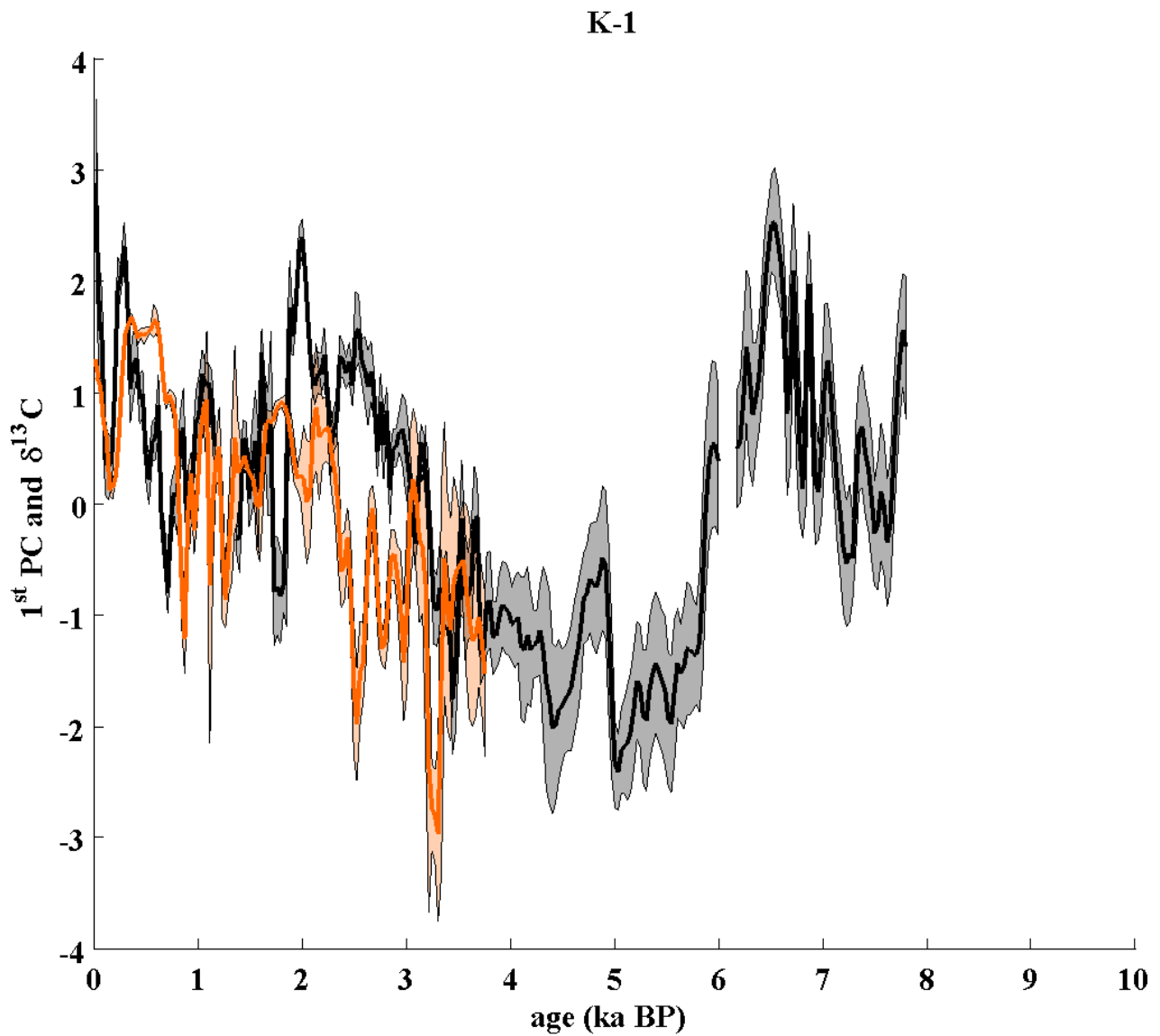


Fig. P.34: The figure is illustrating the computed 1st PC time series for the 8 ka long-term PCA (black line) including its 1-sigma confidence interval (grey shading area). Moreover, the figure pictures the standardised $\delta^{13}\text{C}$ time series of stalagmite K-1 (orange line) with its 1-sigma confidence interval (orange shading area). The 1-sigma confidence interval is computed by using PCA.

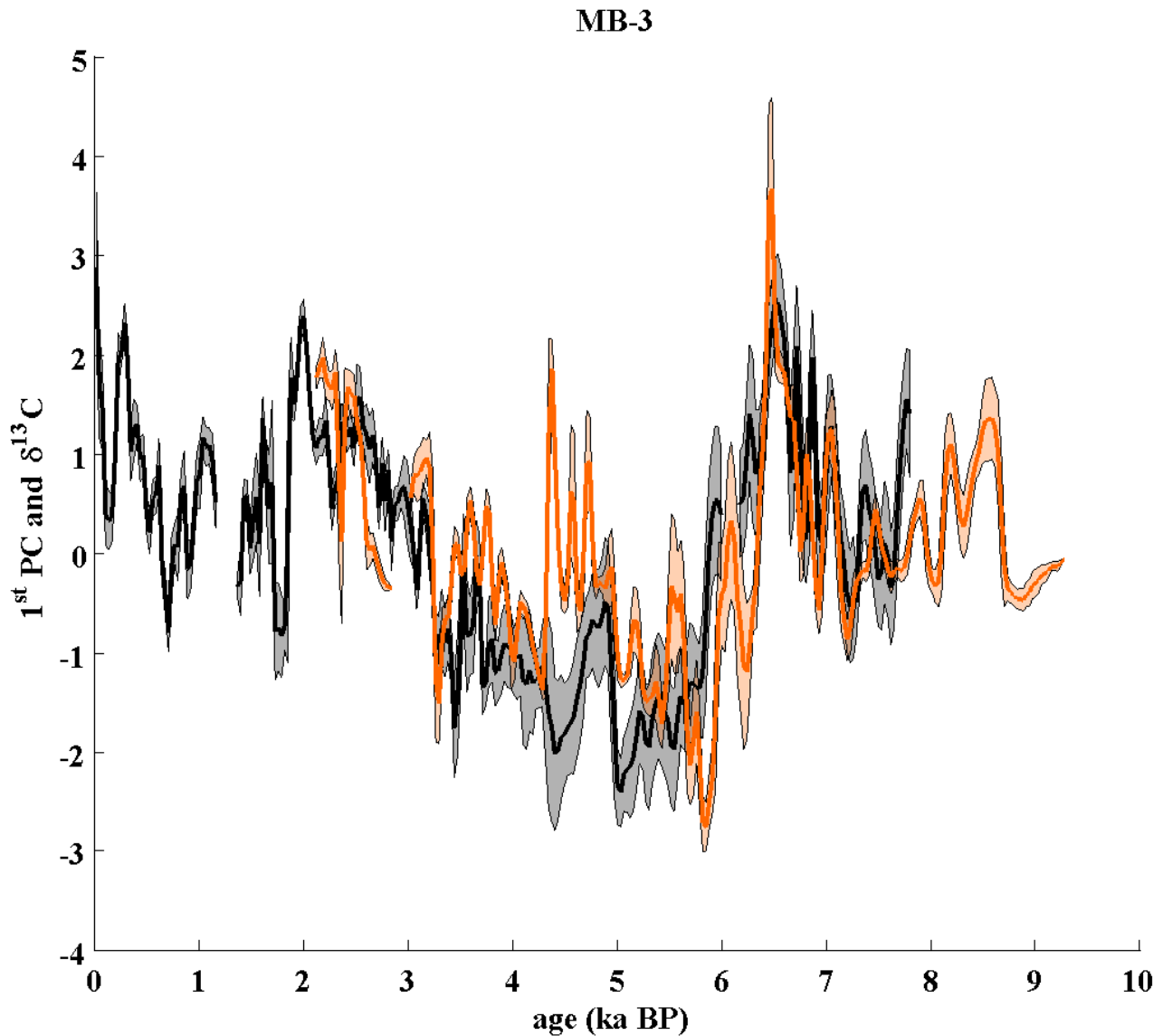


Fig. P.35: The figure is illustrating the computed 1st PC time series for the 8 ka long-term PCA (black line) including its 1-sigma confidence interval (grey shading area). Moreover, the figure pictures the standardised $\delta^{13}\text{C}$ time series of stalagmite MB-3 (orange line) with its 1-sigma confidence interval (orange shading area). The 1-sigma confidence interval is computed by using PCA.

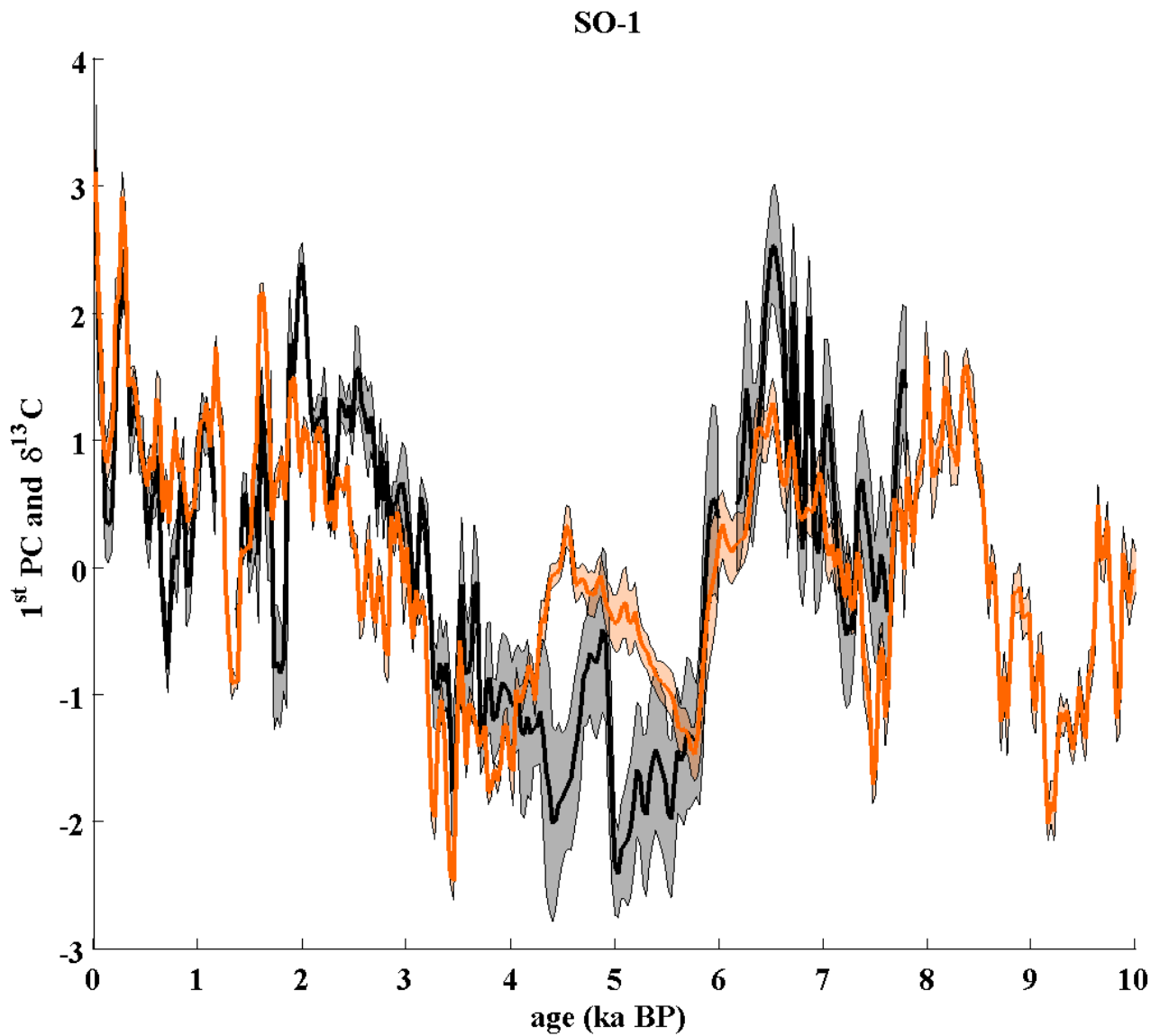


Fig. P.36: The figure is illustrating the computed 1st PC time series for the 8 ka long-term PCA (black line) including its 1-sigma confidence interval (grey shading area). Moreover, the figure pictures the standardised $\delta^{13}\text{C}$ time series of stalagmite SO-1 (orange line) with its 1-sigma confidence interval (orange shading area). The 1-sigma confidence interval is computed by using PCA.

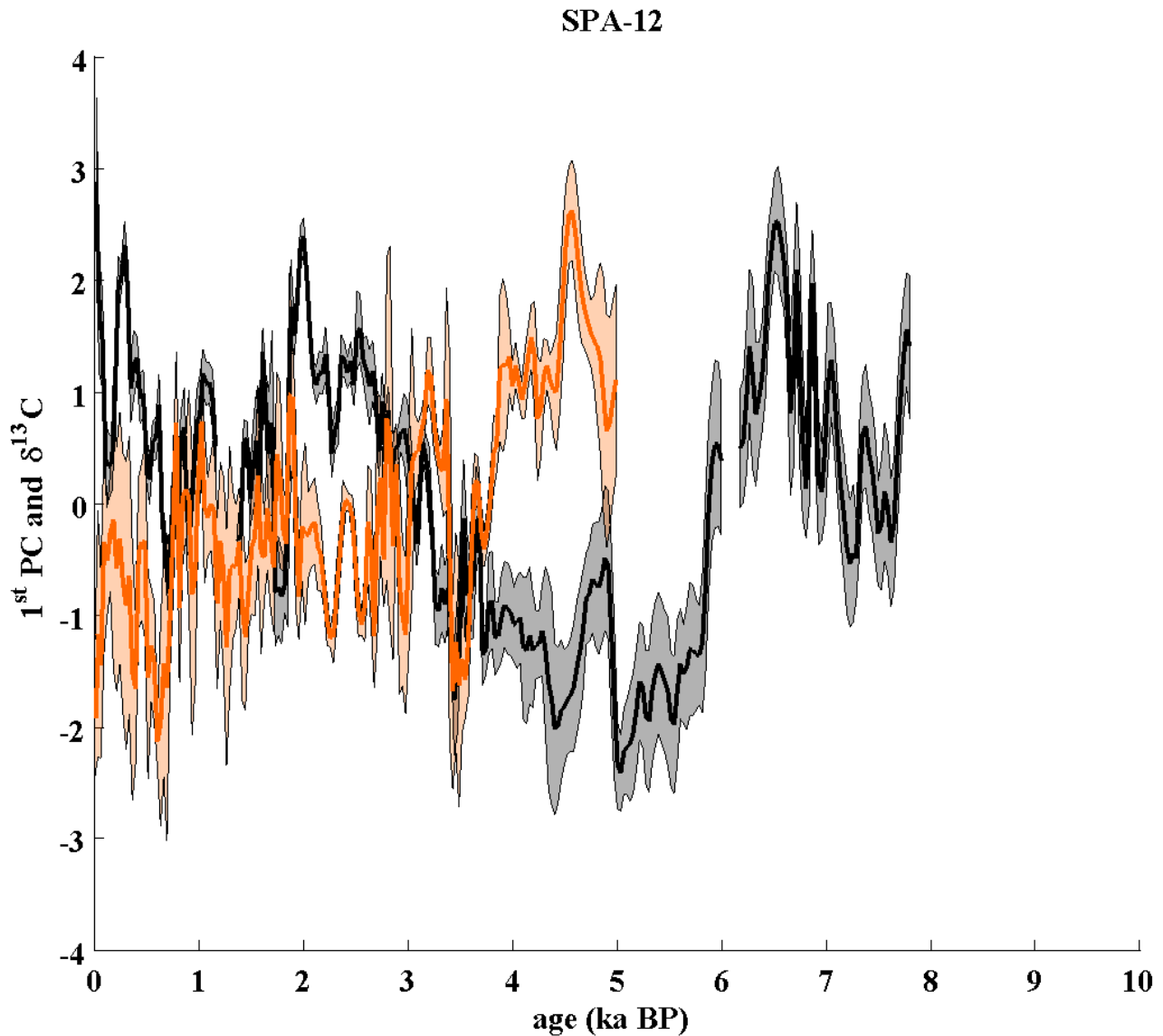


Fig. P.37: The figure is illustrating the computed 1st PC time series for the 8 ka long-term PCA (black line) including its 1-sigma confidence interval (grey shading area). Moreover, the figure pictures the standardised $\delta^{13}\text{C}$ time series of stalagmite SPA-12 (orange line) with its 1-sigma confidence interval (orange shading area). The 1-sigma confidence interval is computed by using PCA.

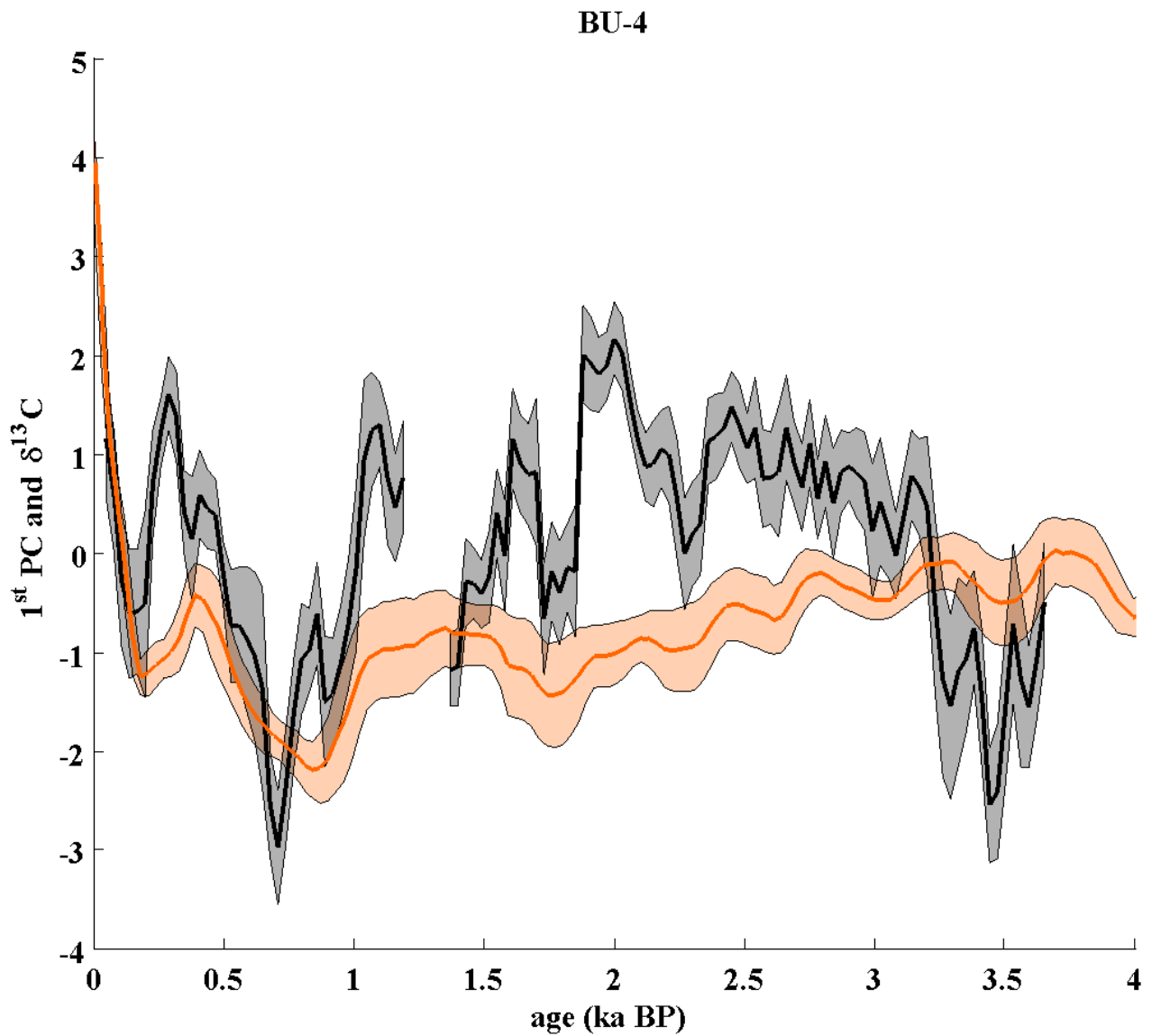


Fig. P.38: The figure is illustrating the computed 1st PC time series for the 4 ka long-term PCA (black line) including its 1-sigma confidence interval (grey shading area). Moreover, the figure pictures the standardised $\delta^{13}\text{C}$ time series of stalagmite BU-4 (orange line) with its 1-sigma confidence interval (orange shading area). The 1-sigma confidence interval is computed by using PCA.

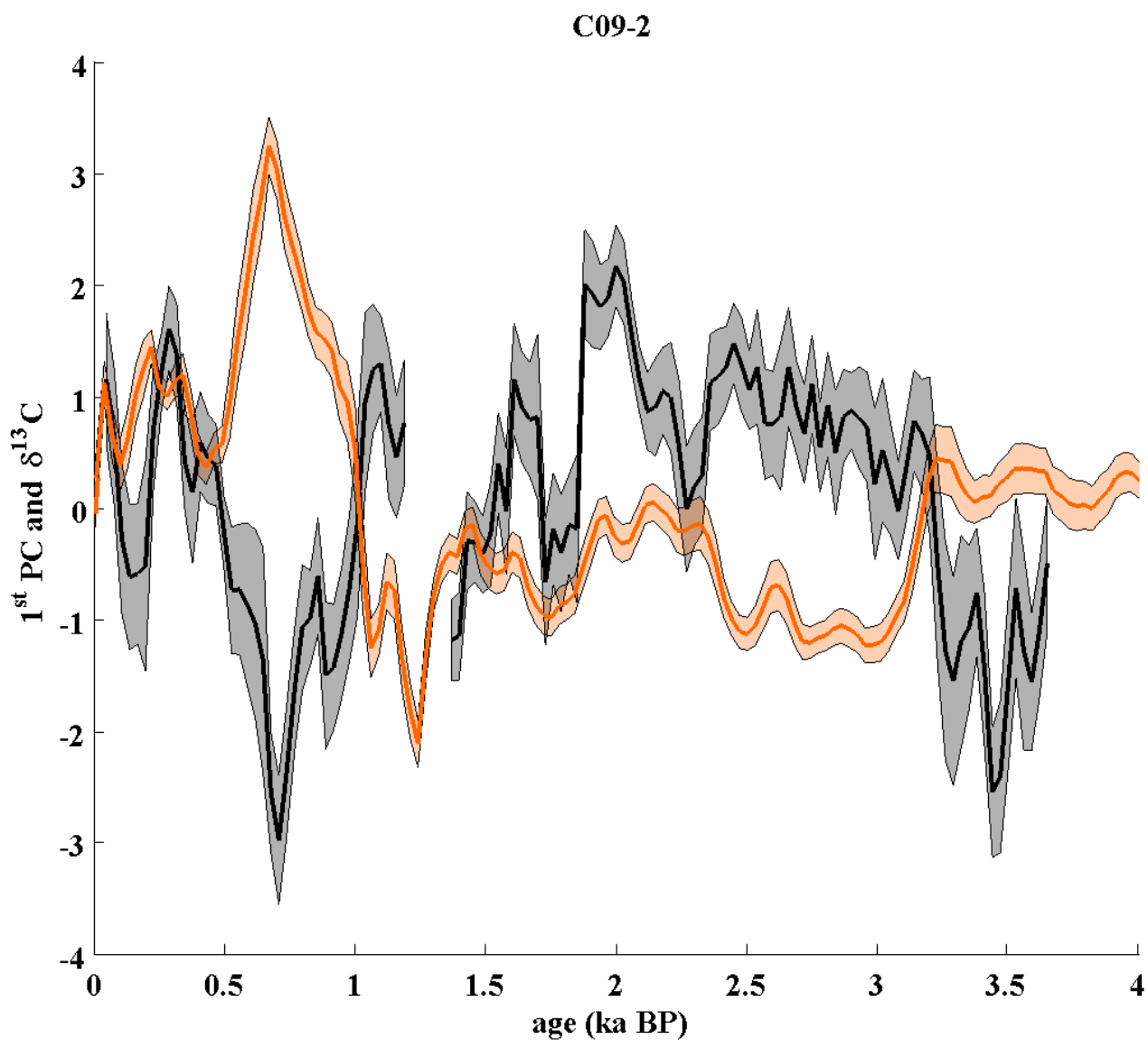


Fig. P.39: The figure is illustrating the computed 1st PC time series for the 4 ka long-term PCA (black line) including its 1-sigma confidence interval (grey shading area). Moreover, the figure pictures the standardised $\delta^{13}\text{C}$ time series of stalagmite C09-2 (orange line) with its 1-sigma confidence interval (orange shading area). The 1-sigma confidence interval is computed by using PCA.

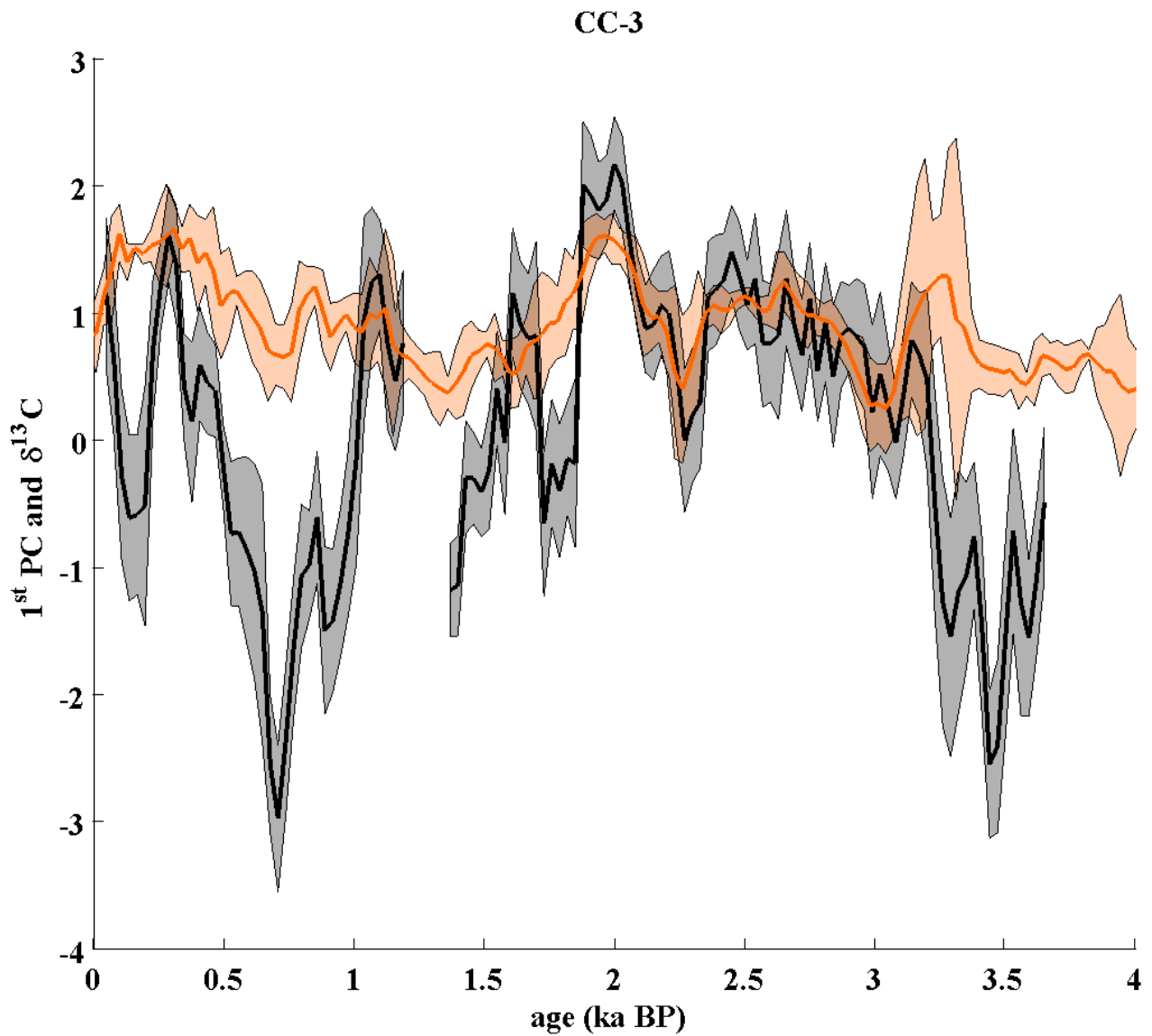


Fig. P.40: The figure is illustrating the computed 1st PC time series for the 4 ka long-term PCA (black line) including its 1-sigma confidence interval (grey shading area). Moreover, the figure pictures the standardised $\delta^{13}\text{C}$ time series of stalagmite CC-3 (orange line) with its 1-sigma confidence interval (orange shading area). The 1-sigma confidence interval is computed by using PCA.

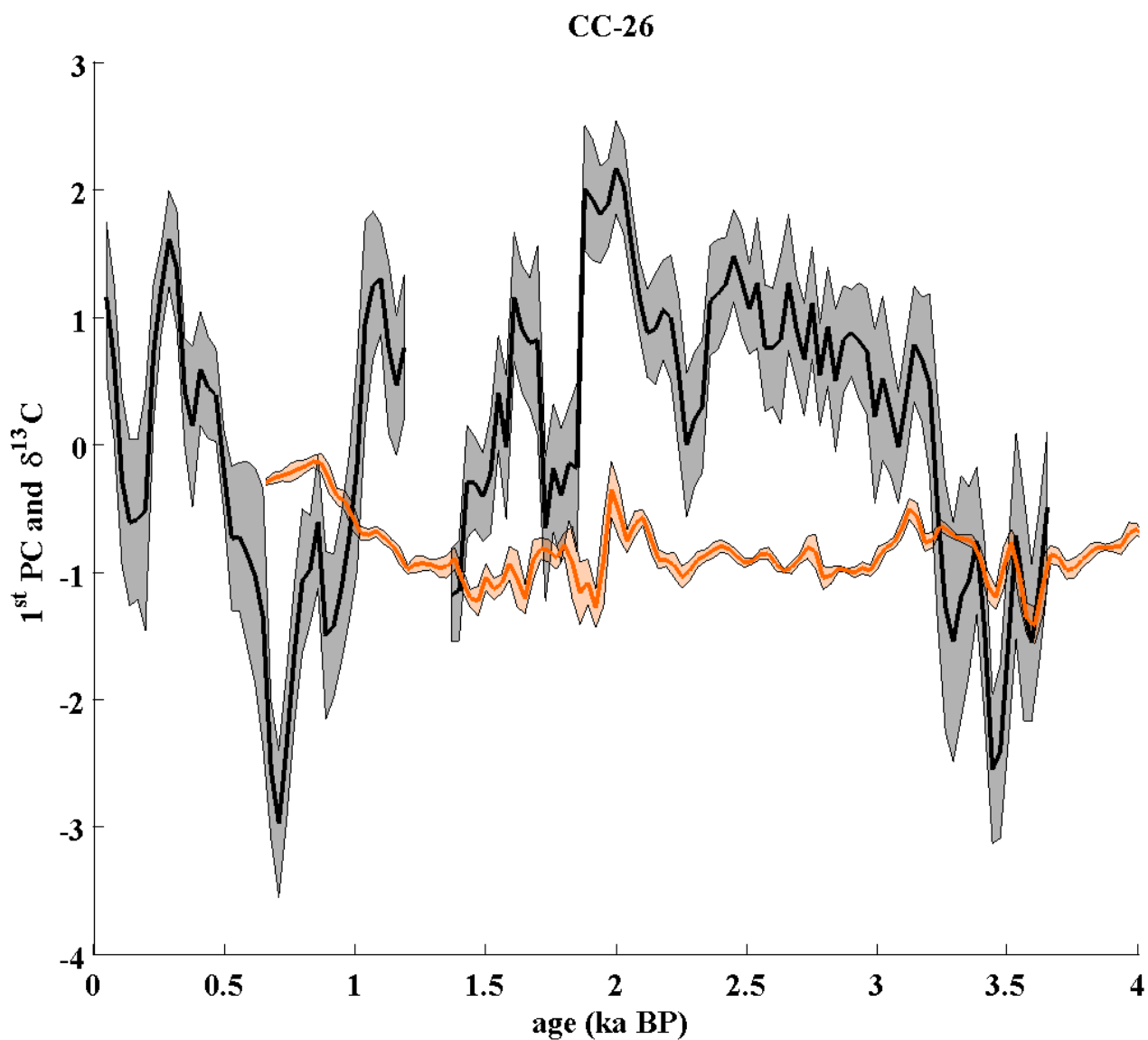


Fig. P.41: The figure is illustrating the computed 1st PC time series for the 4 ka long-term PCA (black line) including its 1-sigma confidence interval (grey shading area). Moreover, the figure pictures the standardised $\delta^{13}\text{C}$ time series of stalagmite CC-26 (orange line) with its 1-sigma confidence interval (orange shading area). The 1-sigma confidence interval is computed by using PCA.

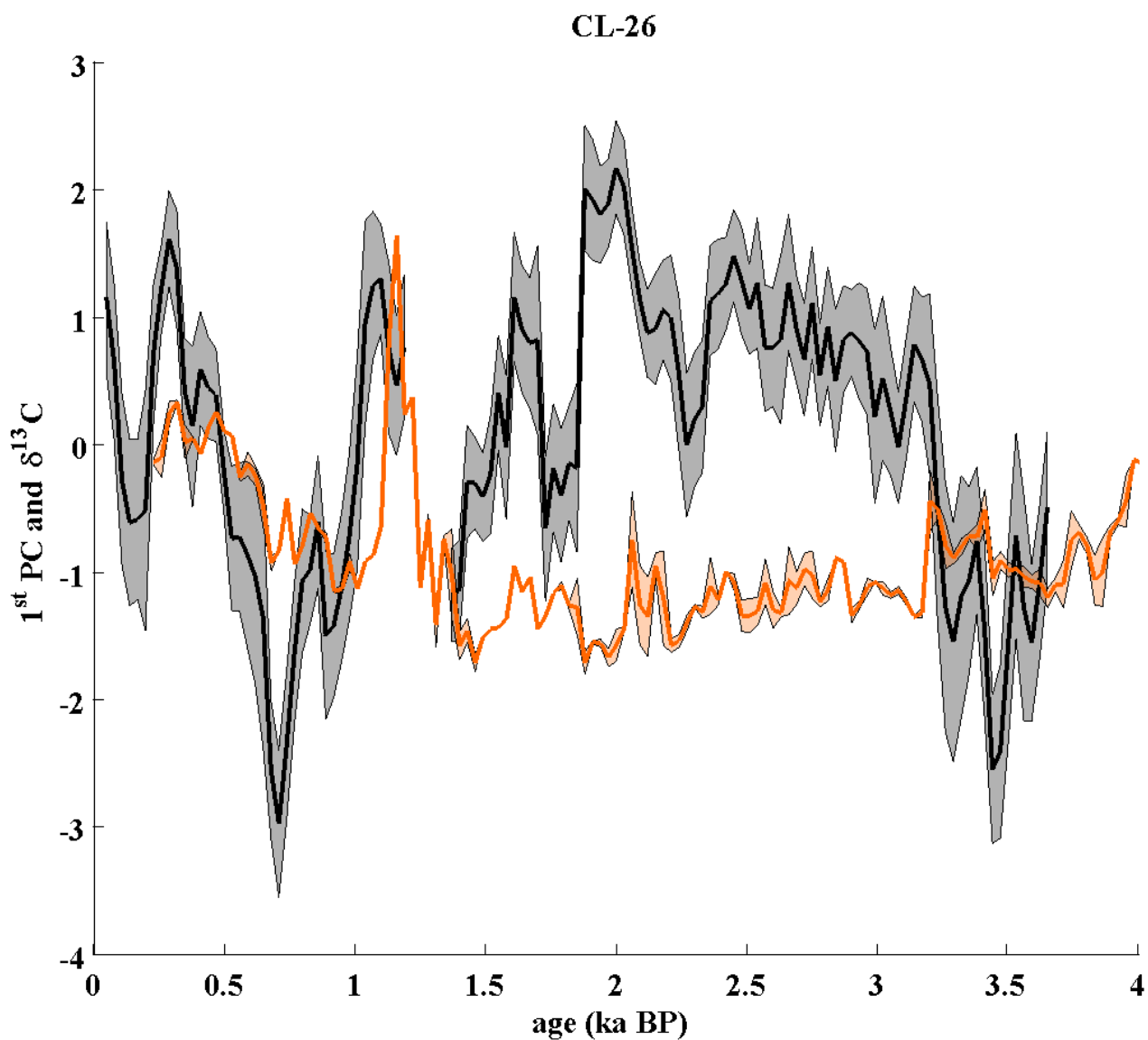


Fig. P.42: The figure is illustrating the computed 1st PC time series for the 4 ka long-term PCA (black line) including its 1-sigma confidence interval (grey shading area). Moreover, the figure pictures the standardised $\delta^{13}\text{C}$ time series of stalagmite CL-26 (orange line) with its 1-sigma confidence interval (orange shading area). The 1-sigma confidence interval is computed by using PCA.

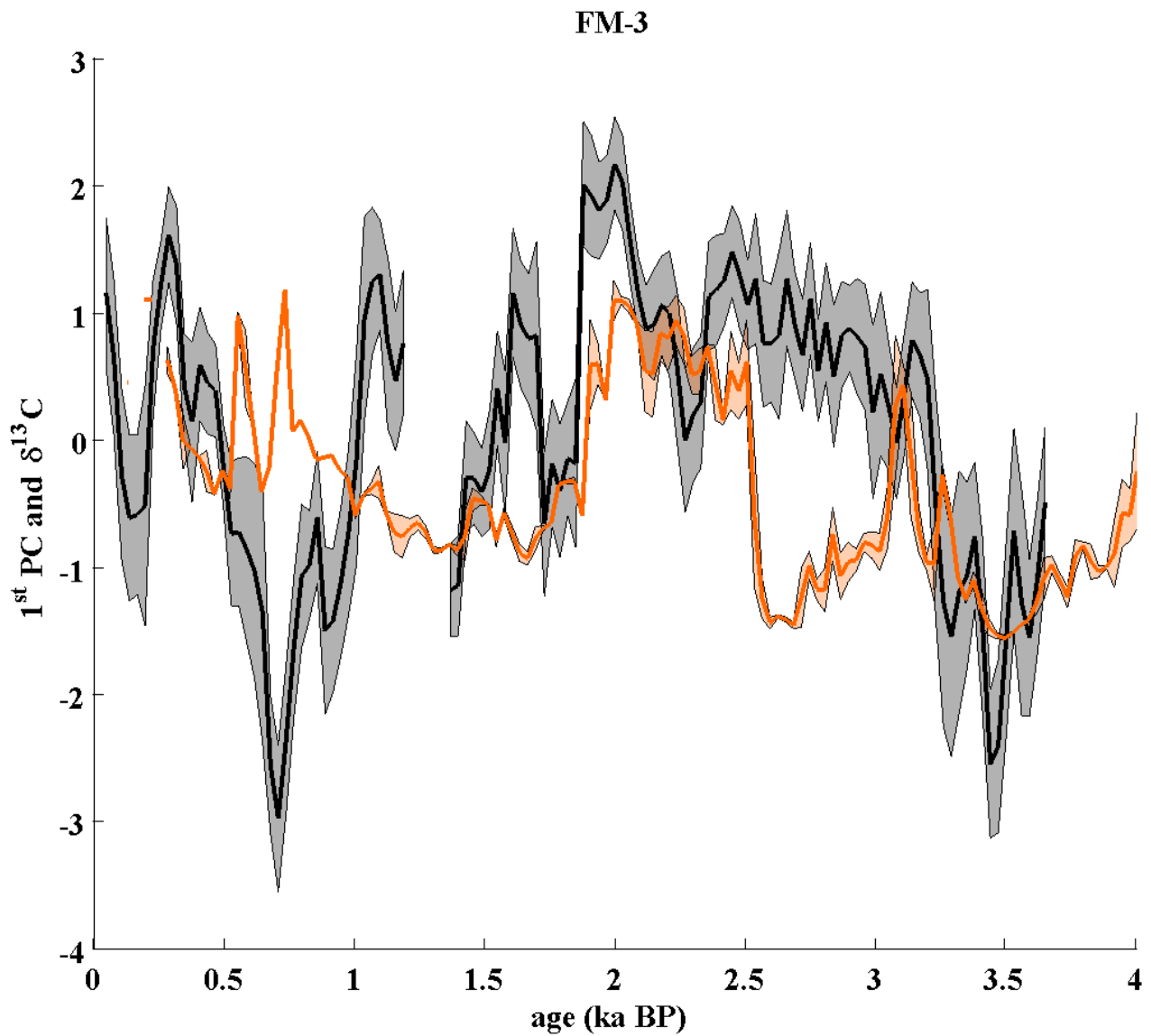


Fig. P.43: The figure is illustrating the computed 1st PC time series for the 4 ka long-term PCA (black line) including its 1-sigma confidence interval (grey shading area). Moreover, the figure pictures the standardised $\delta^{13}\text{C}$ time series of stalagmite FM-3 (orange line) with its 1-sigma confidence interval (orange shading area). The 1-sigma confidence interval is computed by using PCA.

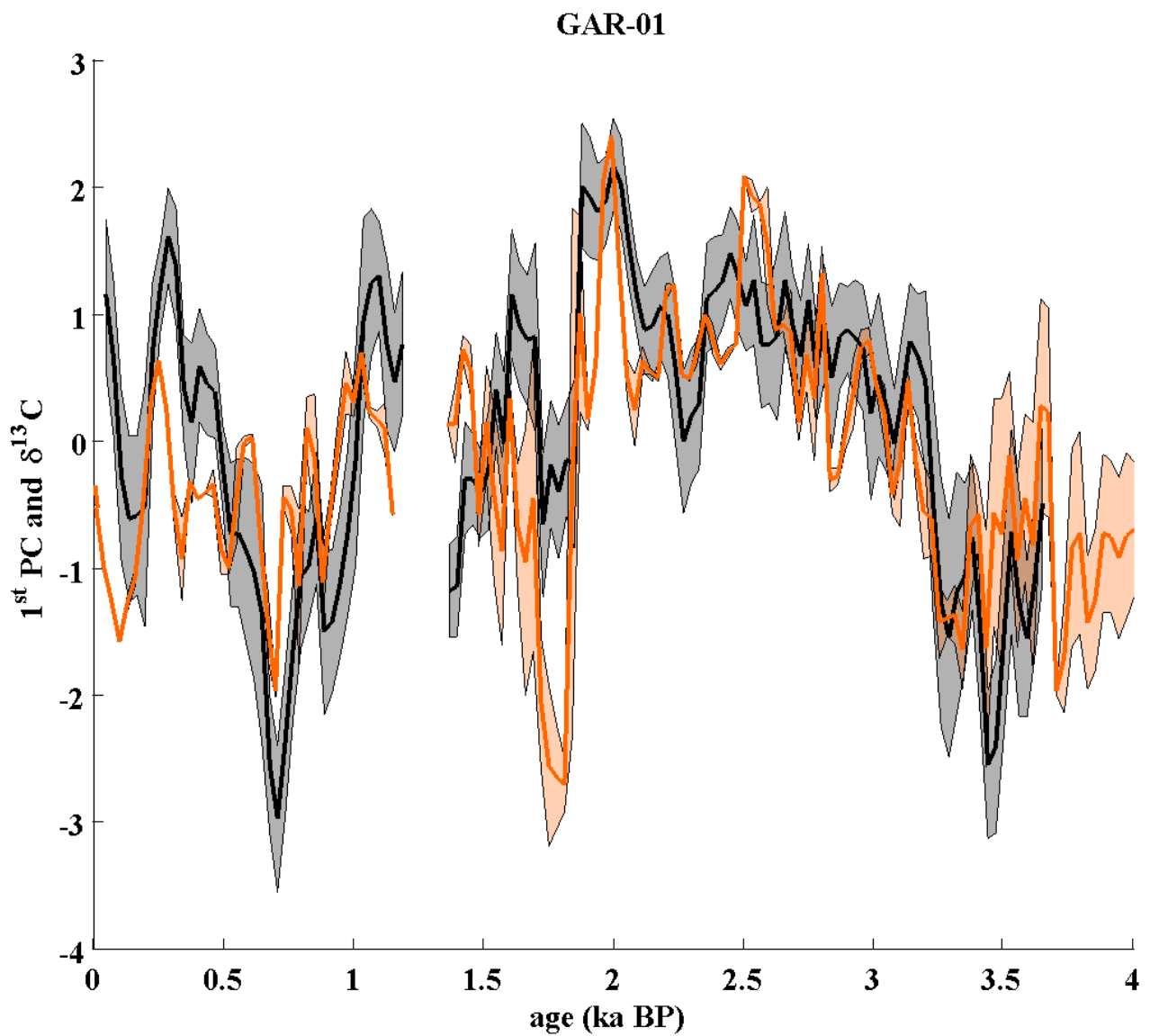


Fig. P.44: The figure is illustrating the computed 1st PC time series for the 4 ka long-term PCA (black line) including its 1-sigma confidence interval (grey shading area). Moreover, the figure pictures the standardised $\delta^{13}\text{C}$ time series of stalagmite GAR-01 (orange line) with its 1-sigma confidence interval (orange shading area). The 1-sigma confidence interval is computed by using PCA.

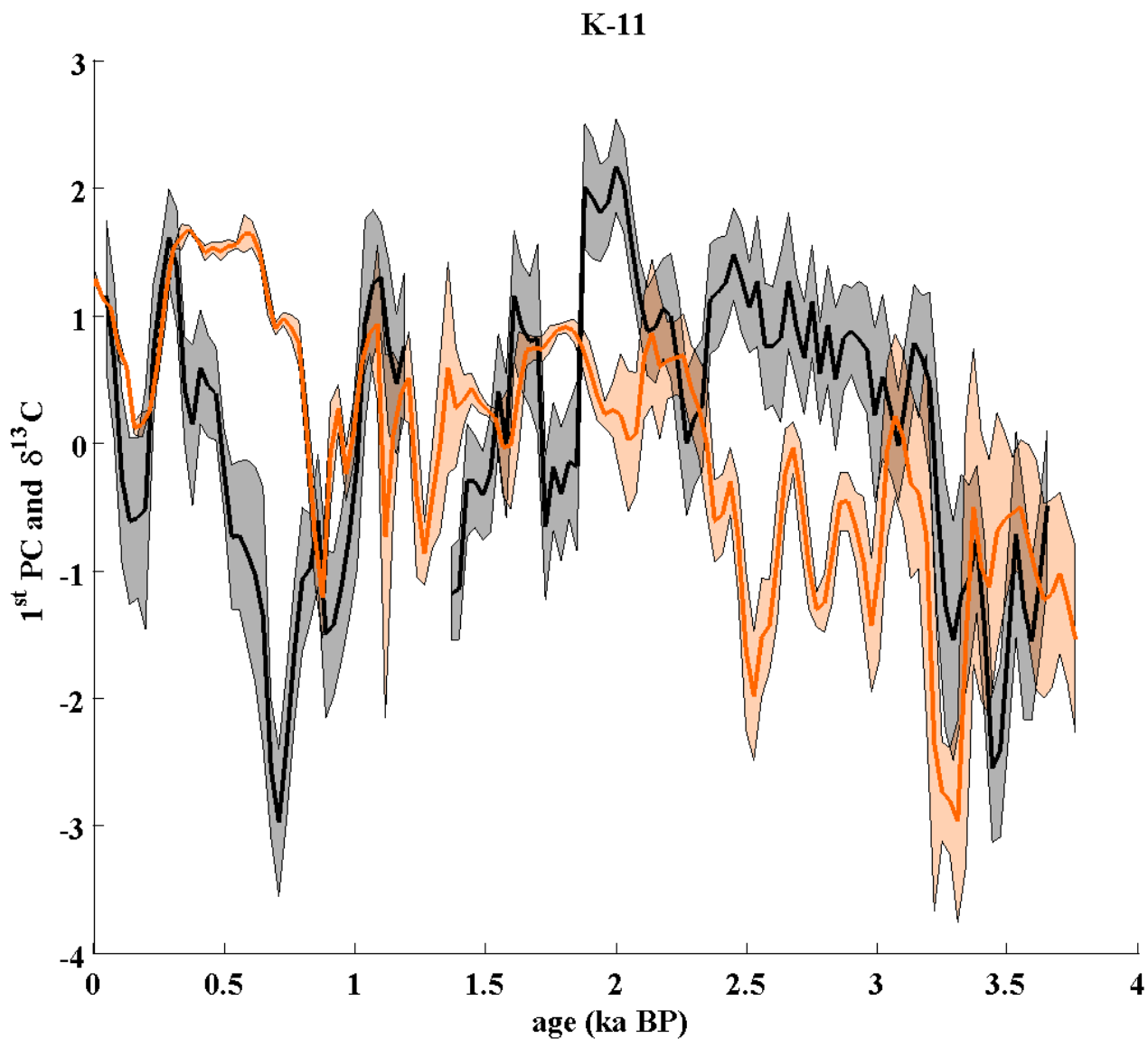


Fig. P.45: The figure is illustrating the computed 1st PC time series for the 4 ka long-term PCA (black line) including its 1-sigma confidence interval (grey shading area). Moreover, the figure pictures the standardised $\delta^{13}\text{C}$ time series of stalagmite K-1 (orange line) with its 1-sigma confidence interval (orange shading area). The 1-sigma confidence interval is computed by using PCA.

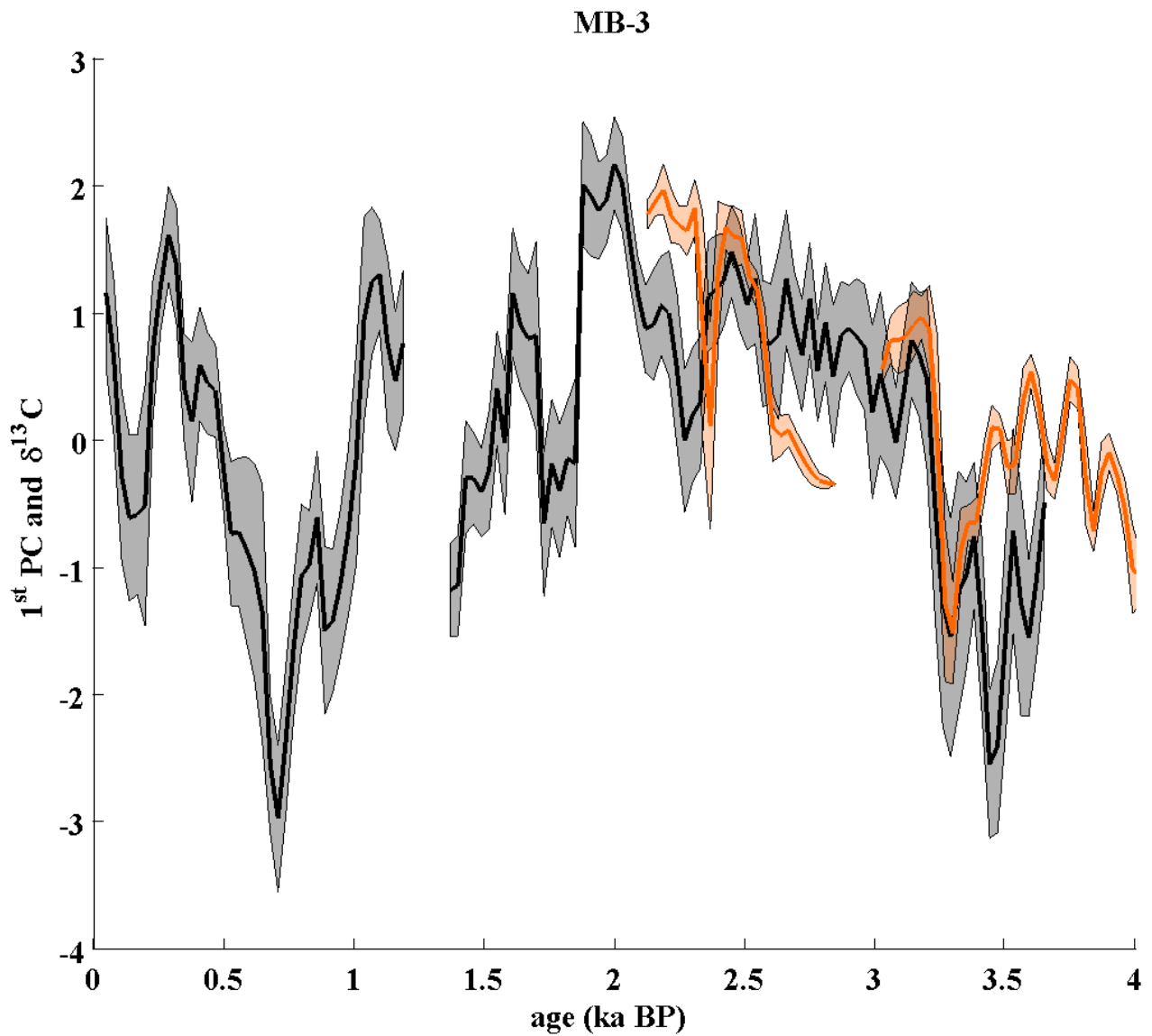


Fig. P.46: The figure is illustrating the computed 1st PC time series for the 4 ka long-term PCA (black line) including its 1-sigma confidence interval (grey shading area). Moreover, the figure pictures the standardised $\delta^{13}\text{C}$ time series of stalagmite MB-3 (orange line) with its 1-sigma confidence interval (orange shading area). The 1-sigma confidence interval is computed by using PCA.

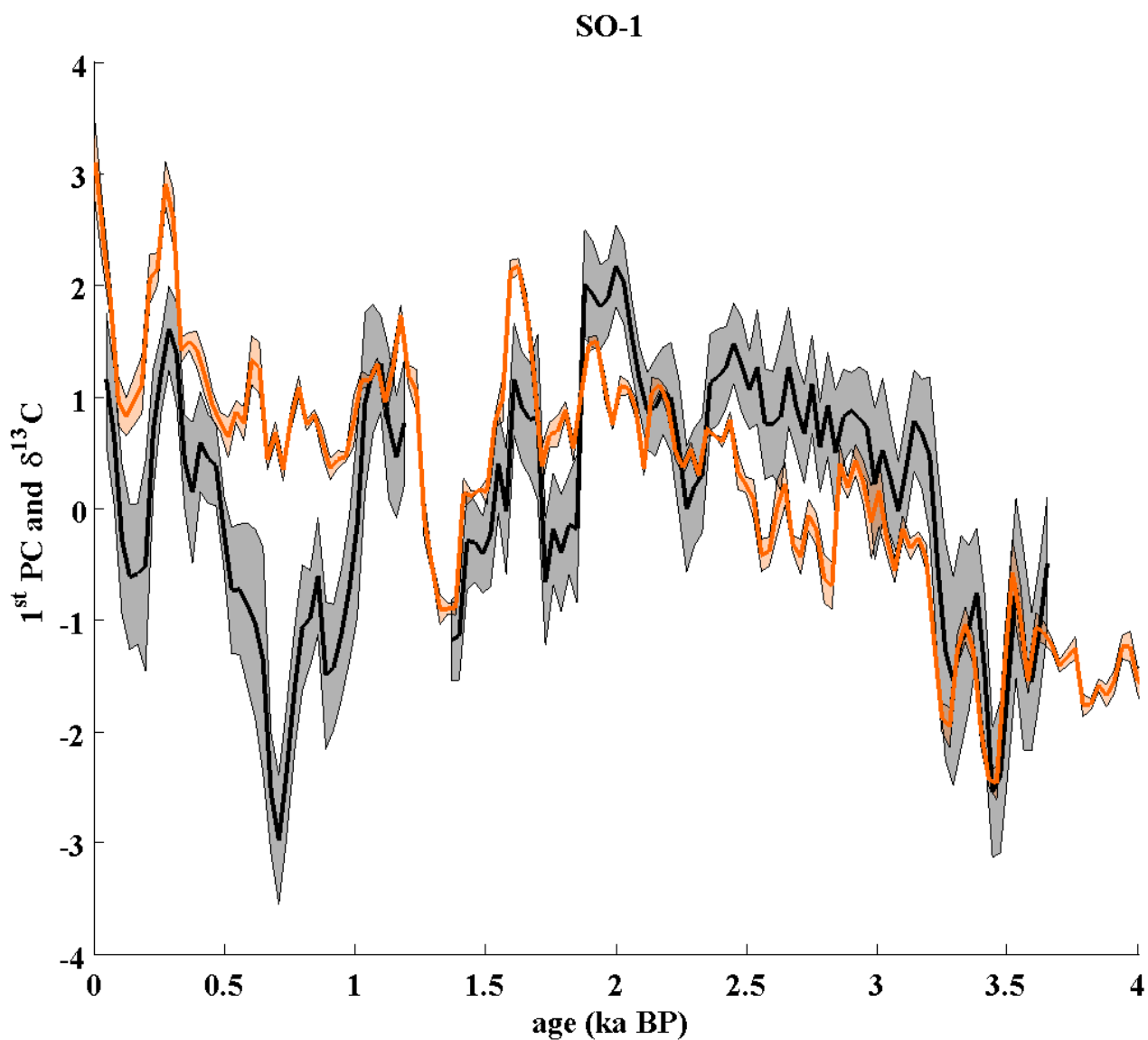


Fig. P.47: The figure is illustrating the computed 1st PC time series for the 4 ka long-term PCA (black line) including its 1-sigma confidence interval (grey shading area). Moreover, the figure pictures the standardised $\delta^{13}\text{C}$ time series of stalagmite SO-1 (orange line) with its 1-sigma confidence interval (orange shading area). The 1-sigma confidence interval is computed by using PCA.

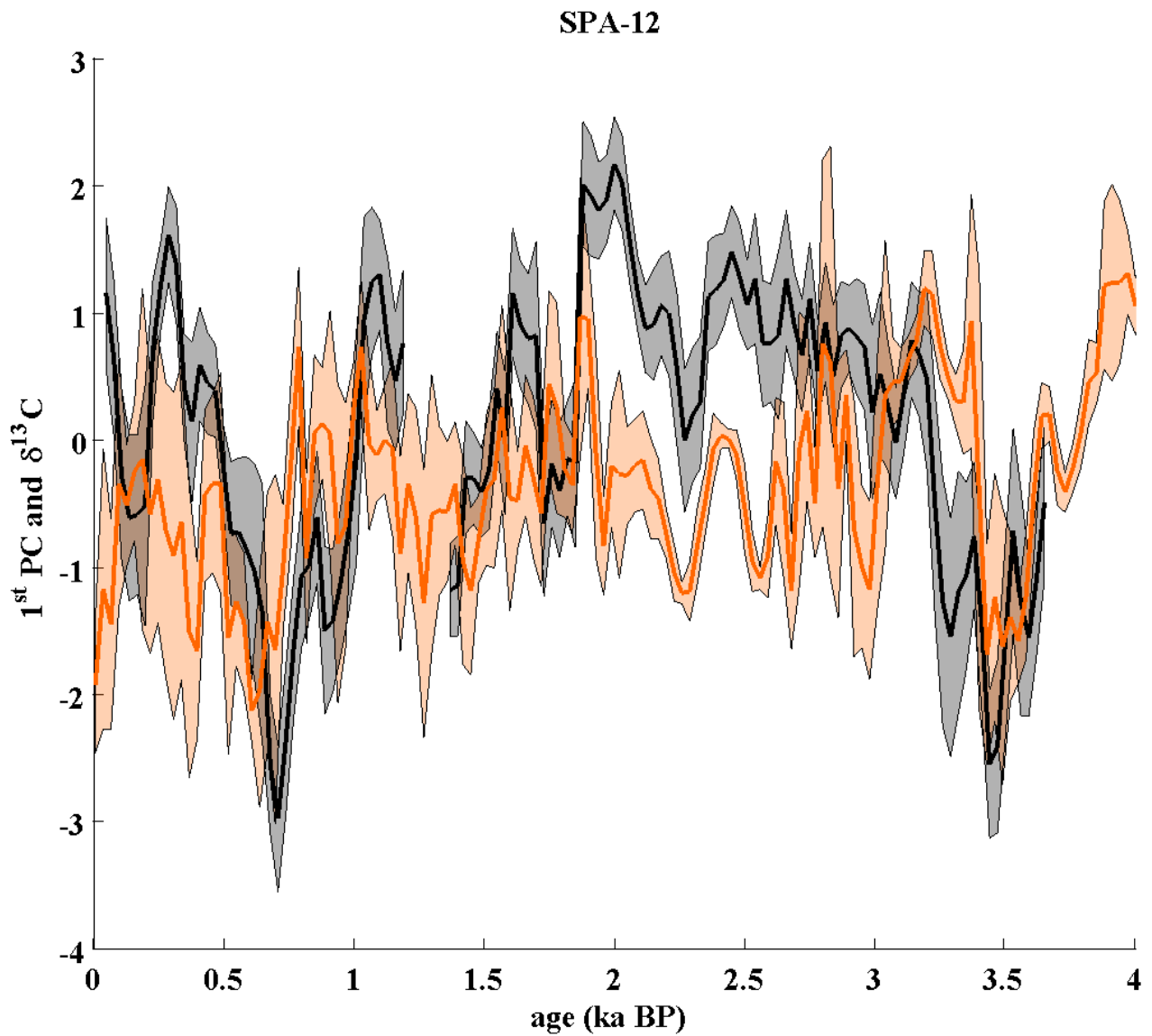


Fig. P.48: The figure is illustrating the computed 1st PC time series for the 4 ka long-term PCA (black line) including its 1-sigma confidence interval (grey shading area). Moreover, the figure pictures the standardised $\delta^{13}\text{C}$ time series of stalagmite SPA-12 (orange line) with its 1-sigma confidence interval (orange shading area). The 1-sigma confidence interval is computed by using PCA.

List of Figures

1.1	Cartoon of the causation of the speleothem formation	4
1.2	A picture from Crag Cave (Ireland)	5
1.3	Chart of the environmental impacts on speleothems	6
3.1	A simple chart of the karst system	13
3.2	TDIC vs pH	17
3.3	The three regions for calcite dissolution	19
3.4	Dissolution rate against. pCO ₂ and pH	20
4.1	Temporal evolution of the 230-Th and 238-U activity ratio	30
6.1	Schematic illustration of a Rayleigh process	40
7.1	Rayleigh approach for carbon isotopes of solution's HCO ₃ ⁻	45
7.2	Rayleigh approach for oxygen isotopes of solution's HCO ₃ ⁻	47
7.3	Illustration of the multi-box model for the solution layer	49
7.4	Illustration of the box model for the solution layer	50
7.5	Sensitivity of calcit's δ ¹⁸ O and δ ¹³ C values on temperature and drip interval	54
7.6	Sensitivity of calcit's δ ¹⁸ O and δ ¹³ C values on drip water's pCO ₂ and cave's air pCO ₂	55
8.1	Schematic illustration of oxygen fractionation effects	58
9.1	Comparison of derived ¹⁸ α _{calcite/H₂O} values from speleothems with the reaktion of Kim and O'Neil (1997)	66
10.1	Illustration of two variables that are anti correlated	77
10.2	Illustration of two variables before and after the PCA	78
10.3	Illustration of the up-side-down effect	79
10.4	Map of spleothem location	80
10.5	Age model of BU-4, CC-26, CC-3, GAR-01, SO-1	81
10.6	proxy-depth relation of BU-4, CC-26, CC-3, GAR-01, SO-1	83
10.7	Temporal resolution of BU-4, CC-26, CC-3, GAR-01, SO-1	84
10.8	Age-depth relation of BU-4	86
10.9	Ensemble of age-depth relations for BU-4 based on 1000 MC simulations .	88
10.10	Age-depth relation and proxy-depth relation for BU-4	89
10.11	Temporal resolution of BU-4	92
10.12	Temporal resolution of BU-4 between 5.0 and 8.0 ka BP	93
10.13	Temporal resolution of BU-4, CC-26, CC-3, GAR-01, SO-1 after equalisation	94

10.14	Re-sampling procedure for the ensemble of the 1st PC	95
10.15	Convergence of eigenvalues for 0-sigma age uncertainty	97
10.16	Convergence of eigenvalues for 1-sigma age uncertainty	99
10.17	Convergence of eigenvalues for 2-sigma age uncertainty	100
10.18	Eigenvalues for 0,1 and 2-sigma age uncertainty	101
10.19	Eigenvalues for AR 1, white noise and single speleothem time series	103
10.20	Effect of the window length on the eigenvalues	105
10.21	Distribution of r_s values between two AR-1 time series	106
10.22	Distribution of r_s values between two identical speleothem proxy time series	108
10.23	Effect of the window length on the eigenvalues for different time windows	109
10.24	Distribution of r_s values for WN time series	112
10.25	Distribution of r_s values for AR-1 time series	113
10.26	Distribution of r_s values for identical proxy time series	114
10.27	Distribution of r_s values for identical proxy time series	115
10.28	Comparison between eigenvalues for a compilation of $\delta^{18}\text{O}$ time series and WN time series.	118
10.29	Comparison between mean long-term and short-term 1 st PC time series	119
10.30	Comparison between mean long-term and short-term 1 st PC time series	120
11.1	Map showing GNIP stations	125
11.2	Map showing the transect T1 and T2	127
11.3	Stable isotopes in precipitation for T1	135
11.4	Oxygen isotope composition in drip water for T1	136
11.5	Oxygen isotope composition in calcite for T1	137
11.6	Stable isotopes in precipitation for T2	139
11.7	Oxygen isotope composition in calcite for T2	141
11.8	Stable isotopes in precipitation for different climates	143
11.9	Oxygen isotope composition in calcite for T1	144
11.10	Stable isotopes in precipitation along T1 for positive and negative NAO phases	146
11.11	Oxygen isotope composition in drip water for T1 for positive and negative NAO phases	148
11.12	Oxygen isotope composition in calcite for T1 for positive and negative NAO phases	149
12.1	The Global Speleothem Network	151
12.2	Map that shows the location of speleothems used for PCA	153
12.3	Mean temporal resolution of pre-selected speleothem proxy time series	155
12.4	Infiltration of water at selected cave locations	157
13.1	Age-models for the speleothems for 8000 year long-term and short-term PCA	161
13.2	1st PC time series for the last 8,000 years based on $\delta^{18}\text{O}$ time series	162
13.3	1st PC time series for the last 8,000 years based on $\delta^{13}\text{C}$ time series	163

13.4	The figure illustrates the spatio-temporal coherency pattern of the 1 st PC time series for three different compilations of $\delta^{18}\text{O}$ (right column) and $\delta^{13}\text{C}$ (left column) time series. For this the mean r_s values between the 1 st PC time series and the speleothem proxy time series are illustrated.	165
14.1	Age models of stalagmites used for long-term PCA of the last 4000 years .	168
14.2	1 st long-term PC time series of the last 4000 years.	169
14.3	1 st long-term PC time series of the last 4000 years.	170
14.4	Spatio-temporal coherence pattern for long-term PCA of the last 4000 years	171
14.5	1 st PC time series for the short-term PCA of the last 4000 years	179
14.6	Spatio-temporal coherence pattern for short-term PCA of the last 4000 years	180
14.7	Spatio-temporal coherence pattern for short-term PCA of the last 4000 years	181
14.8	Spatio-temporal coherence pattern for short-term PCA of the last 4000 years	182
14.9	1 st PC time series for the short-term PCA of the last 4000 years	183
14.10	Spatio-temporal coherence pattern for short-term PCA of the last 4000 years	184
14.11	Spatio-temporal coherence pattern for short-term PCA of the last 4000 years	185
14.12	Spatio-temporal coherence pattern for short-term PCA of the last 4000 years	186
15.1	1 st PC time series for the short-term PCA of the last 8000 years	189
15.2	1 st PC time series for the short-term PCA of the last 8000 years	190
15.3	Spatio-temporal coherence pattern for short-term PCA of the last 8000 years	192
15.4	Spatio-temporal coherence pattern for short-term PCA of the last 8000 years	193
15.5	Spatio-temporal coherence pattern for short-term PCA of the last 8000 years	195
15.6	Spatio-temporal coherence pattern for short-term PCA of the last 8000 years	196
16.1	10 ka 1st PC time series of a compilation of $\delta^{18}\text{O}$ time series	199
16.2	10 ka 1st PC of a compilation of $\delta^{13}\text{C}$ time series	200
16.3	Long-term spatio-temporal coherency pattern for the last 10 ka for $\delta^{18}\text{O}$ time series	202
16.4	Long-term spatio-temporal coherency pattern for the last 10 ka for $\delta^{13}\text{C}$ time series	203
17.1	Computed slope of speleothem $\delta^{18}\text{O}$ gradients for the Holocene	208
17.2	Computed slope of precipitation $\delta^{18}\text{O}$ gradients for the Holocene	211
17.3	Computed sensitivity of calcite and precipitation $\delta^{18}\text{O}$ gradients on $\Delta\gamma$. .	214
17.4	Computed sensitivity of calcite and precipitation $\delta^{18}\text{O}$ gradients on ΔP . .	215
17.5	Speleothem $\delta^{18}\text{O}$ at a 10 °W intercept	216
17.6	Comparison between the 1 st PC time series for the 8k and 4k long-term of the compilation of $\delta^{18}\text{O}$ time series	223
17.7	Comparison between the 1 st PC time series for the 8k and 4k long-term of the compilation of $\delta^{13}\text{C}$ time series	226
A.1	Distribution of r_s values for 8000 years long-term PCA on $\delta^{18}\text{O}$ time series	240
A.2	Distribution of r_s values for 8000 years long-term PCA on $\delta^{18}\text{O}$ time series	241

A.3	Distribution of r_s values for 8000 years long-term PCA on $\delta^{18}\text{O}$ time series	242
A.4	Distribution of r_s values for 8000 years long-term PCA on $\delta^{18}\text{O}$ time series	243
A.5	Distribution of r_s values for 8000 years long-term PCA on $\delta^{18}\text{O}$ time series	244
A.6	Distribution of r_s values for 8000 years long-term PCA on $\delta^{18}\text{O}$ time series	245
A.7	Distribution of r_s values for 8000 years long-term PCA on $\delta^{18}\text{O}$ time series	246
A.8	Distribution of r_s values for 8000 years long-term PCA on $\delta^{18}\text{O}$ time series	247
A.9	Distribution of r_s values for 8000 years long-term PCA on $\delta^{18}\text{O}$ time series	248
A.10	Distribution of r_s values for 8000 years long-term PCA on $\delta^{18}\text{O}$ time series	249
A.11	Distribution of r_s values for 8000 years long-term PCA on $\delta^{18}\text{O}$ time series	250
A.12	Distribution of r_s values for 8000 years long-term PCA on $\delta^{18}\text{O}$ time series	251
B.1	Temperature and precipitation for T1	253
B.2	Temperature, precipitation for T2	254
B.3	Temperature and Precipitation changes for the sensitivity study of the SIP model	255
B.4	Temperature, precipitation and evapo-transpiration for positive and negative wNAO phases	256
C.1	The European speleothem network	257
C.2	Number of speleothems records against time for speleothems usable for PCA	262
D.1	Eigenvalues of the 8k long-term PCA	264
D.2	Eigenvalues of the 8k long-term PCA	265
E.1	Distribution of r_s values for 8000 years long-term PCA on $\delta^{18}\text{O}$ time series of run #1	267
E.2	Distribution of r_s values for 8000 years long-term PCA on $\delta^{18}\text{O}$ time series of run #2	268
E.3	Distribution of r_s values for 8000 years long-term PCA on $\delta^{18}\text{O}$ time series of run #2	269
E.4	Distribution of r_s values for 8000 years long-term PCA on $\delta^{18}\text{O}$ time series of run #3	270
E.5	Distribution of r_s values for 8000 years long-term PCA on $\delta^{18}\text{O}$ time series of run #3	271
E.6	Distribution of r_s values for 8000 years long-term PCA on $\delta^{13}\text{C}$ time series of run #1	273
E.7	Distribution of r_s values for 8000 years long-term PCA on $\delta^{13}\text{C}$ time series of run #2	274
E.8	Distribution of r_s values for 8000 years long-term PCA on $\delta^{13}\text{C}$ time series of run #2	275
E.9	Distribution of r_s values for 8000 years long-term PCA on $\delta^{13}\text{C}$ time series of run #3	276
E.10	Distribution of r_s values for 8000 years long-term PCA on $\delta^{13}\text{C}$ time series of run #3	277

J.13	Distribution of r_s values for 4000 years short-term PCA on $\delta^{18}\text{O}$ time series	366
J.14	Distribution of r_s values for 4000 years short-term PCA on $\delta^{18}\text{O}$ time series	367
J.15	Distribution of r_s values for 4000 years short-term PCA on $\delta^{18}\text{O}$ time series	368
J.16	Distribution of r_s values for 4000 years short-term PCA on $\delta^{18}\text{O}$ time series	369
J.17	Distribution of r_s values for 4000 years short-term PCA on $\delta^{18}\text{O}$ time series	370
J.18	Distribution of r_s values for 4000 years short-term PCA on $\delta^{18}\text{O}$ time series	371
J.19	Distribution of r_s values for 4000 years short-term PCA on $\delta^{13}\text{C}$ time series	373
J.20	Distribution of r_s values for 4000 years short-term PCA on $\delta^{13}\text{C}$ time series	374
J.21	Distribution of r_s values for 4000 years short-term PCA on $\delta^{13}\text{C}$ time series	375
J.22	Distribution of r_s values for 4000 years short-term PCA on $\delta^{13}\text{C}$ time series	376
J.23	Distribution of r_s values for 4000 years short-term PCA on $\delta^{13}\text{C}$ time series	377
J.24	Distribution of r_s values for 4000 years short-term PCA on $\delta^{13}\text{C}$ time series	378
J.25	Distribution of r_s values for 4000 years short-term PCA on $\delta^{13}\text{C}$ time series	379
J.26	Distribution of r_s values for 4000 years short-term PCA on $\delta^{13}\text{C}$ time series	380
J.27	Distribution of r_s values for 4000 years short-term PCA on $\delta^{13}\text{C}$ time series	381
J.28	Distribution of r_s values for 4000 years short-term PCA on $\delta^{13}\text{C}$ time series	382
J.29	Distribution of r_s values for 4000 years short-term PCA on $\delta^{13}\text{C}$ time series	383
J.30	Distribution of r_s values for 4000 years short-term PCA on $\delta^{13}\text{C}$ time series	384
J.31	Distribution of r_s values for 4000 years short-term PCA on $\delta^{13}\text{C}$ time series	385
J.32	Distribution of r_s values for 4000 years short-term PCA on $\delta^{13}\text{C}$ time series	386
J.33	Distribution of r_s values for 4000 years short-term PCA on $\delta^{13}\text{C}$ time series	387
J.34	Distribution of r_s values for 4000 years short-term PCA on $\delta^{13}\text{C}$ time series	388
J.35	Distribution of r_s values for 4000 years short-term PCA on $\delta^{13}\text{C}$ time series	389
J.36	Distribution of r_s values for 4000 years short-term PCA on $\delta^{13}\text{C}$ time series	390
K.1	Eigenvalues of the 10k long-term PCA	392
L.1	Distribution of r_s values for 10,000 years long-term PCA on $\delta^{18}\text{O}$ time series	394
L.2	Distribution of r_s values for 10,000 years long-term PCA on $\delta^{18}\text{O}$ time series	395
L.3	Distribution of r_s values for 10,000 years long-term PCA on $\delta^{13}\text{C}$ time series	396
M.1	Computed slope of speleothem $\delta^{18}\text{O}$ gradients against wNAO index	398
M.2	Computed slope of precipitation $\delta^{18}\text{O}$ gradients against wNAO index . . .	399
N.1	$\delta^{18}\text{O}$ time series for the sea level and temperature effect for the 10 °W intercept	401
O.1	$\delta^{18}\text{O}$ values of evaporative moisture in dependence on T and h	403
P.1	Comparison of the 1 st PC time series with the $\delta^{18}\text{O}$ time series of BU-4 for the last 8000 years	405
P.2	Comparison of the 1 st PC time series with the $\delta^{18}\text{O}$ time series of C09-2 for the last 8000 years	406
P.3	Comparison of the 1 st PC time series with the $\delta^{18}\text{O}$ time series of CC-3 for the last 8000 years	407

List of Figures

P.4	Comparison of the 1 st PC time series with the $\delta^{18}\text{O}$ time series of CC-26 for the last 8000 years	408
P.5	Comparison of the 1 st PC time series with the $\delta^{18}\text{O}$ time series of CL-26 for the last 8000 years	409
P.6	Comparison of the 1 st PC time series with the $\delta^{18}\text{O}$ time series of CR-1 for the last 8000 years	410
P.7	Comparison of the 1 st PC time series with the $\delta^{18}\text{O}$ time series of FM-3 for the last 8000 years	411
P.8	Comparison of the 1 st PC time series with the $\delta^{18}\text{O}$ time series of GAR-01 for the last 8000 years	412
P.9	Comparison of the 1 st PC time series with the $\delta^{18}\text{O}$ time series of GP-2 for the last 8000 years	413
P.10	Comparison of the 1 st PC time series with the $\delta^{18}\text{O}$ time series of K-1 for the last 8000 years	414
P.11	Comparison of the 1 st PC time series with the $\delta^{18}\text{O}$ time series of MB-3 for the last 8000 years	415
P.12	Comparison of the 1 st PC time series with the $\delta^{18}\text{O}$ time series of SO-1 for the last 8000 years	416
P.13	Comparison of the 1 st PC time series with the $\delta^{18}\text{O}$ time series of SPA-12 for the last 8000 years	417
P.14	Comparison of the 1 st PC time series with the $\delta^{18}\text{O}$ time series of Sv-1 for the last 8000 years	418
P.15	Comparison of the 1 st PC time series with the $\delta^{18}\text{O}$ time series of BU-4 for the last 4000 years	419
P.16	Comparison of the 1 st PC time series with the $\delta^{18}\text{O}$ time series of C09-2 for the last 4000 years	420
P.17	Comparison of the 1 st PC time series with the $\delta^{18}\text{O}$ time series of CC-3 for the last 4000 years	421
P.18	Comparison of the 1 st PC time series with the $\delta^{18}\text{O}$ time series of CC-26 for the last 4000 years	422
P.19	Comparison of the 1 st PC time series with the $\delta^{18}\text{O}$ time series of CL-26 for the last 4000 years	423
P.20	Comparison of the 1 st PC time series with the $\delta^{18}\text{O}$ time series of FM-3 for the last 4000 years	424
P.21	Comparison of the 1 st PC time series with the $\delta^{18}\text{O}$ time series of GAR-01 for the last 4000 years	425
P.22	Comparison of the 1 st PC time series with the $\delta^{18}\text{O}$ time series of K-1 for the last 4000 years	426
P.23	Comparison of the 1 st PC time series with the $\delta^{18}\text{O}$ time series of SO-1 for the last 4000 years	427
P.24	Comparison of the 1 st PC time series with the $\delta^{18}\text{O}$ time series of SPA-12 for the last 4000 years	428

P.25 Comparison of the 1 st PC time series with the $\delta^{18}\text{O}$ time series of SV-1 for the last 4000 years	429
P.26 Comparison of the 1 st PC time series with the $\delta^{13}\text{C}$ time series of BU-4 for the last 8000 years	430
P.27 Comparison of the 1 st PC time series with the $\delta^{13}\text{C}$ time series of C09-2 for the last 8000 years	431
P.28 Comparison of the 1 st PC time series with the $\delta^{13}\text{C}$ time series of CC-3 for the last 8000 years	432
P.29 Comparison of the 1 st PC time series with the $\delta^{13}\text{C}$ time series of CC-26 for the last 8000 years	433
P.30 Comparison of the 1 st PC time series with the $\delta^{13}\text{C}$ time series of CL-26 for the last 8000 years	434
P.31 Comparison of the 1 st PC time series with the $\delta^{13}\text{C}$ time series of CR-1 for the last 8000 years	435
P.32 Comparison of the 1 st PC time series with the $\delta^{13}\text{C}$ time series of FM-3 for the last 8000 years	436
P.33 Comparison of the 1 st PC time series with the $\delta^{13}\text{C}$ time series of FM-3 for the last 8000 years	437
P.34 Comparison of the 1 st PC time series with the $\delta^{13}\text{C}$ time series of K-1 for the last 8000 years	438
P.35 Comparison of the 1 st PC time series with the $\delta^{13}\text{C}$ time series of MB-3 for the last 8000 years	439
P.36 Comparison of the 1 st PC time series with the $\delta^{13}\text{C}$ time series of SO-1 for the last 8000 years	440
P.37 Comparison of the 1 st PC time series with the $\delta^{13}\text{C}$ time series of SPA-12 for the last 8000 years	441
P.38 Comparison of the 1 st PC time series with the $\delta^{13}\text{C}$ time series of BU-4 for the last 4000 years	442
P.39 Comparison of the 1 st PC time series with the $\delta^{13}\text{C}$ time series of C09-2 for the last 4000 years	443
P.40 Comparison of the 1 st PC time series with the $\delta^{13}\text{C}$ time series of CC-3 for the last 4000 years	444
P.41 Comparison of the 1 st PC time series with the $\delta^{13}\text{C}$ time series of CC-26 for the last 4000 years	445
P.42 Comparison of the 1 st PC time series with the $\delta^{13}\text{C}$ time series of CL-26 for the last 4000 years	446
P.43 Comparison of the 1 st PC time series with the $\delta^{13}\text{C}$ time series of FM-3 for the last 4000 years	447
P.44 Comparison of the 1 st PC time series with the $\delta^{13}\text{C}$ time series of GAR-01 for the last 4000 years	448
P.45 Comparison of the 1 st PC time series with the $\delta^{13}\text{C}$ time series of K-1 for the last 4000 years	449

List of Figures

P.46 Comparison of the 1 st PC time series with the $\delta^{13}\text{C}$ time series of MB-3 for the last 4000 years	450
P.47 Comparison of the 1 st PC time series with the $\delta^{13}\text{C}$ time series of SO-1 for the last 4000 years	451
P.48 Comparison of the 1 st PC time series with the $\delta^{13}\text{C}$ time series of SPA-12 for the last 4000 years	452

List of Tables

5.1	Used isotope fractionation factors	37
11.1	Used GNIP station data	134
11.2	Used GNIP station data	138
11.3	GNIP station data of T1 for NAO plus and minus phases	145
12.1	Selected European speleothem studies for PCA use	154
13.1	Results of TEV for long-term analysis of the last 8,000 years.	160
14.1	TEV of short-term 1st PC time series for the 4k run	174
15.1	TEV of short-term 1st PC time series for the 8k run	191
16.1	Results of TEV for long-term analysis of the last 10,000 years.	198
17.1	Slope of the $\delta^{18}\text{O}$ gradient of CE speleothems	209
C.1	Compilation of European speleothem studies	258
C.2	Compilation of European speleothem studies	259
C.3	Compilation of European speleothem studies	260
C.4	Compilation of European speleothem studies	261

Acknowledgments

Wow, it's almost done, ... I'd like to thank (formally) my supervisor Prof. Augusto Mangini who gave me the opportunity and the freedom to begin this journey on the wide fields of palaeo climate and speleothem science. The benefit for my personal development is not measurable in SI units and is far beyond of what I have imagined when I started to work in his group five years ago as laboratory assistant. His trust in me and my work gave me the energy to continue my studies during the heavy passages of my PhD journey. Now I almost succeed (I'm writing at the moment) and only a few lines are (yet) missing. To bring this PhD project to an END I simply say (personally) "THANK YOU!" Augusto you are the supervisor of my heart! and a true friend!

However, there was of course not only Prof. Augusto Mangini who supported me. I'd really like to THANK (formally and personally) Prof. Frank McDermott who supported me at some stages (throughout) of my PhD journey whenever we've seen each other. Frank "THANK YOU!" for all the feedback you gave me and for the change that I could stay at UCD (Dublin, Ireland) for some month. I must note that my theses were really pushed forward during these (I think it was) two month. THANKS! again! Frank!

PS: And what people tell about Ireland is not true, it is not that rainy there! There are sunny days, I've seen them, felt them! I actually had more sunny days than rainy days (I think)! I love Ireland!

I also thank Prof. Werner Aeschbach Hertig who is the second supervisor of PhD thesis. I hope it is not too long, ...

Here we are - the University family: I don't know where to start, because there are many of them, colleges-friends, ... Well lets go: Thank you Jörg L., Jens F., Andrea S.-R., Anne W., Daniela P., Evelyn B., Christoph S., Adrian I., Denis S., Rene E., Wolfgang D., Manfred M., Nicole V., Dirk H., Sophie W., Patrick B., Benny A., Tobi T., Claudia F., Gabi S., Caro M., Chris K., Alex V. (the order of the names states nothing! Really!).

Also many thanks to PhD students from various Universities who become friends: Laia, Domi, Inga, Meithe, Meighan, Yuval, Kerstin, Ana, Dana, Simon, S⁴ ... (I'm sure I forgot some people, ...)

Family: Thank you, Thank you, Thank you **Agnes D., Manfred D. and Anne D.**

CA-Family: Thank you, Thank you, Thank you **Richard and JoAnne S.**

Family again: Thank you Family!

Finally: Thank you Thomas A., Bernd, J., Christian J. who are friends for a very long time; Matthias W., Raphael W. Sara-Ann L., Tina B. who are the other part of my family. Thank you! to the numerous people who were/are still part of my life and have influenced my evolution!

THANK YOU TO ALL OF YOU!

References

- Ahmed M., Anchukaitis K.J., Asrat A., Borgaonkar H.P., Braida M., Buckley B.M., Büntgen U., Chase B.M., Christie D.A. and Cook E.R. (2013). “Continental-scale temperature variability during the past two millennia.” *Nature Geoscience*.
- Anchukaitis K.J. and Tierney J.E. (2012). “Identifying coherent spatiotemporal modes in time-uncertain proxy paleoclimate records.” *Climate Dynamics*: 1–16.
- Anderson T.F. (1969). “Self-diffusion of carbon and oxygen in calcite by isotope exchange with carbon dioxide.” *Journal of Geophysical Research*, 74(15): 3918–3932.
- Andrews J. (2006). “Palaeoclimatic records from stable isotopes in riverine tufas: synthesis and review.” *Earth-Science Reviews*, 75(1): 85–104.
- Atkinson T. (1977). “Carbon dioxide in the atmosphere of the unsaturated zone: an important control of groundwater hardness in limestones.” *Journal of Hydrology*, 35(1): 111–123.
- Bahr A., Lamy F., Arz H.W., Major C., Kwiecien O. and Wefer G. (2008). “Abrupt changes of temperature and water chemistry in the late Pleistocene and early Holocene Black Sea.” *Geochemistry Geophysics Geosystems*, 9(1): Q01004.
- Baker A., Genty D., Dreybrodt W., Barnes W.L., Mockler N.J. and Grapes J. (1998). “Testing theoretically predicted stalagmite growth rate with recent annually laminated samples: Implications for past stalagmite deposition.” *Geochimica et Cosmochimica Acta*, 62(3): 393–404.
- Baldini L.M., McDermott F., Foley A.M. and Baldini J.U. (2008). “Spatial variability in the European winter precipitation $\delta^{18}\text{O}$ -NAO relationship: Implications for reconstructing NAO-mode climate variability in the Holocene.” *Geophysical Research Letters*, 35(4): L04709.
- Bar-Matthews M., Ayalon A., Matthews A., Sass E. and Halicz L. (1996). “Carbon and oxygen isotope study of the active water-carbonate system in a karstic Mediterranean cave: Implications for paleoclimate research in semiarid regions.” *Geochimica et Cosmochimica Acta*, 60(2): 337–347.
- Beck W.C., Grossman E.L. and Morse J.W. (2005). “Experimental studies of oxygen isotope fractionation in the carbonic acid system at 15, 25, and 40 C.” *Geochimica et Cosmochimica Acta*, 69(14): 3493–3503.
- Broecker W.S., *The glacial world according to Wally*. Eldigio Press, 1995.

- Broecker W.S., Olson E.A. and ORR P.C. (1960).** “Radiocarbon measurements and annual rings in cave formations.”
- Brutsaert W. (1975a).** “The roughness length for water vapor sensible heat, and other scalars.” *Journal of the Atmospheric Sciences*, 32(10): 2028–2031.
- Brutsaert W. (1975b).** “A theory for local evaporation (or heat transfer) from rough and smooth surfaces at ground level.” *Water Resources Research*, 11(4): 543–550.
- Buhmann D. and Dreybrodt W. (1985a).** “The kinetics of calcite dissolution and precipitation in geologically relevant situations of karst areas: 1. Open system.” *Chemical Geology*, 48(1): 189–211.
- Buhmann D. and Dreybrodt W. (1985b).** “The kinetics of calcite dissolution and precipitation in geologically relevant situations of karst areas: 2. Closed system.” *Chemical Geology*, 53(1): 109–124.
- Busenberg E. and Plummer L. (1986).** “A comparative study of the dissolution and crystal growth kinetics of calcite and aragonite.” *US Geol. Surv. Bull.*, 1578: 139–168.
- Cheng H., Edwards R., Hoff J., Gallup C., Richards D. and Asmerom Y. (2000).** “The half-lives of uranium-234 and thorium-230.” *Chemical Geology*, 169(1): 17–33.
- Christiansen B. and Charpentier Ljungqvist F. (2012).** “The extra-tropical Northern Hemisphere temperature in the last two millennia: reconstructions of low-frequency variability.” *Climate of the Past*, 8(2): 765–786.
- Comas-Bru L. and McDermott F. (2013).** “Impacts of the EA and SCA patterns on the European twentieth century NAO-winter climate relationship.” *Quarterly Journal of the Royal Meteorological Society*.
- Coplen T.B. (2007).** “Calibration of the calcite–water oxygen-isotope geothermometer at Devils Hole, Nevada, a natural laboratory.” *Geochimica et Cosmochimica Acta*, 71(16): 3948–3957.
- Coplen T.B., Winograd I.J., Landwehr J.M. and Riggs A.C. (1994).** “500,000-year stable carbon isotopic record from Devils Hole, Nevada.” *Science*, 263(5145): 361–365.
- Craig H., Gordon L. and Horibe Y. (1963).** “Isotopic exchange effects in the evaporation of water: 1. Low-temperature experimental results.” *Journal of Geophysical Research*, 68(17): 5079–5087.
- Craig H. and Gordon L.I.,** *Deuterium and oxygen 18 variations in the ocean and the marine atmosphere.* Consiglio nazionale delle ricerche, Laboratorio de geologia nucleare, 1965.
- Cruz F.W., Vuille M., Burns S.J., Wang X., Cheng H., Werner M., Edwards R.L., Karmann I., Auler A.S. and Nguyen H. (2009).** “Orbitally driven east–west antiphasing of South American precipitation.” *Nature Geoscience*, 2(3): 210–214.

- Dambach F. (2012).** “Tropfsteine als Palaeoklimaarchive - Kartographische Darstellung und wissenschaftliche Einordnung einer Auswahl weltweiter Untersuchungen seit 1995.” *Bachelor Thesis*.
- Dansgaard W. (1964).** “Stable isotopes in precipitation.” *Tellus*, 16(4): 436–468.
- Darling W. (2004).** “Hydrological factors in the interpretation of stable isotopic proxy data present and past: a European perspective.” *Quaternary Science Reviews*, 23(7): 743–770.
- Davis B., Brewer S., Stevenson A. and Guiot J. (2003).** “The temperature of Europe during the Holocene reconstructed from pollen data.” *Quaternary Science Reviews*, 22(15): 1701–1716.
- Day C. and Henderson G. (2011).** “Oxygen isotopes in calcite grown under cave-analogue conditions.” *Geochimica et Cosmochimica Acta*, 75(14): 3956–3972.
- Deines P. (1980).** “The isotopic composition of reduced organic carbon.” *Handbook of environmental isotope geochemistry*: 329–406.
- Deininger M., Fohlmeister J., Scholz D. and Mangini A. (2012).** “Isotope disequilibrium effects: The influence of evaporation and ventilation effects on the carbon and oxygen isotope composition of speleothems-A model approach.” *Geochimica et Cosmochimica Acta*.
- Dennis P., Rowe P. and Atkinson T. (2001).** “The recovery and isotopic measurement of water from fluid inclusions in speleothems.” *Geochimica et Cosmochimica Acta*, 65(6): 871–884.
- DePaolo D.J. (2011).** “Surface kinetic model for isotopic and trace element fractionation during precipitation of calcite from aqueous solutions.” *Geochimica et Cosmochimica Acta*, 75(4): 1039–1056.
- Dietzel M., Tang J., Leis A. and Köhler S.J. (2009).** “Oxygen isotopic fractionation during inorganic calcite precipitation-Effects of temperature, precipitation rate and pH.” *Chemical Geology*, 268(1): 107–115.
- Dreybrodt W.,** *Processes in karst systems*. Springer, 1988.
- Dreybrodt W. (1999).** “Chemical kinetics, speleothem growth and climate.” *Boreas*, 28(3): 347–356.
- Dreybrodt W. (2008).** “Evolution of the isotopic composition of carbon and oxygen in a calcite precipitating H₂O–CO₂–CaCO₃ solution and the related isotopic composition of calcite in stalagmites.” *Geochimica et Cosmochimica Acta*, 72(19): 4712–4724.
- Dreybrodt W. (2012).** “Comment on “Oxygen isotopes in calcite grown under cave-analogue conditions” by C.C. Day and G.M. Henderson.” *Geochimica et Cosmochimica Acta*, 85: 383–387.

- Dreybrodt W. and Deininger M. (accepted manuscript).** “The impact of evaporation to the isotope composition of DIC in calcite precipitating water films in equilibrium and kinetic fractionation models.” *Geochimica et Cosmochimica Acta*.
- Dreybrodt W., Eisenlohr L., Madry B. and Ringer S. (1997).** “Precipitation kinetics of calcite in the system CaCO₃-H₂O-CO₂: The conversion to CO₂ by the slow process H⁺ + HCO₃⁻ → CO₂ + H₂O as a rate limiting step.” *Geochimica et Cosmochimica Acta*, 61(18): 3897–3904.
- Dreybrodt W. and Scholz D. (2011).** “Climatic dependence of stable carbon and oxygen isotope signals recorded in speleothems: From soil water to speleothem calcite.” *Geochimica et Cosmochimica Acta*, 75(3): 734–752.
- Duplessy J.C., Labeyrie J., Lalou C. and Nguyen H. (1970a).** “Continental climatic variations between 130,000 and 90,000 years BP.” *Nature*, 226: 631–633.
- Duplessy J.C., Labeyrie J., Lalou C. and Nguyen H. (1970b).** “Continental climatic variations between 130,000 and 90,000 years BP.” *Nature*, 226: 631–633.
- Edwards R.L., Cheng H., Murrell M. and Goldstein S. (1997).** “Protactinium-231 dating of carbonates by thermal ionization mass spectrometry: Implications for Quaternary climate change.” *Science*, 276(5313): 782–786.
- Fairbanks R.G. (1989).** “A 17, 000-year glacio-eustatic sea level record: influence of glacial melting rates on the Younger Dryas event and deep-ocean circulation.” *Nature*, 342(6250): 637–642.
- Fairchild I., Frisia S., Borsato A. and Tooth A., *Speleothems*. Blackwells, Oxford, 2006a.**
- Fairchild I.J. and Baker A., *Speleothem science: from process to past environments*, vol. 2. Wiley, 2012.**
- Fairchild I.J., Smith C.L., Baker A., Fuller L., Spötl C., Matthey D. and McDermott F. (2006b).** “Modification and preservation of environmental signals in speleothems.” *Earth-Science Reviews*, 75(1): 105–153.
- Fairchild I.J. and Treble P.C. (2009).** “Trace elements in speleothems as recorders of environmental change.” *Quaternary Science Reviews*, 28(5): 449–468.
- Feng W., Banner J.L., Guilfoyle A.L., Musgrove M. and James E.W. (2012).** “Oxygen isotopic fractionation between drip water and speleothem calcite: A 10-year monitoring study, central Texas, USA.” *Chemical Geology*, 304: 53–67.
- Fleitmann D., Burns S.J., Neff U., Mudelsee M., Mangini A. and Matter A. (2004).** “Palaeoclimatic interpretation of high-resolution oxygen isotope profiles derived from annually laminated speleothems from Southern Oman.” *Quaternary Science Reviews*, 23(7): 935–945.

- Fleitmann D., Cheng H., Badertscher S., Edwards R., Mudelsee M., Göktürk O., Fankhauser A., Pickering R., Raible C. and Matter A. (2009). "Timing and climatic impact of Greenland interstadials recorded in stalagmites from northern Turkey." *Geophysical Research Letters*, 36(19).
- Fleitmann D. and Spötl C. (2008). "Editorial: advances in speleothem research." *Pages News*, 16(2).
- Fohlmeister J., Scholz D., Kromer B. and Mangini A. (2011). "Modelling carbon isotopes of carbonates in cave drip water." *Geochimica et Cosmochimica Acta*, 75(18): 5219–5228.
- Ford D. and Williams P. (2007). "Karst hydrology and geomorphology." *John Willey and Sons Ltd.*
- Frank N., Braum M., Hambach U., Mangini A. and Wagner G. (2000). "Warm period growth of travertine during the last interglaciation in southern Germany." *Quaternary Research*, 54(1): 38–48.
- Frisia S., Borsato A., Preto N. and McDermott F. (2003). "Late Holocene annual growth in three Alpine stalagmites records the influence of solar activity and the North Atlantic Oscillation on winter climate." *Earth and Planetary Science Letters*, 216(3): 411–424.
- Gascoyne M., Schwarcz H. and Ford D. (1978). "Uranium series dating and stable isotope studies of speleothems: Part I theory and techniques." *Trans. Brit. Cave Res. Assoc*, 5: 91–112.
- Gat J.R. (1996). "Oxygen and hydrogen isotopes in the hydrologic cycle." *Annual Review of Earth and Planetary Sciences*, 24(1): 225–262.
- GNIP Team I. (2013). "Brochure: Global Network of Isotopes in Precipitation, available on the GNIP website."
- Gorham E. (1955). "On the acidity and salinity of rain." *Geochimica et Cosmochimica Acta*, 7(5): 231–239.
- Griffiths M., Fohlmeister J., Drysdale R., Hua Q., Johnson K., Hellstrom J., Gagan M. and Zhao J.x. (2012). "Hydrological control of the dead carbon fraction in a Holocene tropical speleothem." *Quaternary Geochronology*, 14: 81–93.
- Hansen M., Dreybrodt W. and Scholz D. (2013). "Chemical evolution of dissolved inorganic carbon species flowing in thin water films and its implications for (rapid) degassing of CO₂ during speleothem growth." *Geochimica et Cosmochimica Acta*, 107: 242–251.
- Harmon R.S., Schwarcz H.P. and Ford D.C. (1978). "Late Pleistocene sea level history of Bermuda." *Quaternary Research*, 9(2): 205–218.

- Harmon R.S., Schwarcz H.P. and O'Neil J.R. (1979).** "D/H ratios in speleothem fluid inclusions: A guide to variations in the isotopic composition of meteoric precipitation?" *Earth and Planetary Science Letters*, 42(2): 254–266.
- Haul R. and Stein L. (1955).** "Diffusion in calcite crystals on the basis of isotopic exchange with carbon dioxide." *Transactions of the Faraday Society*, 51: 1280–1290.
- Henderson G.M. (2006).** "Climate. Caving in to new chronologies." *Science*, 313(5787): 620–2. Henderson, Gideon M New York, N.Y. Science. 2006 Aug 4;313(5787):620-2.
- Hendy C. and Wilson A. (1968).** "Palaeoclimatic data from speleothems."
- Hendy C.H. (1971).** "The isotopic geochemistry of speleothems—I. The calculation of the effects of different modes of formation on the isotopic composition of speleothems and their applicability as palaeoclimatic indicators." *Geochimica et Cosmochimica Acta*, 35(8): 801–824.
- Hoefs J.,** *Stable isotope geochemistry.* Springer, 2009.
- Hoffmann D.L., Beck J.W., Richards D.A., Smart P.L., Singarayer J.S., Ketchmark T. and Hawkesworth C.J. (2010).** "Towards radiocarbon calibration beyond 28ka using speleothems from the Bahamas." *Earth and Planetary Science Letters*, 289(1): 1–10.
- Hoffmann D.L., Prytulak J., Richards D.A., Elliott T., Coath C.D., Smart P.L. and Scholz D. (2007).** "Procedures for accurate U and Th isotope measurements by high precision MC-ICPMS." *International Journal of Mass Spectrometry*, 264(2): 97–109.
- Hoffmann G., Werner M. and Heimann M. (1998).** "Water isotope module of the ECHAM atmospheric general circulation model: A study on timescales from days to several years." *Journal of Geophysical Research*, 103(D14): 16871–16,896.
- Jaffey A., Flynn K., Glendenin L., Bentley W.t. and Essling A. (1971).** "Precision Measurement of Half-Lives and Specific Activities of ^{235}U and ^{238}U ." *Physical Review C*, 4(5): 1889.
- Jex C.N., Phipps S., Baker A. and Bradley C. (2013).** "Reducing uncertainty in the climatic interpretations of speleothem $\delta^{18}\text{O}$." *Geophysical Research Letters*.
- Johnston V., Borsato A., Spötl C., Frisia S. and Miorandi R. (2013).** "Stable isotopes in caves over altitudinal gradients: fractionation behaviour and inferences for speleothem sensitivity to climate change." *Climate of the Past*, 9: 99–118.
- Jolliffe I. (2002).** "Principal component analysis. 1986." *Spring-verlag, New York*.
- Jouzel J. and Koster R.D. (1996).** "A reconsideration of the initial conditions used for stable water isotope models." *Journal of Geophysical Research*, 101(D17): 22933–22,938.

- Jouzel J. and Merlivat L. (1984).** “Deuterium and oxygen 18 in precipitation: Modeling of the isotopic effects during snow formation.” *Journal of Geophysical Research: Atmospheres (1984–2012)*, 89(D7): 11749–11757.
- Jouzel J., Russell G., Suozzo R., Koster R., White J. and Broecker W. (1987).** “Simulations of the HDO and H₂ 18O atmospheric cycles using the NASA GISS general circulation model: The seasonal cycle for present-day conditions.” *Journal of Geophysical Research: Atmospheres (1984-2012)*, 92(D12): 14739–14760.
- Kaufman A. (1993).** “An evaluation of several methods for determining ²³⁰ThU ages in impure carbonates.” *Geochimica et Cosmochimica Acta*, 57(10): 2303–2317.
- Kaufman A. and Broecker W. (1965).** “Comparison of Th²³⁰ and C¹⁴ ages for carbonate materials from lakes Lahontan and Bonneville.” *Journal of Geophysical Research*, 70(16): 4039–4054.
- Kaufmann G. (2003).** “Stalagmite growth and palaeo-climate: the numerical perspective.” *Earth and Planetary Science Letters*, 214(1): 251–266.
- Kaufmann G. and Dreybrodt W. (2004).** “Stalagmite growth and palaeo-climate: an inverse approach.” *Earth and Planetary Science Letters*, 224(3): 529–545.
- Keeling C.D. (1958).** “The concentration and isotopic abundances of atmospheric carbon dioxide in rural areas.” *Geochimica et Cosmochimica Acta*, 13(4): 322–334.
- Keeling C.D. (1979).** “The Suess effect:¹³Carbon-¹⁴Carbon interrelations.” *Environment International*, 2(4): 229–300.
- Kim S.T. and O’Neil J.R. (1997).** “Equilibrium and nonequilibrium oxygen isotope effects in synthetic carbonates.” *Geochimica et Cosmochimica Acta*, 61(16): 3461–3475.
- Lachniet M.S. (2009).** “Climatic and environmental controls on speleothem oxygen-isotope values.” *Quaternary Science Reviews*, 28(5): 412–432.
- Langebroek P., Werner M. and Lohmann G. (2011).** “Climate information imprinted in oxygen-isotopic composition of precipitation in Europe.” *Earth and Planetary Science Letters*.
- LeGrande A. and Schmidt G. (2009).** “Sources of Holocene variability of oxygen isotopes in paleoclimate archives.” *Climate of the Past Discussions*, 5: 1133–1162.
- Linge H., Lauritzen S.E., Andersson C., Hansen J., Skoglund R.O. and Sundqvist H. (2009).** “Stable isotope records for the last 10 000 years from Okshola cave (Fauske, northern Norway) and regional comparisons.” *Climate of the Past*, 5: 667–682.
- Majoube M. (1971a).** “Fractionnement en oxygene 18 entre la glace et la vapeur d’eau.” *J. Chem. Phys*, 68: 625–636.

- Majoube M. (1971b).** “Fractionnement en oxygene-18 et en deuterium entre l’eau et sa vapeur.” *J. Chim. phys*, 68(10): 1423–1436.
- Mangini A., Spötl C. and Verdes P. (2005).** “Reconstruction of temperature in the Central Alps during the past 2000 yr from a $\delta^{18}\text{O}$ stalagmite record.” *Earth and Planetary Science Letters*, 235(3): 741–751.
- Mann M.E., Zhang Z., Hughes M.K., Bradley R.S., Miller S.K., Rutherford S. and Ni F. (2008).** “Proxy-based reconstructions of hemispheric and global surface temperature variations over the past two millennia.” *Proceedings of the National Academy of Sciences*, 105(36): 13252–13257.
- Marcott S.A., Shakun J.D., Clark P.U. and Mix A.C. (2013).** “A reconstruction of regional and global temperature for the past 11,300 years.” *Science*, 339(6124): 1198–1201.
- McDermott F. (2004).** “Palaeo-climate reconstruction from stable isotope variations in speleothems: a review.” *Quaternary Science Reviews*, 23(7): 901–918.
- McDermott F., Atkinson T., Fairchild I.J., Baldini L.M. and Matthey D.P. (2011).** “A first evaluation of the spatial gradients in $\delta^{18}\text{O}$ recorded by European Holocene speleothems.” *Global and Planetary Change*, 79(3): 275–287.
- Merlivat L. (1978a).** “The dependence of bulk evaporation coefficients on air-water interfacial conditions as determined by the isotopic method.” *Journal of Geophysical Research: Oceans (1978-2012)*, 83(C6): 2977–2980.
- Merlivat L. (1978b).** “Molecular diffusivities of H_2^{16}O , HD^{16}O , and H_2^{18}O in gases.” *The Journal of Chemical Physics*, 69: 2864.
- Merlivat L. and Coantic M. (1975).** “Study of mass transfer at the air-water interface by an isotopic method.” *Journal of Geophysical Research*, 80(24): 3455–3464.
- Merlivat L. and Jouzel J. (1979).** “Global climatic interpretation of the deuterium-oxygen 18 relationship for precipitation.” *Journal of Geophysical Research: Oceans (1978-2012)*, 84(C8): 5029–5033.
- Mickler P.J., Stern L.A. and Banner J.L. (2006).** “Large kinetic isotope effects in modern speleothems.” *Geological Society of America Bulletin*, 118(1-2): 65–81.
- Mills G.A. and Urey H.C. (1940).** “The Kinetics of Isotopic Exchange between Carbon Dioxide, Bicarbonate Ion, Carbonate Ion and Water1.” *Journal of the American Chemical Society*, 62(5): 1019–1026.
- Mitchell T.D. and Jones P.D. (2005).** “An improved method of constructing a database of monthly climate observations and associated high-resolution grids.” *International Journal of Climatology*, 25(6): 693–712.
- Mook W. and de Vries J. (2000).** “Environmental Isotopes in the Hydrological Cycle

- Principles and Applications-Volume I: Introduction-Theory.” *Methods, Review, IAEA, Vienna*.
- Mook W.G. (2006).** “Introduction to isotope hydrology.” *Taylor and Francio*, 8.
- Mudelsee M.,** *Climate time series analysis: classical statistical and bootstrap methods*, vol. 42. Springer, **2010**.
- Mühlinghaus C., Scholz D. and Mangini A. (2007).** “Modelling stalagmite growth and $\delta^{13}\text{C}$ as a function of drip interval and temperature.” *Geochimica et Cosmochimica Acta*, 71(11): 2780–2790.
- Mühlinghaus C., Scholz D. and Mangini A. (2009).** “Modelling fractionation of stable isotopes in stalagmites.” *Geochimica et Cosmochimica Acta*, 73(24): 7275–7289.
- Münnich K. (1978).** “Soil-water-plant relationships.”
- Neff U., Burns S., Mangini A., Mudelsee M., Fleitmann D. and Matter A. (2001).** “Strong coherence between solar variability and the monsoon in Oman between 9 and 6 kyr ago.” *Nature*, 411(6835): 290–293.
- Niggemann S., Mangini A., Richter D.K. and Wurth G. (2003).** “A paleoclimate record of the last 17,600 years in stalagmites from the B7 cave, Sauerland, Germany.” *Quaternary Science Reviews*, 22(5): 555–567.
- O’Neil J.R., Clayton R.N. and Mayeda T.K. (1969).** “Oxygen isotope fractionation in divalent metal carbonates.” *The Journal of Chemical Physics*, 51: 5547.
- Osmond J., Cowart J. and Ivanovich M. (1983).** “Uranium isotopic disequilibrium in ground water as an indicator of anomalies.” *The International Journal of Applied Radiation and Isotopes*, 34(1): 283–308.
- Plummer L., Wigley T. and Parkhurst D. (1978).** “The kinetics of calcite dissolution in CO₂-water systems at 5° to 60°C and 0.0 to 1.0 atm CO₂.” *American Journal of Science*, 278(2): 179–216.
- Polag D., Scholz D., Mühlinghaus C., Spötl C., Schröder-Ritzrau A., Segl M. and Mangini A. (2010).** “Stable isotope fractionation in speleothems: Laboratory experiments.” *Chemical Geology*, 279(1): 31–39.
- Preisendorfer R.W. and Mobley C.D.,** *Principal component analysis in meteorology and oceanography*, vol. 17. Elsevier Amsterdam, **1988**.
- Rayleigh L. (1902).** “LIX. On the distillation of binary mixtures.” *The London, Edinburgh, and Dublin Philosophical Magazine and Journal of Science*, 4(23): 521–537.
- Reardon E. and Fritz P. (1978).** “Computer modelling of groundwater ^{13}C and ^{14}C isotope compositions.” *Journal of Hydrology*, 36(3): 201–224.

- Richards D.A. and Dorale J.A. (2003).** “Uranium-series chronology and environmental applications of speleothems.” *Reviews in Mineralogy and Geochemistry*, 52(1): 407–460.
- Riechelmann D.F., Deininger M., Scholz D., Riechelmann S., Schröder-Ritzrau A., Spötl C., Richter D.K., Mangini A. and Immenhauser A. (2012).** “Disequilibrium carbon and oxygen isotope fractionation in recent cave calcite: Comparison of cave precipitates and model data.” *Geochimica et Cosmochimica Acta*.
- Rogers J. and Adams J. (1969).** “Uranium (92) In Handbook of Geochemistry Wedepohl, KH,(Ed.): II-4.”
- Romanek C.S., Grossman E.L. and Morse J.W. (1992).** “Carbon isotopic fractionation in synthetic aragonite and calcite: Effects of temperature and precipitation rate.” *Geochimica et Cosmochimica Acta*, 56(1): 419–430. Hb840 Times Cited:447 Cited References Count:39.
- Rosholt J. and Antal P. (1962).** “Evaluation of the $^{231}\text{Pa}/\text{U}$ - $^{230}\text{Th}/\text{U}$ method for dating Pleistocene carbonate rocks.” *US Geological Survey Professional Paper*, 450: E108–E111.
- Rozanski K. (1985).** “Deuterium and oxygen-18 in European groundwaters—Links to atmospheric circulation in the past.” *Chemical Geology: Isotope Geoscience section*, 52(3): 349–363.
- Rozanski K., Sonntag C. and Münnich K. (1982).** “Factors controlling stable isotope composition of European precipitation.” *Tellus*, 34(2): 142–150.
- Rubinson M. and Clayton R.N. (1969).** “Carbon-13 fractionation between aragonite and calcite.” *Geochimica et Cosmochimica Acta*, 33(8): 997–1002.
- Rudzka D., McDermott F., Baldini L.M., Fleitmann D., Moreno A. and Stoll H. (2011).** “The coupled $\delta^{13}\text{C}$ -radiocarbon systematics of three Late Glacial/early Holocene speleothems; insights into soil and cave processes at climatic transitions.” *Geochimica et Cosmochimica Acta*, 75(15): 4321–4339.
- Salomons W. and Mook W. (1986).** “Isotope geochemistry of carbonates in the weathering zone.” *Handbook of environmental isotope geochemistry*, (2): 239–269.
- Scholz D., Frisia S., Borsato A., Spötl C., Fohlmeister J., Mudelsee M., Miorandi R. and Mangini A. (2012a).** “Holocene climate variability in north-eastern Italy: potential influence of the NAO and solar activity recorded by speleothem data.” *Climate of the Past Discussions*, 8(2): 909–952.
- Scholz D. and Hoffmann D.L. (2011).** “StalAge—an algorithm designed for construction of speleothem age models.” *Quaternary Geochronology*, 6(3): 369–382.
- Scholz D., Hoffmann D.L., Hellstrom J. and Bronk Ramsey C. (2012b).** “A comparison of different methods for speleothem age modelling.” *Quaternary Geochronology*, 14: 94–104.

- Scholz D., Mühlinghaus C. and Mangini A. (2009). “Modelling $\delta^{13}\text{C}$ and $\delta^{18}\text{O}$ in the solution layer on stalagmite surfaces.” *Geochimica et Cosmochimica Acta*, 73(9): 2592–2602.
- Schwarcz H.P., Harmon R.S., Thompson P. and Ford D.C. (1976). “Stable isotope studies of fluid inclusions in speleothems and their paleoclimatic significance.” *Geochimica et Cosmochimica Acta*, 40(6): 657–665.
- Sharp Z., *Principles of stable isotope geochemistry*. Pearson Education Upper Saddle River, NJ, USA, 2007.
- Sonntag C., Klitzsch E., Löhnert E., El-Shazly E., Münnich K., Junghans C., Thorweihe U., Weistroffer K. and Swailem F. (1979). “Palaeoclimatic information from deuterium and oxygen-18 in carbon-14 dated north Saharian groundwaters; groundwater formation in the past.” *Proceedings Series-International Atomic Energy Agency*.
- Sonntag D. (1990). “Important new values of the physical constants of 1986, vapour pressure formulations based on the ITS-90, and psychrometer formulae.” *Z. Meteorol.*, 70(5): 340–344.
- Spötl C., Mangini A. and Richards D.A. (2006). “Chronology and paleoenvironment of Marine Isotope Stage 3 from two high-elevation speleothems, Austrian Alps.” *Quaternary Science Reviews*, 25(9): 1127–1136.
- Spötl C. and Matthey D. (2006). “Stable isotope microsampling of speleothems for palaeoenvironmental studies: a comparison of microdrill, micromill and laser ablation techniques.” *Chemical Geology*, 235(1): 48–58.
- Suess H.E. (1955). “Radiocarbon concentration in modern wood.” *Science*, 122(3166): 415–417.
- Taylor S.R. and McLennan S.M. (1995). “The geochemical evolution of the continental crust.” *Reviews of Geophysics*, 33(2): 241–265.
- Thorstenson D.C. and Parkhurst D.L. (2004). “Calculation of individual isotope equilibrium constants for geochemical reactions.” *Geochimica et Cosmochimica Acta*, 68(11): 2449–2465.
- Tremaine D.M., Froelich P.N. and Wang Y. (2011). “Speleothem calcite farmed in situ: Modern calibration of $\delta^{18}\text{O}$ and $\delta^{13}\text{C}$ paleoclimate proxies in a continuously-monitored natural cave system.” *Geochimica et Cosmochimica Acta*, 75(17): 4929–4950.
- Uzdowski E., Hoefs J. and Menschel G. (1979). “Relationship between ^{13}C and ^{18}O fractionation and changes in major element composition in a recent calcite-depositing spring - A model of chemical variations with inorganic CaCO_3 precipitation.” *Earth and Planetary Science Letters*, 42(2): 267–276.

- Von Storch H. and Zwiers F.W.**, *Statistical analysis in climate research*. Cambridge University Press, 2001.
- Wackerbarth A., Langebroek P., Werner M., Lohmann G., Riechelmann S., Borsato A. and Mangini A. (2012)**. “Simulated oxygen isotopes in cave drip water and speleothem calcite in European caves.” *Climate of the Past*, 8(6): 1781–1799.
- Wackerbarth A., Scholz D., Fohlmeister J. and Mangini A. (2010)**. “Modelling the $\delta^{18}\text{O}$ value of cave drip water and speleothem calcite.” *Earth and Planetary Science Letters*, 299(3): 387–397.
- Wallace J.M. and Gutzler D.S. (1981)**. “Teleconnections in the Geopotential Height Field during the Northern Hemisphere Winter.” *Monthly Weather Review*, 109: 784.
- Wang Y.J., Cheng H., Edwards R.L., An Z., Wu J., Shen C.C. and Dorale J.A. (2001)**. “A high-resolution absolute-dated late Pleistocene monsoon record from Hulu Cave, China.” *Science*, 294(5550): 2345–2348.
- Wanner H., Beer J., Butikofer J., Crowley T.J., Cubasch U., Fluckiger J., Goosse H., Grosjean M., Joos F., Kaplan J.O., Kuttel M., Muller S.A., Prentice I.C., Solomina O., Stocker T.F., Tarasov P., Wagner M. and Widmann M. (2008)**. “Mid- to Late Holocene climate change: an overview.” *Quaternary Science Reviews*, 27(19–20): 1791–1828. 373YD Times Cited:229 Cited References Count:455.
- Wassenburg J., Dietrich S., Fietzke J., Fohlmeister J., Wei W. and Peter K.**, “The variability of the North Atlantic Oscillation throughout the Holocene.” In “EGU General Assembly Conference Abstracts,” vol. 15. 2013, 846.
- Watson E.B. (2004)**. “A conceptual model for near-surface kinetic controls on the trace-element and stable isotope composition of abiogenic calcite crystals.” *Geochimica et Cosmochimica Acta*, 68(7): 1473–1488.
- Wedepohl H.K. (1995)**. “The composition of the continental crust.” *Geochimica et Cosmochimica Acta*, 59(7): 1217–1232.
- Werner M., Langebroek P.M., Carlsen T., Herold M. and Lohmann G. (2011)**. “Stable water isotopes in the ECHAM5 general circulation model: Toward high-resolution isotope modeling on a global scale.” *Journal of Geophysical Research: Atmospheres (1984–2012)*, 116(D15).
- Wiedner E., Scholz D., Mangini A., Polag D., Mühlinghaus C. and Segl M. (2008)**. “Investigation of the stable isotope fractionation in speleothems with laboratory experiments.” *Quaternary International*, 187(1): 15–24.
- Wigley T., Plummer L. and Pearson Jr F. (1978)**. “Mass transfer and carbon isotope evolution in natural water systems.” *Geochimica et Cosmochimica Acta*, 42(8): 1117–1139.
- Winograd I.J., Landwehr J.M., Coplen T.B., Sharp W.D., Riggs A.C., Ludwig**

-
- K.R. and Kolesar P.T. (2006).** “Devils Hole, Nevada, $\delta^{18}\text{O}$ record extended to the mid-Holocene.” *Quaternary Research*, 66(2): 202–212.
- Zeebe R. (2007).** “An expression for the overall oxygen isotope fractionation between the sum of dissolved inorganic carbon and water.” *Geochemistry Geophysics Geosystems*, 8(9): Q09002.
- Zeebe R.E. (1999).** “An explanation of the effect of seawater carbonate concentration on foraminiferal oxygen isotopes.” *Geochimica et Cosmochimica Acta*, 63(13): 2001–2007.
- Zeebe R.E. (2011).** “On the molecular diffusion coefficients of dissolved, and their dependence on isotopic mass.” *Geochimica et Cosmochimica Acta*, 75(9): 2483–2498.
- Zimmermann U., Ehhalt D. and Münnich K. (1967).** “Soil-Water Movement and Evapotranspiration: Changes in the Isotopic Composition of the Water.”

